Polymeric arsenicals as a platform for functional biomaterials

Joji Tanaka

A thesis submitted in partial fulfilment of the requirements for the degree of

Doctor of Philosophy in Mathematical Biology and Biophysical Chemistry

Molecular Organisation and Assembly in Cells Doctoral Training Centre

University of Warwick

September 2018

Table of contents

List of Figures

List of Tables

List of Schemes

Abbreviations

143B	Human osteosarcoma cells
AAS	Atomic absorption spectroscopy
AIBN	2,2'-Azobisisobutyronitrile
AFM	Atomic Force Microscopy
AgNPs	Silver nanoparticles
ANOVA	Analysis of variance
ANT	Adenine nucleotide translocase
APL	Promyelocytic leukaemia
As	Arsenic
AsAm	Arsenical acrylamide
$AsAm(pin)_2$	Pinacol protected Arsenical Acrylamide
AsBr	As(V)-functional α-haloamide initiator
AsCy3	Cyanine-based bisarsenical
AsPC-1	Adenocarcinoma pancreatic cell lines
ATO	Arsenic trioxide
ATRP	Atom Transfer Radical Polymerisation
b	*block*
BArNile	Biarsenical Nile red
$CDCl_3$	Deuterated Chloroform
CI_{50}	Chemotherapeutic index
$CHCl_3$	Chloroform
Cmc	Critical micelle concentration
co	copolymer
CrAsH	Carboxy-FlAsH
CTA	Chain Transfer Agent
CuBr	Copper (I) Bromide
Cys	Cysteine
$\boldsymbol{Đ}$	Dispersity
D_2O	Deuterium oxide
DBM	Dibromomaleimide

DEB	*p/m*-diethynylbenzene
D_h	Hydrodynamic Diameter
DP	Degree of Polymerisation
DLS	Dynamic Light Scattering
DMA	Dynamic Mechanical Analysis
DMAD	Dimethyl acetylenedicarboxylate
DMAm	Dimethyl acrylamide
DMAP	4-Dimethylaminopyridine
DMF	Dimethylformamide
DMEM	Dulbecco's Modified Eagle Medium
DMSO	Dimethyl sulfoxide
dn/dc	Refractive index increment
DRI	Differential refractive index
DSPC	1,2-Distearoyl-*sn*-glycero-3-phosphocholine
DTPA	Diethylenetriaminepentaacetic acid
DTT	Dithiothreitol
EC_{50}	Half maximum effective concentration
EDT	Ethane dithiol
EDX	Energy-Dispersive X-ray
Eq	Equivalence
F2FlAsH	Difluro-FlAsH
F4FlAsH	Tetrafluro-FlAsH
FA-HSA	Folate-labelled Human-Serum-Albumin
FBS	Fetal bovine serum
FDA	Food and drug administration
FlAsH	Fluorescein arsenical hairpin binder
FRβ	Folate receptor-β
FRET	Forster resonance energy transfer
FRP	Free radical polymerisation
FT	Fourier transform
G'	Storage modulus
G''	Loss modulus

GC	Gas chromatography
GFP	Green fluorescent protein
GPC	Gel Permeation Chromatography
GSAO	4-(*N*-(*S*-Glutathionylacetyl)amino) phenylarsonous acid
GSH	Glutathione
HDT	Hexa(ethylene glycol) dithiol
HEAm	2-Hydroxyethyl acrylamide
HeLaS3	Human cervix carcinoma
HepG2	Human liver cancer cell line
HMPA	*N*-(2-Hydroxypropyl)methacrylamide
HL60	Human leukemia cell line
HPLC	High Performance Liquid Chromatography
HSA	Human-Serum-Albumin
Hsp90	90 kDa Heat shock protein
HUVEC	Human umbilical vein endothelial cells
IC_{50}	Half maximum inhibitory concentration
ICP-OES	Inductively coupled plasma optical emission spectroscopy
K562	Myelogenous leukemia cell line
K_d	Dissociation constant
KI	Potassium iodide
MALS	Multi-angle light scattering
MDA-231	Human breast adenocarcinoma cell line
MDA-MB-435	Human melanoma cell line
Me	Methyl
MMA	Methyl methacrylate
$M_{n,Theory}$	Theoretical Number average molar mass
$M_{n,SEC}$	Experimental Number average molar mass
MPTP	Mitochondrial permeability transition pore
MRI	Magnetic resonance Imaging
M_w	Weight Average molecular weight.
m/z	Mass/charge ratio
N_{agg}	Number of aggregation

NAM	4-Acryloylmorpholine
Nd-YAG	Neodymium doped yttrium aluminum garnet
NEM	*N*-ethyl maleimide
NIH/3T3	Mouse embryo fibroblasts
NIPAm	N-isopropylacrylamide
NLO	Non-linear optical
NMP	Nitroxide-mediated polymerization
NMR	Nuclear Magnetic Resonance
NP	Nanoparticle
nMWCO	Nominal molecular weight cutoff
o	*ortho*
p	*para*
PABTC	2-(((Butylthio)-carbonothioyl)thio)propanoic acid
PANC-1	Epithelioid carcinoma pancreatic cell lines
PAO	Phenylarsine oxide
PAzPAO	*p*-Azidophenyl arsenoxide
PBS	Phosphate buffer solution
PC	Phosphatidylcholine
PC3	Human Prostate adenocarcinoma
PCCL	Poly(α-carboxylate-ε-caprolactone)
PCCLSH	Mercaptohexylamine functionalised PCCL
PDi	Polydispersity index
PDI	Protein disulfide isomerase
PEG	Poly(ethylene glycol)
PEGA	Poly(ethylene glycol) methyl ether acrylate (average M_n = 480 $gmol^{-1}$)
PENAO	4-(*N*-(*S*-Penicillaminylacetyl)amino) phenylarsonous acid
PENAOMAm	4-*N*-(*S*-Penicillaminylacetyl)amino phenylarsonous acid Methacrylamide
PET	Positron emission tomography
PeT	Photoinduced electron transfer
Ph	Phenyl

pin	Pinacol
PMMA	Poly(methyl methacrylate)
ppm	Parts per million
PTM	Pentaerythritol tetrakis(3-mercaptopropionate)
RAFT	Reversible addition Fragmentation Chain Transfer
RAME	Rat adrenal medullary endothelial cells
rBSA	Reduced Bovine serum albumin
RCRAC	Ring Collapse Radical Alternating copolymerization
RDRP	Reversible Deactivation Radical Polymerisation
ReAsH	Resorufin arsenical hairpin binder
R_h	Hydrodynamic Radius
ROP	Ring Opening Polymerisation
RPMI-1640	Roswell Park Memorial Institute 1640 cell Medium
RpoA	RNA polymerase
SAMs	Self-assembled monolayers
sCT	Salmon calcitonin
SEC	Size Exclusion Chromatography
SET-LRP	Single Electron Transfer Living Radical Polymerisation
SD	Standard deviation
SH	Thiol
SLS	Static Light scattering
SPECT/CT	Single-Photon Emission Computed Tomography / Computed Tomography
SPR	Surface Plasmon resonance
STORM	Stochastic Optical Reconstruction Microscopy
Sty	Styrene
TC	Tetracysteine
TEM	Transmission Electron Microscopy
T_g	Glass transition temperature
THF	Tetrahydrofuran
TFE	2,2,2-Trifluoroethanol
TTM	Trimethylolpropane tris(3-mercaptopropionate)

UV	Ultraviolet
VA-044	2,2'-Azobis[2-(2-imidazolin-2-yl)propane]dihydrochloride
V601	Dimethyl 2,2’-azobis(2-methylpropionate)
WI-38	Embryonic human lung fibroblasts
w.r.t	With respect to
XTT	Triphenyl tetrazolium chloride
ZIO-101	*S*-Dimethylarsino-glutathione

Acknowledgements

I would like to take this opportunity to thank all the people who has provided help during my PhD and has helped to develop to be a better person.

First and foremost, I thank Paul Wilson for being the best mentor and PhD supervisor I could ever have. I would've never got this far without him. I really appreciated every help I got from him even when I lacked focus due to life crisis. I hope that in the future I will be able to give back to him all the time he gave to me.

I thank Seb for letting me join his group. It would've not been possible to obtain the same level of knowledge and experience had I have been in other group. I greatly appreciate his advice and scientific wisdom. The regular biweekly team meetings was paramount importance for learning during my PhD.

I thank Dave for funding me for 6 months during my PhD and letting me involved in his group too. I really appreciated his wise advice across the years, all the way back from 2012.

I thank Guilleaume Moriceau who has been emotional support and best friend during my PhD. Living together was definitely one of the best decision made during my time. I thank George, Dan L, Sam Lawton and Marie who added more colours in my life outside work. I thank, Rachel Hodgson, for helping me when I was in desperate need and providing me stability during most part of my PhD.

I thank original members of the Seb's group at warwick: Ming, Johannes, Gody, Tammie, Sophie, Junliang and Liam. I thank Liam and Junliang, both who helped me transcended me from copper mediated polymerisation to RAFT polymerisation!! I especially thank Junliang who worked together on many of my crazy ideas and being a mentor in life and in science.

I thank the people in the bionano team, Alex and Pratik who I both respect for their science. We shared many great ideas and discussions, which contributed to much of the work carried out during my PhD. I also thank the people who joined our team in the expansion pack: Mathias, Agnes, Fannie, Tom, Andy K., Andy L., Carlos, Ed and all the summer students and Master students for contributing towards scientific discussions in the meeting.

I thank all the other members of Perrier group: Ximo, Jie, Qiao, Robert, Sean, Julia, Majda, Raoul, Caroline and Sylvain. I especially thank Satu, who I worked closely with towards the end of my PhD, and for helping me move to USA post PhD.

I thank all the members of Haddleton group too: Atty, George, Evelina, Athina, Vasiliki, Alex Simula, Rachel Hand, Sam Lowe, Qiang, Jenny and Patrick. I especially thank Glen and Richard who both helped me with copper mediated polymerisations.

Abstract

Arsenic exhibits diverse chemical reactivity depending upon its oxidation state. This distinctive reactivity has been largely overlooked in the field of polymer and biomaterials science, owing to concerns about the toxicity of arsenic. However, a recent clinical renaissance in the use of arsenicals suggests the possibility of broader acceptance and application. The aim of this work is to stimulate interest in and highlight the potential of polymeric arsenicals as a novel platform for functional and responsive biomaterials (Literature review discussed in Chapter 1).

Cross-linking of polymers through pendent organic arsenic functional groups is demonstrated using three different chemistries: 1) reductive coupling forming arsine oligomers, $As(I)_n$ (Chapter 2) 2) forming arsenic-thiolate bonds with poly-thiol cross-linkers (Chapter 3) 3) polymerizing As(I) via the addition of acetylenes to form vinylene-acetylene bonds (Chapter 4). All three methods of cross-linking were able to cross-link thermally self-assembled NIPAm-PEG diblock copolymers with an arsenical acrylamide (AsAm) monomer incorporated in the NIPAm core. The first two were found to be responsive towards GSH and H_2O_2 under model physiological conditions. The stability of the particles can be finely tuned through varying the amounts of arsenic or varying the nature of the thiol-functional external cross-linker. The last form of cross-linking was found to be non-responsive towards the given stimuli however it enabled incorporation of further functionality to the nanoparticle, such as Rhodamine B, which helped determine the co-localization of the nanoparticle. Notably, in all three chemistries, the nanoparticles produced were not found to be toxic at 2 mg/ml by cell viability assays.

Finally using the $As(I)_n$ cross-linking strategy, the formation of hydrogels (with DMA-AsAm copolymers made by FRP), was demonstrated which were responsive towards oxidation with H_2O_2. Synthesised hydrogels were responsive towards oxidation. 3D cell culturing of these gels were carried out by rehydration of dialyzed/lyophilized gels with trypsinized solution of cells. (Chapter 5).

In addition to the investigation of polymeric arsenicals, synthesis of microscale

multiblock copolymers are described (Appendix A). This enabled generation and characterisation of polymers at 2 μL scale, and procedure to synthesise Multi-block copolymers at 10 μL scale (DP_n = 25, 5 blocks, 2 μL per block).

Chapter 1 : Organic arsenicals as functional motifs in polymer and biomaterials science

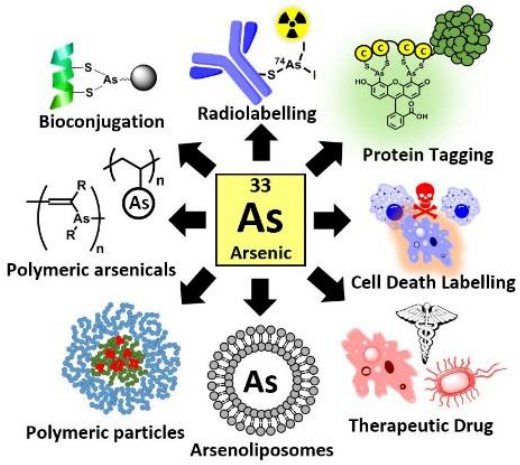

The materials presented in this chapter is directly reproduced with permission from the publishers, a review (with the exceptions of pages 11-12) where I was the first Author: *Macromol. Rapid Commun.* **2018**, 1800205. This was published together with Thomas P. Davis and Paul Wilson (supervisor) who are both corresponding authors and principle investigators.

Abstract

Arsenic (As) exhibits diverse (bio)chemical reactivity and biological activity depending upon its oxidation state. However, this distinctive reactivity has been largely overlooked across many fields owing to concerns regarding the toxicity of arsenic. Recently, a clinical renaissance in the use of arsenicals, including organic arsenicals that are known to be less toxic than inorganic arsenicals, alludes to the possibility of broader acceptance and application in the field of polymer and biomaterials science. Here the present examples of polymeric/macromolecular arsenicals are reported to stimulate interest and highlight their potential as a novel platform for functional, responsive and bioactive materials.

1.1 Introduction

Arsenic exists as a dichotomous enigma between toxicity and therapy in (bio)chemistry and medicine. It is ubiquitously distributed in the Earth's crust and despite being a well-known contaminant of base water supplies, it is an essential dietary element and has historically been employed to treat malignancies, most notably in the form of Arsphenamine/Salvarsan, Paul Ehrlich's first 'magic bullet' chemotherapeutic.[1] More recently, following a demise in use due to concerns over formulation and toxicity, arsenic trioxide (Trisenox, As_2O_3) has revitalised the therapeutic potential of (in)organic arsenicals in the treatment of blood born malignancies such as acute promyelocytic leukaemia (APL).[2] This has stimulated the development of a number of new (in)organic arsenicals which have been shown to exhibit improved efficacy and reduced toxicity compared to As_2O_3 in pre-clinical and early-stage clinical trials against both haematological and solid malignancies, highlighting their potential as future chemotherapies.[3, 4]

Arsenic can adopt two biologically relevant oxidation states, trivalent arsonous acid (As(III)) and pentavalent arsonic acid (As(V)) which are chemically distinct. An example of the interesting reactivity of arsenicals is the synthesis of Salvarsan which was prepared by reductive coupling of 3-amino-4-hydroxyphenylarsenic(V) to form a mixture of homocyclic 3-amino-4-hydroxyphenylarsenic(I) species.[5] The ensuing core of cyclic As-As single bonds can act as a reservoir for biologically relevant As(III). Inorganic arsonic acid, or arsenate (As(V)), exhibits chemical similarities to phosphate (P(V)).[6] Biochemically, arsenate is purported to enter the cell through phosphate transporters where it is either metabolised, via reduction and methylation processes, or can interfere with phosphate dependent biosynthetic pathways.[7] Chemically, phenylarsonic acids (As(V)) can undergo condensation with chelating 1,2- and 1,3-diols to form *spiro*-arsoranes in both organic and aqueous media. The *spiro*-arsoranes derived from vicinal 1,2-diols are favoured and hydrolytically stable at neutral and acidic pH.[8] Analogous *spiro*-arsoranes can be formed via condensation of 1,2-amino alcohols[9] but there is little propensity for covalent bond formation between As(V) and thiols, which prefer to undergo single electron transfer redox reactions, which occurs naturally via thiol-disulfide rich reductase enzymes.[10]

Reduction of arsenate (As(V)), furnishes trivalent arsenicals (As(III)), which dominate the therapeutic and toxic potential of arsenic due to their high affinity for thiols. For example, the activity of As_2O_3 is believed to be underpinned by the affinity of arsonous acid (As(III)), formed in aqueous solutions of As_2O_3, for thiol groups, readily forming up to three As-S covalent bonds.[11] In the intra- and extracellular milieu thiols are present as free thiols or intra-/intermolecular disulfides and it has been postulated that the affinity of As(III) for thiols is enhanced for chelating vicinal or neighbours-through-space (proximal) dithiols, such as those presented by naturally occurring disulfide bonds.[12]

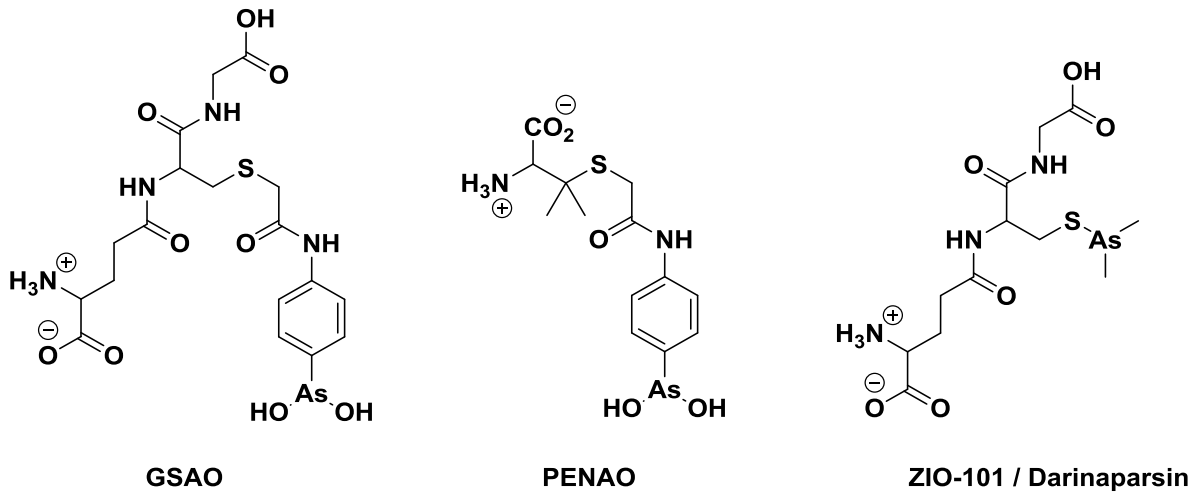

Figure 1.1: Structure of clinically relevant organic arsenical chemotherapeutics.

The activity of clinically relevant organic arsenicals 4-(*N*-(*S*-glutathionylacetyl)amino) phenylarsonous acid (GSAO),[13] 4-(*N*-(*S*-penicillaminylacetyl)amino) phenylarsonous acid (PENAO)[14] and *S*-dimethylarsino-glutathione (ZIO-101; Darinasparin)[15] is associated with disruption of mitochondrial functional (Figure 1.1). In the case of GSAO and PENAO, Cys^{57} and Cys^{257} of mitochondrial adenine nucleotide translocase (ANT) are cross-linked, leading to opening of the mitochondrial permeability transition pore (MPTP) and loss of mitochondrial membrane potential.[16] The specificity of GSAO and PENAO for the ANT dithiols exemplifies the thermodynamically driven sequence specificity of As(III)-arsenicals for Cys-Xxx-Xxx-Cys and proximal dithiols. The specificity can be enhanced further by protein engineering and/or molecule design

strategies. Tetra-cysteine sequences Cys-Cys-Xxx-Xxx-Cys-Cys engineered into native protein sequences bind organic bis-arsenicals with much greater affinity than mono- and native dithiol equivalents and has been utilized to develop highly specific fluorescent labels (*vide infra*).[17-19] More notably, controlling the spacing between the arsenical functional groups in bis- and tris-arsenicals elicits stronger binding (K_d ~ 50 nM)[20] to native proteins that contain redox-active thiol and disulfide rich domains,[21, 22] such as those associated with protein folding (*e.g.* protein disulfide isomerase, PDI) and redox homeostasis (*e.g.* thioredoxin), than mono-arsenical analogues (K_d ~ 1 μM).[23]

Notwithstanding the clinical renaissance in the use of the arsenicals in chemotherapy, or their discrete and distinctive (bio)chemical reactivity, particularly the high affinity and tunable specificity for (di)thiols, the application of organic arsenicals in polymer and biomaterials science has been limited. Here we aim to compile the present literature pertaining to polymeric arsenicals and organic arsenicals employed in biomaterials science, particularly focusing on bio-imaging and self-assembled (polymeric and liposomal) nanoparticles. We hope to stimulate interest in an area where we see great potential and synergy between the chemical and biological activity of arsenic, which, if harnessed appropriately could lead to the development of potent, highly specific macromolecular arsenicals for therapeutic and/or diagnostic nanomedicine.

1.2 Polymeric arsenicals; synthesis and applications

Metal-based polymers and organometallic polymers can be synthesized in a number of ways resulting in polymers with metals distributed either through the main polymer chain or pendent side chain groups. Chain-growth polymerization is possible via anionic or radical mechanisms while step-growth polycondensation, of organopolysiloxanes for example, is an academically and industrially significant process generating materials rich in functionality and application. Appending appropriate ligands through polymer chains also makes the formation of coordination polymers possible. Here we will focus on the methods employed to date to prepare organoarsenic polymers and discuss the potential applications of these materials.

1.2.1 Backbone functional polymeric arsenicals

1.2.1.1 Polycondensation

Interfacial polycondensation emerged as an efficient technique for the synthesis of organometallic polymers in the 1960's and 1970's,[24] gaining popularity as the method of choice for the synthesis of Group 14/15 metal-containing polymers.[25] The process exploits the low-energy barriers of Lewis acid – Lewis base reactions interacting at the interface of an immiscible aqueous/organic solvent mixture generated under mechanically stirred conditions. A variety of polymers have been prepared employing Group 14/15 organometallic dihalides as Lewis acid monomers and organic di- or multifunctional nucleophiles (*e.g.* diols, diamines, diacids) as the Lewis base monomers. An early example of the synthesis of an arsenic (As) containing polymer utilized triphenylarsine dichloride as the Lewis acid, and a range of diamines as Lewis bases, resulting in the formation of the As(V)-polyamines.[26] Polymerisation was rapid, occurring within 20 secs with the precipitated polymers isolated in modest yields (< 50%). The weight average molecular weight (M_w) of the soluble fraction of the precipitated polymers was of the order of 10^5 g.mol^{-1}.

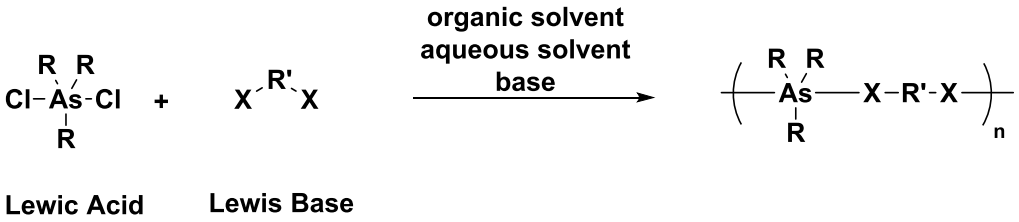

Scheme 1.1 General reaction scheme and conditions for the interfacial polymerisation of lewis acidic arsenic dihalides (here dichlorides) and a complimentary lewis basic where X = OH / NH_2 / COOH.

Inspired by the clinical resurgence of (in)organic arsenic reagents,[27] particularly their potential as anticancer, antiviral and antibacterial agents, Gallaher and his team have prepared a library of the organoarsenic polymers by the interfacial polycondensation approach, utilizing bioactive Lewis bases as comonomers. The rationale for their design came from potential synergy between the bioactive metal-centre and Lewis base (Scheme 1.1), and their inspiration is drawn from data that suggests that Group-15 containing polymers can inhibit the growth of some pancreatic cancer cell lines.

Triterpenoid natural product, glycyrrhetinic acid, derived from herb liquorice was initially investigated as the Lewis base, being able to react with the organoarsenic reagent through both the carboxylic acid and alcohol groups.[28] Structurally, it is similar to cortisone and other corticosteroids and is implicated in the anti-inflammatory properties of liquorice. Furthermore, it has been shown to inhibit prostaglandin metabolism and it is a potent inducer of mitochondrial permeability transition which can trigger reactive oxygen species induced apoptosis. This is significant as this is also the mechanism by which clinically relevant organic arsenicals GSAO and PENAO stimulate cell death through cross-linking the proximal thiols of Cys^{57} and Cys^{257} of mitochondrial transmembrane protein adenine nucleotide translocase (ANT).[29]

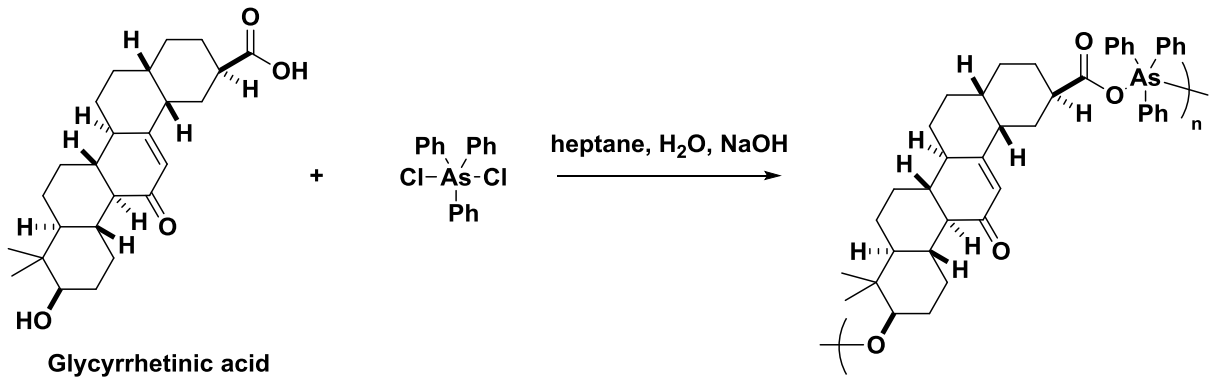

Scheme 1.2 Reaction scheme and conditions for the interfacial polymerisation of triphenylarsenic dichloride and glycyrrhetinic acid yielding the As(V)-poly(ether ester) within 15 seconds M_w = 210000 g.mol^{-1}; DP_n ~ 270.28

The interfacial polymerisation with triphenylarsenic dibromide was complete within 15 seconds yielding As(V)-poly(ether esters) with DP_n ~ 270 and M_w of 210000 g/mol^{-1} (from light scattering photometry) (Scheme 1.2). When unsymmetrical Lewis bases such as these are employed, polymers derived from Group-15 Lewis acids can exist with three possible bonding arrangements around the metal centre (Figure 1.2). Two of these are referred to as symmetrical, *i.e.* alternating metal centre bonding through the alcohol only (**1**) and the acid only (**2**), with the other being unsymmetrical, *i.e.* each metal bonding through the acid and the alcohol (**4**) simultaneously. Furthermore, when bonding to the

metal occurs symmetrically through the acid group, the resulting structure can be 'linear' (**2**) or bridged/distorted (**3**) through back-bonding the carbonyl of the acid to the metal centre, which is also typical for Group-15 polyesters. Using IR spectroscopy, the resulting As-poly(ether ester) was identified to exist predominantly as non-distorted unsymmetrical and symmetrical structures.

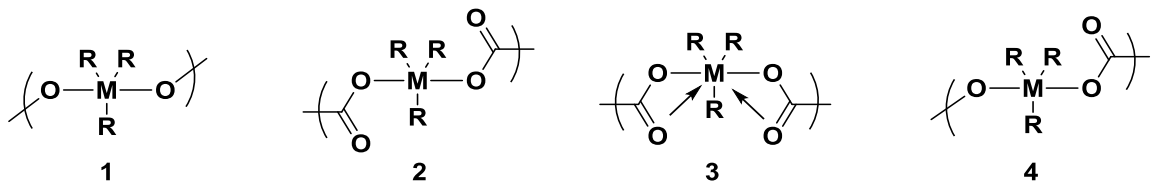

Figure 1.2 Possible bonding configurations of As(V)-poly(ether esters) derived from unsymmetrical Lewis base comonomers; symmetrical (1, 2), distorted symmetrical (3) and unsymmetrical (4).

Analogous organotin polymer drugs have been shown to be cytotoxic with cell death occurring via necrosis.[25] Therefore, the ability of the As-poly(ether esters) to arrest cancer cell growth was assessed by measurement of the effective concentration (EC_{50}) against adenocarcinoma (AsPC-1) and epithelioid carcinoma (PANC-1) pancreatic cell lines. Moreover, the chemotherapeutic index (CI_{50}) was also determined by comparison of the cytotoxicity against non-malignant cell lines, in this case mouse embryo fibroblasts (NIH/3T3) and embryonic human lung fibroblasts (WI-38). The As-poly(ether esters) were effective against PANC-1 (EC_{50} = 2.5 μg/mL) compared to Cisplatin (EC_{50} = 0.34 μg/mL) but ineffective against AsPC-1, which justified further investigation of related polymers.

As-polyesters have been synthesized using thiodiglycolic acid,[30] chelidonic acid[31] and camphoric acid (Figure 1.3).[32] The diacid functionality of the Lewis bases employed in these polymerisations results in the polymers adopting the symmetrical bridged (**3**) or non-bridged bonding around the As centre. Using triphenylarsenic dichloride the As-polyesters derived from thiodiglycolic acid and chelidonic acid were obtained with M_w = 82000 g/mol^{-1}, DP_n = 180 and M_w = 170000 g/mol^{-1}, DP_n = 350 respectively. In the case

of camphoric acid, triphenylarsenic dibromide was employed as the Lewis acid furnished an As-polyester with M_w = 140000 g/mol^{-1}, DP$_n$ = 250.

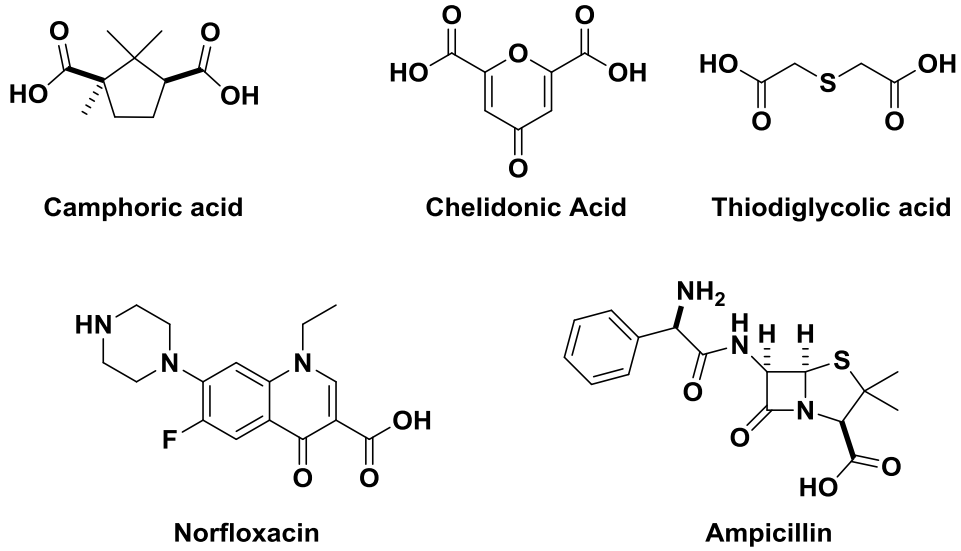

Figure 1.3 Other bioactive Lewis base monomers used for the preparation of As(V)-polyesters (camphoric acid,[32] chelidonic acid,[31] thiodiglycolic acid[30]) and As(V)-poly(amine esters) (norfloxacin,[33] ampicillin[34]).

When antibiotics ampicillin and norfloxacin were used as the Lewis base, reaction with triphenylarsenic dichloride through their amine and acid functional groups formed As-poly(amine esters).[33, 34] Both antibiotics yield polymers with lower chain lengths and M_w (ampicillin DP$_n$ = 81; M_w = 53000 g.mol^{-1} and norfloxacin DP$_n$ = 38; M_w = 24000 g.mol^{-1}) than obtained for the polyesters and poly(ether esters), and like the poly(ether esters) the bonding through the arsenic centre can be symmetrical or unsymmetrical (Figure 1.2). The anticancer activity of the As-polyesters and the As-poly(amine esters) was assessed against a range of pancreatic and non-pancreatic cancer cell lines relative to the constituent monomers and Cisplatin used as a clinical reference. The activity of the Lewis acid monomers was presented with caution in each case due to rapid hydrolysis and accumulation of HX (X = Cl, Br) under the assay conditions. In all cases the Lewis base alone was shown to be ineffective at inhibiting cancer cell growth against all cell lines, so any activity observed was attributed to the As-polymers. The As-polyesters with thiodiglycolic acid exhibited stronger inhibition (EC$_{50}$ = 0.052 μg/mL)[30] of the AsPC-1

cell line than Cisplatin, whilst the chelidonic acid As-polyester also inhibited the AsPC-1 (EC_{50} = 1.9 μg/mL) as well as estrogen-independent breast adenocarcinoma cells (7233/MDA, 0.0044 μg/mL).[31] The As-poly(amine ester) derived from norfloxacin also inhibited AsPC-1 (16 μg/mL),[33] whilst the ampicillin containing polymer was effective against PANC-1 (6.43 ng/mL) and estrogen-independent MCF-7/7233 (0.0014 ng/mL).[34] The activities of the As-polymers are indeed promising, however the CI_{50} (against WI-38 and 3T3 cells) values are erratic and warrant further investigation to identify trends.

1.2.1.2 Free radical alternating copolymerization

The incorporation of metal or metalloid elements into the unsaturated polymer backbones is an attractive prospect for the generation of (semi)conductive and optically active materials.[35-37] The key step in any such process is carbon-metal bond formation, which is usually achieved by classical electrophilic/nucleophilic substitution pathways or hydrometallation.[38] An alternative, atom economical approach to the formation of carbon-metal bonds is radical bismetallation of alkynes,[39] which has been employed in organic synthesis for the synthesis of metal substituted 1,2-diethylenes.[40] This process relies on the homolysis of relatively weak metal-metal bonds, initiated thermally or photochemically, in the presence of alkynes to trap the metal radicals formed.

Organoarsenic homocycles, or cyclooligoarsines (RAs_n)[41, 42] have been known since the 19th century yet as recently as 2005 the composition of Arsphenamine/Salvarsen was resolved as a mixture of organoarsenic homocycles.[5] Such structures are composed of multiple As-As bonds, the number and stability of which depends largely on the nature of the R-groups. For example, when R = Me, five-membered rings are formed and the As-As bonds are prone to spontaneous homolysis; whereas if R = Ph six-membered rings are exclusively formed which are stable in air, moisture and refluxing benzene. The cyclic structures are readily accessible by reduction of the corresponding arsonic acids using hypophosphorus acid in the presence of catalytic amounts of KI (Scheme 1.3).[43] The insoluble product of the spontaneous homolysis of $(MeAs)_5$ has been proposed to be open chain oligoarsines, consisting of an As-As backbone, that stack together in ladder-like structures.[44] Chujo and Naka recognized the potential of these oligomeric As-As structures, particularly the organoarsenic homocycles, to act as comonomers for

alternating copolymerisation via radical bismetallation in the presence of alkynes to form poly(vinylene-arsines).[45]

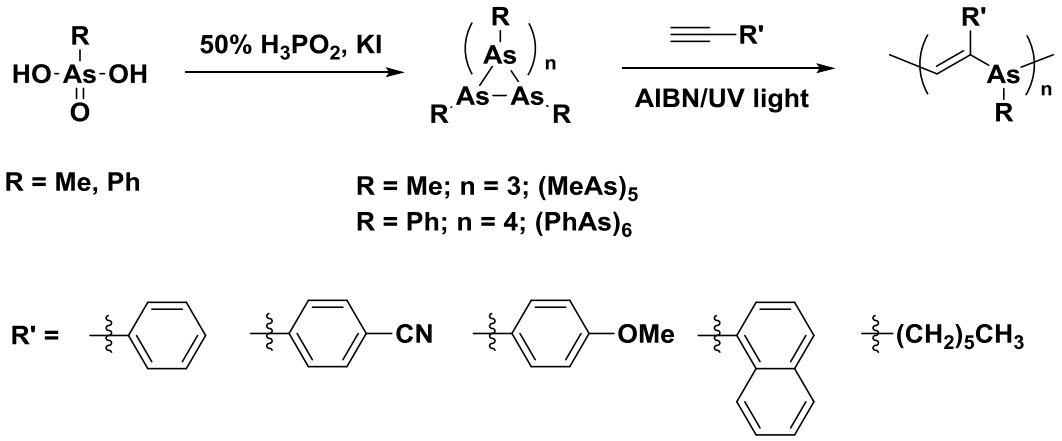

Scheme 1.3 Synthesis of poly(vinylene-arsines) from methy/phenyl arsonic acid via cyclic homoarsines $(MeAs)_5$ and $(PhAs)_6$.

Organoarsenic homocycles $(MeAs)_5$ and $(PhAs)_6$ have been employed as As-functional monomers with aromatic terminal acetylenes employed as comonomers. Whilst polymerisation of $(MeAs)_5$ can occur spontaneously, reactions are typically initiated by thermal decomposition of a radical initiator (2,2'-azobisisobutyronitrile, AIBN) or irradiation with a xenon lamp to catalyse homolysis of the As-As bonds, with AIBN decomposition being essential for the polymerisation of $(PhAs)_6$. The initial investigation[45] employing phenylacetylene as the terminal alkyne reported number average molecular weights (M_n) up to 11500 g.mol^{-1} for $(MeAs)_5$ and $M_n \sim 4000$ g.mol^{-1} for $(PhAs)_6$. Structural characterization of the products by ^{1}H and ^{13}C NMR confirmed the poly(vinylene-arsine) structure with a backbone composed of As-substituted vinylene groups with a *trans*-1,2 geometry. Comparison of the backbone vinyl proton with the sidechain protons and elemental analysis implied the 1:1 stoichiometry of the monomers, which was maintained irrespective of the initial monomer feed ratio.

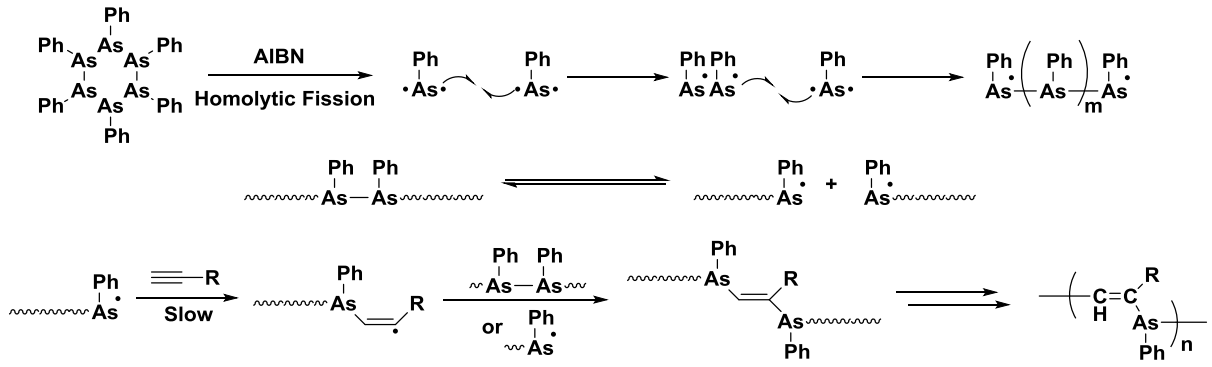

Scheme 1.4. Proposed mechanism for the formation of poly(vinylene-arsines) via ring-collapsed radical alternating copolymerization (RCRAC).

Mechanistically the polymerisation is initiated by cleavage of an As-As bond present in the organoarsenic homocycles, followed by spontaneous homolysis of the remaining As-As bonds and collapse of the ring structure (Scheme 4). The resulting arsenic radicals can either recombine to form labile As-As bonds, or add to the acetylene monomer leading to formation of a new As-carbon bond and vinyl radical, which is proposed to be the rate determining step. Vinyl radicals are very short-lived, reacting rapidly with another As-radical or an As-As bond. The former results in irreversible termination of the polymerisation whilst the latter results in formation of an As-radical chain end which can either reversibly terminate by recombination, or react with another acetylene molecule. Propagation of the vinyl radical chain end by addition to alkyne is not likely. Likewise, recombination of vinyl radical chain ends is prohibited by their low concentration (due to instability and high reactivity). Thus, the combined sequence of events has been named ring-collapsed radical alternating copolymerization (RCRAC) and it is not a classical chain-growth mechanism, with conversion and molecule weight analysis by GC (Figure 1.4A) and SEC (Figure 1.4B/D) respectively indicating step-growth characteristics (Figure 1.4).[46]

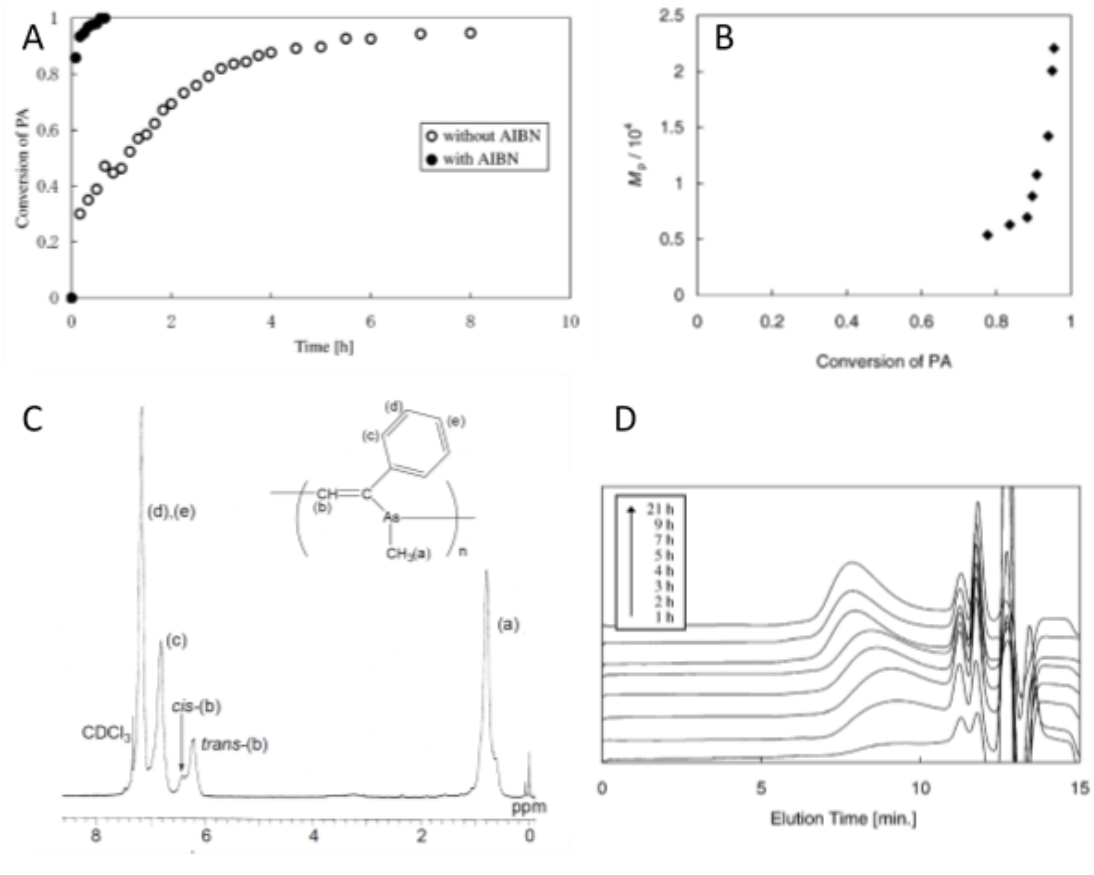

Figure 1.4 Typical data of RCRAC reaction of $(MeAs)_5$ with phenylacetylene showing A) conversion of phenyl acetylene in presence and absence of radical initiation (GC); B) the build-up of molecular weight (M_p) as a function of conversion; C) polymer structure according to ^{1}H NMR; D) the molecular weight distribution as a function of time measured by SEC.[46]

The alternating vinylene-arsine backbone imparts interesting electronic structures and optical properties onto the resulting polymers as a result of strong absorbance UV region ($\pi - \pi^*$, C=C) which extends into the visible (n - π^*, As-C=C), the latter of which confers emissive properties onto the polymers. Specific excitation (λ_{ex}) and emission (λ_{em}) wavelengths have been determined by fluorescence spectroscopy and are dependent upon on the substituents present in both monomers.[47] For example, poly(vinylene-arsines) composed of $(MeAs)_5$ and phenylacetylene (PA) give λ_{ex} = 396 nm and λ_{em} = 485 nm which are blue-shifted when $(PhAs)_6$ is employed (λ_{ex} = 375 nm; λ_{em} = 437 nm). The electronic nature of the acetylene can be altered by the addition of substituents to the phenyl ring,[47] or by changing to an aliphatic acetylene which only copolymerize with $(MeAs)_5$ (Table 1.1).[48] When more electron withdrawing acetylenes (4-

cyanophenylacetylene, 4-CPA) were polymerized with $(PhAs)_6$ faster reactions, higher conversions and higher M_n were obtained and the resulting excitation and emission spectra of the poly(vinylene-arsines) were red-shifted (λ_{ex} = 394 nm; λ_{em} = 443, 466 nm). Conversely, use of an electron-donating acetylene (4-methoxyphenylacetylene, 4-MPA) resulted in slower reaction kinetics, lower conversions and blue shifted excitation and emission spectra (λ_{ex} = 341 nm; λ_{em} = 402nm) relative to phenylacetylene. In the poly(vinylene-arsine) backbone, a donor-acceptor pair exists between an As-lone pair and vinylene unit. The presence of an electron-withdrawing group in conjugation with the vinylene unit improves the acceptor ability, narrowing the band gap and lowering the energy of emission.

Table 1.1 Synthesis and optical properties of poly(vinylene-arsines)[47]

M1	M2	M_n[a] g.mol^{-1}	M_w[a] g.mol^{-1}	M_w/M_n[a]	Yield[b] %	$\lambda_{max,em}$[c] nm	$\lambda_{max,ex}$[c] nm
$(MeAs)_5$	PA	11500	48700	4.3	46	485	396
$(PhAs)_6$	PA	3900	5600	1.4	35	437	375
$(PhAs)_6$	4-CPA	8400	15100	1.8	29	443, 466	394
$(PhAs)_6$	4-MPA	3700	5100	1.4	22	402	341
$(PhAs)_6$	1-NA[d]	7600	9900	1.3	33	350	315
$(MeAs)_5$[e]	1-Oct	6500	7800	1.2	45	450	350

[a)]SEC, $CHCl_3$; [b)]isolated yields after precipitation in hexane; [c)]in $CHCl_3$ at RT; [d)]1-naphthylacetylene; [e)]M2 = 1-octyne, reaction performed in bulk in the presence of AIBN.[48]

More complex terpolymer and block copolymer compositions are accessible by exploiting the relative reactivity of the As-radicals with other Group-15 radicals, such as those derived from organostibine (antimony, Sb) homocycles, or through copolymerization with more tradition vinyl monomers.[49] As-radicals react more readily with electron poor acetylenes, such as dimethyl acetylenedicarboxylate (DMAD), than Sb-radicals.[50] However, the corresponding vinyl radicals react preferentially with Sb-radicals. Consequently, in the copolymerization of $(MeAs)_5/(PhSb)_6$/DMAD = 1/1/2 the relative reactivities of the Group-15 radicals furnished a periodic terpolymer composed

of the vinylene-arsine-vinylene-stibine repeating unit. Increasing the $(MeAs)_5$ monomer feed had little effect on the final polymer composition whereas increasing the $(PhSb)_6$ monomer feed to $(MeAs)_5/(PhSb)_6$/DMAD = 1/1/2 resulted in a higher molecular weight terpolymer with a higher proportion of the Sb-units compared to As-units. This was attributed to the vinylene-arsine-vinylene-stibine periodic structure initially being formed until all the $(MeAs)_5$ was consumed, at which point the $(PhSb)_6$ and DMAD continued to copolymerize via the RCRAC mechanism (Scheme 1.5A).

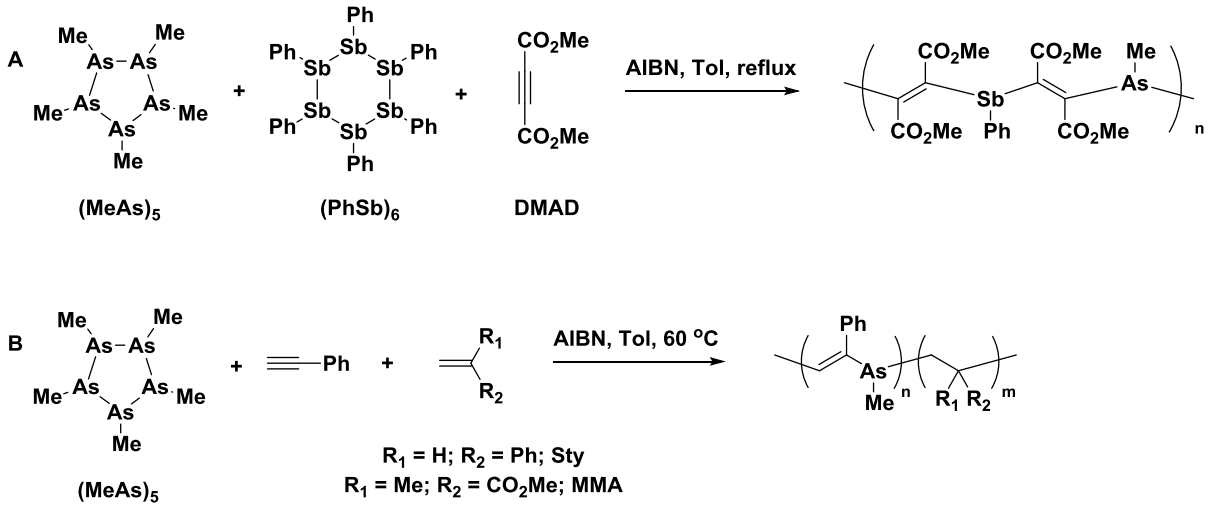

Scheme 1.5 Synthesis of organic arsenical terpolymers via copolymerization in the presence of A) *cyclo*-organostibine $(PhSb)_6$; B) activated vinyl groups styrene (Sty) and methyl methacrylate (MMA)

Terpolymerisation of $(MeAs)_5$ and phenylacetylene in the presence of activated vinyl groups styrene (Sty) and methyl methacrylate (MMA) resulted in block-like copolymers with one block composed of the vinylene-arsine repeating unit and the other being composed of Sty/MMA (Scheme 1.5B).[51] Using the copolymerisation with Sty as a model, reducing the activated monomer feed ratio resulted in small reductions in M_n whilst increasing the Sty feed ratio resulted in polymers with higher M_n values (10200 to 15500 g.mol^{-1}). The block-like structures were inferred by NMR and SEC. The presence of the conjugated vinylene-arsine block was also supported by UV-vis and fluorescence spectroscopy whereby the terpolymers formed exhibited comparable absorption and emission profiles to the copolymers derived from RCRAC of $(MeAs)_5$ and phenylacetylene, in the absence of Sty, with increasing the Sty feed resulting in a blue

shift in both λ_{ex} and λ_{em}. When 2,3-dimethyl-1,3-butadiene was employed as the activated vinyl monomer, a random terpolymer composed of a random distribution of the both vinylene-arsine and arsine-butadiene repeating units was obtained.[51] Interestingly, whilst probing the mechanism of this polymerisation it was recognized that the reaction $(MeAs)_5$ with 2,3-dimthyl-1,3-butadiene under incandescent light, in the absence of other radical initiators, furnished a cyclic diarsine.[52] As observed for organoarsenic homocycles, the As-As bond in cyclic diarsines is prone to homolysis in the presence of catalytic amounts of AIBN, and the As-radicals formed readily copolymerize with activated vinyl monomers such as Sty and MMA resulting in unconjugated polymers with As-units distributed through the backbone. These methods represent novel routes to the formation of polymers with As distributed through the polymer backbone. Additionally, these can have pendent functionalities for specific properties and/or reactivities incorporated by simply varying the styrenic or (meth)acrylic comonomers.

Extended conjugated polymer networks have been synthesized by terpolymerisation of organoarsenic homocycles $(PhAs)_6$ with phenylacetylene and *p/m*-diethynylbenzene (DEB).[53] The *p/m*-DEB monomers reacted faster than phenylacetylene with the *p*-DEB exhibiting the faster rate of conversion. This was reflected in the polymers obtained with increasing the *p/m*-DEB monomer feed from 0 – 10 – 30 % (w.r.t to total acetylene monomer feed) resulting in an increase in M_w (3100 – 11800 g.mol^{-1}) and T_g (92.9 – 101.7 °C). The enhanced reactivity of both the acetylene moieties of *p*-DEB compared to *m*-DEB was confirmed during polymerisation of equimolar amounts of phenylacetylene and *p/m*-DEB. Macroscopic precipitation as a result of gelation occurred when *p*-DEB was employed whereas a soluble crosslinked polymer (M_w = 8000 g.mol^{-1}, T_g = 103.7 °C) was obtained in the presence of *m*-DEB. The soluble crosslinked polymers presented red-shifted excitation and emission relative to linear poly(vinylene-arsine) analogues increasing from λ_{ex} = 375 nm to 394 nm and λ_{em} = 437 nm to 473 nm respectively indicating that increasing the level of crosslinking resulted in extended conjugation and a narrower band gap between the donor and accepter groups. Finally, the film forming abilities of the polymers was assessed by drop-casting and performing a qualitative peel test, which revealed that increasing the *p,m*-DEB content increased the film forming properties.

The presence of As-lone pairs throughout the backbone of poly(vinylene-arsines) has been exploited to prepare coordination polymers with transition metal salts and complexes.[54] Polymers derived from $(PhAs)_5$ formed metal coordinated polymers upon addition of $CoCl_2$ in acetone at various ratios of polymer:$CoCl_2$. However, coordination to polymers derived from $(PhAs)_6$ was not observed due to the more sterically encumbered poly(vinylene-arsine) backbone. When formed at a 1 : 1 stoichiometry of $CoCl_2$: As the bivalent Co^{II} was oxidatively labile forming a more stable trivalent species upon oxidation. However, the bivalent metal centre could be stabilized by complexation with an excess of polymer $CoCl_2$: As = 1 : > 4. The Co^{II} content in the coordination polymers was determined using an EDTA assay to sequester unbound Co^{II} in solution and the electronic structures were confirmed by UV-vis spectroscopy through which $CoCl_2$: As = 1 : 1 showed a signal for metal-ligand charge transfer, indicative of an oxidized trivalent Co-species, which was not present upon increasing the polymer concentration ($CoCl_2$: As = 1 : > 4). Ruthenium-poly(vinylene arsine) complexes have also been reported using a *cis*-$(bpy)_2RuCl_2.2H_2O$ complex. At a ratio of Ru : As = 1 : 2 up to 20 % of the arsine units in the polymers derived from $(MeAs)_5$ were bound to Ru-complexes, and no coordination was reported for polymers derived from $(PhAs)_6$. Finally, the coordination ability between As and transition metals has been exploited for stabilization of colloidal dispersions of silver nanoparticles (AgNPs) (Figure 1.5).[55] In the absence of the poly(vinylene-arsine) polymers reduction of $AgNO_3$ in DMF resulted in deposition of silver metal. However, in a 1 : 1 ratio of $AgNO_3$: poly(vinylene-arsine) colloidal dispersions were obtained as confirmed by the surface plasmon absorption band at ~400 nm in the UV-vis spectra of the resulting solutions.

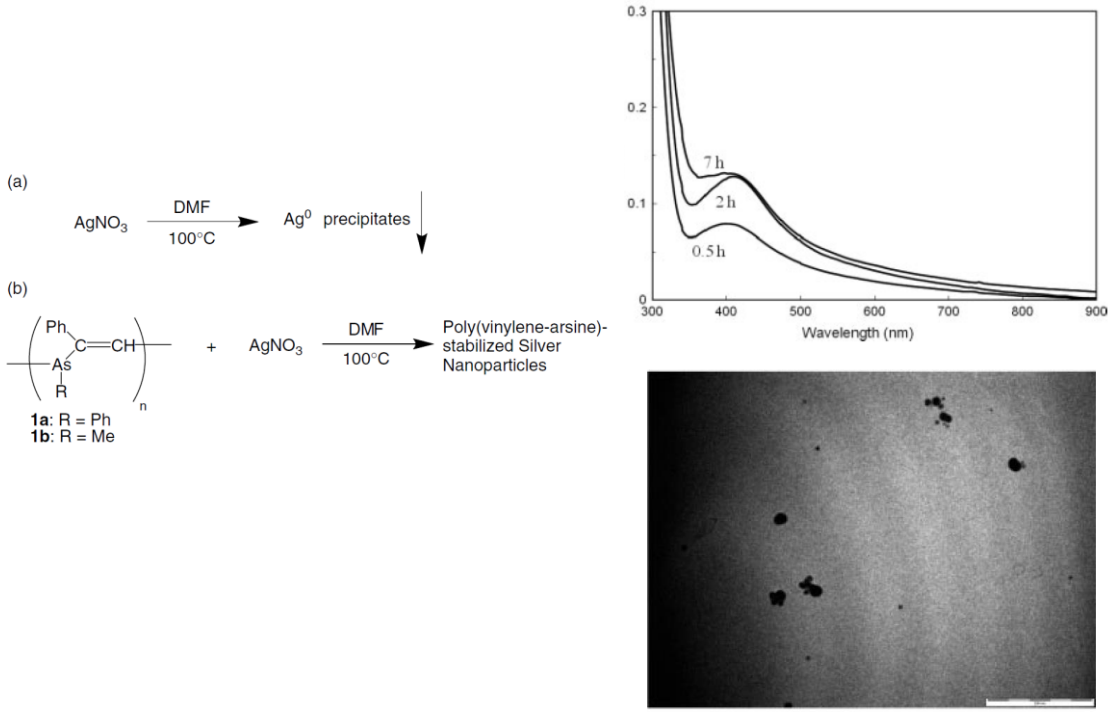

Figure 1.5 Colloidal dispersions of silver nanoparticles can be formed from the reduction of $AgNO_3$ in the presence of coordinating poly(vinylene-arsines). UV-*vis* and TEM confirm the presence of AgNPs within 0.5 hours. Scale bar = 200 nm.[55]

There are exciting potential applications of these conjugated and coordinated polymers in a number of fields including electronics, non-linear optics, catalysis and chemotherapy. As a single example, the ability to coordinate platinum and osmium (and many others) complexes to arsenicals has been demonstrated and in the case of Pt-As complexes,[56] potent inhibition of a broad range of the cancer cells, including Cisplatin-resistant cells, has been demonstrated which certainly encourages further investigation of these materials.

1.2.2 Pendent functional polymeric arsenicals

1.2.2.1 Free radical polymerization (FRP)

There has been interest in the incorporation of the arsonic acid functional group into polymers prepared by FRP since the 1970s based on their polyelectrolyte structure and heavy-metal chelation ability for use in ion exchange resins. In these examples, the arsonic acid functionality was introduced into styrene-divinyl benzene resins post-

polymerisation, via the traditional steps of nitration, reduction and diazotonization of the aromatic groups, followed by substitution using sodium arsenite.[57, 58] This multi-step process allows substitution of up to 50% of the benzene rings present, with little control over the distribution of the functional groups in the resin.

Commercial arsonic acid reagents, for example *o/p*-arsanilic acid, are attractive starting materials for the preparation of arsonic acid functional reagents with the aniline amine group proving to be useful functional handle for synthesis. With respect to arsonic acid functional vinyl-monomers, *o/p*-(meth)acryloylaminophenylarsonic acid monomers have been prepared by amidation of the *o/p*-arsanilic acid using (meth)acryloyl chloride (Scheme 1.6).[59, 60] The crystal structures have been solved[61-63] and *p*-methacryloylaminophenylarsonic acid in particular shows good non-linear optical (NLO) properties, exhibiting a large second-harmonic generation using a 1.06 μm Nd-YAG IR laser which produced a green (534 nm) output. These properties arise from subtle differences in the molecular structure[62] and conformation,[64] in particular the (as)symmetry of the intermolecular hydrogen bonding network. Upon crystallization this results in formation of two crystals structures; noncentrosymmetric orthorhombic crystals which are responsible for producing the second-harmonic generation output and centrosymmetric triclinic crystals which are unable to exhibit the property based on NLO theory.

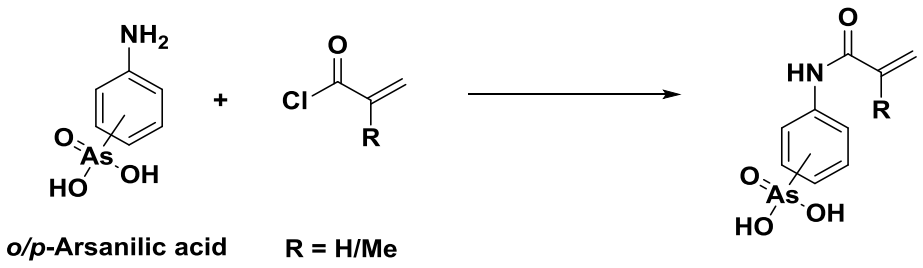

Scheme 1.6 Synthesis of *o/p*-(meth)acryloylaminophenylarsonic acid monomers

o/p-(Meth)acryloylaminophenylarsonic acid monomers have been polymerized by FRP in DMF at 70 °C using AIBN as an initiator.[59, 65] Polymerisation of the monomers in their Na^+ salt forms was also carried out in H_2O at 70 °C using potassium persulfate as a water

soluble initiator. Dilatometry was employed to investigate the kinetics of the polymerisations of *o/p*-methacryloylaminophenylarsonic acid which were shown to be first order in initiator and greater than 1 with respect to monomer, which is not uncommon for electrolyte monomers. Low molecular weight oligomeric species (M_n < 2100 g.mol^{-1}) were formed when *o/p*-methacryloylaminophenylarsonic acid were employed whilst *o/p*-acryloylaminophenylarsonic acid furnished higher molecular weight polymers (M_w < 39000 g.mol^{-1}). The structure of the polymers was confirmed by IR and ^{1}H NMR with the M_n of the methacylamides determined by vapour pressure osmometry, whilst SLS was used to determine M_w of the acrylamides. The colligative properties such as reduced viscosity and flocculation ability, were assessed as a function of the oligomer concentration and pH. Flocculation analyses were performed using a standard jar test in which the polymer was added in variable concentrations (1 – 5 mg.mL^{-1}) to waste sewage water from the authors' institute followed by turbidity measurements. At constant pH (pH = 2), the performance of both polymers as flocculants, in their salt forms, increased as a function of concentration. Increasing the pH reduces the flocculation efficiency rapidly as the pH is raised from 2 to 4, thus passing the pK_{a1} of the arsonic acid moiety, before steadily increasing with increasing pH. Reduced viscosity measurements show two maximum values at pH 2 and 10 respectively, with local minima occurring at pH 4. This was attributed to polymer chain expansion and conformation changes as a result coil expansion, which is typical behavior for polyelectrolytes. Therefore, the flocculation efficiency was tentatively attributed to changes in polymer coil expansion.

The sodium salts of *o/p*-methacryloylaminophenylarsonic acid have been copolymerized, using a range of monomer feed ratios, with sodium (meth)acrylate and acrylamide by FRP in H_2O at 70°C using potassium persulfate as an initiator and their physiochemical properties have been evaluated by on-line (with SEC) and off-line multi-angle light scattering (MALS).[66, 67] The experimental copolymer compositions were extrapolated from the As-content which was determined by atomic absorption spectroscopy (AAS). Homopolymers of *o/p*-methacryloylaminophenylarsonic acid reach high molecular weight (M_w = 1.3 x 10^6 g.mol^{-1}) whilst compositional analysis against the monomer feed revealed that all copolymers were richer in sodium (meth)acrylate or acrylamide than the As-monomers. This was reflected by the reactivity ratios which were determined for all

the polymerisation systems in which $r_{As} < 1$ and $r_2 > 1$ (r_{As} = As-monomer; r_2 = sodium (meth)acrylate and acrylamide) suggesting a random copolymer structure. Molecular weights of the copolymers were of the order of $M_w = 10^5$ g.mol^{-1} with the M_w and radius of gyration decreasing with decreasing As-monomer content.

Homopolymers of *o/p*-acryloylaminophenylarsonic acid have been employed for a one-step 'green' synthesis of the Au and Ag colloidal dispersions in H_2O, where the polymers have the dual properties of reducing agent and stabilizer for the nanoparticles formed.[68] The *p*-acryloylaminophenylarsonic acid polymer was able to reduce $HAuCl_4$, according to the emergence of absorption at 557 nm (SPR band). The reaction was slow, reaching completion with 243 h. The resulting particles, stabilized by the polymer, were polydisperse with sizes ranging from 5-80 nm according to TEM (Figure 1.6). Alternatively, *o*-acryloylaminophenylarsonic acid similarly afforded reduction of $HAuCl_4$ over 140 h with an absorbance peak emerging at 547 nm. However, over longer time periods the absorbance decreased which suggested that the *ortho* polymers were insufficient for stabilization, which was confirmed by observed precipitation.

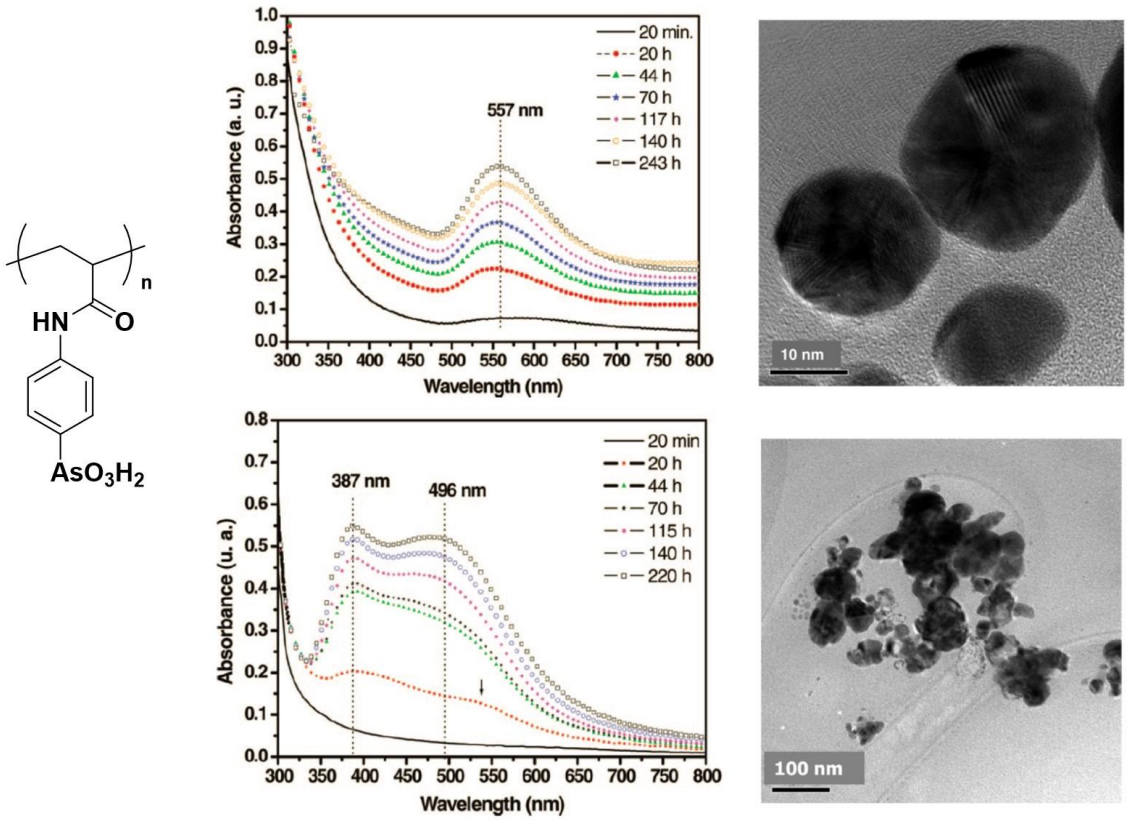

Figure 1.6 Temporal evolution of UV-*vis* absorption and typical TEM images of the nanoparticles formed after addition of $HAuCl_4$ (top) and $AgNO_3$ (bottom) to the polymer derived from *p*-acryloylaminophenylarsonic.[68]

Both polymers were able to reduce $AgNO_3$ and stabilized the Ag^0 particles formed. The mechanism of particle formation is slightly different for each monomer according to differences observed in the absorption spectra. Two distinct maxima emerge with the *para* polymer (387 nm and 496 nm) over 220 h, whilst these peaks coalesce to a single maximum (414 nm) after ~100 hrs. The two maxima were attributed to different size particles which was confirmed by TEM with the *para*-polymer furnishing two distinct distribution of particles at 2-15 nm and 40-60 nm respectively (Figure 1.6). The *ortho*-polymer, exhibiting a single maximum at 414 nm, also yielded particles with two distributions however, TEM revealed that the majority of the particles formed were of a smaller size (2-15 nm) with a minor population of larger particles (25-40 nm). Additional work is perhaps required to improve the particle size distribution of the particles formed in this process but the one-pot, 'surfactant'-free, aqueous conditions of this process are attractive as a relatively 'green' route to metallic nanoparticles.

1.2.2.2 Reversible deactivation radical polymerization (RDRP)

As-functional (co)polymers prepared by FRP have shown some interesting properties, particularly with respect to their use as flocculants and surface-active molecules due to the ionization potential and ion-exchange properties of pendant arsonic acid moieties. The composition, and in some cases the performance, of these materials is somewhat limited by the lack of control over the FRP methodology. One approach to improve compositional control is via reversible deactivation radical polymerization (RDRP) which exploits the activation-deactivation equilibrium of active chain-ends to control radical formation (*i.e.* concentration), monomer addition (*i.e.* chain-growth) and deactivation events during radical polymerizations. Active chain ends include (i) alkyl halides in Cu-mediated radical polymerizations such as atom-transfer radical polymerization (ATRP)[69] and single electron transfer living radical polymerization (SET-LRP);[70, 71] (ii) thiocarbonylthio for reversible addition fragmentation chain-transfer polymerization (RAFT);[72] (iii) alkoxyamines for nitroxide-mediated polymerization (NMP).[73] Recent advances in the field of RDRP allows this activation-deactivation equilibrium to be manipulated to afford unprecedented control over molecular weight and molecular weight distribution (*Đ*). Furthermore, through the use of functional monomers and initiating/mediating reagents, homo- and (multi)block copolymers can be prepared with precise control of the end-group functionality and discrete control over the functional domains present throughout the polymer composition.[74-78]

p-Arsanilic acid has already been shown to be a convenient synthon for the one-step synthesis of (meth)acrylamide monomers.[59, 65] The amine functionality has also been exploited for the one-step synthesis of an arsonic acid, As(V)-functional initiator (AsBr), via amidation using 2-bromoisobutyryl bromide, for Cu-mediated RDRP.[79] The As(V)-functional α-haloamide AsBr was employed to initiate aqueous SET-LRP[80] of a range of acrylamide and acrylate monomers, as well as copolymers with the As(V)-functional acrylamide monomer (AsAm). Homopolymerizations initiated by AsBr, with target $DP_{n,th}$ = 20-100, reached quantitative conversion within 30 minutes and were well controlled (*Đ* < 1.20). Similarly, copolymerizations of variable ratios of PEGA and AsAm with fixed total $DP_{n,th}$ = 20 reached full conversion within 30 minutes and retained good control throughout (*Đ* < 1.30). The differential reactivity of arsenicals for thiols was then

sequentially exploited to achieve highly efficient and highly selective protein/peptide-polymer conjugation.[79]

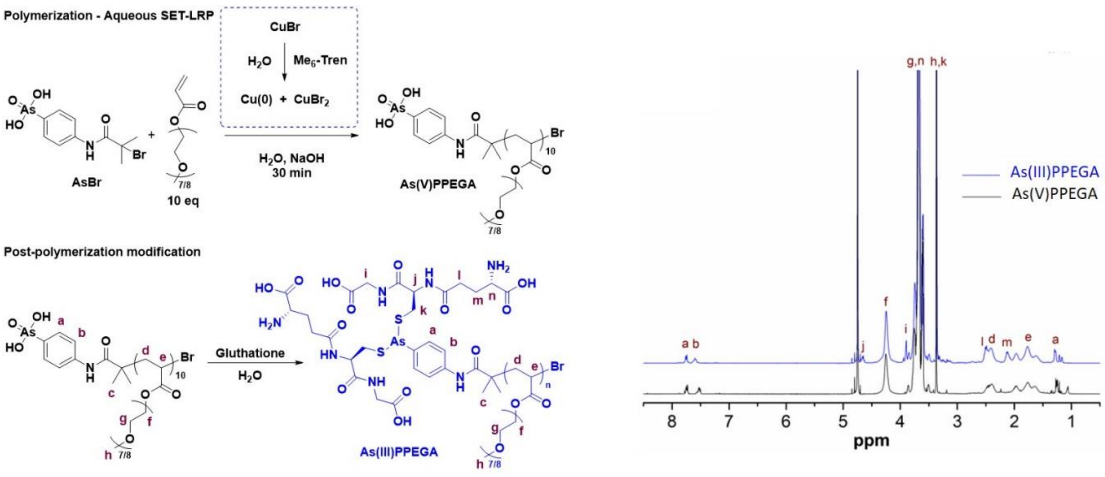

Figure 1.7 Synthesis of As(V)PPEGA$_{480}$ via aqueous SET-LRP followed by post-polymerization modification by reduction and complexation with glutathione (GSH) to form the bis(GSH) As(III)PPEGA adduct.[79]

Pentavalent arsenic (As(V)) does not form covalent bonds with thiols, preferring to undergo two consecutive single electron transfer reductions to yield trivalent arsenic (As(III)) which has a high affinity for thiols, readily forming covalent bonds. An α-As(V)-functional PEGA$_{480}$ homopolymer (As(V)PPEGA) was sequentially reduced and substituted by GSH to yield an α-As(III)-functional homopolymer (As(III)PPEGA) (Figure 1.7). The affinity of As(III) for thiols is markedly enhanced for the proximal, or closely-spaced dithiols, which was utilized to achieve peptide-polymer conjugation via disulfide bond re-bridging using salmon calcitonin (sCT) as a model peptide. Conjugations were fast and efficient reaching full conversion within 45 minutes using a small stoichiometric excess (1.2 eq) of As(III)-functional polymer (Figure 1.8). The selectivity of As(III) for dithiols in the presence of other nucleophilic amino acid residues, including monothiols of free cysteine, was qualitatively exemplified using BSA and reduced BSA (rBSA). Comparison with other thiol reactive reagents, *N*-ethyl maleimide

(NEM) and dibromomaleimide (DBM), showed that whilst NEM and DBM reacted indiscriminately with monothiols and dithiols present in rBSA, As(III) reagents react preferentially to re-bridge the reduced disulfides present in rBSA. This efficient and highly specific approach to conjugation has great potential in the field of drug-delivery, particular with respect to antibody-drug conjugates where heterogeneity in product formulation is a clinical limitation.

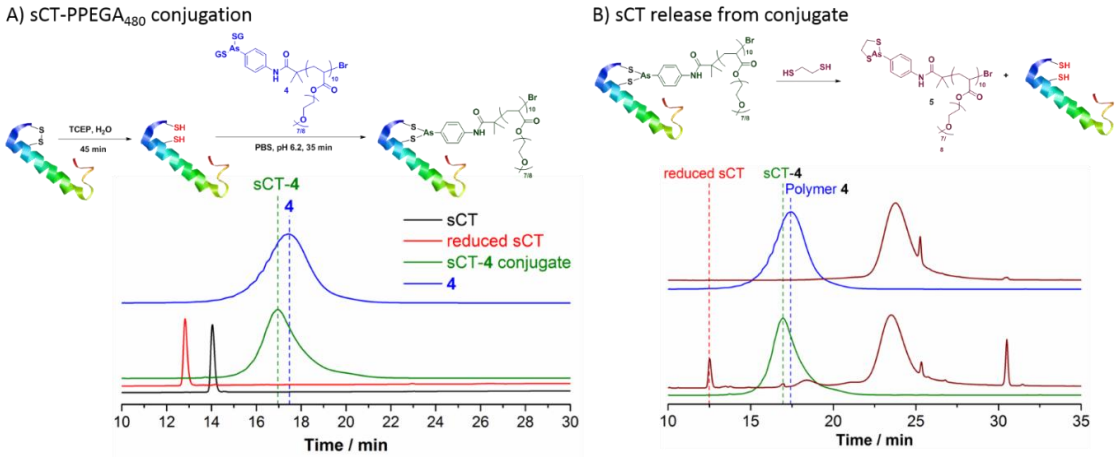

Figure 1.8 A) Conjugation of sCT to $(GSH)_2$-As(III)PPEGA$_{480}$ (2.5 eq) via sequential reduction-conjugation. B) Release of sCT from sCT-4 using EDT (bottom spectra) and control reaction of 4 and EDT (top spectra). [79]

Organic arsenicals are also compatible with RAFT polymerization. This was first reported using a pinacol protected As(V)-acrylamide (AsAm(pin)$_2$) synthesized in a two-step reaction from *p*-arsanilic acid. Homopolymerization of AsAm(pin)$_2$ ($DP_{n,th}$ = 10-50) performed in trifluoroethanol (TFE) at 65 °C using AIBN as initiator and 2-(((butylthio)-carbonothioyl)thio)propanoic acid as the chain-transfer agent was well controlled ($Đ$ < 1.40) (Table 1.2).[81] The livingness of the RAFT polymerization was exemplified by chain extension of a [AsAm(pin)$_2$]$_{10}$-macroCTA with dimethylacrylamide (DMAm) which yielded an amphiphilic block copolymer [AsAm(pin)$_2$]$_{10}$-*b*-DMAm$_{100}$ ($Đ$ = 1.10) which underwent self-assembly in aqueous solution to yield nanoparticles (D_h = 147 nm).

Table 1.2 Synthesis of polymeric arsenicals by RAFT polymerisation.[81]

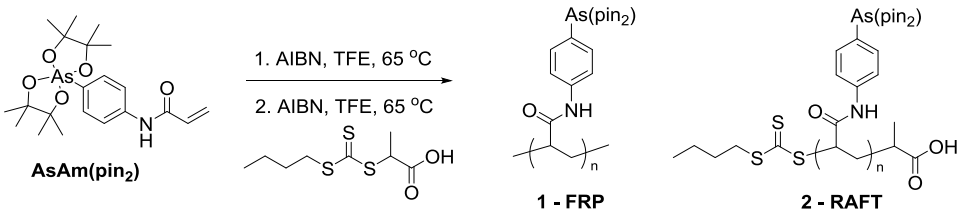

[M]/[CTA]	[CTA]/[I]	Time min	Conv. %	$M_{n,th}$ g.mol^{-1}	$M_{n,SEC}$[b] g.mol^{-1}	M_w/M_n
-[a]	-	330	81	-	39000	2.51
10	10	310	97	4600	4000	1.10
20	10	330	94	8600	5600	1.15
50	5	365	96	22000	10000[c]	1.38

[a]SEC DMF; [b]FRP [M] = 0.5 M, [AIBN] = 1 mol%; [c] SEC_{TD} (DMF): $M_{n,TD}$ = 29500 gmol^{-1}, $Đ$ = 1.36, $R_{h,TD}$ = 2.5 nm, $R_{g,TD}$ = 3.0 nm, α = 0.44.

Statistical copolymers of AsAm(pin)$_2$ and DMAm furnished well controlled DMAm$_{100-n}$-*co*-[AsAm(pin)$_2$]$_n$ copolymer scaffolds (n = 10/20/50, $Đ$ < 1.10). The pendent As(V)-functional group can be manipulated via post-polymerization modification. Initially, under acidic conditions the pinacol groups can be removed to furnish reactive arsonic acid functional groups. Subsequent reduction and substitution in the presence of excess thiol reagents results in transformation of the pendent As(V) group to thiol-substituted As(III) groups. This has been achieved using organic thiols mercaptoethanol and methyl thioglycolate as well as biologically relevant thiols cysteine and GSH to demonstrate the potential of polymeric arsenicals as reactive and responsive polymer scaffolds (Figure 1.9).

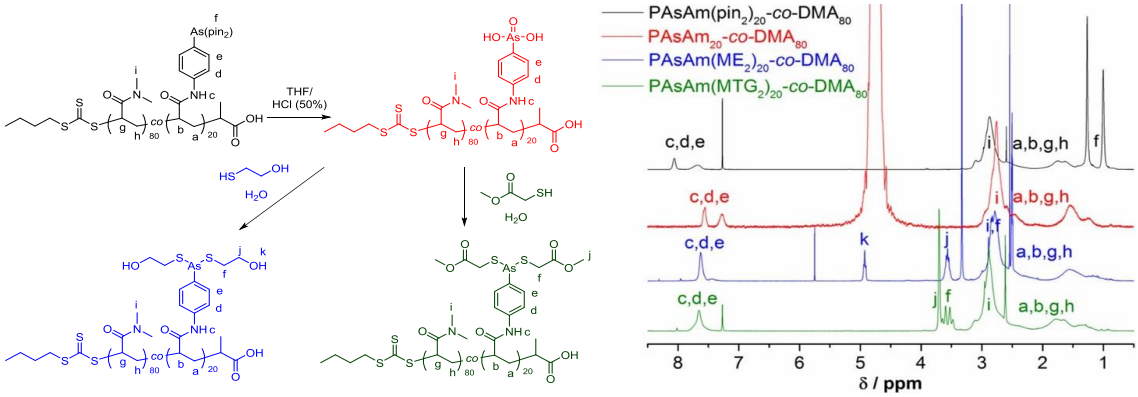

Figure 1.9 Manipulation of the polymeric arsenical scaffolds by sequential treatment with acid and thiols confirmed by ^{1}H NMR, $CDCl_3$.[81]

Most recently, Stenzl and co-workers have prepared an unprotected methacrylamide arsenical monomer derived from organic arsenical drug 4-*N*-(*S*-penicillaminylacetyl)amino phenylarsonous acid (PENAOMAm) (Figure 1.10).[82] This was copolymerized with PEGA (3-15 wt%) to form the hydrophilic block of an amphiphilic block copolymer (MMA-*b*-[PEGA-*co*-PENAOMAm]; M_n = 25-40 x 10^3 g.mol^{-1}; $Đ$ < 1.25). The rationale for this is to improve the bioavailability and efficacy of PENAO which suffers from the typical clinical limitations associated with organic drug molecules. The MMA-*b*-[PEGA-*co*-PENAOMAm] amphiphiles self-assembled in aqueous solution to furnish polymer nanoparticles (D_h = 84-234 nm; cmc = 0.5 – 82 μg.mL^{-1}). The PENAO-functional nanoparticles exhibited greater activity (inhibition; IC_{50} = 0.8 ± 0.02 μM) and cellular uptake compared to free PENAO drug (IC_{50} = 2.7 ± 0.3 μM) when compared using 143B human sarcoma cells. In agreement with preceding work, the reactivity of the pendent arsenous acid (As(III)) groups was confirmed upon reaction with mono and dithiols which has implications on the cellular localization of the nanoparticles. PENAO and related organic arsenical drug GSAO, are proposed to cross-link proximal thiols of mitrochondrial transmembrane protein adenine nucleotide translocase (ANT) which is an important component of the mitrochondial permeability pore. Confocal microscopy suggested that nanoparticles were localized to the mitochondria, suggesting the pendent PENAO groups were inhibiting cell proliferation via a similar mechanism to PENAO and certainly justifies further *in vitro* and *in vivo* investigation of these and related As-functional polymers and particles.

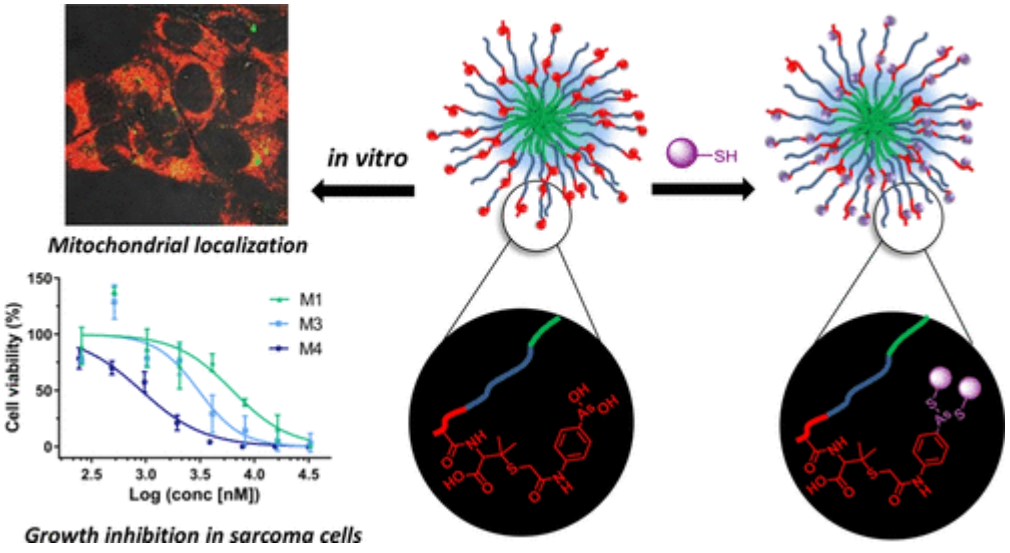

Figure 1.10. PENAO decorated polymer micelles prepared by RAFT polymerisation exhibit high chemical affinity for thiol containing groups and mitochondrial localization in vivo.[82]

1.3 Bio-imaging

Labelling proteins for visualisation is an invaluable technique to help understand the functioning, dynamics and localisation of the biological machinery that drives living organisms. Minimally invasive medical imaging has become crucial to health care, and labelling specific proteins that are markers for diseases is an increasingly attractive method for effective diagnoses. The affinities of arsenic for proteins provide multiple possible opportunities for labelling and biomedical purposes.[83] For example, *p*-azidophenyl arsenoxide (PAzPAO)[84] was incubated with live cells to label arsenic binding proteins without disrupting the membrane. The labelled proteins were then captured by strained alkyne azide cycloaddition with biotin functional dibenzylcyclooctyne and streptavidin coated magnetic beads. The captured proteins were released from the arsenic via addition of DTT and investigated by shotgun proteomics, identifying 48 proteins, including antioxidant proteins (thioredoxin, peroxiredoxin, peroxide reductase, and glutathione reductase) which well-defined dithiols sequences in their active sites.

The affinty of arsenic for protein thiols/disulfides has also been exploited to develop antibody-As-radioisotope conjugates that can undergo positron emission, enabling

tumour specific imaging via positron emission tomography (PET). Jennewein *et al.* employed monoclonal antibody Bavituximab-^{74}As (β^+; $t_{1/2}$ = 17.8 days) conjugate for PET imaging of the 3D vasculature of tumours a rat model (Figure 1.11).[85] Other As-positron emitters for PET imaging include ^{71}As (β^+; $t_{1/2}$ = 64 h) and ^{72}As (β^+; $t_{1/2}$ = 26 h) which has been studied for the development of theranostic radiopharmaceuticals upon conjugation to monoclonal antibodies, dithiol chelating cofactors and thiolated mesoporous silica nanoparticles.[86] Higher energy positron emitters such as ^{76}As (β^-; $t_{1/2}$ = 26.3 h) and ^{77}As (β^-; $t_{1/2}$ = 38.8 h) have also been considered as radiotherapeutics.[87]

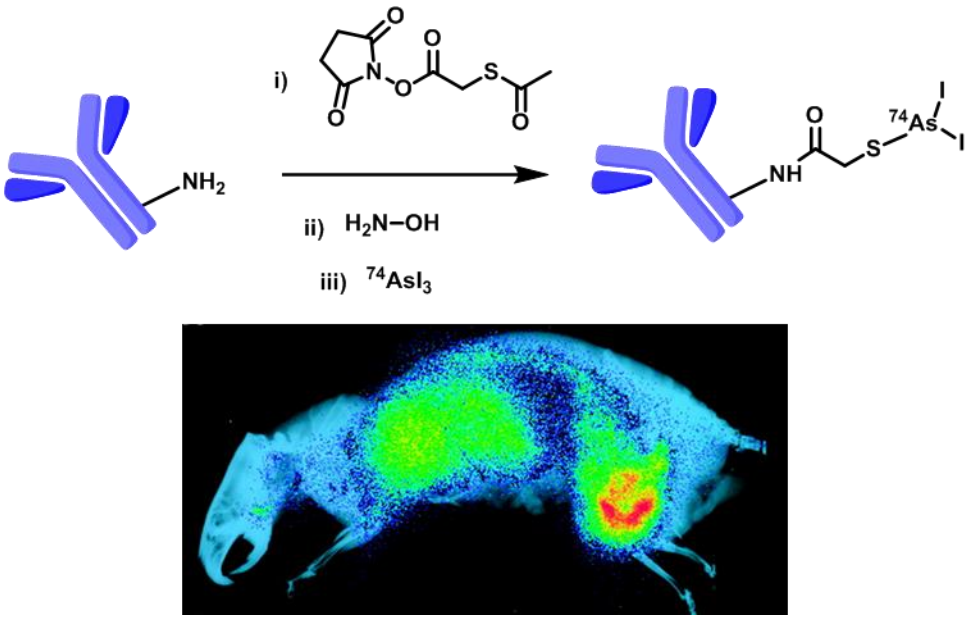

Figure 1.11Antibody functionalised with radioactive arsenic (top) and whole body planar scintigraphy of prostate tumour bearing rat, injected with 5 MBq of ^{74}As-antibody conjugate. The phosphor plate image was overlaid with x-ray picture to provide anatomic correlation.[85]

Polymer scaffolds have also been labelled with As-radioisotopes which is important from a polymer-based nanomedicine perspective, in which non-invasive evaluation of biodistribution and accumulation is highly desirable. An end-group and side-chain thiol functional analogue of FDA-approved polymer *N*-(2-hydroxypropyl)methacrylamide (HMPA) was synthesised by RAFT and conjugated to $^{72/74}$As(III).[88] The relatively long $t_{1/2}$ of ^{72}As and ^{74}As radio-labelled polymer and the stability of the conjugates (> 48 h) in saline implies that such strategies could indeed apply to imaging the long-term fate of polymeric nanomaterials *in vivo*.

Alternatively, the affinity of organic arsenicals for dithiols has been utilized to target imaging modalities (*e.g.* fluorophores, radionuclides) to particular cellular processes. To this end, the limited membrane permeabilty of organic arsenical drug GSAO has proved to be an advantageous property for the imaging of cell death using both fluorophore and radionuclide conjugated GSAO derivatives.[89] Increased accumulation of GSAO fluorophore conjugates in apoptic induced cells led to binding of biotin-GSAO to 90 kDa Heat shock protein (Hsp90), which is abundant, yet inaccessible to GSAO, in the cytoplasm of healthy eukaryotic cells. Furthermore, a rabbit and mouse *in vivo* model has been been developed to image cell death during myocardial infarction.[90] The myocardial accumulation of a radionucluide molecular imaging agent; ^{111}In-GSAO conjugate, was investigated via SPECT/CT and was correlated to both apototic and nectrotic cell death processes (Figure 1.12).

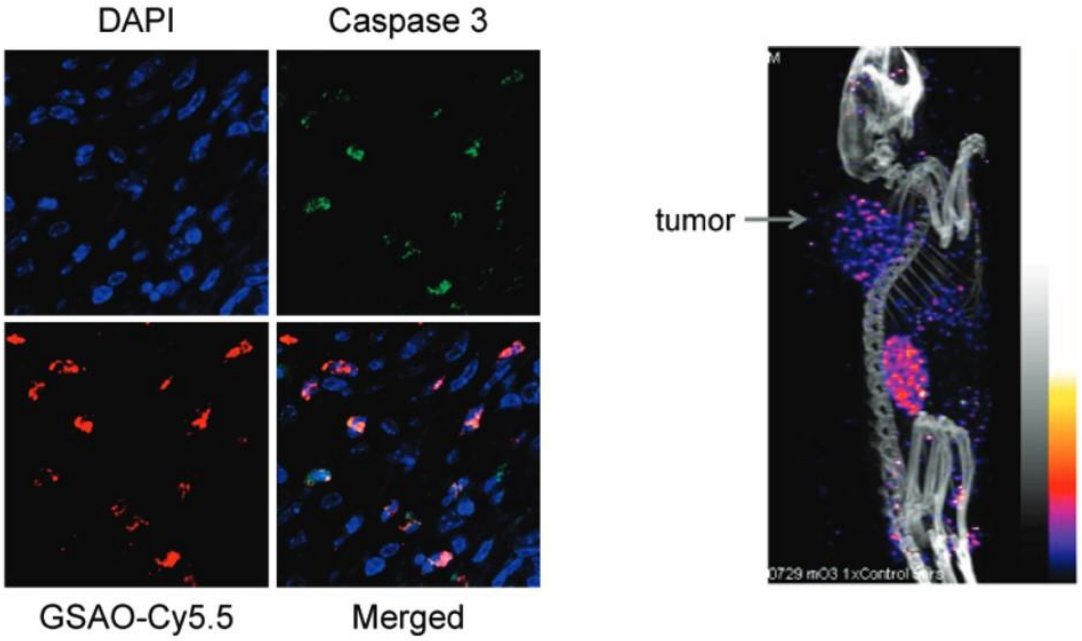

Figure 1.12. Fluorescence confocal microscopy showed cells that were positive for caspase 3 (apoptosis marker) were also positive for Cy5.5-GSAO (left); SPECT/CT image of a mouse bearing a Lewis lung carcinoma tumour in the shoulder area, 5 hours after administered with ^{111}In-DTPA-GSAO in the tail vein (right).[89]

Fluorescent organic (bis)arsenical probes (Figure 1.13) were introduced by Tsein *et al.* 20 years ago and have become the most notable arsenical reagents for imaging

purposes.[17, 91, 92] Fluorescein arsenical hairpin binder bis-EDT (FlAsH-EDT_2) was first reported in 1998[93] followed by resorufin arsenical hairpin binder bisethanedithiol (ReAsH- EDT_2) in 2002.[94] There are two key features of these bis-arsenicals, the first being the arsenic interatomic distances (5-6 Å), which promote strong and highly specific binding to tetracysteine (TC) peptide sequences where two vicinal dicysteines are spaced apart by two intervening amino acid residues (Cys-Cys-Xxx-Xxx-Cys-Cys). The other key feature is rotomer restricted fluorogenicity.[95] FlAsH-EDT_2 and ReAsH-EDT_2 are quenched prior of TC-conjugation and this is thought to be due to photoinduced electron transfer (PET) between freely rotating dithiaarsanes and the fluorophore. Upon TC-conjugation the rotation about the As-Aryl bond is restricted, preventing the PET induced quenching leading to a remarkable (up to 50000x) increase in fluorescent intensity.

The photochemical properties of bis-arsenical fluorescent tags can be readily tuned. While FlAsH-EDT_2 and ReAsH-EDT_2 are green and red emitters respectively, CHoXAsH exhibits blue emission in a region that might be useful as a FRET donor with GFP[94] and fluorescence of BArNile-EDT_2[96] and CrAsH-EDT_2[97] were reported to be dependent upon the environment. Fluorinated bis-arsenical F2FlAsH-EDT_2 has similar wavelength of absorbance and emission compared to FlAsH but with a higher quantum yield and increased photostability. F4FlAsH on the other hand has an emission in a region intermediate to FlAsH and ReAsH and increased fluorescence lifetime. In addition, F2FlAsH and F4FlAsH can both be used as FRET donor and acceptor pairs.[98] Though these tags are optimised for TC-sequences engineered into the termini of native proteons they are less suitable for binding and imaging of dynamic, independently folded CxxC sequences which are ubiquitous in proteins that maintain redox homeostasis. Such targets have been successfully targeted using organic bis-/tris-arsenicals[20] and there is great potential for precision, polymeric arsenicals to be developed to interface, probe and effect (*e.g.* inhibit) these natural redox and protein-folding processes.

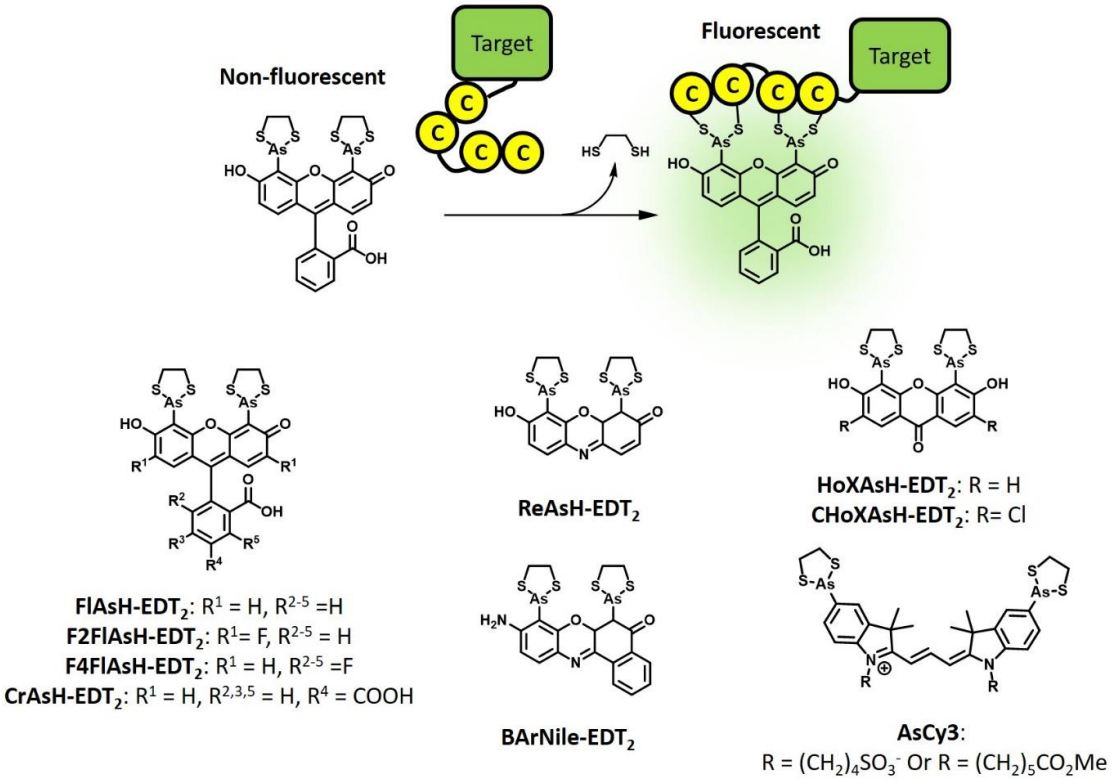

Figure 1.13 Schematic representation of the specificity of bis-arsenicals for tetracysteine sequences and structure for bis-arsenicals synthesized with a range of emission profiles.

A complementary red emitting cyanine-based bisarsenical, AsCy3[99, 100] with larger interatomic distance between the arsenic atoms (14.5 Å) has also been developed, preferentially binding to longer TC with two helical turns (CCKAEAACC). This makes it possible to distinguish between proteins that are simultaneously labelled with FlAsH. Similarly to FlAsH, the fluorescence is dependent on blocking the quenching by dithiaarsanes through interchanging of EDT with the cysteine pairs. The formation of fluorescent complexes with AsCy3 were also observed to form faster, within seconds (compared to a timescale of minutes for ReAsH and FlAsH).

With the development of super high resolution microscopy (sub-diffraction), and the resulting potential for analysing images more accurately, there is a need for probes that can be used with the technology, to generate high quality images. The combination of Cy3-Cy5 has been reported for use in Stochastic Optical Reconstruction Microscopy (STORM).[101] Pulsed red light is used to excite photoswitchable Cy5 into a long lived dark

state, which is then recovered by excitation of proximal Cy3 with green light. The resulting controlled fluorescence allows the high resolution microscopy (below 20 nm) to form the detailed images, using many pictures made into a composite. Squier *et al* reported Cy3-Cy5 derivative, AsCy3Cy5,[102] with Cy3 component as the bis-arsenical scaffold for targeting TC tag. The separation of Cy3 and Cy5 is less than 2.1 nm, which was important as the distance between the dyes for photoactivation of Cy5 is much steeper than FRET (below 3 nm, below 5 nm for FRET).[103] This allowed single molecule imaging of alpha subunit of the RNA polymerase (RpoA) with resolution below 100 nm and potential to be even further enhanced as low as 20 nm.[102]

1.4 Combining nanoparticles and organic arsenicals

While the focus of this literature review is of organic arsenicals, encapsulation and delivery of As_2O_3 using liposomes, polymer nanoparticles, and inorganic nanoparticles has attracted significant attention in an attempt to improve efficacy and mitigate toxicity of As_2O_3chemotherapies. For example, As_2O_3 has been encapsulated in liposomes[104-107] and polymeric nanoparticles[108, 109] for mono and combination therapies through which active targeting can be improved via incorporation of antibodies and ligands on the surfaces. Likewise, inorganic metal-AsO_n@SiO_2 composite nanoparticles have been developed for improved cellular uptake and pH-dependent release of therapeutic As_2O_3.[110-112]

Organic arsenicals with a single arsonic acid group have been employed as surface active ligands for the formation of 2D self-assembled monolayers (SAMs),[113] and for the 3D modification of the Fe_3O_4 nanoparticles.[114] Alkyl arsonic acids have been shown to be versatile and robust ligands for the formation of SAMs at oxide surfaces including titanium oxide and silicon oxide.[113] The alkyl arsonates were more reactive than the related alkyl phosphonates which was exemplified by the formation of alkyl arsonate SAMs at the surface of borosilicate glass which was not possible with alkyl phosphonates. SAMs were characterized by drop-shape analysis (water contact angle), FT-IR and nanoscratching measurements to determine small-scale mechanical properties. Alkyl arsonate SAMs demonstrate greater potential as wear-protection coatings by providing

better protection against micronewtonian forces (nanoscratch) than the phosphonate counterparts. For example, comparing the normalized percentage protection of titanium oxide shows the alkyl arsonate SAMs provide 100% surface protection against micronewtonian forces up to 105 μN whereas phosphonate equivalents afford between 45-75 % protection of the same range.

Inspired by literature associated with the high affinity of arsenic for iron-oxide based absorbent materials (for water purification),[115, 116] azido-functional *p*-arsanilic acid has been investigated as a functional ligand for the stabilization and modification of Fe_3O_4 nanoparticles (Figure 1.14A).[114] Quantitative comparison of surface coverage and packing density respectively revealed that the arsonic acid ligand (32 $\mu mol.g^{-1}$; 1.1 molecules nm^{-1}) performed better than both catechol (20 $\mu mol.g^{-1}$; 0.67 molecules nm^{-1}) and carboxylate (16 $\mu mol.g^{-1}$; 0.55 molecules nm^{-1}) ligand equivalents (Figure 1.14B). Furthermore, the arsonic acid ligands where also found to be more stable than the catechol and carboxylate in cumulative wash cycles between pH 2-9 (Figure 1.14C&D).

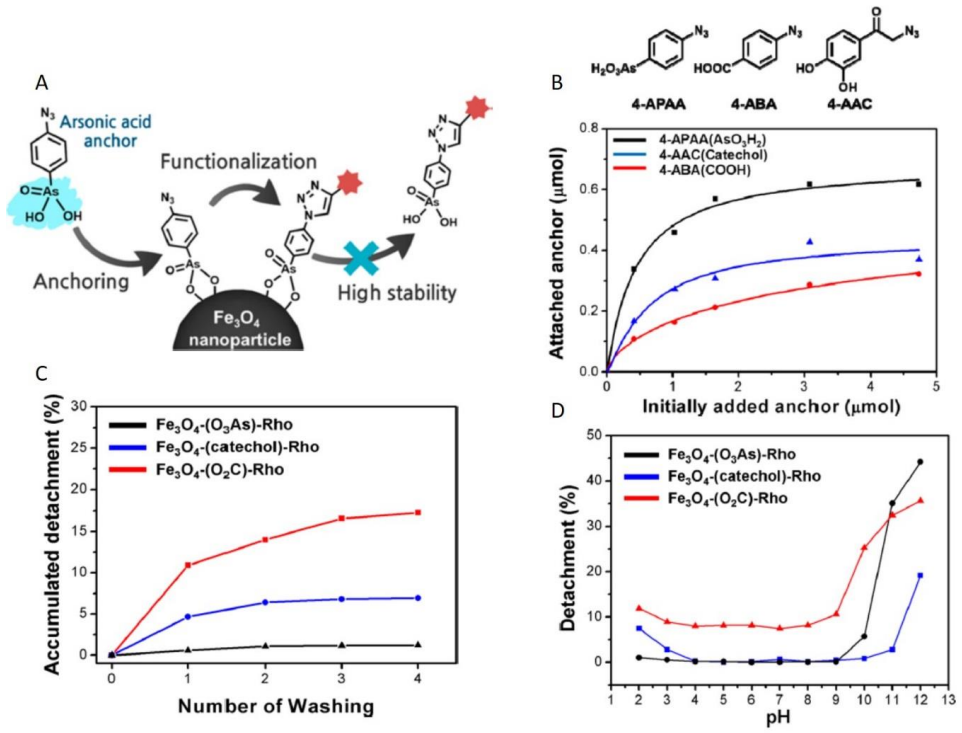

Figure 1.14 A) Schematic representation of the phenylarsonic acid moiety anchoring to the surface of Fe_3O_4; B) Amount of the anchoring as a function of concentration relative to tradition anchoring groups; C) Accumulated detachment of anchoring groups as following aqueous wash cycles; D) anchor stability as a function of pH.[114]

Contrary to this data, arsenoacetic acid ligands, contain both arsonic acid and carboxylic acid functional groups, have been reported to undergo ligand exchange with undecanoic acid ligands at surface of Fe_3O_4 nanoparticles. This exclusively yields the carboxylate coordinated nanoparticles with the arsonic acid group presented at the surface of the particles.[117] In this case, the lability of the C-As bond of alkyl arsonic acids in the presence of thiol reagents was exploited to elicit tumour specific cytotoxicity. The alkyl arsonic acid group (As(V)) presenting nanoparticles were designed as anticancer prodrugs which could be activated in the presence of elevated thiol (GSH) concentrations associated with cancer cells. Using HepG2 and HeLaS3 as model cancer cells and primary mouse hepatocytes as non-malignant controls, reductive cleavage of the alkyl arsonic acid, with release of toxic As(III) species, was shown to be more prevalent in the cancer cell lines reducing viability to 40% (HepG2) and 70% (HeLaS3) at 100 $\mu g.mL^{-1}$ whereas viability of the hepatocytes was maintained across the concentration range (Figure 1.15). As this

specificity is attributed to the redox environment, arsonic acid functional materials combined with imaging modalities (including MRI, fluorescence, radiolabels) could be developed as theranostics for the diagnosis (*e.g.* GSH biomarkers), treatment and tracking of cancer cells.

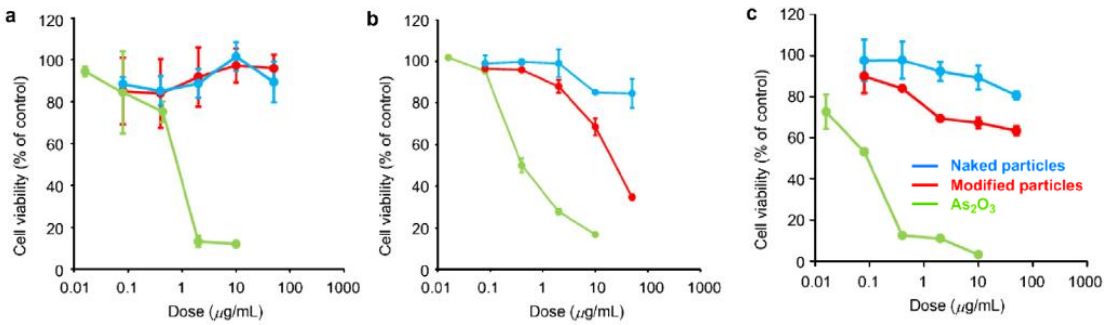

Figure 1.15 Effect of As_2O_3, naked iron oxide nanoparticles, and the modified nanoparticles on the viability of normal cells ((a) primary mouse hepatocytes) and tumor cell lines ((b) HepG2 and (c) HeLaS3). Cells were incubated with various concentrations of the samples for 72 h. Results are expressed as viability (% viable cells in comparison with the control) versus the arsenic content for upper three graphs.[117]

Soft polymer and protein based nanoparticles have also been prepared for the delivery of arsenicals to cancer cells. An amphiphilic, biodegradable diblock copolymer PEG-*b*-(α-carboxylate-ε-caprolactone) (PEG-*b*-PCCL) was synthesized by ROP. Thiol groups, for arsenical conjugation, were introduced into the hydrophobic caprolactone block via amidation of the pendant carboxylate group using mercaptohexylamine (PEG-*b*-PCCLSH).[118] The resulting thiol functional block polymers could be assembled in water, toluene and DMAc forming particles with D_h = 136 nm, 35 nm and 54 nm respectively. In the presence of trivalent organic arsenical phenylarsine oxide (PAO), self-assembly resulted in the formation of PAO-functional nanoparticles whereby the PAO could be covalently bound through conjugation to one or two pendant thiol groups, or physically encapsulated by electrostatic interactions (Scheme 1.7). Particle size analysis revealed that the PAO-functional particles were slightly larger in water (D_h = 151 nm) and more stable with cmc decreasing from 92 $\mu g.mL^{-1}$ to 70 $\mu g.mL^{-1}$ providing indirect evidence for the covalent mode of encapsulation which could proceed with a degree of stabilizing inter-chain cross-linking.

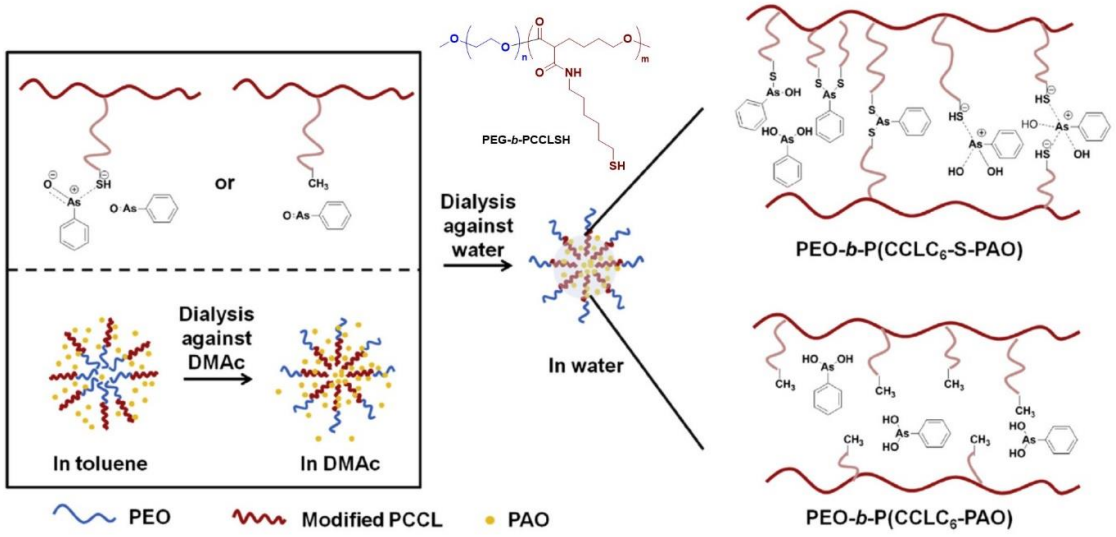

Scheme 1.7 Encapsulation of PAO into PEG-*b*-PCCLSH and PEG-*b*-PCCL micelles. The unloaded PAO was removed by sequential dialysis against DMAc and water. Possible interactions between PAO and polymers include 1 sulfur residue on 1 As atom, 2 sulfur residues on 1 As atom (intra-/interchain) and ionic interactions between thiol groups and hydrolyzed PAO. When no thiol groups exist in PEG-*b*-PCCL, the encapsulation of PAO in PEO-b-PCCL micelles is based on only hydrophobic interaction between PAO and PCCL blocks.[118]

Further evidence for was drawn from maximum loading of PAO into the thiol functional particles (2.4 wt%) which was significantly greater than a non-thiol functional control particles (0.17 wt%). Chemical release studies showed that PAO release could be triggered by the addition of GSH, which is advantageous for targeted release in cancer cells. Indeed, IC_{50} values (MDA-MB-435) of the PAO-functional particles were similar to PAO (< 0.04 mg.mL^{-1}), but there was little selectivity of cancer cells using this formulation as similar IC_{50} values were obtained against health cell lines (human fibroblast BJ cells). This was attributed to the polymer concentration range studied (0.00004-0.04 mg/mL^{-1}) which was below the cmc of the PAO-nanoparticles.

In order to address the thermodynamic stability and improve the cancer cell targeting of As-functional nanoparticles, terpolymers in which the hydrophobic α-carboxylate-ε-caprolactone block has been modified to include additional ε-caprolactone, to increase hydrophobicity, have been prepared.[119] The lowest cmc value was obtained from the triblock PEG-*b*-PCCLSH-*b*-PCL (11 µg.mL^{-1}) compared to PEG-*b*-PCL-*b*-PCCLSH and PEG-*b*-(PCCLSH-*co*-PCL) (36 µg.mL^{-1}). Here, sodium arsenite was used for

encapsulation of a trivalent arsenical and loadings of 3-4 wt% were possible via similarly covalent and physical interactions described above. Release profiles of As-loaded particles derived from the terpolymers correlated with particle stability and As-loading. Finally, cell uptake (MDA-MB-435) was correlated to the properties (stability, surface charge, As-loading/release) of the As-functional particles. It was found that PEG-*b*-PCCLSH-*b*-PCL > PEG-*b*-PCL-*b*-PCCLSH and PEG-*b*-(PCCLSH-*co*-PCL) > free As(III) which raises the possibility of fine-tuning the particle properties by manipulating polymer composition which could be advantageous for arsenical and/or multidrug co-encapsulation for combination chemotherapies (Figure 1.16).

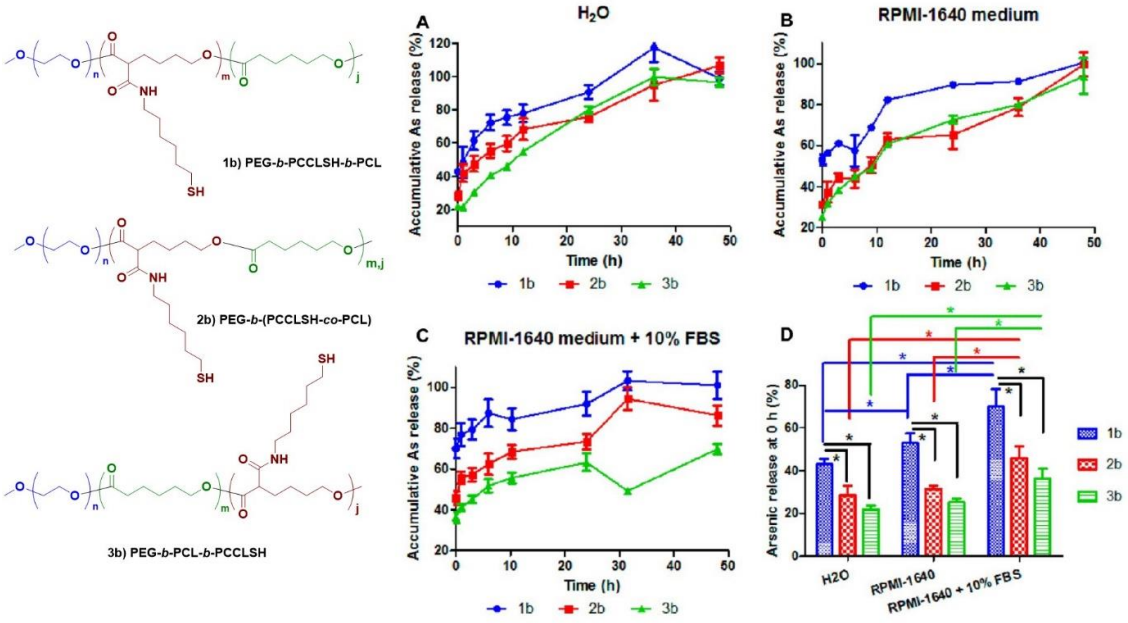

Figure 1.16 In vitro release of As(III) from micelles at 37 °C in (A) water, (B) RPMI-1640 cell culture medium, and (C) RPMI-1640 medium supplemented with 10% FBS. Data are presented as mean ± SD (n = 3) of triplicate samples. The arsenic release from the micelles at 0 h was reorganized into a bar graph (D). One-way ANOVA with post-test of Tukey's multiple comparison test was performed among three types of arsenic encapsulated micelles in a same solvent and among micelle solutions prepared in three different solvents. Micelle 1b had significantly higher initial release than 2b or 3b (*P < 0.05) in H_2O, RPMI-1640, and RPMI 1640 supplemented with 10% FBS. Micelles prepared in RPMI-1640 supplemented with 10% FBS had significantly higher initial release than the corresponsive micelles prepared in H2O or in RPMI-1640 (*P < 0.05).[119]

An alternative method for improving active targeting to cancer cells involves the conjugation of the ligands to the surfaces of nanoparticles. The polymeric system

described above has been adopted to prepare protein-based nanoparticles/nanodrugs. Folate-labelled Human-Serum-Albumin (FA-HSA) contains one free thiol group and 17 disulfide bonds which can readily exposed under reductive conditions in order to interact and form covalent bonds with As(III)-species, in this case arsenic trioxide (ATO).[120] The average loading of ATO (ICP-OES) was found to be ~4 ATO per FA-HSA and discrete particles of D_h = 43 nm were identified by DLS. Release of the ATO was dependent upon the pH and reductive environment with enhanced rates of release as the pH was lowered or [GSH] increased. Competition assays in the presence and absence of free folate revealed that the FA-HSA-ATO particles targeted folate receptor-β (FRβ, K562 cells). Furthermore, treatment of these cells with FA-HAS-ATO stimulated up regulation of the receptor which enhanced cellular uptake and accumulation in a range of FRβ-positive cell lines. This was supported by in-vivo evaluation (Figure 1.17) that demonstrated the FA-HSA-ATO particles had blood circulation half-life, which coupled with the targeting imposed by the FA-ligands resulted in greater tumour growth inhibition (45 day survival) compared to only ATO (28 day survival) and HSA-ATO (36 day survival) in the absence of FA-ligands. This is promising for targeted delivery of arsenicals to a broader range of malignancies (*e.g.* chronic myeloid leukaemia).

k

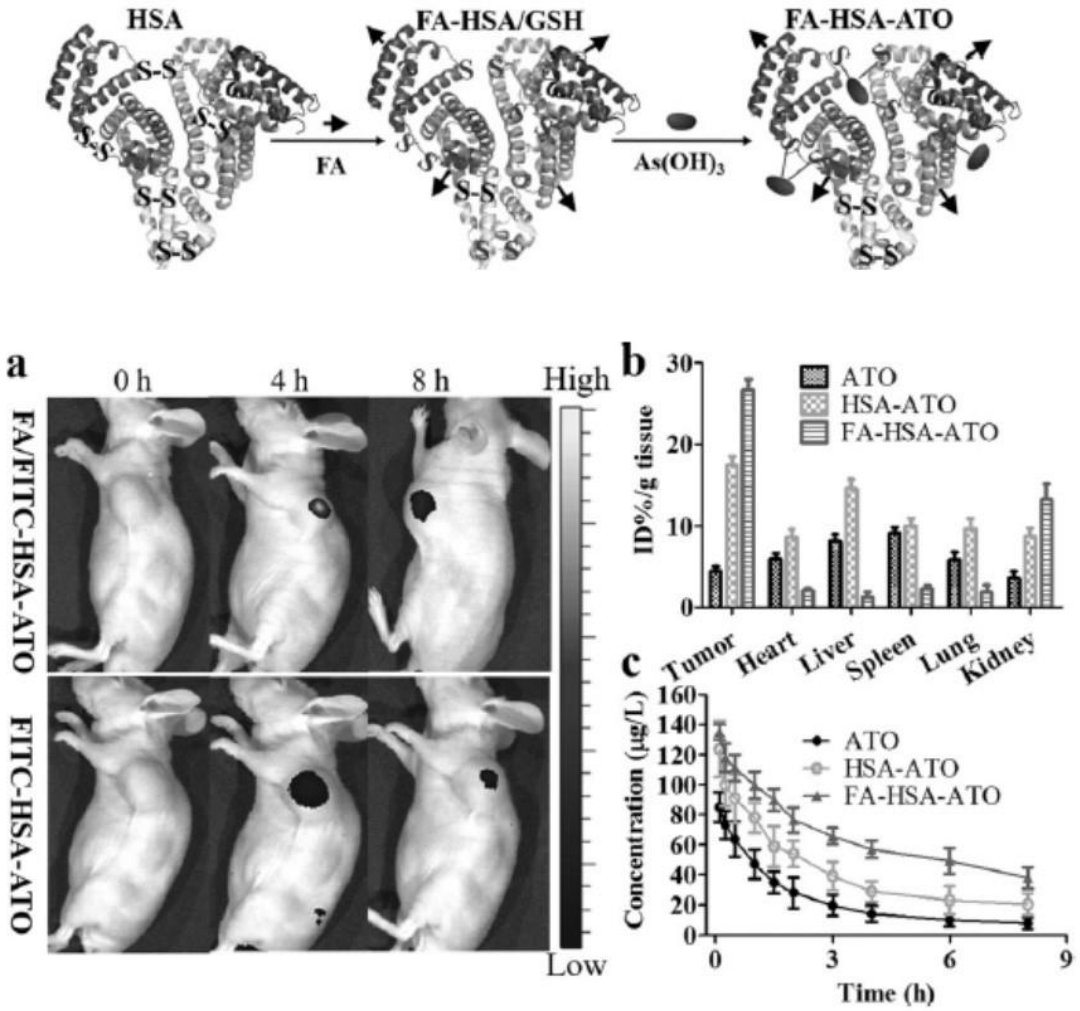

Figure 1.17 Schematic for the synthesis of FA-HAS-ATO and in vivo targeting ability, blood circulation, and tissue biodistribution of FA-HSA-ATO. a) In vivo targeting ability of FITC HSA-ATO injected i.v. in K562 tumor-bearing mouse. b) Biodistribution of ATO, HSA–ATO, and FA-HSA-ATO in main mouse organs, as determined by ICP-OES. Results are expressed as a percentage of the total injected dose per tissue mass (% ID g^{-1}). Data are shown as mean:SD (n=3). c) Blood circulation curves of ATO, HSA–ATO, and FA-HSA-ATO in mice, as determined by ICP-OES. Data are shown as mean:SD (n=3).[120]

1.5 Arsenolipids and arsenoliposomes

The efficacy of ATO against hematologic malignancies is yet to be matched for solid tumours. A number of liposomal strategies have been considered and are under development in order to improve the therapeutic index of ATO as a single and combination chemotherapy.[107, 121-123] These liposomes are formulated from traditional PEG, phosphocholine and cholesterol-based lipids that exploit metal-ion gradient-loading

mechanisms to load inorganic As(III) in the form of arsenous acid. Here we will focus on organic arsenical containing liposomes for the formulation of arsonoliposomes, which have also been reported and investigated for use in drug delivery (Figure 1.18).[124-126]

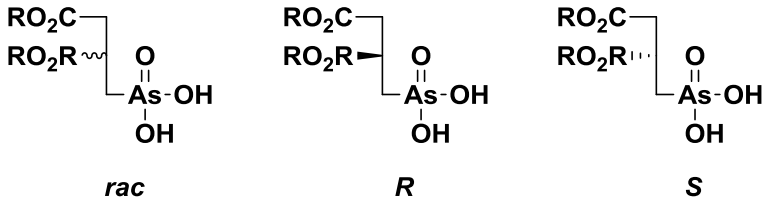

Figure 1.18 General structure of arsonolipid constituents of arsenoliposomes.

Arsonolipids are synthetic analogues of naturally occurring arsenolipids.[127] They are related to conventional phosphonolipids through the polar head group with the phosphonate being replaced by arsonate. The typical route the arsonolipids involves ring-opening of glycidol to with sodium arsenite to give the key 1,2-dihydroxypropyl-3-arsonic acid intermediate as a mixture of diastereomers (*rac*-, *R*-, *S*-).[128] Acylation of the mono- and di-tetrabutylammonium salts of the resulting acids furnishes the arsonolipids in 20-40% yield after neutralization.[129, 130] This yield can be improved by reducing the arsonic acid (As(V)) to a dithioarsonite (As(III)) before diol acylation and oxidation of the As(III) back to As(V) using H_2O_2 (35-55%).[131] Other mono-arsonolipids have been synthesized in this way from 2,3,4-trihydroxybutylarsonic acid, the product of ring-opening of 3,4-epoxybutane-1,2-diol by sodium arsenite.[132] Pseudo-arsonolipids analogues, containing *bis*-arsonic acid groups, have also be synthesized from epihalohydrin[133] and 1,4-dibromo-2,3-butanediol[134] respectively.

Conventional approaches to liposome formation including thin-film hydration, sonication and reversed phase evaporation were not successful for the preparation of arsonoliposomes. However, an adaptation of the 'bubble method'[135] allowed fabrication of pure (C_{12-18}; D_h = 251 – 329 nm) and mixed (with phospholipids; D_h = 247-346 nm) arsonolipids either in the presence or absence of cholesterol the sizes of which could be reduced by ~ 50% when subjected to probe sonication immediately after formation.[136] The physiochemical effects of changing the arsonolipid (C_{12-18})[137] and overall lipid

composition[138] of the vesicles has been evaluated based on the resulting vesicle size distribution, surface charge, encapsulation and retention (of hydrophilic cargo) efficiency. For example, in mixed arsonolipids the size of vesicles increases as function of the arsonolipid content. Incorporation of PEGylated phospholipids into these liposome compositions results in small changes in vesicle sizes (80-100 nm), decreases in surface ζ-potential by a factor of 10 and an enhancement in stability in presence of plasma proteins and divalent cations (*e.g.* Ca^{2+}).[139, 140]

Pharmacokinetics and biodistribution profiles of arsonolipids revealed that lipid composition had a significant effect on liposome stability and distribution after intraperitoneal administration.[141, 142] For example, arsenic levels in the blood were much higher for pegylated-arsonoliposomes and mixed arsonoliposomes containing 1,2-distearoyl-*sn*-glycero-3-phosphocholine (DSPC; 11.1 – 21.7 % of injected dose at 2 h) than for those containing phosphatidylcholine (PC; 0.269 % of injected dose at 3 h).

The intrinsic antiparasitic and anticancer activity of arsonoliposomes, focusing on compositions that include C_{16} arsonolipids (10/27 mol%), pegylated/non-pegylated phospholipids and cholesterol (2 : 1 lipid/cholesterol) have been studied *in vitro* and briefly *in vivo*. Antileishmanial activity was measured again two wild type and two drug-resistant lines of *Leishmania*. Arsonolipids simply dispersed in DMSO were not active (IC_{50} > 100 μg.mL^{-1}), while arsonoliposomes were active (IC_{50} 0.21 – 5.88 μM) with greater activity exhibited against the resistant *Leishmania*. Structurally, the mixed arsonolipids were also show to be more active than the liposomes composed entire of arsonolipids.[143] This trend was also observed against an acute strain of *Trypanosoma brucei brucei* which inspired further *in vitro* and *in vivo* evaluation against a chronic trypanosome model. Here the liposome composition had a significant effect on the antitrypanosomal activity with the PC-based mixed arsonoliposomes showing activity against the acute strain model whilst more stable DSPC-based mixed arsonolipids, hypothesized to be more suitable for treatment of the chronic infection, were inactive.[144] This contradiction of the pharmacokinetics reported[141, 142] indicates that the balance between vesicle membrane fluidity (PC vs DSPC) and hematological stability is crucial

to maximize activity which implies that pegylated PC-based arsonolipids could be candidates for treatment of chronic *Trypanosoma* strains.

Thus far anticancer activity of arsonoliposomes has only been evaluated *in vitro* with particular focus on the effects of the arsonolipid components[137] and the overall liposome composition.[145] Activity has been measured against two 'normal' cell lines (HUVEC, RAME) and a range of cancer cells with conventional phospholipid analogues employed as As-free controls.[145, 146] In line antiparasitic activity, unformulated arsonolipids were not active.[130] Conversely, the preliminary results relating to all arsonoliposomes studied validates the working hypothesis that the presence of arsenic in the vesicle membrane activates arsonoliposomes against cancer cells to much greater extent than 'normal' cells (*e.g.* IC_{50} HL-60 = 0.85 μM; IC_{50} HUVEC = 253 μM). A general mechanism of arsonoliposome toxicity is currently unknown, with C_{12}-based formulations causing cell death by apoptosis in a similar fashion to ATO, whilst $C_{14,16,18}$-based formulations show little evidence of apoptosis. Arsonoliposomes do show enhanced interactions with cancer cells (HL-60) compared to 'normal' cells (HUVEC),[145] which is opposite to what has been reported for conventional phospholipid-based liposomes,[147] and this could be attributed, in part, to the enhanced cellular uptake and toxicity effects of arsonoliposomes. The reactivity of arsonic acid groups, present on the vesicle surface, for thiol groups has also been implicated as a trigger for site specific activity via destabilization of the vesicles at cancer cells which possess higher local concentrations of thiol containing reagents such as GSH.[148] The potential of combining the intrinsic anticancer activity of the arsonoliposomes with the loading of synergistic therapeutics (through control of the vesicle membrane properties) warrants further investigation and *in vivo* evaluation.

1.6 Conclusions and outlook

Though the use of arsenicals in polymer and biomaterials science is not widespread, there are examples of main-chain, side-chain and end-group functional polymeric arsenicals that have been employed for applications ranging from macromolecular chemotherapeutics to flocculants. Appreciation for the distinctive reactivity of the As(V) and As(III) has further been exploited to prepare conjugated vinylene-arsine polymers and highly specific thiol reactive polymeric arsenical scaffolds. Higher order structures including arsenoliposomes and self-assembled polymeric arsenical nanoparticles, with intrinsic bioactivity and/or drug delivery capabilities have also been prepared from discrete arsonolipids and block copolymeric arsenicals respectively. The latter are synthetically accessible through the advances made in RDRP over recent years. We and others have only just started to prepare well-defined As-functional materials, so there is still much, and we are excited to learn about the physiochemical and biochemical properties of these polymers and nanoparticles.

The most recognized application of organic arsenicals is in bio-imaging which has been achieved using pro-fluorescent bis-arsenicals, radiolabelled polymeric arsenicals and radio-labeled protein/antibody-As conjugates. In all cases, the imaging output relies on the affinity of As(III) for thiols, either through simple conjugation of the imaging motif to a synthetic or biological scaffold, or through targeting engineered protein sequences for highly specific, thermodynamically driven labelling. The notion of affinity/avidity in relation to As-(poly)thiol interactions and the chelate effect has been demonstrated using organic arsenicals, whereby bis- and tris-arsenicals bind (di)thiol rich proteins more strongly than mono-arsenical adducts. It is this correlation between protein sequences (*i.e.* (di)thiol distribution) and (poly)arsenical affinity/specificity that is perhaps the most stimulating area of future research. In light of what is already known regarding the chemotherapeutic (and indeed cytotoxic) mechanism of action of organic arsenicals, there is great potential in combining the chemical and biological activity of arsenic to develop of a new platform of reactive/responsive polymers and nanomaterials. Thus, it is possible to imagine that arsenical spacing and distribution can be controlled through the synthetic

strategy, whilst the reactivity of the arsenicals (As(V) vs As(III)), and therefore the specificity for a given protein or family of proteins could be temporally controlled, alluding to the possibility of As-based precision chemotherapy and/or diagnosis in nanomedicine.

1.7 References

1. K. J. Williams, *J. R. Soc. Med.*, 2009, **102**, 343-348.
2. Z.-Y. Wang and Z. Chen, *Blood*, 2008, **111**, 2505-2515.
3. P. J. Dilda and P. J. Hogg, *Cancer Treat. Rev.*, **33**, 542-564.
4. S.-J. Chen, G.-B. Zhou, X.-W. Zhang, J.-H. Mao, H. de The and Z. Chen, *Blood*, 2011.
5. N. C. Lloyd, H. W. Morgan, B. K. Nicholson and R. S. Ronimus, *Angew. Chem., Int. Ed.*, 2005, **44**, 941-944.
6. M. M. Kish and R. E. Viola, *Inorg. Chem.*, 1999, **38**, 818-820.
7. H. B. F. Dixon, in *Adv. Inorg. Chem.*, ed. A. G. Sykes, Academic Press, 1996, vol. Volume 44, pp. 191-227.
8. R. Betz and P. Klüfers, *Inorg. Chem.*, 2009, **48**, 925-935.
9. A. R. Tapia-Benavides, L. H. Mendoza-Huizar, F. Pérez-García, H. Tlahuext, A. Alvarez and M. Tlahuextl, *Inorg. Chem.*, 2010, **49**, 1496-1502.
10. J. Messens and S. Silver, *J. Mol. Biol.*, 2006, **362**, 1-17.
11. A. M. Spuches, H. G. Kruszyna, A. M. Rich and D. E. Wilcox, *Inorg. Chem.*, 2005, **44**, 2964-2972.
12. V. P. Whittaker, *Biochemical Journal*, 1947, **41**, 56-62.
13. L. Horsley, J. Cummings, M. Middleton, T. Ward, A. Backen, A. Clamp, M. Dawson, H. Farmer, N. Fisher, G. Halbert, S. Halford, A. Harris, J. Hasan, P. Hogg, G. Kumaran, R. Little, G. J. M. Parker, P. Potter, M. Saunders, C. Roberts, D. Shaw, N. Smith, J. Smythe, A. Taylor, H. Turner, Y. Watson, C. Dive and G. C. Jayson, *Cancer Chemother. Pharmacol.*, 2013, **72**, 1343-1352.
14. P. J. Dilda, S. Decollogne, L. Weerakoon, M. D. Norris, M. Haber, J. D. Allen and P. J. Hogg, *J. Med. Chem.*, 2009, **52**, 6209-6216.
15. J. Wu, F. Muggia, C. Henderson, L. Feun, P. V. Veldhuizen, P. Gold, H. Zheng, G. A. 66201, J. Lewis and A. X. Zhu, *J. Clin. Oncol.*, 2009, **27**, e15630-e15630.
16. D. Park, J. Chiu, G. G. Perrone, P. J. Dilda and P. J. Hogg, *Cancer Cell Int.*, 2012, **12**, 11.
17. R. A. Scheck and A. Schepartz, *Acc. Chem. Res.*, 2011, **44**, 654-665.
18. A. Pomorski and A. Krężel, *ChemBioChem*, 2011, **12**, 1152-1167.
19. B. Chen, Q. Liu, A. Popowich, S. Shen, X. Yan, Q. Zhang, X.-F. Li, M. Weinfeld, W. R. Cullen and X. C. Le, *Metallomics*, 2015, **7**, 39-55.
20. A. Sapra, D. Ramadan and C. Thorpe, *Biochemistry*, 2015, **54**, 612-621.

21. S. Shen, X.-F. Li, W. R. Cullen, M. Weinfeld and X. C. Le, *Chem. Rev.*, 2013, **113**, 7769-7792.
22. D. Fass and C. Thorpe, *Chem. Rev.*, 2018, **118**, 1169-1198.
23. D. Ramadan, P. C. Rancy, R. P. Nagarkar, J. P. Schneider and C. Thorpe, *Biochemistry*, 2009, **48**, 424-432.
24. C. E. Carraher, *J. Polym. Sci. Part A-1: Polym. Chem.*, 1969, **7**, 2351-2358.
25. C. E. Carraher and M. R. Roner, *J. Organomet. Chem.*, 2014, **751**, 67-82.
26. C. E. Carraher and W. G. Moon, *Eur. Polym. J.*, 1976, **12**, 329-331.
27. J.-X. Liu, G.-B. Zhou, S.-J. Chen and Z. Chen, *Curr. Opin. Chem. Biol.*, 2012, **16**, 92-98.
28. C. E. Carraher, N. T. C. Truong, M. R. Roner, A. Moric and N. T. Trang, *J. Chin. Adv. Mater. Soc.*, 2013, **1**, 134-150.
29. A. S. Don, O. Kisker, P. Dilda, N. Donoghue, X. Zhao, S. Decollogne, B. Creighton, E. Flynn, J. Folkman and P. J. Hogg, *Cancer Cell*, 2003, **3**, 497-509.
30. C. E. Carraher, M. R. Roner, N. Pham and A. Moric-Johnson, *J. Macromol. Sci. Part A*, 2014, **51**, 547-556.
31. C. E. Carraher, M. R. Roner, M. Ayoub, N. Pham and A. Moric-Johnson, *Int. J. Polym. Mater. Polym. Biomater.*, 2015, **64**, 311-319.
32. C. E. Carraher, M. R. Roner, F. Mosca, A. Moric-Johnson, L. C. Miller, J. D. Einkauf, F. Russell and P. Slawek, *J. Inorg. Organomet. Polym. and Mater.*, 2017, **27**, 1627-1639.
33. C. E. Carraher, M. R. Roner, R. Thibodeau and A. M. Johnson, *Inorg. Chim. Acta*, 2014, **423**, 123-131.
34. C. E. Carraher, M. R. Roner, J. Dorestant, A. Moric-Johnson and M. H. Al-Huniti, *J. Inorg. and Organomet. Polym. Mater.*, 2015, **25**, 400-410.
35. *Conjugated Polymer Synthesis*, Wiley-VCH Verlag GmbH & Co. KGaA, 2010, pp. I-XV.
36. K. Naka and Y. Chujo, in *Conjugated Polymer Synthesis*, Wiley-VCH Verlag GmbH & Co. KGaA, 2010, pp. 229-249.
37. J. P. Green, Y. Han, R. Kilmurray, M. A. McLachlan, T. D. Anthopoulos and M. Heeney, *Angew. Chem.*, 2016, **128**, 7264-7267.
38. Y. Chujo, I. Tomita, Y. Hashiguchi, H. Tanigawa, E. Ihara and T. Saegusa, *Macromolecules*, 1991, **24**, 345-348.
39. K. Naka, *Polym. J.*, 2008, **40**, 1031.
40. A. Ogawa, H. Yokoyama, K. Yokoyama, T. Masawaki, N. Kambe and N. Sonoda, *The J. Org. Chem.*, 1991, **56**, 5721-5723.
41. L. R. Smith and J. L. Mills, *J. Organomet Chem.*, 1975, **84**, 1-15.

42. H. J. Breunig, in *Organic Arsenic, Antimony and Bismuth Compounds (1994)*, John Wiley & Sons, Ltd, 2004, pp. 563-577.
43. J. W. B. Reesor and G. F. Wright, *J. Org. Chem.*, 1957, **22**, 382-385.
44. K. Takeda and K. Shiraishi, *Phys Rev. B*, 1998, **57**, 6989-6997.
45. K. Naka, T. Umeyama and Y. Chujo, *J. Am. Chem. Soc.*, 2002, **124**, 6600-6603.
46. T. Umeyama, K. Naka and Y. Chujo, *Macromolecules*, 2004, **37**, 5952-5958.
47. T. Umeyama, K. Naka, A. Nakahashi and Y. Chujo, *Macromolecules*, 2004, **37**, 1271-1275.
48. T. Umeyama, K. Naka and Y. Chujo, *J. Polym. Sci., Part A: Polym. Chem.*, 2004, **42**, 3604-3611.
49. K. Naka, A. Nakahashi and Y. Chujo, *Macromolecules*, 2007, **40**, 1372-1376.
50. K. Naka, A. Nakahashi and Y. Chujo, *Macromolecules*, 2006, **39**, 8257-8262.
51. T. Umeyama, K. Naka and Y. Chujo, *Macromolecules*, 2004, **37**, 3623-3629.
52. T. Umeyama, K. Naka and Y. Chujo, *J. Polym. Sci., Part A: Polym. Chem.*, 2004, **42**, 3023-3028.
53. T. Umeyama, K. Naka, M. D. Bravo, A. Nakahashi and Y. Chujo, *Polym. Bull.*, 2004, **52**, 191-199.
54. A. Nakahashi, M. Bravo, K. Naka and Y. Chujo, *J. Phys: Conf. Ser.*, 2009, **184**, 012021.
55. K. Naka, A. Nakahashi, M. Bravo and Y. Chujo, *Appl. Organomet. Chem.*, 2010, **24**, 573-575.
56. Đ. U. Miodragović, J. A. Quentzel, J. W. Kurutz, C. L. Stern, R. W. Ahn, I. Kandela, A. Mazar and T. V. O'Halloran, *Angew. Chem. Int. Ed.*, 2013, **52**, 10749-10752.
57. R. F. Hirsch, R. E. Gancher and F. R. Russo, *Talanta*, 1970, **17**, 483-489.
58. J. S. Fritz and E. M. Moyers, *Talanta*, 1976, **23**, 590-593.
59. J. García-Serrano, A. M. Herrera, F. Pérez-Moreno, M. A. Valdez and U. Pal, *Journal of Polym. Sci. Part B: Polym. Phys.*, 2006, **44**, 1627-1634.
60. M. J. Percino, V. M. Chapela, R. Gutiérrez-Pérez and A. M. Herrera, *Des. Monomers Polym.*, 2000, **3**, 155-160.
61. M. J. Percino, V. M. Chapela, T. Zayas and C. R. de Barbarín, *J. Chem. Crystallogr.*, 2002, **32**, 307-314.
62. M. J. Percino, V. M. Chapela, C. Rodríguez-Barbarín and S. Bernès, *J. Mol. Struct.*, 2001, **562**, 45-53.
63. A. M. Herrera, J. García-Serrano, J. G. Alvarado-Rodríguez, J. F. Rivas-Silva and U. Pal, *Acta Crystallogr. Sect. E*, 2005, **61**, m2752-m2754.

64. J. M. Hernández, A. M. Herrera, J. García-Serrano and J. F. Rivas-Silva, *Int. J. Quantum Chem*, 2002, **88**, 342-346.
65. T. Zayas, M. J. Percino, J. Cardoso and V. M. Chapela, *Polymer*, 2000, **41**, 5505-5512.
66. B. A. Yáñez-Martínez, J. Percino and V. M. Chapela, *J. Appl. Polym. Sci.*, 2010, **118**, 2849-2858.
67. G. Soriano-Moro, J. Percino, M. Cerón, M. Castro and V. Chapela, *J. Poly. Res.*, 2014, **21**, 1-11.
68. J. García-Serrano, U. Pal, A. M. Herrera, P. Salas and C. Ángeles-Chávez, *Chem. Mater.*, 2008, **20**, 5146-5153.
69. K. Matyjaszewski, *Macromolecules*, 2012, **45**, 4015-4039.
70. A. Anastasaki, V. Nikolaou, G. Nurumbetov, P. Wilson, K. Kempe, J. F. Quinn, T. P. Davis, M. R. Whittaker and D. M. Haddleton, *Chem. Rev.*, 2016, **116**, 835-877.
71. A. Anastasaki, V. Nikolaou and D. M. Haddleton, *Polym. Chem,*, 2016, **7**, 1002-1026.
72. D. J. Keddie, *Chem. Soc. Rev.*, 2014, **43**, 496-505.
73. J. Nicolas, Y. Guillaneuf, C. Lefay, D. Bertin, D. Gigmes and B. Charleux, *Prog. Polym. Sci.*, 2013, **38**, 63-235.
74. G. Gody, T. Maschmeyer, P. B. Zetterlund and S. Perrier, *Nat. Commun.*, 2013, **4**, 2505.
75. N. G. Engelis, A. Anastasaki, G. Nurumbetov, N. P. Truong, V. Nikolaou, A. Shegiwal, M. R. Whittaker, T. P. Davis and D. M. Haddleton, *Nat Chem*, 2017, **9**, 171-178
76. A. Anastasaki, V. Nikolaou, G. S. Pappas, Q. Zhang, C. Wan, P. Wilson, T. P. Davis, M. R. Whittaker and D. M. Haddleton, *Chemical Science*, 2014, **5**, 3536-3542.
77. A. H. Soeriyadi, C. Boyer, F. Nyström, P. B. Zetterlund and M. R. Whittaker, *J. Am. Chem. Soc.*, 2011, **133**, 11128-11131.
78. A. Anastasaki, B. Oschmann, J. Willenbacher, A. Melker, M. H. C. V. Son, N. P. Truong, M. W. Schulze, E. H. Discekici, A. J. McGrath, T. P. Davis, C. M. Bates and C. J. Hawker, *Angew. Chem. Int. Ed.*, 2017, **56**, 14483-14487.
79. P. Wilson, A. Anastasaki, M. R. Owen, K. Kempe, D. M. Haddleton, S. K. Mann, A. P. Johnston, J. F. Quinn, M. R. Whittaker and P. J. Hogg, *J. Am. Chem. Soc.*, 2015, **137**, 4215-4222.
80. F. Alsubaie, A. Anastasaki, V. Nikolaou, A. Simula, G. Nurumbetov, P. Wilson, K. Kempe and D. M. Haddleton, *Macromolecules*, 2015, **48**, 6421-6432.
81. C. Footman, P. A. J. M. de Jongh, J. Tanaka, R. Peltier, K. Kempe, T. P. Davis and P. Wilson, *Chem. Commun.*, 2017, **53**, 8447-8450.
82. J.-M. Noy, H. Lu, P. J. Hogg, J.-L. Yang and M. Stenzel, *Bioconjugate Chem.*, 2018, **29**, 546-558.

83. C. Huang, Q. Yin, W. Zhu, Y. Yang, X. Wang, X. Qian and Y. Xu, *Angew. Chem. Int. Ed.*, 2011, **50**, 7551-7556.
84. X. Yan, J. Li, Q. Liu, H. Peng, A. Popowich, Z. Wang, X.-F. Li and X. C. Le, *Angew. Chem. Int. Ed.*, 2016, **55**, 14051-14056.
85. M. Jennewein, M. A. Lewis, D. Zhao, E. Tsyganov, N. Slavine, J. He, L. Watkins, V. D. Kodibagkar, S. O'Kelly, P. Kulkarni, P. P. Antich, A. Hermanne, F. Rösch, R. P. Mason and P. E. Thorpe, *Clin. Cancer Res.*, 2008, **14**, 1377-1385.
86. P. A. Ellison, T. E. Barnhart, F. Chen, H. Hong, Y. Zhang, C. P. Theuer, W. Cai, R. J. Nickles and O. T. DeJesus, *Bioconjugate Chem.*, 2016, **27**, 179-188.
87. A. J. DeGraffenreid, Y. Feng, C. L. Barnes, A. R. Ketring, C. S. Cutler and S. S. Jurisson, *Nucl. med. biol.*, 2016, **43**, 288-295.
88. M. M. Herth, M. Barz, M. Jahn, R. Zentel and F. Rösch, *Bioorg. Med. Chem. Lett.*, 2010, **20**, 5454-5458.
89. D. Park, A. S. Don, T. Massamiri, A. Karwa, B. Warner, J. MacDonald, C. Hemenway, A. Naik, K.-T. Kuan, P. J. Dilda, J. W. H. Wong, K. Camphausen, L. Chinen, M. Dyszlewski and P. J. Hogg, *J. Am. Chem. Soc.*, 2011, **133**, 2832-2835.
90. N. Tahara, H. R. Zandbergen, H. J. de Haas, A. Petrov, R. Pandurangi, T. Yamaki, J. Zhou, T. Imaizumi, R. H. J. A. Slart, M. Dyszlewski, T. Scarabelli, A. Kini, C. Reutelingsperger, N. Narula, V. Fuster and J. Narula, *Sci. Rep.*, 2014, **4**, 6826.
91. J. Zhang, R. E. Campbell, A. Y. Ting and R. Y. Tsien, *Nat. Rev. Mol. Cell Biol.*, 2002, **3**, 906-918.
92. B. A. Griffin, S. R. Adams and R. Y. Tsien, in *Site-Specific Protein Labeling: Methods and Protocols*, eds. A. Gautier and M. J. Hinner, Springer New York, New York, NY, 2015, pp. 1-6.
93. B. A. Griffin, S. R. Adams and R. Y. Tsien, *Science*, 1998, **281**, 269-272.
94. S. R. Adams, R. E. Campbell, L. A. Gross, B. R. Martin, G. K. Walkup, Y. Yao, J. Llopis and R. Y. Tsien, *J. Am. Chem. Soc.*, 2002, **124**, 6063-6076.
95. A. S. Walker, P. R. Rablen and A. Schepartz, *J. Am. Chem. Soc.*, 2016, **138**, 7143-7150.
96. J. Nakanishi, T. Nakajima, M. Sato, T. Ozawa, K. Tohda and Y. Umezawa, *Anal. Chem.*, 2001, **73**, 2920-2928.
97. H. Cao, B. Chen, T. C. Squier and M. U. Mayer, *Chem. Commun.*, 2006, 2601-2603.
98. C. C. Spagnuolo, R. J. Vermeij and E. A. Jares-Erijman, *J. Am. Chem. Soc.*, 2006, **128**, 12040-12041.
99. H. Cao, Y. Xiong, T. Wang, B. Chen, T. C. Squier and M. U. Mayer, *J. Am. Chem. Soc.*, 2007, **129**, 8672-8673.

100. N. Fu, Y. Xiong and T. C. Squier, *Bioconjugate Chem.*, 2013, **24**, 251-259.
101. M. J. Rust, M. Bates and X. Zhuang, *Nature Methods*, 2006, **3**, 793-795.
102. N. Fu, Y. Xiong and T. C. Squier, *J. Am. Chem. Soc.*, 2012, **134**, 18530-18533.
103. M. Bates, T. R. Blosser and X. Zhuang, *Phys. Rev. Lett.*, 2005, **94**, 108101.
104. H. Chen, R. Ahn, J. Van den Bossche, D. H. Thompson and T. V. O'Halloran, *Mol. Cancer Ther.*, 2009, **8**, 1955-1963.
105. H. Chen, S. Pazicni, N. L. Krett, R. W. Ahn, J. E. Penner-Hahn, S. T. Rosen and T. V. O'Halloran, *Angew. Chem.-Int. Ed.*, 2009, **48**, 9295-9299.
106. R. W. Ahn, S. L. Barrett, M. R. Raja, J. K. Jozefik, L. Spaho, H. Chen, M. B. Bally, A. P. Mazar, M. J. Avram, J. N. Winter, L. I. Gordon, L. D. Shea, T. V. O'Halloran and T. K. Woodruff, *PLOS ONE*, 2013, **8**, e58491.
107. R. W. Ahn, F. Chen, H. Chen, S. T. Stern, J. D. Clogston, A. K. Patri, M. R. Raja, E. P. Swindell, V. Parimi, V. L. Cryns and T. V. O'Halloran, *Clin. Cancer Res.*, 2010, **16**, 3607-3617.
108. C. Qian, Y. Wang, Y. Chen, L. Zeng, Q. Zhang, X. Shuai and K. Huang, *Biomaterials*, 2013, **34**, 6175-6184.
109. L. Zhang, H. Xiao, J. Li, D. Cheng and X. Shuai, *Nanoscale*, 2016, **8**, 12608-12617.
110. Z. Zhao, H. Zhang, X. Chi, H. Li, Z. Yin, D. Huang, X. Wang and J. Gao, *J. Mater. Chem. B*, 2014, **2**, 6313-6323.
111. Z. Zhao, X. Wang, Z. Zhang, H. Zhang, H. Liu, X. Zhu, H. Li, X. Chi, Z. Yin and J. Gao, *ACS Nano*, 2015, **9**, 2749-2759.
112. Z. Zhang, H. Liu, H. Zhou, X. Zhu, Z. Zhao, X. Chi, H. Shan and J. Gao, *Nanoscale*, 2016, **8**, 4373-4380.
113. N. A. LaFranzo and J. A. Maurer, *Adv. Funct. Mater.*, 2013, **23**, 2415-2421.
114. J. Ahn, D.-S. Moon and J.-K. Lee, *Langmuir*, 2013, **29**, 14912-14918.
115. D. Mohan and C. U. Pittman, *J. Hazard. Mater.*, 2007, **142**, 1-53.
116. C. T. Yavuz, J. T. Mayo, W. W. Yu, A. Prakash, J. C. Falkner, S. Yean, L. Cong, H. J. Shipley, A. Kan, M. Tomson, D. Natelson and V. L. Colvin, *Science*, 2006, **314**, 964-967.
117. H. Minehara, A. Narita, K. Naka, K. Tanaka, M. Chujo, M. Nagao and Y. Chujo, *Biorg. Med. Chem.*, 2012, **20**, 4675-4679.
118. Q. Zhang, M. R. Vakili, X.-F. Li, A. Lavasanifar and X. C. Le, *Biomaterials*, 2014, **35**, 7088-7100.
119. Q. Zhang, M. R. Vakili, X.-F. Li, A. Lavasanifar and X. C. Le, *Mol. Pharm.* 2016, **13**, 4021-4033.

120. Y. Peng, Z. Zhao, T. Liu, X. Li, X. Hu, X. Wei, X. Zhang and W. Tan, *Angew. Chem. Int. Ed.*, 2017, **56**, 10845-10849.
121. E. P. Swindell, P. L. Hankins, H. Chen, Đ. U. Miodragović and T. V. O'Halloran, *Inorg. Chem.*, 2013, **52**, 12292-12304.
122. N. D. Winter, R. K. J. Murphy, T. V. O'Halloran and G. C. Schatz, *J. Liposome Res.*, 2011, **21**, 106-115.
123. H. Chen, S. Pazicni, N. L. Krett, R. W. Ahn, J. E. Penner-Hahn, S. T. Rosen and T. V. O'Halloran, *Angew. Chem. Int. Ed.*, 2009, **48**, 9295-9299.
124. S. Antimisiaris, *Clin. Lipidol.*, 2009, **4**, 663-675.
125. S. G. Antimisiaris, *J. Drug Delivery Sci. Technol.*, 2007, **17**, 377-388.
126. S. G. Antimisiaris and P. V. Ioannou, in *Liposomes: Methods and Protocols, Volume 1: Pharmaceutical Nanocarriers*, ed. V. Weissig, Humana Press, Totowa, NJ, 2010, pp. 147-162.
127. V. M. Dembitsky and D. O. Levitsky, *Prog. Lipid Res.*, 2004, **43**, 403-448.
128. G. M. Tsivgoulis, D. N. Sotiropoulos and P. V. Ioannou, *Phosphorus, Sulfur, and Silicon and the Related Elements*, 1991, **57**, 189-193.
129. G. M. Tsivgoulis, D. N. Sotiropoulos and P. V. Ioannou, *Phosphorus, Sulfur, and Silicon and the Related Elements*, 1991, **63**, 329-334.
130. S. V. Serves, G. M. Tsivgoulis, D. N. Sotiropoulos, P. V. Ioannou and M. K. Jain, *Phosphorus, Sulfur, and Silicon and the Related Elements*, 1992, **71**, 99-105.
131. G. M. Tsivgoulis and P. V. Ioannou, *Chem. Phys. Lipids*, 2008, **152**, 113-121.
132. M. A. Lala, G. M. Tsivgoulis and P. V. Ioannou, *Phosphorus, Sulfur, and Silicon and the Related Elements*, 2007, **182**, 2747-2760.
133. A. Terzis and P. V. Ioannou, *Chem. Phys. Lipids*, 2002, **117**, 53-61.
134. G. M. Tsivgoulis, M. A. Lala and P. V. Ioannou, *Chem. Phys. Lipids*, 2007, **148**, 97-104.
135. H. Talsma, M. J. Van Steenbergen, J. C. H. Borchert and D. J. A. Crommelin, *J. Pharm. Sci.*, 1994, **83**, 276-280.
136. D. Fatouros, O. Gortzi, P. Klepetsanis, S. G. Antimisiaris, M. C. A. Stuart, A. Brisson and P. V. Ioannou, *Chem. Phys. Lipids*, 2001, **109**, 75-89.
137. O. Gortzi, S. G. Antimisiaris, P. Klepetsanis, E. Papadimitriou and P. V. Ioannou, *Eur. J. Pharm. Sci.*, 2003, **18**, 175-183.
138. S. Piperoudi, P. V. Ioannou, P. Frederik and S. G. Antimisiaris, *J. Liposome Res.*, 2005, **15**, 187-197.
139. S. Piperoudi, D. Fatouros, P. V. Ioannou, P. Frederik and S. G. Antimisiaris, *Chem. Phys. Lipids*, 2006, **139**, 96-106.

140. D. G. Fatouros, S. Piperoudi, O. Gortzi, P. V. Ioannou, P. Frederik and S. G. Antimisiaris, *J. Pharm. Sci.*, 2005, **94**, 46-55.

141. P. Zagana, M. Haikou, P. Klepetsanis, E. Giannopoulou, P. V. Ioannou and S. G. Antimisiaris, *Int. J. Pharm.*, 2008, **347**, 86-92.

142. S. G. Antimisiaris, P. Klepetsanis, V. Zachariou, E. Giannopoulou and P. V. Ioannou, *Int. J. Pharm.*, 2005, **289**, 151-158.

143. S. G. Antimisiaris, P. V. Ioannou and P. M. Loiseau, *J. Pharm. Pharmacol.*, 2003, **55**, 647-652.

144. P. Zagana, P. Klepetsanis, P. V. Ioannou, P. M. Loiseau and S. G. Antimisiaris, *Biomed. Pharmacother.*, 2007, **61**, 499-504.

145. O. Gortzi, E. Papadimitriou, C. G. Kontoyannis, S. G. Antimisiaris and P. V. Ioannou, *Pharm. Res.*, 2002, **19**, 79-86.

146. P. Zagana, M. Haikou, E. Giannopoulou, P. V. Ioannou and S. G. Antimisiaris, *Mol. Nutr. Food Res.*, 2009, **53**, 592-599.

147. E. Papadimitriou and S. Antimisiaris, *J. Drug Targeting*, 2000, **8**, 335-351.

148. M. N. Haikou, P. Zagana, P. V. Ioannou and S. G. Antimisiaris, *J. Nanosci. Nanotechnol.*, 2006, **6**, 2974-2978.

Chapter 2 : Synthesis, aggregation and responsivity of block copolymers containing organic arsenicals

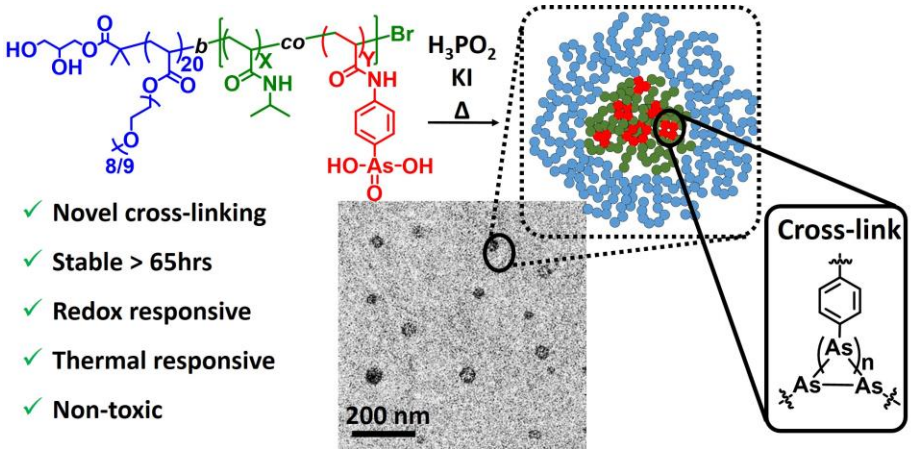

The materials presented in this chapter is directly reproduced from a communication with permission from the publishers, where I was the first Author: *Polym. Chem., 2018, 9, 1551–1556*. This was published together with Seiji Tani (I supervised during his MSc project and has carried out earlier investigation presented in this work in the 2016-17 academic year, Raoul Peltier (who has carried out the XTT presented in this work), Emily H. Pilkington (who has carried out the TEM presented in this work), Andrew Kerr (who has carried out the AFM presented in this work), Thomas P. Davis (collaborator) and Paul Wilson (supervisor and corresponding author).

Abstract

Block copolymers containing an organic arsenical (AsAm) have been synthesised by aqueous SET-LRP**.** The block copolymers are pH and thermoresponsive, forming nanoparticles in aqueous solution. Under reductive conditions the particles are stabilised through the formation of As-As bonds and stability can be tuned as a function of the AsAm monomer feed.

2.1 Introduction

Living systems crosslink (bio)macromolecules in order to stabilise intra- and intermolecular interactions, supporting complex tertiary and quaternary structures and self-assembled (bio)macromolecular complexes. Such biochemical processes have inspired the development of a chemical platform to control the properties and function of polymers through crosslinking. Crosslinking synthetic linear polymers not only alters physical properties such as glass transition temperature, it has been exploited to create architectures beyond one dimensional linear structures such as single chain nanoparticles,[1, 2] star/branched polymers,[3, 4] and nanogels.[5] In particular, responsive materials that utilise reversible covalent bond formation that can be uncrosslinked on demand by specific environmental triggers are attractive targets for drug delivery, sustainability and chemical sensors.[6] In a biological context, boronate esters have been demonstrated by Sumerlin *et al.* as a pH and sugar responsive cross-linker to form hydrogels,[7, 8] with self-healing properties in acidic environment, and self-assembled particles that dissemble in presence of sugars.[9-11] Other types of dynamic cross-linking such as hydrazones[12, 13] and disulfides[14, 15] are reported in the literature for intracellular drug delivery in response to endosomal pH and redox environment.

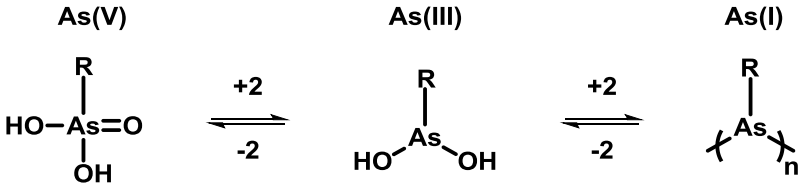

Scheme 2.1 Oxidation states of Arsenic as monovalent arsines (As(I)), trivalent arsenous acid (As(III)) and pentavalent arsenic acid (As(V)).

Arsenic is an interesting candidate for dynamic cross-linking, due to its interchangeable oxidation states each with distinct chemical reactivity. For example, pentavalent arsenic (As(V)) will not form covalent bonds with thiols, preferring to undergo single electron transfer reduction. Trivalent arsenic (As(III)) can be formed from the reduction of As(V) by two equivalents of thiol and in this oxidation state arsenic has a high affinity for thiols, readily forming covalent As-S bonds, which is markedly enhanced for dithiol reagents.[16] The affinity for mono- and dithiols has been exploited for post-polymerisation modification and protein/peptide-polymer conjugation of As-functional polymer

scaffolds.[17, 18] Under stronger reducing conditions, As(V) can be directly reduced to As(I), which has been reported to proceed with reductive coupling to form Asn homocycles comprised of As-As bonds (Scheme 2-1).[19] The As-As bonds are weak but have been exploited in synthesis for the preparation of salvarsan[20] and as a source of monomer for 'ring-collapsed radical alternating copolymerisation' to form poly(vinylene arsines).[21-25]

Until recently, the polymerisation of As-functional monomers by chain-growth polymerisation was only reported by free radical polymerisation.[26-30] The advent of reversible deactivation radical polymerisation (RDRP) techniques such as Reversible Addition-Fragmentation chain-Transfer (RAFT),[31] atom transfer radical polymerisation (ATRP)[32, 33] and single electron transfer living radical polymerisation (SET-LRP)[34] enables exquisite control of chain-end functionality which has been harnessed for the synthesis of well-defined (multi)block copolymers.[35, 36] In previous work, a protected As-functional monomer, prepared in a two-step synthesis from p-arsanilic acid, was employed to prepare As-functional homo- and copolymers by RAFT.[17] In order to access the interesting reactivity of the pendant As-functional groups, the resulting polymers require an additional post-polymerisation processing step to afford deprotection. It would be beneficial to develop a method through which an As-functional monomer could be incorporated into polymers without the need for the additional protection (monomer) - deprotection (polymer) steps.

In this chapter, the synthesis of block copolymers containing an As(V)-functional monomer (AsAm) by aqueous SET-LRP is reported. At elevated temperatures As(V)-functional nanoparticles are formed which, for the first time, are stabilised by crosslinking through the reductive coupling of As(V) to give As(I)n. The stability of the resulting particles as a function of the AsAm monomer feed is also investigated in aqueous and model biological solutions.

2.2 Results and Discussion

2.2.1 Polymeric arsenical synthesis

Poly(ethylene glycol) methyl ether acrylate (PEGA, M_n = 480 g.mol^{-1}) and *N*-

isopropylacrylamide (NIPAm) are hydrophilic monomers that have been successfully polymerised by aqueous SET-LRP previously. Therefore, PEGA was selected as the corona-forming block and NIPAm, with its ability to undergo phase transition at elevated temperatures (LCST = 32 °C), was selected as the core-forming block. For optimal chain extension and block efficiency, the PEGA blocks ($DP_{n,th}$ = 20) were synthesised first then chain extended with NIPAm ($DP_{n,th}$ = 80) via one-pot, sequential chain extension in accordance with previous work.[35] The incorporation of As-functionality was achieved by statistical copolymerisation of varying amounts of AsAm in either the PEGA or NIPAM block, whilst keeping the overall chain length of the polymer constant (DP_n = 100, Scheme 2.2).

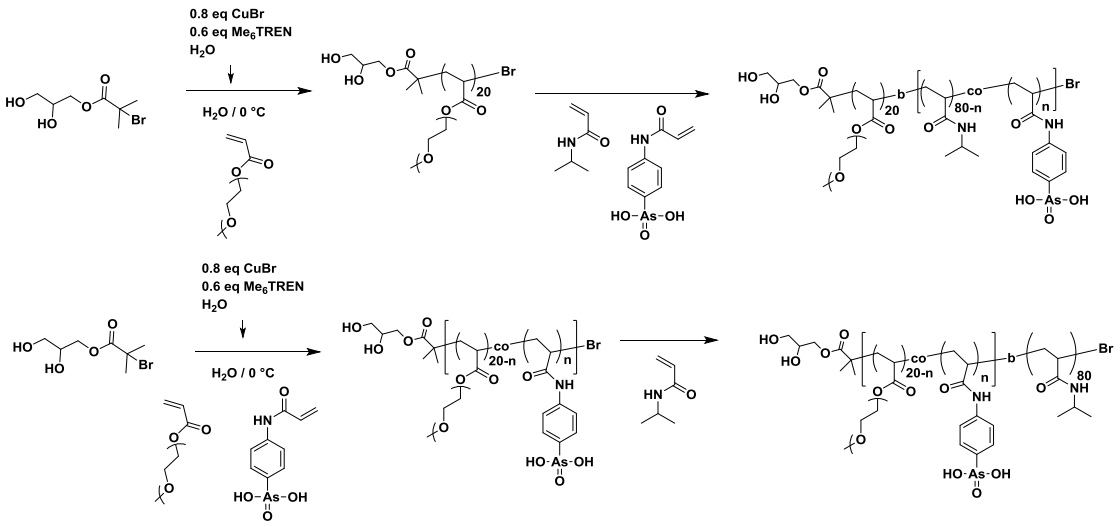

Scheme 2.2 Synthesis of As-functional block copolymers by aqueous SET-LRP

Initially, a non-As functional control polymer $PEGA_{20}$-*b*-$NIPAm_{80}$ was synthesised with homopolymerisation of PEGA in water, complete within 15 mins (>99% conv., $M_{n,SEC}$ = 11800 g.mol^{-1}, $Đ$ = 1.07). Addition of a deoxygenated aliquot of NIPAm then furnished the targeted block copolymer $PEGA_{20}$-*b*-$NIPAm_{80}$ (**P2.1**, 98% conv., $M_{n,SEC}$ = 25400 g.mol^{-1}, $Đ$ = 1.27, Figure 2.1).

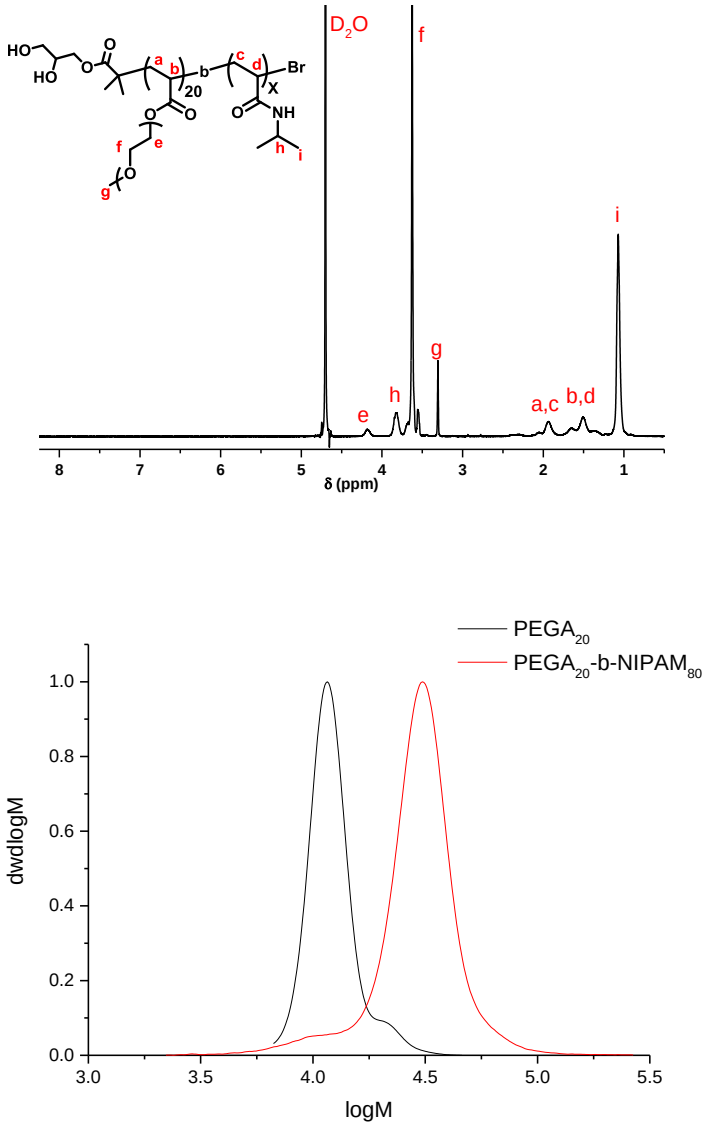

Figure 2.1 ^{1}H NMR spectrum (top) and GPC (DMF, bottom) chromatogram of PEGA$_{20}$-*b*-NIPAm$_{80}$; P2.1, $M_{n,th}$ = 19400 gmol^{-1}, $M_{n,SEC}$ =25400 gmol^{-1}, $Đ$ = 1.27

Arsenical monomer, 4-(*N*-acrylamido)phenylarsonic acid (AsAm), was then incorporated into corona-/core-forming blocks by altering the monomer feed ratio of either the first block (PEGA$_{20-n}$-*co*-AsAm$_n$, **P2.2** n = 3, **P2.3** n = 5) or the chain extension (NIPAm$_{80-n}$-*co*-AsAm$_n$, **P2.4** n = 5, **P2.5** n = 10). Successful inclusion of AsAm into the block copolymer was confirmed by ^{1}H NMR with appearance of aromatic signals of AsAm (H$_{j,k}$ (**P2.2**, **P2.3**) and H$_{l,m}$ (**P2.4**, **P2.5**) Figure 2.2) at 7.5-7.7 ppm in addition to the signals corresponding to PEGA (H$_{g,i}$) and NIPAm (H$_{l,m}$ (**P2.2**, **P2.3**) and H$_{j,k}$ (**P2.4**, **P2.5**)). The relative integrals were translated into an experimental polymer composition which

confirmed the desired increase in AsAm content as a function of the AsAm monomer feed ratio (Figure 2.2, Table 2.3).

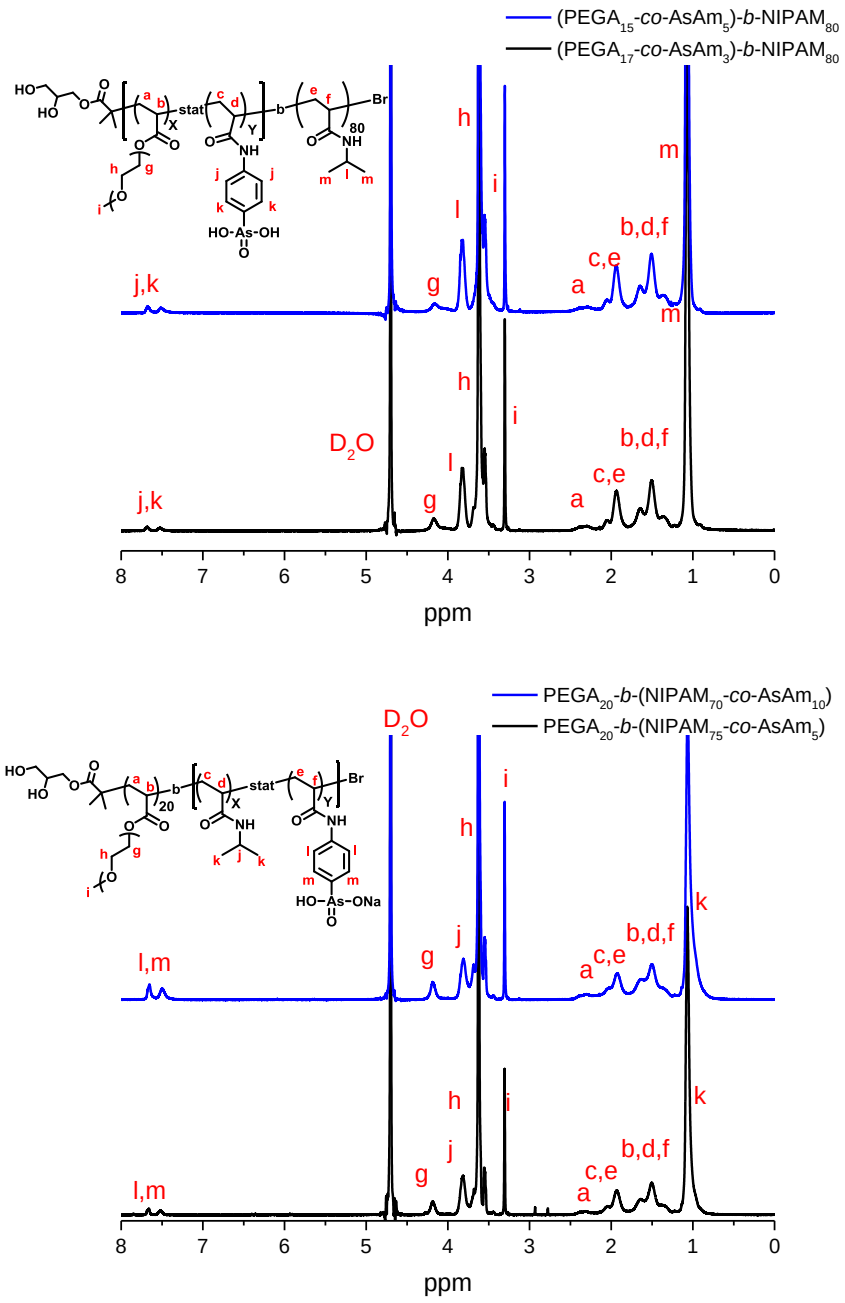

Figure 2.2 ^{1}H NMR of (PEGA$_{20\text{-}n}$-*co*-AsAm$_n$)-*b*-NIPAm$_{80}$ (P2.2, n = 3; P2.3 n = 5) (top) and PEGA$_{20}$-*b*-(NIPAm$_{80\text{-}n}$-*co*-AsAm$_n$) (P2.4, n = 5; P2.5, n = 10)

Block copolymerisation was confirmed by SEC analysis (Figure 2.3) which showed a

shift to higher molecular weight upon chain extension. Increasing the amount of AsAm in either block appeared to have a detrimental effect on the control of the polymerisation as indicated by deviations in theoretical ($M_{n,th}$) and experimental number average molecular weight ($M_{n,SEC}$) and higher dispersities (**P2.2-P2.5**, $Đ = 1.2 – 1.8$) than expected from aqueous SET-LRP polymerisations (Table 2.1).

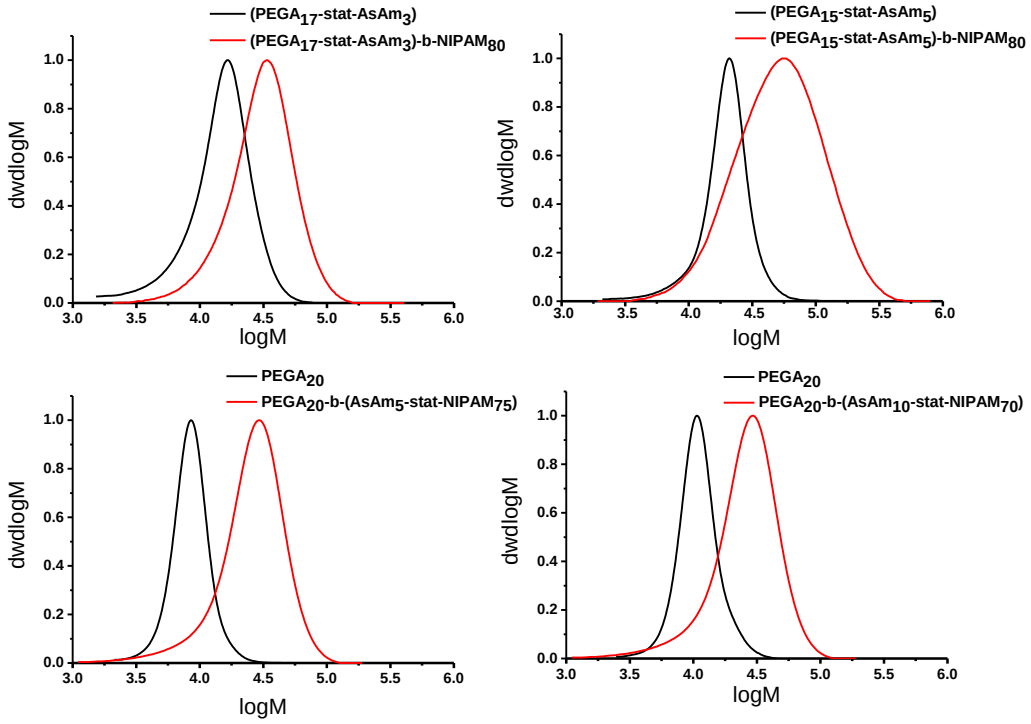

Figure 2.3 GPC (DMF) chromatogram (top left) P2.2: block 1 $M_{n,th}$ = 9200 gmol^{-1}, $M_{n,SEC}$ =11100 gmol^{-1}, $Đ$ = 1.51 (black) and block 2 $M_{n,th}$ = 19400 gmol^{-1}, $M_{n,SEC}$ =25100 gmol^{-1}, $Đ$ = 1.41 (red); (top right) P2.3: block 1 $M_{n,th}$ = 8800 gmol^{-1}, $M_{n,SEC}$ =16500 gmol^{-1}, $Đ$ = 1.51 (black) and block 2 $M_{n,th}$ = 19000 gmol^{-1}, $M_{n,SEC}$ =37500 gmol^{-1}, $Đ$ = 1.81 (red); (bottom left) P2.4: block 1 $M_{n,th}$ = 9800 gmol^{-1}, $M_{n,SEC}$ =7900 gmol^{-1}, $Đ$ = 1.13 (black) and block 2 $M_{n,th}$ = 20700 gmol^{-1}, $M_{n,SEC}$ = 20000 gmol^{-1}, $Đ$ = 1.19 (red); (bottom right) P2.5: block 1 $M_{n,th}$ = 9800 gmol^{-1}, $M_{n,SEC}$ =10100 gmol^{-1}, $Đ$ = 1.16 (black) and block 2 $M_{n,th}$ = 21500 gmol^{-1}, $M_{n,SEC}$ =26000 gmol^{-1}, $Đ$ = 1.19 (red)

2.2.2 Thermoself-assembly

The thermoresponsive behaviour and propensity for aggregation for each polymer was investigated by variable temperature dynamic light scattering (DLS) of aqueous solutions of the polymers (1 mg/ml) at 5 °C intervals between 25-60 °C. PNIPAm$_{80}$ synthesised by aqueous SET-LRP underwent macroscopic precipitation as expected between 35-40 °C (Figure 2.4), whereas the control block copolymer **P2.1** formed small aggregates with hydrodynamic diameters (D_h) of 12 – 15 nm at T > 45 °C (Figure 2.5).

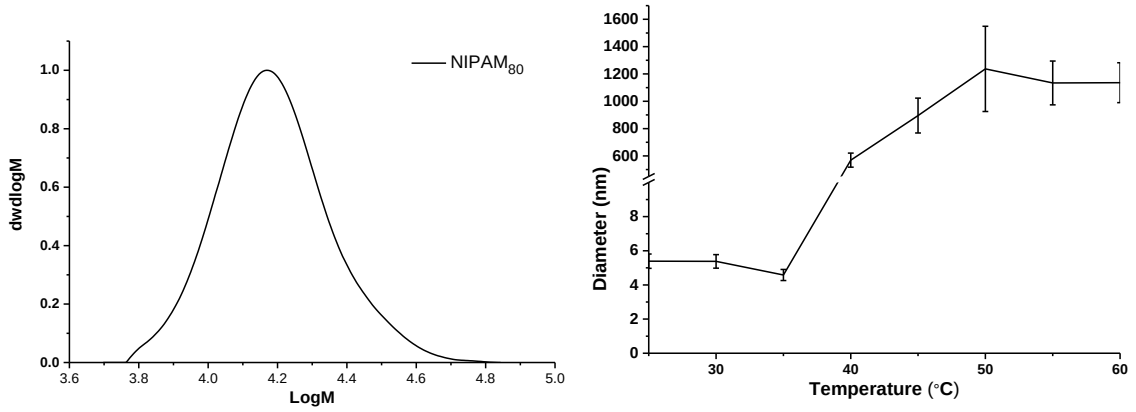

Figure 2.4 GPC (DMF) chromatogram (top) and thermoresponsive behaviour by DLS (bottom) of P(NIPAM)$_{80}$, $M_{n,th}$ = 9300 gmol^{-1} M_{nSEC} = 14500 gmol^{-1}, $\cancel{D}$ = 1.15 in aqueous solution (1 mg/ml) (see Appendix C, S2.4 for supporting information).

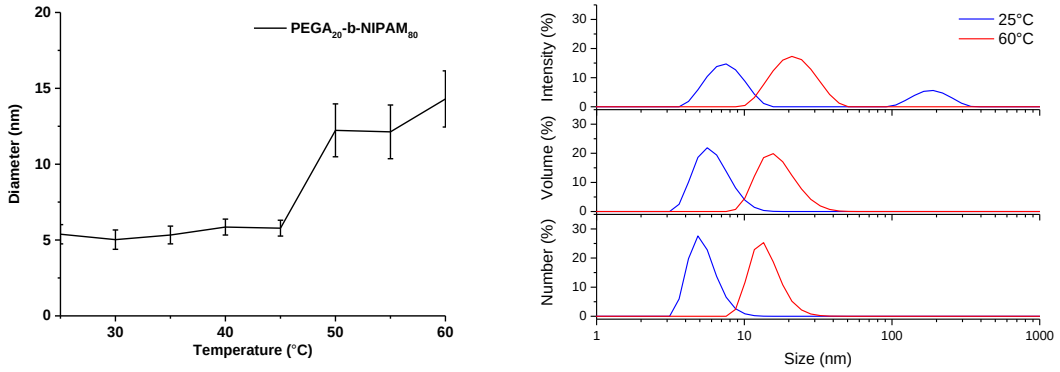

Figure 2.5 Hydrodynamic diameter (number %) as a function of temperature and intensity, number and volume distributions of P2.1, PEGA$_{20}$-*b*-NIPAM$_{80}$ in aqueous solution (1 mg/ml) (see Appendix C, S2.5 for supporting information).

Incorporation of AsAm into the corona-forming block also resulted in the formation of nanoparticles the size of which increased as a function of the AsAm monomer feed (**P2.2,** D_h = 20 nm; **P2.3**, D_h = 33 nm, Figure 2.6).

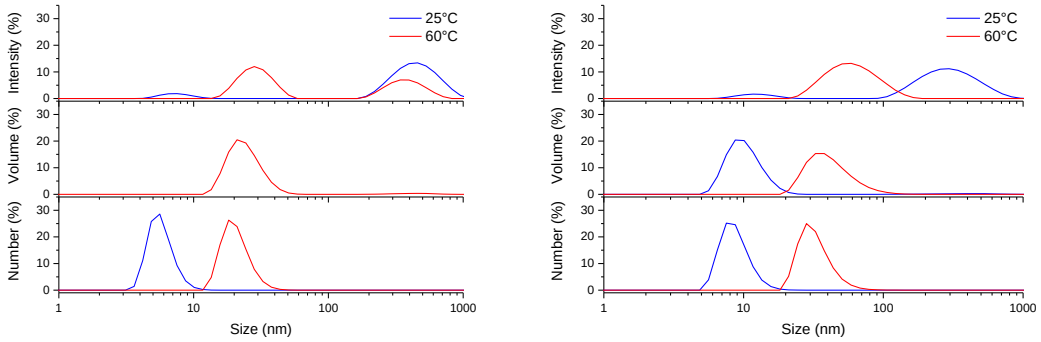

Figure 2.6 DLS, particle size as a function of temperature of P2.2, (PEGA$_{17}$-*co*-AsAm$_3$)-*b*-NIPAM$_{80}$ (left) and P2.3, (PEGA$_{15}$-*co*-AsAm$_5$)-*b*-NIPAM$_{80}$ (right) in aqueous solution (1 mg/ml) (see Appendix C, S2.6 for supporting information).

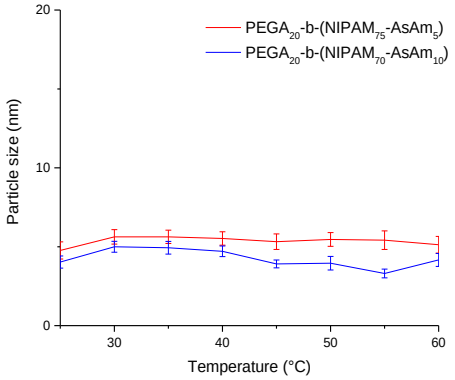

Figure 2.7 Particle size as a function of temperature for PEGA$_{20}$-*b*-(NIPAM$_{80-n}$-*co*-AsAm$_n$) in aqueous solution (1 mg/ml) (see Appendix C, S2.7A and S2.7B for supporting information).

However, when AsAm was incorporated into the core-forming NIPAm block (**P2.4** and **P2.5**) no self-assembly was observed (D_h = 4 nm, Figure 2.7). Under the reaction conditions the pendent arsenic acid group of AsAm is ionised (Na^+ salt) and hydrophilic. It was hypothesised that incorporation into the NIPAm block precluded the expected phase transition. Consequently, the pH of the polymer solutions was measured and found to be 10.3. Acidification of the polymer (**P2.4**) solution using HCl to close to neutral (pH = 6.6) had little effect resulting in no particle formation (D_h = 8 nm). However, further acidification to pH = 2.5, which is closer to the pK_a of arsenic acid (p$K_{a1} \approx 2$)[37] results in protonation of the arsenic acid groups leading to the formation of particles with D_h = 30 nm (Figure 2.8). In an identical titration, polymers **P2.2** and **P2.3** underwent self-

assembly across the pH range forming nanoparticles, the sizes of which increased as the pH decreased (pH 10.3 = 48 nm; pH 2.5 = 98 nm, Figure 2.8).

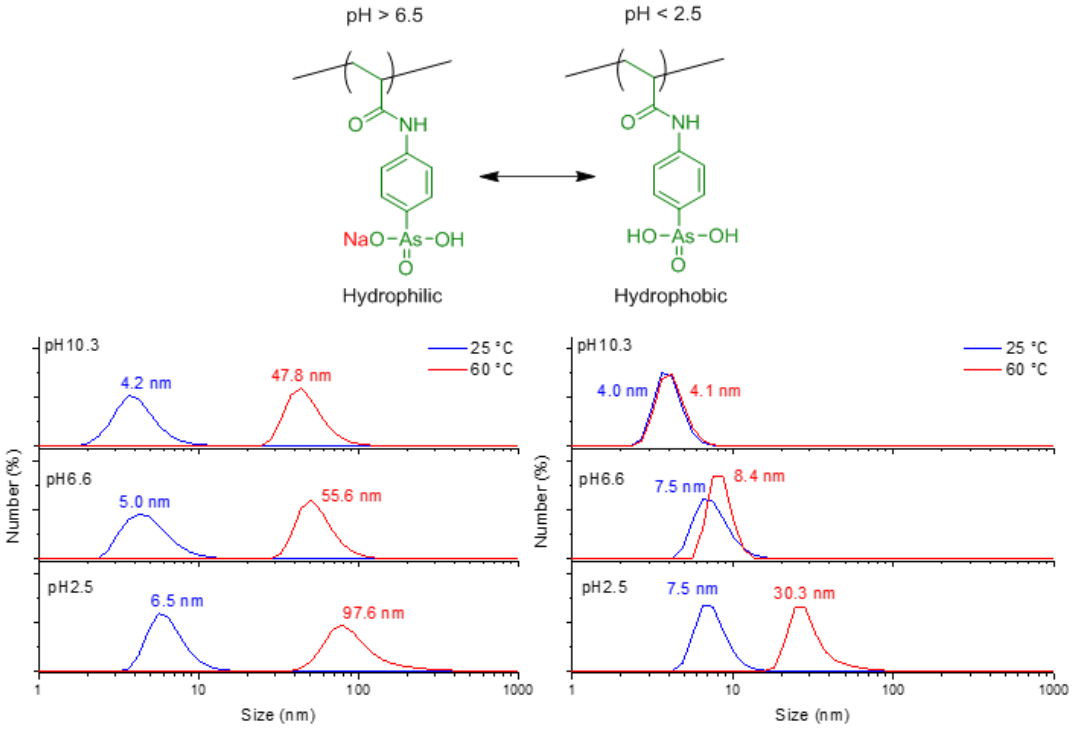

Figure 2.8 Changes in hydrodynamic diameter of ($PEGA_{15}$-*co*-$AsAm_5$)-*b*-$NIPAM_{80}$ (P2.3, left) and $PEGA_{20}$-*b*-($NIPAM_{70}$-*co*-$AsAm_{10}$) (P2.5, right) between 25 °C and 60 °C as a function of pH in aqueous solution (1 mg/ml) (see Appendix C, S2.8A and S2.8B for supporting information).

2.2.3 As(I) stabilised nanoparticles

In pure aqueous solution all the nanoparticles formed from **P2.1** – **P2.5** dissembled upon rehydration of the NIPAm block on cooling to 25 °C. Under reducing conditions (aqueous H_3PO_2), the pendent arsenic acid group (As(V)) can undergo reductive coupling to As(I),[19] with formation of As-As bonds in the form of As_n homocycles. It was hypothesised that reductive coupling could provide a novel approach to crosslinking and stabilisation of the organic arsenical copolymer nanoparticles derived from **P2.2** – **P2.5**. The polymers (10 mg/ml) were dissolved in an aqueous solution of H_3PO_2 prior to heating at 60 °C to facilitate both self-assembly and reduction processes. Under these conditions both **P2.2** and **P2.3** formed particles with D_h of the order of 40 nm and 80 nm respectively by DLS. However, the presence of the AsAm (n = 3, 5) in the corona-forming block was not sufficient to stabilise the particles formed after heating for 10 – 90 minutes, in line

with previous methods employed to achieve reductive coupling.[20] Disassembly was observed within 10 minutes upon cooling back to 25 °C (Figure 2.9).

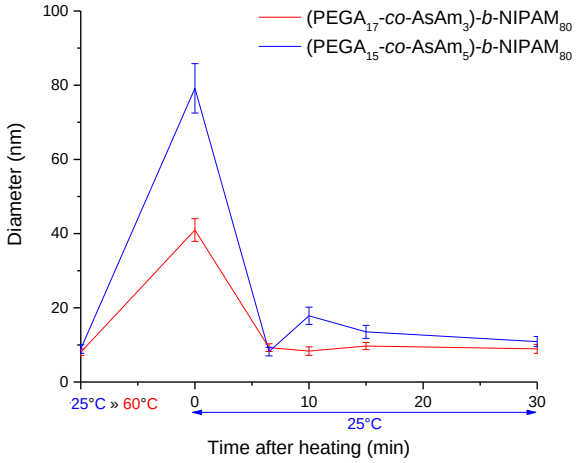

Figure 2.9 Temporal changes in the particle size of the cross-linked particles of (PEGA$_{20-n}$-*co*-AsAm$_n$)-*b*-NIPAM$_{80}$ (P2.2, P2.3) after heating in hypophosphorous solution (10 mins, 10 mg/ml). DLS cell was heated from 25 – 60 °C over 120 secs followed by 60 secs equilibration time before being held at 60 °C for 10 – 90 mins. Cooling of the cell occurred over 120 secs followed by 60 secs equilibration after which measurement of stability commenced (t = 0, 25 °C) (see Appendix C, S2.9A and S2.9B for supporting information).

Conversely, when AsAm was confined to the more densely packed core of the particles derived from **P2.4** (**NP$_{As-5}$**) and **P2.5** (**NP$_{As-10}$**), the particles formed (D_h = 45 nm) upon heating at 60 °C in the presence of H_3PO_2 retained their assembled structure upon cooling for up to 60 minutes, suggesting successful crosslinking through the formation of As-As bonds (Figure 2.10).

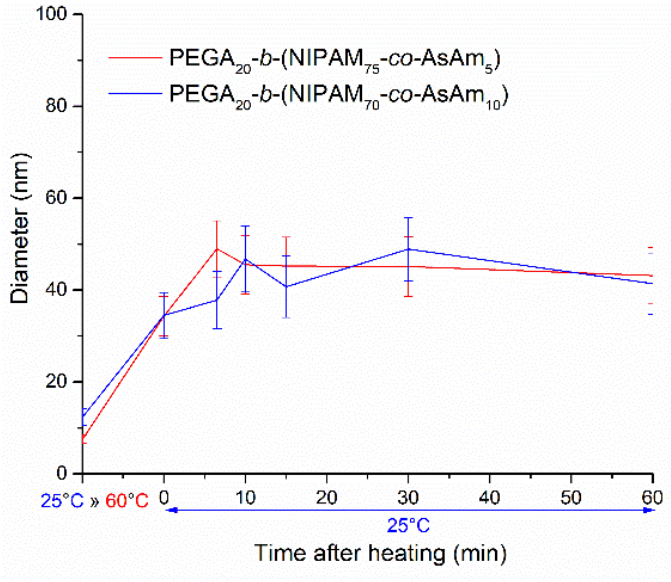

Figure 2.10 Temporal changes in the particle size of the cross-linked particles of $PEGA_{20}$-*b*-($NIPAm_{80-n}$-*co*-$AsAm_n$) (P2.4, P2.5) after heating in hypophosphorous (10 mg/ml). DLS cell was heated from 25 – 60 °C over 120 secs followed by 60 secs equilibration time before being held at 60 °C for 30 mins (P2.4, red) and 10 mins (P2.5, blue) respectively. Cooling of the cell occurred over 120 secs followed by 60 secs equilibration after which measurement of stability commenced (t = 0, 25 °C) (see Appendix C, S2.10A and S2.10B for supporting information).

The nature of the crosslinking was inferred from IR spectroscopy through disappearance of the As-O signals associated with the pendent arsenic acid (As(V)) moieties (Figure 2.11). Increasing the amount of AsAm in the monomer feed from **P2.4** (n = 5) to **P2.5** (n = 10) resulted in the formation of more stable particles, with **P2.5** forming stable particles after only 10 minutes of crosslinking, whereas **P2.4** required at least 30 minutes to form particles that were stable upon cooling to 25 °C (Figure 2.12).

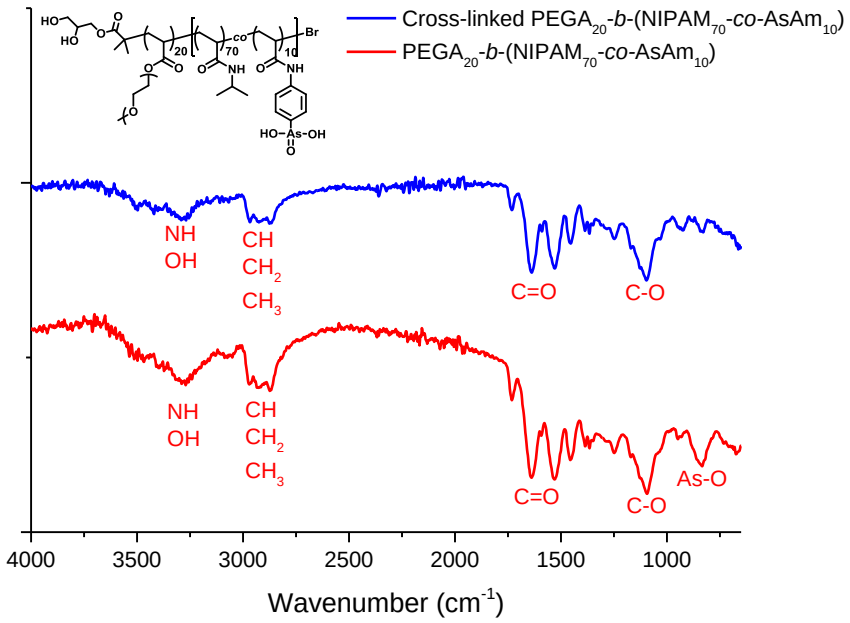

Figure 2.11 IR spectrum of purified $PEGA_{20}$-b-($NIPAm_{70}$-co-$AsAm_{10}$) (P2.4) showing disappearance of the As-O signals upon crosslinking via reductive coupling in H_3PO_2.

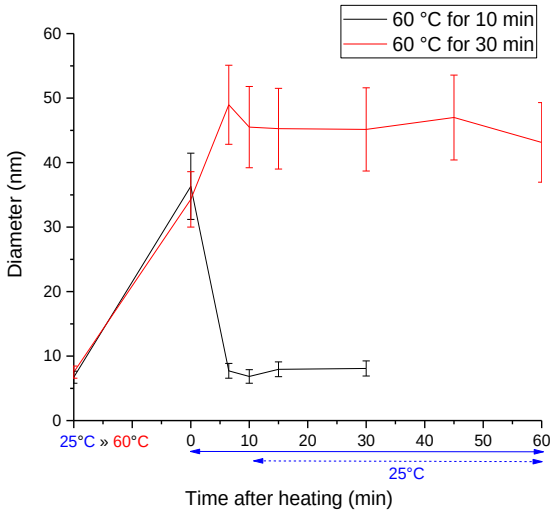

Figure 2.12 Stability of particles derived from $PEGA_{20}$-*b*-($NIPAM_{75}$-*co*-$AsAm_5$) (P2.4) after heating at 60 °C in aqueous H_3PO_2 for 10 mins and 30 mins. DLS cell was heated from 25 – 60 °C for 120 secs followed by 60 secs equilibration time before being held at 60 °C for 10 mins (black) and 30 mins (red) respectively. Cooling of the cell occurred over 120 secs followed by 60 secs equilibration after which measurement of stability commenced (t = 0, 25 °C) (see Appendix C, S2.12 for supporting information).

The particles formed from **P2.5** (**NP_{As-10}**) exhibited thermoresponsive character, reversibly contracting and swelling upon heating and cooling cycles (Figure 2.13), in accordance with the transition of the core from a hydrophobic to hydrophilic state respectively.

Table 2.1 As-functional block copolymers synthesised by aqueous SET-LRP. ^{1}H NMR in D_2O. SEC in DMF.

		First Block				Final Polymer			
Entry	Structures	Con.	$M_{n,th}$ (gmol^{-1})	$M_{n,SEC}$ (gmol^{-1})	Đ	Con.	$M_{n,th}$ (gmol^{-1})	$M_{n,SEC}$ (gmol^{-1})	Đ
	Control								
P2.1	$PEGA_{20}$-*b*-$NIPAm_{80}$	> 99%	9800	11800	1.07	98%	20000	25400	1.27
P2.2	($PEGA_{17}$-*s*-$AsAm_3$)-*b*-$NIPAm_{80}$	> 99%	9200	11100	1.51	> 99%	19400	25100	1.41
P2.3	($PEGA_{15}$-*s*-$AsAm_5$)-*b*-$NIPAm_{80}$	> 99%	8800	16500	1.29	> 99%	19000	37500	1.81
P2.4	$PEGA_{20}$ -*b*-($NIPAm_{75}$-*s*-$AsAm_5$)	> 99%	9800	7900	1.13	> 99%	20700	20000	1.49
P2.5	$PEGA_{20}$ -*b*-($NIPAm_{70}$-*s*-$AsAm_{10}$)	> 99%	9800	10100	1.16	> 99%	21500	26000	1.19
P2.6	$PEGA_{20}$ -*b*-($NIPAm_{65}$-*s*-$AsAm_{15}$)	> 99%	9800	9200	1.18	> 99%	22200	21000	1.42
P2.7	$PEGA_{20}$ -*b*-($NIPAm_{60}$-*s*-$AsAm_{20}$)	> 99%	9800	9200	1.22	> 99%	22900	25600	1.57

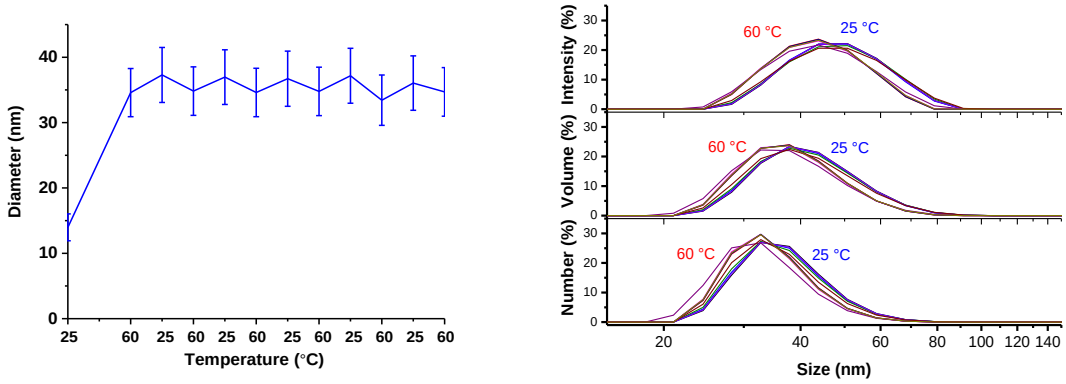

Figure 2.13 Reversible contracting and swelling of particles derived from $PEGA_{20}$-*b*-($NIPAM_{70}$-*co*-$AsAm_{10}$) at 60 °C and 25 °C respectively in aqueous H_3PO_2 (10 mg/ml) (see Appendix C, S2.13 for supporting information).

The enhanced stability of **NP_{As-10}** was further confirmed following purification and re-dispersion of the crosslinked particles in deionised water (1 mg/ml, Figure 2.14). Whereas **NP_{As-5}** was shown to disassemble during the purification process (dialysis against

deionised water), **NP_{As-10}** retained its self-assembled structure and thermoresponsive properties (Figure 2.15). Transmission electron microscopy (TEM) and atomic force microscopy (AFM) of **NP_{As-10}** confirmed the formation of nanoparticles with sizes < 100 nm (Figure 2.16).

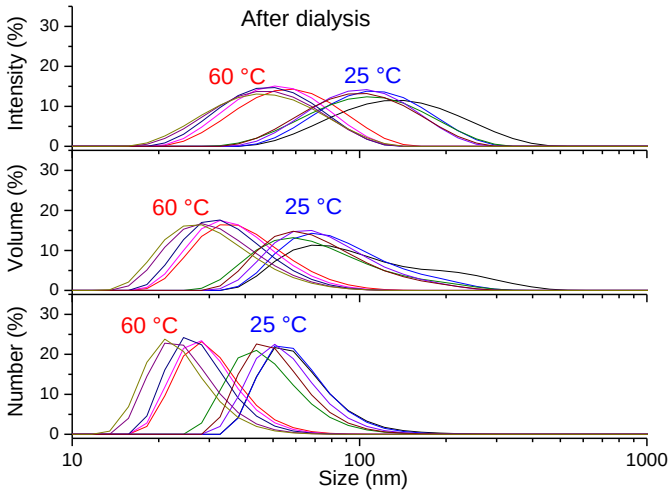

Figure 2.14 The size distribution curves of the cross-linked nanoparticles formed from $PEGA_{20}$-*b*-($NIPAM_{70}$-*co*-$AsAm_{10}$) in deionised water after dialysis at the temperatures of 25 °C and 60 °C. (see Appendix C, S2.14 for supporting information)

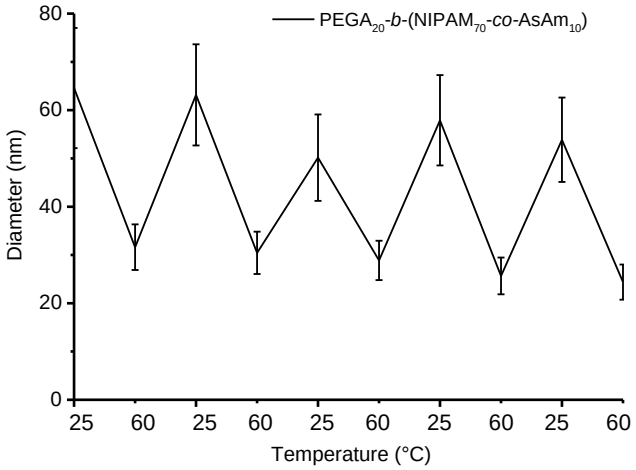

Figure 2.15 Reversible contracting and swelling of the purified particles derived from $PEGA_{20}$-*b*-($NIPAM_{70}$-*co*-$AsAm_{10}$) (P2.5) at 60 °C and 25 °C respectively in aqueous solution (1 mg/ml).

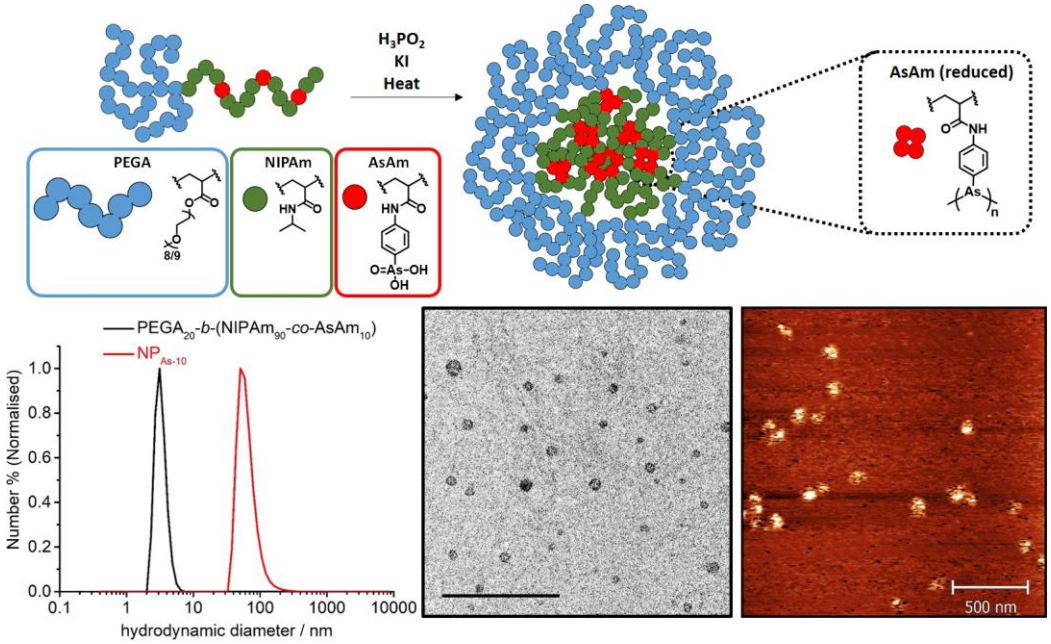

Figure 2.16 A) Schematic for the simultaneous self-assembly and reductive cross-linking of $PEGA_{20}$-*b*-($NIPAM_{70}$-*co*-$AsAm_{10}$) (P2.5) in H_3PO_2; B) Particle size distribution curves (DLS, 1 mg/ml, H_2O) of $PEGA_{20}$-*b*-($NIPAM_{70}$-*co*-$AsAm_{10}$) P2.5 (black) and the corresponding corsslinked nanoparticle NP_{As-10} (red); C) TEM image of NP_{As-10} (scale bar = 500 nm); D) AFM image if NP_{AS-10} (scale bar = 500 nm) (see Appendix C, S2.16 for supporting information).

Two additional polymers were then synthesised to investigate the effect of AsAm monomer feed on self-assembly and particle stability. Thus, $PEGA_{20}$-*b*-$NIPAm_{80-n}$-*co*-$AsAm_n$ (**P2.6**, n = 15; **P2.7**, n = 20) were prepared. These were treated with Hydrochloric acid to deionise the polymer before dialysis. In line with the previous syntheses both blocks reached high conversion (> 99%), the presence of each monomer was confirmed by ^{1}H NMR (Figure 2.17) and successful chain extension was confirmed by SEC analysis (Figure 2.18). The experimental monomer feed was again confirmed by ^{1}H NMR (Table 2.2); the PEGA feed was determined by t = 0 of the residual reaction mixture, NIPAm was calculated from side chain C***H*** (H_j, Fig 2.17) w.r.t PEGA methoxy C***H***$_3$ (H_i, Fig 2.17) and AsAm was calculated from the aromatic protons ($H_{l,m}$, Fig 2.17).This was supported by cryo-probe ^{13}C NMR which was performed to quantitatively confirm the AsAm monomer feed ratio present in the block copolymers capable of forming self-assembled nanoparticles (**P2.4-P2.7**, Figure 2.19, Table 2.2). Backbone secondary carbon, ***C***H_2 ($C_{a,c,e}$, Fig 2.19), was used as a reference to calculate the relative monomer feed by comparing side chain carbons. Depending on the choice of the carbon the monomer feed varied slightly, however successive increase in overall AsAm was consistent with targeted

polymer composition (Table 2.2).

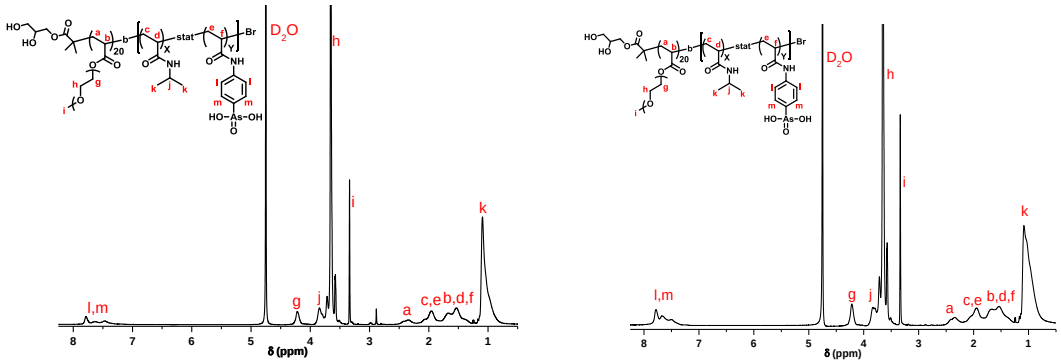

Figure 2.17 ^{1}H NMR spectrum of PEGA$_{20}$-*b*-(NIPAM$_{65}$-*co*-AsAm$_{15}$) (P2.6, top) and PEGA$_{20}$-*b*-(NIPAM$_{65}$-*co*-AsAm$_{15}$) (P2.7, bottom)

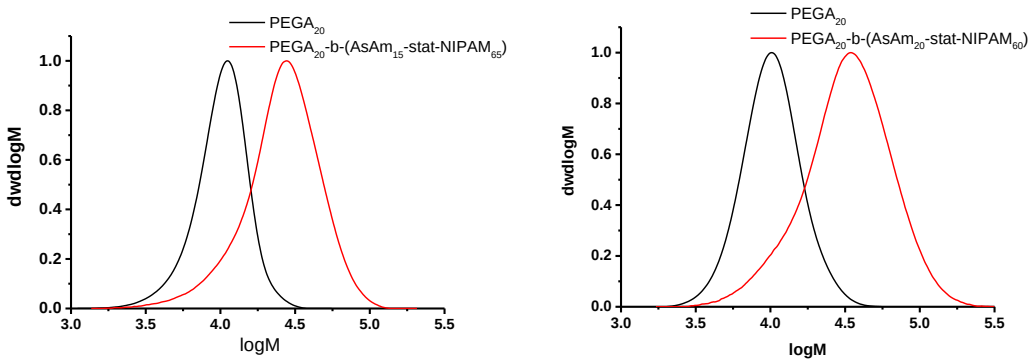

Figure 2.18 GPC (DMF) chromatogram of P(PEGA$_{20}$) $M_{n,th}$ = 9800 gmol^{-1}, $M_{n,SEC}$ = 9200 gmol^{-1}, $Đ$ = 1.18 and PEGA$_{20}$-*b*-(NIPAM$_{65}$-*co*-AsAm$_{15}$) $M_{n,th}$ = 22200 gmol^{-1}, $M_{n,SEC}$ =21000 gmol^{-1}, $Đ$ = 1.42 (P2.6, left); P(PEGA$_{20}$) $M_{n,th}$ = 9800 gmol^{-1}, $M_{n,SEC}$ =9200 gmol^{-1}, $Đ$ = 1.22 and (PEGA$_{20}$-*b*-(NIPAM$_{60}$-*co*-AsAm$_{20}$) $M_{n,th}$ = 22900 gmol^{-1}, $M_{n,SEC}$ =25600 gmol^{-1}, $Đ$ = 1.57 (P2.7, right).

Table 2.2 Experimental polymer chomposition based on ^{1}H NMR

	PEGA		NIPAM		AsAm	
Entry	**Theoretical**	**^{1}H NMR**	**Theoretical**	**^{1}H NMR**	**Theoretical**	**^{1}H NMR**
P2.1	20	15.1	80	84.9	0	0
P2.2	17	15.3	80	82.4	3	2.3
P2.3	15	13.7	80	83.6	5	2.7
P2.4	20	13.7	75	82.2	5	4.1
P2.5	20	15.9	70	74.6	10	9.5
P2.6	20	18.3	65	71.5	15	14.3
P2.7	20	22.8	60	92.6	20	26.3

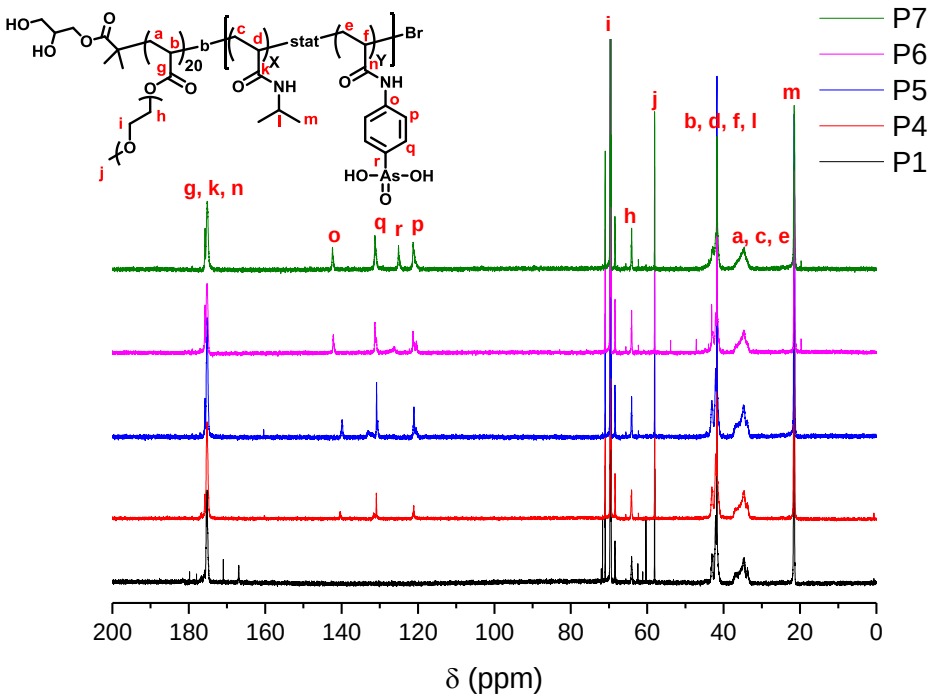

Figure 2.19 Cryoprobe ^{13}C NMR spectrum of PEGA$_{20}$-b-NIPAm$_{80}$ (P2.1) and PEGA$_{20}$-b-(NIPAm$_{80-n}$-co-AsAm$_n$) (P2.4 n = 5; P2.5 n = 10; P2.6 n = 15; P2.7 n = 20)

Table 2.3: Table of summary polymer composition based on cryoprobe ^{13}C NMR (Figure 2.37)

	AsAm content %			NIPAM content %			PEGA content %		
	Theoretical	∫ o	∫ p	Theoretical	∫ m	∫ l	Theoretical	∫ h	∫ j
P2.1	0	0	0	80	89	97	20	16	23
P2.4	5	3	4	75	78	83	20	13	17
P2.5	10	9	9	70	76	72	20	14	16
P2.6	15	14	14	65	68	68	20	19	26
P2.7	20	17	20	60	70	74	20	21	24

Monomer % based on integrals of **a,c** and **e** at ∫32.5 – 38.0 ppm as a constant.

Owing to the deionisation treatment, **P2.6** and **P2.7** underwent self-assembly in aqueous solution at elevated temperature (Figure 2.20). **P2.6** self-assembled at lower temperature (40 °C) than **P2.7** with higher AsAm content (45 °C), as a result of incorporation of AsAm into the NIPAm block. Nevertheless, the temperature for the self-assembly occurred at much lower temperature than the conditions used for the reductive coupling cross-linking.

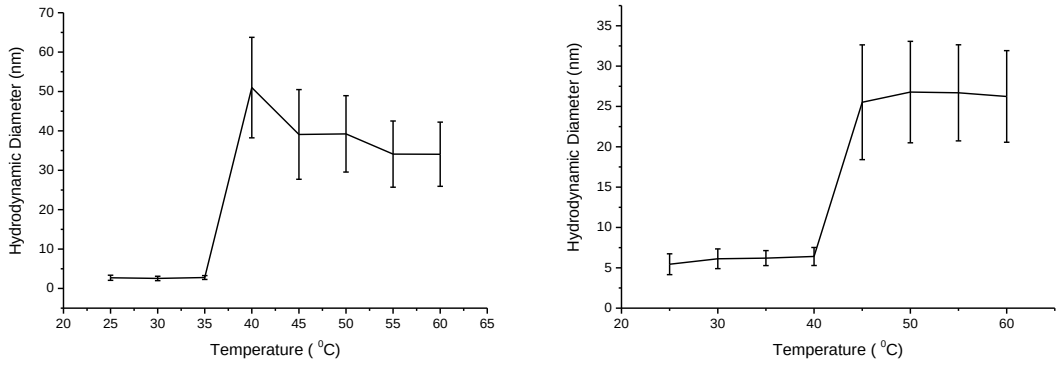

Figure 2.20 Thermal-induced self-assembly of PEGA$_{20}$-*b*-(NIPAM$_{65}$-*co*-AsAm$_{15}$) (P2.6, left) and PEGA$_{20}$-*b*-(NIPAM$_{60}$-*co*-AsAm$_{20}$) (P2.7, right). Hydrodynamic diameter (number %) versus temperature plotted (see Appendix C, S2.20A and S2.20B for supporting information).

Under the same conditions as **P2.5**, the following polymers **P2.6** and **P2.7** were cross-linked, as expected, the resulting nanoparticles were sufficiently stabilised through reductive coupling to be re-dispersed in water, whereby the stabilised particles (**NP$_{As-10}$**, **NP$_{As-15}$**, **NP$_{As-20}$**) were analysed by DLS (Figure 2.21), TEM, and AFM (Figure 2.22 and Figure 2.23). The data obtained for **NP$_{As-15}$** was in good agreement revealing particle sizes < 50 nm whereas for **NP$_{As-20}$** DLS and AFM were in good agreement but the TEM revealed much larger particle sizes (≈ 200 nm). However, in the absence of staining with uranyl acetate, TEM of **NP$_{As-20}$** furnished smaller particles with sizes comparable to those obtained from DLS and AFM (Figure 2.24).

Table 2.4 Light scattering (DLS, SLS) of NP$_{As-10}$, NP$_{As-15}$, NP$_{As-20}$. DLS measured in aqueous solution (1 mg/ml). SLS measured at variable concentration (Figure 2.25). $M_{w,NP}$ was determined using Eq 2.2-2.4. $N_{agg} = M_{w,NP}/M_{n,SEC}$. R_g is the gradient of Zimm plots (Figure 2.25, left) using [NP$_{As-n}$] = 1 mg/ml.

Polymer			SLS			DLS	
	NP	*dn/dC* (mL/g)	$M_{w,NP}$ (g/mol)	N_{agg}	R_g (nm)	D_h (nm)	PDi
P2.5	NP$_{As-10}$	0.144	1.33×10^6	62	32	43	0.06
P2.6	NP$_{As-15}$	0.176	1.13×10^6	51	28	26	0.06
P2.7	NP$_{As-20}$	0.129	4.00×10^6	148	15	36	0.05

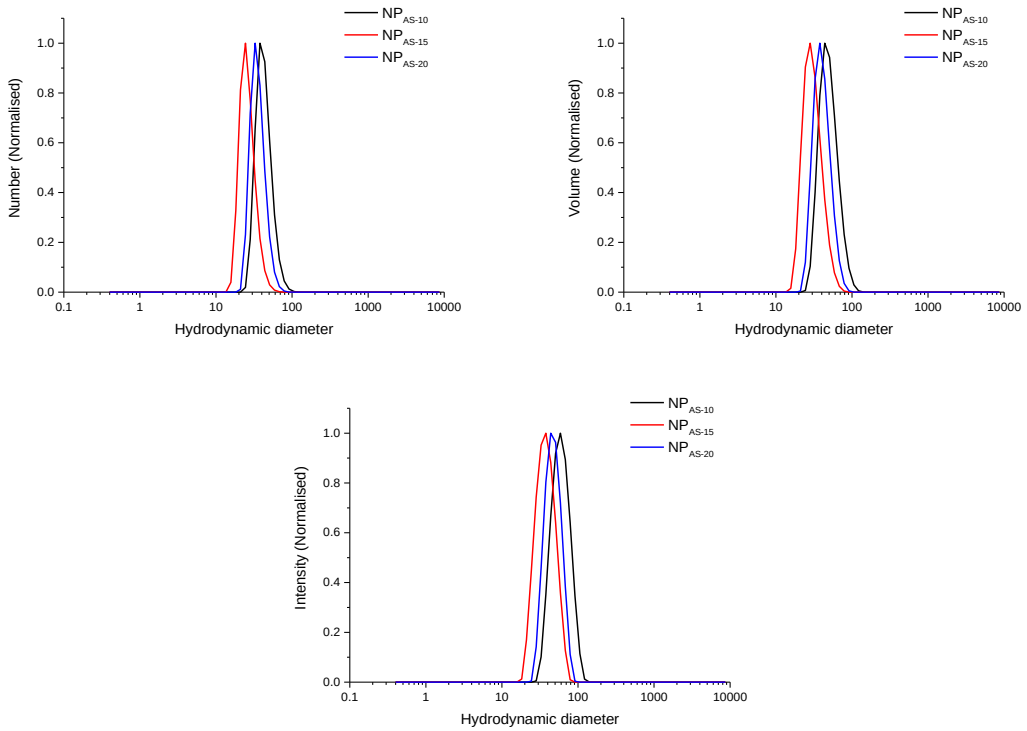

Figure 2.21 Particle size distribution (DLS) curves for NP_{As-10}(black), NP_{As-15}(red), NP_{As-20}(blue) (Table 2.4) (see Appendix C, S2.21 for supporting information).

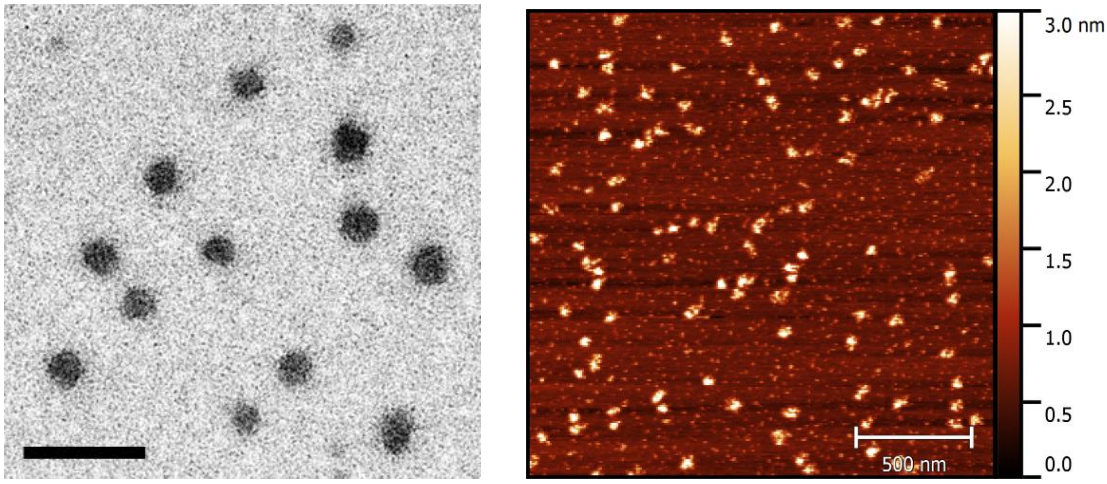

Figure 2.22 Representative TEM (left) and AFM (right) of NP_{As-15}. TEM stained with uranyl acetate. Scale = 500 nm

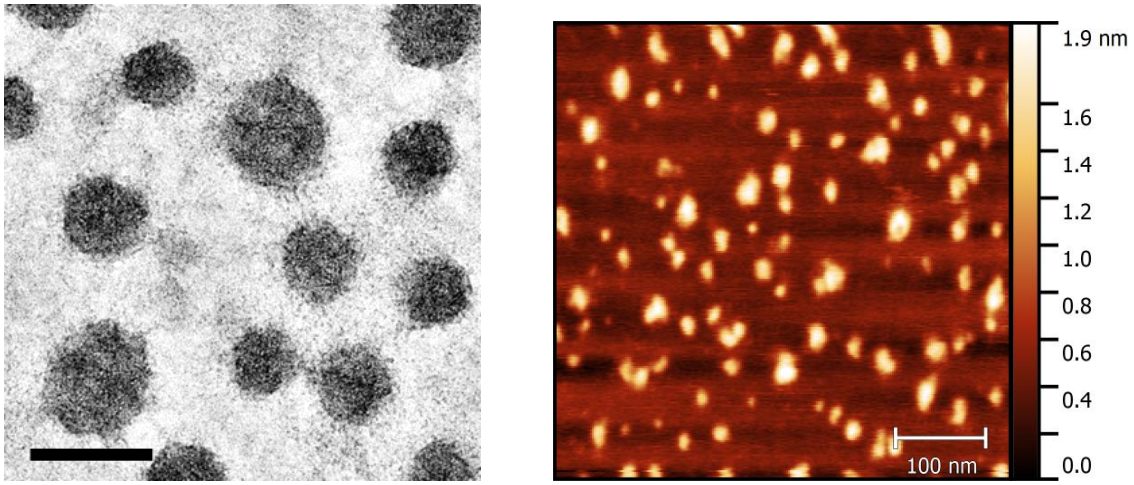

Figure 2.23 Representative TEM (left) and AFM (right) of NP_{As-20}. TEM stained with uranyl acetate. Scale = 100 nm

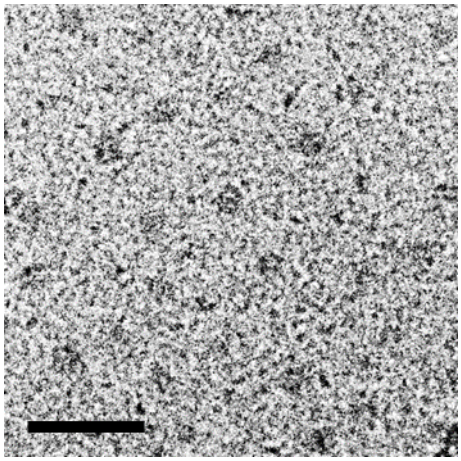

Figure 2.24 Representative TEM without staining (left) of NP_{As-20}. Scale = 100 nm

To determine more accurate particle size data (Radius of gyration - R_g, aggregation number - N_{agg} and nanoparticle molecular weight - $M_{w,NP}$) static light scattering (SLS) was performed (Figure 2.25), where multiple scattering angles were measured as function of concentration to extrapolate the molecular weight at infinite dilutions (Fig 2.25). According to SLS analysis, particles **NP_{As-10}** and **NP_{As-15}** were similar, whereas increasing the AsAm monomer feed to n = 20 (**NP_{As-20}**) resulted in the formation of more densely packed particles as indicated by the increase in the $M_{w,NP}$ (1 x 10^6 – 4 x 10^6 g/mol) and N_{agg} (62 -148), which coincided with a decrease in the D_h obtained from DLS (43 – 36 nm) (Table 2.4).

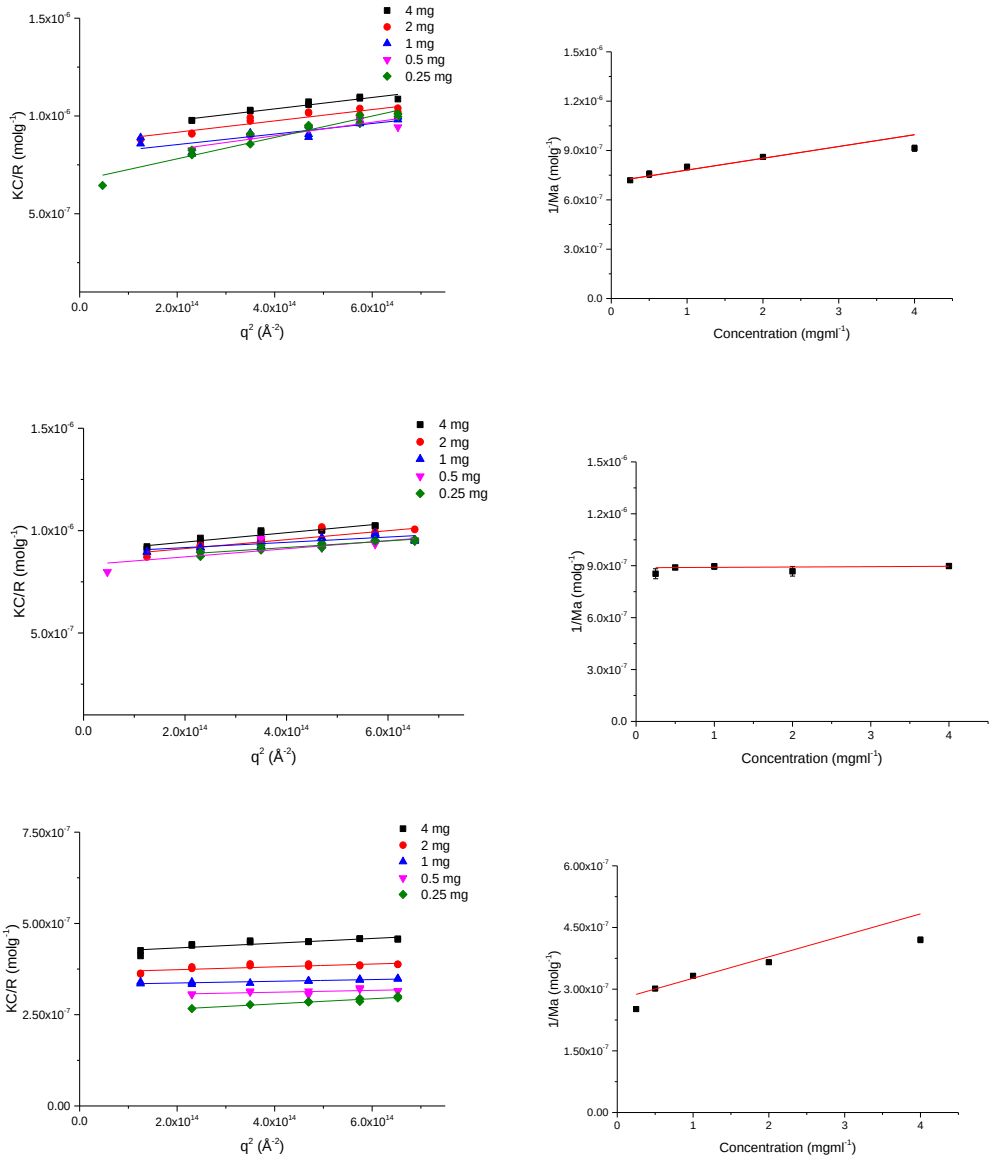

Figure 2.25 Evolution of KC/R in water as function of q^2 and concentration for NP_{As-10} (top), NP_{As-15} (middle), NP_{As-20} (bottom), obtained by SLS.

The relative stabilities of **NP_{As-10}**, **NP_{As-15}** and **NP_{As-20}**, were initially investigated in aqueous solution at 37 °C, in which **NP_{As-10}** was found to be stable for 48 hours where **NP_{As-15}** and **NP_{As-20}** remained stable for at least 96 hours (Figure 2.26).

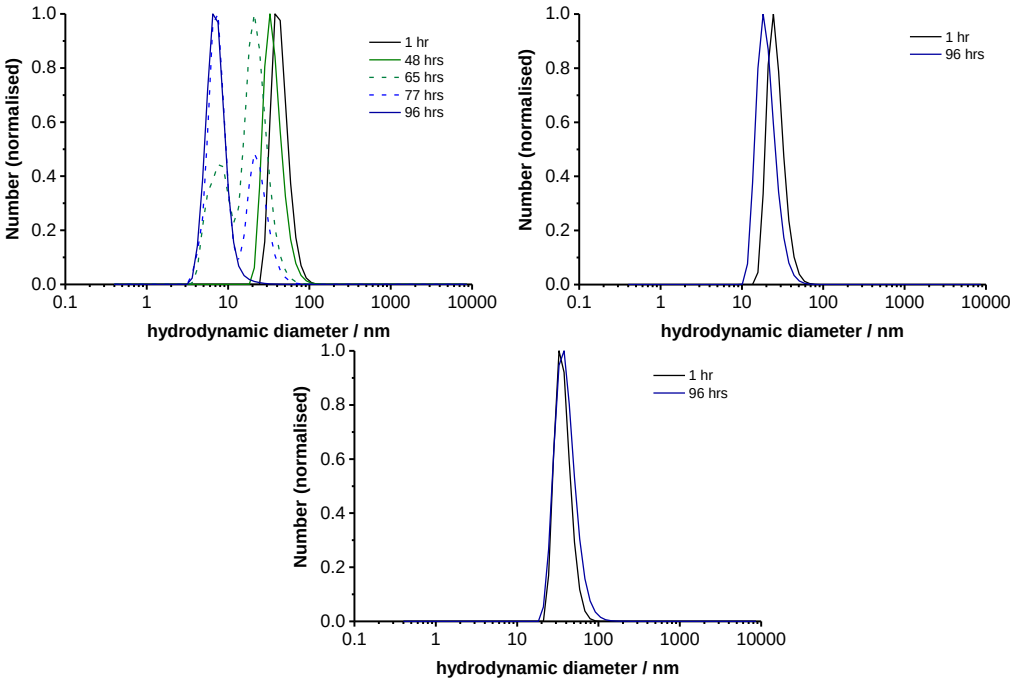

Figure 2.26 Particle size distribution curves of NPAs-10 (left), NPAs-15 (centre), NPAs-20 (right) as a function of time in aqueous solution (1 mg/ml) (see Appendix C, S2.26A, S2.26B and S2.26C for supporting information).

In aqueous glutathione (GSH) at a concentration mimicking intracellular conditions ([GSH] = 5 mM), further differentiation in particle stability was observed. $\mathbf{NP_{As\text{-}10}}$ was stable for only 1 hr with the majority of the nanoparticles undergoing disassembly within 3 hrs. The faster rate of disassembly was mirrored by $\mathbf{NP_{As\text{-}15}}$ and $\mathbf{NP_{As\text{-}20}}$ which disassembled within 12 hrs and 20 hrs respectively (Figure 2.27). The enhanced rate of disassembly is attributed to the formation of more enthalpically favoured As-S bonds in favour of the weak As-As bonds originally formed through reductive coupling. The trend suggests that particle stability can be tuned by adjusting the AsAm monomer feed which could be advantageous for applications such as drug delivery.

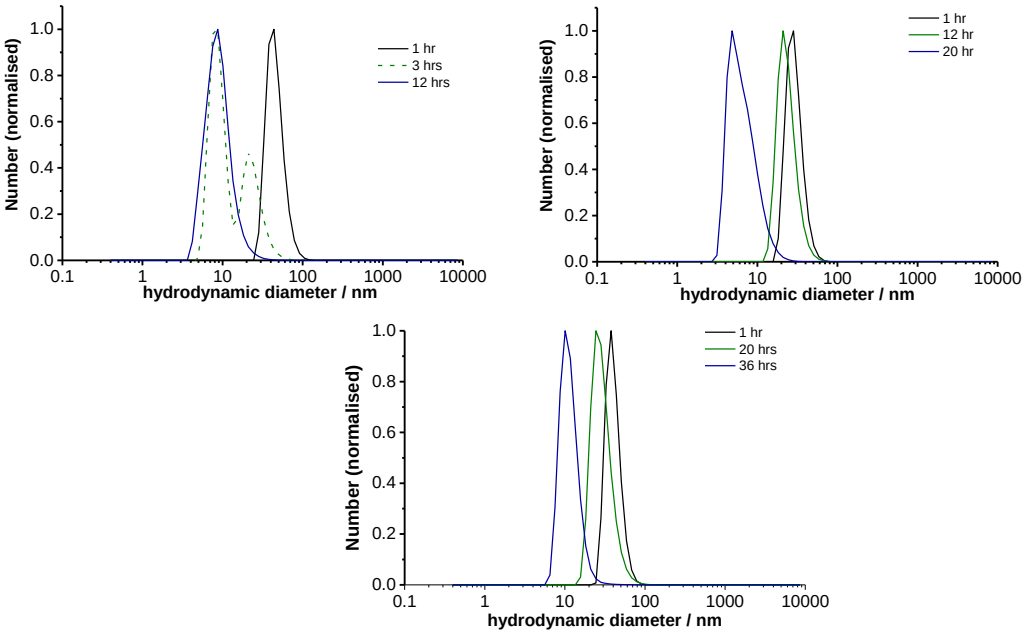

Figure 2.27 Particle size distribution (DLS), illustrating the relative stability of $NP_{As\text{-}10}$ (left), $NP_{As\text{-}15}$ (centre) and $NP_{As\text{-}20}$ (right) in aqueous GSH (5 mM, 1 mg/ml) (see Appendix C, S2.27A, S2.27B and S2.27C for supporting information)

Finally, the stability was investigated under aggressive oxidative conditions (aqueous H_2O_2, 5 mM). Under these conditions all nanoparticles were completely disassembled within 1 hr (Figure 2.28). As the particles were originally crosslinked via reductive coupling, it is likely that disassembly occurs under the strong oxidative conditions in aqueous solution through hydrolysis of the As-As bonds and oxidation of As(I) back to As(V).

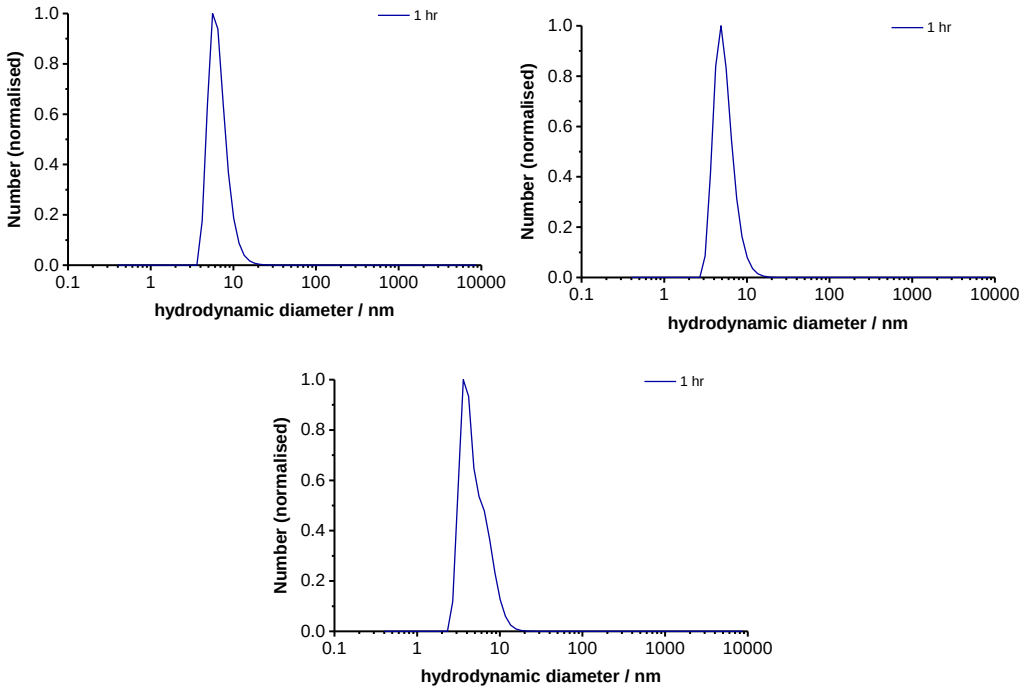

Figure 2.28 Particle size distribution curves of NP_{As-10} (left), NP_{As-15} (centre), NP_{As-20} (right) as a function of time in aqueous H_2O_2 (5 mM, 1 mg/ml) (see Appendix C, S2.28A, S2.28B and S2.28C for supporting information)

2.2.4 Cytoxicity of the polymeric arsenical nanoparticles

Considering the successful synthesis, self-assembly and responsive crosslinking of As-functional block copolymers and with potential biomedical applications in mind, evaluation of their toxicity is essential. It has recently been reported that polymeric arsenicals exhibit limited toxicity *in vitro*.[17, 18] Here, the acute toxicity of the As-functional block copolymers (**P2.2-P2.7**) and the nanoparticles (**NP_{As-10}, NP_{As-15}, NP_{As-20}**) were determined *in vitro* via a standard XTT assay using the human PC3 cell line as model. PC3 (human prostate carcinoma) cells were obtained from the European Collection of Cell Cultures (ECACC). Pleasingly, it was found that all polymers (**P2.2-P2.7**) and their associated nanoparticles (**NP_{As-10}, NP_{As-15}, NP_{As-20}**) were not toxic at concentrations up to 2.0 mg/ml (Figure 2.29).

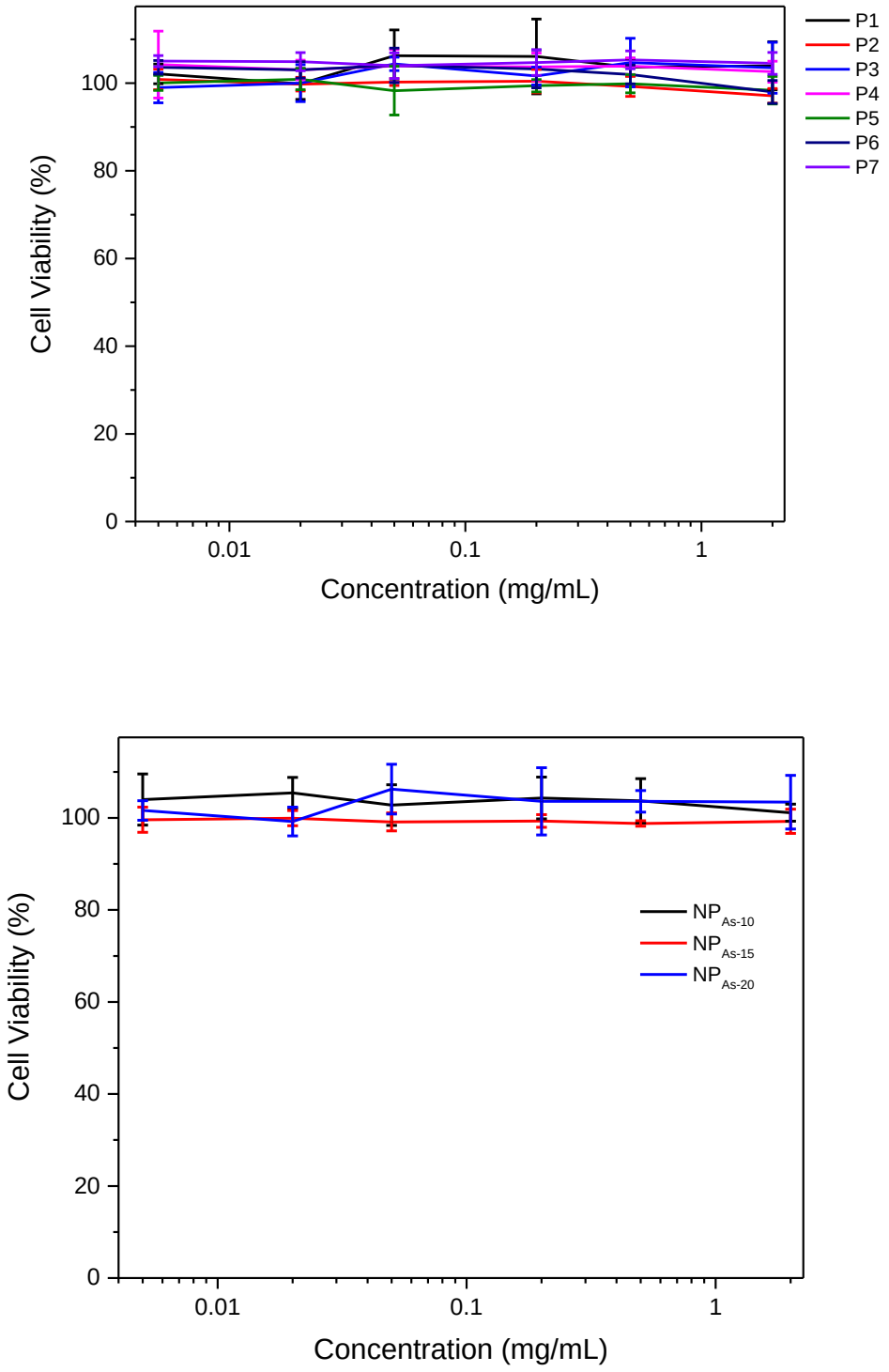

Figure 2.29 In vitro cell viability of polymers P2.1-P2.7 (top) and nanoparticles NP_{As-10}, NP_{As-15}, NP_{As-20}, (bottom) (XTT viability assay using PC3 cell line).

2.3 Conclusions

Block copolymers containing an As-functional monomer (AsAm) have been synthesised by aqueous SET-LRP. Various amounts of AsAm have been incorporating into the hydrophilic corona-forming block ((PEGA$_{20-n}$-*co*-AsAm$_n$)-*b*-NIPAm$_{80}$) or the thermoresponsive core-forming block (PEGA$_{20}$-*b*-NIPAm$_{80-n}$-*co*-AsAm$_n$)). The block copolymers undergo self-assembly at elevated temperatures (60 °C) to form nanoparticles (D_h < 50 nm). Reductive coupling of pendent arsenic acid (As(V)) functional groups has been investigated for the first time for crosslinking and stabilisation. The presence of AsAm in the corona forming block (n = 3, 5) is insufficient for particle stabilisation upon cooling to ambient temperature. Conversely, incorporation of AsAm (n = 5, 10, 15, 20) into the more densely packed core of the nanoparticles affords particles that are stable upon cooling to ambient temperature. The nanoparticles and the polymers they are derived from are non-toxic and the stability of the nanoparticles in aqueous solution and model biological solutions (GSH, H_2O_2) increases as a function of the AsAm monomer feed, both of which we believe could be advantageous of biomedical applications.

2.4 Experimental

2.4.1 Materials and methods

p-Arsanilic acid, acryloyl chloride, glutathione (GSH), hypophosphorous acid (50%), *N*-Isopropylacrylamide (NIPAm, 97%) and poly(ethylene glycol) methyl ether acrylate (PEGA, average M_n = 480) were purchased from Sigma Aldrich and used as received. HPLC grade water (H_2O, VWR international, LLC) was used as the solvent for disproportionation and polymerisation. Copper(I) bromide (CuBr, 98%, Sigma-Aldrich) was purified prior to use via sequentially washing with acetic acid and ethanol and then dried under vacuum. *Tris*(2-(dimethylamino)ethyl)amine[1] and 2,3-dihydroxypropyl 2-bromo-2-methylpropanoate[2] were prepared as reported in the literature. was synthesized according to the literature procedure. Membrane dialysis tubing (nMWCO 3.5 kDa) was obtained from Spectrum Laboratories. All other solvents and reagents were purchased from commercial suppliers (Sigma-Aldrich, Fisher Scientific) and use as received unless otherwise stated.

Nuclear Magnetic Resonance (NMR) spectroscopy (^{1}H NMR) spectra were recorded on a Bruker HD 300 spectrometer (300 MHz) at 27 °C in deuterated water (D_2O). Chemical shift values (δ_{ppm}) are reported in ppm. The residual proton signal of the solvent (δ_H = 4.79 ppm) was used as internal reference. ACDLABS software was used to analyse the data obtained. Number-average molar masses ($M_{n,SEC}$) and dispersity values ($Đ$) were determined using Size exclusion Chromatography (SEC) with DMF as an eluent. SEC analysis was conducted on Polymer Laboratories PL-GPC 50 Plus system using a Polar Gel-M guard column (7.5 × 50 mm) followed by two Polar Gel-M columns (7.5 ×300 mm). DMF (0.1% LiBr) was used as eluent at 1.0 mL min^{-1} at 50 °C. All polymer samples were filtered through a nylon membrane with 0.45 µm pore size before injection (100 µL). Commercial narrow linear poly(methyl methacrylate) (PMMA) standards in range of 2.0 × 10^2 − 1.0 × 10^6 gmol^{-1} were used to calibrate the DMF SEC system. The SEC data obtained were analysed using Agilent technologies GPC/SEC software to determine $M_{n,SEC}$ and $Đ$ based on the PMMA calibration. Hydrodynamic diameters (D_h) and size distributions were determined by Dynamic Light Scattering (DLS) on a MALVERN Zetasizer Nano ZS operating at 25 °C with a 4 mW He-Ne 633 nm laser module. Measurements were made at a detection angle of 173° (back scattering). Measurements were repeated three times with automatic attenuation selection and measurement position. The results were analysed using Malvern DTS 6.20 software. PDI values were calculated using equation Eq 2.1

$$PDI = \sigma^2/d^2 \quad \text{(Eq 2.1)}$$

Where σ is the standard deviation, and d is the diameter, both obtained from the number distribution.

2.4.2 Determination of M_w by Static Light Scattering.

The incremental refractive index, dn/dC, was determined by measuring the refractive index of the polymer over a range of concentrations (1.33, 0.66, 0.33, 0.167 mg/ml) . The RI was determined using a Shodex RI detector, operating at a wavelength of 632 nm. Multiplying the gradient, of the plot of RI vs. concentration, by the refractive index of the solvent (water = 1.3325) and dividing by the RI constant of the instrument (−1398000) gives the dn/dC of the polymer (table 2.3). Light scattering measurements were obtained using an ALV-CGS3 system operating with a vertically polarized laser with the

wavelength $\lambda = 632$ nm. The measurements were taken at 20 °C over a range of scattering wave vectors ($q = 4\pi n\sin(\theta/2)/\lambda$, with θ being the angle of observation and n the refractive index of the solvent). The Rayleigh ratio, R_θ, was determined using Eq 2.2;

$$R_\theta = \frac{I_{solution}(\theta) - I_{solvent}(\theta)}{I_{toluene}(\theta)} \cdot \left(\frac{n_{solution}}{n_{toluene}}\right)^2 \cdot R_{toluene} \qquad \text{(Eq 2.2)}$$

Where $I_{solution}$, $I_{solvent}$ and $I_{toluene}$ are the scattering intensities of the solution, solvent and reference (toluene) respectively, n is the refractive index (n_{water}=1.333, $n_{toluene}$=1.496) and $R_{toluene}$ the Rayleigh ratio of toluene ($R_{toluene}$= 1.35 × 10^{-5} cm^{-1} for λ = 632.8 nm). The optical constant, K, is defined by Eq 2.3, where N_a is the Avogadro number and dn/dC is the incremental refractive index.

$$K = \frac{4\pi^2 {n_{solvent}}^2}{\lambda^4 N_a}\left(\frac{\partial n}{\partial C}\right)^2 \qquad \text{(Eq 2.3)}$$

In all cases it was verified that the apparent radius of gyration of the systems verified $q \times Rg < 1$. The Zimm approximation can thus be used to obtain Eq 2.4. Plotting KC/R_θ as a function of q^2 for each concentration yielded the apparent radius of gyration Rg of the scatterers as well as their apparent molecular weight extrapolated to zero angle, $\boldsymbol{M_a}$. Representative plots are shown in the Figure 2.21.

$$\frac{KC}{R_\theta} = \frac{1}{M_a}\left(1 + \frac{{q^2 R_g}^2}{3}\right) \quad \text{(Eq 2.4)}$$

At a given concentration the Rayleigh ratio, Rθ, is related to the apparent molecular weight of the sample, given by Eq 2.4. It is only at infinite dilutions, where the interactions between scattering particles are negligible, that the apparent molecular weight is equal to the true molecular weight. Multiple concentrations were measured and a plot of linear regression was used to determine the apparent molecular weight at a concentration of 0 $mgml^{-1}$.

2.4.3 Cell viability

PC3 (human prostate cancer) cells were cultured in High Glucose DMEM medium supplemented with 10% fetal bovine serum. For cell viability evaluation, PC3 cells were seeded in a 96 well plate at a density of 1×10^4 cells per well. After 16 hours, the culture medium was replaced by fresh media containing a series of dilution of the polymers (0.0625, 0.125. 0.25, 0.5, 1 and 2 mg/ml), prepared from stock solutions in PBS at 500 µM. Following 24 hours incubation, the medium was removed and replaced with fresh

medium. The cells were incubated with a freshly prepared solution of XTT (0.2 mg/mL^{-1}) and N-methyl dibenzopyrazine methyl sulfate (250 µM) in medium for 16 hours. Absorbance of the samples was finally measured using a plate reader at 450 nm and 650 nm. The data presented are representative of a minimum of two independent experiments where each sample was measured in triplicate. Errors reported correspond to the standard deviation of the mean.

2.4.4 Atomic Force Microscopy (AFM)

AFM images were acquired in AC mode on a Cypher S system (Asylum Research). The probes used were the AC160TS from Olympus probes with a nominal resonant frequency of 300 kHz and a spring constant of approximately 40 N m^{-1} on a Multimode AFM (Asylum Research). Images were acquired at a pixel resolution of 512 and a scan rate of 1 Hz. Samples were diluted to 0.1 mg mL^{-1} in water and 4 µL of solution was drop-deposited onto freshly cleaved mica discs. The data were analyzed by the Asylum Research software.

2.4.5 Transmission Electron Microscopy (TEM)

Nanoparticle solutions at a concentration of 0.1 mg/ml were deposited as 5 µl aliquots on 400 mesh carbon-coated Formvar copper grids and allowed to dry completely. Once dry, grids were stained with 1% aqueous uranyl acetate (UA) by touching the grid to 5 µl UA and drawing off stain immediately, followed by placing the grid atop a 5 µl drop of UA for 15 s in the dark, and drawing off excess liquid as before. Samples were imaged on a FEI Tecnai F20 transmission electron microscope, utilising a Gatan Ultrascan 1000 (2k x 2k) CCD camera

2.4.6 Synthetic procedures

Synthesis of As functional monomer 4-(*N*-acrylamido)phenylarsonic acid [38, 39]

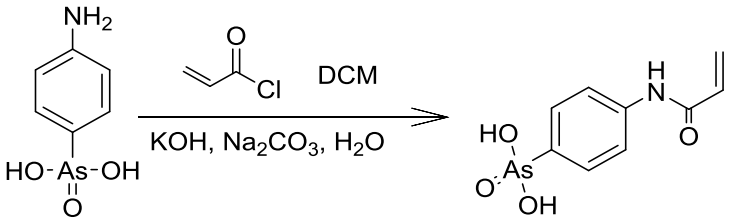

p-arsanilic acid

4-(*N*-acrylamido)phenylarsonic acid

Potassium hydroxide (5.1 g, 91.8 mmol) was dissolved in deionised water (125 mL). The mixture of *p*-arsanilic acid (10.0 g, 46.1 mmol) and Na_2CO_3 (14.5 g, 137.1 mmol) was added portionwise to the KOH to afford dissolution. Acryloyl chloride (5.6 mL, 68.9 mmol), in dichloromethane (25 mL) was quickly added into the *p*-arsanilic acid solution at 0 °C. and stirred for 15 minutes. The aqueous phase was collected are carefully acidified (to minimise effervescence) to pH 1 through the addition of H_2SO_4 (98%) which resulted in precipitation of product. The precipitate was collected by filtration, washed with cold water and dried in the vacuum oven overnight to afford the title compound as a white solid. (Yielded 11.2 g, 90%) The spectroscopic data matched the reported values in the literature.

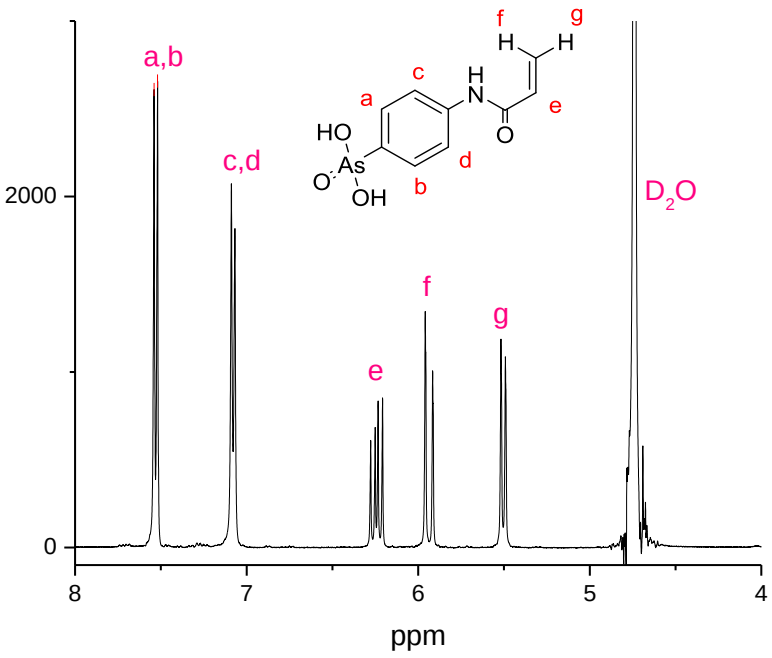

^{1}H NMR spectrum of 4-(*N*-acrylamido)phenylarsonic acid

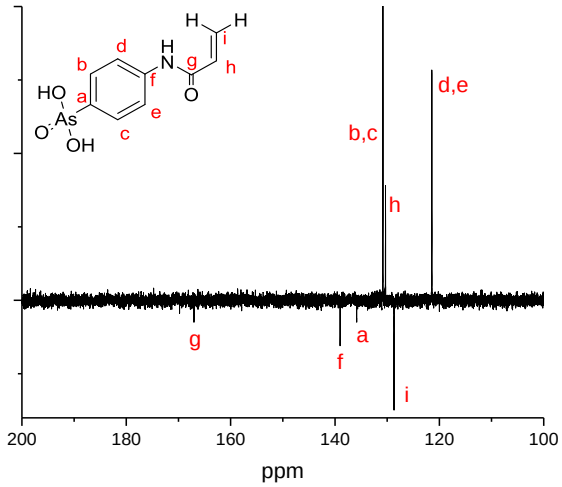

^{13}C NMR spectrum of 4-(*N*-acrylamido)phenylarsonic acid

General procedure for synthesis of [PPEGA$_{20-n}$-*co*-AsAm$_n$]-*b*-NIPAm$_{80}$ by aqueous SET-LRP.

Me$_6$Tren (14 µL, 52 µmol, 0.6 eq) was dissolved in HPLC grade H_2O (1 ml) prior to addition of CuBr (10 mg, 70 µmol, 0.8 eq). The resulting solution was deoxygenated with N_2 affording disproportionation as indicated by the strong blue colour of the solution and precipitation of Cu(0). Simultaneously, in a separate vessel 2,3-dihydroxypropyl-2-bromo-2-methylpropanoate (1 eq) and PEGA (20-n eq, M_n = 480 g.mol^{-1}) were dissolved in HPLC grade H_2O prior to addition of AsAm (n eq) dissolved in 0.5 M NaOH (n eq) to give a total volume of 2.5 ml. The resulting solution was also deoxygenated by bubbling N_2 for 15 mins. The monomer/initiator mixture was then added as a single portion to the disproportionation solution via deoxygenated syringe. The progress of the reaction was followed by ^{1}H NMR and SEC analysis. Upon completion (typically >99% conversion in 15-30 mins) a deoxygenated solution of NIPAm (80 eq) in HPLC grade H_2O (3 mL) was added as a single portion to the polymerisation solution via deoxygenated syringe. The progress of the chain extension was followed by ^{1}H NMR and SEC. Upon completion the Cuprisorb® was added the reaction mixture to remove the (in)soluble copper species prior to dialysis (nMWCO 3.5 KDa) against de-ionised water. The purified polymers were isolated by lyophilisation to obtain white solid (yielded approximately between 70 -90 %).

General procedure for synthesis of PPEGA$_{20}$-*b*-[NIPAm$_{80-n}$-*co*-AsAm$_n$] by aqueous SET-LRP.

Me$_6$Tren (14 µL, 52 µmol, 0.6 eq) was dissolved in HPLC grade H_2O (1 ml) prior to addition of CuBr (10 mg, 70 µmol, 0.8 eq). The resulting solution was deoxygenated with N_2 affording disproportionation as indicated by the strong blue colour of the solution and precipitation of Cu(0). Simultaneously, in a separate vessel 2,3-dihydroxypropyl-2-bromo-2-methylpropanoate (1 eq) and PEGA (20 eq, M_n = 480 g.mol^{-1}) were dissolved in HPLC grade H_2O (1 mL). The resulting solution was also deoxygenated by bubbling N_2 for 15 mins. The monomer/initiator mixture was then added as a single portion to the disproportionation solution via deoxygenated syringe. The progress of the reaction was followed by ^{1}H NMR and SEC analysis. Upon completion (typically >99% conversion in 15-30 mins) a solution of AsAm (n eq) dissolved in 0.5 M NaOH (n eq) was added to a solution of NIPAm (80-n eq) in HPLC grade H_2O give a total volume of 4.0 ml and the resulting mixture was deoxygenated with N_2 prior to addition to the polymerisation solution as a single portion via deoxygenated syringe. The progress of the chain extension was followed by ^{1}H NMR and SEC. Upon completion the Cuprisorb® was added the reaction mixture to remove the (in)soluble copper species prior to dialysis (nMWCO 3.5 KDa) against de-ionised water. The purified polymers were isolated by lyophilisation. Alternatively, following completion of the second block, 1 M HCl was added until the blue colour of the Cu(II)-Me$_6$Tren complex disappeared and the insoluble Cu(0) was filtered off to afford a homogeneous colourless solution which was then dialysed (nMWCO 3.5 KDa) against de-ionised water for 2 days changing the water twice. The purified polymers were isolated by lyophilisation to obtain white solid (yielded approximately between 70 -90 %).

General procedure for self-assembly and crosslinking of [PEGA$_{20-n}$-*co*-AsAm$_n$]-*b*-NIPAm$_{80}$ and PEGA$_{20}$-*b*-[NIPAm$_{80-n}$-*co*-AsAm$_n$].

The procedure reported for the reductive coupling of organic arsenicals was translated to the As-functional block copolymers. Briefly, As-functional polymer was dissolved in a deoxygenated aqueous solution of hypophosphorus acid (H_3PO_2, 10 wt%, 10 mg/ml polymer) and deoxygenated KI (1 vol% from a 3 wt% aq solution) was added. The

solution was allowed to equilibrate for 16 hrs before heating at 60 ^{0}C for 2 hrs. The resulting solution was dialysed against deionised water (nMWCO 3.5 KDa) to remove the electrolytes for no longer than 24 hrs and changing the water 4 times. The crosslinked particles were isolated by lyophilisation to obtain white solid (yielded approximately between 90-98 %) and were readily re-dispersed in H_2O.

General procedure for particle stability and disassembly.

Polymer nanoparticles **NP_{As-10}, NP_{As-15}, NP_{As-20},** were dissolved separately in deionised water, glutathione (5 mM) and H_2O_2 (5 mM) (1 mg/ml). The solutions were filtered through (450 µm nylon filters) into separate plastic cuvettes (with a lid) and incubated at 37 ^{0}C in water bath. Disassembly was monitored through the measurement of changes in particle size (D_h) as a function of time by DLS.

2.5 References

1. J. Zhang, G. Gody, M. Hartlieb, S. Catrouillet, J. Moffat and S. Perrier, *Macromolecules*, 2016, **49**, 8933-8942.
2. J. Zhang, J. Tanaka, P. Gurnani, P. Wilson, M. Hartlieb and S. Perrier, *Polym. Chem,*, 2017, **8**, 4079-4087.
3. M. Hartlieb, T. Floyd, A. B. Cook, C. Sanchez-Cano, S. Catrouillet, J. A. Burns and S. Perrier, *Polym. Chem,*, 2017, **8**, 2041-2054.
4. C. Bray, R. Peltier, H. Kim, A. Mastrangelo and S. Perrier, *Polym. Chem,*, 2017, **8**, 5513-5524.
5. X. Zhang, S. Malhotra, M. Molina and R. Haag, *Chem. Soc. Rev.*, 2015, **44**, 1948-1973.
6. R. J. Wojtecki, M. A. Meador and S. J. Rowan, *Nat Mater*, 2011, **10**, 14-27.
7. J. J. Cash, T. Kubo, A. P. Bapat and B. S. Sumerlin, *Macromolecules*, 2015, **48**, 2098-2106.
8. C. C. Deng, W. L. A. Brooks, K. A. Abboud and B. S. Sumerlin, *ACS Macro Lett.*, 2015, **4**, 220-224.
9. D. Roy and B. S. Sumerlin, *ACS Macro Lett.*, 2012, **1**, 529-532.
10. A. P. Bapat, D. Roy, J. G. Ray, D. A. Savin and B. S. Sumerlin, *J. Am. Chem. Soc.*, 2011, **133**, 19832-19838.
11. D. Roy, J. N. Cambre and B. S. Sumerlin, *Chem. Commun.*, 2008, 2477-2479.
12. Z. Zhou, L. Li, Y. Yang, X. Xu and Y. Huang, *Biomater.*, 2014, **35**, 6622-6635.
13. S. Binauld, W. Scarano and M. H. Stenzel, *Macromolecules*, 2012, **45**, 6989-6999.
14. H.-Y. Wen, H.-Q. Dong, W.-j. Xie, Y.-Y. Li, K. Wang, G. M. Pauletti and D.-L. Shi, *Chem. Commun.*, 2011, **47**, 3550-3552.
15. Y. Zhang, J. Zhou, C. Yang, W. Wang, L. Chu, F. Huang, Q. Liu, L. Deng, D. Kong, J. Liu and J. Liu, *Int. J. Nanomed.*, 2016, **11**, 1119-1130.
16. V. P. Whittaker, *Biochem. J.*, 1947, **41**, 56-62.
17. C. Footman, P. A. de Jongh, J. Tanaka, R. Peltier, K. Kempe, T. P. Davis and P. Wilson, *Chem. Commun.*, 2017, **53**, 8447-8450.
18. P. Wilson, A. Anastasaki, M. R. Owen, K. Kempe, D. M. Haddleton, S. K. Mann, A. P. Johnston, J. F. Quinn, M. R. Whittaker and P. J. Hogg, *J. Am. Chem. Soc.*, 2015, **137**, 4215-4222.
19. L. R. Smith and J. L. Mills, *J. Organomet. Chem.*, 1975, **84**, 1-15.
20. N. C. Lloyd, H. W. Morgan, B. K. Nicholson and R. S. Ronimus, *Angew. Chem. Int. Ed.*, 2005, **44**, 941-944.

21. K. Naka, T. Umeyama and Y. Chujo, *J. Am. Chem. Soc.*, 2002, **124**, 6600-6603.
22. T. Umeyama, K. Naka and Y. Chujo, *J. Polym. Sci., Part A: Polym. Chem.*, 2004, **42**, 3023-3028.
23. T. Umeyama, K. Naka and Y. Chujo, *J. Polym. Sci., Part A: Polym. Chem.*, 2004, **42**, 3604-3611.
24. T. Umeyama, K. Naka and Y. Chujo, *Macromolecules*, 2004, **37**, 5952-5958.
25. T. Umeyama, K. Naka, A. Nakahashi and Y. Chujo, *Macromolecules*, 2004, **37**, 1271-1275.
26. M. J. Percino, V. M. Chapela, R. Gutiérrez-Pérez and A. M. Herrera, *Des. Monomers Polym.*, 2000, **3**, 155-160.
27. T. Zayas, M. J. Percino, J. Cardoso and V. M. Chapela, *Polymer*, 2000, **41**, 5505-5512.
28. M. J. Percino, V. M. Chapela and A. Jiménez, *J. Appl. Polym. Sci.*, 2004, **94**, 1662-1669.
29. B. A. Yáñez-Martínez, J. Percino and V. M. Chapela, *J. Appl. Polym. Sci.*, 2010, **118**, 2849-2858.
30. G. Soriano-Moro, J. Percino, M. Cerón, M. E. Castro and V. M. Chapela, *J. Polym. Res.*, 2014, **21**, 492.
31. J. Chiefari, Y. K. Chong, F. Ercole, J. Krstina, J. Jeffery, T. P. T. Le, R. T. A. Mayadunne, G. F. Meijs, C. L. Moad, G. Moad, E. Rizzardo and S. H. Thang, *Macromolecules*, 1998, **31**, 5559-5562.
32. M. Kato, M. Kamigaito, M. Sawamoto and T. Higashimura, *Macromolecules*, 1995, **28**, 1721-1723.
33. J.-S. Wang and K. Matyjaszewski, *J. Am. Chem. Soc.*, 1995, **117**, 5614-5615.
34. A. Anastasaki, V. Nikolaou, G. Nurumbetov, P. Wilson, K. Kempe, J. F. Quinn, T. P. Davis, M. R. Whittaker and D. M. Haddleton, *Chem. Rev.*, 2016, **116**, 835-877.
35. F. Alsubaie, A. Anastasaki, P. Wilson and D. M. Haddleton, *Polym. Chem,*, 2015, **6**, 406-417.
36. G. Gody, T. Maschmeyer, P. B. Zetterlund and S. Perrier, *Nat. Commun.* 2013, **4**, 2505.
37. S. A. Pergantis, *Analyst*, 1997, **122**, 1063-1068.
38. J. García-Serrano, A. M. Herrera, F. Pérez-Moreno, M. A. Valdez and U. Pal, *J. Polym. Sci., Part B: Polym. Phys.*, 2006, **44**, 1627-1634.
39. J. García-Serrano, U. Pal, A. M. Herrera, P. Salas and C. Ángeles-Chávez, *Chem. Mater.*, 2008, **20**, 5146-5153.

Chapter 3 : Responsivity of polymeric arsenical self-assemblies cross-linked via multifunctional thiol agents

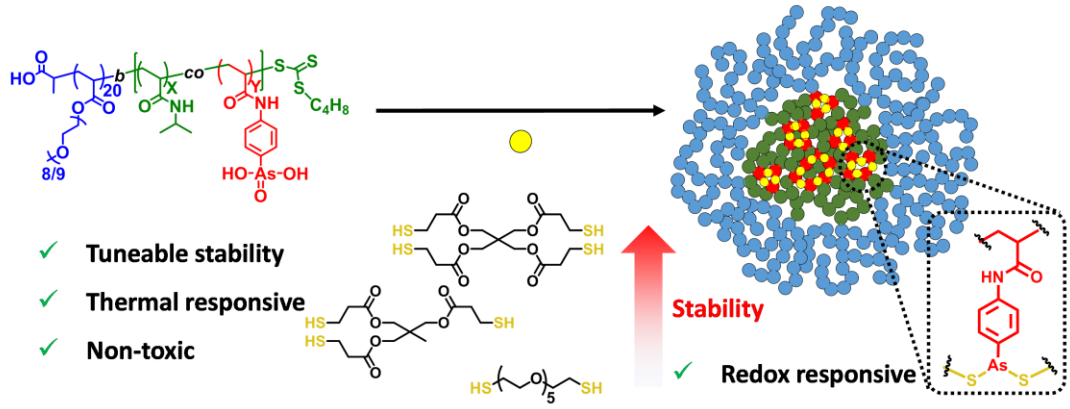

Abstract

The discovery of novel methods to cross-link polymeric particles has been of growing interest in polymer science. To date, using arsenic to cross-link polymers has not been well reported despite its versatile chemistry. The interchangeable oxidation states of arsenic and subsequent changes in chemical properties makes it a promising candidate for redox responsive materials. To this end, we have synthesised thermoresponsive, organic arsenical containing block copolymers using reversible addition fragmentation chain transfer (RAFT) polymerisation capable of simultaneous self-assembly and cross-linking, via the organic arsenical pendant groups, at elevated temperatures in the presence of polythiol cross-linkers. The formation of As(III)-S bonds subsequently stabilises the nanoparticles formed (D_h = 19 - 29 nm) which were characterised by DLS, SLS, TEM and AFM. The stability of the particles was tuned by altering the number of thiol groups in the polythiol cross-linker and by changing the SH : As stoichiometric ratio. The parent block copolymers and nanoparticles are non-toxic and the stability of the nanoparticles in aqueous and model biological solutions (5 mM GSH/H_2O_2) increased with increasing thiol functionality (di- < tri- < tetrathiol) and thiol stoichiometry (SH : As = 2.0 : 1.0 > 1.0 : 1.0). To the best our knowledge, this is the first time that arsenic-thiolate bonding has been employed for redox responsive cross-linking of polymeric nanoparticles. Moreover, the tuneable responsivity of these nanoparticles and the (bio)chemical activity

of organic arsenical reagents could be advantageous for targeted drug delivery and the other biomedical applications.

3.1 Introduction

Supramolecular self-assembly of polymers has been an emerging theme in polymer science, however the dynamic nature of supramolecular self-assemblies often limits its applications in the real world. Although covalent stabilisation can tune the dynamic nature of polymeric nanoparticles, the presence of functional groups required for cross-linking can often limit polymerisation protocols. The emergence of Reversible Deactivation Radical Polymerisation (RDRP) such as Reversible Addition Fragmentation Transfer (RAFT)[1, 2] and copper mediated polymerisation[3-5] has allowed incorporation of monomers of various functionality,[6-13] and thus permitted orthogonality between cross-linking and polymerisation of the cross-linkable monomers. Recently these RDRP protocols has allowed generation of complex block-copolymers[14, 15] and a means of introducing cross-linkable functionalities to generate complex nanostructures.[16, 17] Although considerable work has been focused on covalent chemistry that permanently cross-links self-assembled structures, recently more attention has been steered towards using dynamic covalent bonds for cross-linking polymers that breaks in response to an environmental stimuli. Biodegradability is important property to consider for drug delivery and other biomedical applications, as it prevents materials from accumulating in the body and often correlates to lower toxicity, thus using biologically relevant chemical stimuli to trigger disassembly is quintessential and key for designing nanoparticle system for drug delivery. Most notably disulfides,[18] boronate esters[19] and imines (including hydrazones[20] and oximes[21, 22])[23] have been widely reported in this area, with biologically relevant stimuli such as glutathione, sugars and pH employed to elicit a desired response. This has increasingly attracted interests in various fields beyond drug delivery such as biosensors,[24] and sustainability,[25] thus demonstrating unexplored cross-linking methods that are "responsive" can add value in this field. Recently Yang *et al* has demonstrated, the use of 3-methylmaleamidic acid moiety as a pH responsive amide bond linker, using 2-propionic-3-methylmaleic anhydride as a cross-linker between two polymers to make an amphiphilic block copolymer for self-assembly, whilst triggering its collapse under acidic conditions due to cleavage of the linker.[26, 27]

Interesting, arsphenamine, which is As(I) containing therapeutic drug used to treat syphilis, consists of homocyclic oligomers composed of labile As-As bonds forming the core, which oxidatively hydrolyses to form active As(III). The synthesis of arsphenamie involves heating an arsonic acid (As(V)) precursor in the presence of a suitable reducing agent to As(V) to As(I) which proceeds with the formation of As-As bonds.[28] In chapter 1, As(I) to cross-link micelles formed from block-copolymer containing As(V) in the core forming block were developed.[29] The resulting nanoparticles were responsive towards biologically relevant stimuli, accelerating its degradation with glutathione (GSH) and instantly losing its structure with hydrogen peroxide. The stability of the nanoparticles increased with increasingly number of Arsenic functionality.

In the present study, the use of arsenic to cross-link polymers is not just limited to homocyclisation of As(I). It is widely known that, arsenous acid (As(III)) has high affinity towards thiols, which is implicated in biological toxicity as a result of cross-linking cysteines of important housekeeping proteins inside cells and has been exploited in arsenic based chemotherapeutics.[30, 31] The affinity of As(III) towards dithiols has been demonstrated for peptide-polymer conjugation, in presence of dithiols.[32] Previously polymers with pendant arsenic groups have been synthesised as scaffolds for post-polymerisation thiol modification.[33] The nucleophilic exchangeability of thiols with arsenic-thiolate bonds are well known, and it's the basis for widely used fluorescent bis-arsenicals to bind to thermodynamically favourable tetracysteine tags, through thiol exchanges with ethane dithiol adduct.[34-38] One of the unique properties of arsenic is it's interchangeable oxidation states, between As(III) and As(V) states, due to the subsequent changes in soft to hardness of its Lewis acidity,[39] using biologically relevant oxidising agents to investigate the changes in thiol affinity to As(III) is therefore interesting.

Herein the cross-linking the self-assembled polymeric arsenicals using multi-functional thiol cross-linkers is investigated along with the responsivity of the generated nanoparticles towards redox stimuli in particular to hydrogen peroxide.

3.2 Results and Discussion

In Chapter 2, the possibility of synthesising block copolymers consisting of poly(ethylene glycol) methyl ether acrylate (PEGA, M_n 480 gmol^{-1}) and *N*-isopropylacrylamide (NIPAm) using aqueous single electron transfer-living radical polymerisation (SET-LRP) was reported. Arsenic was incorporated into this copolymer composition through addition of organic arsenical monomer, 4-(*N*-acrylamido)phenyl arsonic acid (AsAm), at various feed ratio's into either the corona forming (PEGA) block or the core-forming (NIPAm) block. The block copolymeric arsenicals were shown to undergo simultaneous self-assembly and reductive cross-linking at elevated temperature in the presence of a reductive environment (H_3PO_2/KI). Though aqueous SET-LRP is the ideal system for the polymerisation of hydrophilic acrylamides and acrylates, hydrolysis of the ω-bromine end group can limit further block extension, and the use of relatively high concentrations of copper can add additional processing steps. RAFT has numerous benefits, such as solvent versatility, as well temporal control over the reaction, allowing the monomer feed of the reaction mixture to be calculated before the polymerisation, which is not feasible with continually initiating catalyst systems such as those in SET-LRP and ATRP systems.

3.2.1 Polymeric arsenical synthesis

To investigate the effect of cross-linking with polythiol reagents on the formation and stability of polymeric arsenical nanoparticles, the polymer composition with the lowest mole fraction of the AsAm capable of forming stable nanoparticles ($PEGA_{20}$-*b*-[$NIPAm_{70}$-*co*-$AsAm_{10}$]) via the reductive coupling method, was targeted. Furthermore, the corona-functional polymeric arsenical [$PEGA_{15}$-*co*-$AsAm_5$]-*b*-$NIPAm_{80}$ which was unable to stabilise nanoparticles was also targeted to determine if these structures could be stabilised using polythiol cross-linkers. Having previously used RAFT polymerisation for the homopolymerisation of an organic arsenical acrylamide ($AsAm(pin)_2$) this method was employed here to synthesise thermoresponsive block copolymeric arsenicals, expanding their versatility in polymer synthesis.

The polymerisations were carried out in 2,2,2-trifluoroethanol (TFE).[40] For optimal chain extension and block efficiency with RAFT polymerisation, the acrylate based PEGA

block was synthesised first, followed by chain extension with the NIPAm block, in a one-pot, sequential chain extension.

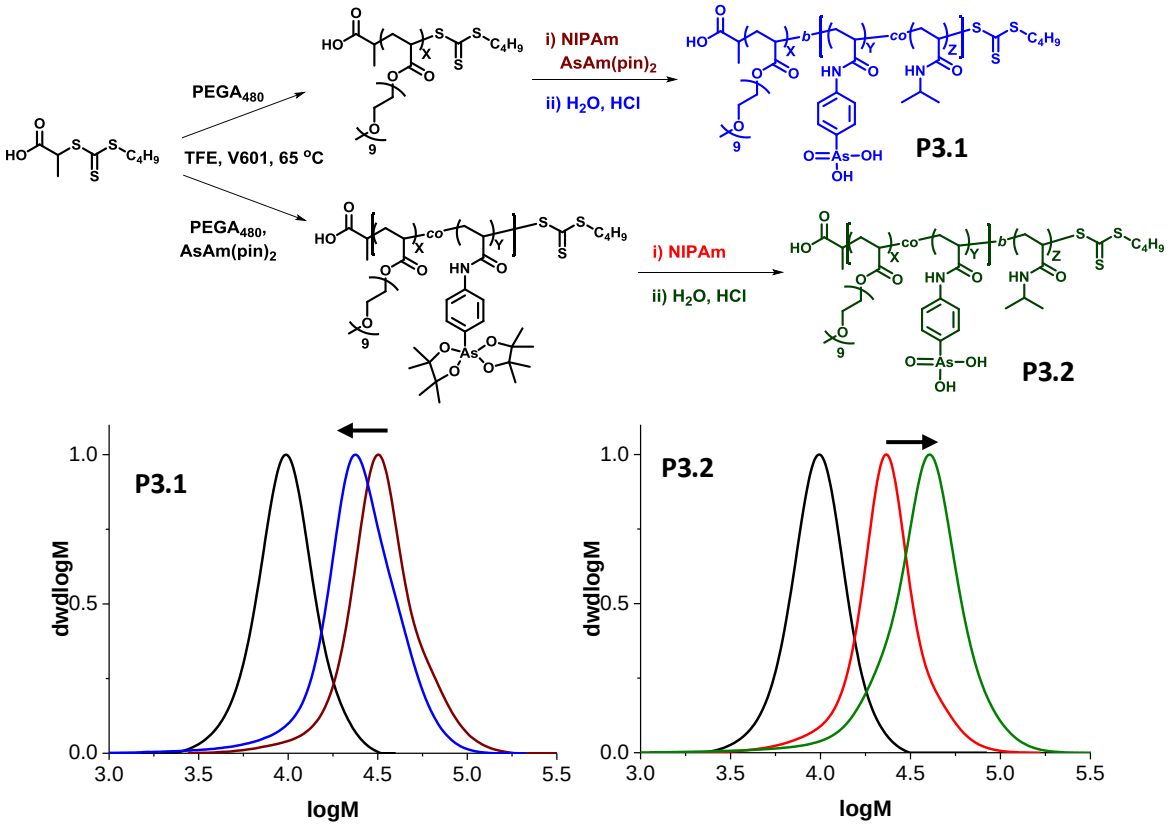

Figure 3.1: Scheme of polymer synthesis of Poly(PEGA-NIPAm) diblock copolymers through sequential chain extension using RAFT polymerisation. Arsenical monomer (AsAm) initially incorporated as pinacol protected AsAm(pin$_2$), subsequently deprotected by acidic dialysis, is either fabricated in the NIPAM block (top, P3.1) or PEGA block (bottom, P3.2). All polymerisations were done in TFE at 65 °C for 24 hours using V601 as an initiator. SEC (DMF) of Arsenic functional block copolymers showing: first block (black), block chain extension (red), after removing pinacol groups (blue) of P3.1 (left) and P3.2 (right). Note that for SEC analysis, the shift in molecular weight distribution after deprotection varies depending which block the arsenic is incorporated.

For the synthesis of the targeted 'core-functional' polymer **P3.1** (PEGA$_{20}$-*b*-[NIPAm$_{70}$-*co*-AsAm$_{10}$]), the polymerisation of the PEGA corona-forming block, in TFE gave good control ($M_{n,th}$ = 10800 gmol^{-1}, $M_{n,SEC}$ = 8900 gmol^{-1}, $Đ$ = 1.16) using PABTC as the RAFT agent. An initial monomer concentration of 1 M of PEGA and initiator (V601) concentration of 9 x 10^{-4} M ([CTA]$_0$/[I]$_0$ = 50) led to near quantitative conversion (98%) at 65 °C after 24 hours. The ratio of monomer feed to CTA was determined from the integral of the acrylic vinyl proton at 5.85 ppm and -C***H***$_3$ of the Z-group belonging to the PABTC (δ = 0.91 ppm). This was subsequently chain extended with AsAm(pin)$_2$ and

NIPAm with combined monomer concentration of 3 M and 1 x 10^{-3} M initiator concentration ($[MacroCTA]_0/[I]_0$ = 16), reaching full conversion of both monomers in the final block after 24 hours. In contrast to the previous study where the sodium salt of the arsenic monomer was polymerised in aqueous solution and subsequently ^{1}H NMR carried out in D_2O, the aromatic peaks can be reliable integrated as in the $CDCl_3$ the aromatic peaks and the acrylamide N-***H*** peaks do not overlap (Figure 3.2). From the aromatic signal at 7.68 ppm (or alternatively 8.00 ppm) it was possible to accurately determine the proportion of $AsAm(pin)_2$ in the monomer feed, furnishing **P3.1** with the composition $PEGA_{22}$-*b*-[$NIPAm_{106}$-*co*-$AsAm(pin_2)_{15}$]. It's important to note, to determine sequential monomer feed to Macro-CTA the acrylic back bone (-C***H***-) between 2.0 -2.5 ppm was used as a reference to the initial block, however alternatively the methoxy (–OC$\boldsymbol{H}_3$) at 3.34 ppm can also be used as reliable reference. The block copolymerisation was also successfully demonstrated by SEC analysis showing shift to a higher molecular weight ($M_{n,th}$ = 29600 gmol^{-1}, $M_{n,SEC}$ = 29300 gmol^{-1}, $Đ$ = 1.27) (Figure 3.1).

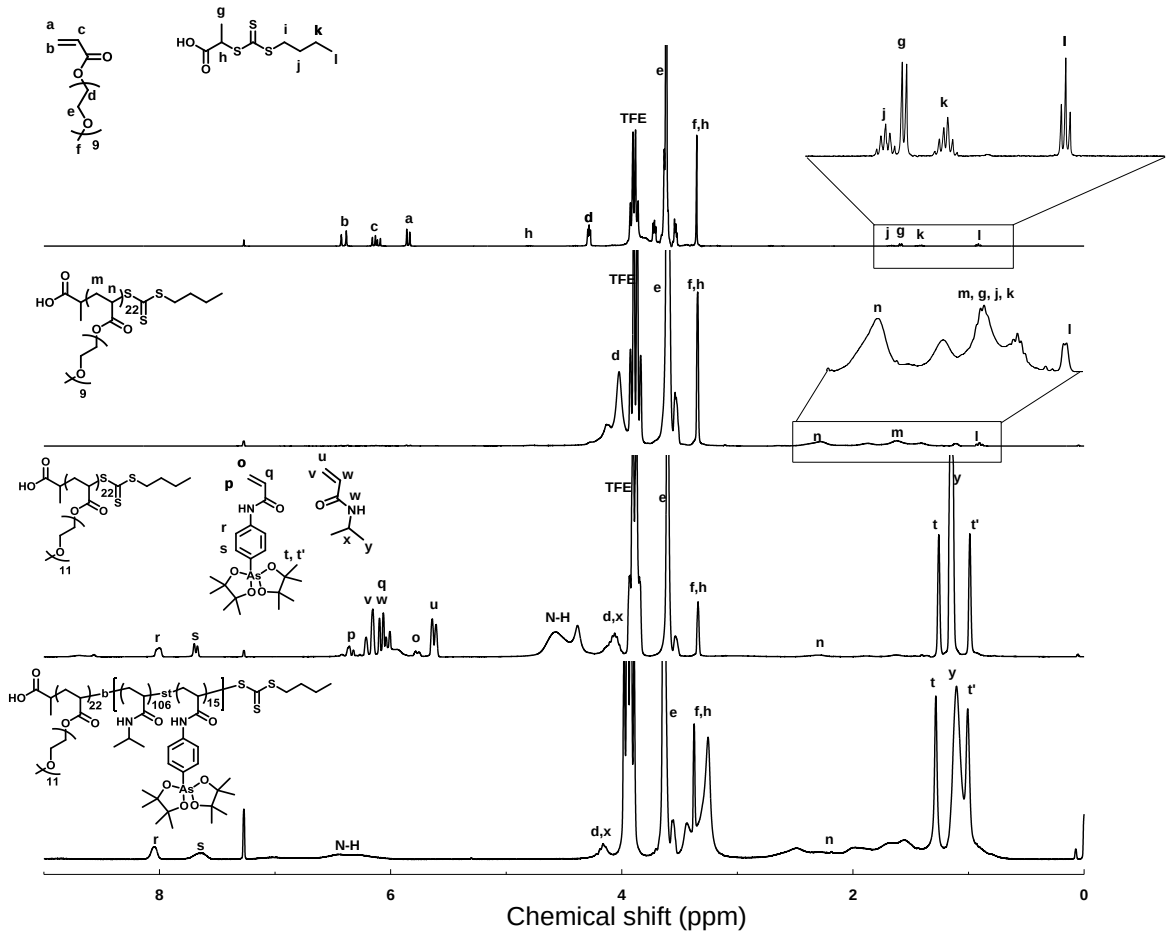

Figure 3.2 ^{1}H NMR ($CDCl_3$) of monomer feed before and after polymerisation of each block for the synthesis of P3.1.

An identical approach was followed for the synthesis of targeted 'corona-functional' polymer **P3.2** ([$PEGA_{15}$-*co*-$AsAm_5$]-*b*-$NIPAm_{80}$). A combined initial monomer concentration of 1 M for the PEGA and $AsAm(pin)_2$ monomers with PABTC and V601 (9×10^{-4} M) ($[CTA]_0/[I]_0 = 39$) gave quantitative conversion (98.5 %). The aromatic signal corresponding to the $AsAm(pin_2)$ monomer at 7.68 ppm was used to determine the proportion of $AsAm(pin_2)$ in the initial block (Figure 3.3). The ratio of monomer feed to CTA was determined by integration of vinylic protons belonging to both monomers (5.63 ppm) with the Z-group of the PABTC as previously, however as the pinacol groups were overlapping with the $-CH_3$ this was taken into account by considering a difference of three protons between the two pinacols peaks each with 6 proton's per $AsAm(pin_2)$ monomer at 1.28 ppm and 1.01 ppm. The conversion of both monomers were determined

by using the aromatic peak at 7.80-7.50 ppm, which was also used as an internal reference for subsequent chain extension with NIPAm to determine the monomer feed to macro-CTA ratio. The chain extension with NIPAm following the similar procedure ($[MacroCTA]_0/[I]_0 = 16$) yielded with quantitative monomer conversion furnishing **P3.2** with a composition of $[PEGA_{17.5}$-*co*-$AsAm_{5.5}]$-*b*-$NIPAm_{97}$ and successful chain extension was further demonstrated by the SEC analysis, showing successful re-initiation of the PEGA-*co*-AsAm(pin_2) as a macro-CTA ($M_{n,th} = 22100$ gmol^{-1}, $M_{n,SEC} = 20500$ gmol^{-1}, $Đ = 1.24$) (Figure 3.1).

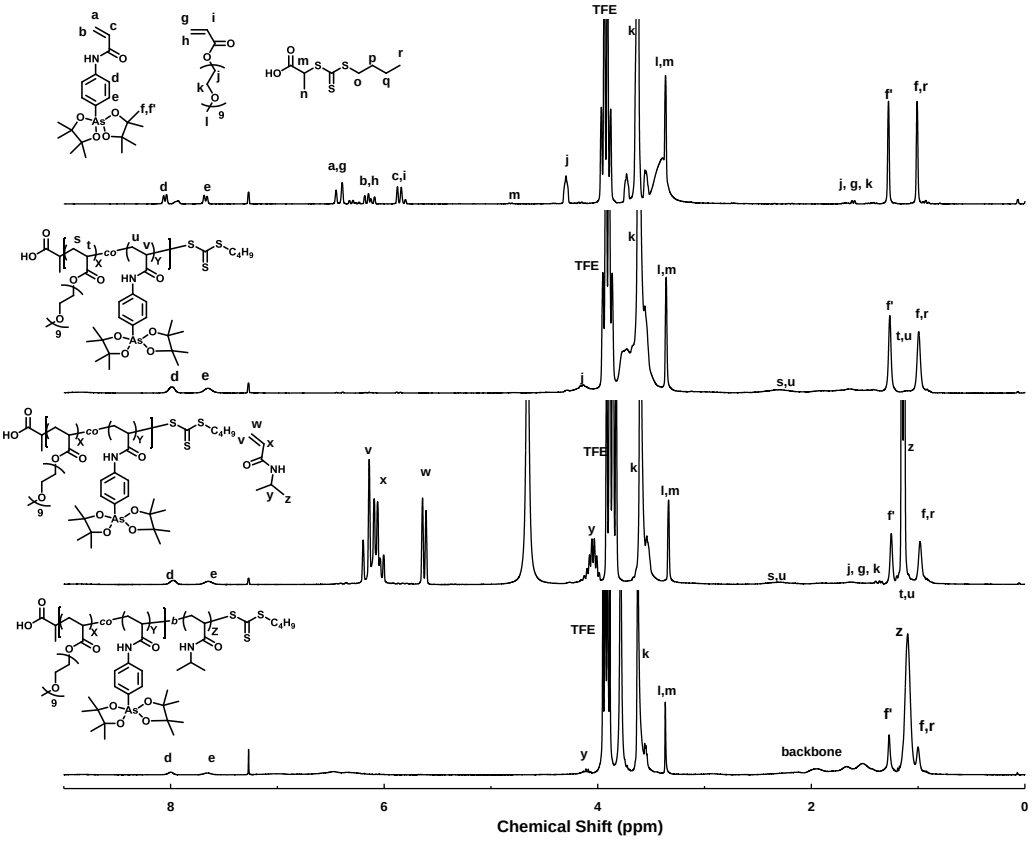

Figure 3.3. ^{1}H NMR ($CDCl_3$) of monomer feed before and after polymerisation of each block for the synthesis of P3.2.

To unleash the reactive arsenic acid As(V) group the pinacol groups of the AsAm(pin_2) were removed by dialysis against 0.1 M HCl overnight. This was done directly from the polymerisation mixture, where both polymers initially precipitated during the dialysis as a result of phase separation during solvent exchange. Switching the dialysis media to pure

H_2O resulted in dissolution of the deprotected polymers which were isolated by lyophilisation to obtain the final polymers (Table3.1). The deprotection of the AsAm(pin)$_2$ units was confirmed by ^{1}H NMR with the disappearance of the pinacol groups at 1.28 and 1.01 ppm (t and t' respectively in Figure 3.2 and 3.3). The dispersity of the final polymers were similar to values reported previously. Consistent with the decrease in $M_{n,th}$ as a result of loss of pinacol groups, deprotection of **P3.1** resulted in a shift to towards lower molecular by SEC analysis (**P3.1**, $M_{n,th}$ = 27100 gmol^{-1}, $M_{n,SEC}$ = 20800 gmol^{-1}, $Đ$ = 1.35). Interestingly, the deprotection of **P3.2** resulted in a higher apparent molecular weight (**P3.2**, $M_{n,th}$ = 21200 gmol^{-1}, $M_{n,SEC}$ = 30500 gmol^{-1}, $Đ$ = 1.35) (Figure 3.1).

Table 3.1 Arsenic functional block copolymers synthesised by RAFT. ^{1}H NMR of polymerisation mixture in $CDCl_3$ and after deprotection done in D_2O. SEC carried out with DMF as an eluent.

	Polymer Composition	Polymerisation mixture				After deprotection		
		Con.	$M_{n,th}$ (g mol^{-1})	$M_{n,SEC}$ (g mol^{-1})	$Đ$	$M_{n,th}$ (g mol^{-1})	$M_{n,SEC}$ (g mol^{-1})	$Đ$
P3.1	P[PEGA$_{22}$]	98 %	10800	8900	1.16			
	P[PEGA$_{22}$-*b*-(NIPAm$_{106}$-*co*-AsAm$_{15}$)]	> 99 %	29600	29300	1.27	27100	20800	1.35
P3.2	P[PEGA$_{17.5}$-*co*-AsAm$_{5.5}$]	98.5 %	11100	9000	1.15			
	P[(PEGA$_{17.5}$-*co*-AsAm$_{5.5}$)-*b*-NIPAm$_{97}$]	> 99 %	22100	20500	1.24	21200	30500	1.40

Prior to cross-linking, the thermoresponsive behaviour and propensity for self-assembly of each polymer was investigated by variable temperature dynamic light scattering (DLS) in aqueous solutions (1 mg ml^{-1}) by increasing the temperature between 25-60 °C at 5 °C intervals. Both **P3.1** and **P3.2** underwent self-assembly in aqueous solution at elevated temperature. When the AsAm units were incorporated into the core-forming NIPAm block (**P3.1**), self-assembly occurred at T = 50 °C (D_h = 33 nm), and the nanoparticles contracted further with increasing temperature (D_h = 21 nm at T = 60 °C) (Figure 3.4). Interestingly, **P3.2** with AsAm units incorporated in the corona forming PEGA block underwent self-assembly at lower temperatures (T = 40 °C, D_h = 21 nm), with contraction again observed with increasing temperature (D_h = 15 nm, at 60 °C) (Figure 3.5), forming smaller aggregates across the temperature range compared to **P3.1**.

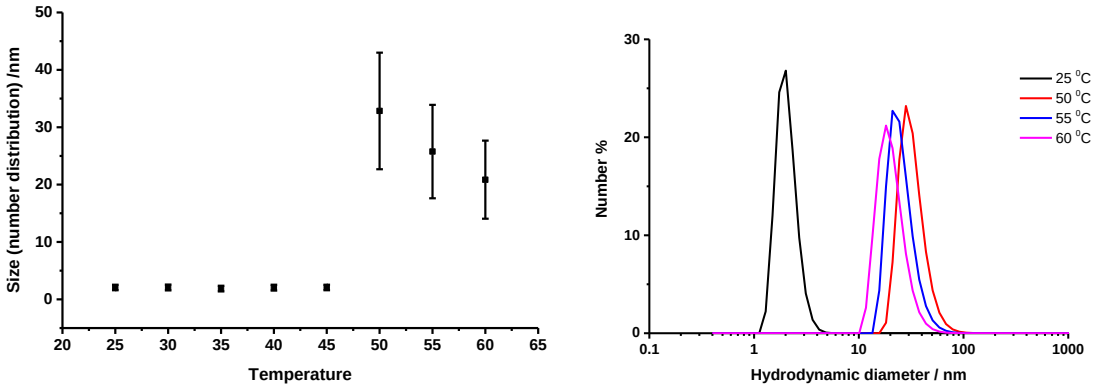

Figure 3.4 DLS analysis of thermally induced self-assembly of P3.1. Hydrodynamic diameter (number %) versus temperature plotted (left). The changes in size distribution curves with temperature plotted (right) (see Appendix C, S3.4 for supporting information).

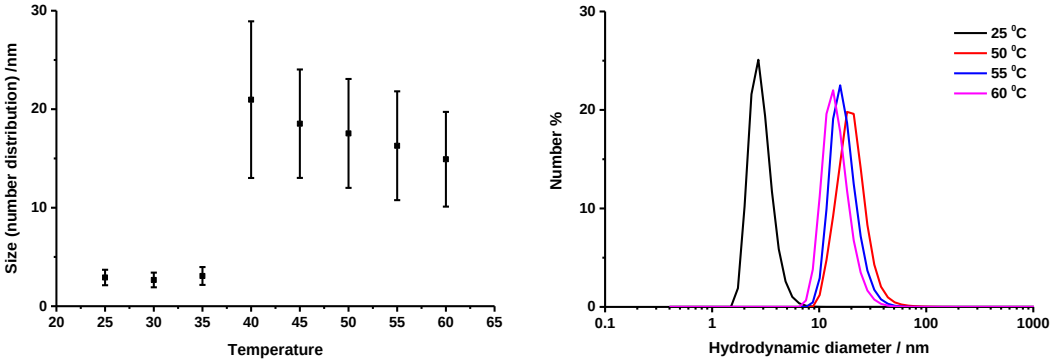

Figure 3.5 DLS analysis of thermally induced self-assembly of P3.2. Hydrodynamic diameter (number %) versus temperature plotted (left). The changes in size distribution curves with temperature plotted (right) (see Appendix C, S3.5 for supporting information).

One of the benefits of cross-linking thermoresponsive self-assembled polymers is being able to follow the success of cross-linking using DLS, by returning the temperature back to that which the polymers would otherwise dissemble to unimer's without successful stabilisation. Sumerlin *et al* have demonstrated retention of nanostructures at ambient temperature from polymerisation induced thermal self-assembly (PISA) of NIPAm via cross-linking at elevated temperatures.[41] Previously, self-assembled thermoresponsive polymeric arsenicals were cross-linked by reductive coupling using aqueous H_3PO_2 to reduce As(V) to As(I) which proceeds with the formation of As-As bonds in the form of As_n homocycles. Cross-linking through the corona-forming PEGA block (**P3.2**) using this strategy was re-investigated here (Figure 3.6A), but consistent with the previous work, it did not result in successfully cross-linked nanoparticles. Cross-linking through the core-

forming NIPAm block (**P3.1**) was however successful yielding stable polymer nanoparticles (**$NP_{As(I)}$**), as confirmed by light scattering (D_h = 29 nm, N_{agg} = 23, Figure 3.6 B/E/F, Table 3.2) and microscopy (TEM and AFM: Figure 3.6 C/D) techniques. However, in contrast to the previous work, the nanoparticles were less stable in comparison, as these particles disassembled in response to glutathione much faster (3 hr compared to 12-20 hr with equivalent amount of AsAm units per chain) (Figure 3.7). This is attributed to a lower relative density of AsAm units within the NIPAm core (NIPAm : AsAm = 106 : 15 vs 75/72/93 : 10/14/26).

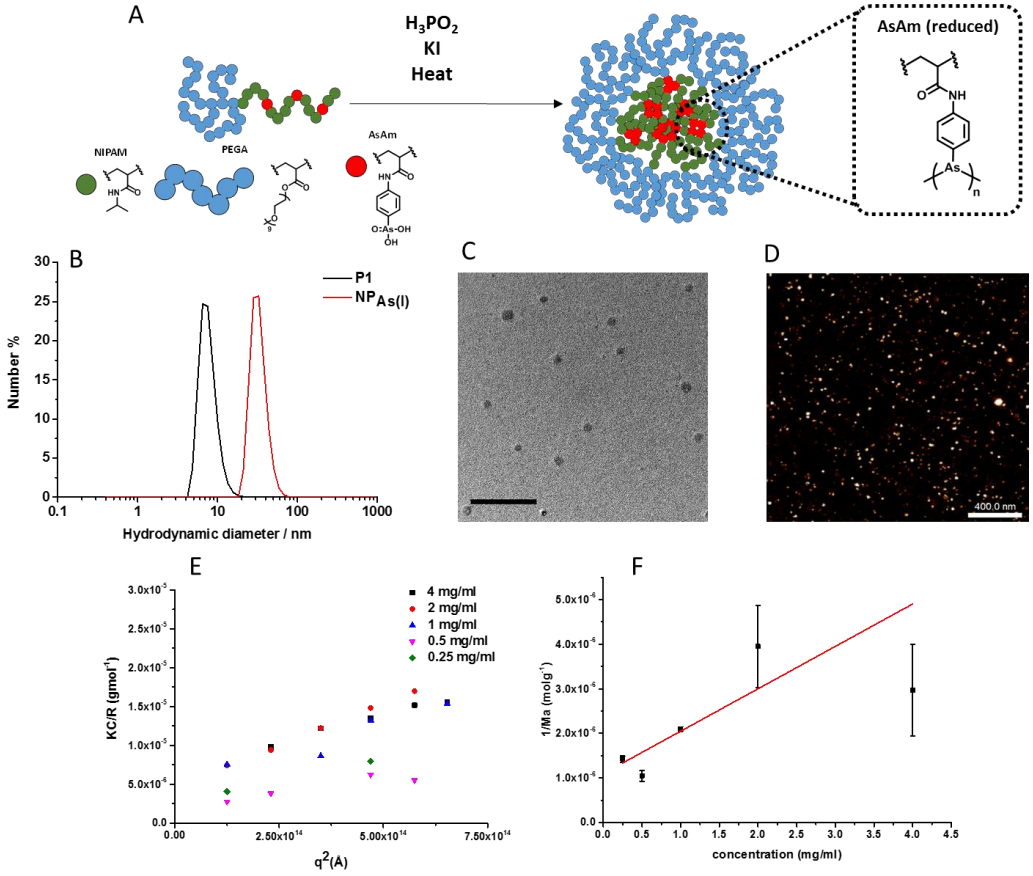

Figure 3.6 A) Schematic for simultaneous self-assembly and reductive cross-linking of P3.1 in H_3PO_2 B) particle size distrubtion curves (DLS. 1 mgml^{-1}, H_2O) of P3.1 and corresponding nanoparticle $NP_{As(I)}$ C) TEM of $NP_{As(I)}$ (scale bar 400 nm) D) AFM of $NP_{As(I)}$ (scale bar = 400 nm) E) Evolution of KC/R in water as function of q^2 and concentration for $NP_{As(I)}$ obtained by SLS. F) M_w of $NP_{As(I)}$ obtained by SLS as function of concentration.

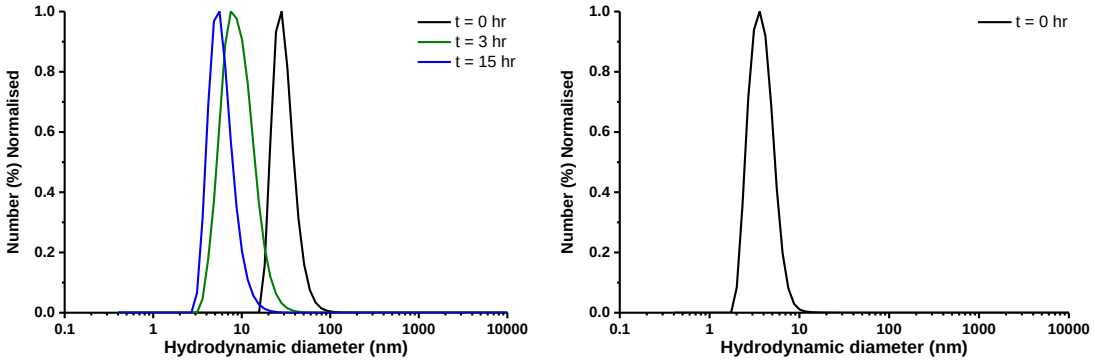

Figure 3.7 Particle size distribution (DLS) of aqueous solution of $NP_{As(I)}$ (1 mg/ml) in presence 5 mM Glutathione (left) and 5 mM H_2O_2 (right) as function of time (see Appendix C, S3.7A and S3.7B for supporting information).

3.2.2 Stabilisation of polymeric arsenical nanoparticle with multi-thiol cross-linker

Due to the lability of the As-As bonds to hydrolysis and oxidation which results in disassembly over time, polythiol reagents were investigated as external cross-linkers (scheme 3.1) to cross-link the self-assembled nanoparticles through more stable As(III)-S bonds. Although trivalent arsenic (As(III)) readily reacts with thiols to form As(III)-S covalent bonds, pentavalent arsenic (As(V)) must first undergo reduction to As(III). This can be achieved via addition of excess thiol, with 2 equivalents required for reduction and a further 2 equivalents for bonding. In the context of this work, it was hypothesised that this would limit the cross-linking efficiency by diminishing the number of reactive thiol groups due to their oxidation (during the initial reduction process) to disulfides. Alternatively, non-thiol reducing agents could be considered to achieve *in-situ* reduction prior to addition of the polythiol cross-linkers. With this in mind the reductive conditions reported previously (H_3PO_2, KI, 60 °C) were adopted to afford simultaneous self-assembly and initiate reduction of As(V). It was proposed that the introduction of polythiol cross-linkers would pull the redox equilibrium towards the thiol cross-linked As(III) state, due to the formation of more enthalpically favoured As(III)-S bonds. Consequently, the polythiol cross-linker would be fed into the reaction as a single portion

after 10 minutes of heating to react with and intercept As(III), before reduction to As(I) was complete. This hypothesis was verified by heating *p*-arsanilic acid under reductive conditions for 10 minutes prior to addition of a monothiol reagent (thiogylcerol, 2 eq, Fig 3.8A), which resulted in the trapping of the As(III)-*bis*-thiogycerol adduct of *p*-arsanilic acid (Fig 3.8B).

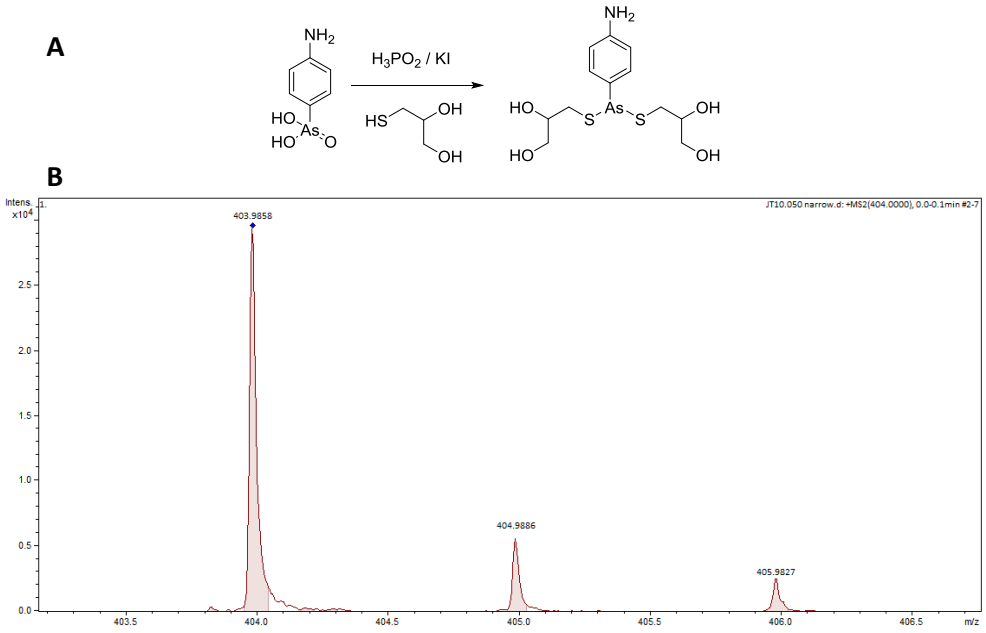

Figure 3.8 A) schematic of arsanilic acid with thiogycerol (2 eq) in reductive conditions (H_3PO_2 / KI). B) HRMS of the reaction mixture with isotopic distribution corresponding to $[C_{12}H_{20}AsO_4S_2 + Na]^+$ species.

Commercially available polythiol cross-linkers with similar interatomic distances between each thiol were identified. Pentaerythritol tetrakis(3-mercaptopropionate), (PTM), trimethylolpropane tris(3-mercaptopropionate) (TTM) and hexa(ethylene glycol) dithiol (HDT) were selected as a tetra- tri- and di-functional cross-linkers respectively (Scheme 3.1).

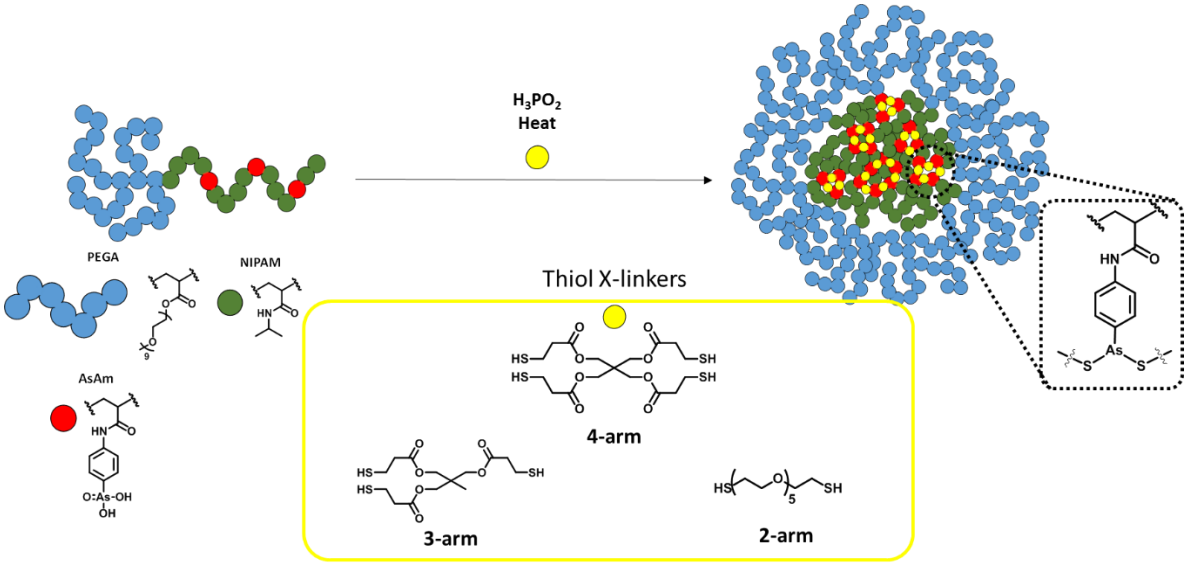

Scheme 3.1 Thermal induced self-assembly and cross-linking of P3.2 using multi-functional thiol cross-linkers in reductive conditions. The cross-linker(s) is added after 10 minutes of heating in the reductive conditions. Hypophosphorous acid is used as reducing agent with catalytic amount of potassium iodide.

Considering that the pendant As(III) groups can form two bonds to thiols, and to investigate the effect of thiol valency of the cross-linkers the stoichiometry of cross-linker was set so that [SH]/[As] = 2, for each combination of polymer and cross-linker. For example, **P3.2** [PEGA$_{17.5}$-*co*-AsAm$_{5.5}$]-*b*-NIPAm$_{97}$, which does not form stable nanoparticles when subjected to reductive conditions alone, was initially reacted with tetra-functional PTM (2.75 eq *i.e.* 11 eq [SH] w.r.t. [As]) in an attempt to stabilise the resulting nanoparticles. However, in line with previous work the formation of stable cross-linked nanoparticles was not possible as evidenced by DLS analysis at room temperature which showed only unimers (Fig 3.9). This is attributed to the relatively low functional density of the As-groups in the corona which is naturally more diffuse than the core, thus limiting the proximity of As(III) groups during the cross-linking process.

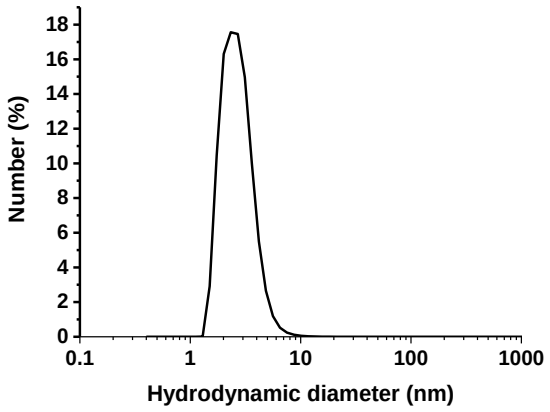

Figure 3.9 Size distribution (DLS) of P3.2 at room temperature after cross-linking with PTM under elevated temperature (60 °C) (see Appendix C, S3.9 for supporting information).

Hitherto, cross-linking of core-functional **P3.1** ($PEGA_{22}$-*b*-[$NIPAm_{106}$-*co*-$AsAm(pin_2)_{15}$]) with the polythiol reagents will be the focus of this investigation. Thus, when **P3.1** was subjected to reductive conditions, addition of PTM (7.5 eq) furnished stable nanoparticles $\mathbf{NP_{As\text{-}S4}}$, as observed by DLS ($D_h$ = 29 nm, PDI = 0.06) measured at room temperature (Figure 3.10). Transmission Electron Microscopy (TEM) shows range of sizes (Figure 3.10). Owing to the thermoresponsive nature of the NIPAm core, the nanoparticles were able to contract (D_h = 23.0 nm) at elevated temperature and swell (D_h = 27.2 nm) again upon cooling (Figure 3.11).

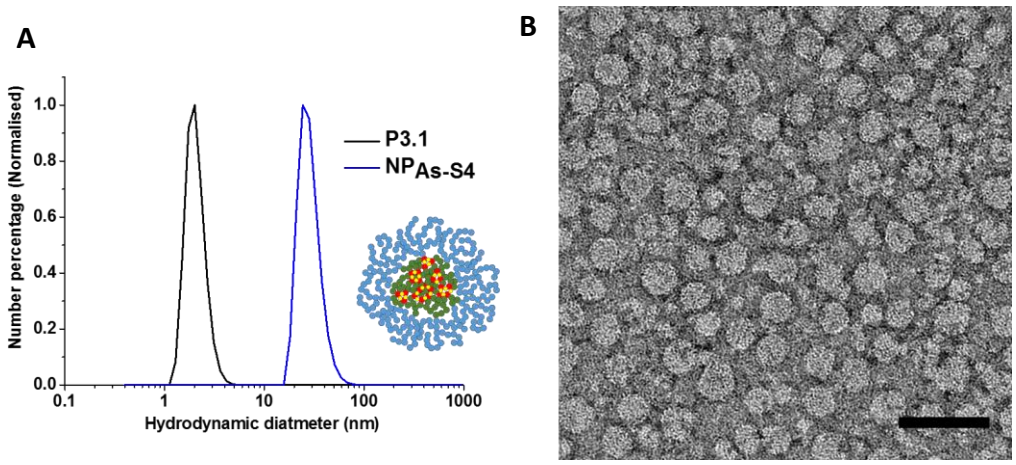

Figure 3.10 A) Particle size distribution (DLS) of P3.1(black) and corresponding cross-linked nanoparticle NP_{As-S4} (blue). B) TEM image of NP_{AS-S4} (scale bar = 100 nm) (see Appendix C, S3.10 for supporting information).

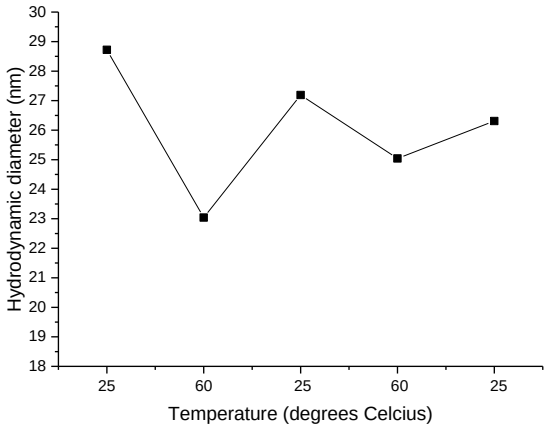

Figure 3.11 Reversible contracting and swelling of particles derived of NP_{As-S4} at 60 °C and 25 °C respectively in deionised water (1 mg/ml) (see Appendix C, S3.11 for supporting information).

Static light scattering (SLS) was used to determine the absolute molecular weight from the Zimm plot and therefore the number of polymer chains per particle. Interestingly, **NP_{As-S4}** was estimated to have an aggregation number (N_{agg}) of 278 chains per particle (at infinite dilution), which was considerably higher than our previous As-As cross-linked nanoparticles. As observed in the Zimm plot, the molecular weight of the nanoparticles decreased with concentration, indicative of inter-particle interactions and inter-particle

crosslinking at higher concentration (Fig 3.12). An additional feature of the SLS, is the radius of gyration (R_g) which can be obtained by extrapolating the Zimm plot. The ratio (ρ) of the R_g and radius of hydration (R_h) (scattering measured at 90°) can provide topological information, with $R_g/R_h = 0.778$ for a compact hard sphere, and 2.36 for a stiff rod.[42, 43] **NP_{As-S4}** had a ρ value of 1.39, at 1 mg/ml, which increased to 2.04 at higher concentration (4 mg/ml), indicating a change in topology, deviating further from spherical geometry as a result of inter-nanoparticle clustering (Table 3.2).

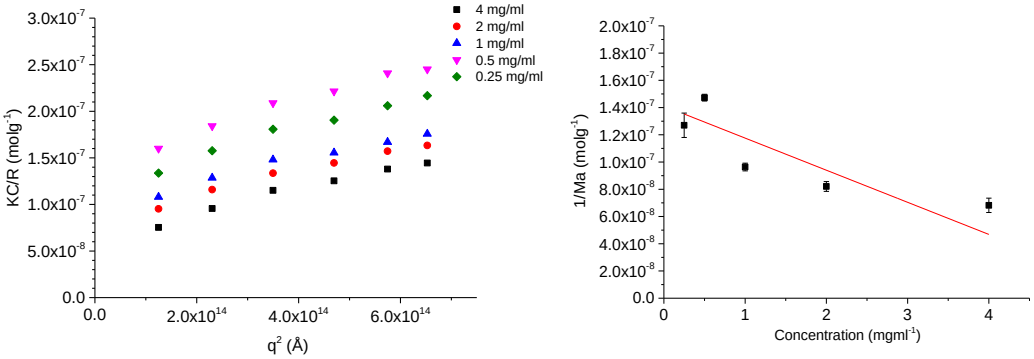

Figure 3.12 Evolution of KC/R in water as function of q^2 and concentration for NP_{As-S4}, obtained by SLS.

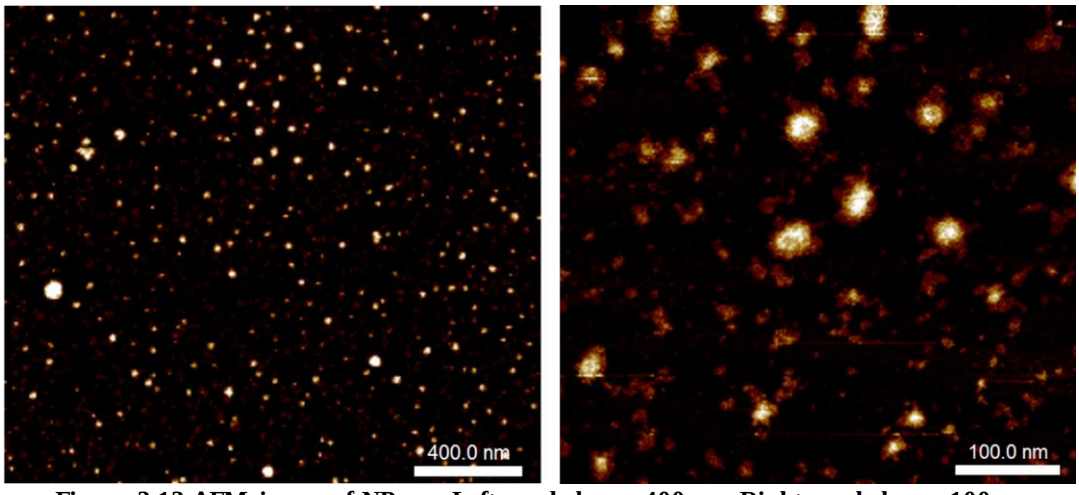

Figure 3.13 AFM image of NP_{As-S4}. Left: scale bar = 400 nm. Right: scale bar = 100 nm.

The inter-nanoparticle interaction was observed by Atomic Force Microscopy, (AFM), where close examination indicates clustering of the particles is evident (Fig 3.13). Although As(III)-S bonds are more stable than the As-As bonds reported previously, the bonding can be dynamic particularly in the presence of exchangeable thiols. The stability

and responsivity of $\mathbf{NP_{As\text{-}S4}}$ to glutathione (5 mM, 37 °C) was therefore investigated. The nanoparticles remained intact, even after one week, as observed by no change in the hydrodynamic size (D_h = 30.5 nm, PDi = 0.07) by DLS analysis (Fig 3.14). This is in contrast, to the results of Le *et al* who demonstrated release of phenylarsine oxide (As(III)) with glutathione, from the core of a thiol-functional particle stabilised by As(III)-S bonds (80% released within the first few hours, with 5 mM GSH).[44] This suggests that the interaction between arsenicals incorporated into polymer chains with PTM is more entropically favourable than the interaction between thiol functional polymers and phenylarsine oxide.

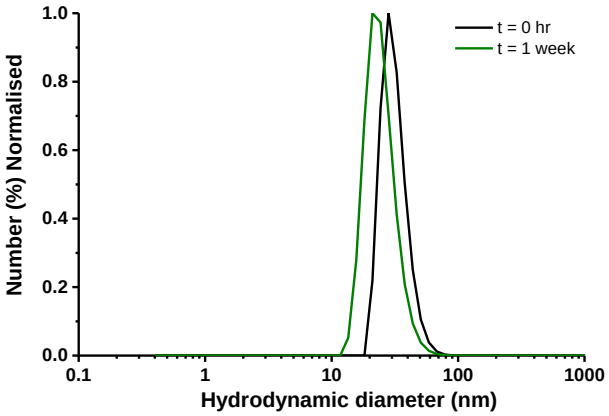

Figure 3.14 Particle size distribution curves of $NP_{As\text{-}S4}$ as a function of time in aqueous GSH (GSH = 5 mM, nanoparticle concentration = 1 mg/ml) (see Appendix C, S3.14 for supporting information).

To synthesise nanoparticles that were less densely cross-linked, the amount of cross-linker was reduced to half the stoichiometry ([SH]/[As] = 1, *i.e.* 3.75 eq PTM w.r.t. **P3.1**). The resulting nanoparticle, $\mathbf{NP_{As\text{-}S4/2}}$ was successfully prepared and stable at room temperature (D_h = 23 nm, PDi = 0.11, Fig 3.15).

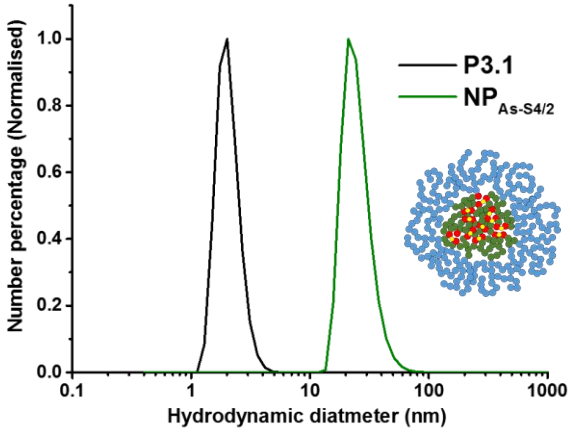

Figure 3.15 DLS analysis of P3.1 (1 mg/ml) showing the success of nanoparticle formation with half the stoichiometric ratio of PTM cross-linker ($NP_{AS-S/4}$, 1 mg/ml) after dialysis at room temperature (see Appendix C, S3.15 for supporting information).

Further SLS analysis indicated a smaller molecular weight for these nanoparticles compared to when stoichiometric cross-linker was used, with fewer polymer chains (N_{agg} = 53) per particle (Fig 3.16).

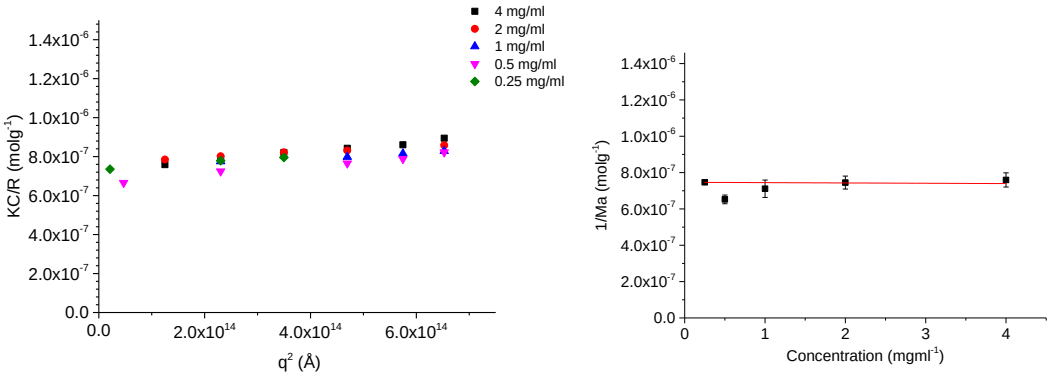

Figure 3.16 Evolution of KC/R in water as function of q^2 and concentration for, $NP_{As-S4/2}$ obtained by SLS.

Heating and cooling cycles of $\mathbf{NP_{As-S4/2}}$ revealed more pronounced contraction (D_h = 19.2 nm) and expansion (D_h= 24.2 nm) compared to $\mathbf{NP_{As-S4}}$ (Fig 3.17), indicative of more diffuse cross-linking within the core of $\mathbf{NP_{As-S4/2}}$.

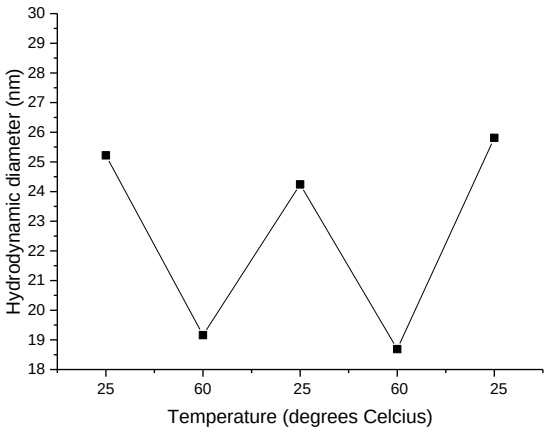

Figure 3.17 Reversible contracting and swelling of particles derived of $NP_{As\text{-}S4/2}$ at 60 °C and 25 °C respectively in deionised water (1 mg/ml) (see Appendix C, S3.17 for supporting information).

The Zimm plot reveals less concentration dependency on molecular weight (Fig 3.16), indicating the absence of inter-particle clustering at higher concentrations which is supported by the ρ value of $\mathbf{NP_{As\text{-}S4/2}}$ being lower (1.13) than $\mathbf{NP_{As\text{-}S4}}$ (2.04) across the concentration range (Table 3.2). The AFM data for $\mathbf{NP_{As\text{-}S4/2}}$ shows less clustering and a more regular distribution of the nanoparticles in contrast to $\mathbf{NP_{As\text{-}S4}}$ (Fig 3.18).

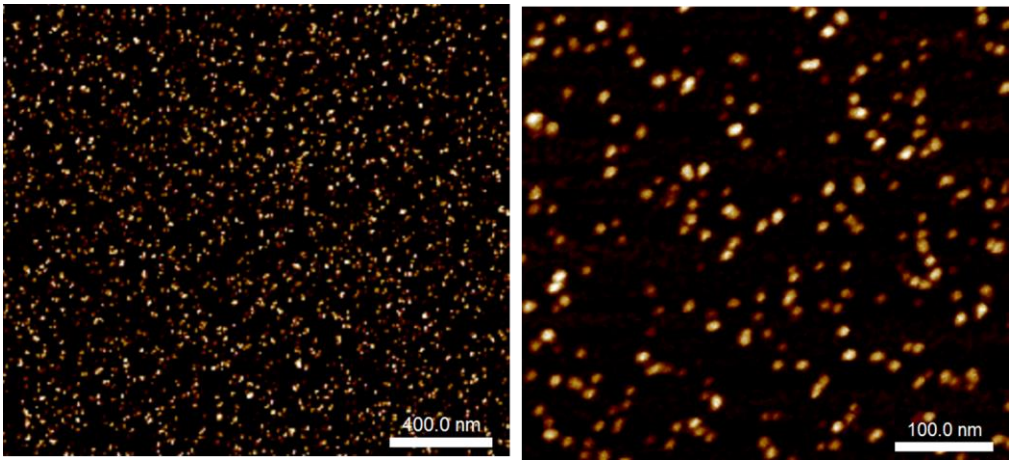

Figure 3.18 AFM image of $NP_{As\text{-}S4/2}$. Left: scale bar = 400 nm. Right: scale bar = 100 nm.

Despite reducing the cross-linking density by 50%, $\mathbf{NP_{As\text{-}S4/2}}$ also did not show responsivity to GSH even after a week at the physiological temperature (5 mM, 37 °C, Fig 3.19).

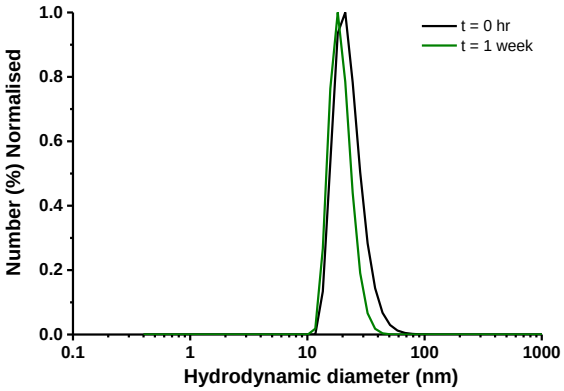

Figure 3.19 Particle size distribution curves of $NP_{As-S4/2}$ as a function of time in aqueous GSH (GSH = 5 mM, nanoparticle concentration = 1 mg/ml) (see Appendix C, S3.19 for supporting information).

An alternative way of tuning the cross-linking density is through the thiol valency in the polythiol cross-linkers. When **P3.1**, was subjected to reductive conditions and tri-functional cross-linker TTM (10 eq w.r.t. **P3.1**) was added stable nanoparticles $\mathbf{NP_{As-S3}}$ were retained (D_h = 25, PDI = 0.09, Fig 3.20) at room temperature and whilst maintaining nanostructure.

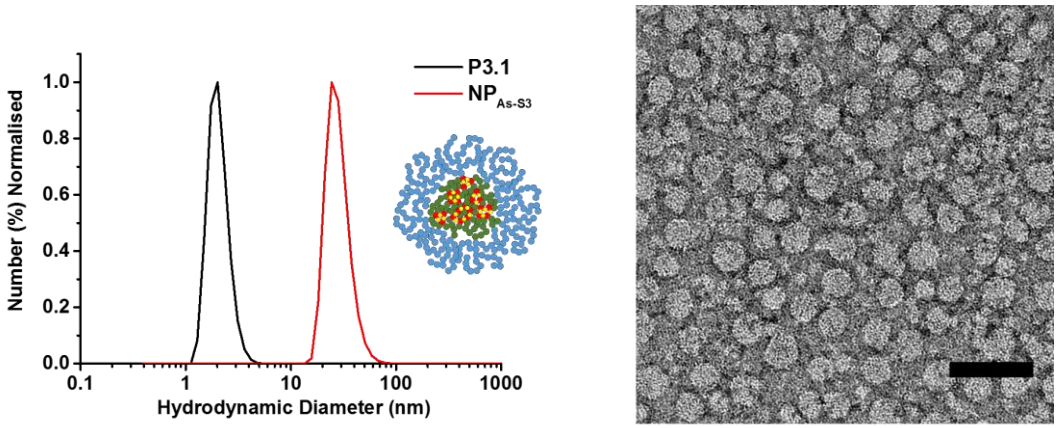

Figure 3.20 A) Particle size distribution (DLS) of P3.1(black) and corresponding cross-linked nanoparticle NP_{As-S3} (red). B) TEM image of NP_{AS-S3} (scale bar = 100 nm) (see Appendix C, S3.20 for supporting information) .

With the stoichiometry such that [SH]/[As] = 2, SLS revealed that $\mathbf{NP_{As-S3}}$ (N_{agg} = 204) was similar to $\mathbf{NP_{As-S4}}$ with the Zimm-plot showing a molecular weight dependency on concentration, indicative of inter-particle clustering at higher concentrations (Fig 3.21). This is further evidenced by the increasing ρ value at higher concentrations (Table 3.2) and noticeable clustering the AFM of the $\mathbf{NP_{As-S3}}$ (Fig 3.22).

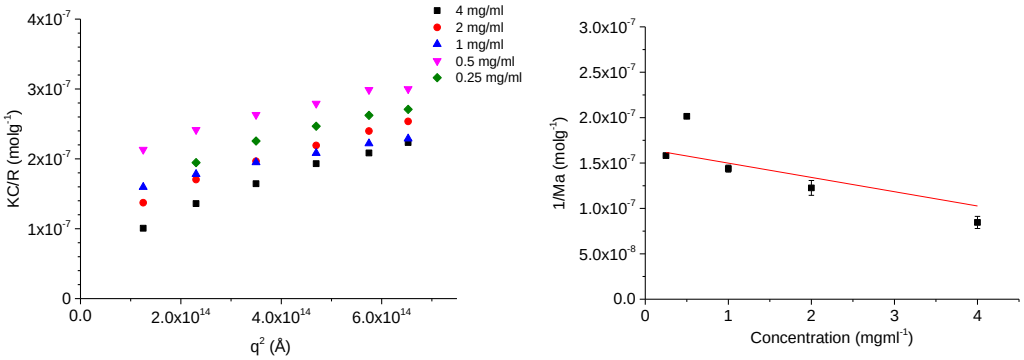

Figure 3.21 Evolution of KC/R in water as function of q^2 and concentration for $NP_{As\text{-}S3}$ obtained by SLS.

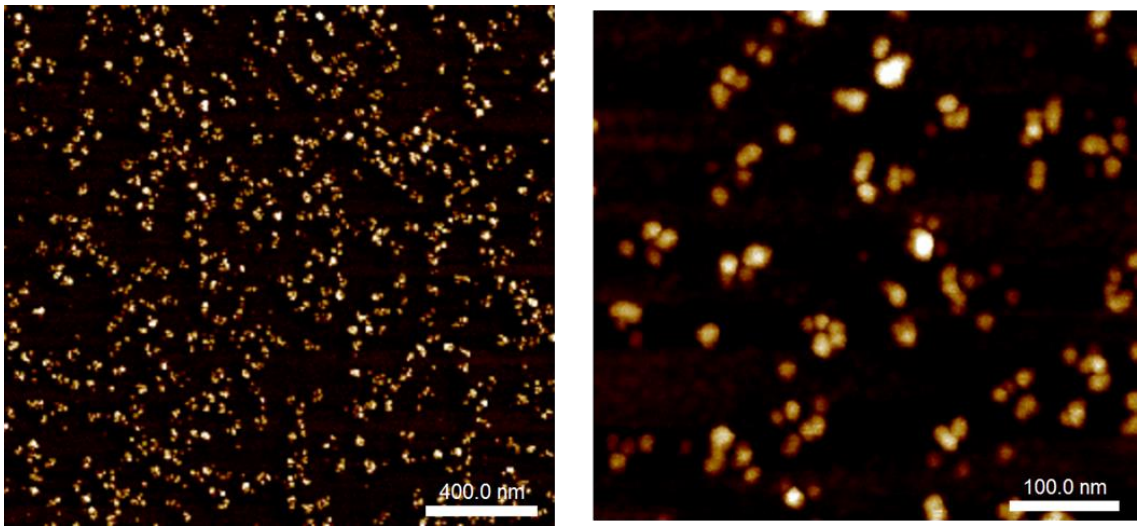

Figure 3.22 AFM image of $NP_{As\text{-}S3}$ depicting the clustering when stoichiometric TTM cross-linker is used, similar to $NP_{As\text{-}S4}$. Left: scale bar = 400 nm. Right: scale bar = 100 nm

Reducing the stoichiometric equivalence of TTM (5 eq) furnished stable nanoparticles $\mathbf{NP_{As\text{-}S3/2}}$ and similar to $\mathbf{NP_{As\text{-}S4/2}}$ these were slightly smaller size according to DLS (D_h = 21 nm, PDi = 0.11), but significantly smaller by SLS (N_{Agg} = 26). The same trend was observed with respect to the ρ value of $\mathbf{NP_{As\text{-}S3/2}}$ (1.08, 4 mg/ml), which was smaller than $\mathbf{NP_{As\text{-}S3}}$ (2.48, 4 mg/ml) and AFM of the $\mathbf{NP_{As\text{-}S3/2}}$ was found to be similar to $\mathbf{NP_{As\text{-}S4/2}}$ showing little evidence of particle clustering.

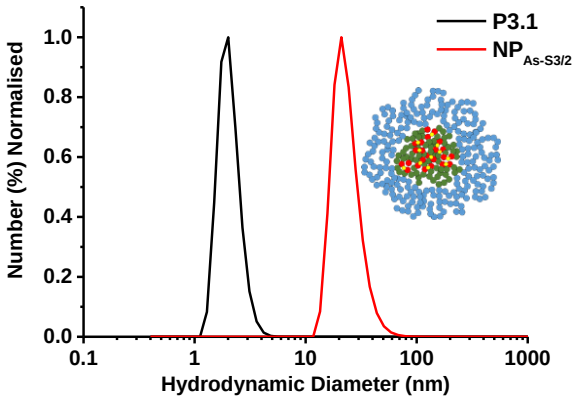

Figure 3.23 Particle size distribution (DLS) of P3.1(black) and corresponding cross-linked nanoparticle $NP_{As\text{-}S3/2}$ (red) (see Appendix C, S3.23 for supporting information).

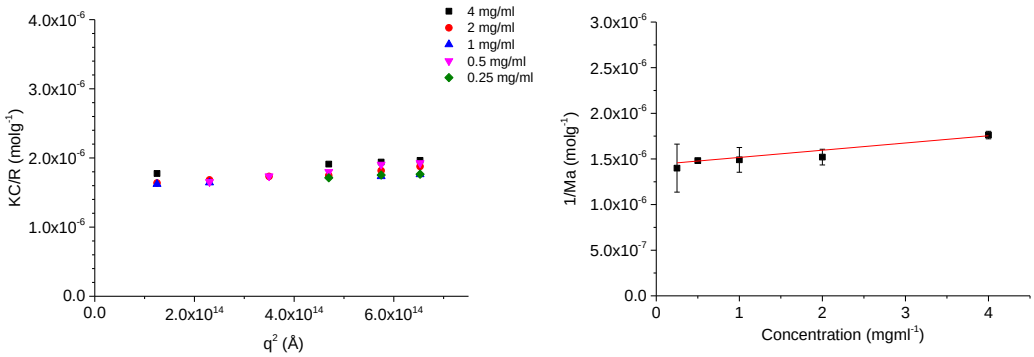

Figure 3.24 Evolution of KC/R in water as function of q^2 and concentration for $NP_{As\text{-}S3/2}$, obtained by SLS.

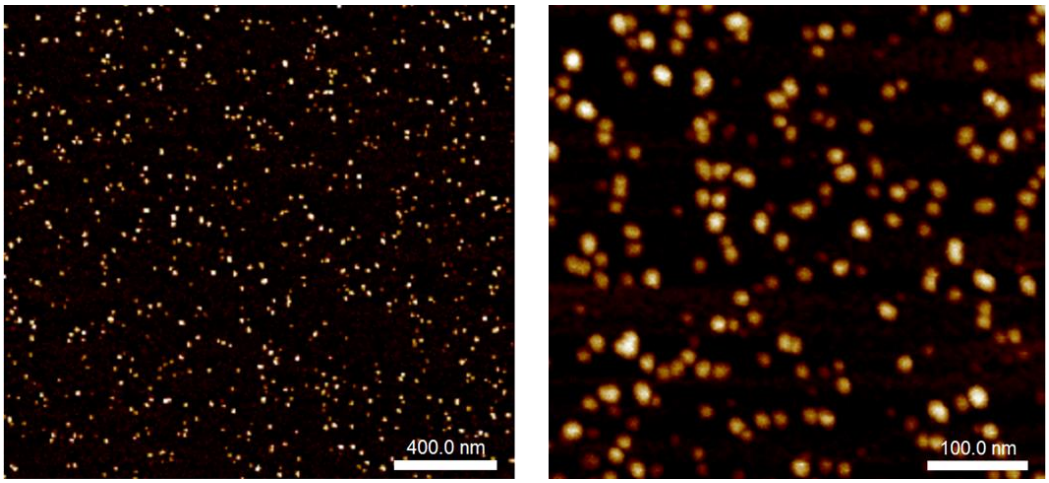

Figure 3.25 AFM image of $NP_{As\text{-}S3/2}$. Left: scale bar = 400 nm. Right: scale bar = 100 nm

The stability and responsivity to GSH (5 mM, 37 °C) was also similar to $\mathbf{NP_{As\text{-}S4}}$ and $\mathbf{NP_{As\text{-}S4/2}}$ as both $\mathbf{NP_{As\text{-}S3}}$ and $\mathbf{NP_{As\text{-}S3/2}}$ remained intact even after a week according to DLS (D_h = 29.1 nm, PDi = 0.08 and D_h = 23.5 nm, PDi = 0.14 Fig 3.26). This indicates that the tri-functional thiol cross-linker has similar entropic barrier to exchange with monothiol reagents such as GSH.

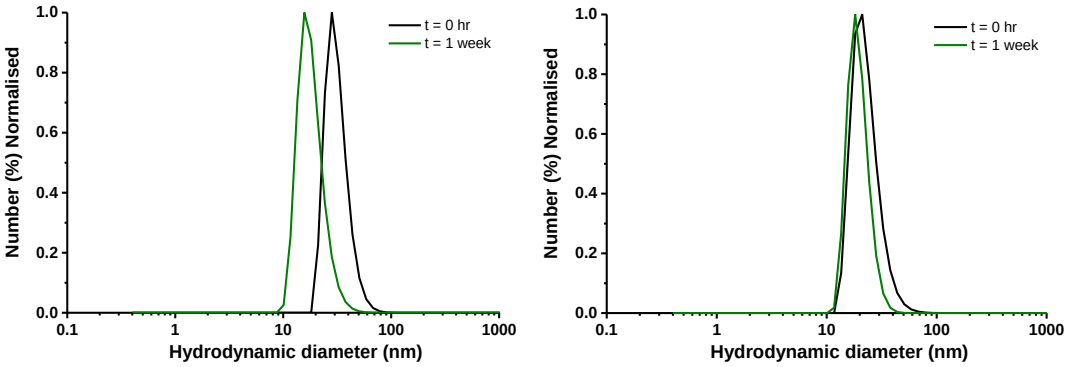

Figure 3.26 Particle size distribution curves of $NP_{As\text{-}S3}$ (left) and $NP_{As\text{-}S3/2}$ (right) as a function of time in aqueous GSH (GSH = 5 mM, nanoparticle concentration = 1 mg/ml) (see Appendix C, S3.26A and S3.26B for supporting information).

Table 3.2 Light scattering (DLS and SLS) of the nanoparticles. DLS was measured in aqueous solution (1 mg/ml). SLS measured at variable concentration. $M_{w,NP}$ was determined using Eq 2-4. $N_{agg} = M_{w,NP}/M_{n,th}$. R_g is the gradient of Zimm plots and R_h is determined as the size measured from the scattering angle at 90 ° from SLS. The ratio R_g/R_h at 4 mg/ml and 1 mg/ml is displayed for comparison.

		SLS				DLS	
NP	***dn/dC*** **(mL/g)**	$M_{W,NP}$ (g/mol)	N_{agg}	R_g/R_h (4 mg/ml)	R_g/R_h (1 mg/ml)	D_h **(nm)**	**PDi**
$\mathbf{NP_{S4}}$	0.137	7.5×10^6	277	2.04	1.39	29	0.06
$\mathbf{NP_{As\text{-}S4/2}}$	0.189	1.4×10^6	52	1.13	0.90	23	0.11
$\mathbf{NP_{As\text{-}S3}}$	0.133	5.5×10^6	203	2.48	1.28	25	0.09
$\mathbf{NP_{As\text{-}S3/2}}$	0.190	7.2×10^5	27	1.08	1.11	21	0.11
$\mathbf{NP_{As\text{-}S2}}$	0.174	7.0×10^5	26	1.64	1.60	19	0.11
$\mathbf{NP_{As\text{-}S2/2}}$	-	-	-	-	-	5.4	0.07
$\mathbf{NP_{As(I)}}$	0.164	6.3×10^5	23	3.42	1.27	29	0.12

Finally, the bi-functional cross-linker HDT (15 eq w.r.t. **P3.1**) was added to **P3.1** under reductive conditions, yielding stable nanoparticles, $\mathbf{NP_{As\text{-}S2}}$ (D_h = 19 nm, PDi = 0.11,

Figure 3.27) which were retained at room temperature.

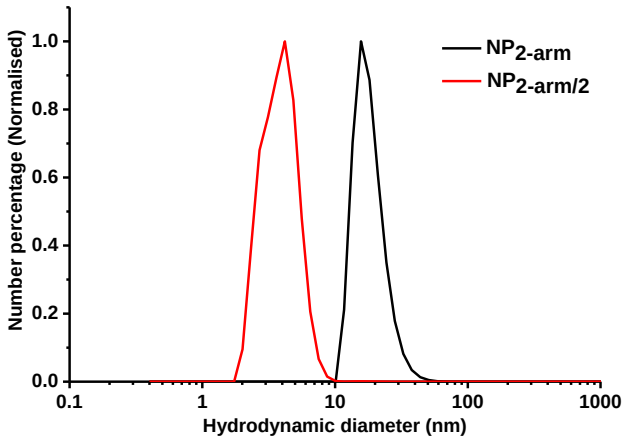

Figure 3.27 DLS analysis (top) showing the nanoparticle formed with stoichiometric equivalence of HBT cross-linker (see Appendix C, S3.27 for supporting information).

SLS analysis also indicated that $\mathbf{NP_{As\text{-}S2}}$ ($N_{agg}=26$) had similar molecular weight to $\mathbf{NP_{As\text{-}S3/2}}$, therefore representing similar number cross-linked polymer chains per nanoparticle. Unlike $\mathbf{NP_{As\text{-}S4}}$ and $\mathbf{NP_{As\text{-}S3}}$ the nanoparticles prepared with stoichiometric amount of cross-linker $\mathbf{NP_{As\text{-}S2}}$ did not show concentration dependence on molecular weight, and the ρ value, although relatively high is not concentration dependent (Figure 3.28, table 3.2).

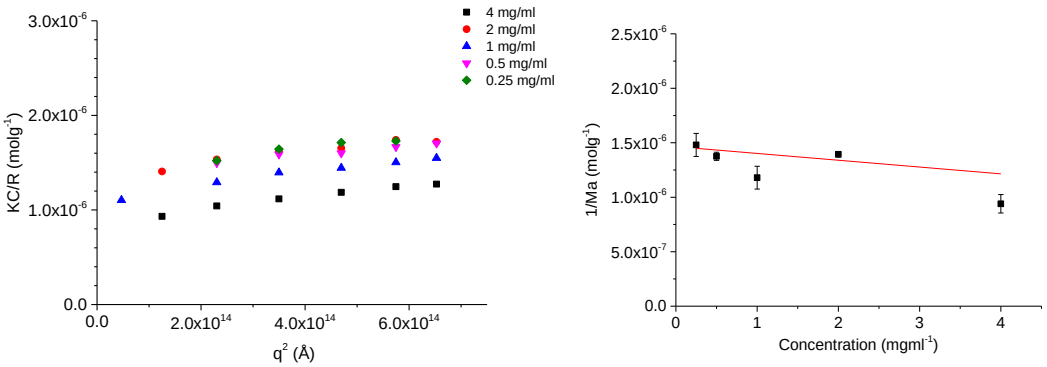

Figure 3.28 Evolution of KC/R in water as function of q^2 and concentration for $NP_{As\text{-}S2}$ obtained by SLS.

The relatively high ρ value of suggests a prolate ellipsoid topology, by AFM the nanoparticles appears more clustered (Fig 3.29).

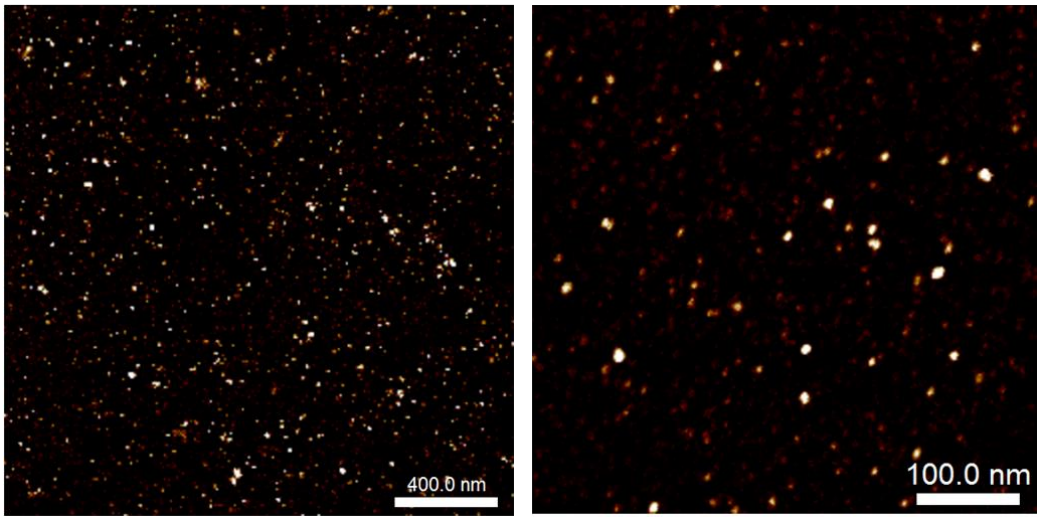

Figure 3.29 AFM (bottom) depicting the clustering of NP_{As-S2}, similar to NP_{As-S4} and NP_{As-S3}. Scale bar of AFM: right = 400 nm, left = 100 nm.

Reducing the stoichiometry (HDT = 7.5 eq) also resulted in stable particles (**$NP_{As-S2/2}$**) being retained at room temperature, however the particles were not stable to purification by dialysis against H_2O, with unimers being observed by DLS (Fig 3.27). This indicated that **NP_{As-S2}** was less stable than **NP_{As-S3}** and **NP_{As-S4}** and more likely to respond to GSH (5 mM, 37 °C) stimulus. Indeed, this was the case with **NP_{As-S2}** disassembling between 48 to 72 hrs (Fig 3.30).

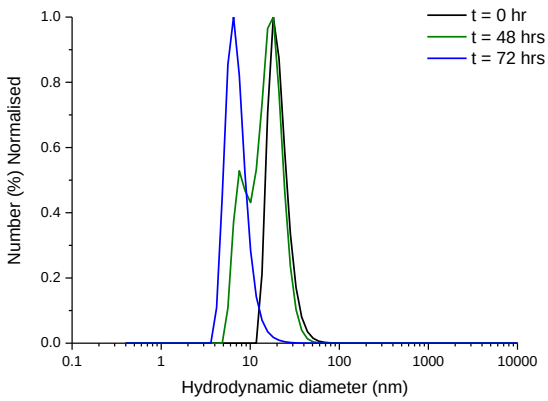

Figure 3.30 Particle size distribution curves of NP_{As-S2} as a function of time in aqueous GSH (GSH = 5 mM, nanoparticle concentration = 1 mg/ml) (see Appendix C, S3.30 for supporting information).

The dynamic redox chemistry of As is a distinctive characteristic of organic and polymeric arsenicals that lends itself to application in the development of responsive (bio)nanomaterials. It is known that As(III) can be readily oxidise to As(V) by reactive oxygen species (ROS) such as hydrogen peroxide (H_2O_2).[45] Suzuki *et al* have treated blood and organ lysates from animal models (Hamsters and Rats) with hydrogen peroxide to liberate As(III) bound proteins as arsenates (As(V)) for arsenic biodistribution and metabolite assays.[46] Computational studies by Villamena *et al* suggests As(III) oxidation to As(V) by ROS species including hydrogen peroxide is exoergic, and highlight the possibility of arsenic cytotoxicity by GSH depletion due to the redox cycling events between GSH (As(V) reduction) and ROS (As(III) oxidation).[47]

The responsivity of the As(III)-S cross-linked nanoparticles to H_2O_2 (5 Mm. 37 °C) was investigated with the proposed response to As-S bond cleavage and oxidation monitored as a function of the particle size using DLS (Figure 3.31). The nanoparticles stabilised by As(III)-S cross-linking (**$NP_{As\text{-}S4}$**, **$NP_{As\text{-}S4/2}$**, **$NP_{As\text{-}S3}$**, **$NP_{As\text{-}S3/2}$**, **$NP_{As\text{-}S2}$**) did not disassemble instantly, maintaining the hydrodynamic particle sizes over the first 3 hours. This is in contrast to the nanoparticles cross-linked by reductive coupling with As-As bond formation prepared here as a control (Fig 3.7), and in previous work, which fully disassembled within 1 hour after addition of H_2O_2 (5 mM, 37 °C). Pleasingly, a trend was observed relating the nanoparticle stability to the structure of the polythiol cross-linkers and the cross-linking density. Thus the stability of the particles decreased with decreasing thiol valency in the cross-linkers ([SH] : [As] = 2; **$NP_{As\text{-}S4}$** > **$NP_{As\text{-}S3}$** > **$NP_{As\text{-}S2}$**) with **$NP_{As\text{-}S4}$** undergoing disassembly over 44 hours and **$NP_{As\text{-}S3}$** and **$NP_{As\text{-}S2}$** disassembling over 18 hours and 6 hours respectively (Fig 3.31). When the cross-linking density was reduced ([SH] : [As] = 1; **$NP_{As\text{-}S4/2}$** and **$NP_{As\text{-}S3/2}$**) the stability was reduced further with the onset of disassembly occurring within 3 hours (Fig 3.31). This trend can be attributed to the thiol valency in the cross-linkers *i.e.* increasing valency PTM > TTM > HDT increases the likelihood of inter-chain As(III)-S bonds forming, constituting cross-linking, which have to be broken under the oxidative conditions. Intra-chain As(III)-S bonding is also possible, and this will have a more detrimental effect when HDT is employed (**$NP_{As\text{-}S2}$**) as a single intra-chain reaction will consume both the thiol groups present in HDT, whereas when PTM and TTM are employed (**$NP_{As\text{-}S4}$** and **$NP_{As\text{-}S3}$**), latent thiol groups

remain available for cross-linking. These results demonstrate for the first time that nanoparticles compromised of polymeric arsenicals, cross-linked via As(III)-S bonds have tuneable responsivity to H_2O_2, which is an attractive stimulus for drug delivery, particularly as a responsive linker for peroxisomes targeted delivery is also particularly interesting, especially in intracellular infections.[48] Furthermore, H_2O_2 is indigenously produced inside cells for natural cellular processing[49] and it's concentration is increased in environments of oxidative stress which occurs in response to inflammation associated with a number of disease states including cancer and atherosclerosis and cystic fibrosis.

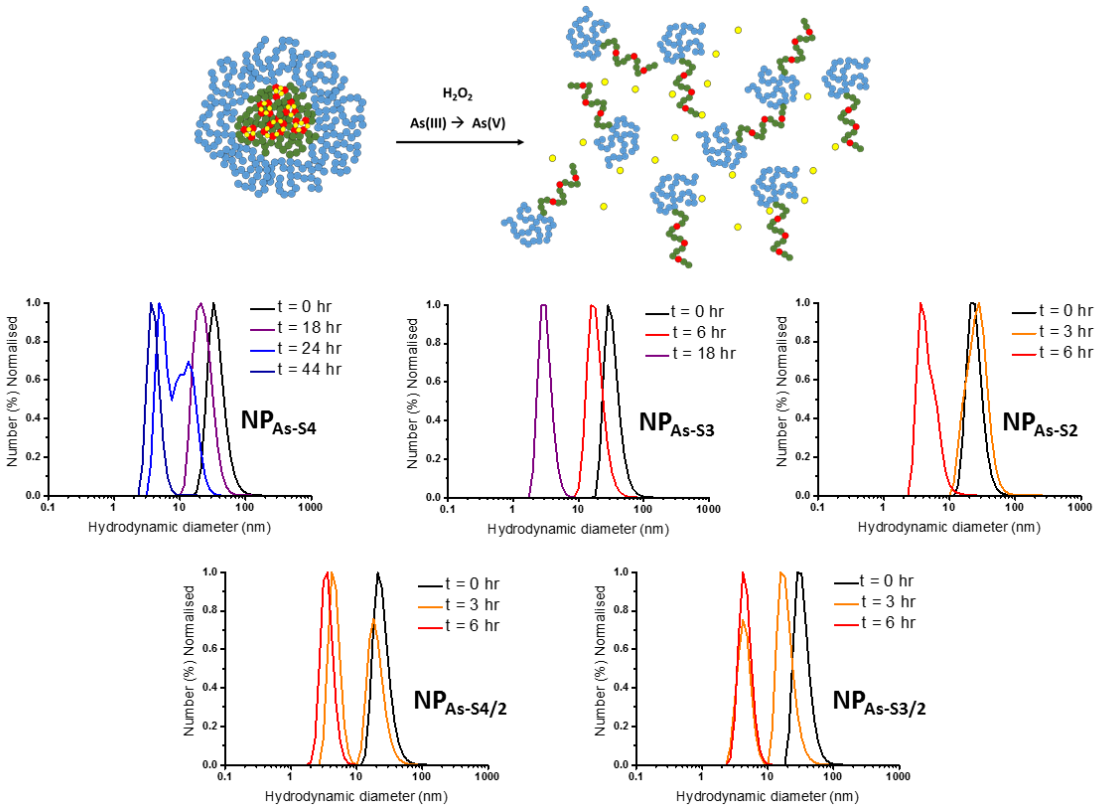

Figure 3.31 Scheme: disassembly of the nanoparticles through release of the cross-linker mediated by oxidation of the As(III) to As(V) with hydrogen peroxide. DLS analysis of the disassembly with time (black = 0 hr, orange = 3 hr, red = 6 hr, purple = 18 hr, blue = 24 hr, Navy = 44hr) (see Appendix C: S3.31A, S3.31B, S3.31C, S3.31D and S3.31D for supporting information).

3.2.3 Cytotoxicity of polymeric arsenical nanoparticles

Finally, to dispel concerns regarding the toxicity of organic and polymeric arsenicals, which are known to be less toxic than inorganic counterparts, *in vitro* toxicity of the polymeric arsenical **P3.1** and the resulting nanoparticles was determined using a standard XTT assay with a human breast adenocarcinoma cell line (MDA-231). Using an identical

protocol, polymeric arsenical scaffolds have been shown to be non-toxic between 2 – 20 μM against MDA-231, whilst nanoparticles derived from thermoresponsive block copolymeric arsenicals, similar to those reported here but consisting of As-As cross-linking, were also non-toxic up to 2 mg/ml against a Prostate cancer cell line (PC3). In this work **P3.1** was non-toxic up to 5 mg/ml and the nanoparticles were non-toxic up to 2 mg/ml with the exception of the $\mathbf{NP_{As\text{-}S2}}$ which showed a decrease in cell viability at concentration > 0.2 mg/ml (Fig 3.32). This is attributed to the lower stability of $\mathbf{NP_{As\text{-}S2}}$ leading to an earlier onset of disassembly, with the products of the disassembly being responsible the change in viability. The origin of the toxicity is not known at this stage but the released cross-linker is implicated considering that **P3.1** is non-toxic over the concentration range. Despite this result, and since it occurs at high concentration (from a clinical perspective), these results support the potential of using polymeric arsenicals as a platform for drug delivery.

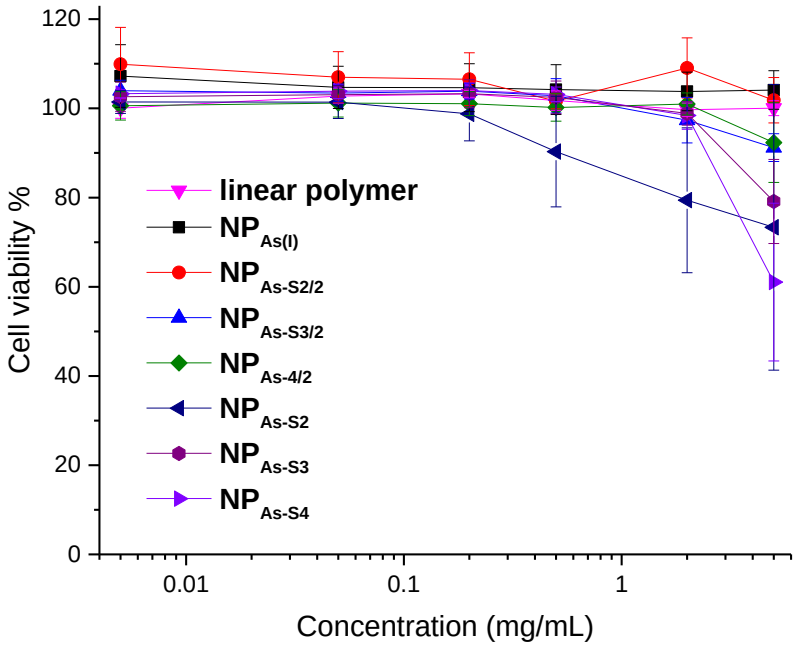

Figure 3.32 ***In vitro*** **cell viability of polymers P3.1 and nanoparticles,** $\mathbf{NP_{As\text{-}S4}}$**,** $\mathbf{NP_{As\text{-}S4/2}}$**,** $\mathbf{NP_{As\text{-}S3}}$**,** $\mathbf{NP_{As\text{-}S3/2}}$**,** $\mathbf{NP_{As\text{-}S2}}$**,** $\mathbf{NP_{As(I)}}$ **(XTT viability assay using MDA cell line).**

3.3 Conclusion

Thermoresponsive block copolymeric arsenicals comprised of PEGA and NIPAm, with incorporation of organic arsenical acrylamide monomer (AsAm(pin$_2$)) into either the core-forming NIPAm block (PEGA$_{22}$-*b*-(NIPAm$_{106}$-*co*-AsAm(pin$_2$)$_{15}$, **P3.1**) or the corona-forming PEGA block ([PEGA$_{17.5}$-*co*-AsAm(pin$_2$)$_{5.5}$]-*b*-NIPAm$_{97}$, **P3.2**), have been synthesised by RAFT for the first time. Removal of the pinacol groups of AsAm(pin$_2$) furnished reactive As(V)-functional groups and the resulting polymers formed nanoparticles at elevated temperatures. The reactive As(V)-functional groups were targeted for cross-linking under reductive conditions (H_3PO_2, KI, 60 °C) in the presence of polythiol reagents (PTM, TTM, HDT) exploiting the high affinity of the As(III) for thiols and affording cross-linking through the formation of As(III)-S bonds. The corona-functional polymer **P3.2** was not able to be cross-linked even in the presence of tetra-thiol cross-linker PTM and targeting 100% cross-linking ([SH] : [As] = 2). However, the core-functional polymer **P3.1** formed stable nanoparticles in the presence of tetra- (PTM, $\mathbf{NP_{As\text{-}S4}}$), tri- (TTM, $\mathbf{NP_{As\text{-}S3}}$) and di-thiol (HDT, $\mathbf{NP_{As\text{-}S2}}$) cross-linkers ([SH] : [As] = 2), which were more stable than analogous nanoparticles cross-linked by complete reductive coupling via As-As bond formation. Characterisation of the nanoparticles by SLS and AFM revealed that N_{agg} and R_g/R_h increased as a function of concentration for $\mathbf{NP_{As\text{-}S4}}$ and $\mathbf{NP_{As\text{-}S3}}$ which was manifest as changes in nanoparticle topology as a result of inter-particle interactions and aggregation. Conversely, $\mathbf{NP_{As\text{-}S2}}$ and nanoparticles prepared targeting 50% cross-linking ([SH] : [As] = 1; $\mathbf{NP_{As\text{-}S4/2}}$, $\mathbf{NP_{As\text{-}S3/2}}$) and exhibited more spherical structures and showed little change in N_{agg} and R_g/R_h. With respect to stability and responsivity of these nanoparticles only $\mathbf{NP_{As\text{-}S2}}$ was shown to disassemble in the presence GSH (5 μM, 37 °C) which occurred over 72 hours. In contrast, a trend was observed pertaining to disassembly in under conditions mimicking oxidative stress H_2O_2 (5 μM, 37 °C), whereby the stability of the particles followed the trend $\mathbf{NP_{As\text{-}S4}} > \mathbf{NP_{As\text{-}S3}} > \mathbf{NP_{As\text{-}S2}} > \mathbf{NP_{As\text{-}S4/2}} \approx \mathbf{NP_{As\text{-}S3/2}}$. To the best of our knowledge this is the first report in the literature to demonstrate the using polymeric arsenicals cross-linked via As(III)-S bonding as a responsive mechanism for polymeric nanoparticles. The diverse chemistry and non-toxic nature of the polymeric arsenicals and nanoparticles demonstrated here and in our previous work, combined with the potential synergy with respect to biological activity, strengthens the case for broader acceptance and adoption of

polymeric arsenicals as functional and responsive platform for biomaterials science.

3.4 Experimental

3.4.1 Methods and materials

Dimethyl 2,2'-azobis(2-methylpropionate) (V601), *N*-(4-(2,2,3,3,7,7,8,8-octamethyl-1,4,6,9-tetraoxa-5λ^5-arsaspiro[4.4]non-5-yl)-phenyl-2-propenamide) (AsAm(pin$_2$)) was synthesised as previously reported[33] 2-((butylthio)-carbonothioyl) thio propanoic acid (PABTC) was synthesised according to the reported literature.[50] *N*-Isopropylacrylamide (NIPAm, 97%) was purchased from sigma and recrystallized in hexane from diethyl ether. Potassium Iodide, glutathione (GSH), hydrogen peroxide (30 % w/w), hypophosphorous acid (50% w/w), poly(ethylene glycol) methyl ether acrylate (PEGA, average M_n = 480), tetrakis(3-mercaptopropionate), trimethylolpropane tris(3-mercaptopropionate), and hexa(ethylene glycol) dithiol) were purchased from Sigma Aldrich and used as received. Nuclear Magnetic Resonance (NMR) spectroscopy (^{1}H NMR) spectra were recorded on a Bruker HD 300 spectrometer (300 MHz) at 27 °C in either deuterated chloroform ($CDCl_3$) or deutrated water (D_2O). Chemical shift values (δ) are reported in ppm. The residual proton signal of the solvent (δ H = 7.26 ppm for $CDCl_3$, δ H = 2.50 ppm for D_2O) was used as internal reference. ACDLABS software was used to analyse the data obtained. Number-average molar masses ($M_{n,SEC}$) and dispersity values ($Đ$) were determined using Size exclusion Chromatography (SEC) with DMF as an eluent. SEC analysis was conducted on Polymer Laboratories PL-GPC 50 Plus system using a Polar Gel-M guard column (7.5 × 50 mm) followed by two Polar Gel-M columns (7.5 ×300 mm). DMF (0.1% LiBr) was used as eluent at 1.0 mL min^{-1}at 50 °C. All polymer samples were filtered through nylon membrane with 0.45 µm pore size before injection (100 µL). Commercial narrow linear poly(methyl methacrylate) (PMMA) standards in range of 2.0 × 10^2 −1.0 × 10^6 gmol^{-1} were used to calibrate the DMF SEC system. The SEC data obtained were analysed using Agilent technologies GPC/SEC software to determine $M_{n,SEC}$ and $Đ$ based on the PMMA calibration. Hydrodynamic diameters (D_h) and size distributions were determined by Dynamic Light Scattering (DLS) on a MALVERN Zetasizer Nano ZS operating at 25 °C with a 4 mW He-Ne 633 nm laser module. Measurements were made at a detection angle of 173° (back scattering). Measurements

were repeated three times with automatic attenuation selection and measurement position. The results were analysed using Malvern DTS 6.20 software. PDI values were calculated using equation Eq 3.1

$$PDi = \frac{\sigma^2}{d^2} \qquad \text{(Eq 3.1)}$$

Where σ is the standard deviation, and d is the diameter both obtained from the number distribution.

3.4.2 Determination of M_w by Static Light Scattering

The incremental refractive index, dn/dC, was determined by measuring the refractive index of the polymer over a range of concentrations (1.33, 0.66, 0.33, 0.167 mg/ml) . The RI was determined using a Shodex RI detector, operating at a wavelength of 632 nm. Multiplying the gradient, of the plot of RI vs. concentration, by the refractive index of the solvent (water = 1.3325) and dividing by the RI constant of the instrument (−1398000) gives the dn/dC of the polymer (table 3.2). Light scattering measurements were obtained using an ALV-CGS3 system operating with a vertically polarized laser with the wavelength λ = 632 nm. The measurements were taken at 20 °C over a range of scattering wave vectors ($q = 4\pi n \sin(\theta/2)/\lambda$, with θ being the angle of observation and n the refractive index of the solvent). The Rayleigh ratio, R_θ, was determined using Eq 3.2;

$$R_\theta = \frac{I_{solution}(\theta) - I_{solvent}(\theta)}{I_{toluene}(\theta)} . \left(\frac{n_{solution}}{n_{toluene}}\right)^2 . R_{toluene} \qquad \text{(Eq 3.2)}$$

Where $I_{solution}$, $I_{solvent}$ and $I_{toluene}$ are the scattering intensities of the solution, solvent and reference (toluene) respectively, n is the refractive index (n_{water}= 1.333, $n_{toluene}$=1.496) and $R_{toluene}$ the Rayleigh ratio of toluene ($R_{toluene}$= 1.35 × 10^{-5} cm^{-1} for λ = 632.8 nm). The optical constant, K, is defined by Eq 3.3, where N_a is the Avogadro number and dn/dC is the incremental refractive index.

$$K = \frac{4\pi^2 {n_{solvent}}^2}{\lambda^4 N_a} \left(\frac{\partial n}{\partial C}\right)^2 \qquad \text{(Eq 3.3)}$$

In all cases it was verified that the apparent radius of gyration of the systems verified q × Rg < 1. The Zimm approximation can thus be used to obtain Eq 3.4. Plotting KC/R_θ as a function of q^2 for each concentration yielded the apparent radius of gyration Rg of the scatterers as well as their apparent molecular weight extrapolated to zero angle, $\boldsymbol{M_a}$. Representative plots are shown in the Figures 3.6(e-f), 3.12, 3.16, 3.21, 3.24 and 3.27.

$$\frac{KC}{R_\theta} = \frac{1}{M_a}\left(1 + \frac{q^2 R_g{}^2}{3}\right) \quad \text{(Eq 3.4)}$$

At a given concentration the Rayleigh ratio, Rθ, is related to the apparent molecular weight of the sample, given by Eq 3.4. It is only at infinite dilutions, where the interactions between scattering particles are negligible, that the apparent molecular weight is equal to the true molecular weight. Multiple concentrations were measured and a plot of linear regression was used to determine the apparent molecular weight at a concentration of 0 $mgml^{-1}$.

3.4.3 Atomic Force Microscopy (AFM)

AFM images were recorded on a Bruker Dimension Icon instrument operated in peak force tapping mode. The probes used were ScanAsyst silicon tips with a resonance frequency of 70 kHz and a spring constant of 0.4 N/m. Samples were prepared by drop casting 5 µl of a 1 mg/ml aqueous nanoparticle solution onto a freshly cleaved sheet of mica, left to stand for 30 seconds and then dried under a stream of Nitrogen.

3.4.4 Transmission Electron Microscopy (TEM)

Samples were prepared by placing a 400 mesh carbon coated Formvar copper grid onto a 20 µL droplet of aqueous nanoparticles (1 mg/ml) in a petri dish, leaving it for 10 minutes before drawing off the solution. The grid was then stained by placing onto a 20 µl droplet of aqueous solution of uranyl acetate (0.2 wt%), leaving it for 10 minutes before drawing off excess liquid and allowed to air-dry overnight. TEM images were acquired using a JEOL 2100 transmission electron microscope operating at a 200 kV accelerating voltage. Images were captured using Digital Micrograph® and analyzed with ImageJ.

3.4.5 General procedure for RAFT polymerisation.

A typical synthesis of the first block (A_1 described here) is the following: CTA PABTC (24.8 mg, 0.1 mmol), PEGA (M_{n480}) (1000 mg, 2.1 mmol), V601 (0.5 mg, 2.2 µmol) and trifluoroethanol (1.5 ml, 1 $moldm^{-3}$ monomer concentration) was charged into a vial equipped with a magnetic stirrer, the vial was then sealed with rubber septum and

deoxygenated by stream of bubbling nitrogen for 15 minutes with stirring. The vial was suspended in a preheated oil bath at 65^0C for 24 hrs. NMR of the reaction mixture was used to compare monomer consumption before and after the polymerisation and GPC sample was taken. No purification was required before chain extension.

3.4.6 A typical chain extension (P3.1):

The vial with reaction mixture of the first block was cooled before opening to air. NIPAm (1136 mg, 10 mmol), AsAmpin$_2$ (644 mg, 1.4 mmol), V601 (1.26 mg, 5.5 2.2 μmol) and trifluoroethanol (3.8 ml, 3 mldm^{-3} monomer concentration) was added directly to reaction mixture of first block and mixture was well stirred. The vial was then re-sealed with rubber septum and deoxygenated by stream of bubbling nitrogen for 15 minutes with stirring. NMR of the reaction mixture was used to compare monomer consumption before and after the polymerisation and GPC sample was taken. No purification was required before deprotection.

3.4.7 Deprotection AsAm(pin)$_2$ units / removal of pinacol groups (P3.1 and P3.2):

The polymerisation reaction mixture of **P3.1** (and **P3.2**) was dialysed in 0.1 moldm^{-3} HCl solution over night before changing to deionised water and further dialysed for 24 hours in deionised water, changing the water up to 3 times. The dialysed (3.5 K polymer solution was lyophilised to yielded **P3.1** as white powder (2.4 g, 85 % yield). Similarly for **P3.2** yielded as white powder (2.0 g, 94 % yield).

3.4.8 Determination of monomer conversions and Monomer to CTA /Macro-CTA ratio

The conversions of the monomers were determined by comparing the vinyl protons (δ 6.50 - 5.50 ppm) to the integration of an internal reference. In the case of **P3.1** the three methyl protons belonging to the Z group of the PABTC chain transfer agent (–CH_2–C***H***$_3$) before and after polymerization was used as a reference. For the following chain extension (**P3.1**), the back bone -C***H***- (∫ δ 2.0 -2.5 ppm) was used as reference to determine the monomer to macro CTA ratio.

For the synthesis of **P3.2** the overlapping pinacol groups with RAFT agent were taken into account to get a difference of three protons between the pinacol C$\boldsymbol{H}_3$ (Figure S) to get an accurate estimate of the CTA to monomer ratio. For the following chain extension (**P3.2**), the aromatic groups of the AsAm(pin$_2$) units ∫ δ 7.8 -7.5 ppm were used as an internal reference to determine the macro-CTA to monomer ratio and monomer conversion.

3.4.9 Calculation of $M_{n,th}$,

The theoretical number average molar mass ($M_{n,th}$) is calculated using equation (Eq 3.5).

$$M_{n,th} = \rho M_M \frac{[M]_0}{[CTA]_0} + M_{CTA} \quad \text{(Eq 3.5)}$$

Where $[M]_0$ and $[CTA]_0$ are the initial concentrations of the monomer and chain transfer agent respectively; ρ is the monomer conversion as determined by ^{1}H NMR, M_M and M_{CTA} are the molar molar masses (gmol^{-1}) of the monomer and chain transfer agent respectively.

3.4.10 General Procedure for Arsenic-thiolate cross-linked nanoparticle synthesis

AsAm functional polymer (100 mg) was dissolved in deoxygenated aqueous solution (10 ml) of hypophosphorous acid (H_3PO_2, 10 wt%, 10 mg/ml polymer) and deoxygenated KI (1 vol% from a 3 wt % aq solution) was added. The solution was heated at 60 °C for 10 minutes before adding the cross-linker. Stock solutions (100 mg/ml in dioxane) of cross-linkers were prepared and added to preassembled nanoparticle solution to synthesise the following; tetrakis(3-mercaptopropionate) was used as a cross-linker to synthesise **NP$_{As\text{-}S4}$** (12.4 mg, 123 µL of cross-linker solution, 7.5 eq with respect to **P3.1**) and to synthesis **NP$_{As\text{-}S4/2}$** (6.18 mg, 61.8 µL of cross-linker solution, 3.75 eq with respect to **P3.1**); trimethylolpropane tris(3-mercaptopropionate) was used as a cross-linker to synthesise **NP$_{As\text{-}S3}$** (13.5 mg, 135 µL of cross-linker solution, 10 eq with respect to **P3.1**) and to synthesis **NP$_{As\text{-}S3/2}$** (6.73 mgs, 67.3 µL of cross-linker solution, 5 eq with respect to **P3.1**); hexa(ethylene glycol) dithiol) was used as a cross-linker to synthesise **NP$_{As\text{-}S2}$** (11.5 mg, 115 µL of cross-linker solution, 15 eq with respect to **P3.1**). The cross-linking reaction was left for 2 hours at 60 °C. The resulting solution was dialysed (nMWCO 3.5 KDa) for

3 days with deionised water, changing the water twice a day to remove electrolytes and dioxane. The cross-linked particles were isolated by lyophilisation to obtain white solid (yielded approximately between 95 - 99%) and were readily dispersed in H_2O.

3.4.11 General procedure for particle stability and disassembly.

Polymer nanoparticles (1 mg/ml), were dissolved separately in deionised water, glutathione (5 mM) and H_2O_2 (5 mM). The solutions were filtered through (450 µm nylon filters) into separate plastic cuvettes (with a lid) and incubated at 37 ^{0}C in water bath. Disassembly was monitored through the measurement of changes in particle size (D_h) as a function of time by DLS.

3.4.12 Cell viability

Cell viability was assessed against MDA-231 (human breast adenocarcinoma) cell lines. Cells were seeded into a 96-well plate, (1.5 x 10^4 cells per well), cultured in basal medium DMEM (Dublecco's Modified Eagle Medium) with 10% foetal bovine serum and allowed to grow for 24 hours. The medium was then replaced with fresh media and complemented with solutions of polymer (0.313, 0.625, 1.25, 2.50, 5.00 mgml^{-1}) prepared from stock solutions in PBS (500 µM). Cells were further incubated for 24 hours. The medium was replaced with fresh medium containing a solution of XTT (0.2 mg mL^{-1}) and N-methyl dibenzopyrazine methyl sulphate (250 µM) and incubated for 16 hours. Cells were then transferred to a plate reader and absorbance at 450 and 650 nm was assessed.

3.5 References

1. G. Gody, T. Maschmeyer, P. B. Zetterlund and S. Perrier, *Macromolecules*, 2014, **47**, 3451-3460.
2. G. Gody, T. Maschmeyer, P. B. Zetterlund and S. Perrier, *Nat. Commun.*, 2013, **4**, 2505.
3. Q. Zhang, P. Wilson, Z. Li, R. McHale, J. Godfrey, A. Anastasaki, C. Waldron and D. M. Haddleton, *J. Am. Chem. Soc.*, 2013, **135**, 7355-7363.
4. A. Anastasaki, V. Nikolaou and D. M. Haddleton, *Polym. Chem,*, 2016, **7**, 1002-1026.
5. A. Anastasaki, V. Nikolaou, Q. Zhang, J. Burns, S. R. Samanta, C. Waldron, A. J. Haddleton, R. McHale, D. Fox and V. Percec, *J. Am. Chem. Soc.*, 2014, **136**, 1141-1149.
6. G. Moriceau, G. Gody, M. Hartlieb, J. Winn, H. Kim, A. Mastrangelo, T. Smith and S. Perrier, *Polym. Chem,*, 2017, **8**, 4152-4161.
7. A. Kuroki, P. Sangwan, Y. Qu, R. Peltier, C. Sanchez-Cano, J. Moat, C. G. Dowson, E. G. L. Williams, K. E. S. Locock, M. Hartlieb and S. Perrier, *ACS Appl. Mater. Interfaces*, 2017, **9**, 40117-40126.
8. J. Tanaka, A. S. Gleinich, Q. Zhang, R. Whitfield, K. Kempe, D. M. Haddleton, T. P. Davis, S. b. Perrier, D. A. Mitchell and P. Wilson, *Biomacromolecules*, 2017, **18**, 1624-1633.
9. C. Bray, R. Peltier, H. Kim, A. Mastrangelo and S. Perrier, *Polym. Chem,*, 2017, **8**, 5513-5524.
10. R. Whitfield, A. Anastasaki, N. P. Truong, P. Wilson, K. Kempe, J. A. Burns, T. P. Davis and D. M. Haddleton, *Macromolecules*, 2016, **49**, 8914-8924.
11. T. R. Barlow, J. C. Brendel and S. Perrier, *Macromolecules*, 2016, **49**, 6203-6212.
12. E. H. Discekici, A. Anastasaki, R. Kaminker, J. Willenbacher, N. P. Truong, C. Fleischmann, B. Oschmann, D. J. Lunn, J. Read de Alaniz, T. P. Davis, C. M. Bates and C. J. Hawker, *J. Am. Chem. Soc.*, 2017, **139**, 5939-5945.
13. P. Gurnani, A. M. Lunn and S. Perrier, *Polymer*, 2016, **106**, 229-237.
14. A. Kerr, M. Hartlieb, J. Sanchis, T. Smith and S. Perrier, *Chem. Commun.*, 2017, **53**, 11901-11904.
15. J. Zhang, R. Deubler, M. Hartlieb, L. Martin, J. Tanaka, E. Patyukova, P. D. Topham, F. H. Schacher and S. Perrier, *Macromolecules*, 2017, **50**, 7380-7387.
16. J. Zhang, J. Tanaka, P. Gurnani, P. Wilson, M. Hartlieb and S. Perrier, *Polym. Chem,*, 2017, **8**, 4079-4087.
17. J. Zhang, G. Gody, M. Hartlieb, S. Catrouillet, J. Moffat and S. Perrier, *Macromolecules*, 2016, **49**, 8933-8942.

18. J. F. Quinn, M. R. Whittaker and T. P. Davis, *Polym. Chem,*, 2017, **8**, 97-126.
19. W. L. A. Brooks and B. S. Sumerlin, *Chem. Rev.*, 2016, **116**, 1375-1397.
20. J.-Z. Du, X.-J. Du, C.-Q. Mao and J. Wang, *J. Am. Chem. Soc.*, 2011, **133**, 17560-17563.
21. S. Mukherjee, M. R. Hill and B. S. Sumerlin, *Soft Matter*, 2015, **11**, 6152-6161.
22. S. Mukherjee, A. P. Bapat, M. R. Hill and B. S. Sumerlin, *Polym. Chem,*, 2014, **5**, 6923-6931.
23. D. K. Kölmel and E. T. Kool, *Chem. Rev.*, 2017, **117**, 10358-10376.
24. S. Hagihara, H. Tanaka and S. Matile, *J. Am. Chem. Soc.*, 2008, **130**, 5656-5657.
25. K. Fukuda, M. Shimoda, M. Sukegawa, T. Nobori and J.-M. Lehn, *Green Chem.*, 2012, **14**, 2907-2911.
26. C.-Y. Sun, S. Shen, C.-F. Xu, H.-J. Li, Y. Liu, Z.-T. Cao, X.-Z. Yang, J.-X. Xia and J. Wang, *J. Am. Chem. Soc.*, 2015, **137**, 15217-15224.
27. C. Y. Sun, Y. Liu, J. Z. Du, Z. T. Cao, C. F. Xu and J. Wang, *Angew. Chem. Int. Ed.*, 2016, **55**, 1010-1014.
28. N. C. Lloyd, H. W. Morgan, B. K. Nicholson and R. S. Ronimus, *Angew. Chem. Int. Ed.*, 2005, **44**, 941-944.
29. J. Tanaka, S. Tani, R. Peltier, E. H. Pilkington, A. Kerr, T. P. Davis and P. Wilson, *Polym. Chem,*, 2018, **9**, 1551-1556.
30. L. Horsley, J. Cummings, M. Middleton, T. Ward, A. Backen, A. Clamp, M. Dawson, H. Farmer, N. Fisher, G. Halbert, S. Halford, A. Harris, J. Hasan, P. Hogg, G. Kumaran, R. Little, G. J. M. Parker, P. Potter, M. Saunders, C. Roberts, D. Shaw, N. Smith, J. Smythe, A. Taylor, H. Turner, Y. Watson, C. Dive, G. C. Jayson and U. K. D. D. O. P. I. Canc Res, *Cancer Chemother. Pharmacol.*, 2013, **72**, 1343-1352.
31. P. J. Dilda, S. p. Decollogne, L. Weerakoon, M. D. Norris, M. Haber, J. D. Allen and P. J. Hogg, *J. Med. Chem.*, 2009, **52**, 6209-6216.
32. P. Wilson, A. Anastasaki, M. R. Owen, K. Kempe, D. M. Haddleton, S. K. Mann, A. P. Johnston, J. F. Quinn, M. R. Whittaker and P. J. Hogg, *J. Am. Chem. Soc.*, 2015, **137**, 4215-4222.
33. C. Footman, P. A. de Jongh, J. Tanaka, R. Peltier, K. Kempe, T. P. Davis and P. Wilson, *Chem. Commun.*, 2017, **53**, 8447-8450.
34. B. A. Griffin, S. R. Adams and R. Y. Tsien, in *Site-Specific Protein Labeling: Methods and Protocols*, eds. A. Gautier and M. J. Hinner, Springer New York, New York, NY, 2015, pp. 1-6.
35. R. A. Scheck and A. Schepartz, *Acc. Chem. Res.*, 2011, **44**, 654-665.

36. G. T. Dempsey, M. Bates, W. E. Kowtoniuk, D. R. Liu, R. Y. Tsien and X. Zhuang, *J. Am. Chem. Soc.*, 2009, **131**, 18192.
37. S. R. Adams, R. E. Campbell, L. A. Gross, B. R. Martin, G. K. Walkup, Y. Yao, J. Llopis and R. Y. Tsien, *J. Am. Chem. Soc.*, 2002, **124**, 6063-6076.
38. B. A. Griffin, S. R. Adams and R. Y. Tsien, *Science*, 1998, **281**, 269-272.
39. P. Roy, N. K. Mondal, S. Bhattacharya, B. Das and K. Das, *Appl Water Sci.*, 2013, **3**, 293-309.
40. A. Anastasaki, B. Oschmann, J. Willenbacher, A. Melker, M. H. C. V. Son, N. P. Truong, M. W. Schulze, E. H. Discekici, A. J. McGrath, T. P. Davis, C. M. Bates and C. J. Hawker, *Angew. Chem. Int. Ed.*, 2017, **56**, 14483-14487.
41. C. A. Figg, A. Simula, K. A. Gebre, B. S. Tucker, D. M. Haddleton and B. S. Sumerlin, *Chem. Sci.*, 2015, **6**, 1230-1236.
42. B. M. Tande, N. J. Wagner, M. E. Mackay, C. J. Hawker and M. Jeong, *Macromolecules*, 2001, **34**, 8580-8585.
43. A. K. Brewer and A. M. Striegel, *Analyst*, 2011, **136**, 515-519.
44. Q. Zhang, M. R. Vakili, X.-F. Li, A. Lavasanifar and X. C. Le, *Biomaterials*, 2014, **35**, 7088-7100.
45. H. V. Aposhian, R. A. Zakharyan, M. D. Avram, M. J. Kopplin and M. L. Wollenberg, *Toxicol. Appl. Pharmacol.*, 2003, **193**, 1-8.
46. H. Naranmandura, N. Suzuki, K. Iwata, S. Hirano and T. Suzuki, *Chem. Res. Toxicol.*, 2007, **20**, 616-624.
47. P. L. Zamora, A. Rockenbauer and F. A. Villamena, *Chem. Res. Toxicol.*, 2014, **27**, 765-774.
48. F. Di Cara, A. Sheshachalam, N. E. Braverman, R. A. Rachubinski and A. J. Simmonds, *Immunity*, 2017, **47**, 93-106.e107.
49. C. Lennicke, J. Rahn, R. Lichtenfels, L. A. Wessjohann and B. Seliger, *Cell Communication and Signaling : CCS*, 2015, **13**, 39.
50. C. J. Ferguson, R. J. Hughes, D. Nguyen, B. T. T. Pham, R. G. Gilbert, A. K. Serelis, C. H. Such and B. S. Hawkett, *Macromolecules*, 2005, **38**, 2191-2204.

Chapter 4 : Stabilisation and functionalisation of polymeric arsenical self-assembly through vinylene-arsine copolymerisation

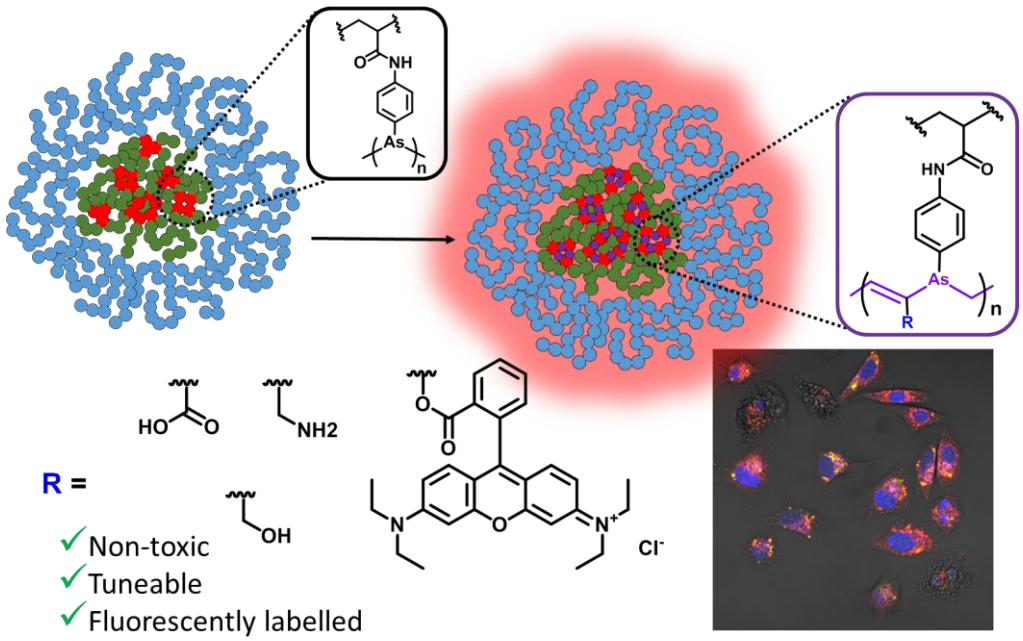

The research presented in this chapter was performed in collaboration with Mr Alex Evans during his MChem project in the 2017-18 academic year. I supervised the project and directed the progress of the research and together we conducted the experimental and analytical work. All the discussion was written independently by myself and the data was processed and resulted figures formatted to be consistent with the other chapters in this thesis.

Abstract

The chemical reactivity of arsenic is a unique feature which changes upon it's interchangeable oxidation states. Alkyl and aryl arsines As(I) exists as oligomers, composed of labile and redox responsive As-As bonds. In chapter 2, As(I) was used as a cross-linker to form responsive nanoparticles by reductive coupling of arsenous acid present in the core of the nanostructure. In the present work, the cross-linking As(I) within

the nanoparticles is further elaborated with functional acetylenes in presence of radical initiators, to form vinylene-arsine cross-linked particles. This enables further stabilisation of the nanoparticles, rendering it non-responsive towards oxidation. Furthermore, fluorescent a label was introduced through the incorporation of the *O*-propargyl Rhodamine-B ester as the functional acetylene reagent. Subsequently these fluorescent nanoparticles were tracked with *in-vitro* fluorescent confocal microscopy with the PC3 cell-line, which showed strong mitochondrial co-localisation, indicating the mitochondrial tagging effect of arsenic observed in organoarsenical chemotherapeutics. Thus this work demonstrates a novel strategy of cross-linking polymeric nanostructures with arsenic whilst retaining the biochemical properties.

4.1 Introduction

The use of arsenic trioxide (Trisenox, As_2O_3) for effective treatment for acute promyelocytic leukaemia has revitalised the therapeutic potential of arsenicals. [1] Such clinical renaissance in the use of arsenicals, has increased the acceptance of the use of arsenic in the field of polymer and biomaterials science. More recently, organic arsenicals 4-(*N*-(*S*-glutathionylacetyl)amino) phenylarsonous acid (GSAO),[2] 4-(*N*-(*S*-penicillaminylacetyl)amino) phenylarsonous acid (PENAO)[3] and S-dimethylarsino-glutathione (ZIO-101; Darinasparin)[4] have gained much attention for use as mitochondrial targeting chemotherapeutic drugs. These trivalent arsenicals (As(III)) drugs, work due to their natural high affinity for proximal cellular dithiols, for example it has been postulated that GSAO and PENAO, leads to loss of mitochondrial membrane potential by cross-linking Cys^{57} and Cys^{257} of mitochondrial adenine nucleotide translocase, leading to opening of the mitochondrial permeability transition pore.[5] Recently, Stenzel and co-workers have copolymerised a methacrylamide PENAO derived monomer, to incorporate the drug into the corona of polymer nanoparticles to improve its bioavailability and drug efficacy. More interestingly, the natural targeting properties of As(III) leads to mitochondrial colocalisation of the nanoparticles by confocal microscopy. The mitochondrial targeting properties of arsenic are an attractive feature and it is an excellent target for chemotherapy, considering the essential energy production required to maintain cell viability.

The biochemical properties of arsenic is dependent on oxidation state of the As(X) (e.g. X = V, III, I), with As(III) being the most widely used for therapeutic applications. Arsines (As(I)) or cyclic oligoarsines (RAs_n)[6, 7] have been known since the 19^{th} century and have been used as chemotherapeutic agents to treat syphilis, yet it was only as recent as 2005, that the structure of Arsphenamine/Salvarsen was elucidated as a mixture of organoarsenic homocycles.[8] These cyclic structures are readily accessible by reduction of the corresponding arsonic acids using hypophosphorus acid in the presence of catalytic amounts of KI.[9] As(I) are known to oxidatively hydrolyze, to form arsenous acid As(III). This unique redox responsive oligocyclisation of arsenic oxidation state inspired the previous chapter where As(I) was utilised for cross-linking self-assembled structures.[10] These As(I) stabilised particles were shown to dissemble under model biologically

relevant redox conditions and found to be non-toxic (up to 2 mg/ml, Chapter 2).

In 2004, Chujo and Naka recognized the potential of these oligomeric As-As structures to act as comonomers for alternating copolymerisation with alkynes to form poly(vinylene-arsines) via ring-collapsed radical alternating copolymerization (RCRAC).[11] These were typically initiated by thermal decomposition of a radical initiator (2,2'-azobisisobutyronitrile, AIBN) to catalyse the homolysis of labile As-As bonds. The resulting arsenic radicals can either recombine to form labile As-As bonds, or add to the acetylene monomer leading to formation of a new As-carbon bond (reviewed in Chapter 1, Scheme 1.4). The structural characterization confirmed the poly(vinylene-arsine) structure with a backbone composed of As-substituted vinylene groups with a *trans*-1,2 geometry.[11] Irrespective of the initial monomer feed ratio, 1:1 stoichiometry of the monomers was maintained as determined through elemental analysis and comparison of the backbone vinyl proton with the sidechain protons. Oligo-phenylarsine were found to be homolytically more stable than oligo-methyl-arsines, and also required more reactive acetylene comonomers. It was reported that aromatic acetylenes derivatives can react efficiently with oligo-phenylarsine, as the aromatic stabilization of the vinyl radical was essential for the addition of the As radical species. It was also reported that electron withdrawing groups (EWG) can stabilize the resulting radical and thus facilitate the polymerisation.[12]

The aim of the work in this chapter was to cross-link self-assembled polymeric arsenicals through arsenic displayed on the side chains via the aforementioned RCRAC method. As well as stabilising the target nanoparticles, an additional purpose of this work is introduce new functionality into the core of the nanoparticles through RCRAC using functional alkyne motifs.

4.2 Results and discussion

4.2.1 Polymeric arsenical synthesis

An identical strategy to that applied in Chapter 3 was employed to synthesis block copolymer composed of corona forming poly(ethylene glycol) methyl ether acrylate

(PEGA, $M_n = 480$ gmol^{-1}) block and core forming *N*-isopropylacrylamide (NIPAm) block, which self-assembles at elevated temperature owing to the thermoresponsive nature of Poly(NIPAm). Previously, these polymers were thermally self-assembled and successfully crossed-linked through the incorporation of the arsenical functional group in the core forming NIPAm block. From the earlier investigation with cyclooligoarsine cross-linking, the arsenical monomer feed was observed to influence the particle stability as function of cross-linking density. This steered the initial focus of this work to vary the arsenical monomer feed in the core forming NIPAm block, whilst keeping the corona forming PEGA block length constant to investigate the effect of cross-linking density of the stability of the corresponding particles. Therefore, in this study polymer compositions of P(PEGA$_{20}$-*b*-[NIPAM$_{80-n}$-*co*-AsAm$_n$]) (**P4.1** *n = 5,* **P4.2** *n = 10,* **P4.3** *n = 15,* **P4.4** *n = 20*) were targeted.

So far two approaches to generate the arsenical functional diblock copolymers have been demonstrated. In Chapter 2, diblock copolymers were generated with unprotected arsenical acrylamide (AsAm) using sodium hydroxide to aid the solubility of the monomer, via sequential chain extension by aqueous SET-LRP. However, for more precise determination of the block co-monomer feed ratio for subsequent cross-linking in Chapter 3, a pinacol protected arsenic acrylamide AsAm(pin)$_2$ was polymerised by RAFT polymerisation, with deprotection of the pinacol group yielding polymers with the reactive arsenic acid functional group required for cross-linking. It's noteworthy that 2,2-trifluoroethanol (TFE) was used a solvent, which is known to be a good solvent for hydrophobic and hydrophilic monomers, but also due to its miscibility with water it allowed facile aqueous acid dialysis for subsequent deprotection and purification.[13] Considering the former factor, we decided to use the RAFT approach in this investigation.

Using the previous RAFT conditions, the initial PEGA block (targeting DP 20) was polymerised, with PABTC as the RAFT agent, and subsequently chain extended with varying amounts of AsAm(pin)$_2$ and NIPAm (targeting overall DP 80). Conversion was monitored *via* ^{1}H NMR comparing vinyl signals at 5.50 – 6.50 ppm with an internal reference (-*CH$_3$* of the Z-group belonging to the PABTC ($\delta = 0.91$ ppm)) for the initial block and methoxy (-*OCH$_3$* at 3.34 ppm) of the PEGA for the chain extension (see

Chapter 3). In all cases the initial blocks were close to the desire target DP_n ($PEGA_n$ DP = 20) with narrow molecular weights distributions ($M_{n,SEC}$ = 8400-10400 $gmol^{-1}$, $Đ$ = 1.16-1.27, Table 4.1) and good agreement with $M_{n,th}$. The block copolymerisation was successfully demonstrated by SEC analysis showing a shift to higher molecular weight ($M_{n,SEC}$ = 17500-22000, $Đ$ =1.25-1.40, Fig 4.1, Table 4.1), owing to efficient re-initiation from the PEGA block with acrylamide based monomers. The removal of the pinacol groups was carried out using acidic dialysis in accordance to the previous study (Chapter 3). The deprotection of the $AsAm(pin)_2$ units was confirmed by ^1H NMR with the disappearance of pinacol groups at 0.95 – 1.35 ppm and further confirmed by SEC analysis, showing a shift to lower molecular weight after deprotection ($M_{n,SEC}$ = 9900-13900, $Đ$ =1.19-1.53; Fig 4.1, table 4.1). Successful inclusion of AsAm into the block copolymers was confirmed by ^1H NMR with appearance of aromatic signals of AsAm ($H_{j,k}$, Fig. 4.2) at 7.5 – 7.7 ppm.

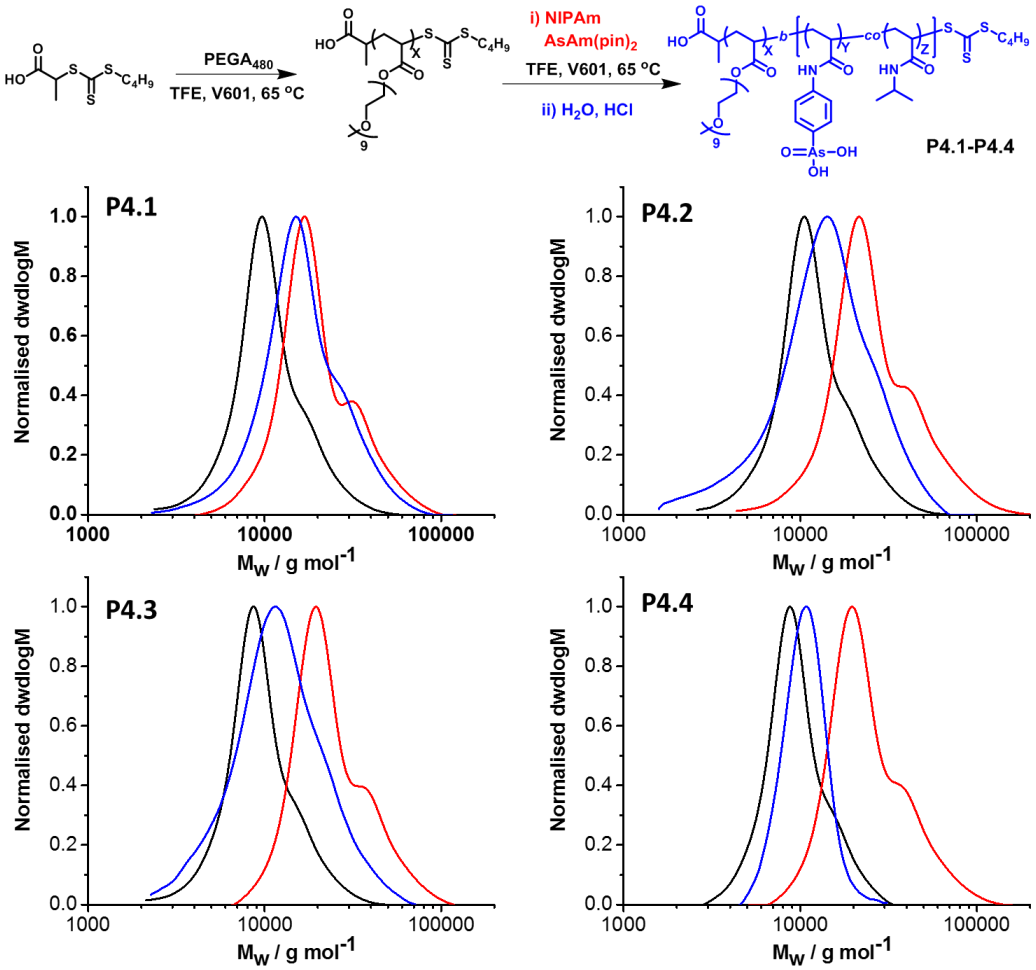

Figure 4.1 Scheme of Poly(PEGA-NIPAm) diblock through sequential chain extension using RAFT polymerisation (as carried out in chapter 2) with varying amount of Arsenical acrylamide in the NIPAm block (P4.1 z = 5, P4.2 z = 10, P4.3 z = 15, P4.4 z = 20). SEC (DMF) of the arsenic functional block copolymer showing the first block (black), block extension (red) and removing the pinacol groups (blue).

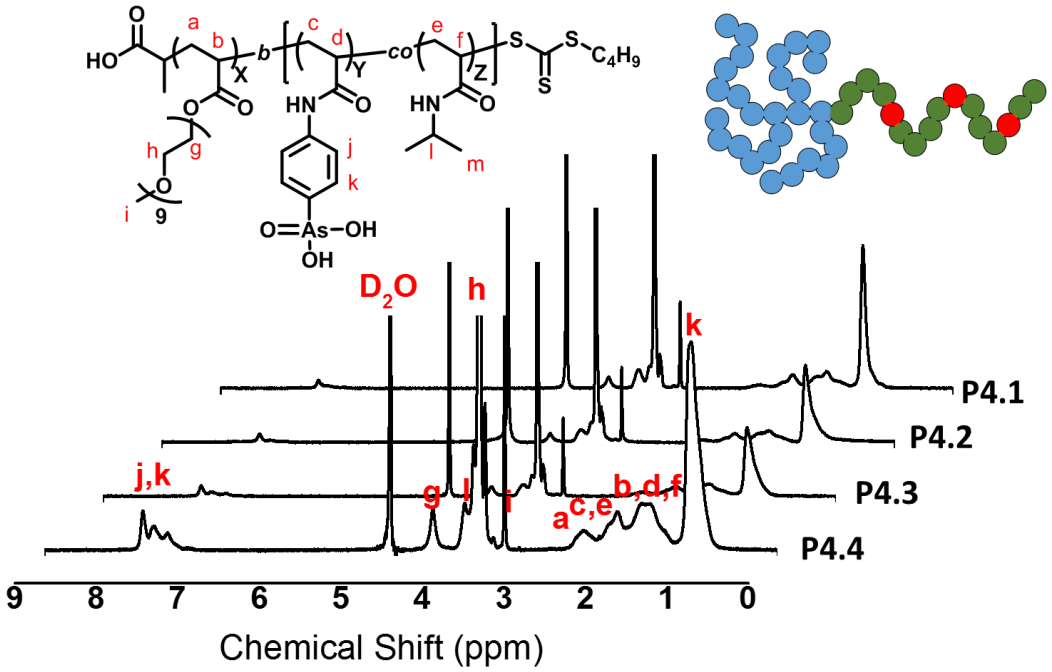

Figure 4.2 ^{1}H NMR (D_2O) of the final polymer P4.1-P4.4

Table 4.1 Arsenic functional block copolymers synthesised by RAFT. ^{1}H NMR of polymerisation mixture in $CDCl_3$ and after deprotection done in D_2O. SEC carried out with DMF as an eluent.

	Polymer Composition	Polymerisation mixture				After deprotection		
		Con.	$M_{n,th}$ (g mol^{-1})	$M_{n,SEC}$ (g mol^{-1})	$Đ$	$M_{n,th}$ (g mol^{-1})	$M_{n,SEC}$ (g mol^{-1})	$Đ$
P4.1	P[PEGA$_{23}$]	> 99%	18000	9400	1.23			
	P[PEGA$_{23}$-*b*-(NIPAm$_{73}$-*co*-AsAm$_4$)]	> 99%	21800	17500	1.27	21200	13900	1.33
P4.2	P[PEGA$_{27}$]	> 99%	13200	10400	1.27			
	P[PEGA$_{27}$-*b*-(NIPAm$_{80}$-*co*-AsAm$_{11}$)]	> 99%	21800	22000	1.40	25400	10500	1.53
P4.3	P[PEGA$_{23}$]	> 99%	11300	8400	1.23			
	P[PEGA$_{23}$-*b*-(NIPAm$_{66}$-*co*-AsAm$_{15}$)]	> 99%	25500	21000	1.25	23100	9900	1.44
P4.4	P[PEGA$_{24}$]	> 99%	11800	8700	1.16			
	P[PEGA$_{24}$-*b*-(NIPAm$_{56}$-*co*-AsAm$_{18}$)]	> 99%	26300	21300	1.27	23300	10200	1.19

The thermal stability of all the polymers was evaluated by thermogravimetric analysis (TGA), which revealed evolution of mass loss between 300-400 °C to correlate with incorporation of AsAm in the copolymer. However, between 450-600 °C the plateau of percentage mass remaining was proportional to the presence of Arsenic. Nevertheless, all polymers are stable at < 300 °C (Fig. 4.3).

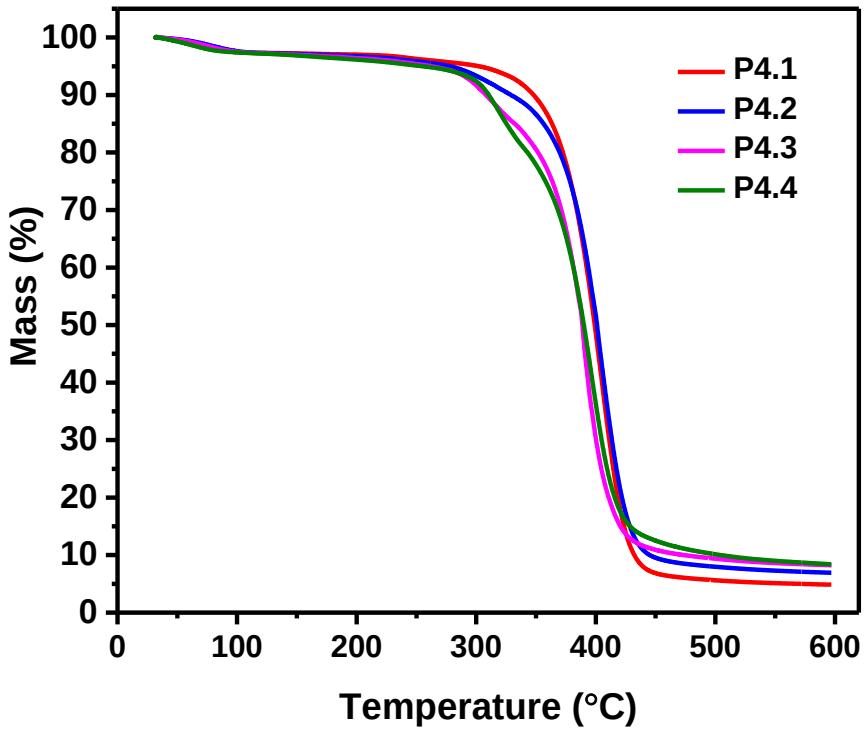

Figure 4.3 Evolution of mass loss with temperature of arsenic functional polymers (P4.1-P4.4) by Thermogravimetric analysis.

The thermoresponsive nature of the As(V)-functional polymers and propensity for self-assembly was investigated by variable temperature dynamic light scattering (DLS). The aqueous solutions of all the arsenic functional polymers (1 mg ml^{-1}) exhibiting an increase in hydrodynamic diameters (D_h) from 2.1-3.1 nm at 25 °C to 14-20 nm with uniform particle sizes at 60 °C, owing to the phase transition of the NIPAm block (Figure 4.4).

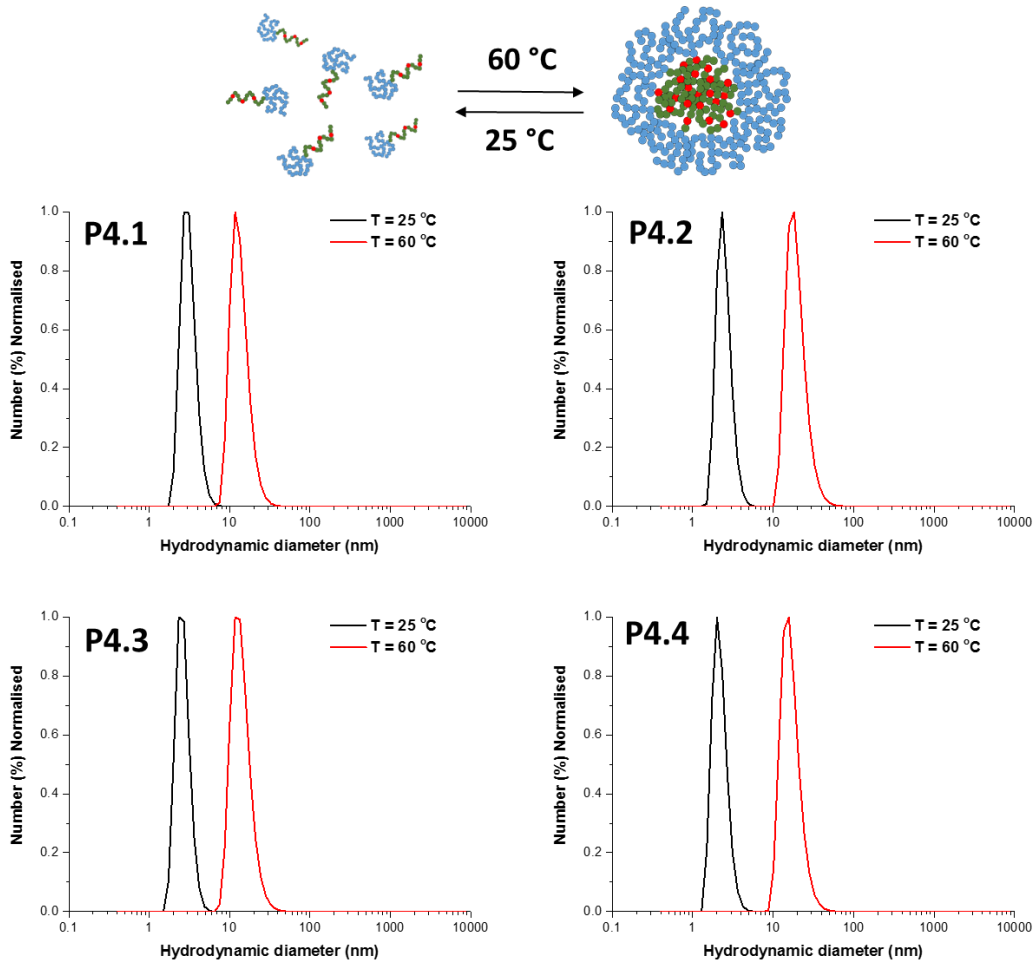

Figure 4.4 Particle size distribution curves of P4.1-P4.4 by dynamic light scattering (1 mg/ml, H_2O) analysis at 25 °C and 60 °C (see Appendix C: S4.4A, S4.4B, S4.4C and S4.4D for supporting information).

Using the method described in Chapter 2, which was inspired by the synthesis and structural elucidation of Salvarsen, the polymers were first cross-linked *via* the reductive coupling of the arsenical motifs, forming cyclic oligoarsines, during self-assembly (10 mg ml^{-1}) at 60 °C. These As(I) cross-linked nanoparticles (termed here as $\mathbf{NP_{As(I)-n}}$) formed stable particles, as previously reported, when sufficient AsAm units were incorporated. This was consistent with the previous study when less than 5 AsAm residues were incorporated into the chain (**P4.1**) the nanoparticles dissembled ($\mathbf{NP_{As(I)-4}}$) during the purification process, whereas the polymers containing more than 10 AsAm residues (**P4.2-P4.4**) maintained the self-assembly even after dialysis ($\mathbf{NP_{As(I)-11}}$, $\mathbf{NP_{As(I)-15}}$, $\mathbf{NP_{As(I)-18}}$) (Fig 4.5). The stable nanoparticles also exhibited thermoresponsive NIPAm

character, causing a decrease in D_h of 1-6 nm at elevated temperature.

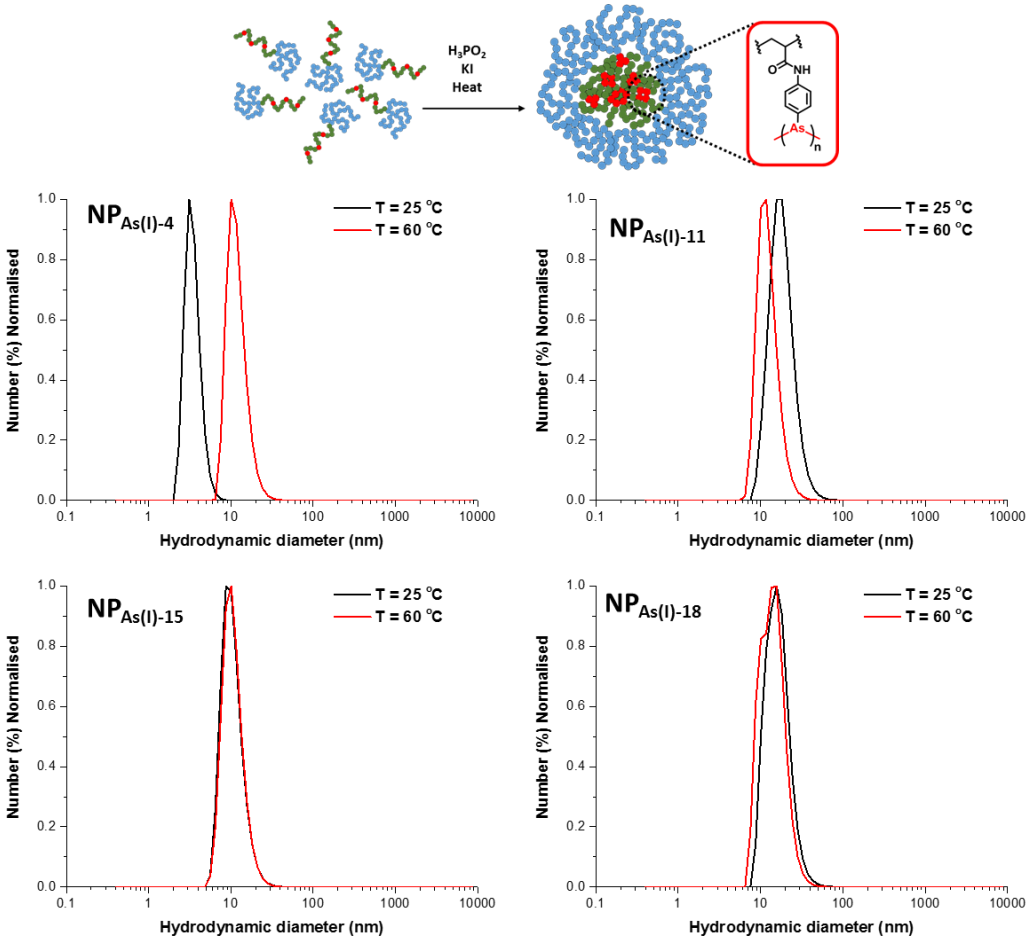

Figure 4.5 Particle size distribution curves of $NP_{As(I)-n}$ (n = 4, 11, 15, 18) by dynamic light scattering (1 mg/ml, H_2O) analysis at 25 °C and 60 °C (see Appendix C: S4.5A, S4.5B, S4,5C and S4.5D for supporting information).

Atomic force microscopy (AFM) and transition electron microscopy (TEM) of **NP_{As-18}** confirmed the formation of nanoparticles with sizes < 25 nm (Fig. 4.6).

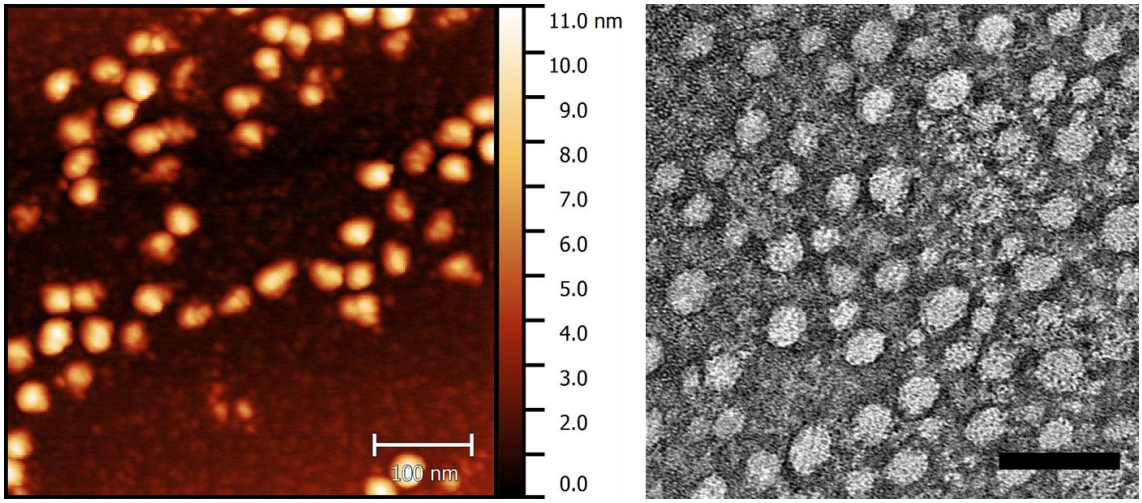

Figure 4.6 AFM (left, scale bar = 100 nm) and TEM (right, scale bar = 100 nm) of $NP_{As(I)-18}$

The formation of cyclic oligoarsines was inferred by the disappearance of the As-O signals associated with the pendent arsenic acid moieties by Fourier transform-infra-red (FT-IR) spectroscopy (Fig 4.7). This allowed progression to further functionalise and stabilise the nanoparticles through RCRAC.

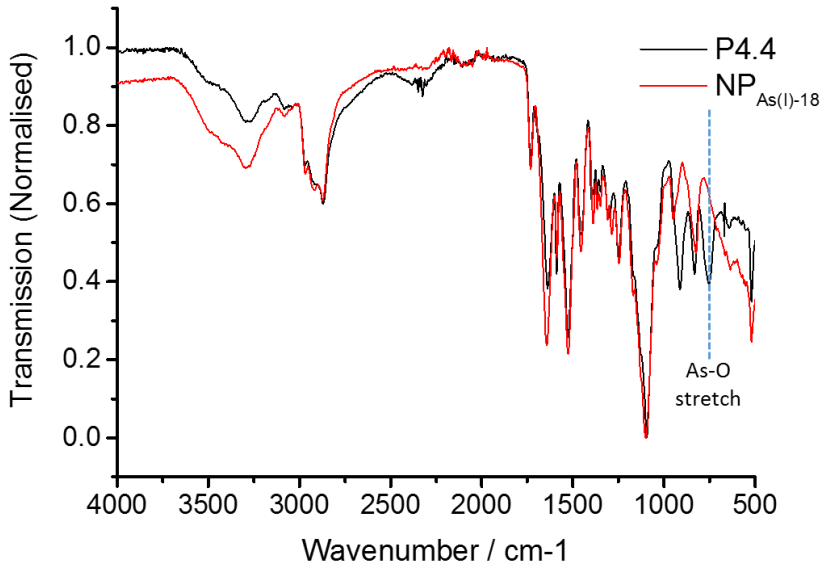

Figure 4.7 Infrared spectra of $NP_{As(I)-18}$ (red) indicating the absence of As-O stretch (750 cm^{-1}) present in the parent polymer, P4.4 (black)

4.2.2 Stabilisation of polymeric arsenical nanoparticle via arsine-vinylene cross-linking

In order to combine Chujo's RCRAC strategy with the present work, propargyl alcohol and 2,2'-azobis[2-(2-imidazolin-2-yl)propane]dihydrochloride (VA-044) was used as water soluble alkyne and azoinitiator respectively. These two reagents were added as deoxygenated aliquots after 30 minutes of initial reductive coupling to form As(I) cross-linking with **P4.1**-**P4.4**, and then left for 16 h at 60 ºC (scheme 4.1). Pleasingly all the nanoparticles generated retained the self-assembled structures when cooled back to room temperature and survived purification via dialysis (Fig 4.8). RCRAC of phenylarsine was previously reported with aromatic acetylenes with electron withdrawing group greatly enhancing the propensity for polymerisation, in contrast authors noted that polymers were not obtained with aliphatic acetylenes, however in the case of propargyl alcohol, sufficient number of vinylene-arsine bonds were formed to successfully yield stabilised nanoparticles.

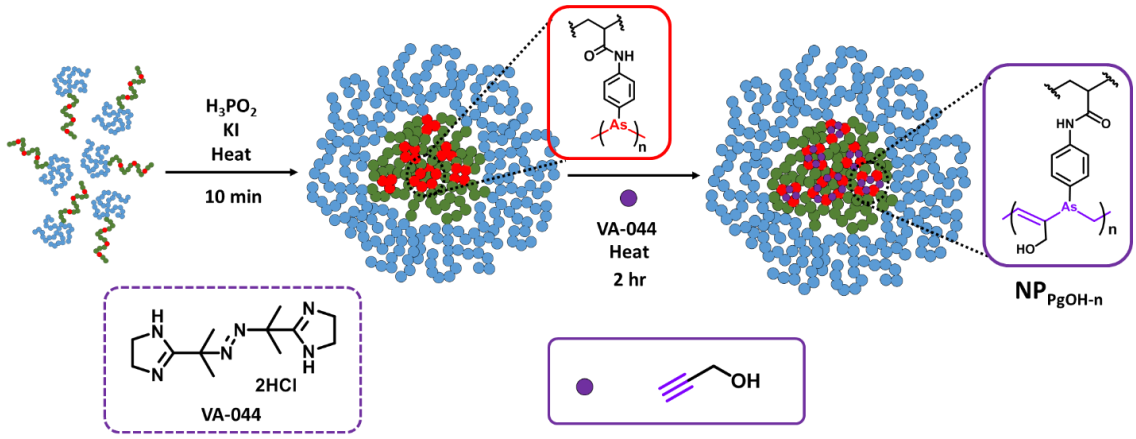

Scheme 4.1 Cross-linking of Poly(PEGA-NIPAm) diblock copolymer through RCRAC of As(I) in the core of the self-assembly and water soluble acetylenes (Propargyl alcohol). The As(I) cross-link nanoparticles is initially generated under elevated temperature using H_3PO_2 to reductive couple the arsenic side chains for 10 minutes before the addition of VA-044 and acetylene then left for 2 hours.

Interestingly, whereas nanoparticles generated from **P4.1** via reductive coupling alone ($\mathbf{NP_{As(I)-4}}$) did not survive dialysis, the particle cross-linked via reductive coupling in the presence of propargyl alcohol and VA-044 retained its self-assembled structure. We attribute this increased stability in vinylene-arsine cross-linking to three factors, 1) increased degree of cross-linking through polymerisation (versus oligomerization of

cyclicooligoarsines) 2) the trivalent arsenic (As(III)) bridging the vinylene-arsine chain has increased inertia towards oxidation 3) stronger relative bond strength through As-C (607 KJ mol^{-1}) (versus As-As (382 KJ mol^{-1}))[14] which is further stabilised through π-π conjugation.[15] These nanoparticles also exhibited thermoresponsive character less than the As(I) analogues, with decrease in D_h of 1-2.5 nm upon heating at 60 ºC (Fig 4.8). This can be ascribed with the factors above yielding a more densely packed and ridged core.

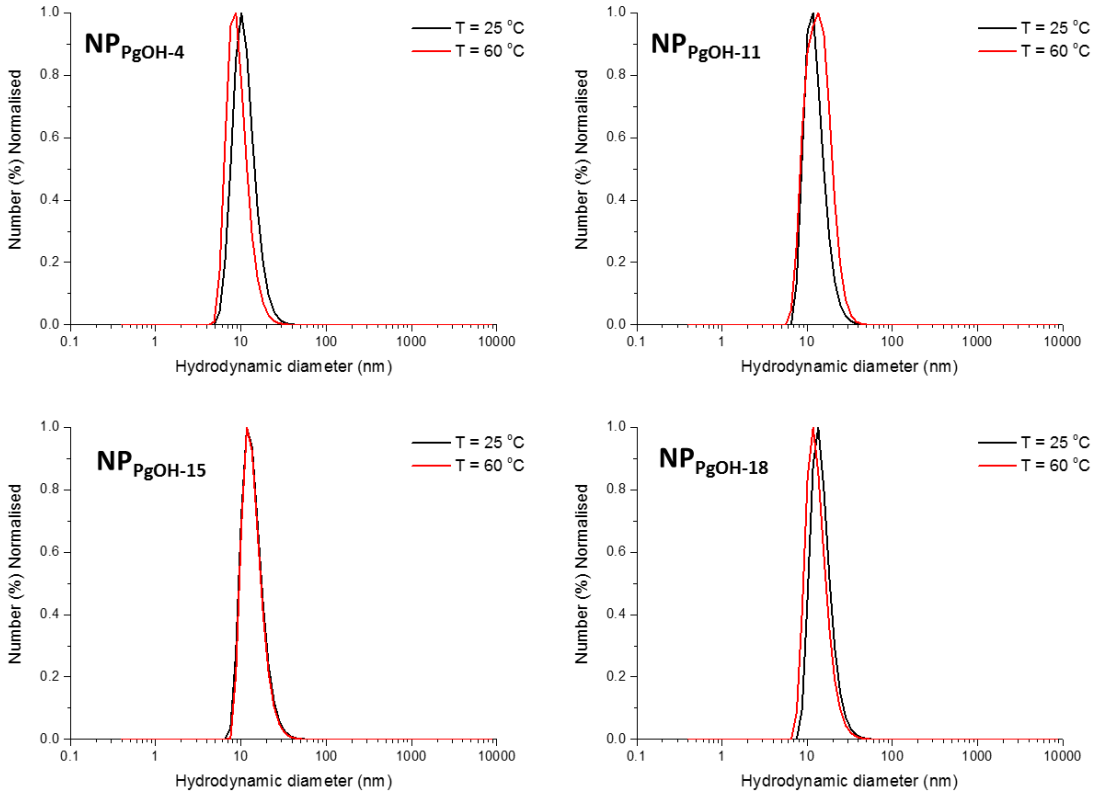

Figure 4.8 Particle size distribution curves of NP_{PgOH-n} (n = 4, 11, 15, 18) by dynamic light scattering (1 mg/ml, H_2O) analysis at 25 °C and 60 °C (see Appendix C: S4.8A, S4.8B, S4.8C and S4.8D for supporting information).

Transmission electron microscopy (TEM) and atomic force microscopy (AFM) of **$NP_{PgOH-18}$** confirmed the formation of spherical nanoparticles with sizes < 35 nm, which are the ideal shape and size for *in vivo* tumour accumulation (Fig 4.9).[16, 17]

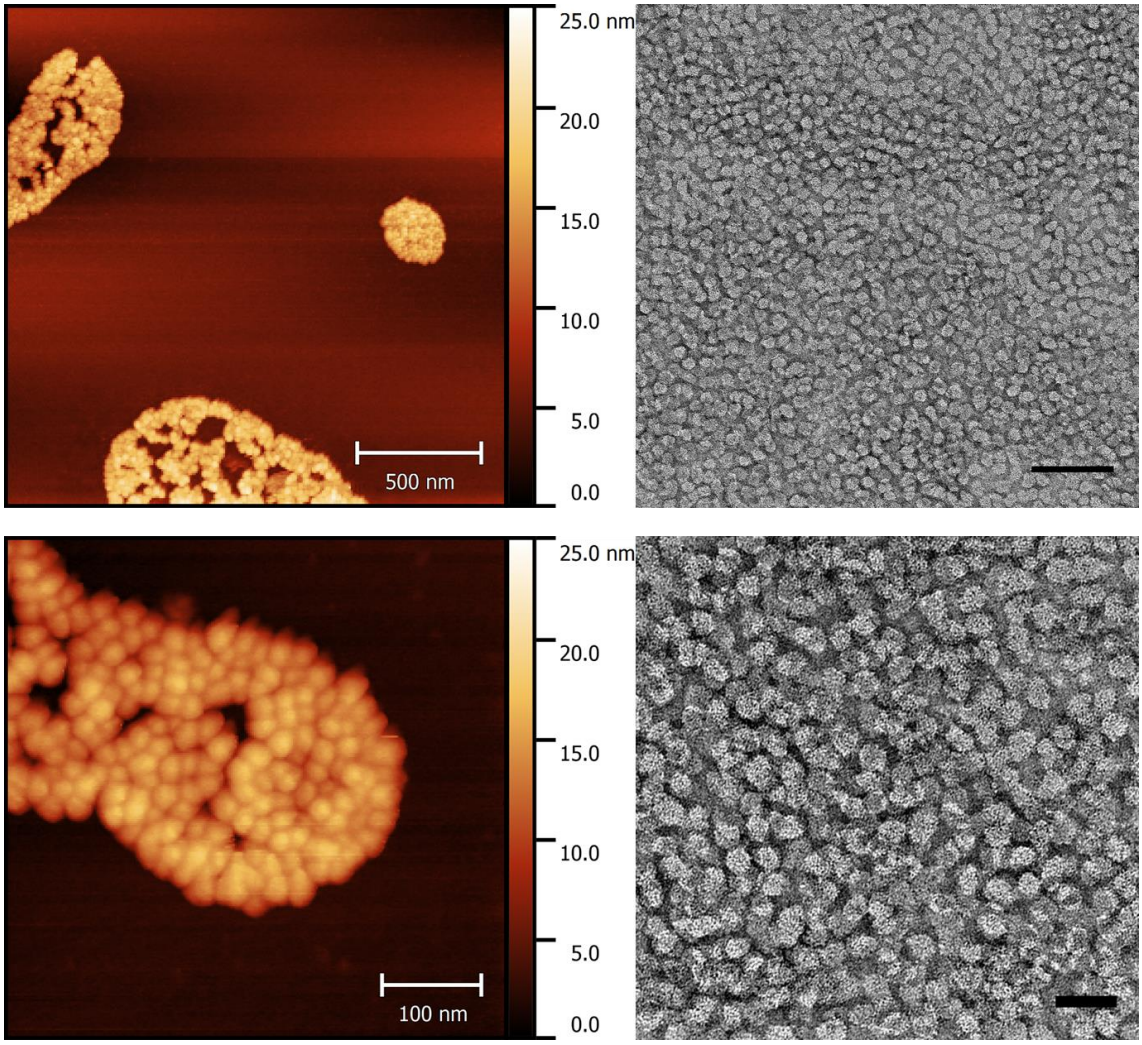

Figure 4.9 AFM (left column) and TEM (right column) of $NP_{PgOH-18}$ (bottom row scale bar = 100 nm, top row scale bar = 500 nm)

The stability of these vinylene-arsine cross-linked nanoparticles under model biological redox conditions were initially investigated in presence of reduced glutathione (GSH) at 37 °C, mimicking intracellular conditions ([GSH] = 5 mM). In Chapter 2, As(I) cross-linked particles were shown to slowly dissemble (over 96 hrs) by DLS analysis due to the formation of more enthalpically favoured As-S bonds (425 kJ mol^{-1})[14] over the weaker As-As bonds. In the present work, all the propargyl alcohol cross-linked nanoparticles ($\mathbf{NP_{PgOH-n}}$) remained unchanged over a week, due to the stronger As-C bonds along the vinylene-arsine bridges (Fig 4.10).

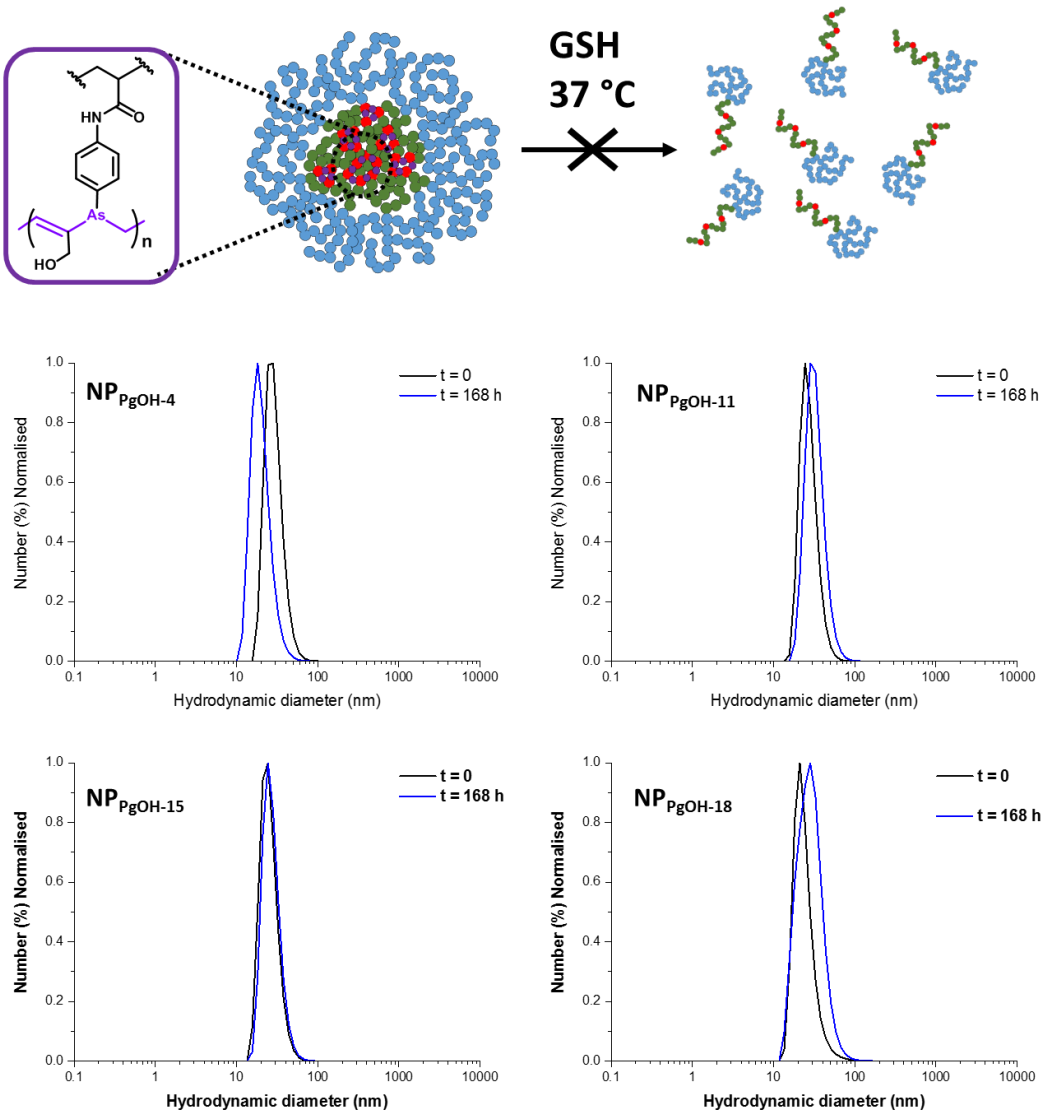

Figure 4.10 Particle size distribution curves of NP_{PgOH}-n (n = 4, 11, 15, 18) by dynamic light scattering (1 mg/ml, H_2O) as function of time in aqueous GSH (5mM) (see Appendix C: S4.10A, S4.10B, S4.10C and S4.10D for supporting information).

The stability of the nanoparticles in the presence of hydrogen peroxide at 37 °C to mimic lysosomal oxidative conditions conditions ($[H_2O_2]$ = 5 mM) was then investigated. All the $\mathbf{NP_{PgOH-n}}$ were found to more stable than the nanoparticles reported in Chapter 2 and 3, retaining their structures over a week under these conditions (Fig 4.11).

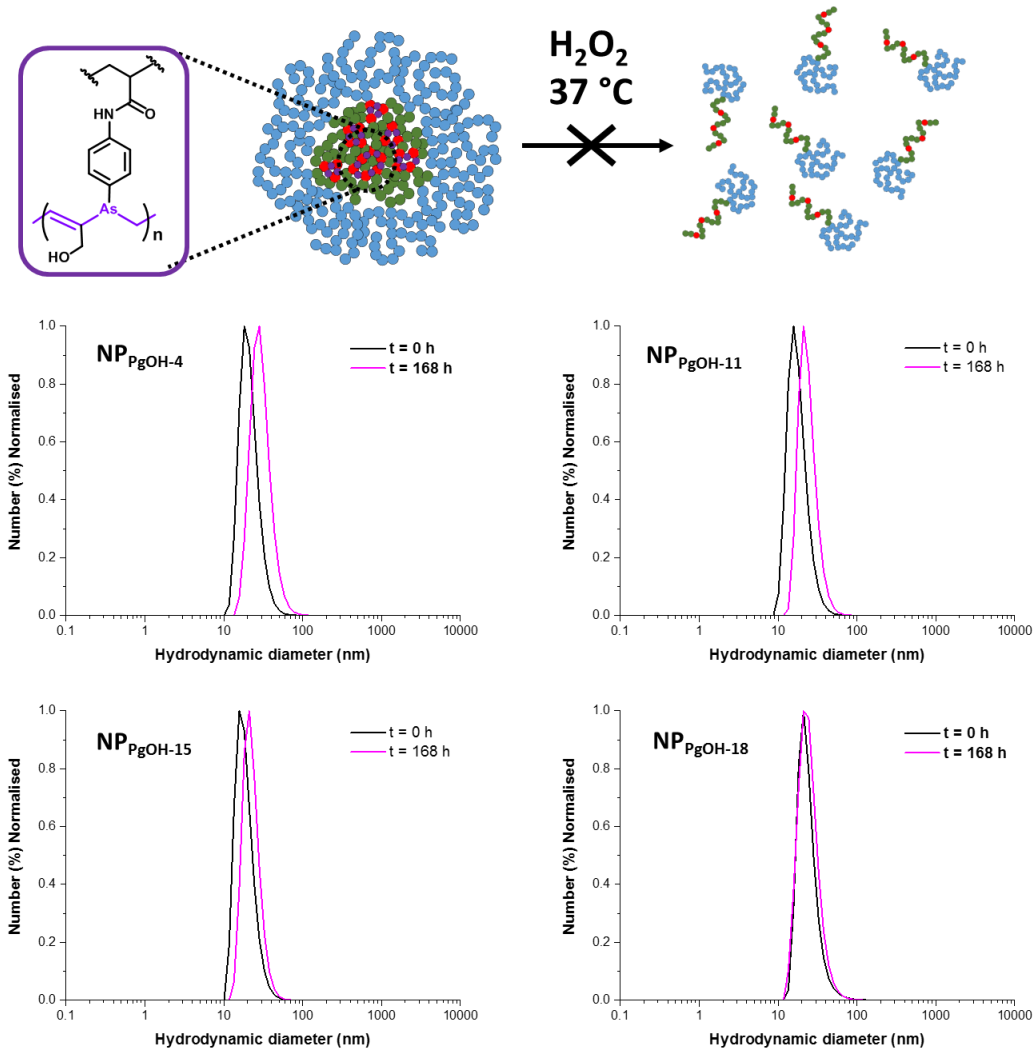

Figure 4.11 Particle size distribution curves of NP_{PgOH}-n (n = 4, 11, 15, 18) by dynamic light scattering (1 mg/ml, H_2O) as function of time in aqueous H_2O_2 (5mM) (see Appendix C: S4.11A, S4.11B, S4.11C and S4.11D for supporting information).

Observed increase in stability compared to the analogues in in chapter 2 and 3 where the NPs were cross-linked through formation of As-As and As-S bond formation. In particular, the resilience to oxidation, in agreement with the seminal work of Chujo *et al*, was taken as an indirect indication of vinylene-arsine bond formation. Attempts to detect the vinyl protons by ^{1}H NMR were unsuccessful. Alternative methods of detection, not employed here, include IR, Raman and oxidative staining using osmium tetroxide.

To further demonstrate the applicability of the RCRAC a range of functional water soluble

alkynes were examined as co-monomer for cross-linking. Given the mechanism of RCRAC, it was hypothesised that there would be orthogonality with functional groups such as nucleophilic amines and carboxylic acids, in addition, allowing positively and negatively charged core nanoparticles to be generated. To this end, propargyl amine and propiolic acid were screened as the alkyne comonomers and successfully generated stabilised nanoparticles $\mathbf{NP_{PgNH\text{-}n}}$ and $\mathbf{NP_{PAc\text{-}n}}$ respectively with the library of arsenical polymers (Scheme 4.2).

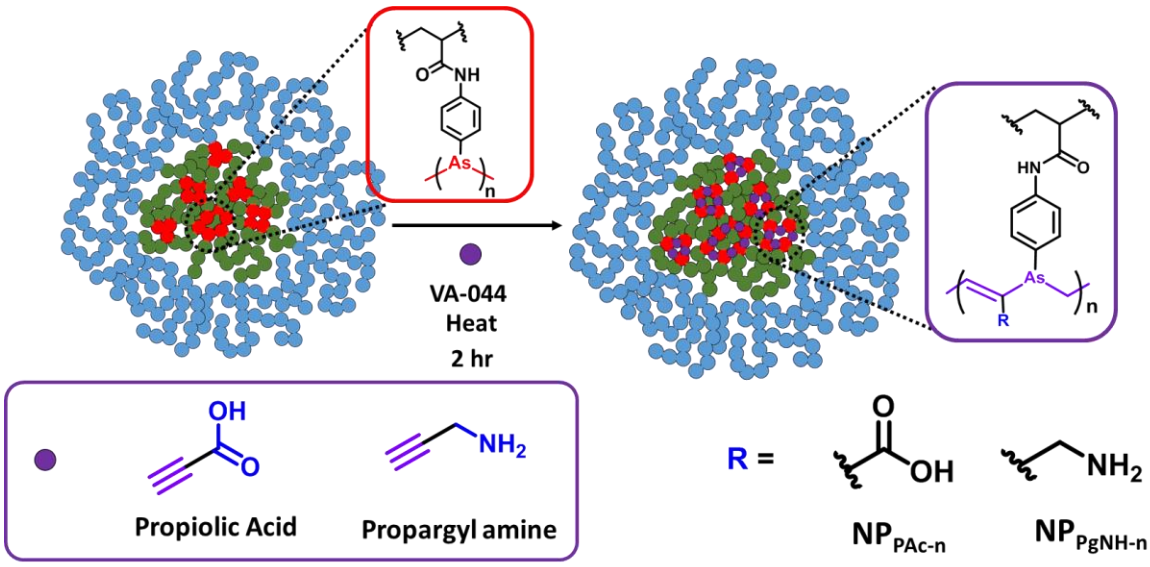

Scheme 4.2 Cross-linking of Poly(PEGA-NIPAm) diblock copolymer through RCRAC of As(I) in the core of the self-assembly and water soluble functional acetylenes: propiolic acid and propargyl amine to generate nanoparticles: $NP_{PAc\text{-}n}$, $NP_{PgNH\text{-}n}$ (n = 4, 11, 15, 18)

These all behaved similarly to the nanoparticles generated with RCRAC cross-linking with propargyl alcohol when the temperature was elevated to 60 °C, demonstrated consistent rigid cross-linking (Fig 4.12, Fig 4.13, Table 4.2, D_h = 12 – 31 nm).

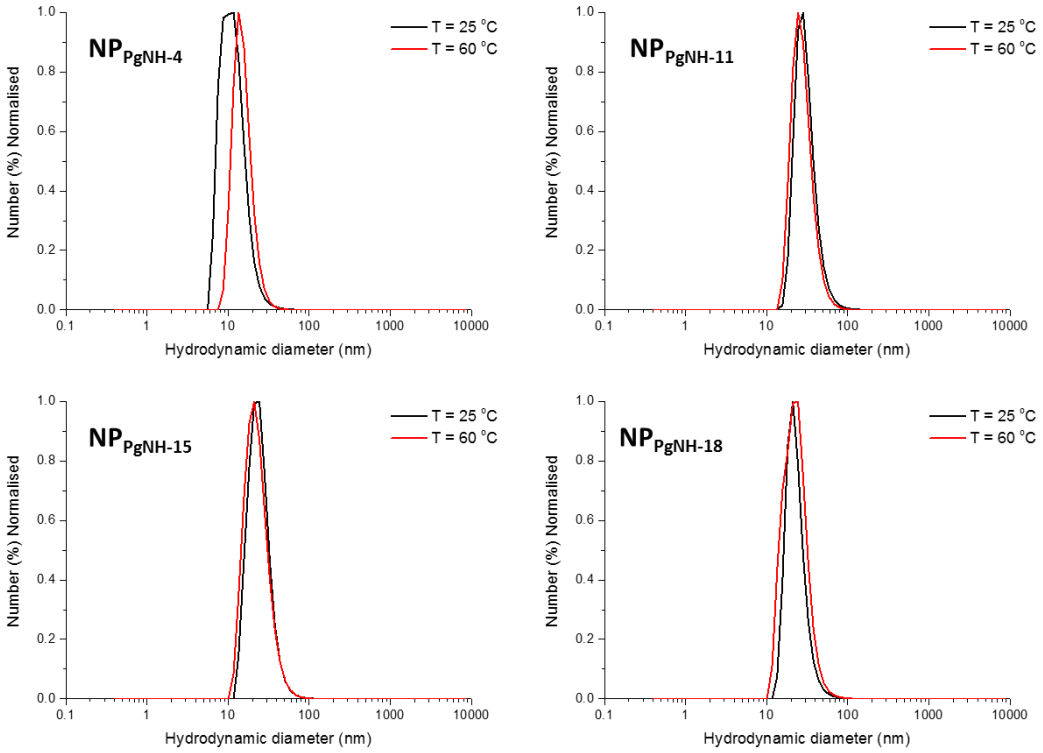

Figure 4.12 Particle size distribution curves of NP_{PgNH-n} (n = 4, 11, 15, 18) by dynamic light scattering (1 mg/ml, H_2O) analysis at 25 °C and 60 °C (see Appendix C: S4.12A, S4.12B, S4.12C and S4.12D for supporting information).

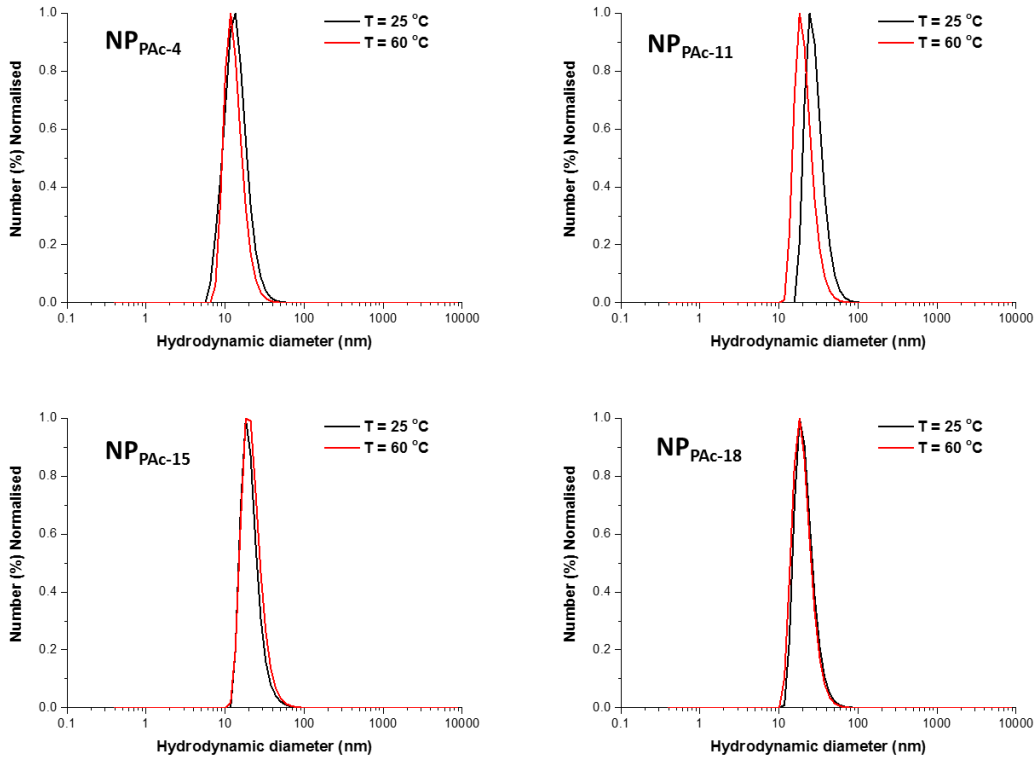

Figure 4.13 Particle size distribution curves of NP_{PAc-n} (n = 4, 11, 15, 18) by dynamic light scattering (1 mg/ml, H_2O) analysis at 25 °C and 60 °C (see Appendix C: S4.13A, S4.13B, S4.13C and S4.13D for supporting information).

TEM and AFM of **$NP_{PgNH-18}$** and **NP_{PAc-18}** further confirms formation of nanoparticles (Fig 4.14, Fig 4.15, Diameter =20-30 nm).

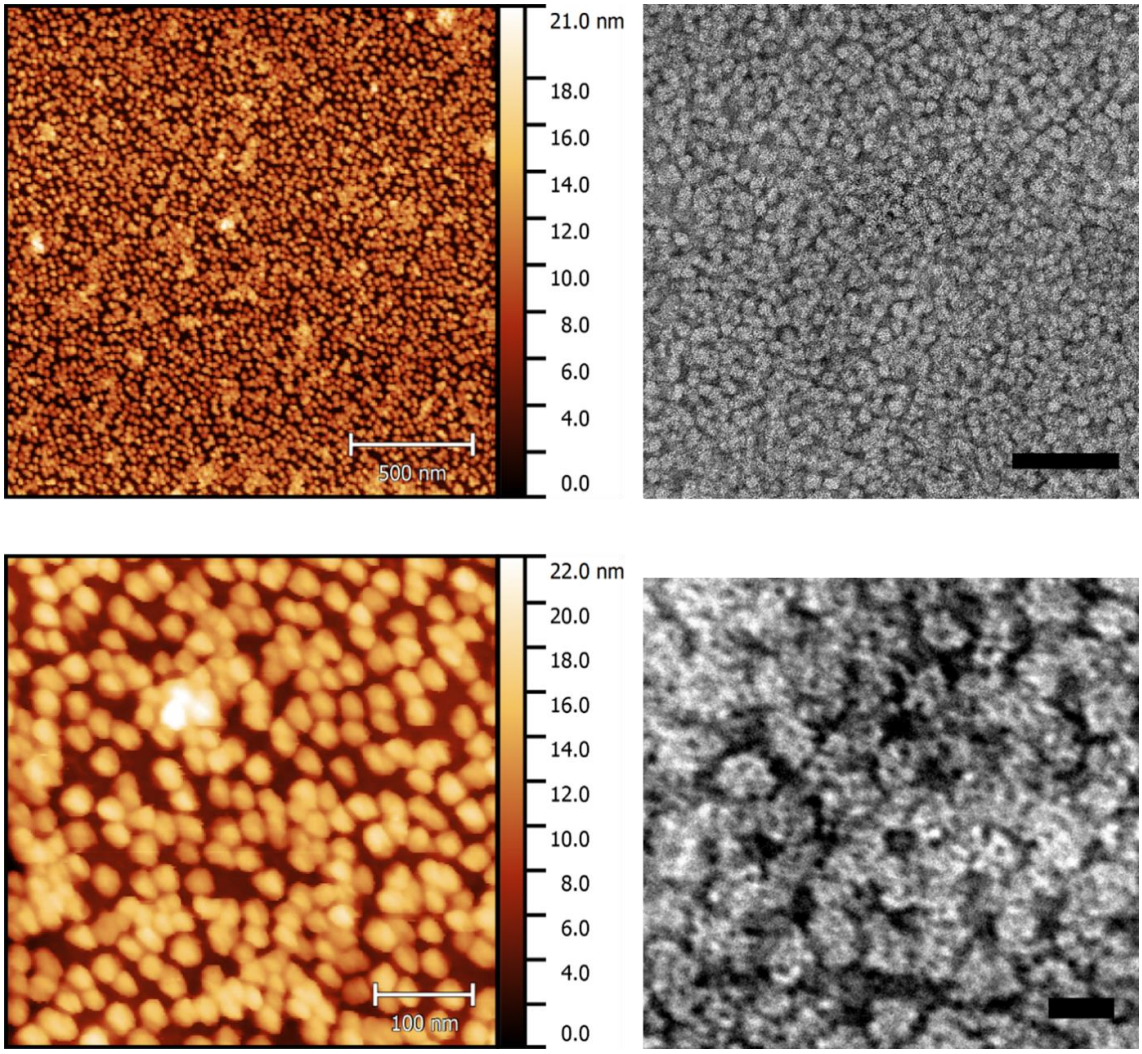

Figure 4.14 AFM (left column) and TEM (right column) of NP_{PNH-18} (bottom row scale bar = 100 nm, top row scale bar = 500 nm)

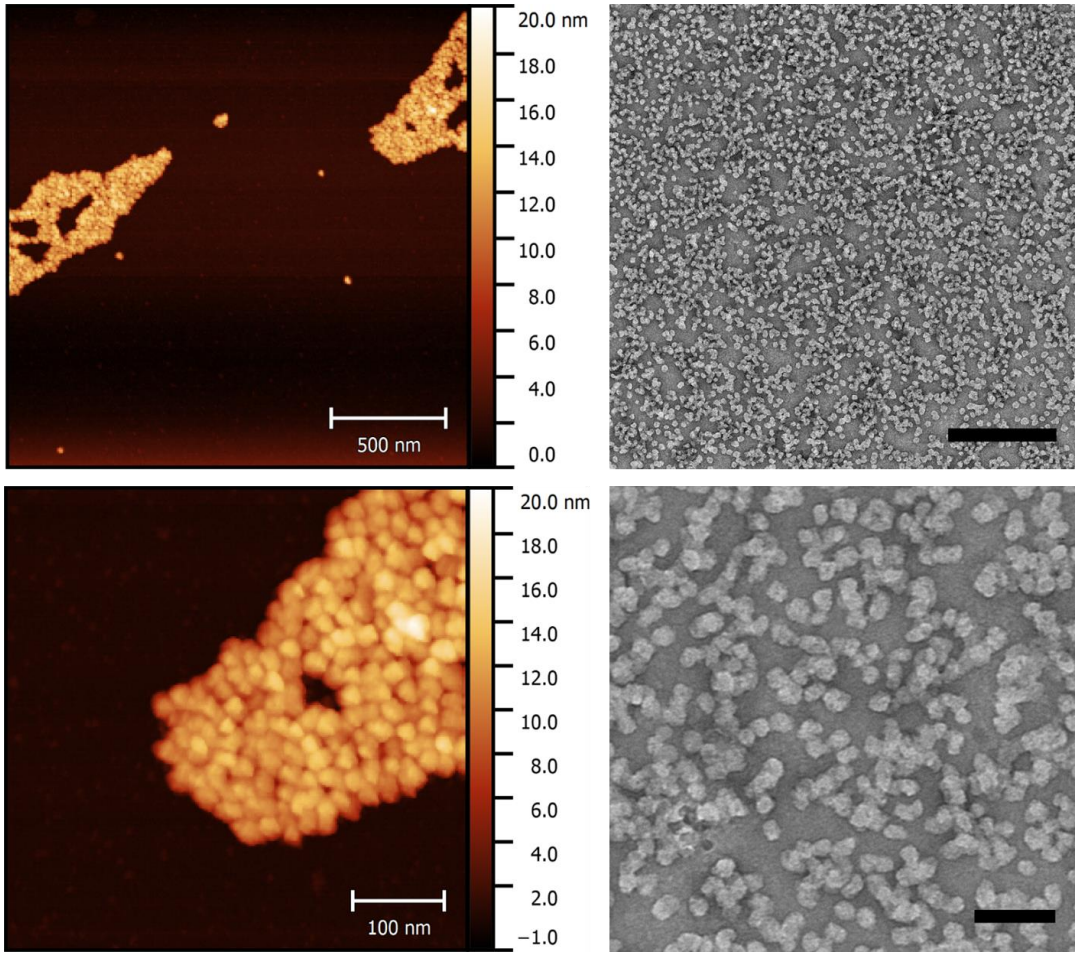

Figure 4.15 AFM (left column) and TEM (right column) of NP_{PAc-18} (bottom row scale bar = 100 nm, top row scale bar = 500 nm)

The stability of the particles was subsequently examined with the redox conditions above. Interestingly, the nanoparticles cross-linked with propiolic acid degraded over the course of a week in hydrogen peroxide, with the lowest arsenic content (**P4.1**, $\mathbf{NP_{PAc-4}}$) dissembling within 24 hours. However, they were stable in presence of glutathione for a week (Fig 4.16). In contrast all the nanoparticles generated with propagyl amine were stable in oxidative conditions over a week even with **P4.1**, however **P4.1** was unstable in presence of glutathione, showing decrease in size after 72 hours (Fig 4.17), however these were still larger than unimers. This observation could be due to unreacted AsAm units reacting with GSH, changing the size in the process.

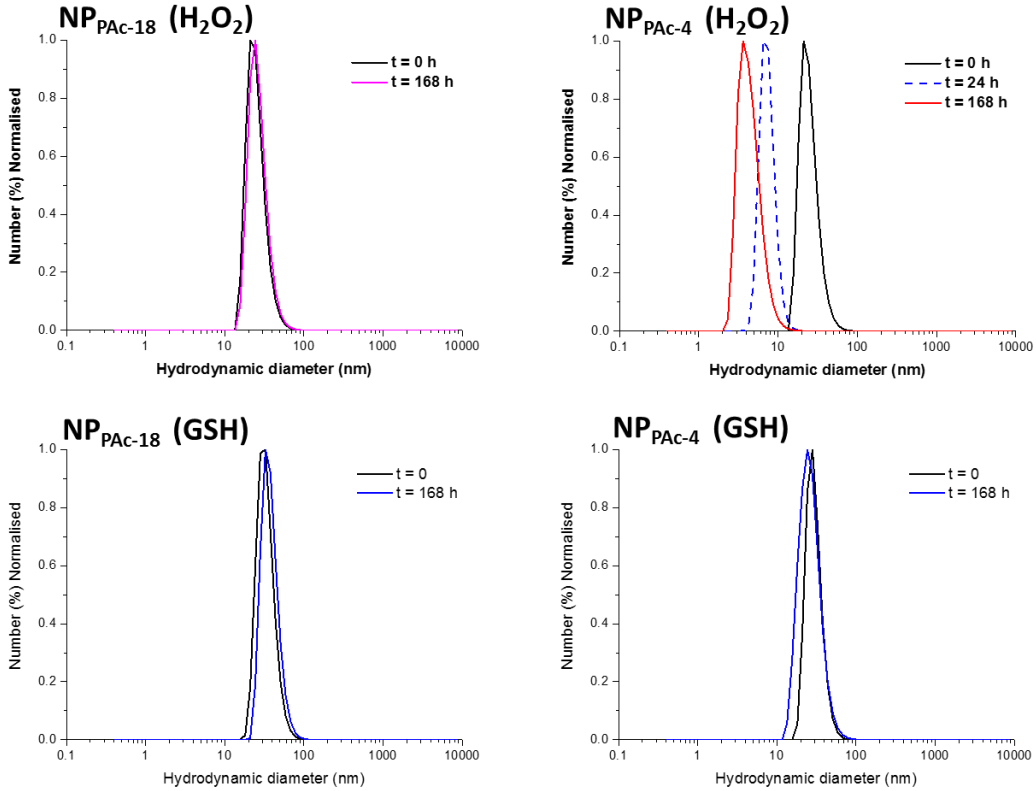

Figure 4.16 Particle size distribution curves of $NP_{PAc\text{-}n}$ (n = 4, 18) by dynamic light scattering (1 mg/ml) as function of time in aqueous H_2O_2 (5mM, top row) and GSH (5mM. bottom row) (see Appendix C: S4.16A, S4.16B, S4.16C and S4.16D for supporting information).

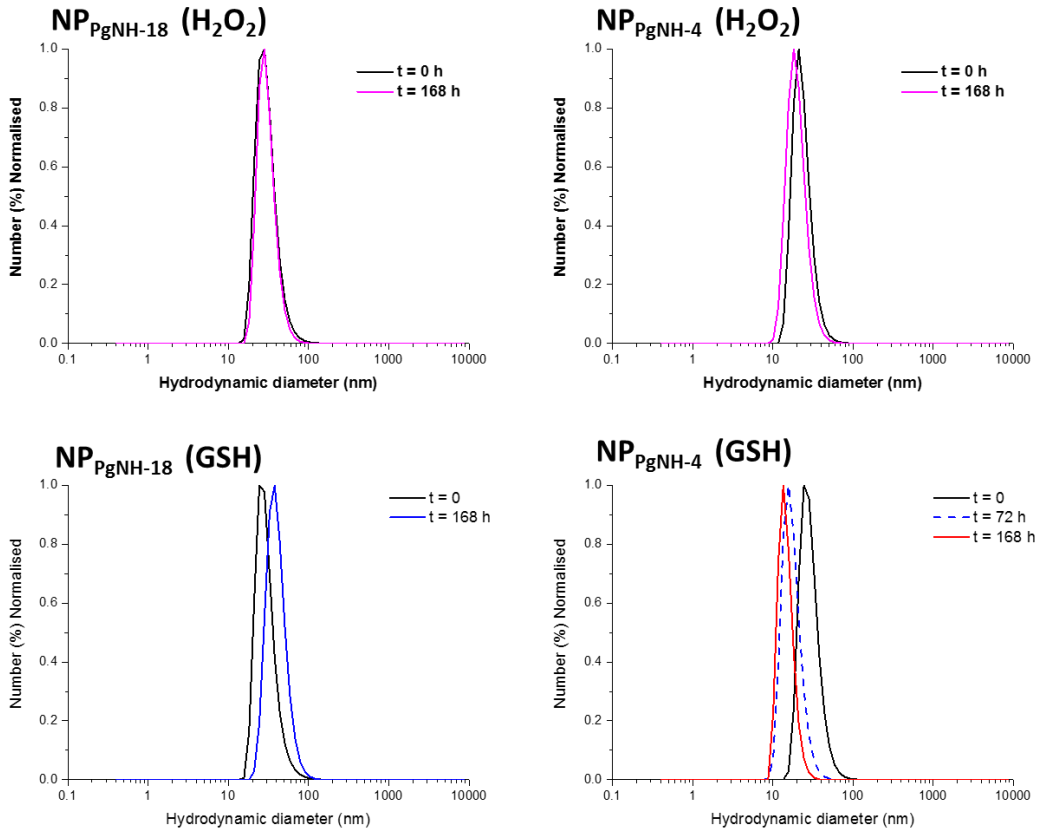

Figure 4.17 Particle size distribution curves of NP_{PNH-n} (n = 4, 18) by dynamic light scattering (1 mg/ml) as function of time in aqueous H_2O_2 (5mM, top row) and GSH (5mM. bottom row) (see Appendix C: S4.17A, S4.17B, S4.17C and S4.17D for supporting information).

4.2.3 Cytotoxicity of polymeric arsenical nanoparticles

Considering the biomedical potential of our nanoparticles it was critical to evaluate their toxicity. In addition to the parent polymeric arsenicals **P4.1-P4.4** the acute toxicity of all the nanoparticles (**NP_{PgOH-n}**, **NP_{PAc-n}**, and **$NP_{PgNH2-n}$**) was determined in vitro via standard XTT assay using Prostate carcinoma cell line (PC3) as a model. The parent polymers and corresponding nanoparticles were non-toxic up to the maximum concentration that was tested (2 mg ml^{-1}) (Fig 4.18). This was consistent with the results reported in Chapter 2 and 3. Polymeric arsenical scaffolds exhibit limited cytotoxicity *in vitro* against the same cell-line,[6, 18] thus with previous result these findings further highlights arsenic as potential component for biomedical application.

Table 4.2 Particle size by dynamic light scattering at 25 °C and 60 °C in aqueous solution (1 mg/ml) (PDi calculated from equation 4.1)

		25 °C		60 °C	
		D_h (nm)	PDi	D_h (nm)	PDi
P4.1	Polymer	3.12	0.052	13.60	0.077
	$NP_{As(I)-4}$	3.47	0.052	12.02	0.086
	NP_{PgOH-4}	11.3	0.108	9.47	0.101
	NP_{PgNH-4}	11.9	0.156	15.4	0.088
	NP_{PgAc-4}	14.2	0.013	13.4	0.094
	NP_{Rh-4}	19.6	0.129	16.0	0.102
P4.2	Polymer	2.47	0.046	19.7	0.097
	$NP_{As(I)-11}$	18.8	0.138	12.58	0.100
	$NP_{PgOH-11}$	12.7	0.095	14.0	0.119
	$NP_{PgNH-11}$	30.9	0.138	28.2	0.126
	$NP_{PgAc-11}$	17.6	0.014	20.3	0.102
	NP_{Rh-11}	26.7	0.098	13.8	0.099
P4.3	Polymer	2.65	0.043	14.2	0.093
	$NP_{As(I)-15}$	10.7	0.107	10.9	0.100
	$NP_{PgOH-15}$	14.1	0.106	140	0.119
	$NP_{PgNH-15}$	24.9	0.122	23.5	0.142
	$NP_{PgAc-15}$	21.5	0.108	22.5	0.110
	NP_{Rh-15}	18.3	0.102	13.8	0.099
P4.4	Polymer	2.20	0.050	16.9	0.090
	$NP_{As(I)-18}$	16.8	0.133	14.5	0.130
	$NP_{PgOH-18}$	15.1	0.099	13.5	0.107
	$NP_{PgNH-18}$	23.5	0.022	23.5	0.143
	$NP_{PgAc-18}$	21.8	0.090	20.5	0.098
	NP_{Rh-18}	16.3	0.131	19.0	0.113

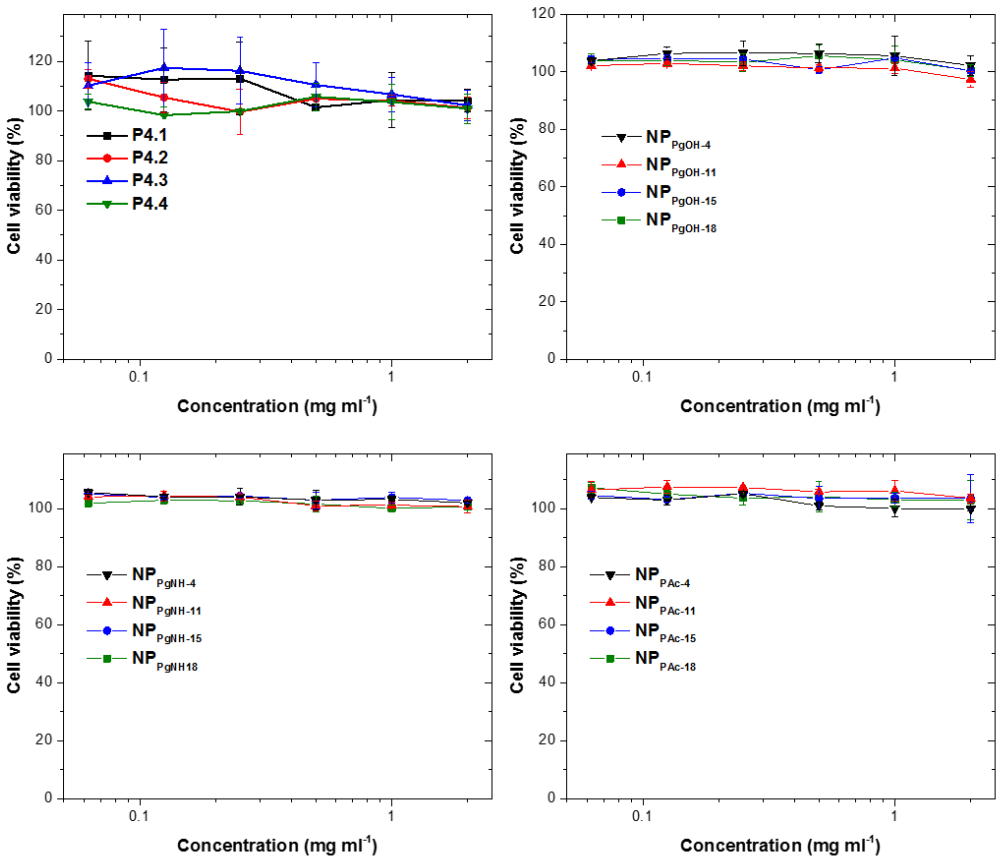

Figure 4.18 In vitro cell viability of polymers P4.1-P4.4 (top left) and nanoparticles NP_{PgOH-n} (top right), NP_{PgNH-n} (bottom left) and NP_{PAc-n} (bottom right) (n = 4, 11, 15 and 18) using XTT viability assay with PC3 cell line.

4.2.4 Cellular tracking of polymeric arsenical nanoparticles

Given that particle size and shape impacts biodistribution *in vivo*; spherical nanoparticles below 50 nm have been reported by many to be the best for tumour accumulation,[16, 17] which makes the cross-linked nanoparticles reported here candidates for drug delivery. In order to establish the cellular uptake of the nanoparticles and determine the localisation within the intracellular framework, incorporation of an appropriate visualisation probe was necessary. The RCRAC method was identified as a possible route to covalently introduce functionality suitable for cellular imaging within the core of our nanoparticle core. Rhodamine B was chosen as a cheap water soluble fluorescent probe, with a convenient handle for alkyne attachment through the esterification of the acid group. The *O*-propargyl-ester derivative of rhodamine B was prepared *via* standard Steglich

conditions, using *N,N'*-dicyclohexylcarbodiimide (DCC), and catalytic quantities of 4-dimethylaminopyridine (DMAP) in anhydrous dichloromethane (DCM). The ester product was purified by flash column to yield iridescent black crystals, **4** (57% yield), and the structure was confirmed by ^{1}H NMR (Figure 4.19).

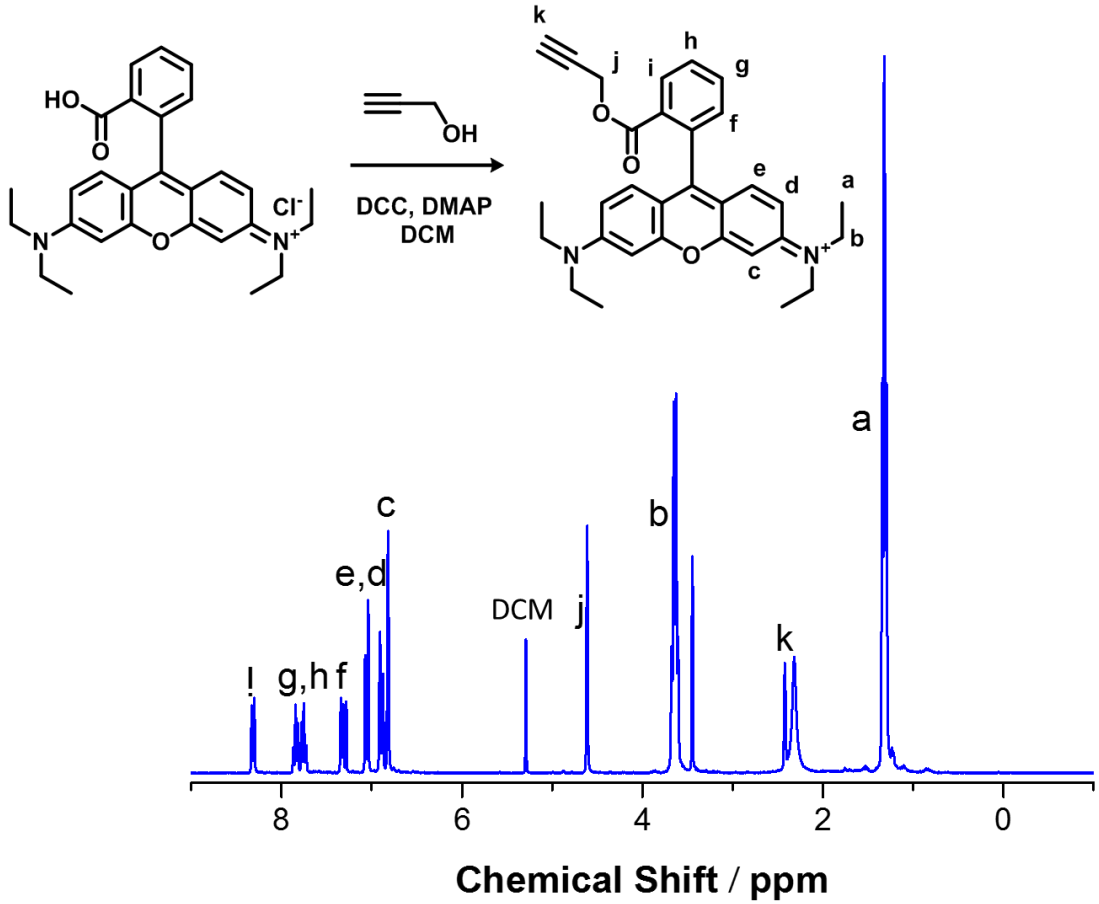

Figure 4.19 ^{1}H-NMR spectrum and synthesis of *O*-propargyl-Rhodamine-B ester

Using the aforementioned RCRAC protocol to cross-link **P4.1-P4.4** with *O*-propargyl-ester rhodamine, fluorescent nanoparticles (**NP$_{Rh-n}$**) were prepared (Fig 4.20). The nanoparticles were purified by acidic dialysis (0.1 M HCl), until no colouration was present in the dialysis media, before switching to neutral deionised water and finally lyophilisation. The nanoparticles generated were comparable in size by DLS analysis (D_h = 16.3– 26.7 nm, Fig 20).

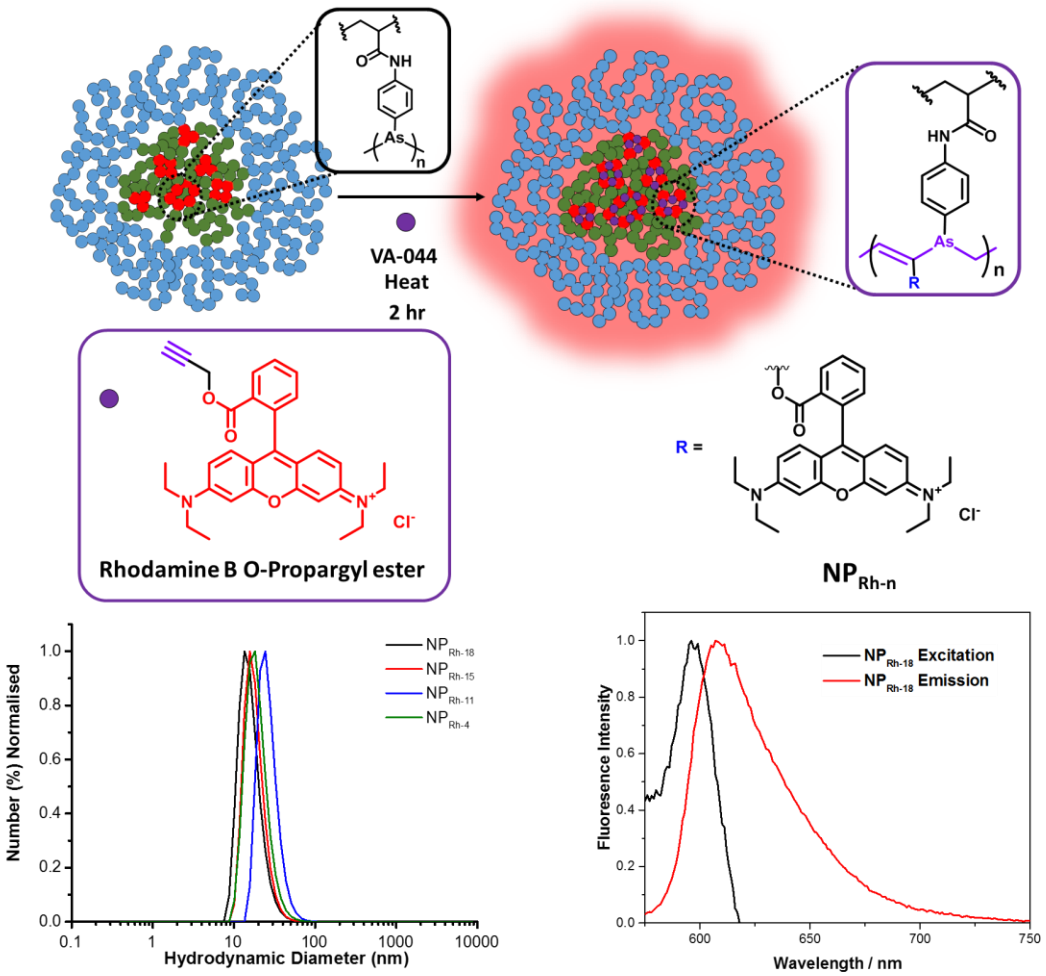

Figure 4.20 Cross-linking of Poly(PEGA-NIPAm) diblock copolymer through RCRAC of As(I) in the core of the self-assembly and O-propargyl Rhodamine B ester to generate fluorescent nanoparticles nanoparticles: $NP_{Rh\text{-}n}$ (n = 4, 11, 15, 18). Particle size distribution curves by DLS (bottom left, 1 mg/ml). Fluorescence spectrum of $NP_{Rh\text{-}18}$ (λ_{Ex} = 553 nm, λ_{Em} = 627 nm).

The nanoparticles exhibited fluorescence properties according to fluorescence spectroscopy confirming successful loading with the rhodamine (Fig 4.20). The quantity of rhodamine was determined using Ultraviolet-visible (UV-Vis) spectroscopy by extrapolating the concentration from calibration graph of rhodamine *O*-propargyl-ester (Fig 4.21). This revealed theoretical cross-linking efficiency of 7 – 32 % through RCRAC assuming 1:1 monomer incorporation with AsAm.

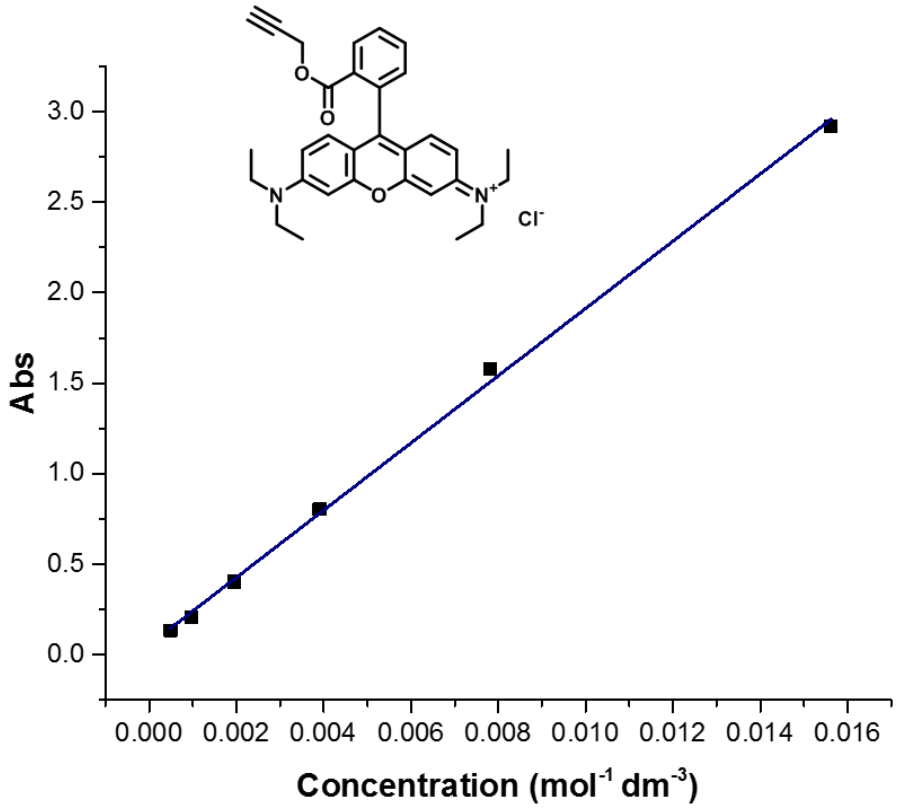

Figure 4.21 UV-Vis calibration curves of O-propargyl Rhodamine B ester yielding theoretical crosslinking densities of NP_{Rh-18} = 12 % ; NP_{Rh-15} = 12 % ; NP_{Rh-11} = 7.1 % ; NP_{Rh-4} = 32 % .

Interestingly $\mathbf{NP_{Rh-n}}$ with the least theoretical cross-linking, $\mathbf{NP_{Rh-11}}$ (7 %) exhibited the most pronounced contraction under elevated temperature (Fig 4.22), consistent with the reduced rigid vinylene-arsine stabilisation.

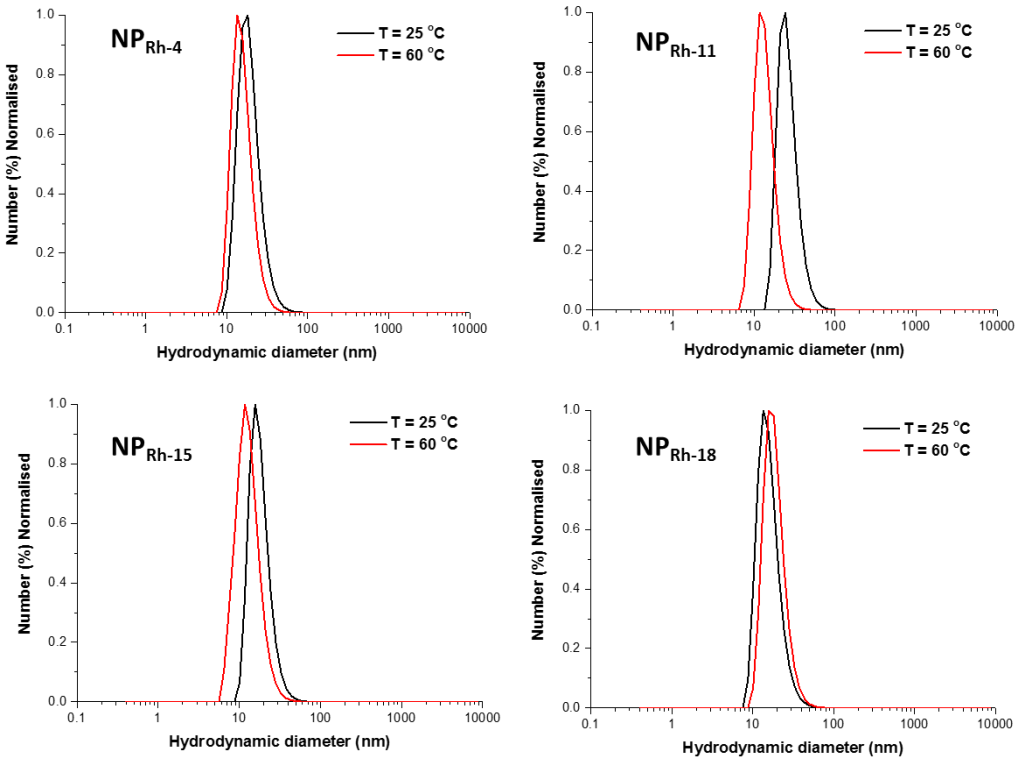

Figure 4.22 Particle size distribution curves of $NP_{Rh\text{-}n}$ (n = 4, 11, 15, 18) by dynamic light scattering (1 mg/ml, H_2O) analysis at 25 °C and 60 °C (see Appendix C: S4.22A, S4.22B, S4.22C and S4.22D for supporting information).

Formation of spherical nanoparticles of **$NP_{Rh\text{-}18}$** was confirmed with AFM and TEM (Diameter = 24-36 nm, Fig 4.23).

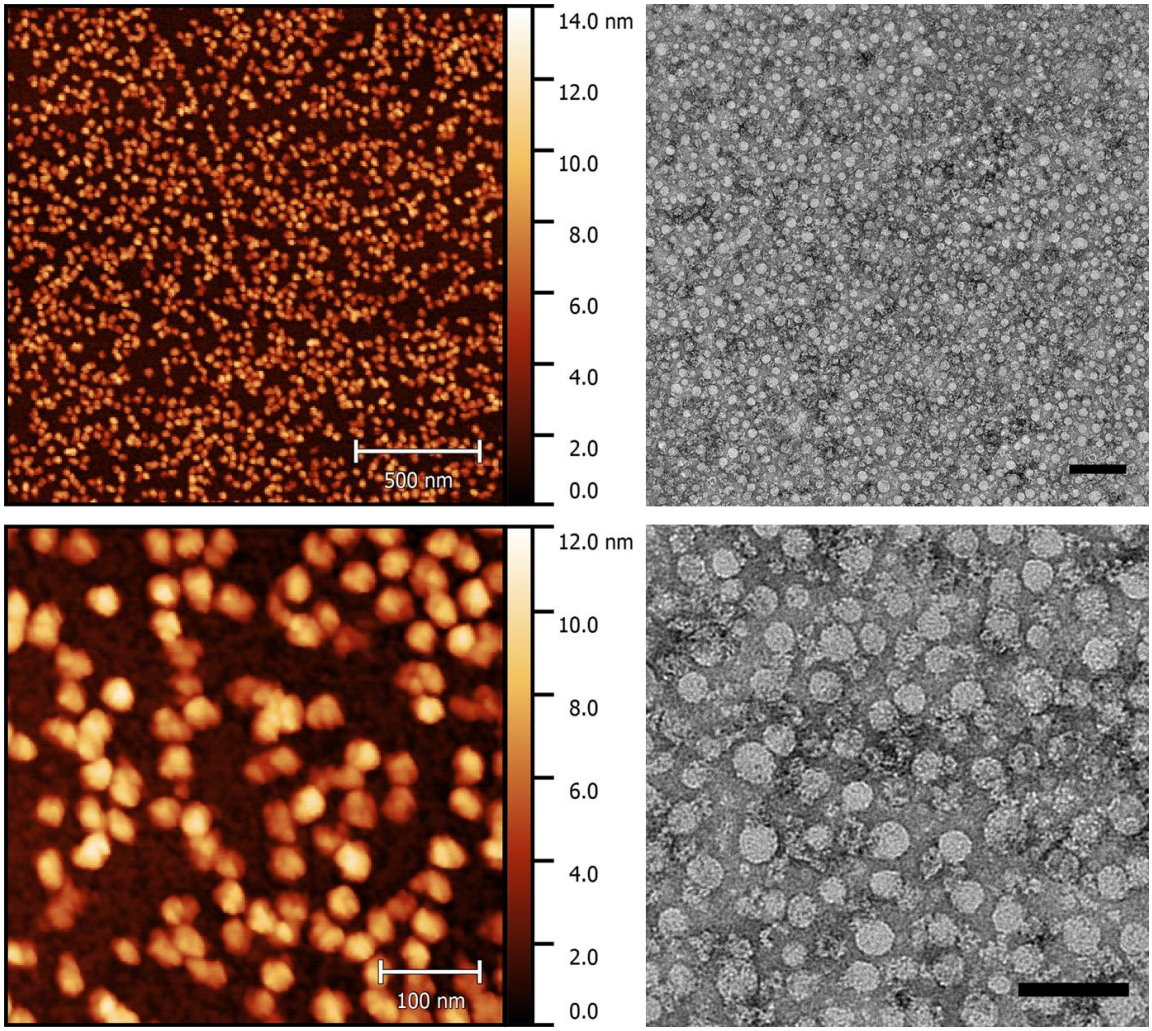

Figure 4.23 AFM (left column) and TEM (right column) of NP_{Rh-18} (bottom row scale bar = 100 nm, top row scale bar = 500 nm)

The rhodamine incorporated nanoparticles, including the one generated from with the lowest arsenic content, were found to be stable under the biologically relevant conditions used above for more than a week, (**P4.1**) (Fig 4.24).

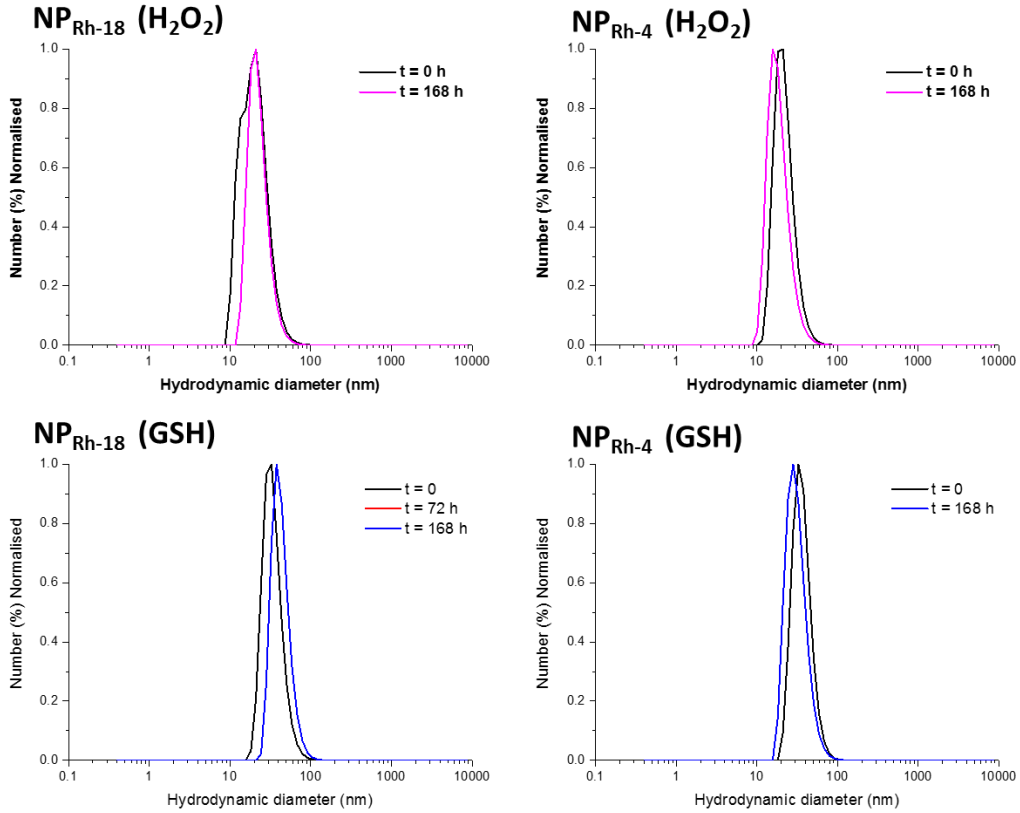

Figure 4.24 Particle size distribution curves of NP_{Rh-n} (n = 4, 18) by dynamic light scattering (1 mg/ml) as function of time in aqueous H_2O_2 (5mM, top row) and GSH (5mM. bottom row) (see Appendix C: S4.24A, S4.24B, S4.24C and S4.24D for supporting information).

Prior to cellular uptake studies, fluorescence normalisation correction curves were plotted (Fig 4.25) for each nanoparticle in order to normalise the intracellular fluorescence with the intrinsic particle fluorescence to quantify the relative uptake. PC3 cells were then incubated with nanoparticles $\mathbf{NP_{Rh-n}}$ (100 μg mL^{-1}) for 2 hr and washed three times with PBS prior to imaging the cellular fluorescence.

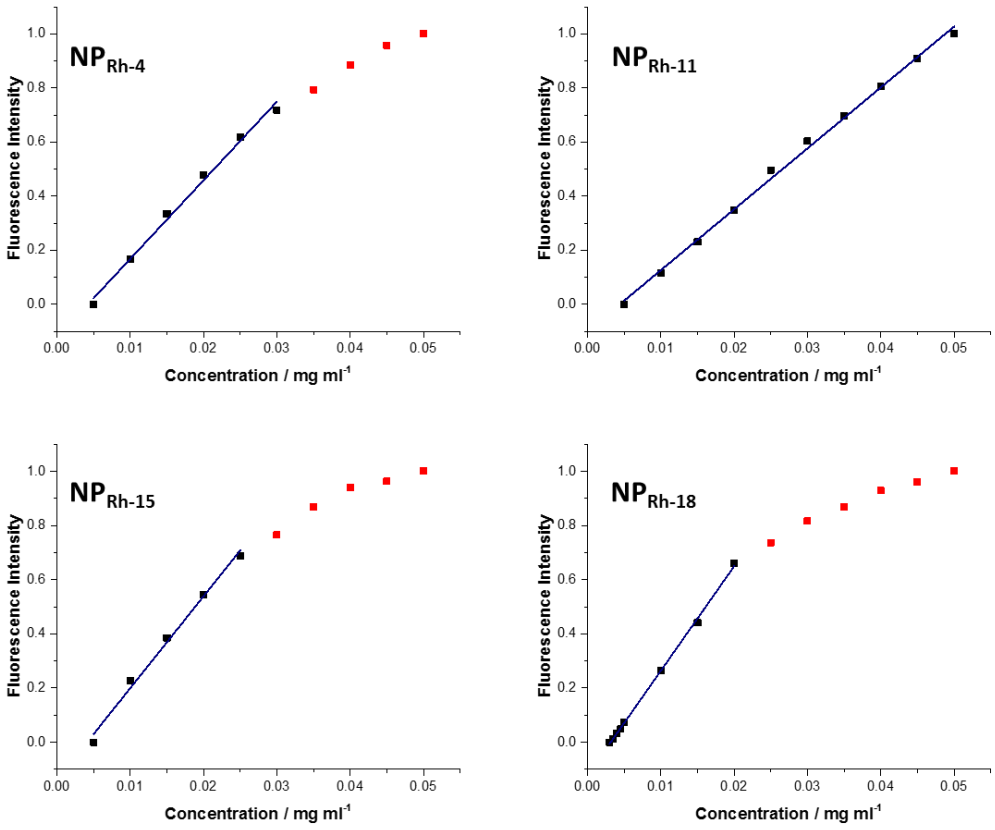

Figure 4.25 Fluorescence calibration curves of NP_{Rh-n} (n = 4, 11, 15, 18). Concentration at the linear region was used for normalisation. At higher concentration, self-quenching of the fluorophore occurs (red dots).

Pleasingly increased intracellular fluorescence was observed as a result of cellular uptake of the fluorescent nanoparticles (Fig 4.26, Fig 4.27). Cellular uptake was observed after 2 hours of incubation with the nanoparticles (Fig 4.26) and did not increase with a longer incubation period of 24 hours (Fig 4.27, Fig 2.28). These findings suggest that the aforementioned cell viability is a result of the intrinsic non-toxic properties of the nanoparticles as oppose to evasion of cellular uptake.

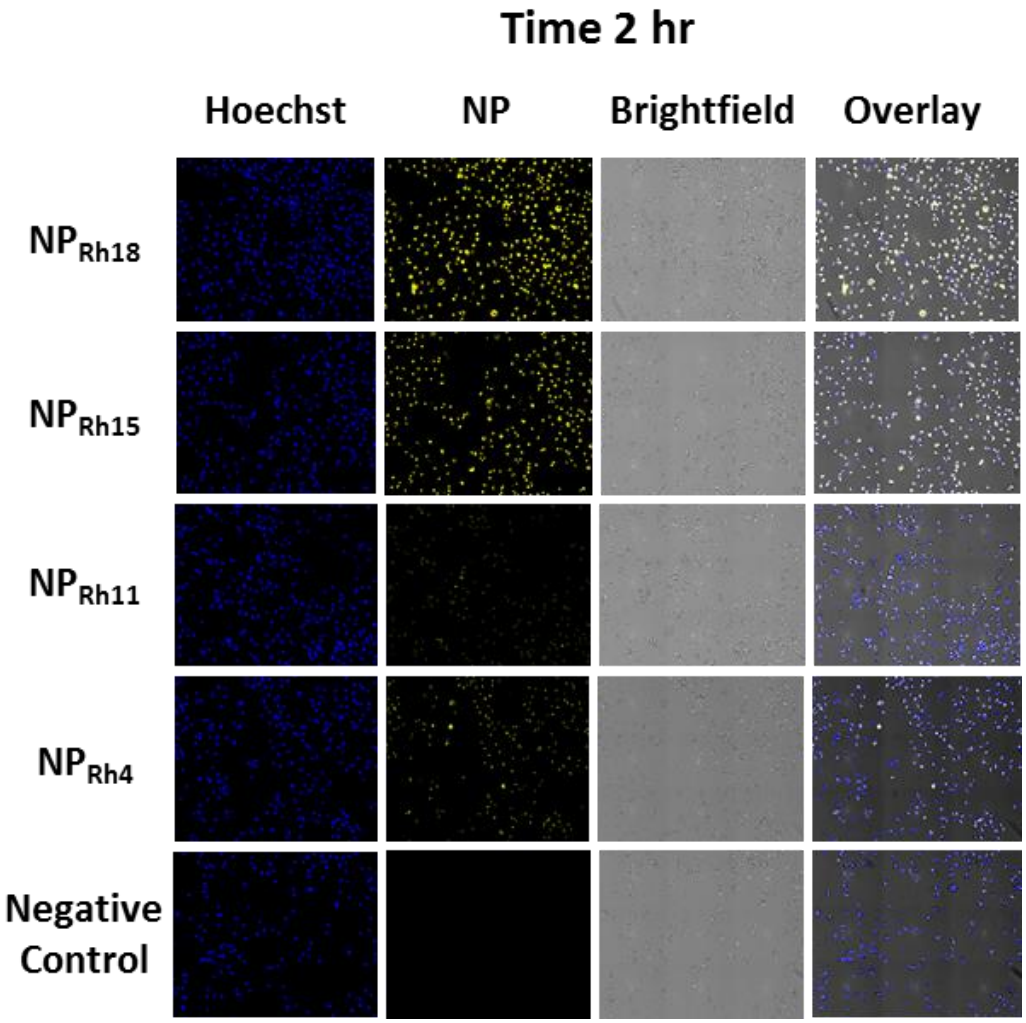

Figure 4.26 Uptake of $NP_{Rh\text{-}n}$ (n = 4, 11, 15 and 18) by PC3 cells with 2 hours of incubation (at 37 °C).

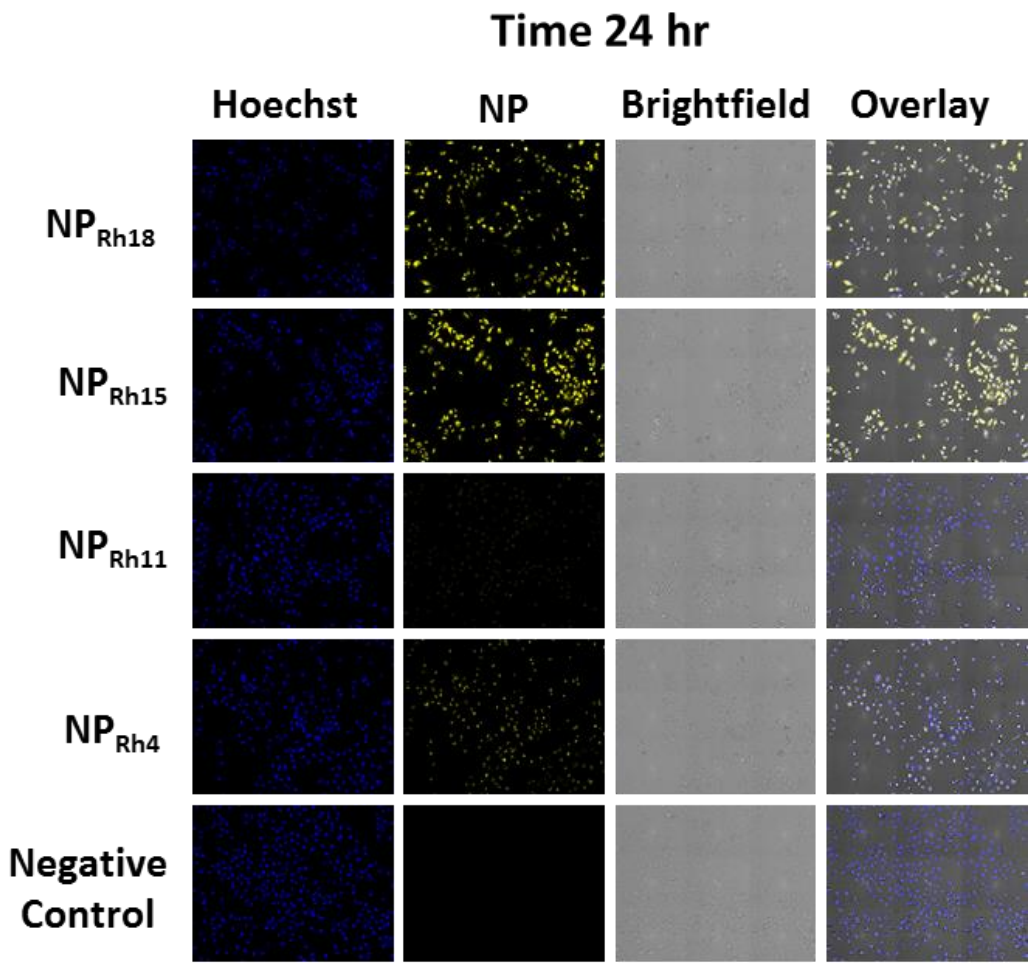

Figure 4.27 Uptake of NP_{Rh-n} (n = 4, 11, 15 and 18) by PC3 cells with 24 hours of incubation (at 37 °C).

Interestingly increasing the proportion of arsenic within the nanoparticle, greater cellular uptake was observed (Fig 4.28), particularly with $\mathbf{NP_{Rh-18}}$ and $\mathbf{NP_{Rh-15}}$ showing higher uptake than $\mathbf{NP_{Rh-10}}$ and $\mathbf{NP_{Rh-4}}$ which can be attributed to increased particle stability as a result of increased cross-linking or potentially due to the targeting effects of As(III).[20]

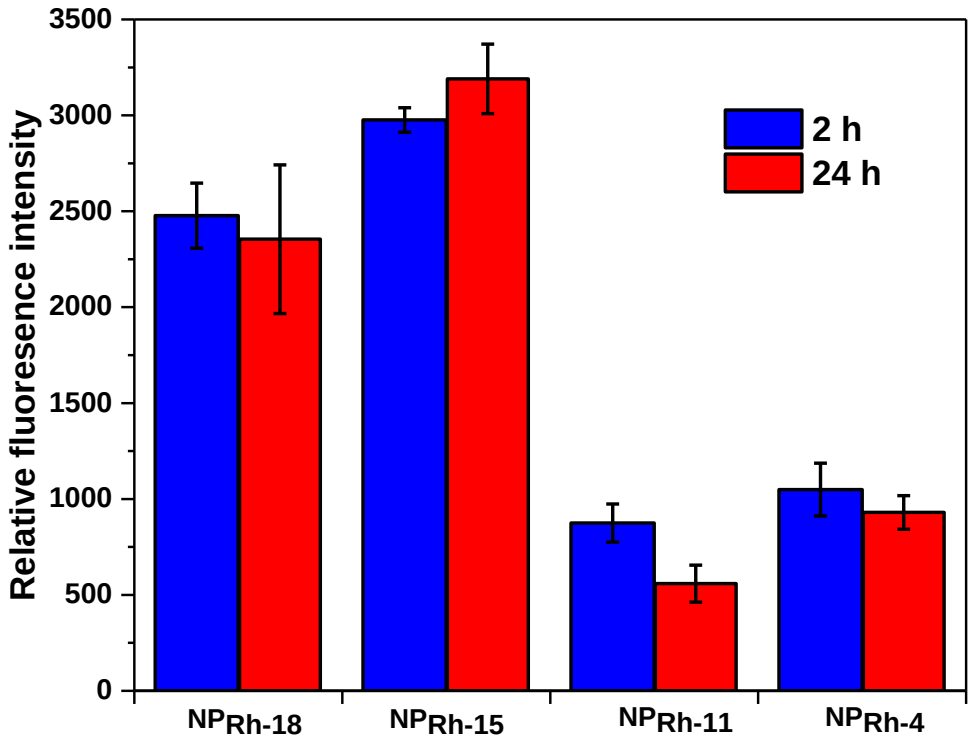

Figure 4.28 Relative fluorescence intensity of NP_{Rh-n} (n = 4, 11, 15 and 18) in PC3 cells with a nanoparticle concentration of 100 µg mL^{-1} after 2 and 24 hours of incubation. Following background reduction using a roll ball model (25 µm), fluorescence associated with rhodamine (RFP filter, λ_{ex} = 531 nm, λ_{em} = 593 nm) was assigned as intracellular fluorescence. Data is represented as the arithmetic mean ± SD with experiment conducted in triplicates.

To further track the internalisation of the nanoparticle, fluorescent confocal microscopy was used investigate the intracellular co-localisation of the internalised nanoparticles. It was hypothesised that, the nanoparticles do not enter the cells passively through direct translocation across the plasma membrane due to their size, but instead enter through an energy depend mechanism involving trafficking through a probable endosomal pathway.[21] It was therefore reasonable to assume possible trafficking of the nanoparticles to the lysosomes upon cellular entry, thus we initially stained PC3 cells with lysosomal stain, lysotracker green, and incubated with $\mathbf{NP_{Rh-18}}$ (100 µg mL^{-1}) for 24 hours prior to imaging to investigate the possible lysosomal co-localisation of the nanoparticles. The nanoparticle appears to be punctuated across the cell as observed by the confocal microscopy, however they do not appear to co-localise in the lysosomes (Fig 4.29). These results suggest avoidance of the nanoparticle towards the lysosomes, in comparison to free Rhodamine B which appears to be diffusely distributed across the cells, show some

lysomal localisation (yellow regions, Figure 4.30). In addition the nuclei of the cells were stained with Hoechst dye (blue), no nuclear co-localisation of the nanoparticles is highlighted.

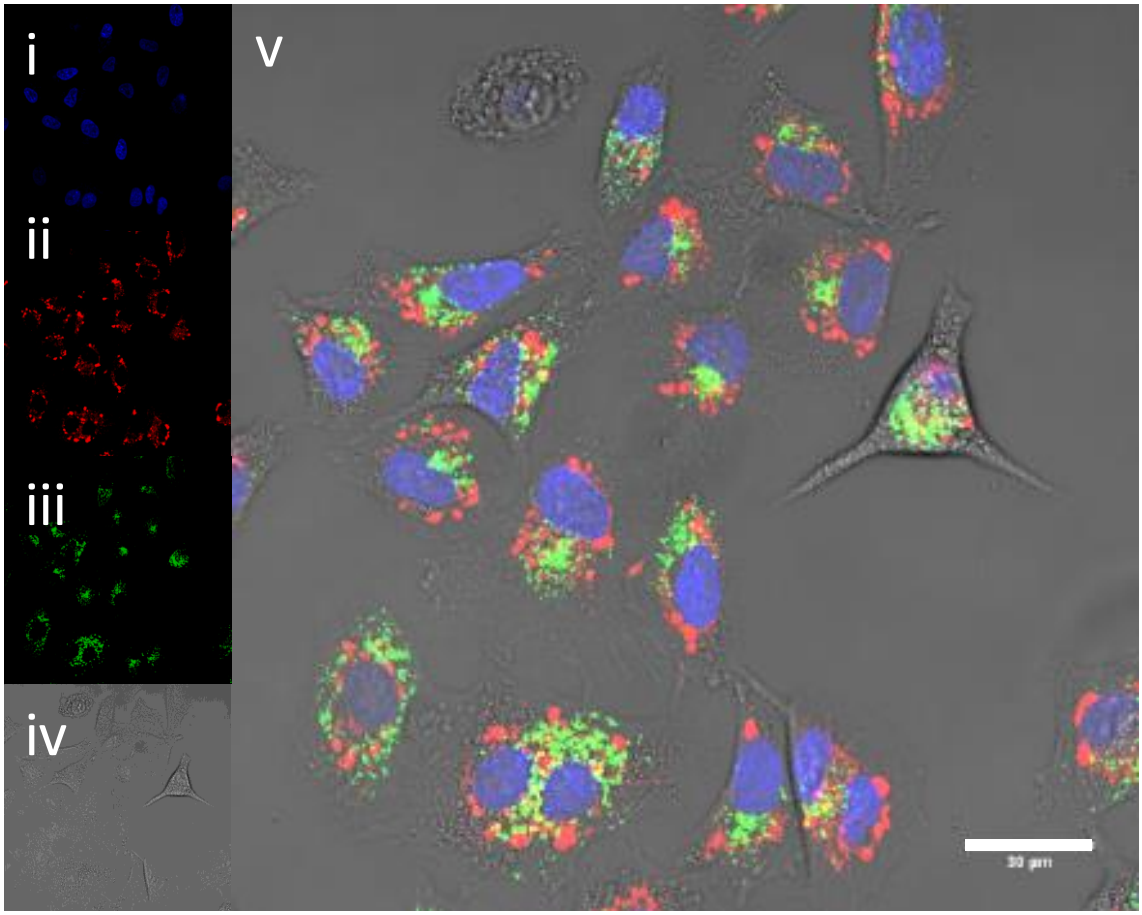

Figure 4.29 Confocal fluorescent microscopy images of PC3 cells with $NP_{Rh\text{-}18}$. i) Hoechst 33258; ii) Rhodamine-B; iii) Lysotracker green; iv) Brightfield image; v) Overlay of channels indicating lack of lysosomal co-localisation of the nanoparticles. Scale bar = 30 µm.

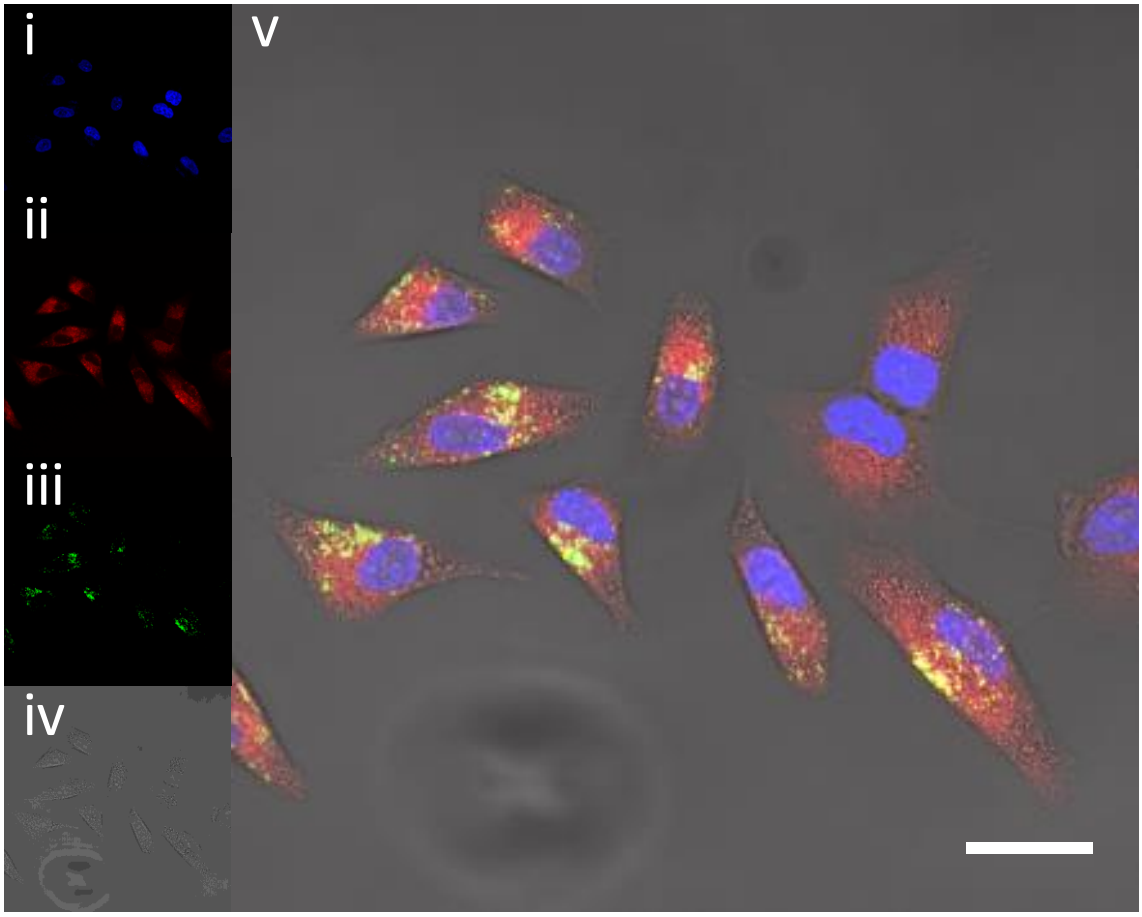

Figure 4.30 Confocal fluorescent microscopy images of PC3 cells with free Rhodamine B. i) Hoechst 33258; ii) Rhodamine-B; iii) Lysotracker green; iv) Brightfield image; v) Overlay of channels showing localisation of Rhodamine B relative to the lysosomes. Scale bar = 30 µm.

Considering the arsenic affinity towards mitochondrial as mentioned earlier, the next step was to determine the mitochondrial co-localisation of the nanoparticles. The mitochondria of PC3 cells were stained with mitotracker-green and incubated with $NP_{Rh\text{-}18}$. Although the nanoparticles are distributed throughout the cell, juxtaposition of the mitochondrial stain and rhodamine shows co-localisation as indicated by in yellow regions as a result of superimposing of the two stains (Fig 4.31). This can be attributed due to targeting effects of unreacted As(III) within the particle, as from the UV-vis spectra 12 % of the rhodamine *O*-propargyl ester (assuming 1:1 / arsine:alkyne) was incorporated in $\mathbf{NP_{Rh\text{-}18}}$ forming stable As-C bonds, suggesting number of uncross-linked arsenic groups are available capable of reacting with cellular thiols and therefore functioning as an active mitochondria tag. To rule out the co-localisation of the nanoparticle as an artefact of free diffusion and mitochondrial affinity of rhodamine, confocal microscopy of free

rhodamine was conducted. As the free rhodamine appears to be distributed throughout the cell with no strong co-localisation with mitotracker green (Fig 4.32), we can attribute our findings as a result of tagging effect of arsenic with thiols present in the mitochondria.

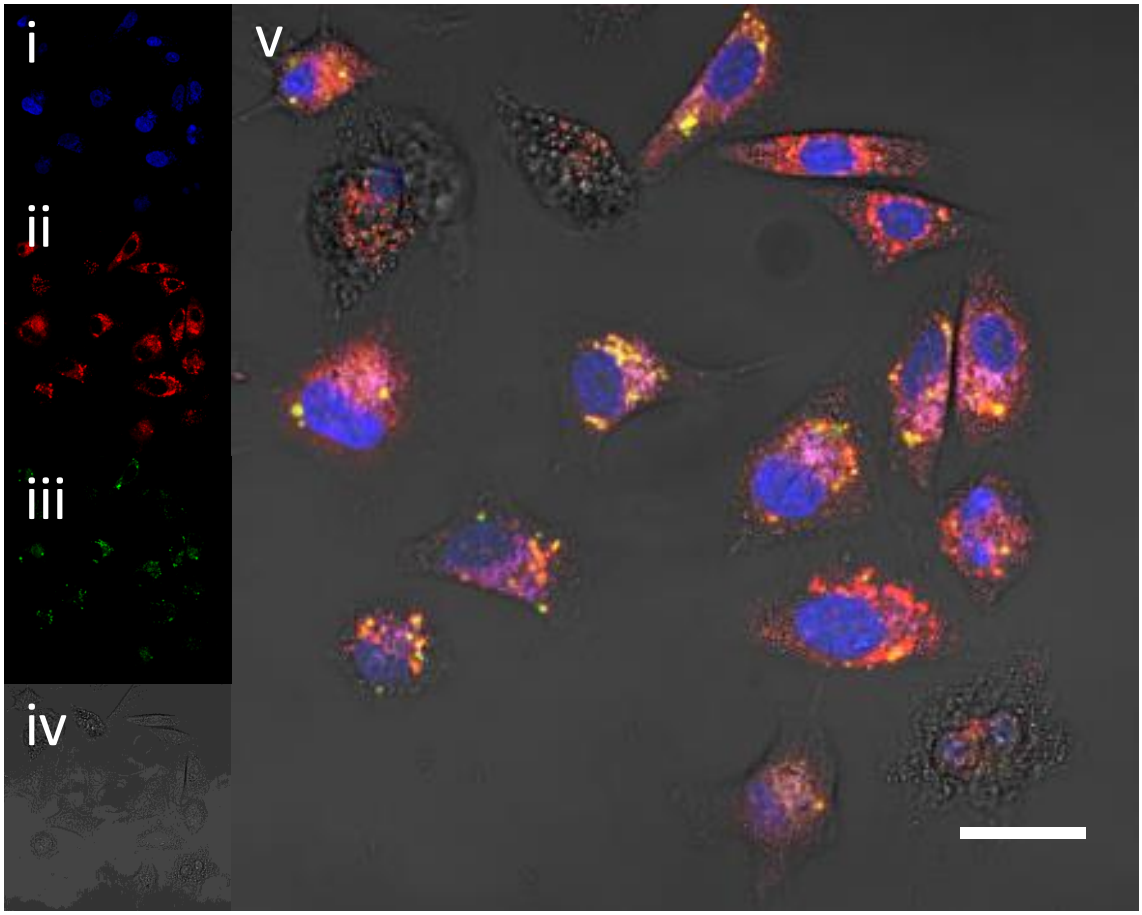

Figure 4.31 Confocal fluorescent microscopy images of PC3 cells with $NP_{Rh\text{-}18}$. i) Hoechst 33258; ii) Rhodamine-B; iii) Mitotracker green; iv) Brightfield image; v) Overlay of channels indicating mitochondrial co-localisation of the nanoparticles. Scale bar = 30 µm.

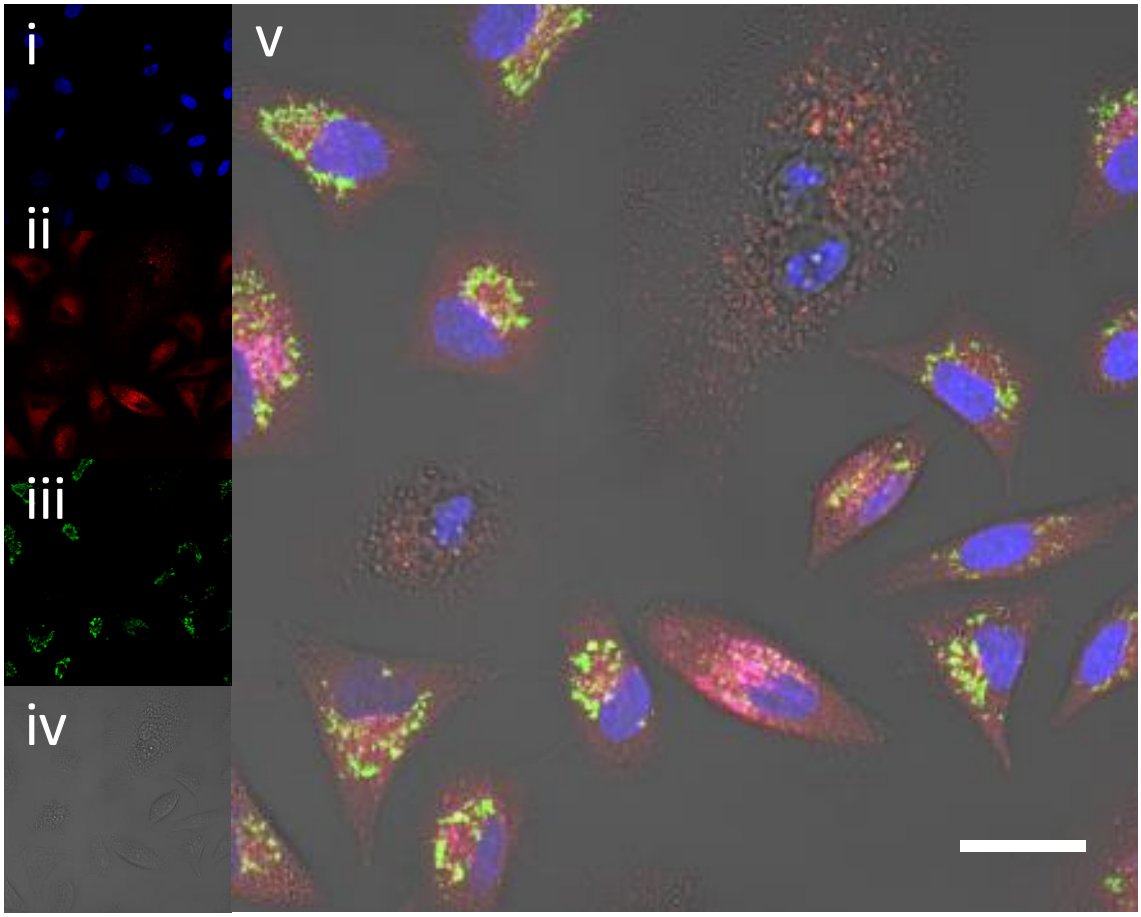

Figure 4.32 Confocal fluorescent microscopy images of PC3 cells with free Rhodamine B (bottom). i) Hoechst 33258; ii) Rhodamine-B; iii) Mitotracker green; iv) Brightfield image; v) Overlay of channels indicating lack of mitochondrial co-localisation is observed with free Rhodamine-B. Scale bar = 30 µm.

4.3 Conclusion

The ability of arsenic to polymerise with acetylenes is a unique semi-metalloid elemental feature. This method was reported to obtain poly(arsine-vinylene) conjugate polymers in 2004, but to date an application of this polymerisation has not yet been reported. As demonstrated in Chapter 2 and 3, nanoparticles can be generated by cross-linking polymers through arsenic by reduction to As(I) or by addition of nucleophilic cross-linkers. This chapter demonstrates the property of arsenic to polymerise with acetylenes as an alternative strategy of cross-linking polymers. In contrast to previous studies, this method of cross-linking yielded nanoparticles resistant to oxidation by H_2O_2. Furthermore, this strategy enabled incorporation of additional properties through the bridging acetylene monomer, allowing the covalent attachment of a fluorescent dye,

Rhodamine B ester. This permitted visualisation for *in-vitro* cellular uptake and tracking of the nanoparticle by confocal fluorescent microscopy. The results indicates successful uptake of the nanoparticles which become diffusely distributed in the cells, with evidence to suggest mitochondrial co-localisation. This mitochondrial targeting property of arsenic has recently been exploited by Stenzel to direct polymeric nanoparticles where the arsenous acid are displayed on the exterior. We show this targeting biochemical property of Arsenic is possibly retained in the even in the core of the nanoparticle. Considering the non-toxic nature of these arsenical nanoparticles as confirmed by standard in-vitro XTT-assay (2 mg/ml), these are promising candidate for benign mitochondrial targeting biomaterials. Further investigation into in-vivo study would be interesting to evaluate in-vivo toxicity and biodistribution of the arsenical nanoparticles.

4.4 Experimental

4.4.1 Materials

Dimethyl 2,2'-azobis(2-methylpropionate) (V601), *N*-(4-(2,2,3,3,7,7,8,8-octamethyl-1,4,6,9-tetraoxa-5λ^5-arsaspiro[4.4]non-5-yl)-phenyl-2-propenamide) (AsAm(pin$_2$)) was synthesised as previously reported[21] 2-((butylthio)-carbonothioyl) thio propanoic acid (PABTC) was synthesised according to the reported literature.[22] *N*-Isopropylacrylamide (NIPAm, 97%) was purchased from sigma and recrystallized in hexane from diethyl ether. Potassium Iodide, glutathione (GSH), hydrogen peroxide (30 % w/w), hypophosphorous acid (50% w/w), and poly(ethylene glycol) methyl ether acrylate (PEGA, average M_n = 480) were purchased from Sigma Aldrich and used as received. Membrane dialysis tubing (nMWCO 3.5 kDa) was obtained from Spectrum Laboratories.

4.4.2 Nuclear Magnetic Resonance

Nuclear Magnetic Resonance (NMR) spectroscopy (^{1}H NMR) spectra were recorded on a Bruker HD 300 spectrometer (300 MHz) at 27 °C in either deuterated chloroform ($CDCl_3$) or deutrated water (D_2O). Chemical shift values (δ) are reported in ppm. The residual proton signal of the solvent (δ H = 7.26 ppm for $CDCl_3$, δ H = 2.50 ppm for D_2O) was used as internal reference. ACDLABS software was used to analyse the data obtained.

4.4.3 Size Exclusion Chromatography

Size Exclusion Chromatography (SEC) was conducted using an Agilent 390-LC MDS instrument equipped with differential refractive index (DRI), viscometry (VS), dual angle light scatter (LS) and dual wavelength UV detectors. The system was equipped with 2 x PLgel Mixed D columns (300 x 7.5 mm) and a PLgel 5 µm guard column. The eluent is DMF with 5 mmol NH_4BF_4 additive. Samples were run at 1 ml min-1 at 50 °C. Poly(methyl methacrylate) (PMMA) standards (Agilent EasyVials) were used for 3rd order calibration between 2 x 10^2 – 1.0 × 10^6 g mol^{-1}. Analyte samples were

filtered through 450 µm nylon filters pore size before injection. $M_{n,SEC}$ and $Đ$ values of synthesized polymers were determined by conventional calibration using Agilent GPC/SEC software.

4.4.4 Dynamic Light Scattering

Hydrodynamic diameters (D_h) and size distributions were determined by Dynamic Light Scattering (DLS) on a MALVERN Zetasizer Nano ZS operating at 25 °C with a 4 mW He-Ne 633 nm laser module. Measurements were made at a detection angle of 173° (back scattering). Measurements were repeated three times with automatic attenuation selection and measurement position. The results were analysed using Malvern DTS 6.20 software. PDI values were calculated using equation Eq 4.1

$$PDI = \frac{\sigma^2}{d^2} \qquad \text{(Eq 4.1)}$$

Where σ is the standard deviation, and d is the diameter both obtained from the number distribution.

4.4.5 Infrared spectroscopy

Infrared (IR) spectra were recorded on a Bruker VECTOR-22 FTIR spectrometer using a Golden Gate diamond attenuated total reflection cell.

4.4.6 Ultraviolet-visible light spectrometer

Ultraviolet-visible (UV-Vis) calibration curves for experimental cross-linking density was recorded on an Agilent Technologies Cary 60 UV-Vis at a wavelength of 531 nm using a cuvette with a 1 cm path length and solutions of 1 mg ml^{-1}.

4.4.7 Fluorescence spectrometer

The fluorescent intensity was monitored using Agilent Technologies Cary Eclipse Fluorescence Spectrophotometer at an excitation wavelength of 553 nm and collection of emission at 627 nm based on rhodamine B using a cuvette with a 1 cm path length and solutions of 1 mg ml^{-1}.

4.4.8 Thermogravimetric Analysis

Thermogravimetric Analysis (TGA) spectra were recorded on a Mettler Toledo TGA/DSC. Samples were heated from 25 to 600 ºC at 10 ºC min^{-1} under N_2 atmosphere.

4.4.9 Atomic Force Microscopy

Atomic Force Microscopy (AFM) images were recorded on a Bruker Dimension Icon instrument operated in peak force tapping mode. The probes used were ScanAsyst silicon tips with a resonance frequency of 70 kHz and a spring constant of 0.4 N m^{-1}. Samples were prepared by drop casting 5 µl of a 1 mg ml^{-1} aqueous nanoparticle solution onto a freshly cleaved sheet of mica, left to stand for 30 seconds and dried under of Nitrogen.

4.4.10 Transition Electron Microscopy

Transition Electron Microscopy (TEM) Samples were prepared by placing a 400 mesh carbon coated Formvar copper grid onto a 20 µL droplet of aqueous nanoparticles (1 mg ml^{-1}) in a petri dish, leaving for 10 minutes prior to drawing off the solution. The grid was then stained by placing onto a 20 µl droplet of aqueous uranyl acetate (0.2 wt%), leaving for 10 minutes before drawing off excess liquid and allowed to air-dry overnight. TEM images were acquired using a JEOL 2100 TEM operating at a 200 kV accelerating voltage. Images were captured using Digital Micrograph® and analysed with ImageJ.

4.4.11 General Cell Culture

PC3 cells were purchased from ECACC and cultured as single monolayers at 310 K in a humidified atmosphere containing 5% CO_2. Cells were sub-cultured at regular intervals, and passages made by trypsinising cells when at 80-90% confluence. Media used was Dulbecco's Modified Eagle Medium (DMEM) supplemented with 10% of foetal calf serum, 1% of L-glutamine and 1% penicillin/streptomycin.

4.4.12 Cell Viability

PC3 cells were cultured in High Glucose DMEM medium supplemented with 10% fetal bovine serum. For cell viability evaluation, PC3 cells were seeded in a 96 well plate at a density of 1 × 104 cells per well. After 16 h, the culture medium was replaced by fresh media containing a series of dilution of the polymers (0.0625, 0.125, 0.25, 0.5, 1 and 2 mg ml^{-1}), prepared from stock solutions in PBS at 500 µM. Following 24 h incubation, the medium was removed and replaced with fresh medium. The cells were incubated with a freshly prepared solution of XTT (0.2 mg mL^{-1}) and N-methyl dibenzopyrazine methyl sulfate (250 µM) in medium for 16 h. Absorbance of the samples was finally measured using a plate reader at 450 nm and 650 nm. The data presented are representative of a minimum of two independent experiments where each sample was measured in triplicate. Errors reported correspond to the SD of the mean.

4.4.13 Cell Uptake

PC3 Cells were seeded into a black 96 imaging well plate with a clear bottom at a density of 5000 cells per well and allowed to grow for 24 h. The culture medium was replaced with media containing rhodamine labelled nanoparticles (100 µg mL^{-1}) 2 h and 24 h prior to imaging. Cellular fluorescence was measured using a Cytation 3 Cell Imaging Multi-Mode ReaderTM from Biotek®, with quantification from the Gen5TM software. Single cells were isolated using the blue channel (Hoechst 33258), and using a secondary mask with an area of 12 µm. Following background reduction using a roll ball model (25 µm), fluorescence associated with rhodamine (RFP filter, λ_{ex} = 531 nm, λ_{em} = 593 nm) was assigned as intracellular fluorescence. Data is represented as the arithmetic mean ± SD with experiments conducted in triplicates.

4.4.14 Confocal Microscopy

7500 PC3 cells were seeded in a 10 well microscopy slide and left to incubate for 24 h, at 37°C in 5% CO2 atmosphere. The culture medium was replaced with media containing nanoparticles (100 µg mL^{-1}) and incubated for 24 h prior to imaging. Cells were stained with 1) Nuclear stain – Hoechst 33258 (0.5 µg mL^{-1}; 30 min), 2) Lysotracker-Green (100

nM; 2 h), 3) Mitotracker green (100 nM; 30 min). Immediately prior to imaging, the cells were washed with PBS 3x, and finally the media replaced with 100 µL of phenol red free DMEM. Cells were imaged with a Zeiss 880 confocal microscope using a 40 x objective, at 37°C with the following laser settings: 1) Hoechst dye (blue channel), 405 nm laser, 420-500 nm emission band. 2) Lysotracker and Mitotracker (green channels), 488 nm laser 500-550 nm emission band. 3) rhodamine labelled compounds and free rhodamine B (red channel), 561 nm laser (570-630 nm emission band). Images were processed with Fiji software.

4.4.15 Synthesis of Propargyl-*O*-Rhodamine B ester

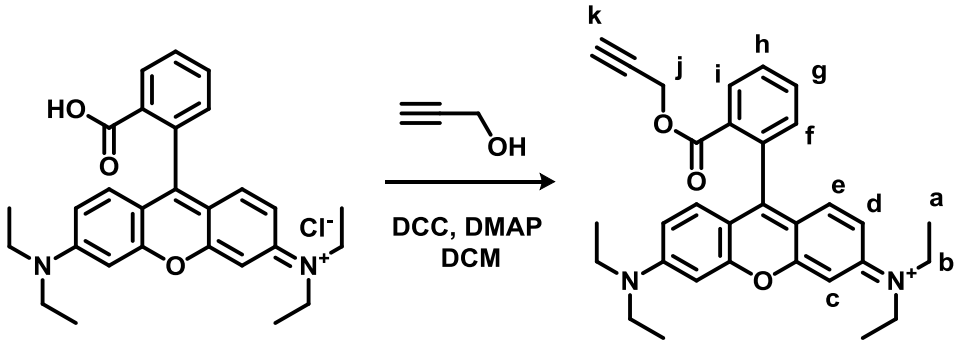

Rhodamine b (1 eq), DCC (1.5 eq), DMAP (0.2 eq) were dissolved in anhydrous DCM (50 ml) and stirred for 30 min. Propargyl alcohol (1.5 eq) were added and stirred at room temperature for 16 h. Product purified by flash column in 1% methanol in DCM, the resulting product fractions combined and the solvent removed in vacuo to yield iridescent black crystals **4** (57% yield). ^{1}H NMR (400 MHz, $CDCl_3$, 298 K) δ = 8.30 (d, J_{HH} = 7.2 Hz, 1H, H_i), 7.84 (dd, J_{HH} = 7.2, 7.3 Hz, 1H, H_g), 7.75 (dd, J_{HH} = 7.9, 7.3 Hz, 1H, H_h), 7.31 (d, J_{HH} = 7.9 Hz, 1H, H_f) 7.06 (d, J_{HH} = 9.5 Hz, 2H, H_e), 6.90 (d, J_{HH} = 9.7 Hz, 2H, H_d) 6.80 (s, 2H, H_c) 4.60 (s, 2H, H_j) 3.63 (q, J_{HH} = 13.3, 6.4 Hz, 8H, H_b) 2.40 (s, 1H, H_k) 1.30 (t, J_{HH} = 6.8, 12H, H_a); ^{13}C NMR (400 MHz, $CDCl_3$ 298 K) δ = 164.2, 75.6, 52.9, 46.2, 12.7,; LR-MS (ESI, +ve) *m/z* ($C_{31}H_{34}N_2O_3$); expected 481.2, obtained 481.4 ($[M+H]^+$).

4.4.16 General procedure for self-assembly and crosslinking of $PEGA_{20}$-*b*-[$NIPAm_{80-n}$-*st*-$AsAm_n$] *via* acetylenes

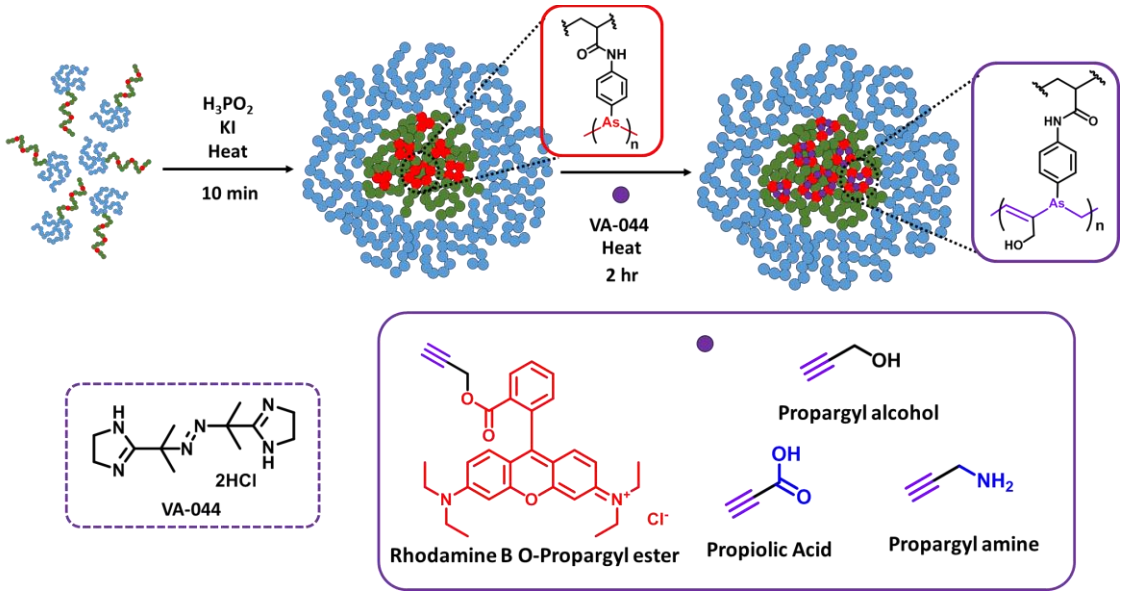

The general procedure for crosslinking through vinyl-arsine required As-functional polymer dissolution in a deoxygenated aqueous solution of hypophosphorus acid (H_3PO_2, 10 wt%, 10 mg/ml polymer) and deoxygenated KI (1 vol% from a 3 wt% aq solution) were added. The solution were heated to 60 °C for 30 min. The functionalised acetyleneS (2.5 eq. w.r.t. [As]) and VA-044 (0.1 eq w.r.t [As]) were separately dissolved in HPLC grade H_2O and sparged with N_2 before addition to the hot polymer solution which were heated for a further 15.5 h. The resulting solution dialysed (nMWCO 3.5 KDa) against deionised water for 24 h and the crosslinked particles isolated by lyophilisation. The resulting solution of Rhodamine-functional nanoparticle were dialysed (nMWCO 3.5 KDa) against dilute hydrochloric acid (HCl, 0.1 M) until no further fluorescence in the dialysis media were visible by UV-Vis, then further dialysis against deionised water for 24 h, the crosslinked particles isolated by lyophilisation.

4.4.17 General procedure for particle stability and disassembly.

Polymer nanoparticles were dissolved separately in deionised water, aqueous glutathione (5 mM) and aqueous H_2O_2 (5 mM) (1 mg ml^{-1}). The solutions were filtered through (450 µm nylon filters) into separate plastic cuvettes (with a lid) and incubated at 37 ^{0}C in water bath. Disassembly was monitored through the measurement of changes in D_h as a function of time by DLS.

4.5 References

1. Z.-Y. Wang and Z. Chen, *Blood*, 2008, **111**, 2505-2515.
2. L. Horsley, J. Cummings, M. Middleton, T. Ward, A. Backen, A. Clamp, M. Dawson, H. Farmer, N. Fisher, G. Halbert, S. Halford, A. Harris, J. Hasan, P. Hogg, G. Kumaran, R. Little, G. J. M. Parker, P. Potter, M. Saunders, C. Roberts, D. Shaw, N. Smith, J. Smythe, A. Taylor, H. Turner, Y. Watson, C. Dive and G. C. Jayson, *Cancer Chemother. Pharmacol.*, 2013, **72**, 1343-1352.
3. P. J. Dilda, S. Decollogne, L. Weerakoon, M. D. Norris, M. Haber, J. D. Allen and P. J. Hogg, *J. Med. Chem.*, 2009, **52**, 6209-6216.
4. J. Wu, F. Muggia, C. Henderson, L. Feun, P. V. Veldhuizen, P. Gold, H. Zheng, G. A. 66201, J. Lewis and A. X. Zhu, *J. Clin Oncol.*, 2009, **27**, e15630-e15630.
5. D. Park, J. Chiu, G. G. Perrone, P. J. Dilda and P. J. Hogg, *Cancer Cell Int.*, 2012, **12**, 11.
6. L. R. Smith and J. L. Mills, *J. Organomet. Chem.*, 1975, **84**, 1-15.
7. H. J. Breunig, in *Organic Arsenic, Antimony and Bismuth Compounds (1994)*, John Wiley & Sons, Ltd, 2004, pp. 563-577.
8. N. C. Lloyd, H. W. Morgan, B. K. Nicholson and R. S. Ronimus, *Angew. Chem. Int. Ed.*, 2005, **44**, 941-944.
9. J. W. B. Reesor and G. F. Wright, *J.Org. Chem.*, 1957, **22**, 382-385.
10. J. Tanaka, S. Tani, R. Peltier, E. H. Pilkington, A. Kerr, T. P. Davis and P. Wilson, *Polym. Chem,*, 2018, **9**, 1551-1556.
11. K. Naka, T. Umeyama and Y. Chujo, *J. Am. Chem. Soc.*, 2002, **124**, 6600-6603.
12. T. Umeyama, K. Naka, A. Nakahashi and Y. Chujo, *Macromolecules*, 2004, **37**, 1271-1275.
13. A. Anastasaki, B. Oschmann, J. Willenbacher, A. Melker, M. H. C. V. Son, N. P. Truong, M. W. Schulze, E. H. Discekici, A. J. McGrath, T. P. Davis, C. M. Bates and C. J. Hawker, *Angew. Chem. Int. Ed.*, 2017, **56**, 14483-14487.
14. D. R. Lide., *CRC Handbook of Chemistry and Physics.*, CRC Press, Boca Raton, Florida, USA, 81 edn., 2000.
15. G. Odian, *Principles of Polymerisation*, John Wiley & Sons, 4th edn., 2004.
16. S. Kaga, N. P. Truong, L. Esser, D. Senyschyn, A. Sanyal, R. Sanyal, J. F. Quinn, T. P. Davis, L. M. Kaminskas and M. R. Whittaker, *Biomacromolecules*, 2017, **18**, 3963-3970.

17. H. Cabral, Y. Matsumoto, K. Mizuno, Q. Chen, M. Murakami, M. Kimura, Y. Terada, M. R. Kano, K. Miyazono, M. Uesaka, N. Nishiyama and K. Kataoka, *Nat. Nanotechnol.*, 2011, **6**, 815.
18. P. Wilson, A. Anastasaki, M. R. Owen, K. Kempe, D. M. Haddleton, S. K. Mann, A. P. R. Johnston, J. F. Quinn, M. R. Whittaker, P. J. Hogg and T. P. Davis, *J. Am. Chem. Soc.*, 2015, **137**, 4215-4222.
19. J.-M. Noy, H. Lu, P. J. Hogg, J.-L. Yang and M. Stenzel, *Bioconjugate Chem.*, 2018, **29**, 546-558.
20. J. Rejman, V. Oberle, I. S. Zuhorn and D. Hoekstra, *Biochem. J*, 2004, **377**, 159-169.
21. A. Schachtschneider, M. Wessig, M. Spitzbarth, A. Donner, C. Fischer, M. Drescher and S. Polarz, *Angew. Chem. Int. Ed.*, 2015, **54**, 10465-10469.
22. C. Footman, P. A. de Jongh, J. Tanaka, R. Peltier, K. Kempe, T. P. Davis and P. Wilson, *Chem. Commun.*, 2017, **53**, 8447-8450.
23. C. J. Ferguson, R. J. Hughes, D. Nguyen, B. T. T. Pham, R. G. Gilbert, A. K. Serelis, C. H. Such and B. S. Hawkett, *Macromolecules*, 2005, **38**, 2191-2204.

Chapter 5 : Polymeric arsenicals as scaffolds for functional and responsive hydrogels

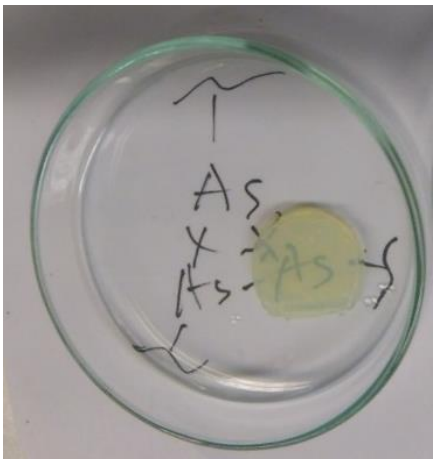

Abstract

Arsenohydrogels are introduced for the first time as tuneable, responsive and biocompatible hydrogels. The distinctive redox reactivity of arsenic has been exploited to crosslink high molecular weight (M_w > 300 kDa) polymeric arsenical scaffolds ($PDMAm_x$-co-$AsAm_y$) via reductive coupling of As(V) to As(I) which proceeds with the formation of As-As in the form of As(I)n homocycles. Arsenohydrogels are formed at 2.5 wt% of polymeric arsenical scaffold (G'~ 400 Pa) and gel strength is significantly increased when the polymer weight fraction is increased to 10 wt% (up to 81 kPa). Increasing the mole fraction of arsenic (AsAm, y) increases the crosslinking density, reduces the degree of swelling and increases the stability of the gel against hydrolysis and oxidation of the As-As crosslinks. The functionality of the polymeric arsenical scaffolds has also been exploited to load arsenohydrogels with a model organic arsenical drug. The rate and degree of release of the loaded organic arsenical under simulated oxidative stress (H_2O_2) is inversely proportional to the mole fraction of arsenic in the original polymer scaffold. Finally, the polymeric arsenical scaffolds and the resulting arsenohydrogels have been shown to be non-toxic and capable of encapsulating trypsinized PC3 cells. The properties and versatility of the arsenohydrogels further alludes to their potential as a functional platform for biomaterials.

5.1 Introduction

Synthetic polymer hydrogels are materials composed of networks of hydrophilic polymers, cross-linked via covalent bonding or physical interactions such as hydrogen bonding,[1] electrostatic interactions[2] and host - guest[3] / metal – ligand[4] complexation.[5, 6] They are defined by their durability and programmable physical and mechanical properties even at high water contents (> 90%), which lends itself to a number of emerging technologies, particularly in healthcare where they are being applied in areas such as wound dressings,[7] diagnostics,[8] drug delivery,[9] 3D cell culture,[10] tissue engineering[11] and wearable technologies.[12]

Hydrogels formed through covalent bonding can exhibit static or dynamic properties based on the nature of the cross-linking involved.[13] For example, the archetypal polyacrylamide hydrogel employed in gel electrophoresis, is an aqueous network of acrylamide irreversibly cross-linked by a bisacrylamide co-monomer.[14] Conversely, incorporation of functional groups capable of forming cleavable and/or dynamic covalent bonds into polymeric scaffolds has been employed to fabricate dynamic hydrogels which elicit spatial and temporal controlled bond formation and degradation, and in some cases self-healing properties.[15, 16] In this context Schiff bases (including hydrazone[17] and oxime[18]), boronate esters[19] and disulfides[20] are amongst those most widely explored in such systems. These dynamic bonds are sensitive to changes in the local pH or redox environment, or are competitively exchanged with biologically relevant nucleophiles to stimulate material response.

Organic arsenicals have diverse and distinct chemical reactivity which is dependent upon the oxidation state of the As(X) (e.g. X = V, III, I) centres present. However, concerns about the toxicity of arsenic have limited the use to organic arsenicals in polymer and materials science. A clinical renaissance in the use of arsenic trioxide to treat blood born malignancies and the subsequent development of more potent organic arsenical analogues,[21] has inspired investigations into the potential of organic and polymeric arsenicals as a platform for functional and responsive (bio)materials.[22] To this end, pentavalent arsenic, As(V), has been incorporated into well-defined polymer chains at the chain-end and/or the side-chains of polymers synthesised by radical deactivation radical

polymerisation (RDRP), employing As-functional initiators and monomers respectively. These polymers have been shown to be non-toxic in vitro and have been exploited as reactive scaffolds for post-polymerisation modification[23] and highly specific disulfide bond targeting linkers for protein/peptide-polymer conjugation[24] via sequential reduction, to trivalent As(III), and reaction with thiol/disulfide containing molecules.

Most recently, thermoresponsive block copolymers containing organic arsenicals have been synthesised and assembled under reductive conditions (H_3PO_2, KI) at elevated temperatures to generate nanoparticles stabilised as a result of reductive coupling from As(V) to As(I).[25] This has previously been reported to proceed with the formation As-As bonds in the form of As(I)$_n$ homocyclic oligomers.[26] The stability of the resulting nanoparticles in aqueous and model biological solutions (5 mM glutathione) was dependent upon the mole ratio of As(V) in the initial monomer feed and all were responsive towards oxidation with hydrogen peroxide. To date, this is the only example of cross-linking polymers ever reported using the redox chemistry of organic arsenicals. Herein, reductive coupling of As(V) to As(I) in hydrophilic polymeric arsenicals is demonstrated to furnish macroscopic arsenohydrogels. The resulting gels are non-toxic and their physical properties depend upon the As(V) mole fraction and the polymer loading in solution (wt%).

5.2 Results and Discussion

5.2.1 Polymeric arsenical synthesis

For the preparation of high molecular weight hydrophilic As(V)-functional polymer scaffolds, the As(V)-functional acrylamide monomer (AsAm) reported in Chapter 2,[25] was copolymerised with hydrophilic acrylamide monomer dimethylacrylamide (DMAm) using free radical polymerisation. Water soluble initiator (VA0-44) was employed at 90 °C targeting high monomer conversions and high molecular weight polymers. The reactions reached full conversion with respect to both monomers within 2 hrs and the resulting polymers were directly lyophilised without further purification. The PDMAm$_x$-co-AsAm$_y$ polymers (**P5.1 – P5.4**, Table 5.1) were synthesised with increasing AsAm functionality as observed by NMR (Fig. 5.1). The percentage of AsAm was calculated by

comparing either -C***H***$_2$- the backbone of DMAm and AsAm (1.0 – 1.8 ppm) or C***H***$_3$- side chain of DMAm with –C***H***- of the backbone (2.1 – 3.0 pm) with aromatic AsAm protons (7.2 – 7.8 ppm).

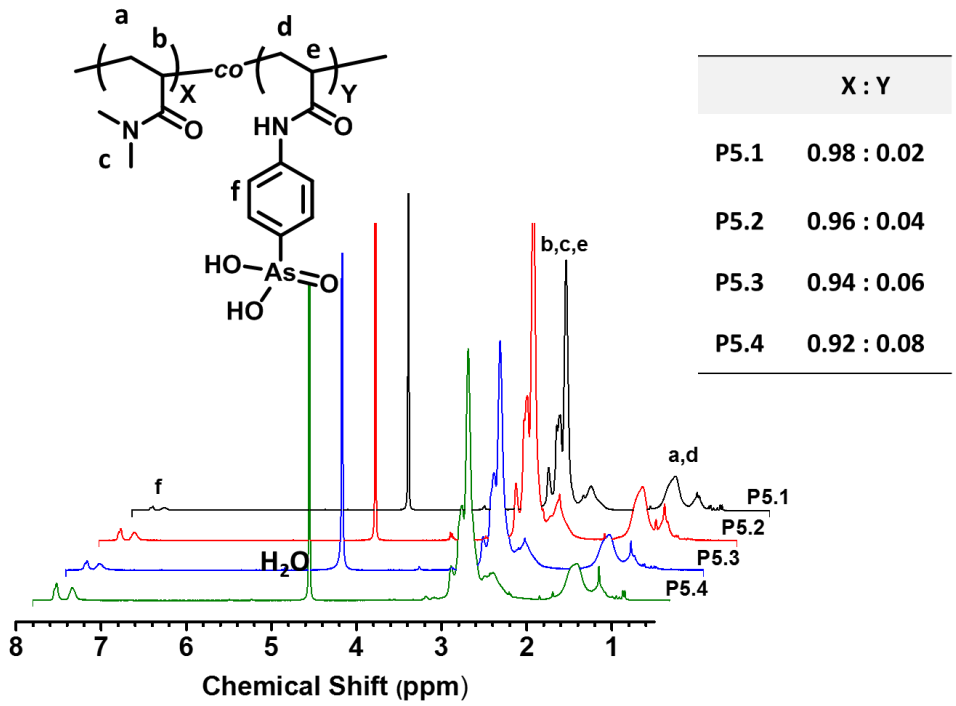

	X : Y
P5.1	0.98 : 0.02
P5.2	0.96 : 0.04
P5.3	0.94 : 0.06
P5.4	0.92 : 0.08

Figure 5.1 NMR of polymeric arsenical scaffolds PDAm$_x$-*co*-AsAm$_y$ synthesised by free radical polymerisation.

Table 5.1 Composition and molecular weight data for the polymeric arsenical scaffolds P5.1 – P5.4

	Composition	M_n^* (gmol^{-1})	M_w^{**} (gmol^{-1})	$Đ^{**}$
P5.1	P(DMAm$_{0.98}$-AsAm$_{0.02}$)	95000	460000	4.8
P5.2	P(DMAm$_{0.96}$-AsAm$_{0.04}$)	81000	330000	4.1
P5.3	P(DMAm$_{0.94}$-AsAm$_{0.06}$)	110000	450000	4.1
P5.4	P(DMAm$_{0.92}$-AsAm$_{0.08}$)	56000	310000	5.5

*** From ^{1}H NMR (*vide supra*) ** from aqueous SEC**

Increasing Arsenic content was also confirmed by the increase in υ = 854 cm-1 corresponding to the As-O absorption in IR spectroscopy (Fig. 5.2). Molecular weight data was obtained by aqueous size exclusion chromatography (SEC) which revealed that each polymer had high molecular weight (M_w > 300 kDa, Fig. 5.3).

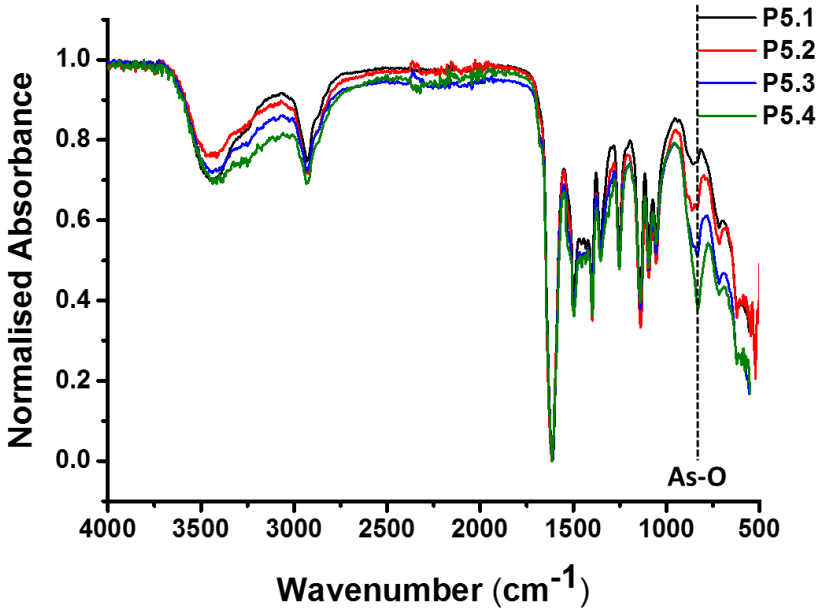

Figure 5.2 **FT-IR of polymeric arsenical scaffolds PDAm$_x$-*co*-AsAm$_y$ synthesised by free radical polymerisation.**

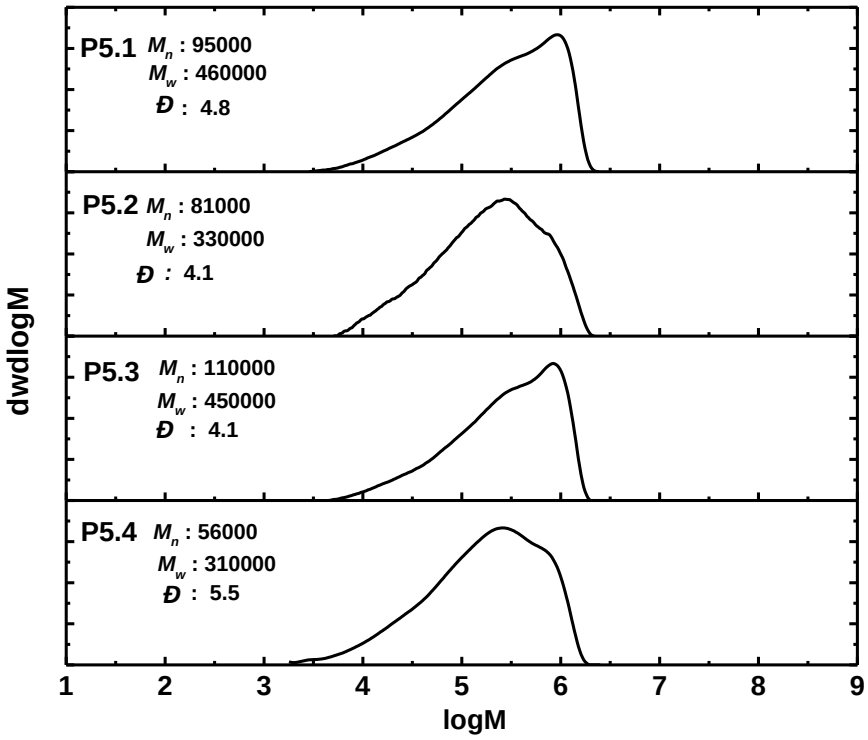

Figure 5.3 Molecular weight data for polymeric arsenical scaffolds P5.1 – P5.4 obtained from aqueous SEC

5.2.2 Hydrogel preparation and characterisation

The polymers were cross-linked via the reductive coupling method described in Chapter 2 which was inspired by the synthesis and structural elucidation of Salvarsen (Scheme 5.1).[27] Hydrogels were formed at 2.5 wt% and 10 wt% polymer after heating at 60 °C in the presence of aqueous H_3PO_2 and KI for 30 minutes, according to qualitative inversion tests (Fig 5.4). Attempts to form gels at 1 wt% of the arsenical polymers were unsuccessful as the gels collapsed to a heterogeneous precipitate.

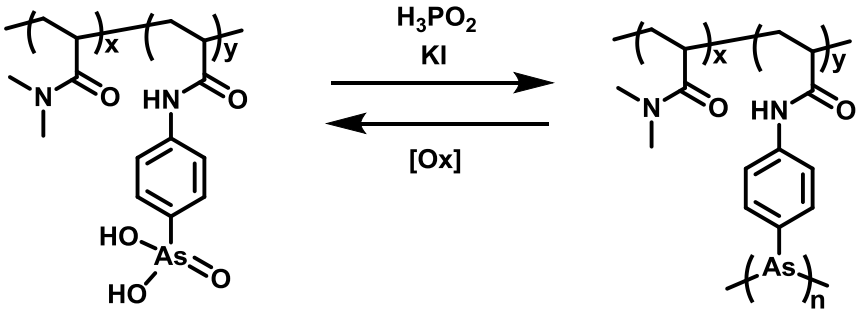

Scheme 5.1 General scheme for the formation of arsenohydrogels by reductive coupling of polymeric arsenical scaffolds

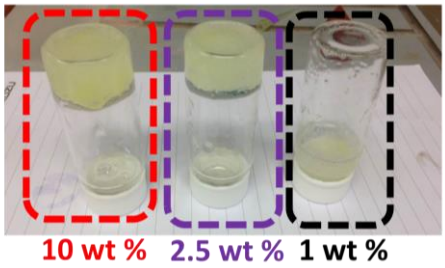

Figure 5.4 Inverse test qualitatively demonstrating gelation at 2.5 wt% and 10 wt% with no gelation occurring at 1 wt%

Interestingly **P5.3** and **P5.4** with increased amounts of AsAm units induced syneresis at 2.5 wt % after the initial gel formation, expelling 40% of the aqueous solution (Fig 5.5). This macroscopic contraction is typically observed with highly cross-linked polymeric gels at low polymer weight concentration.[28]

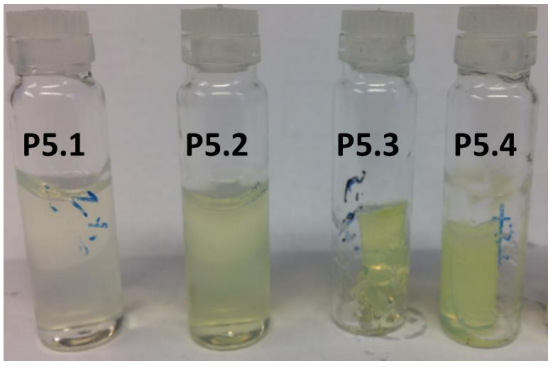

Figure 5.5 Image of 2.5 wt % arsenohydrogels P5.1 – P5.4 in which P1 and P2 formed stable gels P3 and P4 undergo syneresis, expelling up to 40% of the aqueous solution

The formation of the 2.5 wt % gel was followed by rheology in oscillation mode (0.1% strain). The transition from liquid to gel was observed at the cross over point between the storage (G') and loss (G'') moduli (t < 500 secs) and G' values indicated that very soft gels were formed under these conditions (G' < 400 Pa) (Fig. 5.6). At this point the self-healing ability of the arsenohydrogels was briefly investigated.

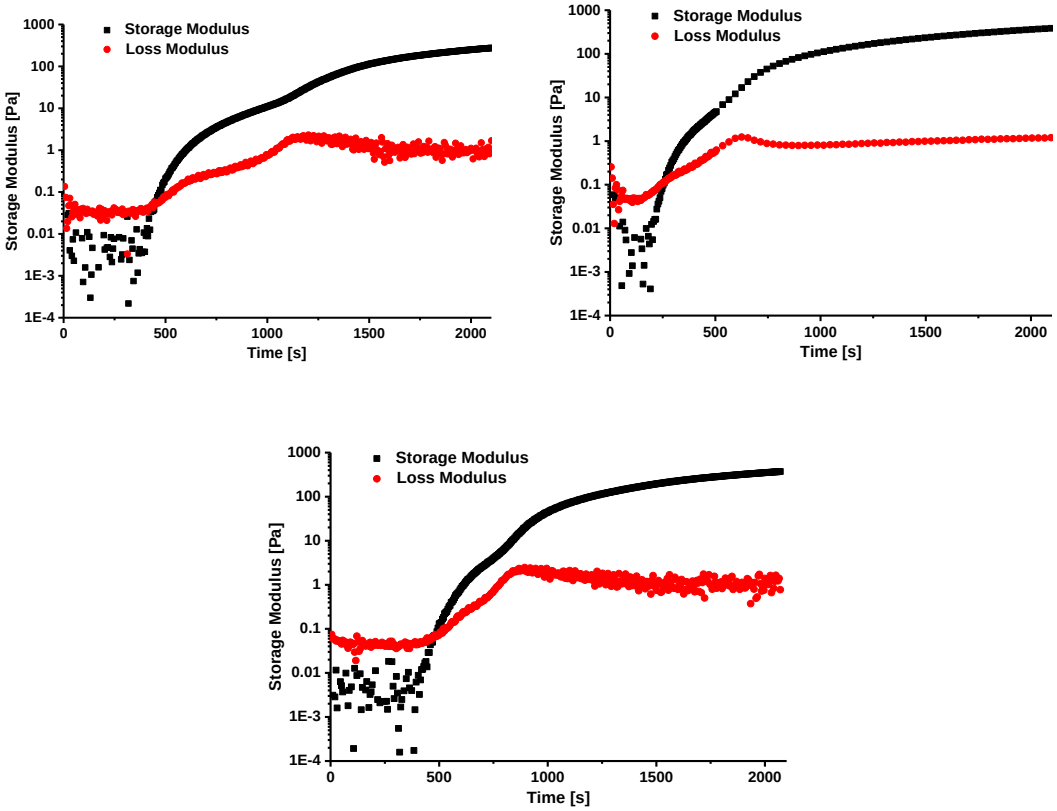

Figure 5.6 Rheology of the arsenohydrogel formation of P5.1 (top left) P5.2 (top right) and P5.3 (bottom) at 2.5 wt %, strain 0.1 % and frequency 1 Hz (oscillation mode).

At this point the self-healing ability of the arsenohydrogels was briefly investigated. However, despite the potentially dynamic nature of the arsine bonds,[29-32] the gels were not self-healable under the conditions investigated in this work. Analytically this was indicated by the loss of gel integrity observed in the 2nd cycle of the amplitude sweep during rheology of **P5.1** (2.5 wt%, Fig. 5.7). Chemically, additional experiments including addition of reductive cross-linking solution at the fracture point to (re)form Arsine(I) bonds, and UV irradiation to reshuffle labile As(I) bonds by homolytic fission and recombination failed to stimulate healing of the fractured gel matrix.

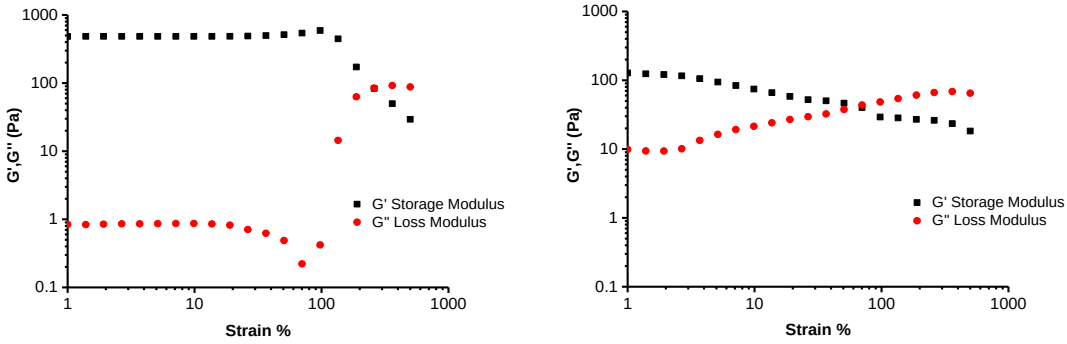

Figure 5.7: Amplitude sweep of hydrogel of P5.1 at 30 °C and frequency of 1 rad s^{-1} 1st cycle (left) and 2nd

When arsenohydrogels were prepared at 10 wt% polymer the macroscopic structure was retained with no syneresis observed irrespective of the AsAm feed ratio. The viscoelastic properties of these hydrogels were determined by Dynamic Mechanical Analysis (DMA) in frequency sweep mode. The G' was consistently higher than G'' across the range of frequency tested, indicating the hydrogels were stable and behaved as viscoelastic solids (Fig. 5.8). Increasing the polymer weight fraction from 2.5 wt% to 10 wt% increased the G' by 2 orders of magnitude from ~400 Pa to 33 – 81 kPa. The data obtained from the DMA was verified by comparison to that obtained from rheology of the same hydrogel formulations (Fig. 5.9).

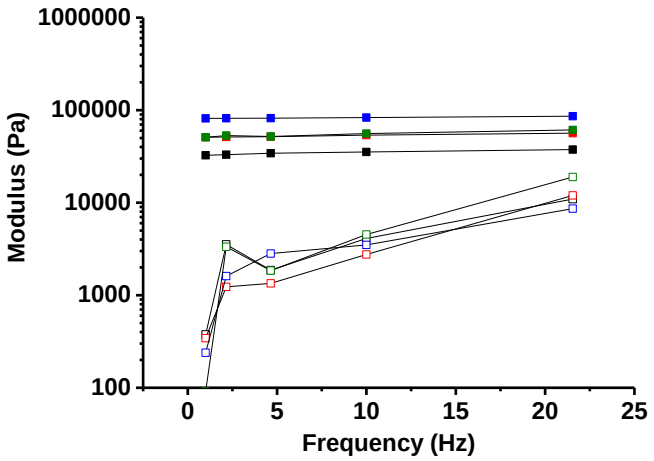

Figure 5.8 Frequency sweep of arsenohydrogels from DMA analysis. Storage moduli (filled in squares) and loss moduli (empty squares) of P1 (black), P2 (red), P3 (blue) and P4 (green).

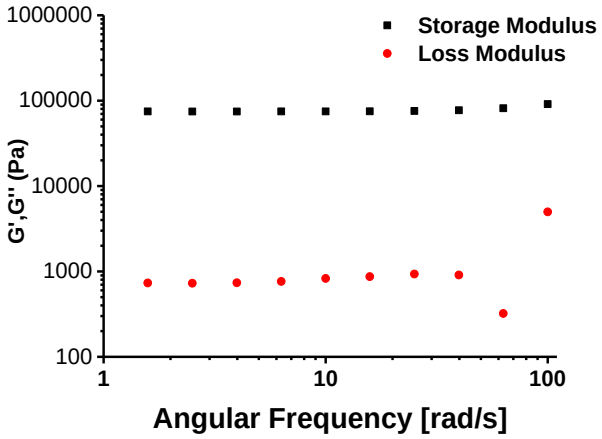

Figure 5.9 Frequency sweep of P5.2 (10 wt%) measured by rheology

The morphology of arsenohydrogels (10 wt%) was investigated by SEM of lyophilised gels after 24 hours of dialysis (Fig 5.10). After dialysis, the gels prepared with higher AsAm mole fraction (**P5.4**) show a retention of more densely cross-linked gel matrix at the microscopic scale. Furthermore, the increasing arsenic content present in the arsenohydrogels was confirmed by Energy-Dispersive X-ray (EDX) Spectroscopy (Table 5.2).

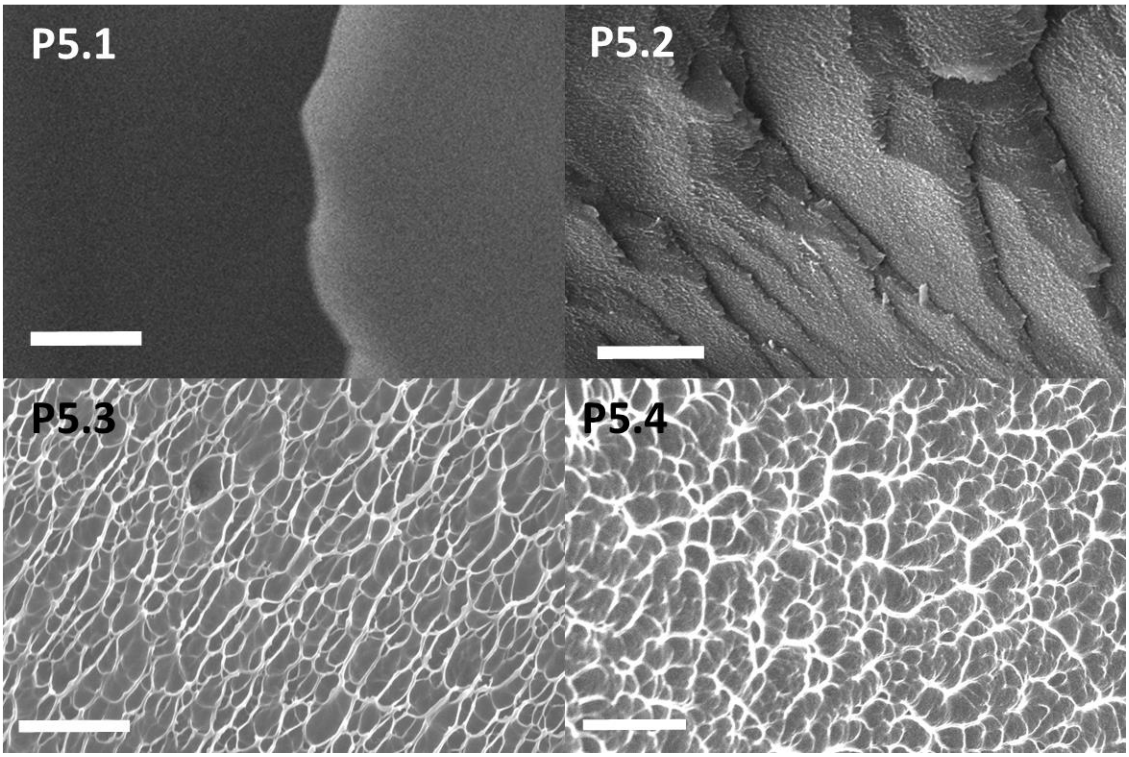

Figure 5.10 Scanning electron microscopy of pore like structures in 10 wt % arsenogels after dialysis (24 hr): P5.1 (top left), P5.2 (top right), P5.3 (bottom left) and P5.4 (bottom right), Scale bar = 2 µm.

Table 5.2: Elemental analysis summary from EDX of the arsenohydrogels.

	Wt %[a]			
	C	N	O	As
P5.1	41.41	9.46	46.52	2.61
P5.2	35.67	9.89	51.24	3.20
P5.3	37.24	9.73	48.15	4.89
P5.4	39.45	11.09	43.06	6.41

[a]Other elements such as potassium, iodide and phosphorous is not taken into account.

The arsenohydrogels (10 wt %) were swollen in water (Fig 5.11). The degree of swelling was determined by the % swelling ($W_s - W_0/W_0$) x 100 (where W_s is the mass of the swollen gel and W_0 is the mass of dried gel). The swelling of the gel derived from **P5.1**, with the smallest AsAm mole fraction was 760% after 24 hours compared to 25% for **P5.4** with the highest AsAm mole fraction (Fig. 5.12). Swelling of **P5.1** continued over 6 days and did not reach equilibrium. The gels derived from **P5.2** and **P5.3** followed the same trend, with **P5.2** reaching 720% and **P5.3** reaching 250% after 6 days of swelling.

Images of the arsenohydrogels swelling show that swelling proceeds with retention of the gel structure (Fig. 5.11). The swelling of **P5.1** indicates that this proceeds to the point at which the swollen gel fills the base of the beaker (Fig. 5.11, $t > 72$ hours). The swelling properties of the arsenohydrogels can be rationalised by the degree of crosslinking the relative susceptibility of the As-As bonds, that constitute the crosslinking, to hydrolysis and then oxidation. Under reductive conditions the formation of As-As bonds is favoured. However, during the swelling experiment, the reducing agent(s) are gradually removed which exposes the relatively weak As-As bonds to hydrolysis and re-oxidation, under ambient condition, of the As(I) to As(III) and As(V). The impact of this on the gel integrity is most prevalent at lower crosslinking densities (**P5.1**). At the highest crosslinking density (**P5.4**) the impact on the gel integrity was minimal.

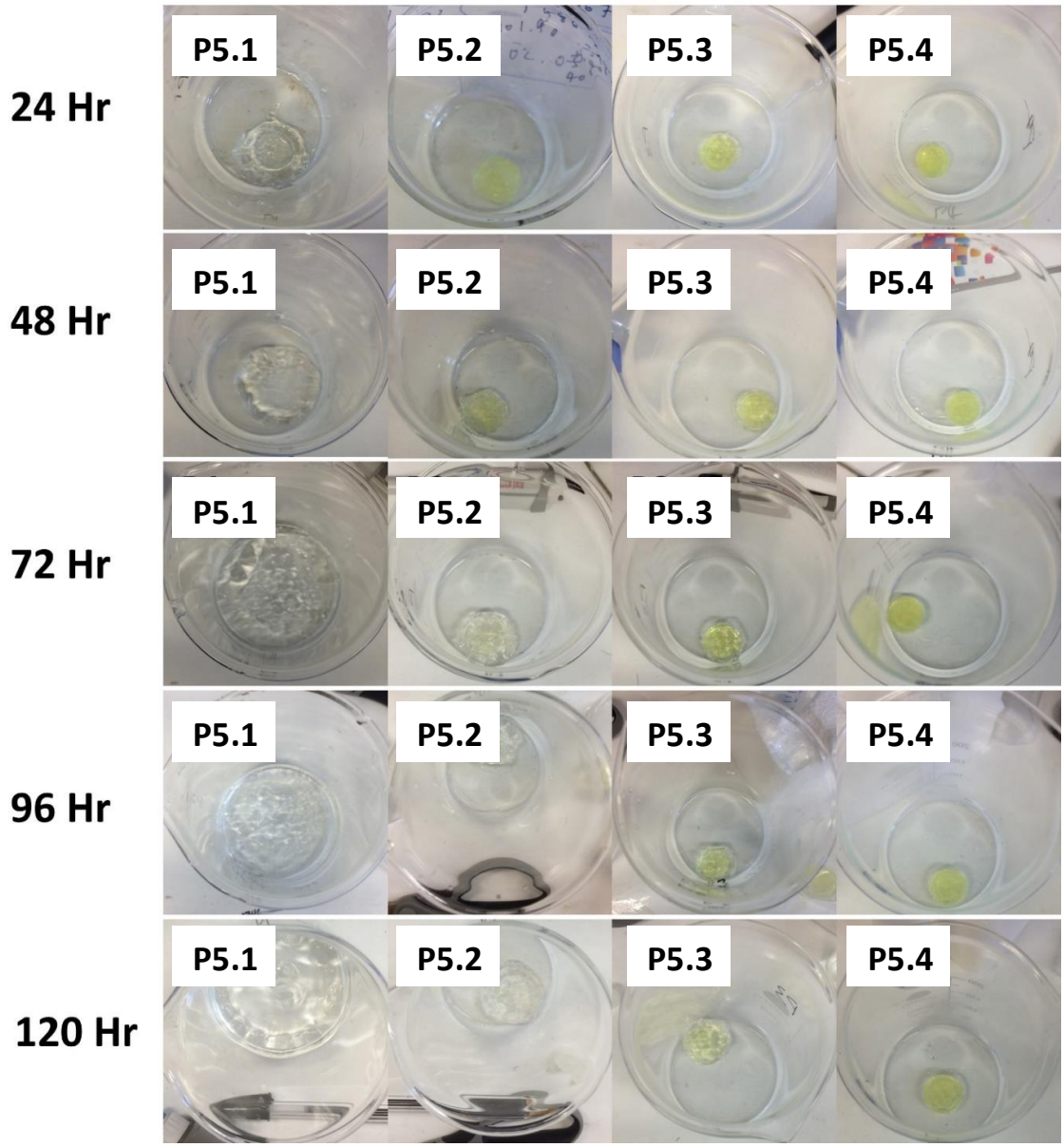

Figure 5.11 Images for the swelling analysis for arsenohydrogels derived from P5.1-P5.4. Numerical data can be found in Table 5.3 (and Graphical data, Fig. 5.12). Swelling was performed in de-ionised water.

Table 5.3: Degree of swelling (W_s-W_0/W_0) x 100 for P5.1-P5.4 in de-ionised water

	Time / hr				
	24	48	72	96	120
P5.1	760	1440	5040	7880	10950
P5.2	160	220	370	540	720
P5.3	100	110	160	170	250
P5.4	25	45	55	65	80

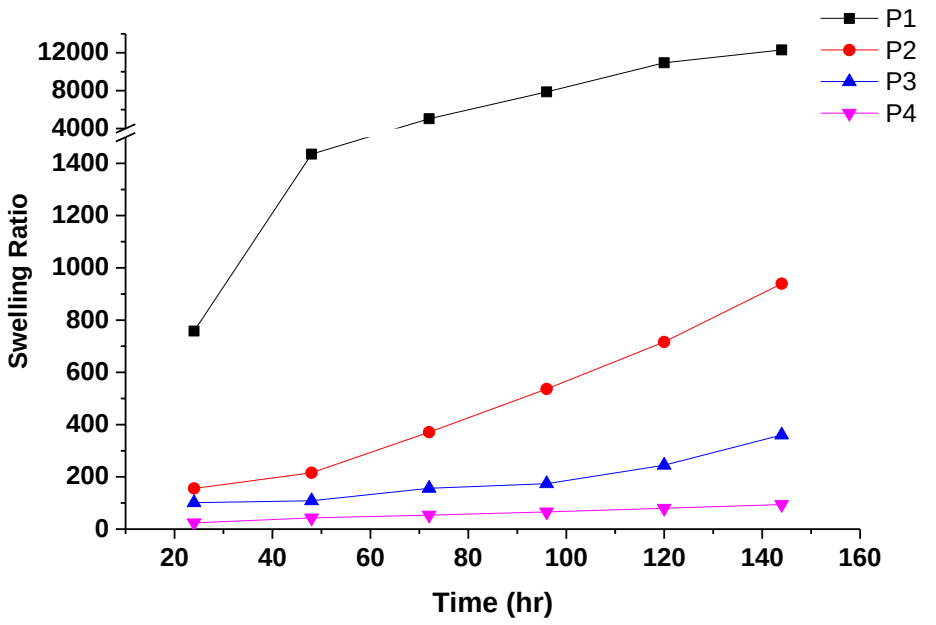

Figure 5.12 Swelling ratio of the arsenohydrogels derived from P5.1-P5.4 calculated as (W_s-W_0)/W_0 x 100 where W_0 is the weight of the hydrogel after drying in the oven and W_s is the weight of the swollen hydrogel at a definite time interval (Table 5.3). Swelling was performed in deionised water.

5.2.3 Biocamptibility of arsenohydrogels

For polymeric arsenicals and arsenohydrogels to be considered for biological applications it is important to consider their cytotoxicity. Thus, polymers **P5.1-P5.4** were investigated for toxicity in vitro using a standard XTT assay. Consistent with our previous results[23-25] the polymers were not toxic up to relatively high concentrations (up to 8 mgml^{-1} Fig. 5.13).

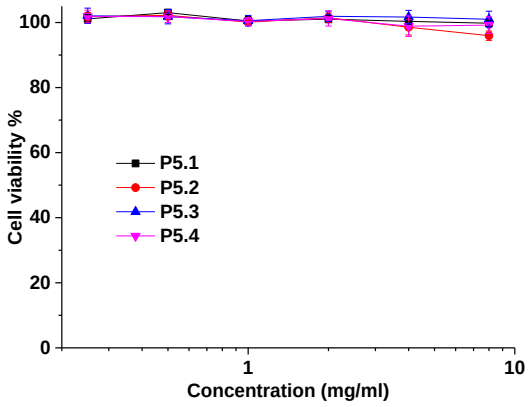

Figure 5.13 XTT cytotoxicity assay of arsenic functional polymers (P5.1-P5.4) with PC3 cells

To investigate the potential use of arsenohydrogels as scaffolds for 3D cell culture, gels were made with **P5.1** and thoroughly purified by dialysis to remove excess H_3PO_2 and KI then dried by lyophilisation. The dried gels were then swollen in the cell growth media containing freshly trypsinized Prostate Cancer cells (PC3), and imaged using confocal fluorescent microscopy. The image of live, replicating cells was conducted using nuclei active staining (Hoechst). The cells retained the spherical morphology (Fig. 5.14) obtained after trypsinisation indicating that the cells were encapsulated in the gel matrix and not fixed to either the surface of the gel or culture plate. This was confirmed by z-stack tomography (Fig. 5.15) which shows that the cells interact with the gel matrix across the entire cell surface which promotes the retention of their spherical morphology.

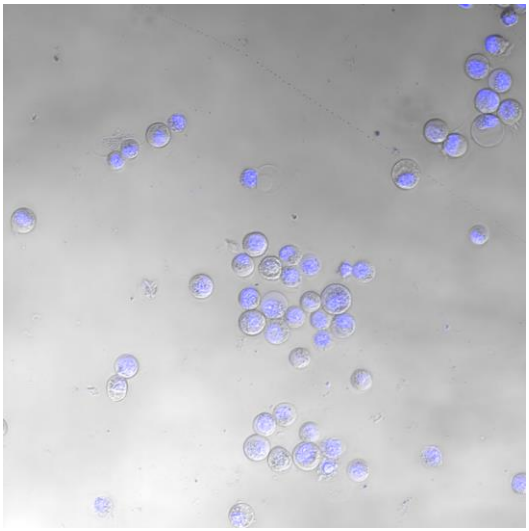

Figure 5.14 Confocal microscopy of arsenohydrogels (P1, 10 wt%, after dialysis and lyophilisation) rehydrated with cell media containing PC3 cells: 20 x magnification with bright field and Hoechst stain.

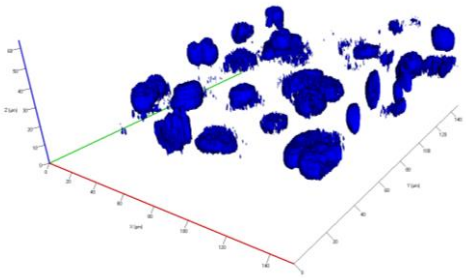

Figure 5.15 z-stack tomography of the PC3 cells encapsulated an arsenohydrogel matrix, imaged with Hoechst dye.

5.2.4 Loading and release of organic arsenicals from arsenohydrogels

The principle of controlled drug release by environmental stimuli has become a central focus in the development of responsive materials for biomedical applications.[33] Considering the oxidative responsive nature of the arsine bonds, and the clinical relevance of organic arsenicals such as 4-(*N*-(*S*-penicillaminylacetyl)amino) phenylarsonous acid (PENAO)[34] and 4-(*N*-(*S*-glutathionylacetyl)amino) phenylarsonous acid (GSAO),[35] the potential to incorporate an organic arsenical as a model therapeutic into the arsenohydrogels was investigated. Thus, it was hypothesised that this could be achieved by physical encapsulation into the gel matrix and/or via covalent incorporation into

domains of As(I)$_n$ cyclooligoarsine crosslinking. To investigate this, arsenohydrogels (2.5 wt%) were prepared in the presence of *p*-arsanilic acid as the model organic arsenical. In the presence of an excess of *p*-arsanilic acid (3.8 wt %), the initial gelation took longer due to incorporation of the monomeric organic arsenical competing with cross-linking between polymeric arsenical chains (4 hours at 60 °C or 2 hours at 80 °C). Interestingly, this competition between cross-linking and incorporation of organic arsenical completely eliminated the syneresis observed previously for the gels derived from **P5.3 and P5.4** at 2.5wt % suggesting a lower degree of cross-linking present in each formulation. The relative release of the *p*-arsanilic acid from the arsenohydrogels at room temperature in aqueous solution and under simulated oxidative stress (aqueous H_2O_2 5 mmol) was monitored by HPLC (Fig. 5.16). In pure aqueous solution, very little release was observed. Conversely, in an aqueous solution containing a stoichiometric amount (with respect to total arsenic content) of H_2O_2, evidence of release of *p*-arsanilic acid was detected over 48 hours until a plateau was reached. A trend in release with respect to copolymer composition was apparent, with the rate and degree of release being inversely proportional to the AsAm mole fraction in the copolymer composition ((**P5.1 > P5.2 > P5.3 > P5.4**). This was attributed to increased covalent incorporation of the *p*-arsanilic acid into the domains of As(I)$_n$ cyclooligoarsine crosslinking.

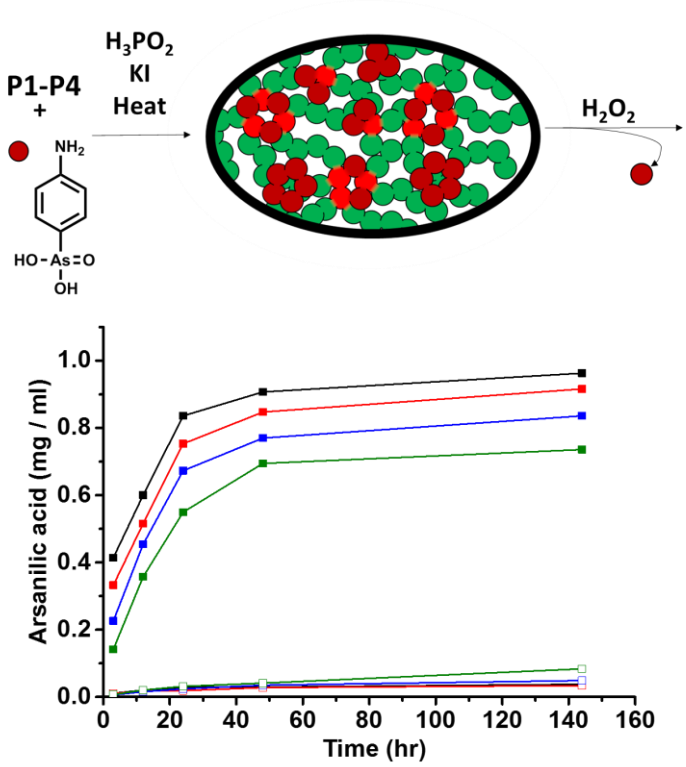

Figure 5.16 Release of p-arsanilic acid from arsenohydrogels from P5.1 (black), P5.2 (red), P5.3 (blue) and P5.4 (green) in aqueous solution (empty) and under simulated oxidative stress using stoichiometric H_2O_2 (filled) (see Appendix C: 5. for supporting information) (see Appendix C, S5.16A, S5.16B, S5.16C, S5.16D and S5.16E for supporting information).

5.3 Conclusions

Arsenohydrogels have been successfully prepared for the first time. Reductive coupling of As(V) to As(I) has been exploited to crosslink high molecular weight (M_w > 300 kDa) polymeric arsenical scaffolds (PDMAm$_x$-*co*-AsAm$_y$). Gels were formed when the polymer weight fraction was ≥ 2.5 wt% with soft gels (G'~ 400 Pa) being formed at 2.5 wt%. Gel strength significantly increased (up to G' = 81 kDa) when the polymer weight fraction was increased to 10 wt%. The properties of the gels depend on the mole fraction of AsAm in the polymer scaffolds as increasing the AsAm mole fraction resulted in increased crosslinking density, reduced swelling capacity and increased resistance to hydrolysis and oxidation of the As-As crosslinks. The polymeric arsenical scaffolds and the resulting arsenohydrogels were found to be non-toxic *in vitro* and the gels were capable of encapsulating PC3 cells within a 3D arsenohydrogel matrix. Finally, the arsenohydrogels have been shown to be functional through the loading of *p*-arsanilic acid

as model arsenical drug. The relative release of model arsenical drug in aqueous solution and under simulated oxidative stress demonstrates the redox responsive characteristics of systems containing organic arsenicals. This investigation further demonstrates the distinctive reactivity and versatility of organic and polymeric arsenicals, and the properties of this first generation of arsenohydrogels are promising for biomaterials applications in the future.

5.4 Experimental

5.4.1 Materials and instruments:

AsAm was synthesised according to the literature.[25] N,N-Dimethylacrylamide (DMA) were filtered through a basic aluminium oxide (activated, basic, Brockman I, standard grade) to remove the radical inhibitor. 2,2′-azobis[2-(2-imidazolin-2yl)propane] dihydrochloride (VA-044, Wako), hypophosphoric acid and HPCL-grade H2O (sigma-aldrich, 50%) were used without further purification.

Nuclear Magnetic Resonance (NMR) spectroscopy (1H NMR spectra) were recorded on a Bruker HD 400 spectrometer (400 MHz) at 27 °C using D2O as solvent and the residual proton signal of the solvent (δ H = 4.75 ppm) was used as internal reference. Chemical shift values (δ) are reported in ppm. ACDLABS software was used to analyse the data obtained. Number-average molar masses (Mn,SEC) and dispersity values (Đ) were determined using Size exclusion Chromatography (SEC). Agilent PL50 instrument equipped with differential refractive index (DRI) detector. The system was equipped with Aquagel OH mixed M column (300 x 7.5 mm) was used alongside with an 8µm aquagel guard column The mobile phase used was 80% NaNO3 in water at 0.1 M and 20% methanol. Samples were run at 1ml/min at 35 °C. Poly(ethylene oxide) standards (Agilent EasyVials) were used for calibration. Analyte samples were filtered through a membrane with 0.45 µm pore size before injection. FT-IR spectrometer using a Golden Gate diamond attenuated total reflection cell and OPUS software was used to analyse the data.

5.4.2 Calculation of AsAm content with respect to DMA by ^{1}H-NMR

Method 1

$$\frac{\int [2[M]_{AsAm} + 2[M]_{DMA}]_{1.0-1.8\,ppm} - \int 4[[M]_{AsAm}]_{7.2-7.8\,ppm}/_2}{2} = [M]_{DMA}$$

Method 2

$$\frac{\int [[M]_{AsAm} + 7[M]_{DMA}]_{2.1-3.0\,ppm} - \int 4[[M]_{AsAm}]_{7.2-7.8\,ppm}/_4}{7} = [M]_{DMA}$$

The value from each method was averaged.

5.4.3 Rheology

The transition from solution phase to gel phase was monitored by following the storage moduli and loss moduli. Measurements were performed on an Anton Paar MCR 302 rheometer using a parallel plate with diameter of x mm and measuring gap of 1 mm. The normal force was kept constant at 1 N during measurements and all measurements were performed at 30 °C (maintained by a Peltier system). All the analysis was conducted by adding pre-gel solution between the plates and forming the gel before or during the analysis. Gel formation was monitored with constant frequency of 1 rad s-1 and a constant strain of 0.1 %. When conducting the amplitude sweep, a constant frequency of 1 rad s-1 was applied and strain was ramped logarithmically from 1 % to 500 %. For the frequency sweep, a constant strain of 0.1 % was applied and frequency was ramped logarithmically from 0.1 to 100 rad s^{-1}. All the data was analysed using RheoCompass software.

5.4.4 Dynamic mechanical analysis (DMA)

Dynamic mechanical analysis was performed on a Perkin Elmer DMA8000 in tension mode. Frequency sweeps were performed from 1 to 25 Hz at room temperature (approximately 25 °C). Hydrogels were prepared in silicone moulds as standard and then cut to size before mounting in the DMA (approximately 13 mm width, 4 mm thickness).

5.4.5 Reverse Phase High performance liquid chromatography (RP-HPLC)

Both sample analysis conducted from a RP-HPLC system (Agilent 1260 infinity series stack) equipped with a 1260 Quat Pump VL, a degasser and a fraction collector (FC-AS). Samples were injected using Agilent 1260 auto-sampler with 5 µL injection (Draw and injection of 200 µL/min). The RP-HPLC was fitted with Eclipse XDB-C18 column (150 x 4.6 mm) 5 micron packing (100Å). Detection was achieved using an Agilent 1260 variable wavelength detector connected in series with UV detection monitored at 280 nm. The total flow rate was set to 1.0 mL/min and the temperature of the column was set to 20 °C. The mobile phase condition is as follows. Mobile phase A: 100% water with 0.04%v/v TFA; Mobile phase B: 100% MeCN with 0.04%v/v TFA (see SI for gradient). The standard analysis method is as followed:

Time (min)	A (%)	B (%)
0.00	90.0	10.0
15.00	50.0	50.0
25.00	0.0	100.0
27.00	90.0	10.0
35.00	90.0	10.0

5.4.6 SEM and EDX analysis

SEM analysis together with EDX was performed to determine the pore structure and arsenic content of the gels. The prepared hydrogels were cut using a scalpel to expose the internal structure, a roughly 3 mm2 fragment was then mounted onto SEM stages using double sided conductive copper tape, which served as an adhesive and provided electrostatic screening. The samples were subsequently coated in gold for 15 seconds using a Polaron 5C 7640 sputter coater and the surface structure visualised using a Zeiss Gemini SEM- field emission scanning electron microscope at an accelerating voltage of

either 10 or 15 keV. Elemental analysis was carried out during SEM imaging on the same samples using an Oxford instruments X-Max 150 large area SDD electron dispersive X-ray analysis (EDX) detector.

5.4.7 Cell viability

Cell viability. PC3 (human prostate cancer) cells were cultured in High Glucose DMEM medium supplemented with 10% fetal bovine serum. For cell viability evaluation, PC3 cells were seeded in a 96 well plate at a density of 1 × 104 cells per well. After 16 hours, the culture medium was replaced by fresh media containing a series of dilution of the polymers (0.25, 0.5, 1, 2, 4 and 8 mgml-1), prepared from stock solutions in PBS at 500 μM. Following 24 hours incubation, the medium was removed and replaced with fresh medium. The cells were incubated with a freshly prepared solution of XTT (0.2 mg/mL-1) and *N*-methyl dibenzopyrazine methyl sulfate (250 μM) in medium for 16 hours. Absorbance of the samples was finally measured using a plate reader at 450 nm and 650 nm. The data presented are representative of a minimum of two independent experiments where each sample was measured in triplicate. Errors reported correspond to the standard deviation of the mean.

5.4.8 Fluorescent confocal imaging of cells seeded in arsenohydrogels

In each chamber slide, 30 000 cells of PC3 (prostate cancer cell-line) in 300 μl of DMEM media were seeded together with the dried hydrogel (vide infra). Also, the control cells without a hydrogel were prepared and incubated for 24 hours at 310 K. The co-culture of PC3 and hydrogel was stained by adding 12 ul dye Hoechst 33342 (1 mg/ml) which targets nucleus (60 min, 310 K). Samples were analysed using a Zeiss LSM710 laser scanning confocal microscope (Diode laser; excitation: 405 nm; blue emission: 410-585 nm). 12-bit images were obtained at room temperature using an EC Epiplan-Neofluar 20x /0.50HD M27 and a C-Apochromat 63X /1.20 W Korr M27 with ImmersolW immersion fluid on the objective lens on the microscope. The image stacks were projected along the z-axis using either sum-intensity or maximum-intensity projections. Data were processed using ZEN 2012 software for Windows (Zeiss).

Synthetic methods

5.4.9 General Procedure for polymer synthesis via Free Radical Polymerisation.

AsAm was solubilised in water with 1 eq of Sodium Hydroxide and added into a cooled aqueous solution of DMA (1 M) with VA-044 (0.01 eq with respect to total monomer content). The solution was degassed for 15 minutes before heating the solution at 90 °C for 2 hours. The full consumption of the monomer was confirmed by NMR before freeze drying directly to yield white solids (> 99 %).

5.4.10 General Procedure for arsenohydrogel synthesis.

For 2.5 wt % gels 25 mg of AsAm bearing polymers (P1-P4) was initially dissolved in 800 µL of HPLC grade water before adding 200 µL of concentrated hypophosphoric acid solution (50%) and 10 µL of 3 wt % potassium iodide solution. The solution was heated at 60 °C for 30 minutes, this resulted in successful clear gel formation however P3 and P4 macroscopic gel contraction was observed. For 10.0 wt % gels 100 mg of AsAm bearing polymers (P1-P4) was initially dissolved in 800 µL of HPLC grade water before adding the 200 µL of concentrated hypophosphoric acid solution (50%) and 10 µL of 3 wt % potassium iodide solution. The solution was heated at 60 °C for 30 minutes, this resulted in formation of pale yellow gels and stable to syneresis.

5.4.11 Gel Prep for Cell seeding

10 wt% arsenohydrogels were prepared as described above, in 2 ml solution on a 3 cm diameter silicon mould. The gels were then dialysed in 100 ml deionised water over 24 hours changing the water 6 to 8 times. Dried arsenohydrogels were obtained by lyophilisation.

5.4.12 Loading arsenohydrogels with model organic arsenical.

For 2.5 wt % gels 250 mg of AsAm bearing polymers (P1-P4) was initially dissolved in 8 ml of HPLC grade water before adding the 2 mL arsanilic acid (380 mg) freshly dissolved in concentrated hypophosphoric acid solution (50%) and 100 µL of 3 wt %

potassium iodide solution. The solution was heated at 60 °C for 4 hrs, this resulted in dark red gels.

5.4.13 Release study of the arsanilic acid loaded arsenohydrogels with RP-HPLC.

The 2.5 wt% gels described above were loaded with arsanilic acid in 50 ml falcon tubes in HPLC grade water, filling up to 50 ml line. The aqueous phase was stirred regularly without disturbing the gels, 200 µL sample from aqueous phase was taken at 3 hr, 12 hr, 24 hr, 48 hr and 144 hr for HPLC analysis. The arsanilic acid released was identified by comparing the arsanilic acid (in hypophosphoric acid solution) to assign the retention time of the arsanilic acid released. The height of the intensity of the peak corresponding to arsanilic acid was measured and compared to the theoretical maximum concentration after release (7.6 $mgml^{-1}$).

5.4.14 Hydrogen peroxide mediated release study of the arsanilic acid loaded arsenohydrogels with RP-HPLC.

200 µL of 30 wt % H_2O_2 (approximately stoichiometrically equivalent to arsanilic acid) was added to the following to study described above in parallel.

5.5 References

1. Z. Yinyu, L. Yongmao and L. Wenguang, *Adv. Funct. Mater.*, 2015, **25**, 471-480.
2. A. Erbas and M. O. de la Cruz, *Acs Macro Lett.*, 2015, **4**, 857-861.
3. E. A. Appel, J. del Barrio, X. J. Loh and O. A. Scherman, *Chem. Soc. Rev.*, 2012, **41**, 6195-6214.
4. A. Gutierres, S. Pascual, L. Fontaine, S. Pioge and L. Benyahia, *Polym. Chem,*, 2018, **9**, 2494-2504.
5. M. J. Webber, E. A. Appel, E. W. Meijer and R. Langer, *Nat. Mater.*, 2016, **15**, 13-26.
6. Y. S. Zhang and A. Khademhosseini, *Science*, 2017, **356**.
7. Z. Chongyu, Z. Jinxin, K. Kristian, W. Paul, W. Jiping, V. Tony, L. Jian, D. T. P., W. M. R. and H. D. M., *Macromol. Biosci.*, 2017, **17**, 1600320.
8. I. Y. Jung, J. S. Kim, B. R. Choi, K. Lee and H. Lee, *Adv. Healthcare Mater.*, 2017, **6**.
9. B. Yang, Y. Zhang, X. Zhang, L. Tao, S. Li and Y. Wei, *Polym. Chem,*, 2012, **3**, 3235-3238.
10. J. Carthew, J. E. Frith, J. S. Forsythe and V. X. Truong, *J. Mater. Chem. B*, 2018, **6**, 1394-1401.
11. M. Liu, X. Zeng, C. Ma, H. Yi, Z. Ali, X. B. Mou, S. Li, Y. Deng and N. Y. He, *Bone Res.*, 2017, **5**.
12. H. Kai, T. Yamauchi, Y. Ogawa, A. Tsubota, T. Magome, T. Miyake, K. Yamasaki and M. Nishizawa, *Adv. Healthcare Mater.*, 2017, **6**.
13. J. J. Cash, T. Kubo, D. J. Dobbins and B. S. Sumerlin, *Polym. Chem,*, 2018, **9**, 2011-2020.
14. H. Towbin, T. Staehelin and J. Gordon, *Proc. Natl. Acad. Sci. U.S.A.*, 1979, **76**, 4350-4354.
15. D. Roy, J. N. Cambre and B. S. Sumerlin, *Prog. Polym. Sci.*, 2010, **35**, 278-301.
16. Y. Yang and M. W. Urban, *Chem. Soc. Rev.*, 2013, **42**, 7446-7467.
17. H. Qian and I. Aprahamian, *Chem. Commun.*, 2015, **51**, 11158-11161.
18. F. Karimi, J. Collins, D. E. Heath and L. A. Connal, *Bioconjugate Chem.*, 2017, **28**, 2235-2240.
19. J. J. Cash, T. Kubo, A. P. Bapat and B. S. Sumerlin, *Macromolecules*, 2015, **48**, 2098-2106.
20. H. S. Yu, Y. A. Wang, H. Y. Yang, K. Peng and X. Y. Zhang, *J. Mater. Chem. B*, 2017, **5**, 4121-4127.

21. P. J. Dilda and P. J. Hogg, *Cancer Treat. Rev.*, 2007, **33**, 542-564.
22. T. Joji, D. T. P. and W. Paul, *Macromol. Rapid Commun.*, **0**, 1800205.
23. C. Footman, P. A. J. M. de Jongh, J. Tanaka, R. Peltier, K. Kempe, T. P. Davis and P. Wilson, *Chem. Commun.*, 2017, **53**, 8447-8450.
24. P. Wilson, A. Anastasaki, M. R. Owen, K. Kempe, D. M. Haddleton, S. K. Mann, A. P. R. Johnston, J. F. Quinn, M. R. Whittaker, P. J. Hogg and T. P. Davis, *J. Am. Chem. Soc.*, 2015, **137**, 4215-4222.
25. J. Tanaka, S. Tani, R. Peltier, E. H. Pilkington, A. Kerr, T. P. Davis and P. Wilson, *Polym. Chem,*, 2018, **9**, 1551-1556.
26. K. Naka, T. Umeyama and Y. Chujo, *J. Am. Chem. Soc.*, 2002, **124**, 6600-6603.
27. L. N. C., M. H. W., N. B. K. and R. R. S., *Angew. Chem. Int. Ed.*, 2005, **44**, 941-944.
28. A. Morales-Burgos, E. Carvajal-Millan, Y. López-Franco, A. Rascón-Chu, J. Lizardi-Mendoza, N. Sotelo-Cruz, F. Brown-Bojórquez, A. Burgara-Estrella and M. Pedroza-Montero, *Polymers*, 2017, **9**, 164.
29. U. Tomokazu, N. Kensuke and C. Yoshiki, *J. Polym. Sci., Part A: Polym. Chem.*, 2004, **42**, 3023-3028.
30. U. Tomokazu, N. Kensuke and C. Yoshiki, *J. Polym. Sci., Part A: Polym. Chem.*, 2004, **42**, 3604-3611.
31. T. Umeyama, K. Naka and Y. Chujo, *Macromolecules*, 2004, **37**, 5952-5958.
32. T. Umeyama, K. Naka, A. Nakahashi and Y. Chujo, *Macromolecules*, 2004, **37**, 1271-1275.
33. P. A. de Jongh, A. Mortiboy, G. S. Sulley, M. R. Bennett, A. Anastasaki, P. Wilson, D. M. Haddleton and K. Kempe, *ACS Macro Lett.*, 2016, **5**, 321-325.
34. P. J. Dilda, S. Decollogne, L. Weerakoon, M. D. Norris, M. Haber, J. D. Allen and P. J. Hogg, *J. Med. Chem.*, 2009, **52**, 6209-6216.
35. L. Horsley, J. Cummings, M. Middleton, T. Ward, A. Backen, A. Clamp, M. Dawson, H. Farmer, N. Fisher, G. Halbert, S. Halford, A. Harris, J. Hasan, P. Hogg, G. Kumaran, R. Little, G. J. M. Parker, P. Potter, M. Saunders, C. Roberts, D. Shaw, N. Smith, J. Smythe, A. Taylor, H. Turner, Y. Watson, C. Dive and G. C. Jayson, *Cancer Chemother. Pharmacol.*, 2013, **72**, 1343-1352.

Chapter 6 : Conclusion and perspective

The use of organoarsenic in the field of polymer and biomaterials science has been largely overlooked due to concerns regarding the toxicity of arsenic. Arsenic is a distinctive element that exhibits diverse chemical reactivity depending upon its oxidation state. It's chemical properties and interaction at the biological interface alludes to potential applications in biomaterial science. Arsenic can exist in various oxidation states, (V, III and I), with As(I) capable of forming cyclic oligomers through the formation of As-As bonds. Polymeric arsenicals have been previously synthesised through polycondensation, exploiting the Lewis acid properties of the arsenic centres (As(V), As(III)). Additionally, As(I) oligomers have been copolymerised with acetylenes through radical mediated homolysis. The focus of the work in this thesis, was to generate nanoparticles and hydrogels with tuneable and functional properties through cross-linking polymers with the unique properties of arsenic and investigate their properties as potential candidates for biomaterials applications.

To this end, acrylamidic monomer(s) with pendant arsanilic acid groups used for cross-linking were synthesised from commercially available phenylarsonic acid derivative, *p*-arsanilic acid. This enabled convenient synthesis one-pot synthesis of the arsenic acid containing monomer (AsAm) by functionalising the aromatic amine.

In Chapter 2, thermoresponsive PEGA-NIPAm diblock copolymers were generated through aqueous SET-LRP, with random incorporation of AsAm in either the PEGA or NIPAm blocks, using sodium hydroxide to solubilise AsAm. The resulting polymers self-assembled at elevated temperatures. When AsAm was presented in the core forming NIPAm block, the self-assembly was found to be pH dependent, forming nanoparticles when the pH was below the pK_a of the arsenic acid. Nevertheless, the aim of this initial investigation was to cross-link polymers through reductive coupling of arsenic acid (As(V)) to oligomeric arsines (As(I)), which involved using hypophosphorous acid as a reducing agent, rendering the pH suitable for self-assembly. The formation of nanoparticles was monitored by dynamic light scattering. Upon cooling back to room temperature, retention of the nanoparticle at room temperature was indicative of

successful cross-linking. Reductive coupling of AsAm stabilised the nanoparticles when AsAm was present in the core forming NIPAm, however it did not yield stable nanoparticles when the AsAm was presented on corona forming PEGA block. Further study showed the stability of the nanoparticle increased with increasing incorporation of AsAm in the polymer.

In Chapter 3, nanoparticles were generated with equivalent polymer scaffolds, synthesised by RAFT polymerisation, through addition of poly-thiol cross-linkers. As an external thiol cross-linker was used to stoichiometrically react with the AsAm units, it was important to determine the monomer feed in the polymer composition as accurately as possible. In this study a pinacol protected arsenical acrylamide was co-polymerised into the core forming NIPAm block using TFE as a solvent. The deprotection undermildly acidic dialysis yielded As(V) functional polymers equivalent to those in chapter 2. The cross-linking density was tuned by thiol functionality of the cross-linker, forming stable nanoparticles with tetra-thiol (PTM), tri-thiol (TTM) and di-thiol (HDT) cross-linkers. When 100% cross-linking was targeted ([SH]:[As] = 2), the N_{agg} and topology of the nanoparticles were concentration dependent due to inter-particle interaction and aggregation. However when 50% cross-linking was targeted the ([SH]:[As] = 1), nanoparticles exhibited more spherical character and less concentration dependency on aggregation. The aim of this work was to investigate arsenic-thiolate bonds as responsive cross-linking form the polymeric arsenical nanoparticles. The stability of the nanoparticles correlated with the thiol functionality of the cross-linker and the targeted [SH]:[As]. As a result, nanoparticles formed with tetra-thiol and tri-thiol cross-linker did not dissemble in presence of glutathione, via thiol exchange due to an entropic barrier, however dissembled when di-thiol cross-linker was observed. The stability towards oxidation by hydrogen peroxide increased with increasing thiol functionality (di- < tri- < tetrathiol) and thiol stoichiometry ([SH] : [As] = 2.0 : 1.0 > 1.0 : 1.0). Interestingly the nanoparticles with 100% cross-linking were more toxic, which was attributed to the release of the cross-linker within the cell. Considering the potential for these nanoparticles as drug delivery vectors, the responsivity of arsenic thiolate-bond demonstrates promising scope for drug release as well as degradability.

Cyclic arsine(I) oligomers are known to undergo RCRAC with acetylenes to form alternating poly(vinylene-arsines), which have been previously reported to be resistant to oxidation by hydrogen peroxide. Considering the previous nanoparticles formed through As(I) oligomerisation and arsenate-thiolate bonds discussed in the chapter 2 and 3 were prone to oxidation and therefore dissembled in presence of hydrogen peroxide, it was therefore interesting to investigate cross-linking through the formation of vinylene-arsine bonds to form resilient nanoparticles in the subsequent Chapter. In Chapter 4, PEGA-NIPAm diblock copolymers with AsAm incorporated in the NIPAm block were generated by RAFT polymerisation as discussed in chapter 3, then As(I) cross-linked nanoparticles were formed *in-situ* via reductive coupling of AsAm as discussed in Chapter 2. When water soluble acetylenes, propargyl alcohol were added with radical initiator source, stable nanoparticles were formed. To study further the robustness of this cross-linking polymerisation strategy, propargyl amine and propiolic acid were also investigated as acetylene source, which yielded stable nanoparticles, thus demonstrating the functional group tolerance of this strategy. It is important to note that all the nanoparticles cross-linked through this strategy did not dissemble in presence of hydrogen peroxide using the previously used condition (chapter 2 and 3), consistent with the reported properties of poly(vinylene-arsine) polymers.

As this unique strategy enables introduction of additional functionality through the acetylene motif, the next goal in this chapter was to incorporate a fluorescent label to help determine the cellular uptake and the co-localization of the nanoparticle. To this end, propargyl-*O*-rhodamine B ester was synthesised and polymerised with As(I) cross-linked nanoparticles. The subsequent fluorescently labelled nanoparticles were shown to be successfully taken up by PC3 cells after 2 hours of incubation. Confocal fluorescent microscopy shows diffuse distribution of the nanoparticles throughout the cell with the lack of lysosomal co-localisation. Interestingly strong mitochondrial co-localisation was observed, suggesting a biochemical property of mitochondrial tagging effect of As(III) was retained.

The focus in chapters 2 to 4 was generating polymeric nanoparticles using arsenical pendant groups presented in well-defined diblock copolymers as cross-linking motifs. In

Chapter 5, the reductive coupling described in chapter 2 is utilised to form chemical cross-linked hydrogels. Poly($DMAm_x$-$AsAm_y$) were synthesised by FRP, and hydrogels were made at concentrations low as 2.5 wt% when cross-linked through the formation of As(I) oligomerisation. However at higher cross-linking density ([DMAm]:[AsAm] < 96 : 4) the hydrogels underwent syneresis, which were preventable at higher weight concentration (10 wt%). The hydrogels were responsive towards oxidation, showing an increasing swelling profile as a result of oxidation, which was sensitive to the cross-linking density. 3D cell culturing of these gels was carried out by rehydration of dialyzed/lyophilized gels with trypsinized solution of cells. Finally, *p*-arsanilic acid, as a model arsenical drug, was encapsulated in the hydrogels by reductive coupling and formation of the bridging polymer-arsanilic acid As(I) mixtures. The release of the *p*-arsanilic acid was stimulated by oxidation with H_2O_2, where increased covalent incorporation of the *p*-arsanilic acid into the domains of $As(I)_2$ cyclooligoarsine crosslinking was found to slow the release, as observed with higher incorporation of AsAm in the polymer.

Further work to generate arsenohydrogels through addition of multithiol cross-linking agent or further curing of As(I) cross-linked arsenohydrogels through RCRAC (used in chapter 4) and investigate the chemical/physical/mechanical properties would be interesting.

In conclusion, this investigation demonstrates the distinctive reactivity and versatility of polymeric arsenicals, and the properties of this first generation of polymeric nanoparticles and arsenohydrogels chemically cross-linked through arsenic centres are promising for biomaterials applications in the future. Furthermore, considering the potential for biomedical application, all the materials polymers and nanoparticles were not toxic (2 mg/ml) when examined by standard XTT assay. In the future, *in-vivo* investigations would be interesting to evaluate the further the biocompatibility of polymeric arsenicals, more specifically long term toxicity and biodistribution.

Chapter 7 Microscale Synthesis of Multi-block Copolymers Using Ultrafast-RAFT Polymerization

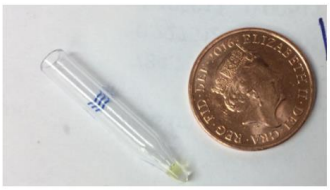

- ✓ Ultralow volume
- ✓ Presence of air
- ✓ No deoxygenation
- ✓ Ultrafast RAFT (3 mins per block)
- ✓ Iterative multichain extensions
- ✓ 2 µL per block
- ✓ 10 µL pentablock copolymer

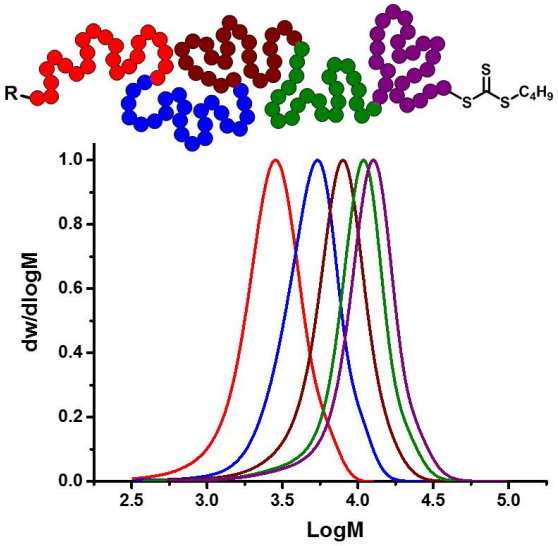

ABSTRACT:

Ultrafast reversible addition-fragmentation chain-transfer polymerization (RAFT) in presence of air was previously described. Herein, we demonstrate this method can be scaled down to 2 µL using inserts typically used in vials for SEC analysis, as a polymerization vessel. By careful cooling and mixing of the sequential monomers between chain extensions, well defined pentablock copolymers were successfully generated with a total volume of 10 µL. This work demonstrates the suitability of scale applicable to microarray combinatorial chemistry.

7.1 Introduction

Polymerization in standard chemistry laboratory reaction vessels becomes increasingly difficult at increasing smaller scales. Transfer of advanced polymer synthesis techniques to smaller scales will allow for the high-throughput screening of polymer composition for biomaterial discovery and has previously been demonstrated by step growth polymerisations.[1, 2] However low scale-screening using controlled polymerizations methods was only recently achieved by Chapman *et al* to investigate the influence of polymer architecture on materials properties.[3]

Typically polymerizations are carried out with reaction volumes between 50 ml and 0.5 ml,[4-7] as these ranges are practical for the conventional reaction vessels and deoxygenation processes necessary for typical Reversible Deactivation Radical Polymerization (RDRP). Note that, the latter condition limits scales of the reactions, as using nitrogen sparging or freeze pump thaw cycles to deoxygenate the reaction media is not practical at ultralow volume, due to inherent loss of volatile monomer and solvents. Hence oxygen tolerant RDRP protocols are necessary to allow polymerizations to be carried out at microscale. To this end, Boyer *et al* have performed ultralow volume reactions (20 μL) in 96 well plates, using photo-catalysed redox Reversible Addition Fragmentation Chain Transfer (RAFT) polymerization without deoxygenation in presence of air.[8] This enabled screening of different homopolymers, diblock copolymers, star architectures and nanoparticles formulations.

RDRP protocols without deoxygenation have become an emerging topic, however many of these protocols requires external stimuli,[9] additives[8] or oxygen scavenging enzymes,[3, 10, 11] which deviates from the simplicity of RDRP protocols. To address this, Gody *et al.* demonstrated standard RAFT polymerization using only conventional ingredients used for RAFT polymerization, without degassing, in vessels open to air.[12] This elegant and simple approach takes advantage of the fast propagation of monomers in water a solvent known to increase the rate of radical polymerization, which is further accelerated at elevated temperatures. This ultrafast RAFT polymerization was generally demonstrated with acrylamide-based monomers with 2,2'-azobis[2-(2-imidazolin-2-yl)propane]dihydrochloride (VA-044) as an initiator (10 hr ½ life = 44 °C) and heating to

100 °C, allowing iterative chain extensions to synthesize multiblock copolymers (MBCPs) within 3 minutes per block such that monomer is fully consumed before the initiator is fully decomposed (approximately 80%).[12]

MBCPs are macromolecules with defined control over block sequence and that can be synthesized from just simple chemical ingredients without complex biological machineries, and are amenable to industrial scales.[13-15] The synthesis of MBCPs has been progressed more recently with RDRP, including copper mediated polymerization[16-24] and RAFT polymerization.[25-31] In spite of the inevitable small number of radical termination events, 21 iterative block extensions have been reliably demonstrated with these methods.[32] Furthermore, these routes are popular as they allow incorporation of monomers of various functional groups[33-38] and do not require exhaustively dried reagents and environments, required for ionic living polymerization systems.[39] Recently, work on sulfur-free RAFT polymerization offers the potential for MBCP synthesis amenable to industrial scales.[32, 40, 41] However, the possible benefits of scaling down MBCP synthesis is often overlooked in academic settings. Industry often relies on the inexpensive small scale combinatorial reactions or optimisation before larger scale synthesis of the preferred choice or optimized conditions. Microscale MBCP synthesis could have applicability in high throughput microarrays,[42] thus allowing the implications in permutations of monomers and block lengths of MBCPs to be rapidly investigated.

Here, it is proposed that the aforementioned ultrafast RAFT protocol could be applicable in microliter scale reactions due to the rapid consumption of the monomer without deoxygenation. Thereby demonstrating the synthesis of MBCPs at a scale suitable for applications such as microarray patterning and combinatorial chemistry with conventional ingredients for RAFT polymerization.

7.2 Results and Discussions

7.2.1 Scaling down

To counteract the inherent problem of increased air/water interface when scaling down the protocol proposed by Gody *et al.*, we used a narrow micro-volume glass inserts (4.6

mm diameter, 200 µL capacity) with conical bottoms (cone volume = approximately 20 µL) that are typically fitted into a standard 2 ml vials for HPLC/GPC analysis for low volume analyses. A master mix of the RAFT agent, monomer, solvent and initiator was made as "all-in-one" stock solution and added into the insert using a standard micropipette (scheme 7.1). This mix was made following closely to the published protocol,[12] using VA0-44 as an initiator (3×10^{-3} M, $[CTA]/[I]_0 = 40$) and *N*-acryloyl morpholine (NAM) as suitable acrylamidic monomer ($[M]_0 = 3$ M) in aqueous mixture and 2-(((butylthio)-carbonothioyl)thio)propanoic acid (PABTC) as a RAFT agent. The inserts were then heated in an oil bath at 100 °C for 3 minutes. In contrast to the previous study where the temperature of the reaction increase was gradual, taking 80 seconds to reach 96 °C,[12] we assume the temperature of the reaction to reach equilibrium almost immediately. Conveniently as the polymerizations were carried in SEC vial inserts, the reaction mixture was directly diluted with SEC eluent within the insert, and injected directly for SEC analysis (Figure 7.1). A duplicate reaction was carried out to dilute with NMR solvent (d_6-DMSO) to measure monomer conversion by NMR.

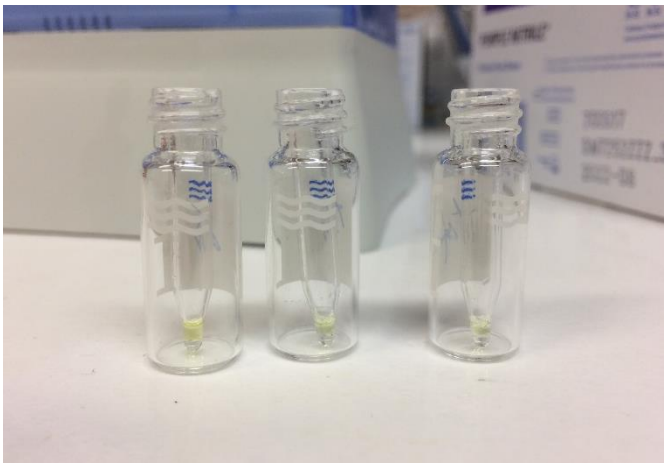

Figure 7.1 Figure Photograph of the inserts in the GPC vials before dilution.

Preliminary experiments were designed to investigate the absolute limit of scale for the solution-based polymerization. Initially this was investigated with a targeted degree of polymerization (DP) of 25 using 20 % dioxane to aid the solubility of the CTA. At 10 µL ($M_{n,SEC}$ = 2200; $Đ$ = 1.23), 5 µL ($M_{n,SEC}$ = 2600; $Đ$ = 1.23), and 2 µL ($M_{n,SEC}$ = 2600; $Đ$ = 1.29) we were able to reproducibly obtain $PNAM_{25}$ as observed by SEC analysis (Figure

7.2) with a slight increase in dispersity at the microliter scale, however comparable to polymerization carried out in 5.4 ml test tubes (termed macroscale in this paper) ($M_{n,SEC}$ = 2700 g mol^{-1}; $Đ$ = 1.19). At 1 µL ($M_{n,SEC}$ = 2600 g mol^{-1}; $Đ$ = 1.42) scale polymers were obtained, but results were not reproducible. The weight loss due to evaporation was also noted (Table 7.1), which suggests that the effect of evaporation was detrimental at 1 µL scale. Hence we presume that 2 µL is the lower scale limit achievable with this method.

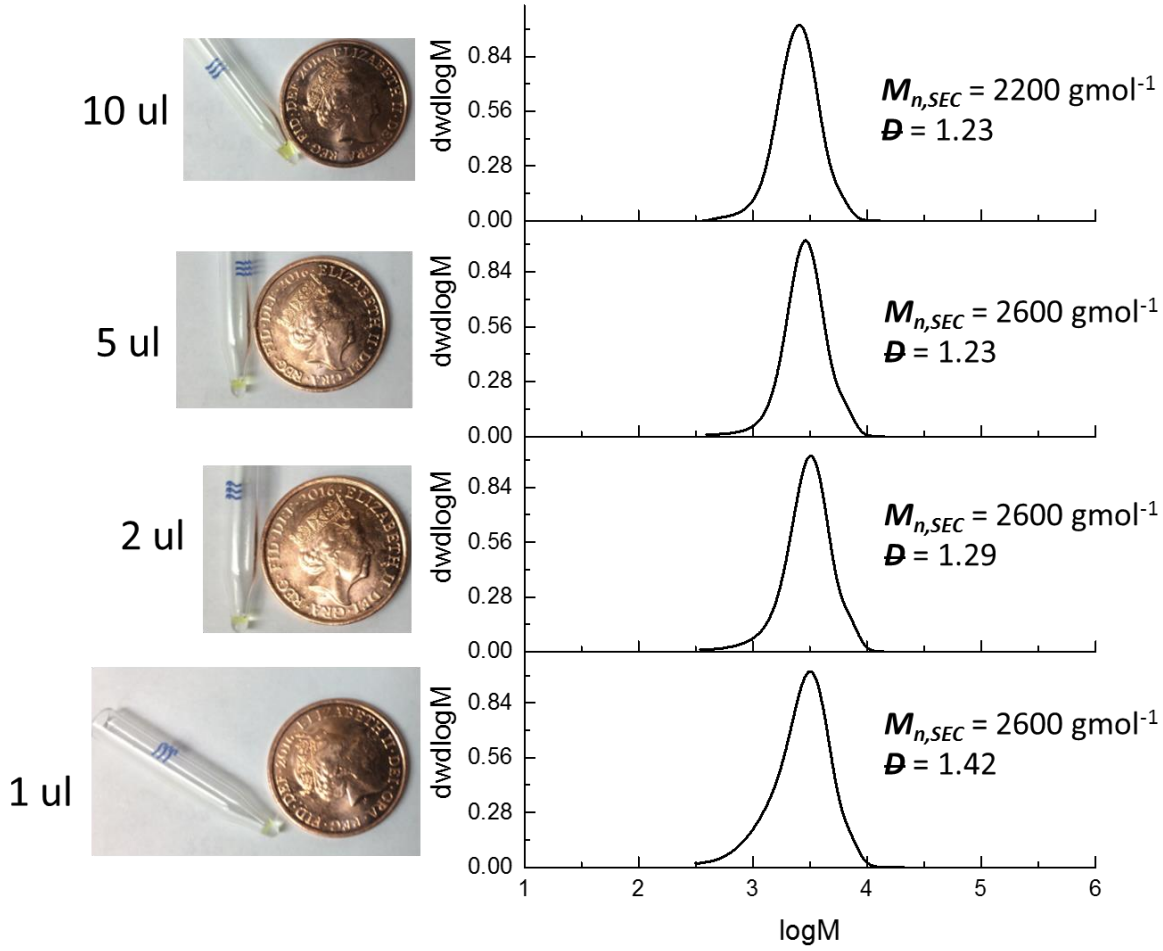

Figure 7.2: Polymerisation of P[NAM]$_{25}$ carried out different scale inside microvolume inserts. At range of scales: 10 µL, 5 µL, 2 µL and 1 µL. It's important to note that at 1 µL scale the results are not reliably reproducible.

Table 7.1: The percentage of the weight loss in the microvolume inserts from evaporation.

Scale	Percentage of weight loss
10 µL	14 %
5 µL	26 %
2 µL	43 %
1 µL	46 %

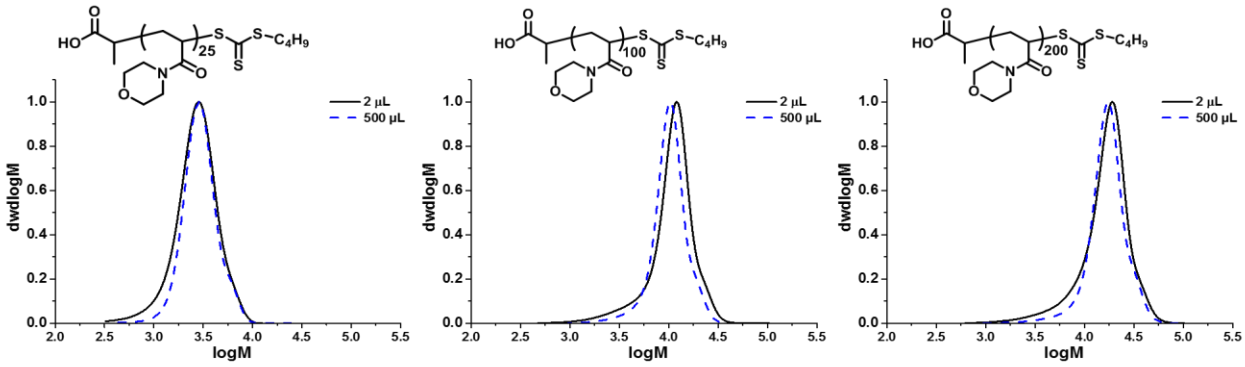

Figure 7.3: SEC analysis (DRI, $CHCl_3$) of $P(NAM)_n$ (n = 25, 100 and 200) in microscale (2 µL) in microvolume inserts and normal scale (500 µL) in conventional test tubes (5.4 ml). All the polymerization carried out under 3 minutes without stirring, deoxygenation and open to air.

7.2.2 Varying DP_n of $P(NAM)_n$ at 2 µL scale

Next, this protocol was applied to synthesise longer polymer chain lengths of $P(NAM)_n$ (Figure 7.3). Increasing the chain length four-fold (DP_n = 100), required a slight modification of the master mix (10 % dioxane; $[I]_0 = 1 \times 10^{-3}$ M, $[CTA]/[I]_0 = 30$). Pleasingly polymerization yielded $PNAM_{100}$ at 2 µL scale ($M_{n,SEC}$ = 9200 g mol^{-1}; $Đ$ = 1.36), in contrast to macroscale the molecular weight distributions was relatively broader by SEC analysis ($M_{n,SEC}$ = 8900 g mol^{-1}; $Đ$ = 1.19). Increasing the length further (DP_n = 200), increased the dispersity at 2 µL scale ($PNAM_{200}$, $M_{n,SEC}$ = 26800 g mol^{-1}; $Đ$ = 1.43), compared to the macroscale equivalent ($M_{n,SEC}$ = 15000 g mol^{-1}; $Đ$ = 1.23). SEC analysis in all cases revealed slightly higher dispersity due to appearance of low molecular tailing.

Also the ^{1}H NMR spectra revealed more residual monomer was present (approximately 2-3 % more). As targeting DP of 25 of NAM yielded relatively narrow dispersity at 2 µL scale, we therefore decided to keep this a constant block length for our MBCPs.

7.2.3 Iterative multi-chain extension at 2 µL per block scale

In order to generate MBCP's through iterative chain extension with the current protocol, it was important to consider the limitation of mixing sequential monomers in the polymerization mixture, as stirring during polymerization is unfeasible at the 2 µL scale. To maximise the mixing of each monomer aliquot the polymerization reaction mixture was cooled prior to addition of new monomer and stirred before heating again at 100 °C for successful sequential chain extension. This circumvented the need for continual stirring during the addition of sequential monomers. Thus by adopting this necessary measure of cooling and mixing before reheating (Scheme 7.1), successive chain extensions were possible within the insert vials to synthesize a homopolymer in five successive chain extensions, $P(NAM_{25})_5$, at 5 µL per block (final $M_{n,SEC}$ = 10600 g mol^{-1}; $Đ$ = 1.25) and 2 µL per block (final $M_{n,SEC}$ = 10000 g mol^{-1}; $Đ$ = 1.31) (Figure 7.2). Centrifugation was necessary to collect the new monomer solution into the bottom the insert before stirring (see experimental info for full details). It is important to note, that the monomer concentration of the chain extension stock solution was kept constant at 3 M, such that the same DP per chain extension could be targeted by sequentially adding the same volume as the original block. It is noteworthy that all the chain extension stock solutions had contained the same initiator concentration of 2.2 x 10^{-3} M. This was designed to give an overall macroCTA/initiator ratio of 40 constant per block, whilst assuming that 20% of initiator is still remaining from the previous block. This gave a good balance of quantitative monomer consumption (>96%, Table 7.1) at each block whilst keeping the theoretical livingness of each block high (>98%, see experimental for calculation and experimental conditions) to prevent dead chains formed (See table 7.7-7.11 for detailed conditions).

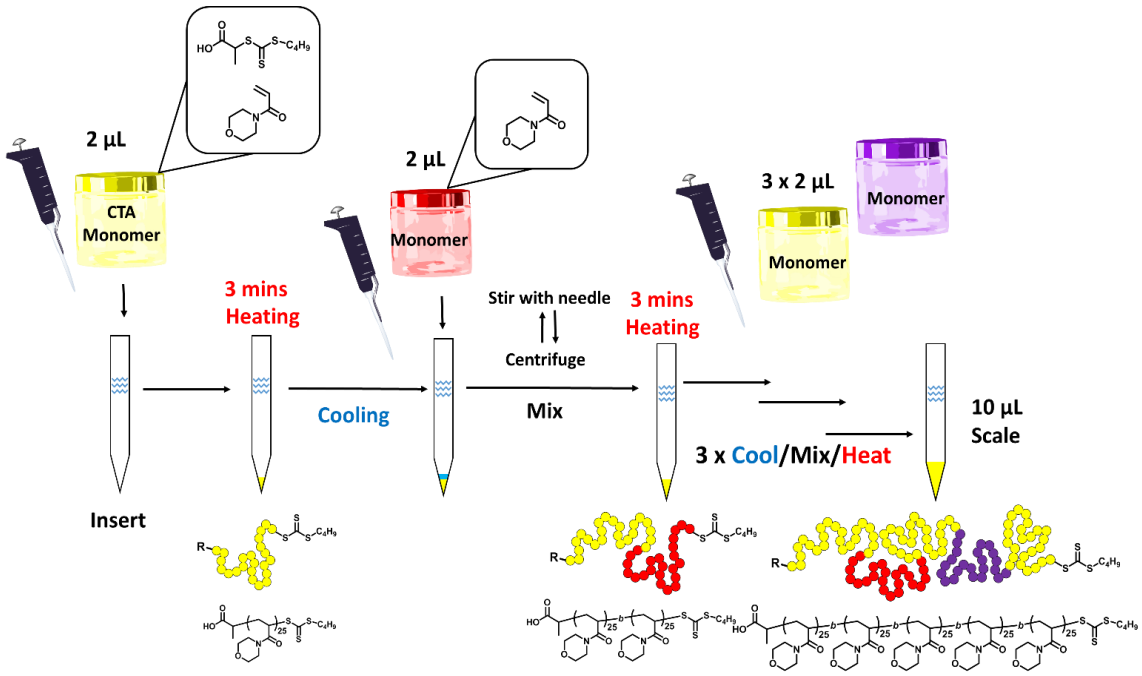

Scheme 7.1: "master mix" (with monomer, CTA, initiator and solvent) is added into the microvolume insert using a regular air displacement micropipettes. After 3 mins of heating at 100 °C in an oil bath polymerisation was complete, the insert was cooled with liquid nitrogen. For sequential chain extension, separate monomer master mix is directly added and mixed by stirring with a needle and centrifugation, before reheating for further 3 minutes for block extension. This cycle was repeated to yield pentablock copolymer. All the polymerisation were carried out without deoxygenation and in presence of open air.

The monomer consumption was followed by ^{1}H NMR spectroscopy and succession of the sequential chain extension was confirmed by GPC analysis of polymerization at each block. To analyze each chain extension, the same number of replicate reactions as the number of iterative blocks was prepared (Scheme 7.2), whereby representative vessel at each stage was used as a whole for each analysis (See experimental section for detail procedure).

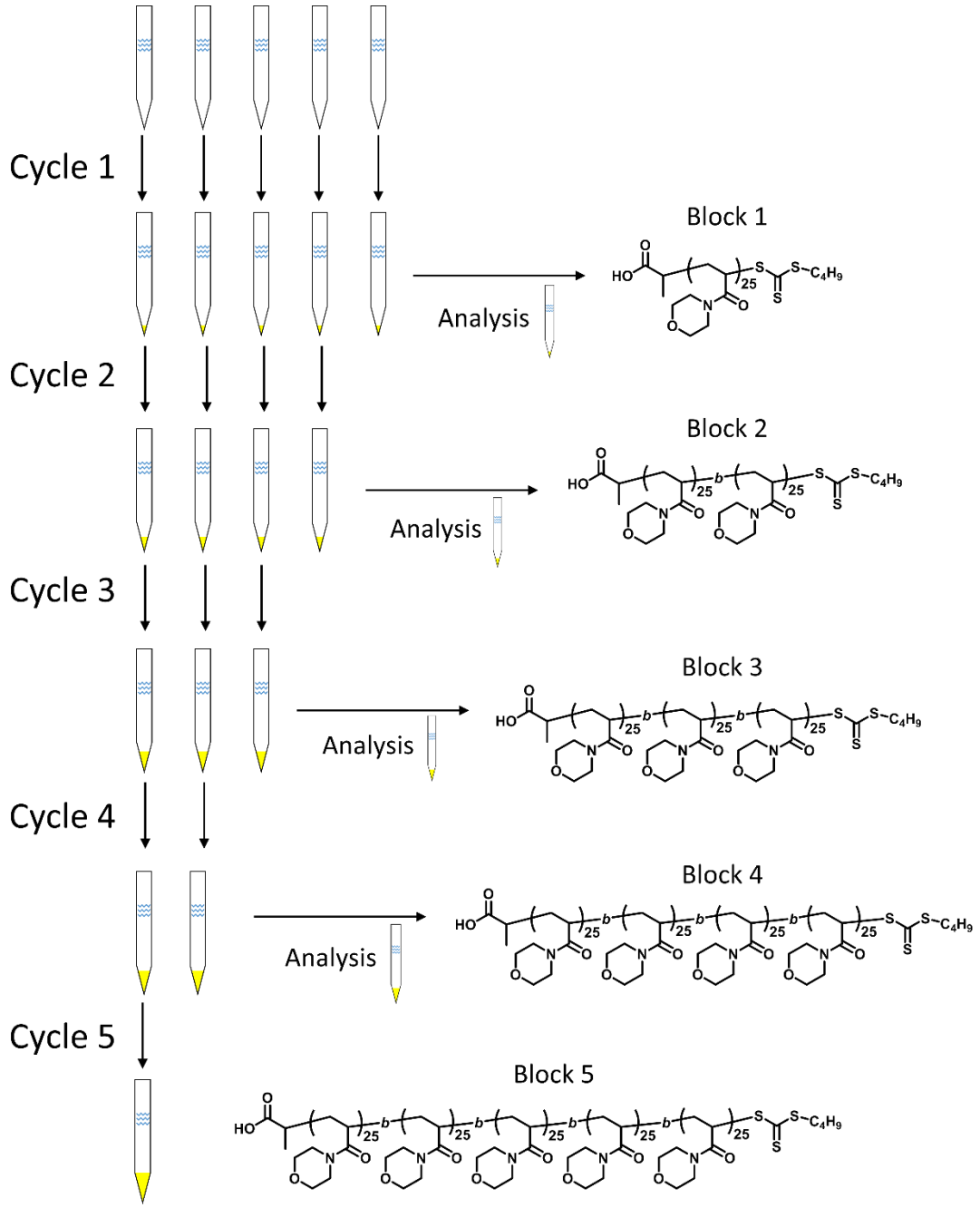

Scheme 7.2: the method for analysis of the multiblock copolymers at microscale.Twice as many reactions are prepared as number of blocks and polymerised simultaneously. After each block cycle a whole insert is taken as a representative sample. Two separate samples per block are required to enable both GPC and NMR analysis.

In all cases, a linear increase in $M_{n,SEC}$ was observed with increasing number of iterative block extensions (Figure 7.5, 5 µL per block; Figure 7.6, 2 µL per block,), suggesting excellent control in polymerization at the microscale. In comparison the molecular weight distributions of P[[NAM]$_{25}$]$_5$ was only slightly broader at microscale compared to

macroscale with our protocol (Figure 7.4, final $M_{n,SEC}$ = 12600 g mol^{-1}; $Đ$ = 1.23). At the macroscale, bimodal distributions were observed, due to back-biting induced β-scission and subsequent branching, with successive chain extensions.[43] Although this is typically characteristic of more labile methine backbone hydrogens of acrylic monomer families, as a result of high temperature this was observed here with an acrylamide monomer. This was indeed the case in previous work which used similar polymer composition, manifest as high molecular weight tailing.[12] At the microscale (25 μL and 10 μL), this feature is still present despite molecular weight distributions appearing to be unimodal, due to the broadening of the molecular weight distribution. We attribute this result to an increased interface between air and solution phase when scaling down, subsequently leading to dead chains as a result of oxygen related termination events. It's noteworthy that the weight loss for each chain extension is considerably greater at the microscale compared to the conventional scale (Table 7.2), however at the 5th block the weight loss was found to be less substantial.

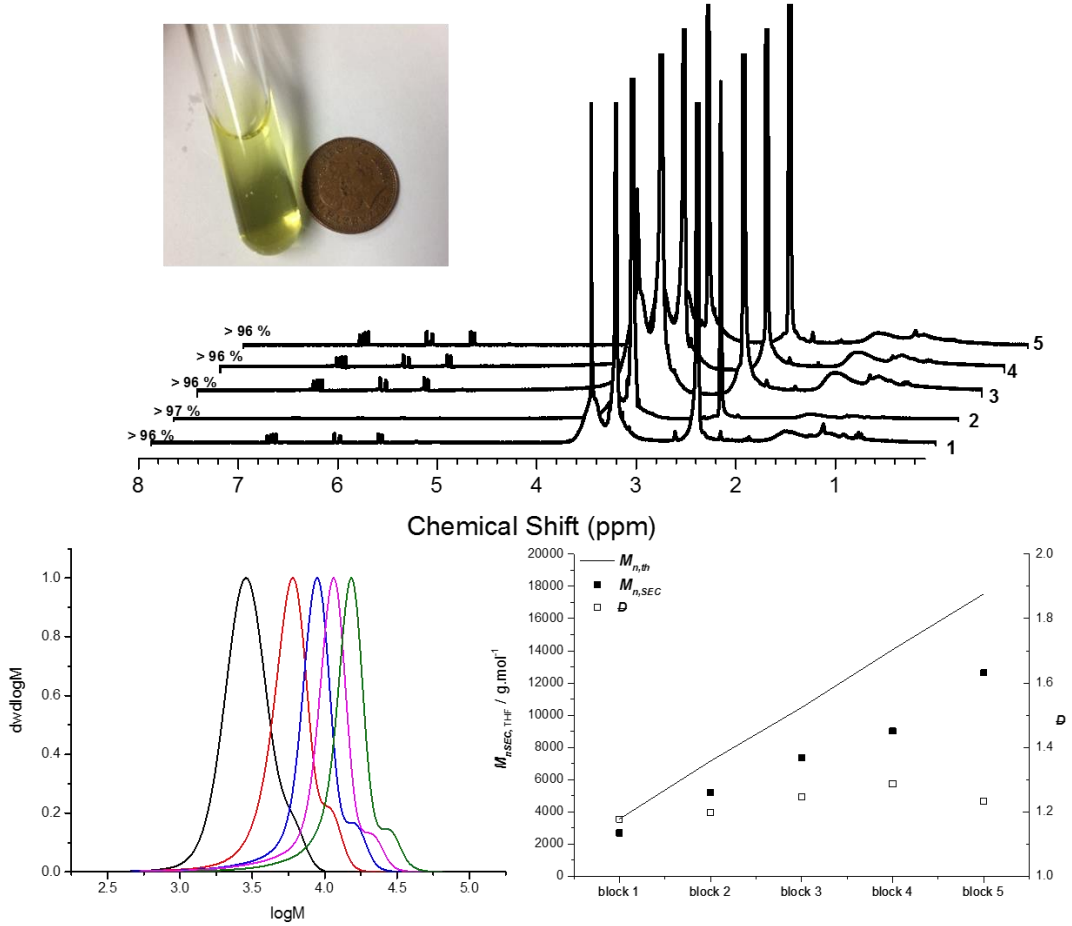

Figure 7.4 Multichain extension to generate $P(NAM_{25})_5$ synthesis with Ultrafast RAFT polymerization through iterative chain extensions at conventional macroscale = 2.5 ml, 0.5 ml per block. Photograph after reaction next to a British penny coin (20.3 mm in diameter) as a reference to the size of the scale. SEC chromatograms for successive chain extensions. Evolution of number-average molar masses and dispersity values with the number of blocks during the preparation of the $P(NAM_{25})_5$. The black line represents the theoretical molar mass calculated from Eqn. A.2. The filled squares represents the experimental molar mass and empty squares represents the dispersity values, both as determined by THF SEC.

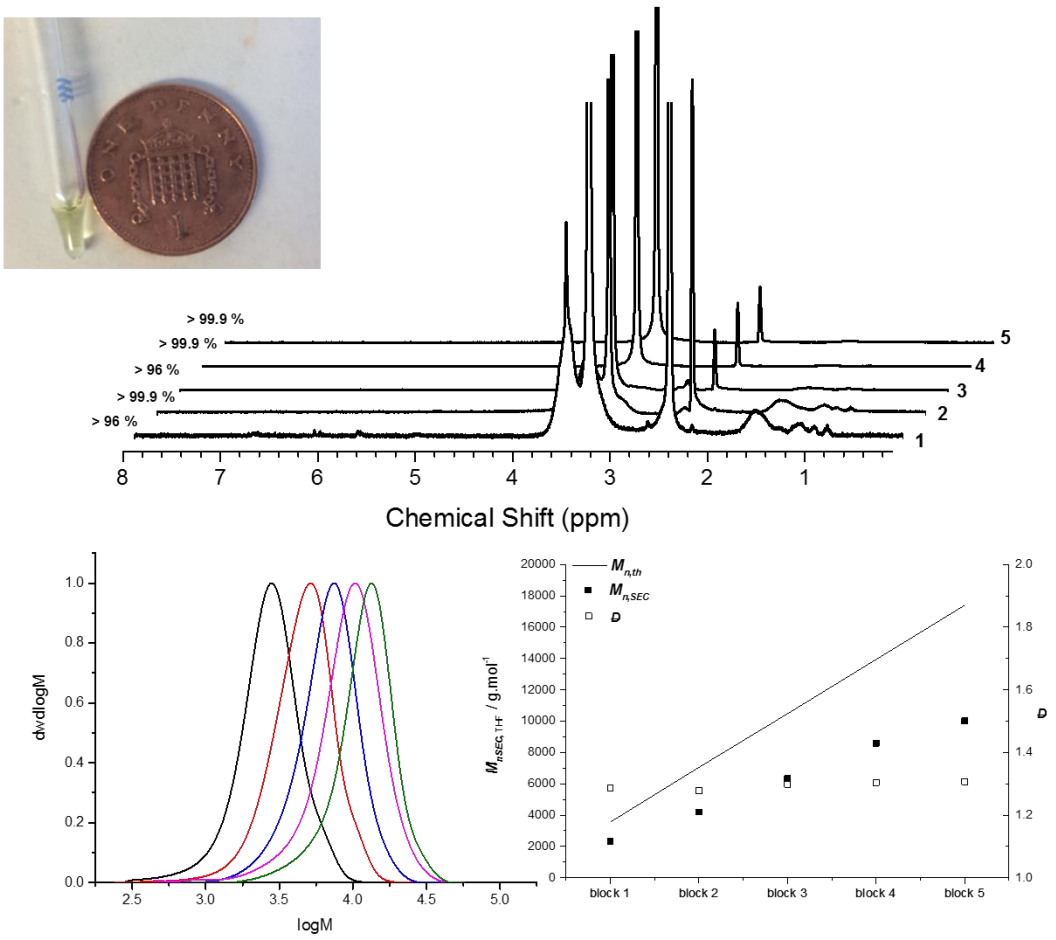

Figure 7.5 Multichain extension to generate $P(NAM_{25})_5$ synthesis with Ultrafast RAFT polymerization through iterative chain extensions at microscale = 25 µL, 5 µL per block. Photograph after reaction next to a British penny coin (20.3 mm in diameter) as a reference to the size of the scale. SEC chromatograms for successive chain extensions. Evolution of number-average molar masses and dispersity values with the number of blocks during the preparation of the $P(NAM_{25})_5$. The black line represents the theoretical molar mass calculated from Eqn A.2. The filled squares represents the experimental molar mass and empty squares represents the dispersity values, both as determined by THF SEC.

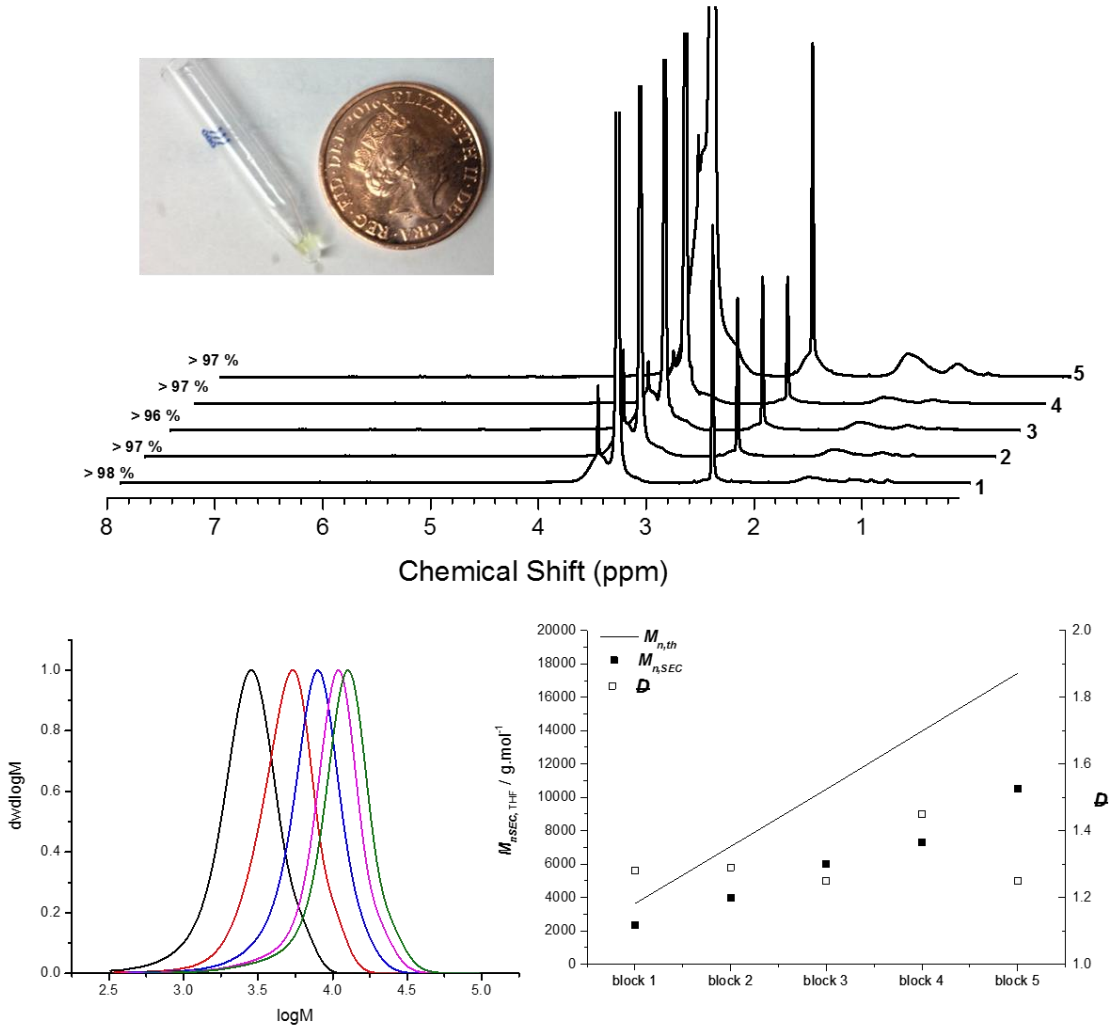

Figure 7.6 Multichain extension to generate P(NAM$_{25}$)$_5$ synthesis with Ultrafast RAFT polymerization through iterative chain extensions at microscale = 10 µL, 2 µL block. Photograph after reaction next to a British penny coin (20.3 mm in diameter) as a reference to the size of the scale. SEC chromatograms for successive chain extensions. Evolution of number-average molar masses and dispersity values with the number of blocks during the preparation of the P(NAM$_{25}$)$_5$. The black line represents the theoretical molar mass calculated from equation Eqn A.2. The filled squares represents the experimental molar mass and empty squares represents the dispersity values, both as determined by THF SEC.

Table 7.2: The percentage of the weight loss after each block extension during the preparation of $P(NAM_{25})_5$ in the microvolume inserts versus conventional test tube (5.4 ml) from evaporation.

	Percentage of weight loss (per block)	
	2 µL per block	500 µL per block
Block 1	43 %	3.7 %
Block 2	39 %	3.6 %
Block 3	40 %	3.6 %
Block 4	44 %	3.3 %
Block 5	28 %	2.7 %

7.2.4 Synthesis of MBCP at 2 µL per block scale

To further demonstrate the robustness of this method MBCPs were synthesized with blocks of different monomers: dimethylacrylamide (DMAm) and hydroxyethylacrylamide (HEAm). Pentablock of $P(NAM)_{25}$-b-$(DMAm)_{25}$-b-$(NAM)_{25}$-b-$(HEAm)_{25}$-b-$(NAM)_{25}$ were prepared in the inserts at the microliter scale (2 µL per block) following this protocol, with well-defined molecular weight distribution ($M_{n,SEC}$ = 14000 g mol^{-1}; $Đ$ = 1.35) which was comparable to macroscale synthesis ($M_{n,SEC}$ = 15100 g mol^{-1}; $Đ$ = 1.32). Note that the theoretical number average molecular ($M_{n,th}$) of this pentablock gave a good agreement with $M_{n,SEC}$ owing to the DMF used an eluent for the SEC analysis (Figure 7.7, 7.8), due to the better agreement of solvation in comparison to PMMA calibrant.

Table 7.3 The range of (micro)scales, monomer conversion, theoretical and experimental number average molar mass and dispersity of homopolymers and multiblock copolymers synthesized

Polymer	Scale[a] (µL)	Conv.[b]	$M_{n,th}$[c] ($gmol^{-1}$)	$M_{n,SEC}$[d] ($gmol^{-1}$)	$Đ$[d]
$P(NAM)_{25}$	500	> 97	3600	2700	1.18
	10	> 98	3600	2200	1.23
	5	> 98	3600	2600	1.23
	2	> 98	3600	2600	1.29
	1[e]	> 96[e]	3600[e]	2600[e]	1.42[e]
$P(NAM)_{100}$	500	> 99	14000	8900	1.19
	2	> 97	13600	9200	1.36
$P(NAM)_{200}$	500	> 98	26800	15000	1.23
	2	> 98	26800	13000	1.43
$P(NAM)_{25}$-*b*-$(NAM)_{25}$–*b*-$(NAM)_{25}$-*b*-$(NAM)_{25}$-*b*-$(NAM)_{25}$	2500	> 99.9	17200	12600	1.23
	25	> 99	17200	10600	1.25
	10	> 99	17200	10000	1.31
$P(NAM)_{25}$-*b*-$(DMAm)_{25}$-*b*-$(NAM)_{25}$-*b*-$(HEAm)_{25}$-*b*-$(NAM)_{25}$	2500	> 96	15400	15100[f]	1.32[f]
	10	> 98	15500	14000[f]	1.35[f]

[a] All polymerizations are carried out in insert vials unless the scale is above or equal to 500 µL are carried out in test tube (5.4 ml). [b] Determined using equation 1 in supporting information. [c] As calculated from equation 2 in supporting information. [d] Determined by SEC with THF as the eluent with PMMA as a calibrant, unless stated otherwise. [e] not reproducible. [f] Determined by SEC with DMF as a eluent with PMMA as a calibrant.

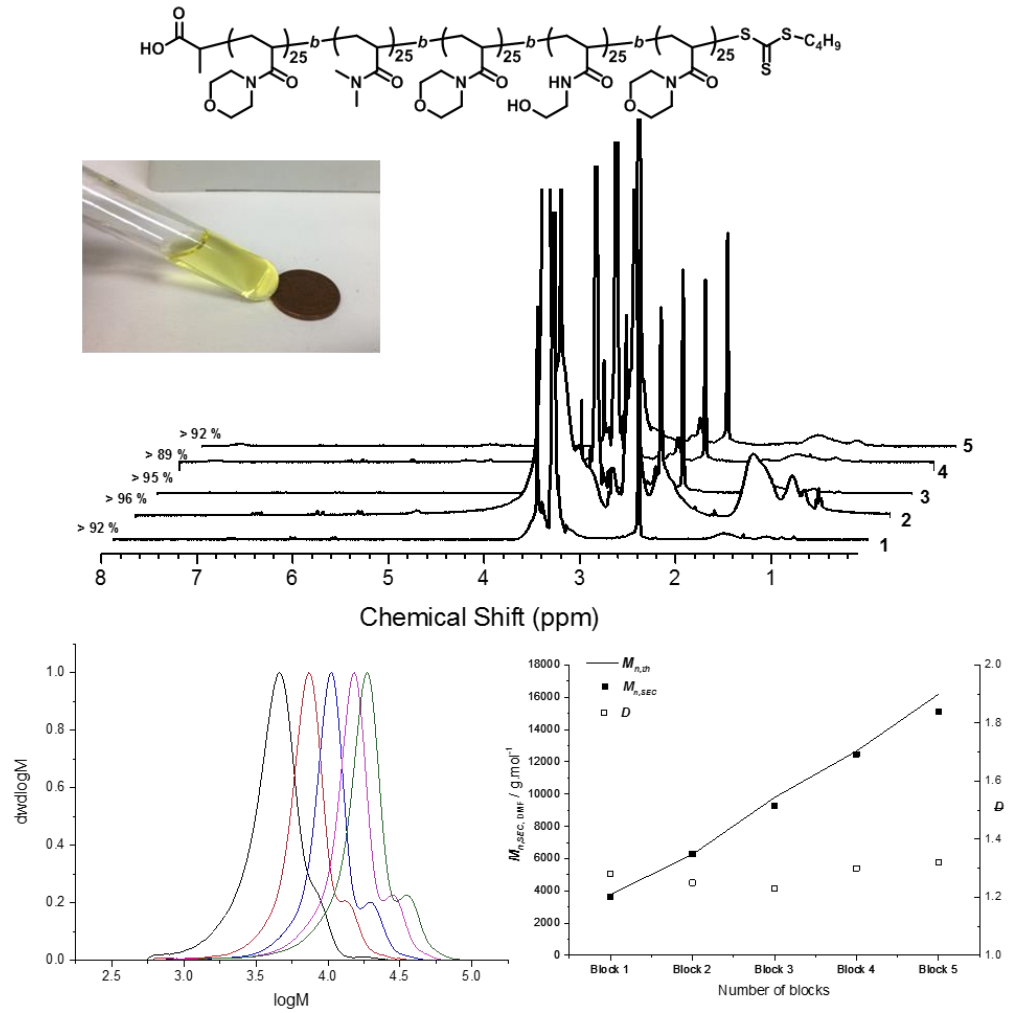

Figure 7.7. (a) ^{1}H NMR spectra (DMSO, 400 MHz) showing the monomer conversion for each new block P[(NAM)$_{25}$-b-(DMAm)$_{25}$-b-(NAM)$_{25}$-b-(HEAm)$_{25}$-b-(NAM)$_{25}$], after 3 mins of iterative RAFT polymerisation at conventional scale (scale = 0.5 ml per each block). SEC chromatograms for successive chain extensions. Evolution of number-average molar masses and dispersity values with the number of blocks during the preparation of the pentablock copolymer. The black line represents the theoretical molar mass calculated from equation A.2. The filled squares represents the experimental molar mass and empty squares represents the dispersity values, both as determined by DMF SEC.

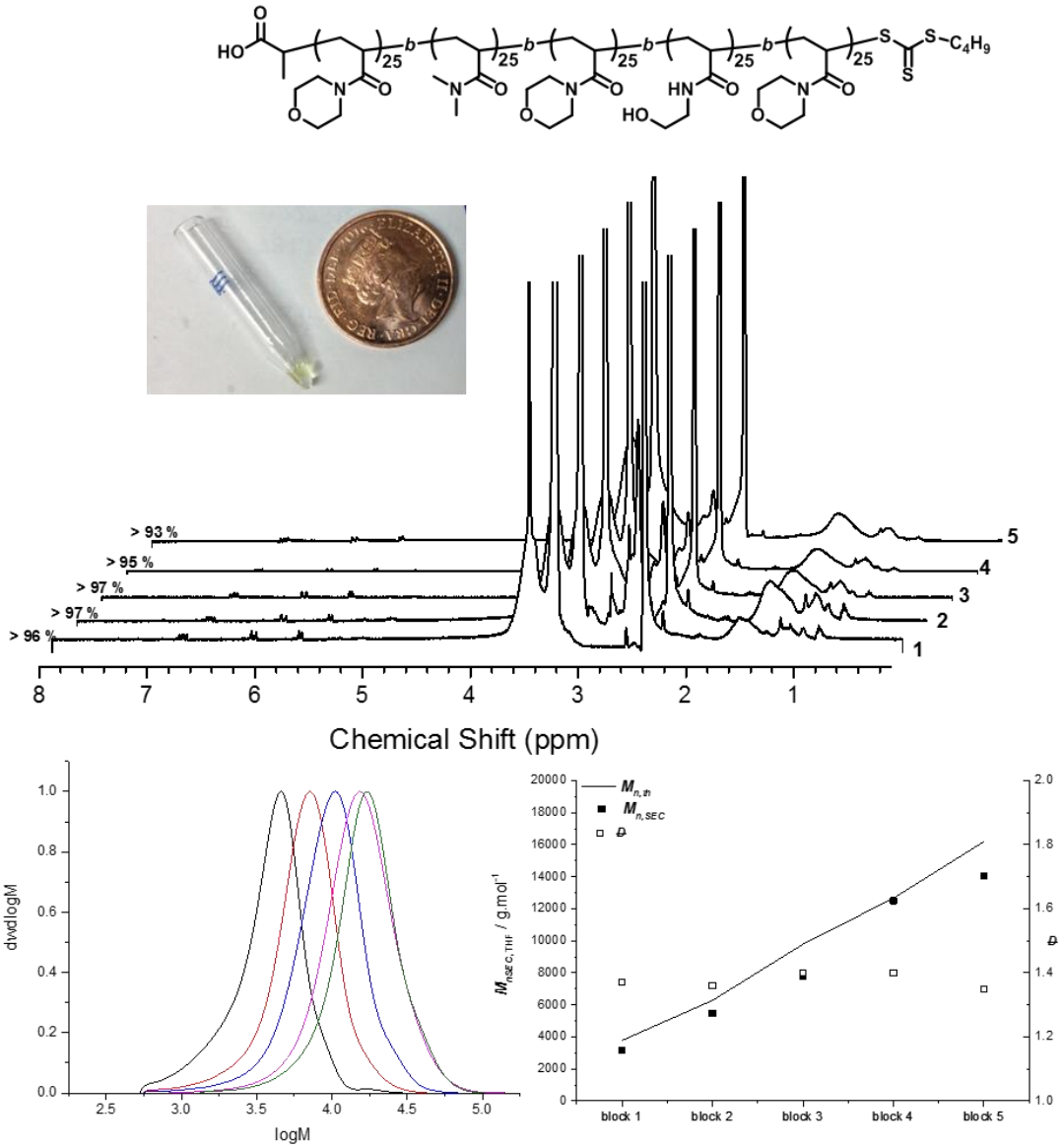

Figure 7.8 ^{1}H NMR spectra (DMSO, 400 MHz) showing the monomer conversion for each new block P[(NAM)$_{25}$-b-(DMAm)$_{25}$-b-(NAM)$_{25}$-b-(HEAm)$_{25}$-b-(NAM)$_{25}$] after 3 mins of iterative RAFT polymerisation inside microvolume inserts (scale = 2 µL per each block). SEC chromatograms for successive chain extensions. Evolution of number-average molar masses and dispersity values with the number of blocks during the preparation of the pentablock copolymer. The black line represents the theoretical molar mass calculated from Eqn A.2. The filled squares represents the experimental molar mass and empty squares represents the dispersity values, both as determined by DMF SEC.

7.3 Conclusion

To conclude, we have demonstrated the robustness of oxygen tolerant ultrafast RAFT polymerization at microscale of 2 µL. By careful consideration of monomer mixing we

generated well-controlled MBCPs (pentablock copolymer) by iterative addition, with an overall scale of 10 µL without continual stirring. Currently ongoing investigation(s) are in progress to investigate the robustness of the protocol for complex architectures, solvent and applicability in biological science.

7.4 Experimental

7.4.1 Materials:

2-((Butylthio)-carbonothioyl) thio propanoic acid (PABTC) was synthesised according to the reported literature and recrystallized at least twice in hexane before use.[44] *N*-Acryloylmorpholine (NAM) *N,N*-Dimethylacrylamide (DMAm) were filtered through a basic aluminium oxide (activated, basic, Brockman I, standard grade) to remove the radical inhibitor. 2,2′-azobis[2-(2-imidazolin-2yl)propane] dihydrochloride (VA-044, Wako), Dioxane (Sigma-Aldrich, >99%), HEAm (Sigma-Aldrich, > 97 %) and HPCL-grade H_2O (sigma-aldrich, > 99%) were used without further purification.

7.4.2 Instruments:

Nuclear Magnetic Resonance (NMR) spectroscopy (^{1}H NMR spectra) were recorded on a Bruker HD 400 spectrometer (400 MHz) at 27 °C using d_6-DMSO as solvent and the residual proton signal of the solvent (δ H = 2.50 ppm) was used as internal reference. Chemical shift values (δ) are reported in ppm. ACDLABS software was used to analyse the data obtained.

Number-average molar masses ($M_{n,SEC}$) and dispersity values ($Đ$) were determined using Size exclusion Chromatography (SEC) with THF or DMF as the eluent, depending on the composition of the copolymer. For conventional scale synthesis (for scales greater than 20 µL) polymer samples diluted with GPC eluent (1.5 ml) were filtered through a nylon membrane with 0.22 µm pore size before injection. For microscale synthesis with the microvolume inserts, the mixture was diluted with GPC eluent (200 µL) in the reaction vessels and were fitted inside a GPC sample vial. These were directly injected (80 µL) in to the SEC system. The THF system, Agilent 390-LC MDS instrument equipped with differential refractive index (DRI), viscometry (VS), dual angle light scatter (LS) and dual wavelength UV detectors. The system was equipped with 2 x PLgel Mixed C columns

(300 x 7.5 mm) and a PLgel 5 µm guard column. The eluent is THF with 2 % TEA (triethylamine) and 0.01 % BHT (butylated hydroxytoluene) additives. Samples were run at 1ml/min at 30 °C. Poly(methyl methacrylate) (PMMA) standards (Agilent EasyVials) were used for calibration between 955,000 – 550 gmol^{-1}. The DMF system was operating on Agilent 390-LC MDS instrument, which was equipped with differential refractive index (DRI), viscometry (VS), dual angle light scatter (LS) and UV detectors. The system was equipped with 2 x PLgel Mixed D columns (300 x 7.5 mm) and a PLgel 5 µm guard column. The DMF eluent had 5 mmol NH_4BF_4 additive. Samples were run at 1 ml/min at 50 °C. PMMA were used for calibration. Both instruments were equipped with an autosampler. Experimental molar mass ($\boldsymbol{M_{n,SEC}}$) and dispersity ($\boldsymbol{Đ}$) values of synthesized polymers were determined based on PMMA calibration using Agilent GPC/SEC software.

7.4.3 Determination of monomer conversions

Monomer conversion (ρ) were calculated from ^{1}H NMR sprectra using the following equation from Gody's protocol:[12]

$$\rho = \frac{[M]_0 - [M]_t}{[M]_0} = 1 - \frac{[M]_t}{[M]_0} = 1 - \frac{\int M_{5.5-7.00\ \mathrm{ppm}} / \int \mathrm{CTA}_{CH3}}{DP_{targeted}} \qquad \text{(Eqn A.1)}$$

Where $[M]_0$ is the initial monomer concentration and $[M]_t$ is the concentrations of the monomer at time t. ($\int M_{5.5\text{-}7.00\ \mathrm{ppm}}$ / ($\int \mathrm{CTA}_{CH3}$) is the corrected integrals for the vinylic protons of the monomer, $DP_{targeted}$ is the degree of the polymeirsation targeted and $\int_{CTA\text{-}CH3}$ is the integral of the 3 methyl protons belonging to the Z group of the RAFT agent (CH_2-CH_3) used as an internal reference. Note, the integral range for the vinylic protons is slightly wider than previously reported, this is to sufficiently cover all the vinylic protons.

7.4.4 Calculation of theoretical number average molar mass $M_{n,th}$

The theoretical number average molar mass ($M_{n,th}$) is calculated using equation (Eq 2).

$$M_{n,th} = \frac{[M]_0 \rho M_M}{[CTA]_0 + 2f[I]_0(1-e^{-k_d t})\left(\frac{1-f_c}{2}\right)} + M_{CTA} \qquad \text{(Eq A.2)}$$

Where $[M]_0$, $[I]_0$and $[CTA]_0$ are the initial concentrations of the monomer, initiator and chain transfer agent respectively; ρ is the monomer conversion as determined by ^{1}H NMR (from Eqn 1), M_M and M_{CTA} are the molar molar masses (gmol^{-1}) of the monomer and chain transfer agent respectively. The factor "2" accounts for two radicals generated from one molecule of azoinitiator with efficiency f (assumed to be 0.5) to react with monomers to initiate propagating chains. The decomposition rate constant, k_d is calculated from the Arrhenius equation for a given temperature (Eqn 3). Time, t is polymerisation time (in seconds). The term (1-f_c/2) represents the number of chains produced in a radical-radical termination events. The coupling factor, f_c has a value between 1 (100% termination occur by bimolecular combination) and 0 (100% termination occurs by disproportionation). For simplicity in this study 100 % termination is assumed to be by disproportionation (fc = 0).

7.4.5 Calculation of the decomposition rate constant kd

$$k_d = Ae^{-E_A/RT} \qquad \text{(Eq A.3)}$$

T is the temperature (in Kelvin). R is the molar gas constant (or universal gas constant) and has a value of 8.314 Jmol^{-1}. E_A is the activation energy, which is 10800 Jmol^{-1} for VA-044 (obtained from wako).[45] The Pre-exponential factor, A is determined using Eqn 4 shown below:

$$A = \frac{k_{d(317K)}}{e^{-Ea/RT_{317K}}} \text{ (Eqn A.4)}$$

Where $k_{d(317K)}$ is the decomposition rate when the initiator has a 10 hr half-life, at the specific temperature of the initiator. This temperature is 44 °C or 317 K for VA-044. The decomposition rate for a given half-life is a mathematical constant (for 10 hrs, it is 1.92 x 10^{-5} s^{-1}). In most cases, where available, the 10 hr half-life temperature and activation

energy of commercial thermal initiators can be obtained from the supplier (Wako).[45] From this the pre-exponential factor of VA-044 has a value of 1.18 x 10^{13}.

7.4.6 Calculation of the theoretical number fraction of living chains (livingness, L)

The number fraction of living chains is calculated using equation 5.

$$L = \frac{[CTA]_0}{([CTA]_0 + 2f[I]_0(1-e^{-k_d t})\left(\frac{1-f_c}{2}\right)} \qquad \text{(Eqn A.5)}$$

All side reactions with oxygen is neglected.

7.4.7 General procedure for microscale polymerisation.

Master mix with CTA, Monomer, initiator and solvent (preparation of the master mix with CTA described below) is added into microvolume inserts using regular air displacement micropipettes (P10's for 1 - 10 µL reactions). The insert is heated for 3 mins at 100 °C in an oil bath. The insert is either directly diluted with GPC eluent and inserted into a GPC vial, directly used for SEC analysis or alternatively diluted with deuterated DMSO for ^{1}H NMR analysis. Duplicate reactions are required to achieve both analysis (one for each).

7.4.8 General Procedure for Conventional scale polymerisation (500 µL scale)

Master mix with CTA, Monomer, initiator and solvent (preparation of the master mix with CTA described below) is added into test tube (with or without stirrer) using a regular air displacement micropipettes (P1000) to pipette 500 µL. The test tube is heated for 3 mins at 100 °C in an oil bath. Approximately 10 µL is used for GPC and NMR analysis.

7.4.9 General procedure preparing the for master mix with CTA (with NAM, 3M, DPn = 25)

The RAFT agent PABTC (67.5 mg, 0.28 mmol, 1 eq), is weighed into a sealable vial. NAM is carefully weighed directly into the same vial (1000 mg, 7.1 mmol, 25 eq).

Dioxane (294 µL) and water (1061 µL) is added and vortexed until the PABTC is completely dissolved. The solution was cooled in fridge or ice until the mixture is sufficiently below the room temperature before adding a stock solution of VA-044 (114.5 µL of 20 mg/ml stock solution) and vortex. Note, the solution may appear cloudy when chilled but will return back to clear solution at ambient temperatures.

In this study, a stock initiator solution is prepared and used to avoid weighing minute amount of initiator (2.29 mg). It is important to note that all initiator stock solution and master mix's once the initiator is added to be kept on ice or stored in the fridge to avoid decomposition of the initiator.

7.4.10 General procedure for microscale multiblock synthesis

2 µL of the master mix with CTA (preparation of the CTA master mix described above) was added into the insert(s) using a regular air displacement micropipettes (P10's). After 3 mins of heating at 100 °C in an oil bath, the insert is cooled with liquid nitrogen until the insert is frozen (approximately 30 seconds). For sequential chain extension, 2 µL of a separate master mix with monomer (with identical Monomer concentration to previous block to target the same DPn), initiator and solvent (no CTA) (preparation of chain extension master described below) was directly added using the micropipette. For thorough mixing, initially the inserts are placed inside an Eppendorf tube and centrifuged at 1.38 x 10^4 rpm for 1 minute to force the newly added monomer solution to bottom of the insert with the previous mixture. The mixtures were then crudely stirred with 23 gauge needle until the solution appeared homogenous and re-centrifuged (1.38 x 10^4 rpm for 1 minute). The mixture was then heated for 3 minutes 100 °C in an oil bath. This process was repeated for additional chain extensions. Tables S6, S7 has detailed conditions for specific multiblock described in the paper. For GPC and NMR analysis of each block see the Scheme S2 for the analysis of the multiblock copolymers at microscale.

7.4.11 General procedure for conventional scale synthesis (done without a stirrer bar)

For comparison study with the microscale synthesis, conventional scale synthesis was carried without stirrer during polymerisation. Procedure follows: 500 µL of the master

mix with CTA is added into insert using a regular air displacement micropipettes (P1000's). After 3 mins of heating at 100 °C in an oil bath, two aliquots of 10 µL of samples were taken out using P200's separately for GPC and NMR analysis. The reaction mixture was allowed to be cooled in ice, until the reaction mixture was sufficiently below room temperature. 500 µL of separate master mix (chain extension master described below) was directly added using the micropipette (P1000's). The layered mixture was carefully mixed thoroughly until the mixture was completely homogenous. Samples taken for GPC and NMR increased by additional 10 µL every 2 blocks i.e. 2 x 20 µL were taken 3rd and 4th block and 2 x 30 µL were taken for 5th (final) block. Multiblock obtained by this appeared identical to the multiblock made with stirring.

7.4.12 General procedure for preparing the chain extension master mix (NAM, 3M)

NAM is carefully weighed directly into the sealable vial (1000 mg, 7.1 mmol). Water (1061 µL) is added and then cool the solution in fridge or ice until the mixture is sufficiently below the room temperature. A stock solution of VA-044 (91.7 µL of 20 mg/ml stock solution) was added and vortexed. Note, combined with the initiator stock solution makes 3 M monomer concentration. The mixture can be used directly and should be stored in the fridge when not in use.

7.4.13 General procedure for preparing the chain extension master mix (DMAm, 3M)

DMAm is carefully weighed directly into the sealable vial (702 mg, 7.1 mmol). Water (1540 µL) is added and the solution was then cooled in fridge or ice until the mixture is sufficiently below the room temperature. A stock solution of VA-044 (91.7 µL of 20 mg/ml stock solution) was added and vortex. Note, combined with the initiator stock solution makes 3 M monomer concentration. The mixture can be used directly and should be stored in the fridge when not in use.

7.4.14 General procedure for preparing the chain extension master mix (HEAm, 3M)

HEAm is carefully weighed directly into the sealable vial (816 mg, 7.1 mmol). Water (1535 µL) is added and then cool the solution in fridge or ice until the mixture is sufficiently below the room temperature. A stock solution of VA-044 (91.7 µL of 20 mg/ml stock solution) and vortex. Note, combined with the initiator stock solution makes 3 M monomer concentration. The mixture can be used directly and should be stored in the fridge when not in use.

Table 7.4 Experimental conditions for the preparation of $P(NAM)_{25}$ at range of scales in H_2O/dioxane at 100 °C with VA-044 as initiator (3 mins per reaction, in presence of air an without degassing).

Scale	500 µL[a]	10 µL[b]	5 µL[b]	2 µL[b]	1 µL[b]
Monomer	NAM	NAM	NAM	NAM	NAM
$DP_{targeted}$	25	25	25	25	25
$m_{monomer\ added}$ (mg)	211.7	4.24	2.12	0.848	0.424
$m_{CTA\ added}$ (mg)	14.3	0.286	0.143	5.73×10^{-2}	2.86×10^{-2}
$m_{VA\text{-}044\ added}$ (mg)	0.48	9.71×10^{-3}	4.86×10^{-3}	1.94×10^{-3}	9.71×10^{-4}
$V_{water\ added}$ (µL)	249	4.986	2.493	0.997	0.499
$V_{dioxane\ added}$ (µL)	62	1.247	0.623	0.249	0.125
$[VA\text{-}044]_{0\ Master\ mix}$ ($moldm^{-3}$)[c]	3.00×10^{-3}	3.00×10^{-3}	3.00×10^{-3}	3.00×10^{-3}	3.00×10^{-3}
$[NAM]_{0\ Master\ mix}$ ($moldm^{-3}$)[c]	3.00	3.00	3.00	3.00	3.00
Water/Dioxane ratio $_{master\ mix}$	80:20	100:0	100:0	100:0	100:0
$V_{master\ mix\ added}$ (µL)[d]	500	10	5	2	1
% H_2O	80 %	80 %	80 %	80 %	80 %
V_{total} (µL)	0.500	0.010	0.005	0.002	0.001
Overall $[VA\text{-}044]_0$ ($moldm^{-3}$)	3.00×10^{-3}	3.00×10^{-3}	3.00×10^{-3}	3.00×10^{-3}	3.00×10^{-3}
Overall $[NAM]_0$ ($moldm^{-3}$)	3	3	3	3	3
$[CTA]_0/[VA\text{-}044]_0$	40	40	40	40	40
L[e] (%)	98.04	98.04	98.04	98.04	98.04

[a] Reaction carried out in a conventional X ml test tube. [b] Reaction carried out in a 200 µL inserts [c] Overall concentration of the master mix (monomer, initiator and solvent), CTA added in the cycle 1 master mix. For subsequent chain extensions (cycles = 2, 3, 4 and 5) the same master mix was used. [d] Volume of the master mix added into the reaction vessel using an air displacement micropipette. [e] Theoretical estimation of the fraction of living chains per block (e.g. extendable chains having the Z group).

Table 7.5 Experimental conditions for the preparation of $P(NAM)_{100}$ at range of scales in H_2O/dioxane at 100 °C with VA-044 as initiator (3 mins per reaction, consuming 80% of initiator; in presence of air and without degassing).

Scale	500 μL[a]	2 μL[b]
Monomer	NAM	NAM
$DP_{targeted}$	100	100
$m_{monomer\ added}$ (mg)	211.7	0.848
$m_{CTA\ added}$ (mg)	35.7	1.43×10^{-2}
$m_{VA\text{-}044\ added}$ (mg)	0.36	6.5×10^{-4}
$V_{water\ added}$ (μL)	280	1.122
$V_{dioxane\ added}$ (μL)	311	0.125
$[VA\text{-}044]_{0\ Master\ mix}$ ($moldm^{-3}$)[c]	1.00×10^{-3}	1.00×10^{-3}
$[NAM]_{0\ Master\ mix}$ ($moldm^{-3}$)[c]	3.00	3.00
Water/Dioxane ratio $_{master\ mix}$	90:10	90:10
$V_{master\ mix\ added}$ (μL)[d]	500	2
% H_2O	90 %	90 %
V_{total} (μL)	500	2
Overall $[VA\text{-}044]_0$ ($moldm^{-3}$)	1.00×10^{-3}	1.00×10^{-3}
Overall $[NAM]_0$ ($moldm^{-3}$)	3.00	3.00
$[CTA]_0/[VA\text{-}044]_0$	30	30
L[e] (%)	97.40	97.40

[a] Reaction carried out in a conventional X ml test tube. [b] Reaction carried out in a 200 μL inserts [c] Overall concentration of the master mix (monomer, initiator and solvent), CTA added in the cycle 1 master mix. For subsequent chain extensions (cycles = 2, 3, 4 and 5) the same master mix was used. [d] Volume of the master mix added into the reaction vessel using an air displacement micropipette. [e] Theoretical estimation of the fraction of living chains per block (e.g. extendable chains having the Z group).

Table 7.6 Experimental conditions for the preparation of $P(NAM)_{200}$ at range of scales in H_2O/dioxane at 100 °C with VA-044 as initiator (3 mins per reaction, consuming 80% of initiator; in presence of air and without degassing).

Scale	500 μL[a]	2 μL[b]
Monomer	NAM	NAM
$DP_{targeted}$	200	200
$m_{monomer\ added}$ (mg)	211.7	0.848
$m_{CTA\ added}$ (mg)	1.79	7.2×10^{-3}
$m_{VA\text{-}044\ added}$ (mg)	0.121	4.9×10^{-4}
$V_{water\ added}$ (μL)	296	1.184
$V_{dioxane\ added}$ (μL)	156	0.062
$[VA\text{-}044]_{0\ Master\ mix}$ ($moldm^{-3}$) [c]	7.50×10^{-4}	7.50×10^{-4}
$[NAM]_{0\ Master\ mix}$ ($moldm^{-3}$) [c]	3.00	3.00
Water/Dioxane ratio $_{master\ mix}$	95:05	95:05
$V_{master\ mix\ added}$ (μL) [d]	500	2
% H_2O	95 %	95 %
V_{total} (μL)	500	2
Overall $[VA\text{-}044]_0$ ($moldm^{-3}$)	7.5×10^{-4}	7.5×10^{-4}
Overall $[NAM]_0$ ($moldm^{-3}$)	3.00	3.00
$[CTA]_0/[VA\text{-}044]_0$	20	20
L[e] (%)	96.15	96.15

[a] Reaction carried out in a conventional X ml test tube. [b] Reaction carried out in a 200 μL inserts [c] Overall concentration of the master mix (monomer, initiator and solvent), CTA added in the cycle 1 master mix. For subsequent chain extensions (cycles = 2, 3, 4 and 5) the same master mix was used. [d] volume of the master mix added into the reaction vessel using an air displacement micropipette. [e] theoretical estimation of the fraction of living chains per block (e.g. extendable chains having the Z group).

Table 7.7. Experimental conditions for the preparation of multichain extension to generate $P[(NAM)_{25}]_5$ at 25 µL scale (5 µL per block) in H_2O/dioxane at 100 °C with VA-044 as initiator (3 mins per block, consuming 80% of initiator; per block in presence of air an without degassing).

Cycles	1	2	3	4	5
Monomer	NAM	NAM	NAM	NAM	NAM
$DP_{targeted}$	25	25	25	25	25
$m_{monomer\ added}$ (mg)	2.117	2.117	2.117	2.117	2.117
$m_{CTA\ added}$ (mg)	0.143	-	-	-	-
$m_{VA\text{-}044\ added}$ (mg)	4.85×10^{-3}	3.88×10^{-3}	3.88×10^{-3}	3.88×10^{-3}	3.88×10^{-3}
$V_{water\ added}$ (µL)	0.997	1.247	1.247	1.247	1.247
$V_{dioxane\ added}$ (µL)	0.249	-	-	-	-
$[VA\text{-}044]_{0\ Master\ mix}$ (moldm^{-3}) [a]	3.00×10^{-3}	2.37×10^{-3}	2.37×10^{-3}	2.37×10^{-3}	2.37×10^{-3}
$[NAM]_{0\ Master\ mix}$ (moldm^{-3}) [a]	3.00	3.00	3.00	3.00	3.00
Water/Dioxane ratio $_{master\ mix}$	80:20	100:0	100:0	100:0	100:0
$V_{master\ mix\ added}$ (µL) [b]	5.00	5.00	5.00	5.00	5.00
% H_2O	80 %	90 %	93 %	95 %	96 %
V_{total}[c] (µL)	5.00	10.00	15.00	20.00	25.00
Overall $[VA\text{-}044]_0$ (moldm^{-3}) [d]	3.00×10^{-3}	1.50×10^{-3}	1.00×10^{-3}	7.5×10^{-4}	6.0×10^{-4}
Overall $[NAM]_0$ (moldm^{-3})	3.00	1.50	1.00	0.75	0.60
$[CTA]_0/[VA\text{-}044]_0$	40	40	40	40	40
L[e] (%)	98.04	98.04	98.04	98.04	98.04
Cumulative L[f] (%)	98.04	96.11	94.23	92.38	90.56

[a] Overall concentration of the master mix (monomer, initiator and solvent), CTA added in the cycle 1 master mix. For subsequent chain extensions (cycles = 2, 3, 4 and 5) the same master mix was used. [b] volume of the master mix added into the reaction vessel using an air displacement micropipette. [c] the sum of volume of the solvent added + volume of monomer + V_{total} previous block. [d] takes into the account the theoretical initiator remaining from the previous block (using the Arrhenius equation). [e] theoretical estimation of the fraction of living chains per block (e.g. extendable chains having the Z group). [f] Theoretical estimation of the cumulated fraction of living chains.

Table 7.8 Experimental conditions for the preparation of multichain extension to generate $P[(NAM)_{25}]_5$ at 10 µL scale (2 µL per block) in H_2O/dioxane at 100 °C with VA-044 as initiator (3 mins per block, consuming 80% of initiator; per block in presence of air an without degassing).

Cycles	1	2	3	4	5
Monomer	NAM	NAM	NAM	NAM	NAM
$DP_{targeted}$	25	25	25	25	25
$m_{monomer\ added}$ (mg)	0.847	0.847	0.847	0.847	0.847
$m_{CTA\ added}$ (mg)	5.73×10^{-2}	-	-	-	-
$m_{VA\text{-}044\ added}$ (mg)	1.94×10^{-3}	1.55×10^{-3}	1.55×10^{-3}	1.55×10^{-3}	1.55×10^{-3}
$V_{water\ added}$ (µL)	0.996	1.247	1.247	1.247	1.247
$V_{dioxane\ added}$ (µL)	0.249	-	-	-	-
$[VA\text{-}044]_{0\ Master\ mix}$ (moldm^{-3}) [a]	3.00×10^{-3}	2.37×10^{-3}	2.37×10^{-3}	2.37×10^{-3}	2.37×10^{-3}
$[NAM]_{0\ Master\ mix}$ (moldm^{-3}) [a]	3.00	3.00	3.00	3.00	3.00
Water/Dioxane ratio $_{master\ mix}$	80:20	100:0	100:0	100:0	100:0
$V_{master\ mix\ added}$ (µL) [b]	2.00	2.00	2.00	2.00	2.00
% H_2O	80 %	90 %	93 %	95 %	96 %
V_{total}[c] (µL)	2.00	4.00	6.00	8.00	10.00
Overall $[VA\text{-}044]_0$ (moldm^{-3}) [d]	3.00×10^{-3}	1.50×10^{-3}	1.00×10^{-3}	7.5×10^{-4}	6.0×10^{-4}
Overall $[NAM]_0$ (moldm^{-3})	3.00	1.50	1.00	0.75	0.60
$[CTA]_0/[VA\text{-}044]_0$	40	40	40	40	40
L[e] (%)	98.04	98.04	98.04	98.04	98.04
Cumulative L[f] (%)	98.04	96.11	94.23	92.38	90.56

[a] Overall concentration of the master mix (monomer, initiator and solvent), CTA added in the cycle 1 master mix. For subsequent chain extensions (cycles = 2, 3, 4 and 5) the same master mix was used. [b] volume of the master mix added into the reaction vessel using an air displacement micropipette. [c] the sum of volume of the solvent added + volume of monomer + V_{total} previous block. [d] takes into the account the theoretical initiator remaining from the previous block (using the Arrhenius equation). [e] theoretical estimation of the fraction of living chains per block (e.g. extendable chains having the Z group). [f] Theoretical estimation of the cumulated fraction of living chains.

Table 7.9 Experimental conditions for the preparation of multichain extension to generate $P[(NAM)_{25}]_5$ at 2.5 ml scale in H_2O/dioxane at 100 °C with VA-044 as initiator (3 mins per block, consuming 80% of initiator; per block in presence of air an without degassing).

Cycles	1	2	3	4	5
Monomer	NAM	NAM	NAM	NAM	NAM
$DP_{targeted}$	25	25	25	25	25
$m_{monomer\ added}$ (mg)	211.7	211.7	211.7	211.7	211.7
$m_{CTA\ added}$ (mg)	14.3	-	-	-	-
$m_{VA\text{-}044\ added}$ (mg)	0.48	0.39	0.39	0.39	0.39
$V_{water\ added}$ (µL)	249	311	311	311	311
$V_{dioxane\ added}$ (µL)	62	-	-	-	-
$[VA\text{-}044]_{0\ Master\ mix}$ ($moldm^{-3}$) [a]	3.00×10^{-3}	2.37×10^{-3}	2.37×10^{-3}	2.37×10^{-3}	2.37×10^{-3}
$[NAM]_{0\ Master\ mix}$ ($moldm^{-3}$) [a]	3.00	3.00	3.00	3.00	3.00
Water/Dioxane ratio $_{master\ mix}$	80:20	100:0	100:0	100:0	100:0
$V_{master\ mix\ added}$ (µL) [b]	500	500	500	500	500
% H_2O	80 %	90 %	93 %	95 %	96 %
V_{total}[c] (µL)	500	1000	1500	2000	2500
Overall $[VA\text{-}044]_0$ ($moldm^{-3}$) [d]	3.00×10^{-3}	1.50×10^{-3}	1.00×10^{-3}	7.5×10^{-4}	6.0×10^{-4}
Overall $[NAM]_0$ ($moldm^{-3}$)	3.00	1.50	1.00	0.75	0.60
$[CTA]_0/[VA\text{-}044]_0$	40	40	40	40	40
L[e] (%)	98.04	98.04	98.04	98.04	98.04
Cumulative L[f] (%)	98.04	96.11	94.23	92.38	90.56

[a] Overall concentration of the master mix (monomer, initiator and solvent), CTA added in the cycle 1 master mix. For subsequent chain extensions (cycles = 2, 3, 4 and 5) the same master mix was used. [b] volume of the master mix added into the reaction vessel using an air displacement micropipette. [c] the sum of volume of the solvent added + volume of monomer + V_{total} previous block. [d] takes into the account the theoretical initiator remaining from the previous block (using the Arrhenius equation). [e] theoretical estimation of the fraction of living chains per block (e.g. extendable chains having the Z group). [f] Theoretical estimation of the cumulated fraction of living chains.

Table 7.10 Experimental conditions for the preparation of the pentablock copolymer P[(NAM)$_{25}$-b-(DMAm)$_{25}$-b-(NAM)$_{25}$-b-(HEAm)$_{25}$-b-(NAM)$_{25}$] at 10 µL scale (2 µL per block)scale in H_2O/dioxane at 100 °C with VA-044 as initiator (3 mins per block, consuming 80% of initiator; per block in presence of air an without degassing).

Cycles	1	2	3	4	5
Monomer	NAM	DMAm	NAM	HEAm	NAM
$DP_{targeted}$	25	25	25	25	25
$m_{monomer\ added}$ (mg)	0.848	0.595	0.848	0.691	0.848
$m_{CTA\ added}$ (mg)	5.72×10^{-2}	-	-	-	-
$m_{VA\text{-}044\ added}$ (mg)	1.94×10^{-3}	1.55×10^{-3}	1.55×10^{-3}	1.55×10^{-3}	1.55×10^{-3}
$V_{water\ added}$ (µL)	0.996	1.382	1.245	1.378	1.245
$V_{dioxane\ added}$ (µL)	0.249	-	-	-	-
$[VA\text{-}044]_{0\ Master\ mix}$ (moldm^{-3}) [a]	3.00×10^{-3}	2.37×10^{-3}	2.37×10^{-3}	2.37×10^{-3}	2.37×10^{-3}
$[M]_{0\ Master\ mix}$ (moldm^{-3}) [a]	3.00	3.00	3.00	3.00	3.00
Water/Dioxane ratio $_{master\ mix}$	80:20	100:0	100:0	100:0	100:0
$V_{master\ mix\ added}$ (µL) [b]	2.00	2.00	2.00	2.00	2.00
% H_2O	80 %	90 %	93 %	95 %	96 %
V_{total}[c] (µL)	2.00	4.00	6.00	8.00	10.00
Overall $[VA\text{-}044]_0$ (moldm^{-3}) [d]	3.00×10^{-3}	1.50×10^{-3}	1.00×10^{-3}	7.5×10^{-4}	6.0×10^{-4}
Overall $[M]_0$ (moldm^{-3})	3.00	1.50	1.00	0.75	0.60
$[CTA]_0/[VA\text{-}044]_0$	40	40	40	40	40
L[e] (%)	98.04	98.04	98.04	98.04	98.04
Cumulative L[f] (%)	98.04	96.11	94.23	92.38	90.56

[a] Overall concentration of the master mix (monomer, initiator and solvent), CTA added in the cycle 1 master mix. For subsequent chain extensions (cycles = 2, 3, 4 and 5) the same master mix was used. [b] volume of the master mix added into the reaction vessel using an air displacement micropipette. [c] the sum of volume of the solvent added + volume of monomer + V_{total} previous block. [d] takes into the account the theoretical initiator remaining from the previous block (using the Arrhenius equation). [e] theoretical estimation of the fraction of living chains per block (e.g. extendable chains having the Z group). [f] Theoretical estimation of the cumulated fraction of living chains.

Table 7.11 Experimental conditions for the preparation of the pentablock copolymer P[(NAM)$_{25}$-b-(DMAm)$_{25}$-b-(NAM)$_{25}$-b-(HEAm)$_{25}$-b-(NAM)$_{25}$] at 2.5 ml scale (500 µL per block)scale in H_2O/dioxane at 100 °C with VA-044 as initiator (3 mins per block, consuming 80% of initiator; per block in presence of air an without degassing).

Cycles	**1**	**2**	**3**	**4**	**5**
Monomer	NAM	DMAm	NAM	HEAm	NAM
$DP_{targeted}$	25	25	25	25	25
$m_{monomer\ added}$ (mg)	212	149	212	173	212
$m_{CTA\ added}$ (mg)	14.3	-	-	-	-
$m_{VA\text{-}044\ added}$ (mg)	0.49	0.39	0.39	0.39	0.39
$V_{water\ added}$ (µL)	249.0	345.5	311.3	344.6	311.3
$V_{dioxane\ added}$ (µL)	62	-	-	-	-
$[VA\text{-}044]_{0\ Master\ mix}$ (moldm^{-3}) [a]	3.00 x 10^{-3}	2.37 x 10^{-3}	2.37 x 10^{-3}	2.37 x 10^{-3}	2.37 x 10^{-3}
$[M]_{0\ Master\ mix}$ (moldm^{-3}) [a]	3.00	3.00	3.00	3.00	3.00
Water/Dioxane ratio $_{master\ mix}$	80:20	100:0	100:0	100:0	100:0
$V_{master\ mix\ added}$ (µL) [b]	500	500	500	500	500
% H_2O	80 %	90 %	93 %	95 %	96 %
V_{total}[c] (µL)	2.00	4.00	6.00	8.00	10.00
Overall $[VA\text{-}044]_0$ (moldm^{-3}) [d]	3.00 x 10^{-3}	1.50 x 10^{-3}	1.00 x 10^{-3}	7.5 x 10^{-4}	6.0 x 10^{-4}
Overall $[M]_0$ (moldm^{-3})	3.00	1.50	1.00	0.75	0.60
$[CTA]_0/[VA\text{-}044]_0$	40	40	40	40	40
L[e] (%)	98.04	98.04	98.04	98.04	98.04
Cumulative L[f] (%)	98.04	96.11	94.23	92.38	90.56

[a] Overall concentration of the master mix (monomer, initiator and solvent), CTA added in the cycle 1 master mix. For subsequent chain extensions (cycles = 2, 3, 4 and 5) the same master mix was used. [b] volume of the master mix added into the reaction vessel using an air displacement micropipette. [c] the sum of volume of the solvent added + volume of monomer + V_{total} previous block. [d] takes into the account the theoretical initiator remaining from the previous block (using the Arrhenius equation). [e] theoretical estimation of the fraction of living chains per block (e.g. extendable chains having the Z group). [f] Theoretical estimation of the cumulated fraction of living chains.

7.5 References

1. D. G. Anderson, S. Levenberg and R. Langer, *Nat. Biotechnol.*, 2004, **22**, 863.
2. J. J. Green, R. Langer and D. G. Anderson, *Acc. Chem. Res.*, 2008, **41**, 749-759.
3. R. Chapman, A. J. Gormley, M. H. Stenzel and M. M. Stevens, *Angew. Chem. Int. Ed.*, 2016, **55**, 4500-4503.
4. G. Moriceau, G. Gody, M. Hartlieb, J. Winn, H. Kim, A. Mastrangelo, T. Smith and S. Perrier, *Polym. Chem,*, 2017, **8**, 4152-4161.
5. J. Tanaka, S. Tani, R. Peltier, E. H. Pilkington, A. Kerr, T. P. Davis and P. Wilson, *Polym. Chem,*, 2018, **9**, 1551-1556.
6. J. Tanaka, A. S. Gleinich, Q. Zhang, R. Whitfield, K. Kempe, D. M. Haddleton, T. P. Davis, S. b. Perrier, D. A. Mitchell and P. Wilson, *Biomacromolecules*, 2017, **18**, 1624-1633.
7. J. Zhang, J. Tanaka, P. Gurnani, P. Wilson, M. Hartlieb and S. Perrier, *Polym. Chem,*, 2017, **8**, 4079-4087.
8. J. Yeow, R. Chapman, J. Xu and C. Boyer, *Polym. Chem,*, 2017, **8**, 5012-5022.
9. J. Tan, D. Liu, Y. Bai, C. Huang, X. Li, J. He, Q. Xu and L. Zhang, *Macromolecules*, 2017, **50**, 5798-5806.
10. R. Chapman, A. J. Gormley, K.-L. Herpoldt and M. M. Stevens, *Macromolecules*, 2014, **47**, 8541-8547.
11. L. Zhifen, L. Yue and A. Zesheng, *Angew. Chem.*, 2017, **129**, 14040-14044.
12. G. Gody, R. Barbey, M. Danial and S. Perrier, *Polym. Chem,*, 2015, **6**, 1502-1511.
13. M. Zamfir and J.-F. Lutz, *Nat. Commun.*, 2012, **3**, 1138.
14. M. Ouchi, N. Badi, J.-F. Lutz and M. Sawamoto, *Nat. Chem.*, 2011, **3**, 917.
15. J.-F. Lutz, *Polym. Chem,*, 2010, **1**, 55-62.
16. A. Anastasaki, B. Oschmann, J. Willenbacher, A. Melker, M. H. C. V. Son, N. P. Truong, M. W. Schulze, E. H. Discekici, A. J. McGrath, T. P. Davis, C. M. Bates and C. J. Hawker, *Angew. Chem. Int. Ed.*, 2017, **56**, 14483-14487.
17. A. Anastasaki, V. Nikolaou and D. M. Haddleton, *Polym. Chem,*, 2016, **7**, 1002-1026.
18. F. Alsubaie, A. Anastasaki, V. Nikolaou, A. Simula, G. Nurumbetov, P. Wilson, K. Kempe and D. M. Haddleton, *Macromolecules*, 2015, **48**, 5517-5525.
19. F. Alsubaie, A. Anastasaki, V. Nikolaou, A. Simula, G. Nurumbetov, P. Wilson, K. Kempe and D. M. Haddleton, *Macromolecules*, 2015, **48**, 6421-6432.
20. C. Waldron, Q. Zhang, Z. Li, V. Nikolaou, G. Nurumbetov, J. Godfrey, R. McHale, G. Yilmaz, R. K. Randev, M. Girault, K. McEwan, D. M. Haddleton, M. Droesbeke, A. J.

Haddleton, P. Wilson, A. Simula, J. Collins, D. J. Lloyd, J. A. Burns, C. Summers, C. Houben, A. Anastasaki, M. Li, C. R. Becer, J. K. Kiviaho and N. Risangud, *Polym. Chem,*, 2014, **5**, 57.

21. Q. Zhang, A. Anastasaki, G.-Z. Li, A. J. Haddleton, P. Wilson and D. M. Haddleton, *Polym. Chem,*, 2014, **5**, 3876-3883.
22. A. Anastasaki, V. Nikolaou, Q. Zhang, J. Burns, S. R. Samanta, C. Waldron, A. J. Haddleton, R. McHale, D. Fox and V. Percec, *J. Am. Chem. Soc.*, 2014, **136**, 1141-1149.
23. Q. Zhang, P. Wilson, Z. Li, R. McHale, J. Godfrey, A. Anastasaki, C. Waldron and D. M. Haddleton, *J. Am. Chem. Soc*, 2013, **135**, 7355-7363.
24. A. H. Soeriyadi, C. Boyer, F. Nyström, P. B. Zetterlund and M. R. Whittaker, *J. Am. Chem. Soc.*, 2011, **133**, 11128-11131.
25. G. Gody, T. Maschmeyer, P. B. Zetterlund and S. Perrier, *Macromolecules*, 2014, **47**, 3451-3460.
26. G. Gody, T. Maschmeyer, P. B. Zetterlund and S. Perrier, *Nat. Commun.*, 2013, **4**, 2505.
27. A. Kerr, M. Hartlieb, J. Sanchis, T. Smith and S. Perrier, *Chem. Commun.*, 2017, **53**, 11901-11904.
28. J. Zhang, R. Deubler, M. Hartlieb, L. Martin, J. Tanaka, E. Patyukova, P. D. Topham, F. H. Schacher and S. Perrier, *Macromolecules*, 2017, **50**, 7380-7387.
29. A. Kuroki, P. Sangwan, Y. Qu, R. Peltier, C. Sanchez-Cano, J. Moat, C. G. Dowson, E. G. L. Williams, K. E. S. Locock, M. Hartlieb and S. Perrier, *ACS Appl. Mater. Interfaces*, 2017, **9**, 40117-40126.
30. J. Zhang, G. Gody, M. Hartlieb, S. Catrouillet, J. Moffat and S. Perrier, *Macromolecules*, 2016, **49**, 8933-8942.
31. C. Bray, R. Peltier, H. Kim, A. Mastrangelo and S. Perrier, *Polym. Chem,*, 2017, **8**, 5513-5524.
32. N. G. Engelis, A. Anastasaki, G. Nurumbetov, N. P. Truong, V. Nikolaou, A. Shegiwal, M. R. Whittaker, T. P. Davis and D. M. Haddleton, *Nat. Chem.*, 2016, **9**, 171.
33. T. R. Barlow, J. C. Brendel and S. Perrier, *Macromolecules*, 2016, **49**, 6203-6212.
34. C. Footman, P. A. de Jongh, J. Tanaka, R. Peltier, K. Kempe, T. P. Davis and P. Wilson, *Chem. Commun.*, 2017, **53**, 8447-8450.
35. V. Nikolaou, A. Simula, M. Droesbeke, N. Risangud, A. Anastasaki, K. Kempe, P. Wilson and D. M. Haddleton, *Polym. Chem,*, 2016, **7**, 2452-2456.
36. J. Collins, J. Tanaka, P. Wilson, K. Kempe, T. P. Davis, M. P. McIntosh, M. R. Whittaker and D. M. Haddleton, *Bioconjugate Chem.*, 2015, **26**, 633-638.
37. Q. Zhang, Z. Li, P. Wilson and D. M. Haddleton, *Chem. Commun.*, 2013, **49**, 6608-6610.

38. C. Boyer and T. P. Davis, *Chem. Commun.*, 2009, 6029-6031.
39. D. R. Carroll, A. P. Constantinou, N. Stingelin and T. K. Georgiou, *Polym. Chem,*, 2018, **9**, 3450-3454.
40. N. G. Engelis, A. Anastasaki, R. Whitfield, G. R. Jones, E. Liarou, V. Nikolaou, G. Nurumbetov and D. M. Haddleton, *Macromolecules*, 2018, **51**, 336-342.
41. A. Lotierzo, R. M. Schofield and S. A. F. Bon, *ACS Macro Lett.*, 2017, **6**, 1438-1443.
42. N. J. Gesmundo, B. Sauvagnat, P. J. Curran, M. P. Richards, C. L. Andrews, P. J. Dandliker and T. Cernak, *Nature*, 2018, **557**, 228-232.
43. A. Postma, T. P. Davis, G. Li, G. Moad and M. S. O'Shea, *Macromolecules*, 2006, **39**, 5307-5318.
44. C. J. Ferguson, R. J. Hughes, D. Nguyen, B. T. T. Pham, R. G. Gilbert, A. K. Serelis, C. H. Such and B. S. Hawkett, *Macromolecules*, 2005, **38**, 2191-2204.
45. http://www.wako-chem.co.jp/kaseihin_en/waterazo/VA-044.htm).

Appendix B: List of Publications

7) Organic arsenicals as functional motifs in polymer and biomaterials science. **Joji Tanaka**, Thomas P. Davis* and Paul Wilson* **Macromolecular Rapid Communications** 2018, 1800205 **DOI:** 10.1002/marc.201800205

6) Synthesis, aggregation and responsivity of block copolymers containing organic arsenicals. **Joji Tanaka**, Seiji Tani, Raoul Peltier, Emily H. Pilkington, Andrew Kerr, Thomas P. Davis and Paul Wilson* **Polymer Chemistry**, 2018,9, 1551-1556 **DOI:** 10.1039/C7PY01852E

5) Evolution of Microphase Separation with Variations of Segments of Sequence-Controlled Multiblock Copolymers. Junliang Zhang , Robert Deubler, Matthias Hartlieb , Liam Martin, **Joji Tanaka,** Elena Patyukova, Paul D. Topham, Felix H. Schacher, and Sébastien Perrier* **Macromolecules**, 2017, 50, 7380-7387 **DOI:** 10.1021/acs.macromol.7b01831

4) Thiol-reactive (co)polymer scaffolds comprised of organic arsenical acrylamides**.** Charlotte Footman, Patrick A.J.M. de Jongh, **Joji Tanaka**, Raoul Peltier, Kristian Kempe, Thomas P. Davis* and Paul Wilson* **Chemical Communications,** 2017, 53, 8447-8450 **DOI:** 10.1039/C7CC03880A

3) Self-assembly and disassembly of stimuli responsive tadpole-like single chain nanoparticles using a switchable hydrophilic/hydrophobic boronic acid cross-linker. Junliang Zhang, **Joji Tanaka**, Pratik Gurnani, Paul Wilson, Matthias Hartlieb and Sébastien Perrier* **Polymer Chemistry**, 2017, 8, 4079-4087 **DOI:** 10.1039/C7PY00828G

2) Specific and Differential Binding of N-Acetylgalactosamine Glycopolymers to the Human Macrophage Galactose Lectin and Asialoglycoprotein Receptor. **Joji Tanaka**, Anne S. Gleinich, Qiang Zhang, Richard Whitfield, Kristian Kempe, David M. Haddleton, Thomas P. Davis, Sébastien Perrier, Daniel A. Mitchell* and Paul Wilson* **Biomacromolecules**, 2017, 18 (5), pp 1624–1633 **DOI:** 10.1021/acs.biomac.7b00228

1) In Situ Conjugation of Dithiophenol Maleimide Polymers and Oxytocin for Stable and Reversible Polymer–Peptide Conjugates Jennifer Collins, **Joji Tanaka**, Paul Wilson, Kristian Kempe, Thomas P. Davis, Michelle P. McIntosh, Michael R. Whittaker, and David M. Haddleton* **Bioconjugate Chemistry**, 2015, 26 (4), pp 633–638 **DOI**: 10.1021/bc5006202

Appendix C: Supporting Information

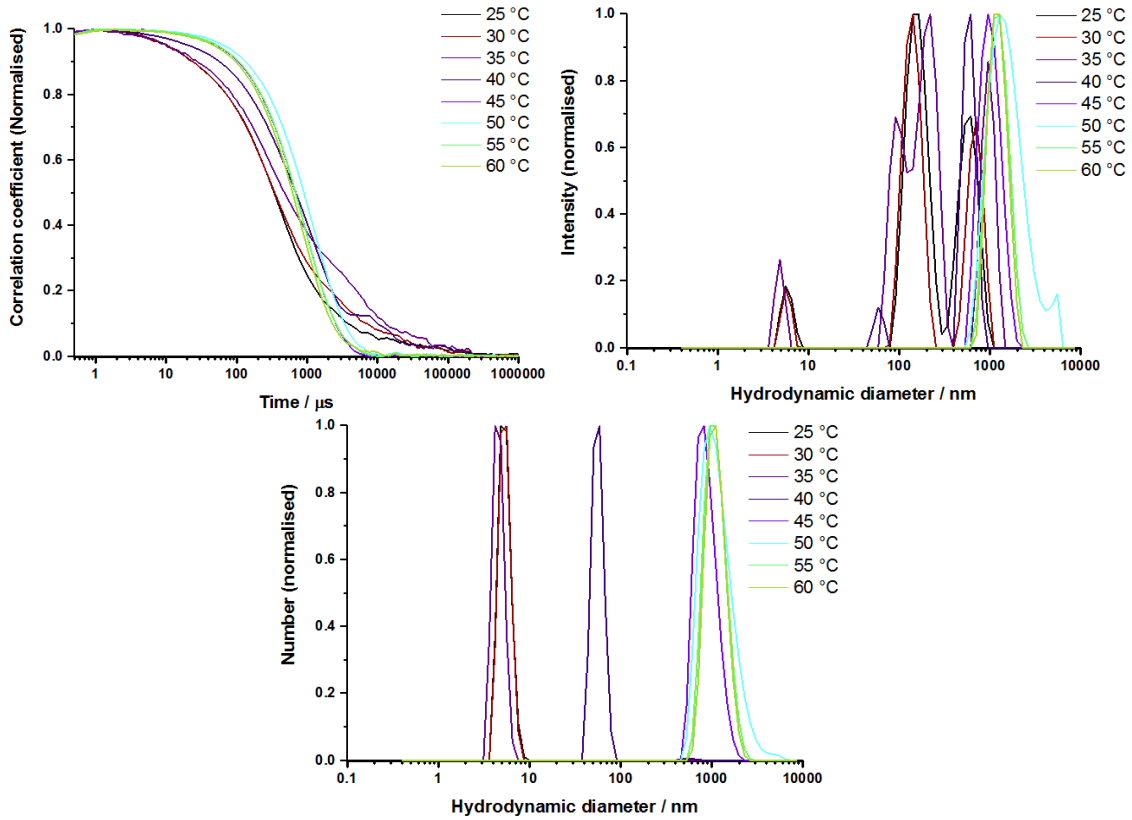

S2.4: DLS Correlation coefficient, intensity distribution and number distribution as a function of temperature for P(NIPAm)$_{80}$ in Figure 2.4

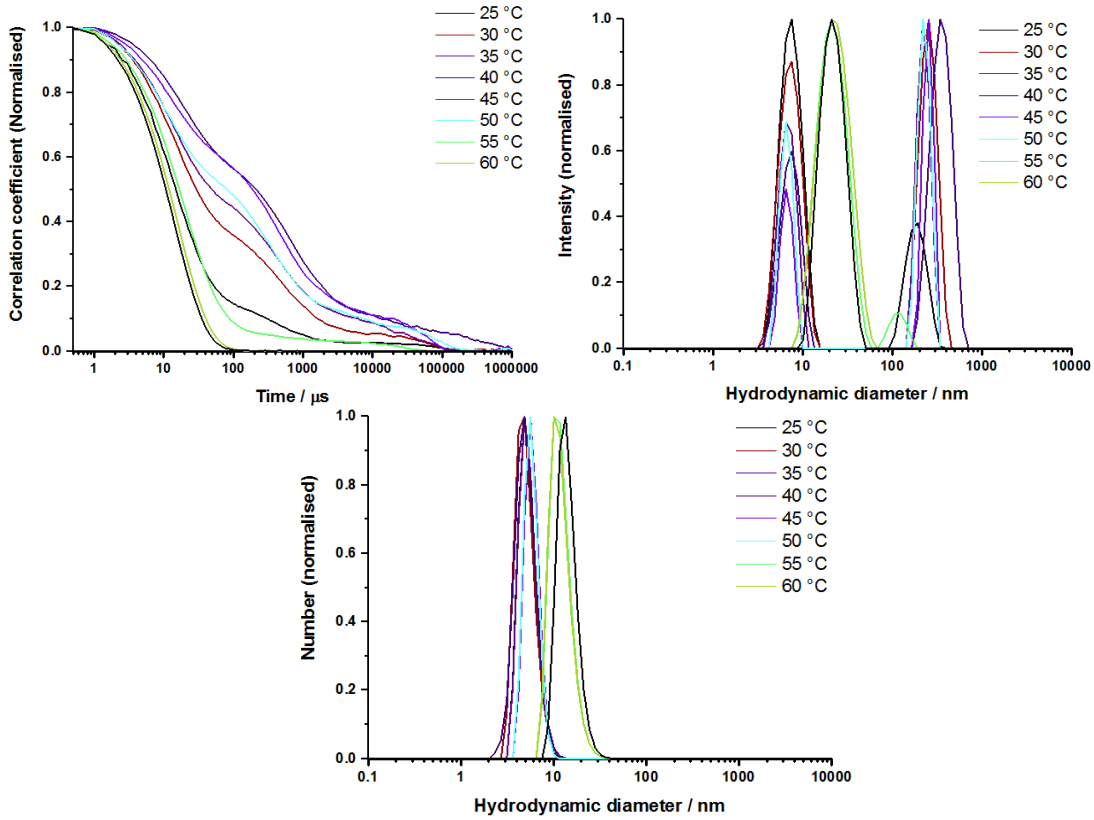

S2.5: DLS Correlation coefficient, intensity distribution and number distribution as a function of temperature for P2.1 in Figure 2.5

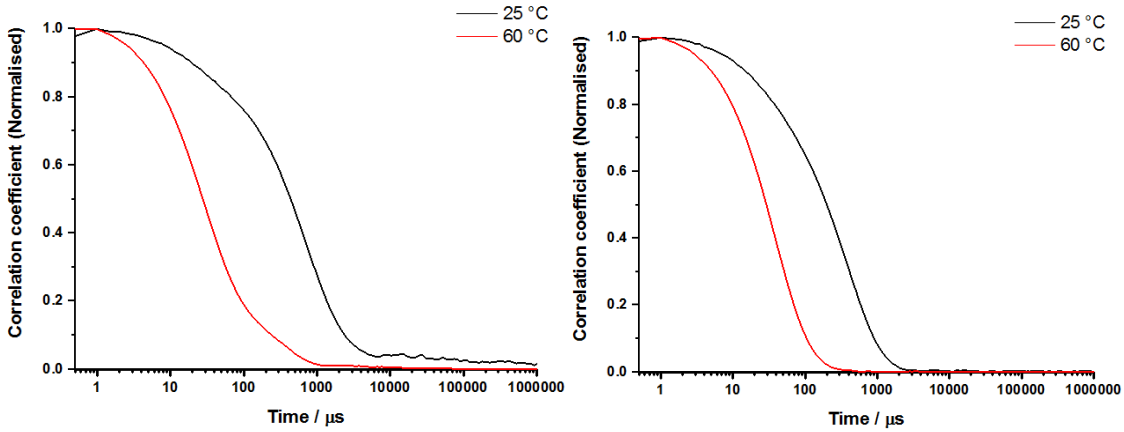

S2.6: DLS Correlation coefficient as a function of temperature for P2.2 (left) and P2.3 (right) in Figure 2.6

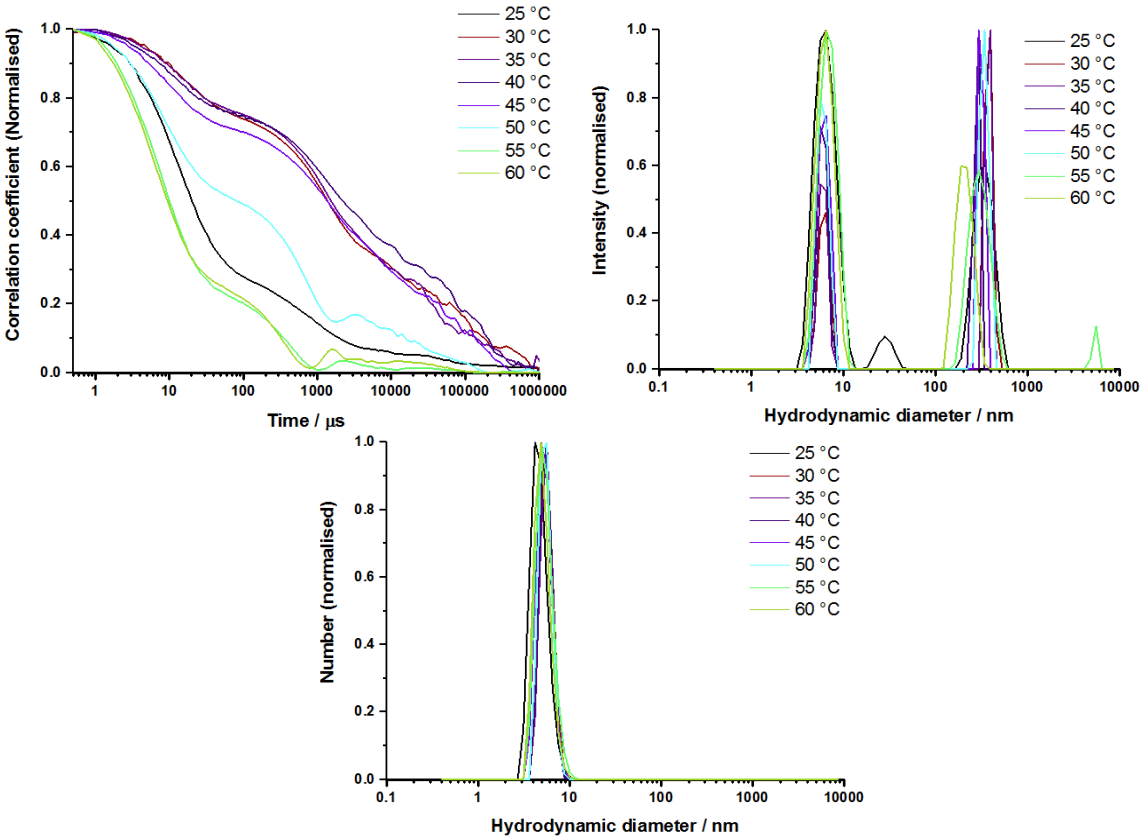

S2.7A: DLS Correlation coefficient, intensity distribution and number distribution as a function of temperature for P2.4 in Figure 2.7

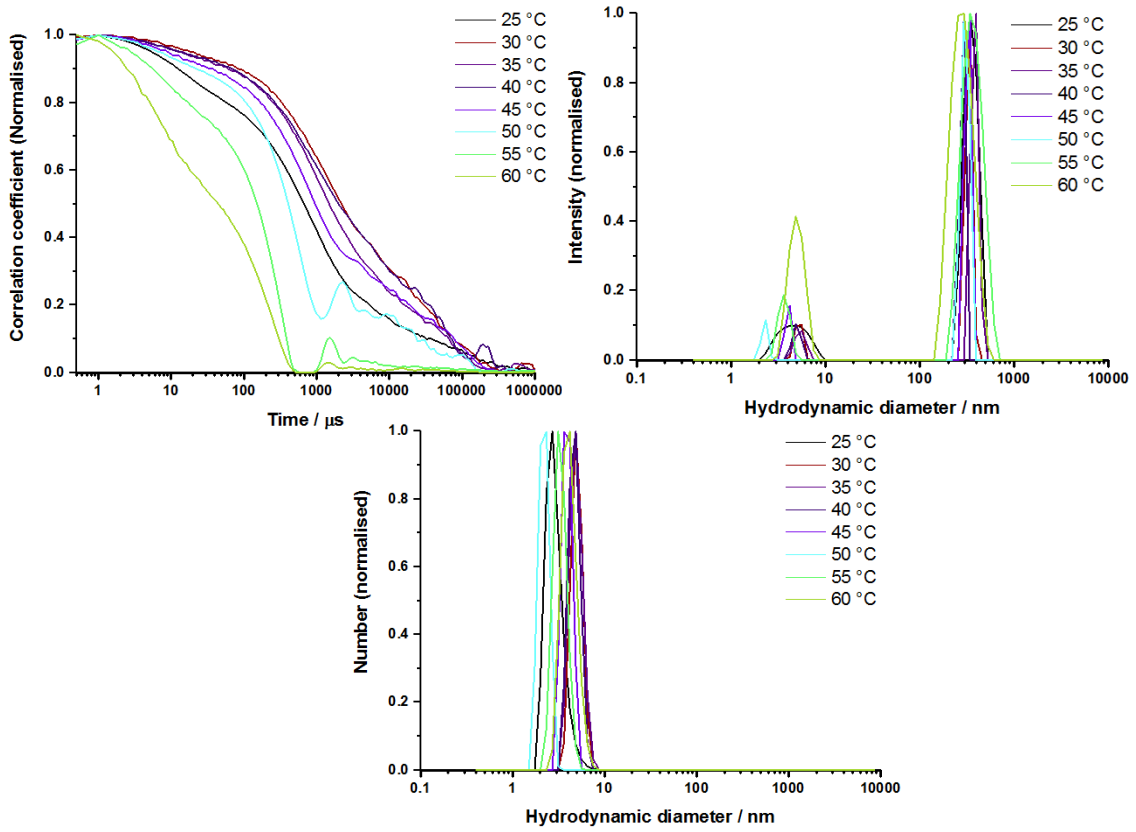

S2.7B: DLS Correlation coefficient, intensity distribution and number distribution as a function of temperature for P2.5 in Figure 2.7

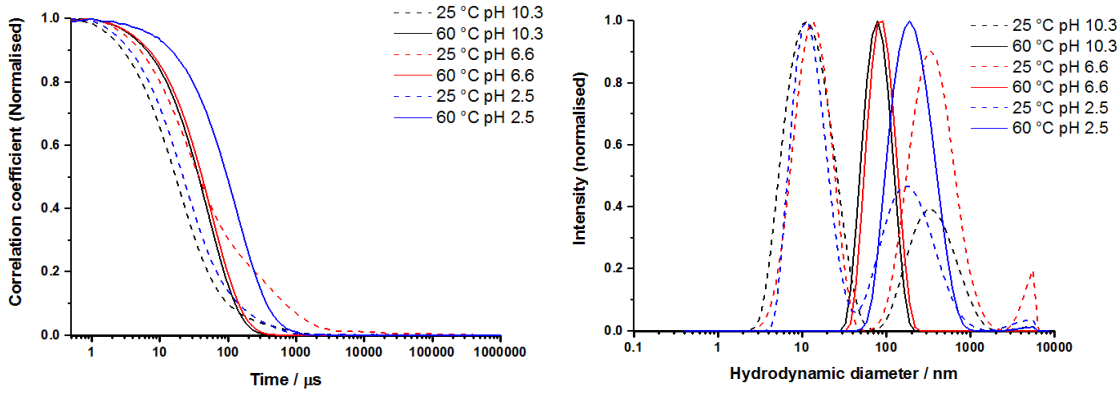

S2.8A: DLS Correlation coefficient and intensity distribution as a function of temperature for P2.3 in Figure 2.8

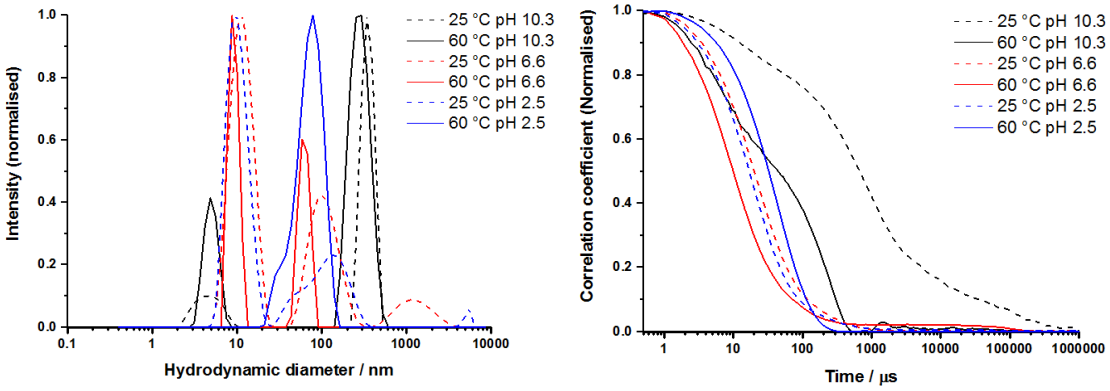

S2.8B: DLS Correlation coefficient and intensity distribution as a function of temperature for P2.5 in Figure 2.8

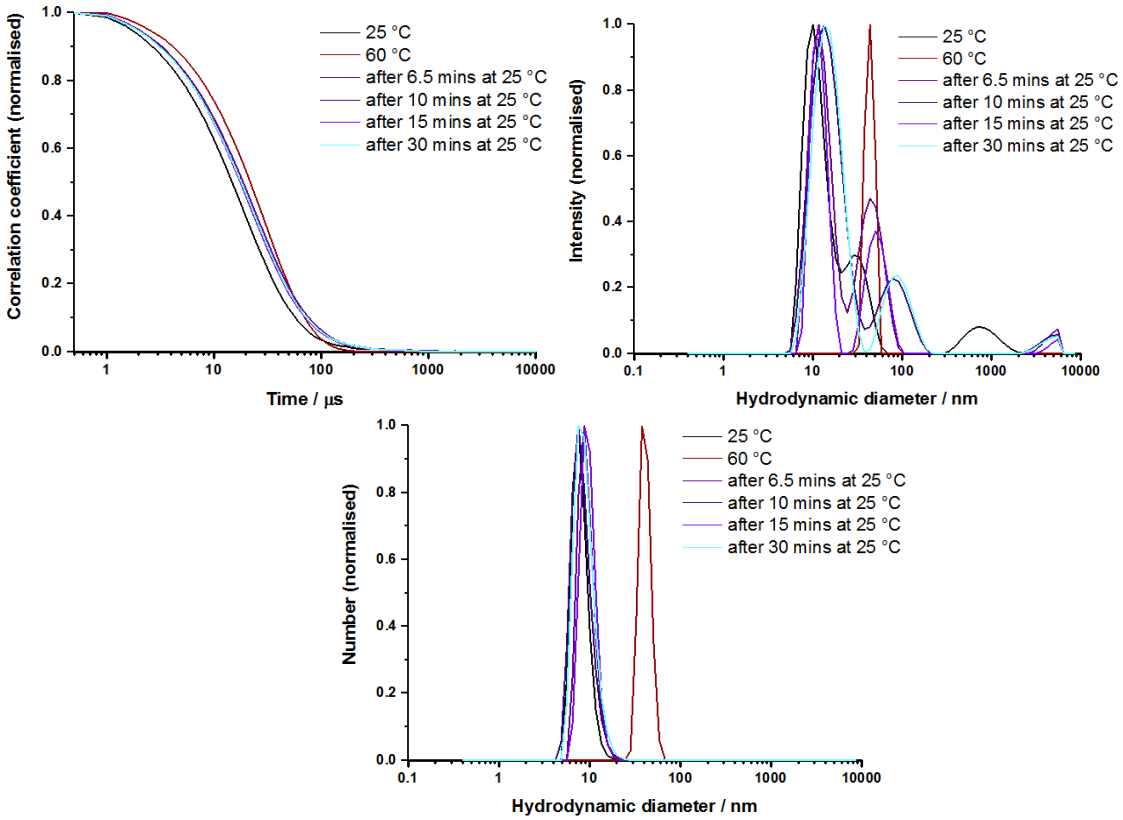

S2.9A DLS Correlation coefficient, intensity distribution and number distribution as a function of temperature for P2.2 in Figure 2.9. Temporal changes in the particle size of the cross-linked particles of (PEGA$_{20-n}$-*co*-AsAm$_n$)-*b*-NIPAM$_{80}$ (P2.2) after heating in hypophosphorous solution (10 mins, 10 mg/ml). DLS cell was heated from 25 – 60 °C over 120 secs followed by 60 secs equilibration time before being held at 60 °C for 10 – 90 mins. Cooling of the cell occurred over 120 secs followed by 60 secs equilibration after which measurement of stability commenced (t = 0, 25 °C).

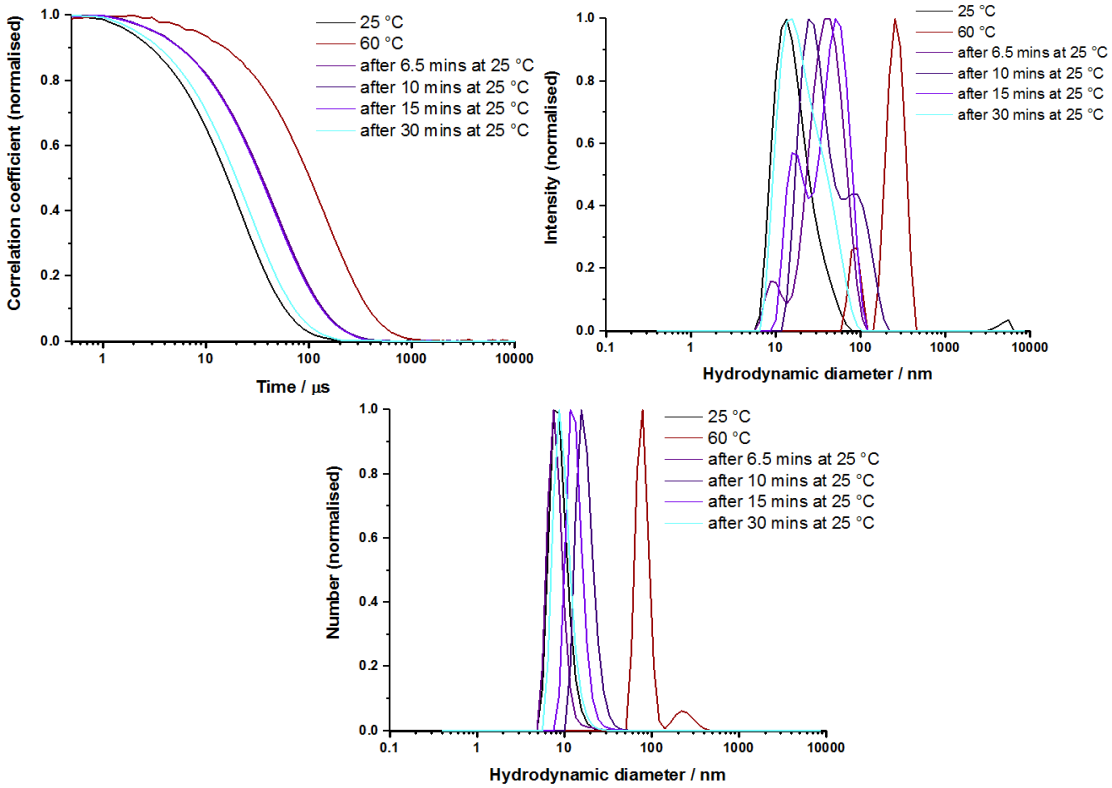

S2.9B DLS Correlation coefficient, intensity distribution and number distribution as a function of temperature for P2.3 in Figure 2.9. Temporal changes in the particle size of the cross-linked particles of (PEGA$_{20-n}$-*co*-AsAm$_n$)-*b*-NIPAM$_{80}$ (P2.3) after heating in hypophosphorous solution (10 mins, 10 mg/ml). DLS cell was heated from 25 – 60 °C over 120 secs followed by 60 secs equilibration time before being held at 60 °C for 10 – 90 mins. Cooling of the cell occurred over 120 secs followed by 60 secs equilibration after which measurement of stability commenced (t = 0, 25 °C).

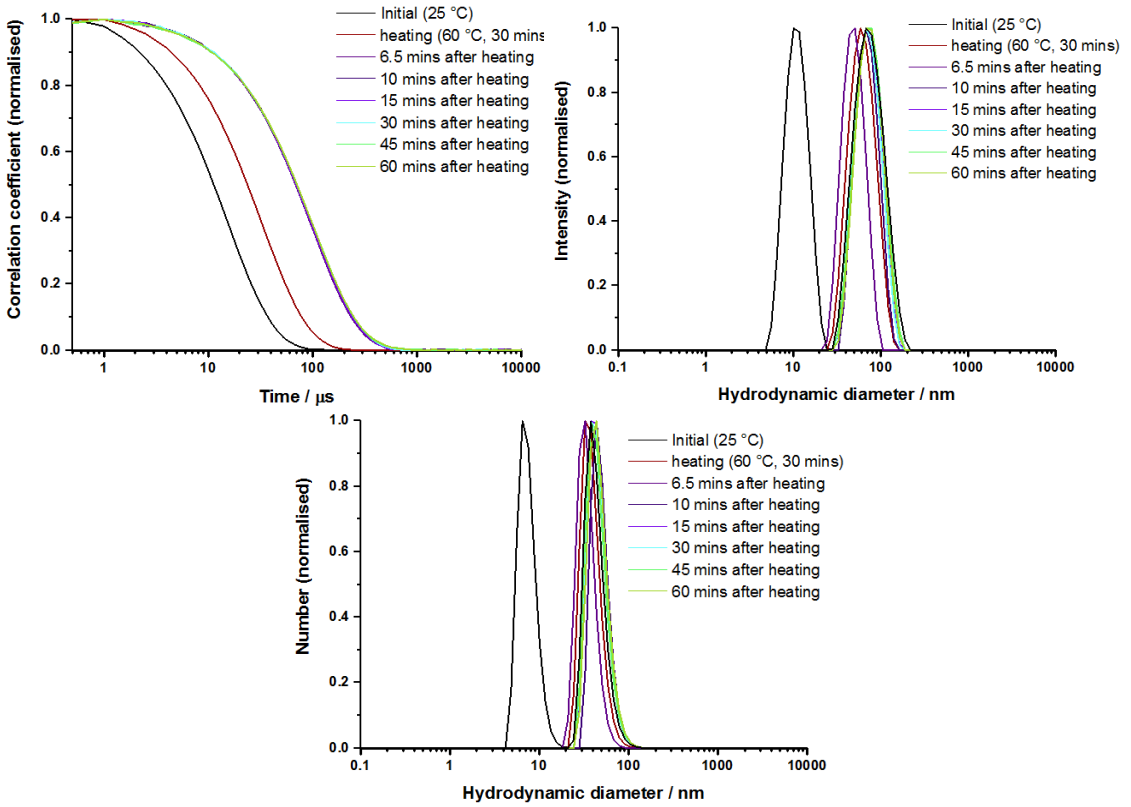

S2.10A DLS Correlation coefficient, intensity distribution and number distribution as a function of temperature for P2.4 in Figure 2.10. Temporal changes in the particle size of the cross-linked particles of $PEGA_{20}$-*b*-($NIPAm_{80-n}$-*co*-$AsAm_n$) (P2.4) after heating in hypophosphorous acid (10 mg/ml). DLS cell was heated from 25 – 60 °C over 120 secs followed by 60 secs equilibration time before being held at 60 °C for 30 mins (P2.4) respectively. Cooling of the cell occurred over 120 secs followed by 60 secs equilibration after which measurement of stability commenced (t = 0, 25 °C).

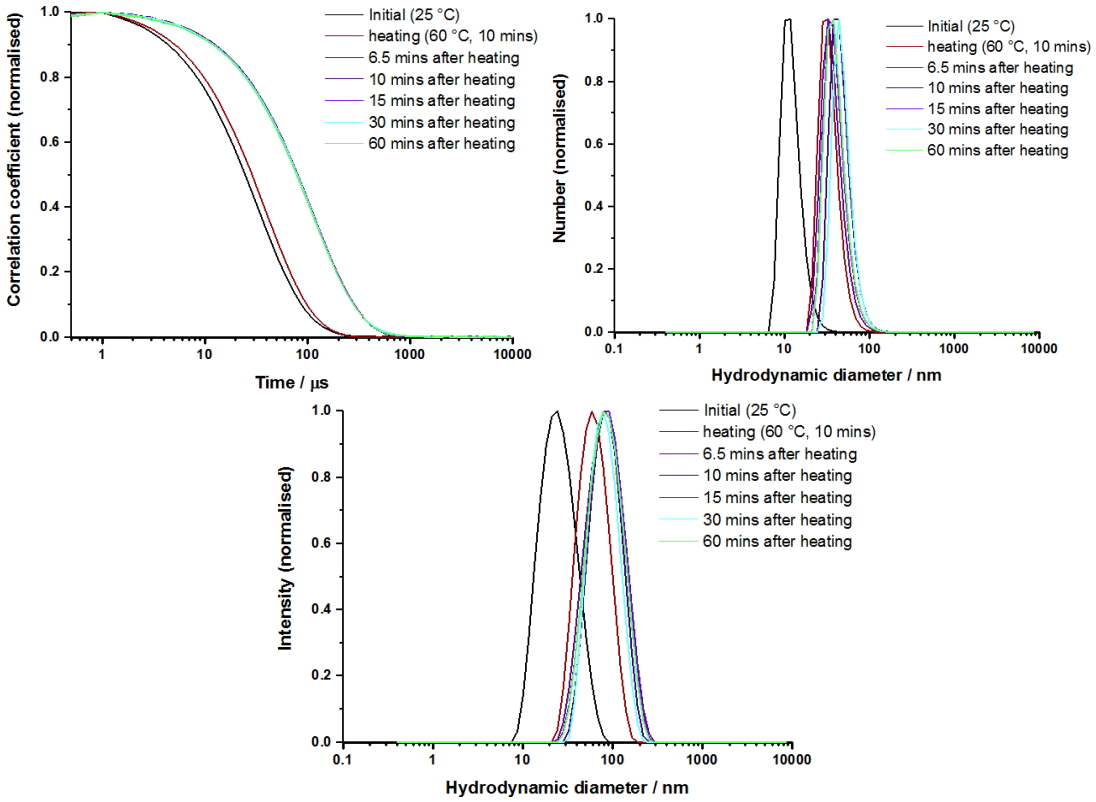

S2.10B DLS Correlation coefficient, intensity distribution and number distribution as a function of temperature for P2.5 in Figure 2.10. Temporal changes in the particle size of the cross-linked particles of $PEGA_{20}$-*b*-($NIPAm_{80-n}$-*co*-$AsAm_n$) (P2.5) after heating in hypophosphorous acid (10 mg/ml). DLS cell was heated from 25 – 60 °C over 120 secs followed by 60 secs equilibration time before being held at 60 °C for 10 mins (P2.5) respectively. Cooling of the cell occurred over 120 secs followed by 60 secs equilibration after which measurement of stability commenced (t = 0, 25 °C).

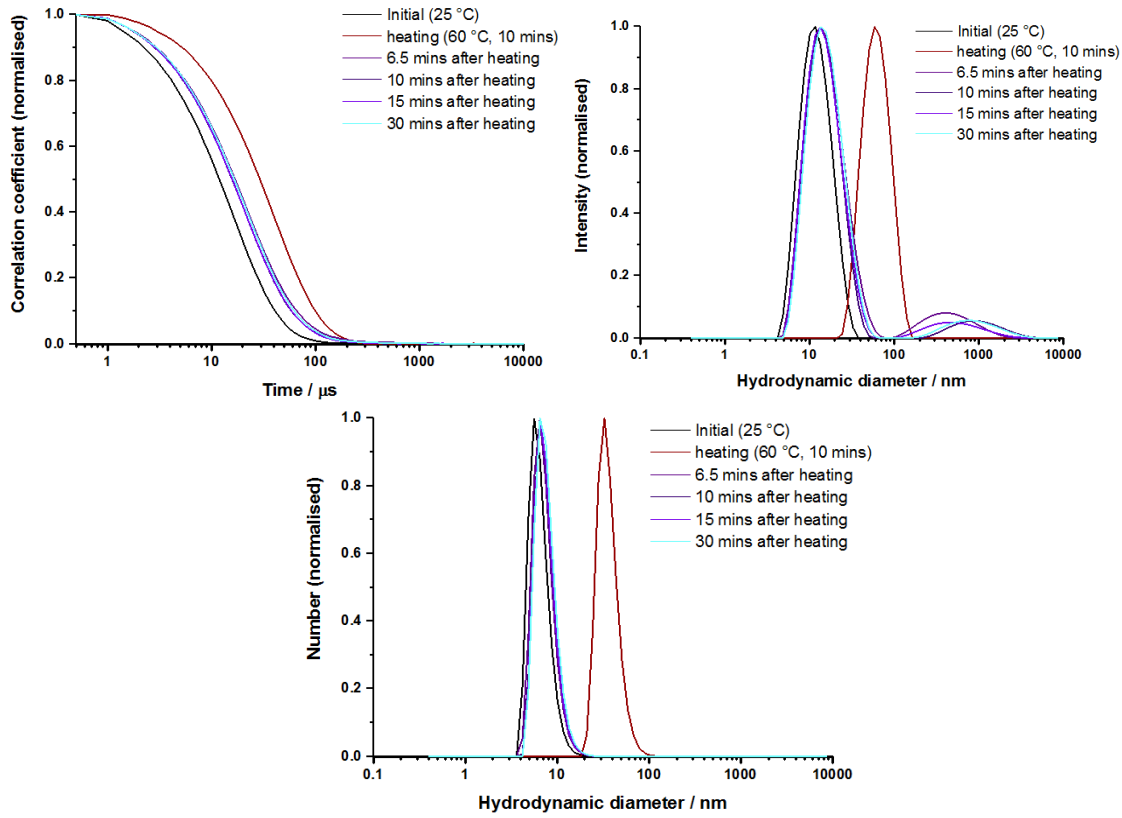

S2.12 DLS Correlation coefficient, intensity distribution and number distribution as a function of temperature for P2.4 in Figure 2.12. Stability of particles derived from PEGA$_{20}$-*b*-(NIPAM$_{75}$-*co*-AsAm$_5$) (P2.4) after heating at 60 °C in aqueous hypophosphorous acid for 10 mins. DLS cell was heated from 25 – 60 °C for 120 secs followed by 60 secs equilibration time before being held at 60 °C for 10 mins. Cooling of the cell occurred over 120 secs followed by 60 secs equilibration after which measurement of stability commenced (t = 0, 25 °C).

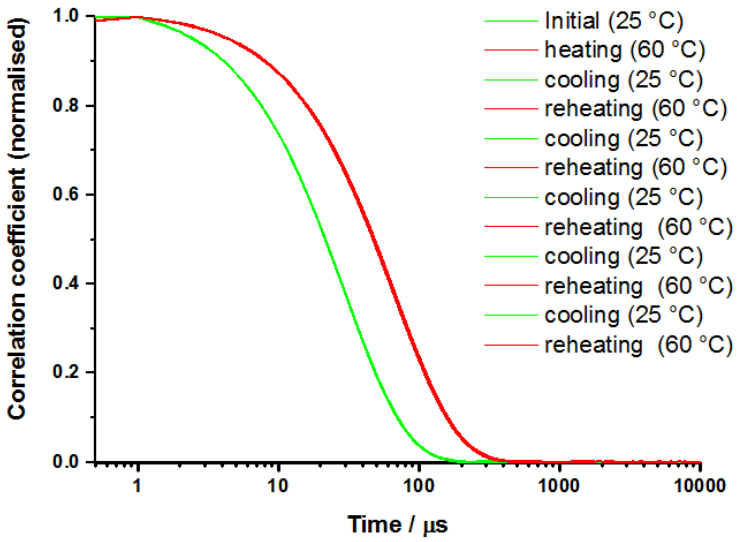

S2.13 DLS Correlation coefficient as a function of temperature for PEGA$_{20}$-*b*-(NIPAm$_{70}$-*co*-AsAm$_{10}$) in hypophosphorous solution Figure 2.13

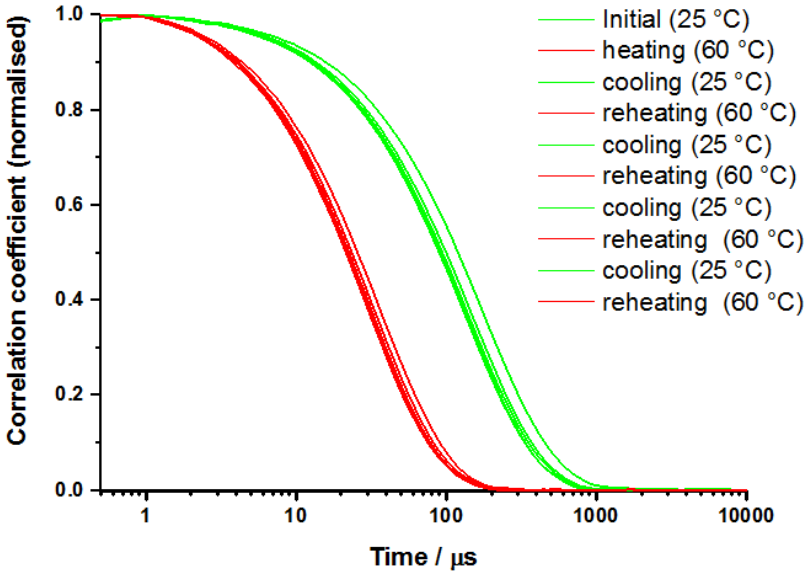

S2.14 DLS Correlation coefficient as a function of temperature for NP$_{As-10}$ Figure 2.14 and Figure 2.15

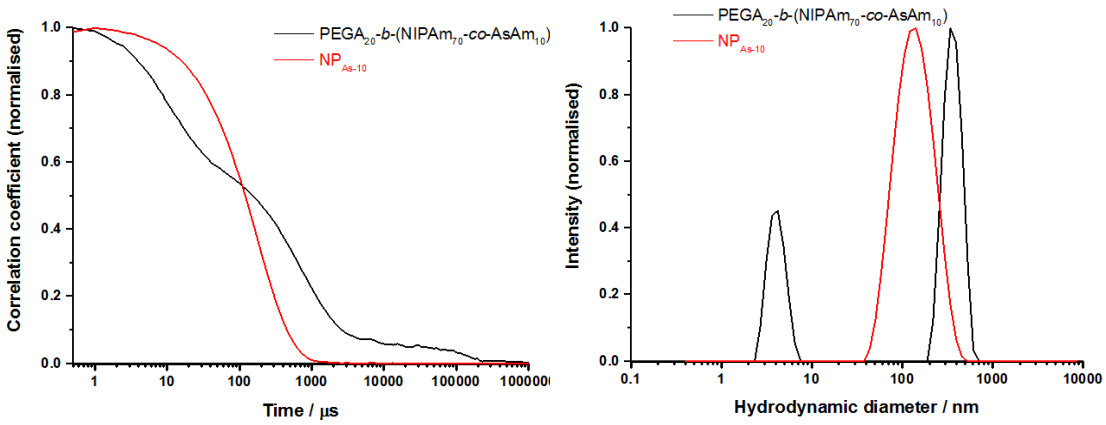

S2.16 DLS Correlation coefficient and intensity distribution of NP_{As-10} (red) and P2.5 (black) in Figure 2.16

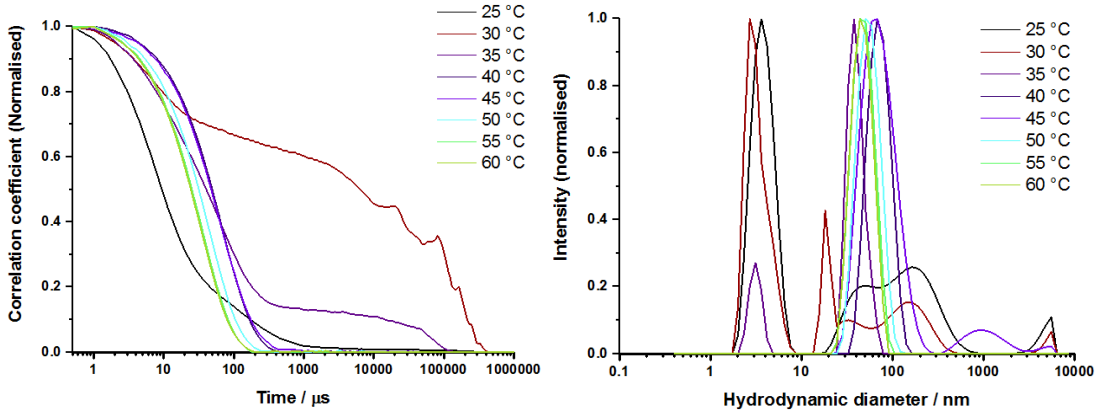

S2.20A DLS Correlation coefficient and intensity distribution of P2.6 in Figure 2.20

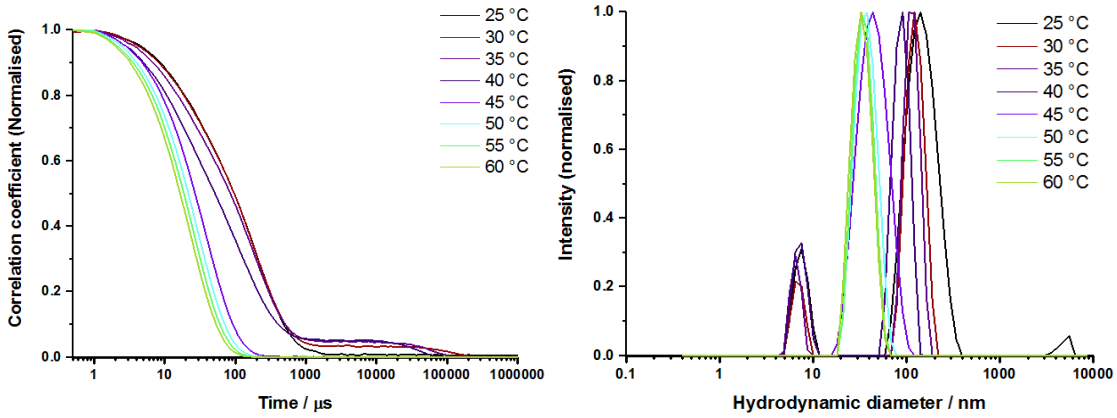

S2.20B DLS Correlation coefficient and intensity distribution of P2.7 in Figure 2.20

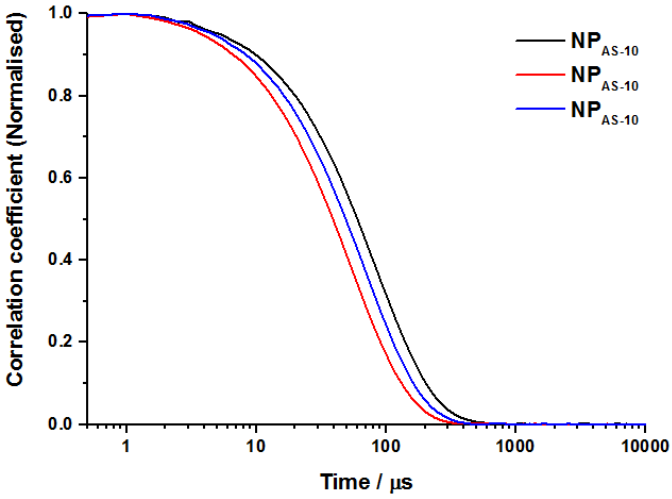

S2.21 DLS Correlation coefficient of NP_{AS-10}, NP_{AS-15} and NP_{AS-20} in Figure 2.21

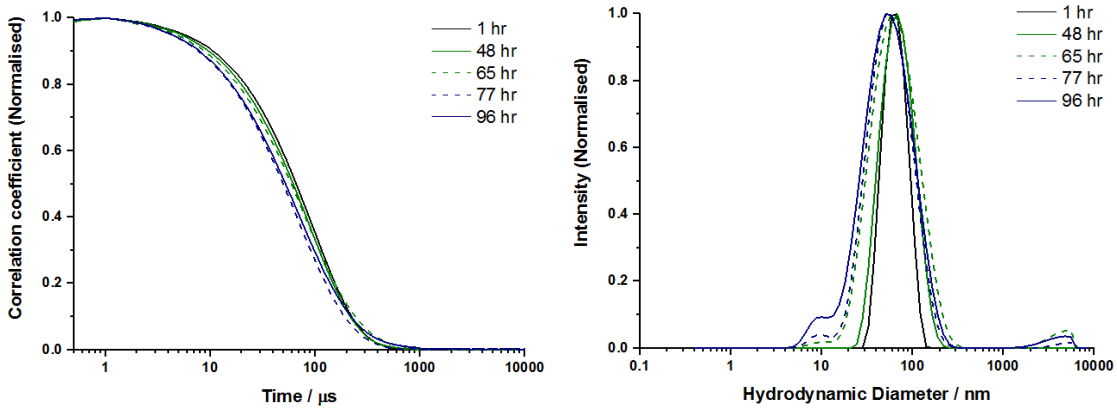

S2.26A DLS Correlation coefficient and intensity distribution for NP_{AS-10} as a function time in aqueous solution in Figure 2.26

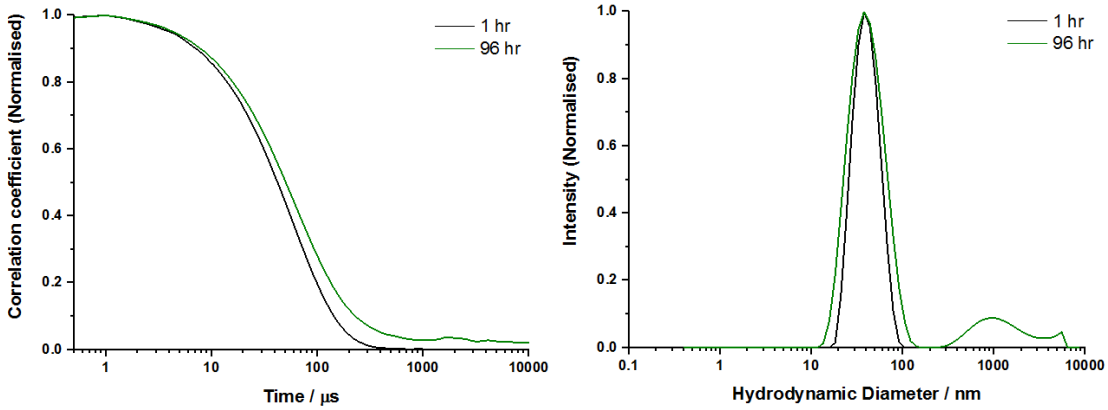

S2.26B DLS Correlation coefficient and intensity distribution for NP_{AS-15} as a function time in aqueous solution in Figure 2.26

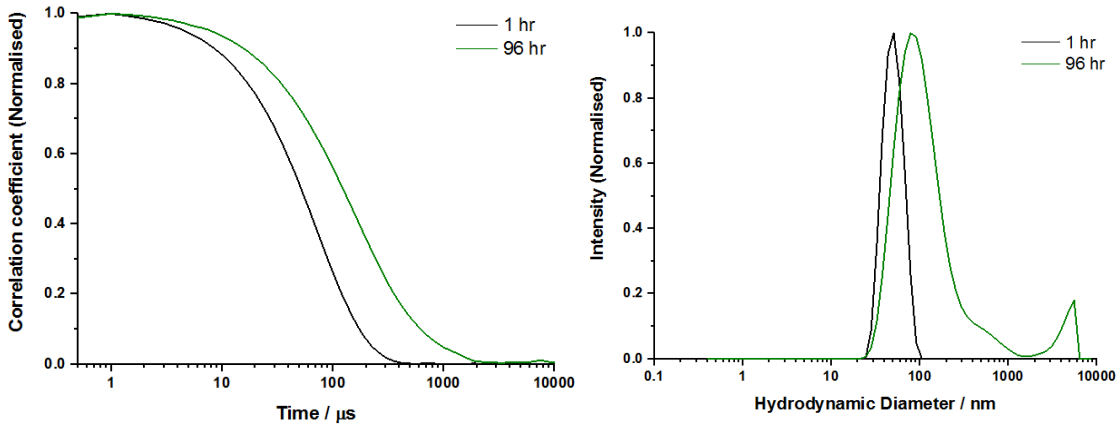

S2.26C DLS Correlation coefficient and intensity distribution for NP_{AS-20} as a function time in aqueous solution in Figure 2.26

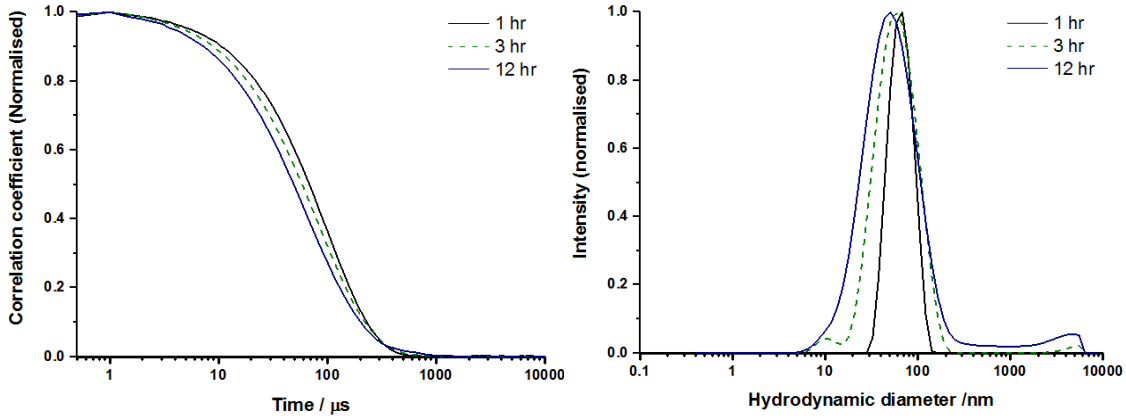

S2.27A DLS Correlation coefficient and intensity distribution for NP_{AS-10} as a function time in aqueous GSH solution (5mM) in Figure 2.27

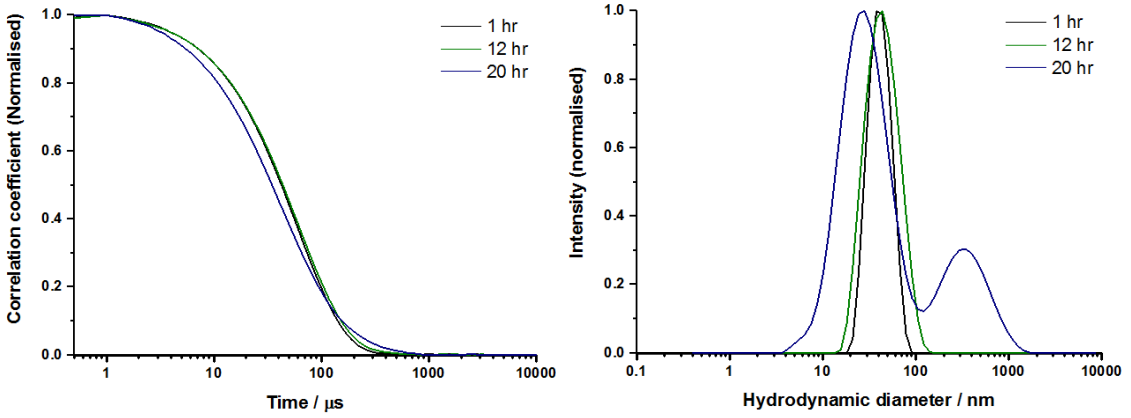

S2.27B DLS Correlation coefficient and intensity distribution for NP_{AS-15} as a function time in aqueous GSH solution (5mM) in Figure 2.27

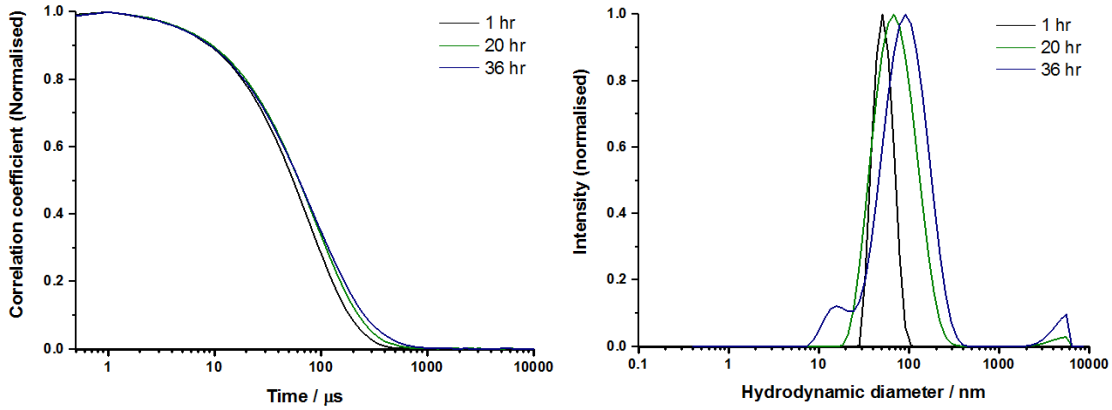

S2.27C DLS Correlation coefficient and intensity distribution for NP_{AS-20} as a function time in aqueous GSH solution (5mM) in Figure 2.27

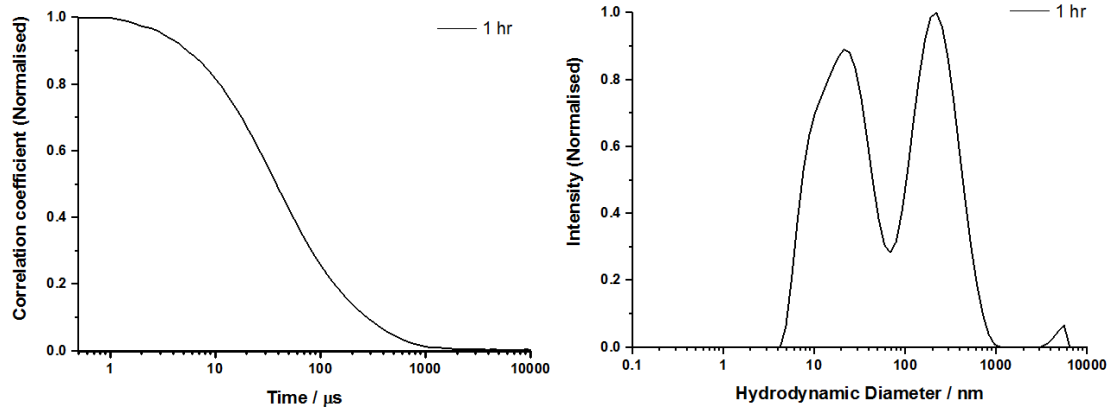

S2.28A DLS Correlation coefficient and intensity distribution for NP_{AS-10} as a function time in aqueous hydrogen peroxide solution (5mM) in Figure 2.28

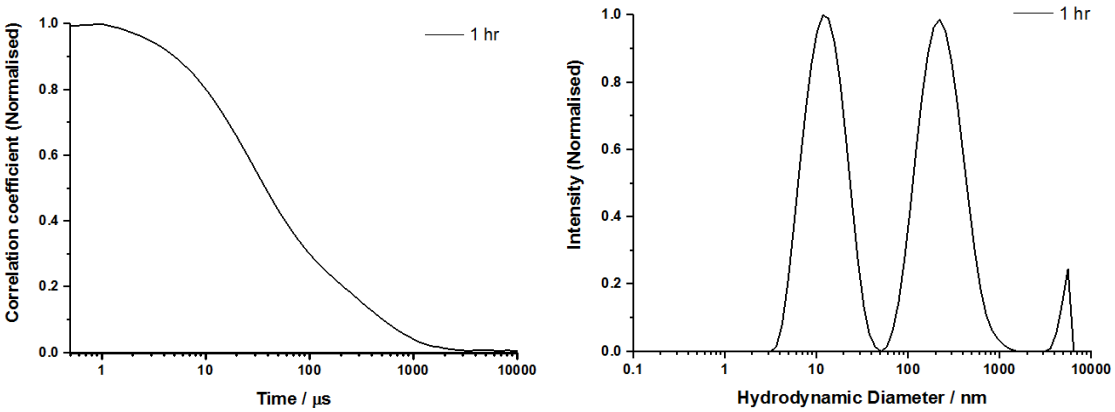

S2.28B DLS Correlation coefficient and intensity distribution for NP_{AS-15} as a function time in aqueous hydrogen peroxide solution (5mM) in Figure 2.28

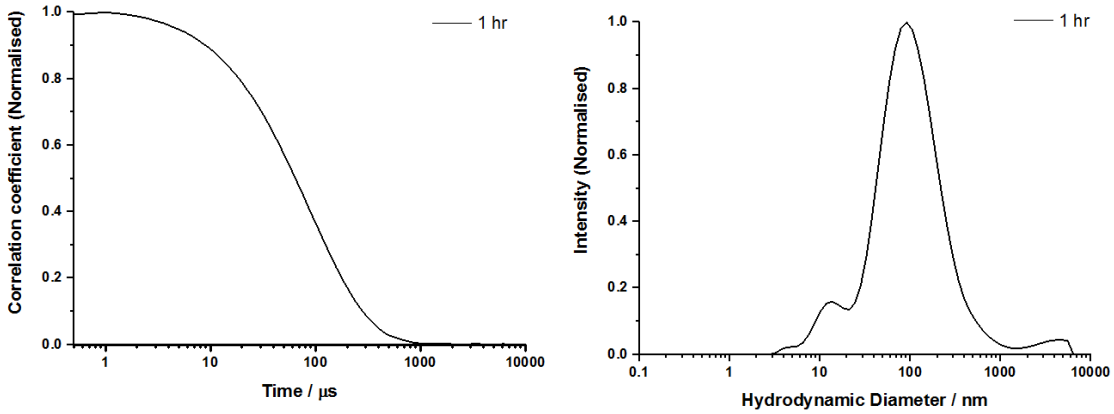

S2.28C DLS Correlation coefficient and intensity distribution for NP_{AS-20} as a function time in aqueous hydrogen peroxide solution (5mM) in Figure 2.28

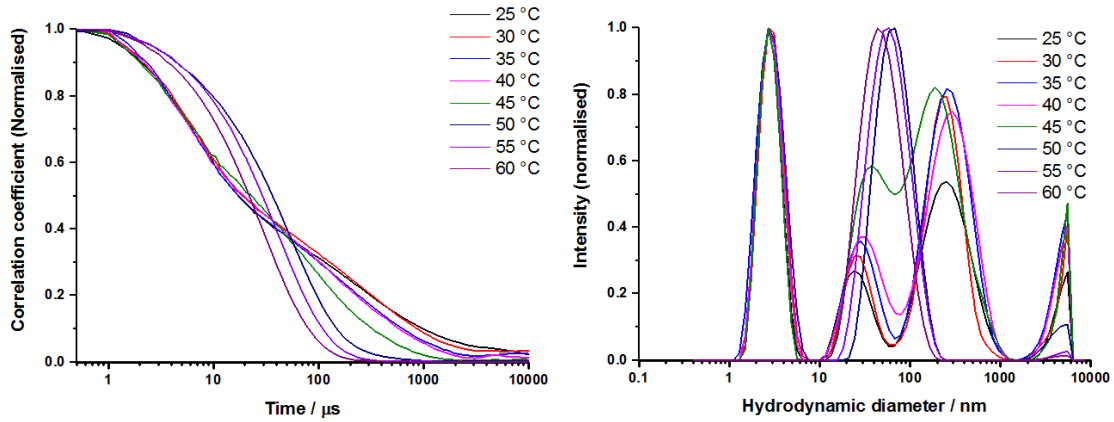

S3.4: DLS Correlation coefficient and intensity distribution as a function of temperature for P3.1 in Figure 3.4

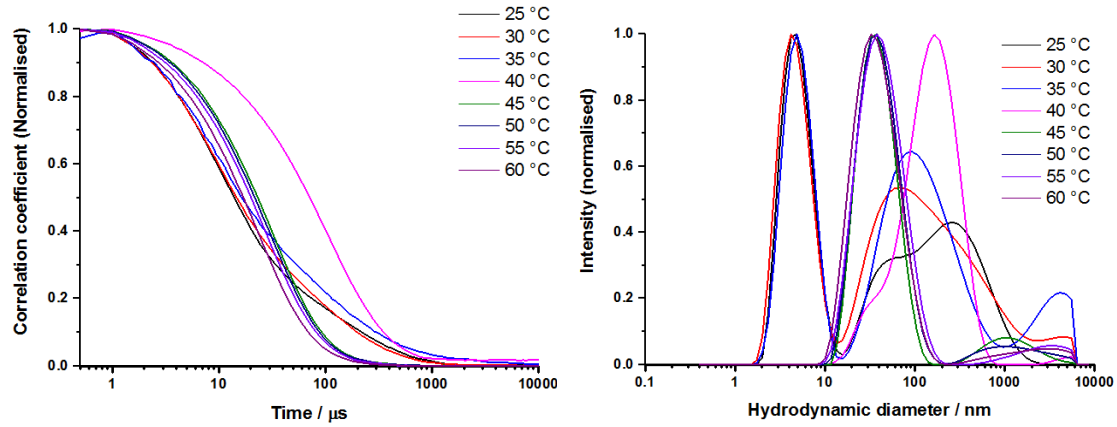

S3.5: DLS Correlation coefficient and intensity distribution as a function of temperature for P3.2 in Figure 3.5

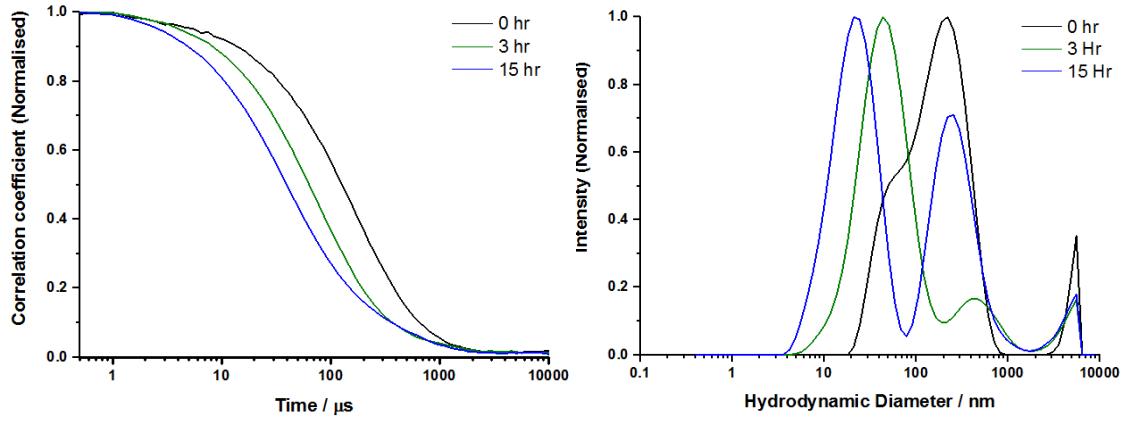

S3.7A: DLS Correlation coefficient and intensity distribution for $NP_{AS(I)}$ as a function time in aqueous GSH solution (5mM) in Figure 3.7

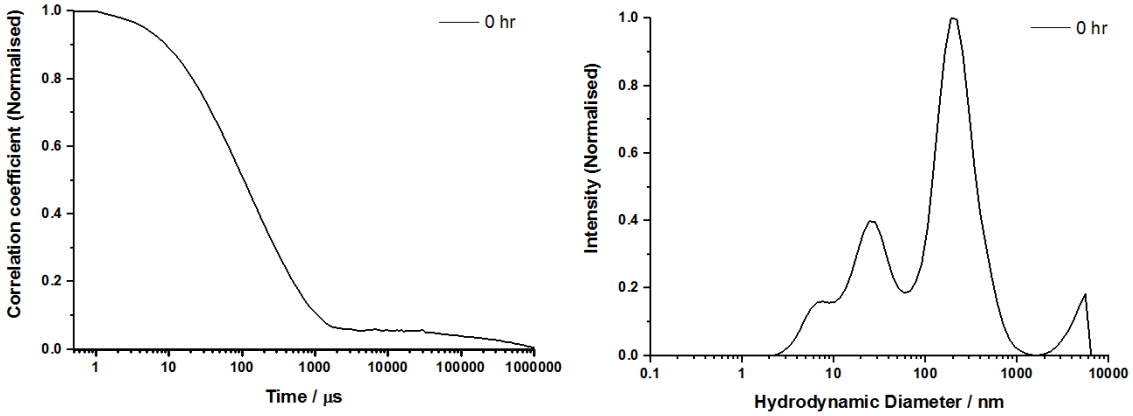

S3.7B: DLS Correlation coefficient and intensity distribution for $NP_{AS(I)}$ as a function time in aqueous hydrogen peroxide solution (5mM) in Figure 3.7

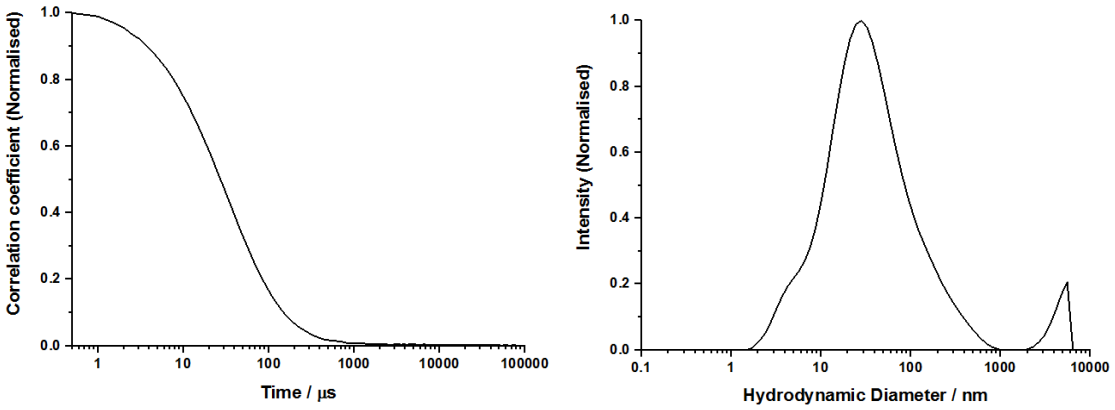

S3.9: DLS Correlation coefficient and intensity distribution of P3.2 after cross-linking with PTM under elevated temperature (60 °C) in Figure 3.9

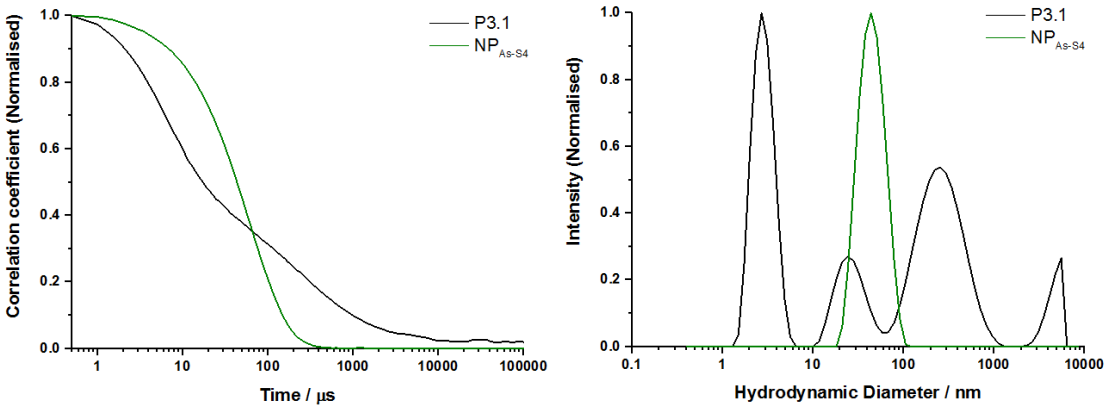

S3.10: DLS Correlation coefficient and intensity distribution of P3.1 (black) and NP_{As-S4} (green) in Figure 3.10

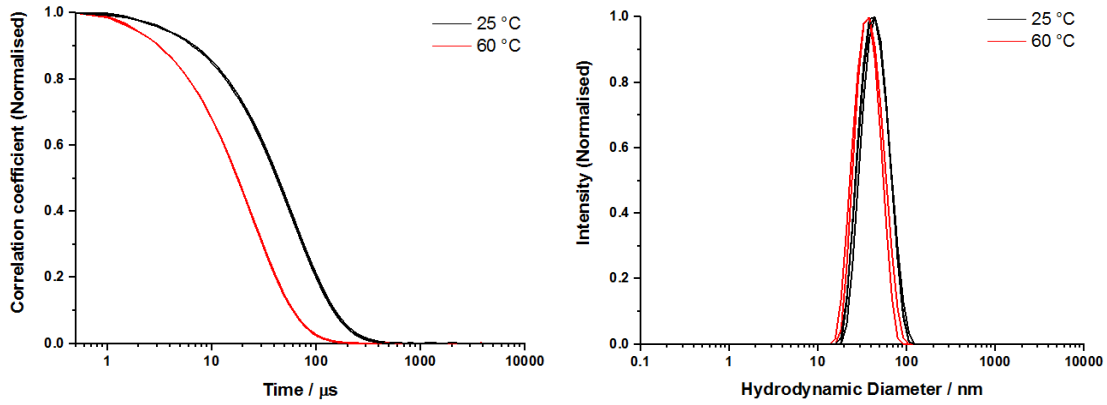

S3.11: DLS Correlation coefficient and intensity distribution of NP_{As-S4} as function of temperature in Figure 3.11

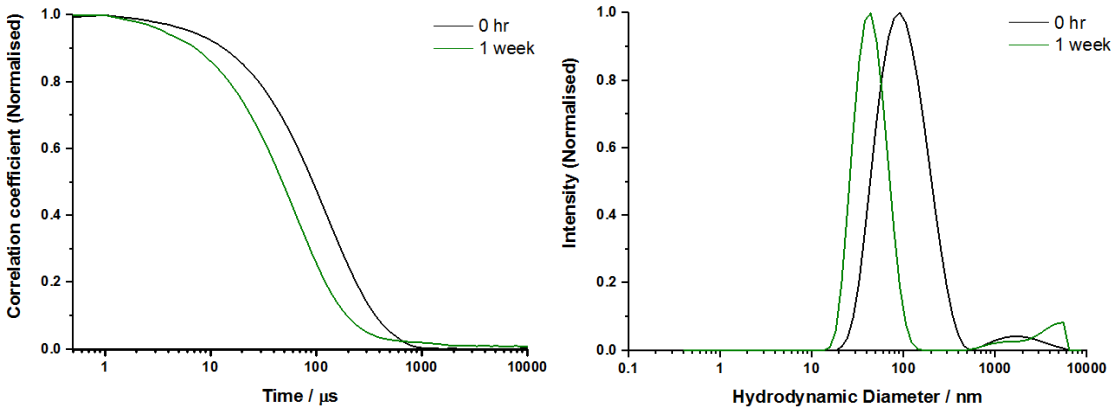

S3.14: DLS Correlation coefficient and intensity distribution for NP_{As-S4} as a function time in aqueous GSH solution (5mM) in Figure 3.14

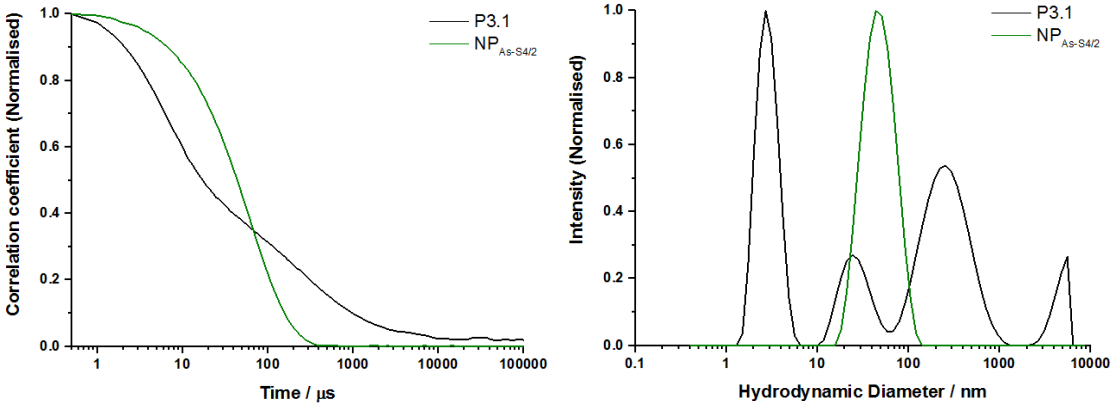

S3.15: DLS Correlation coefficient and intensity distribution for P3.1 (black) and $NP_{As-S4/2}$ (green) in Figure 3.15

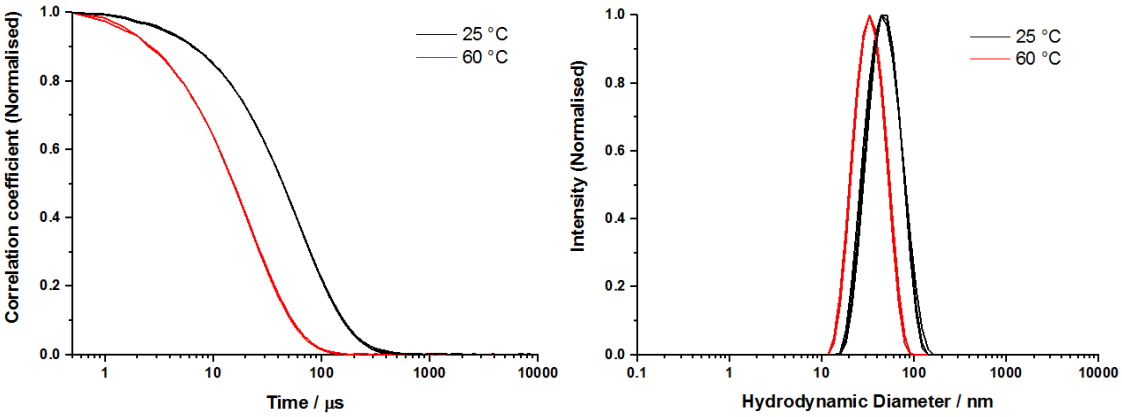

S3.17: DLS Correlation coefficient and intensity distribution of $NP_{As-S4/2}$ as function of temperature in Figure 3.17

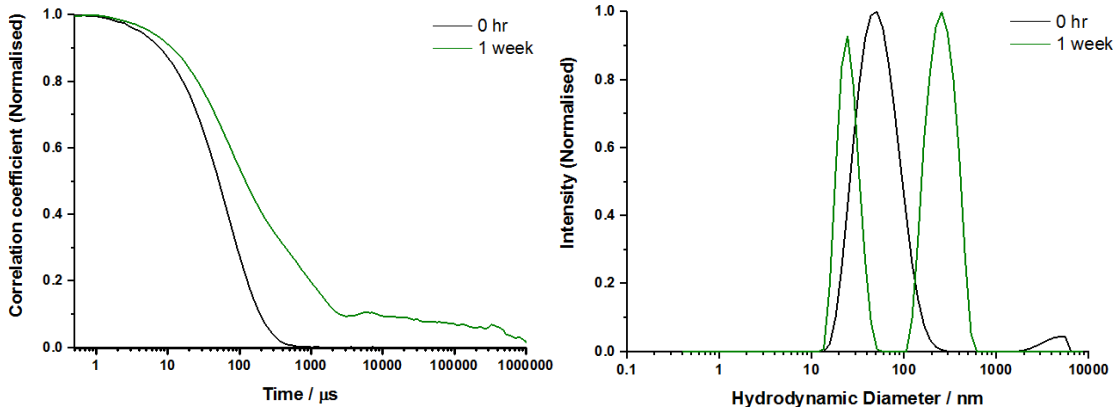

S3.19: DLS Correlation coefficient and intensity distribution for $NP_{As-S4/2}$ as a function time in aqueous GSH solution (5mM) in Figure 3.19

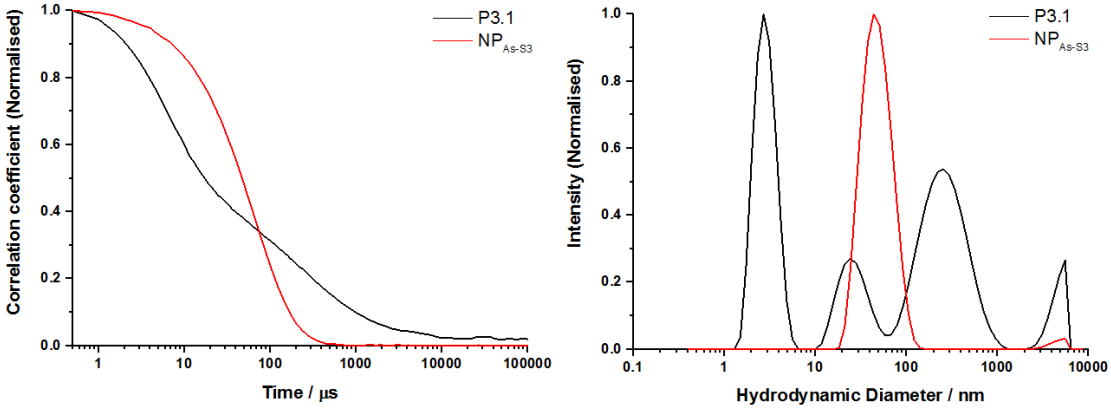

S3.20: DLS Correlation coefficient and intensity distribution for P3.1 (black) and NP_{As-S3} (red) in Figure 3.20

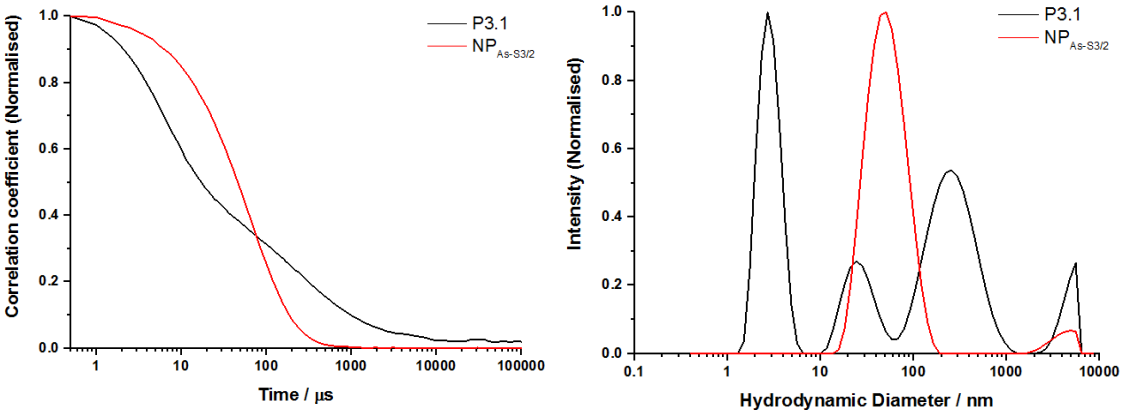

S3.23: DLS Correlation coefficient and intensity distribution for P3.1 (black) and $NP_{As-S3/2}$ (red) in Figure 3.23

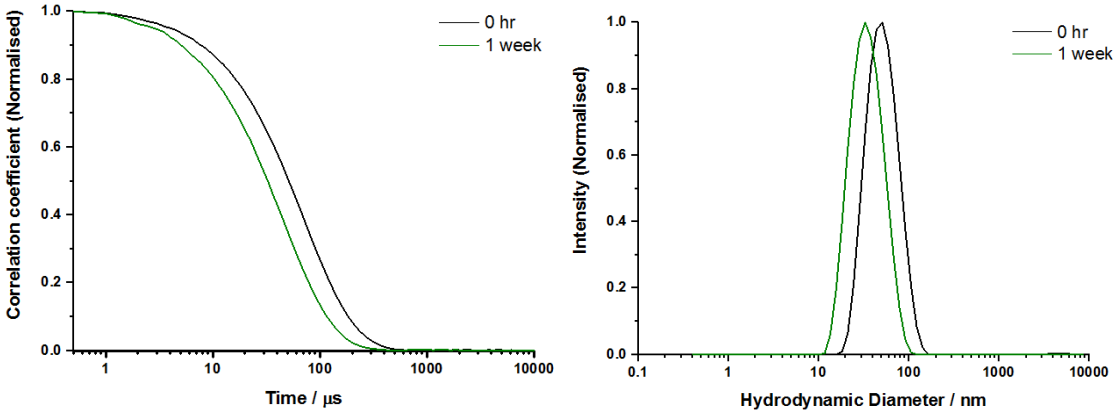

S3.26A: DLS Correlation coefficient and intensity distribution for NP_{As-S3} as a function time in aqueous GSH solution (5mM) in Figure 3.26

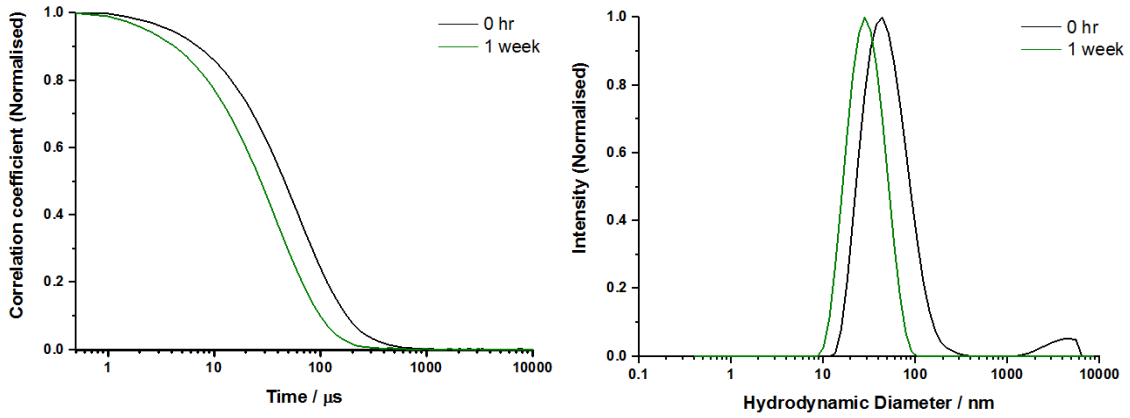

S3.26B: DLS Correlation coefficient and intensity distribution for $NP_{As-S3/2}$ as a function time in aqueous GSH solution (5mM) in Figure 3.26

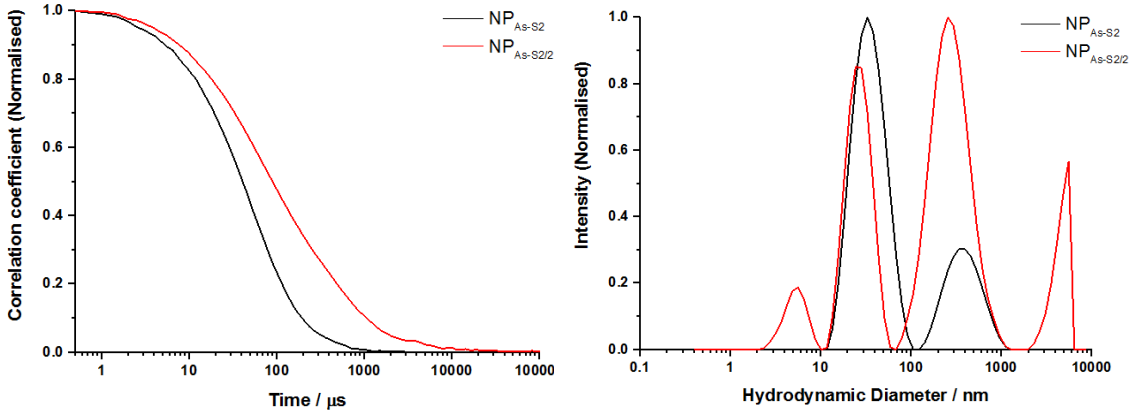

S3.27: DLS Correlation coefficient and intensity distribution of P3.1 with stoichiometric HBT cross-linker (black) and half the stoichiometric HBT cross-linker (red) in Figure 3.27

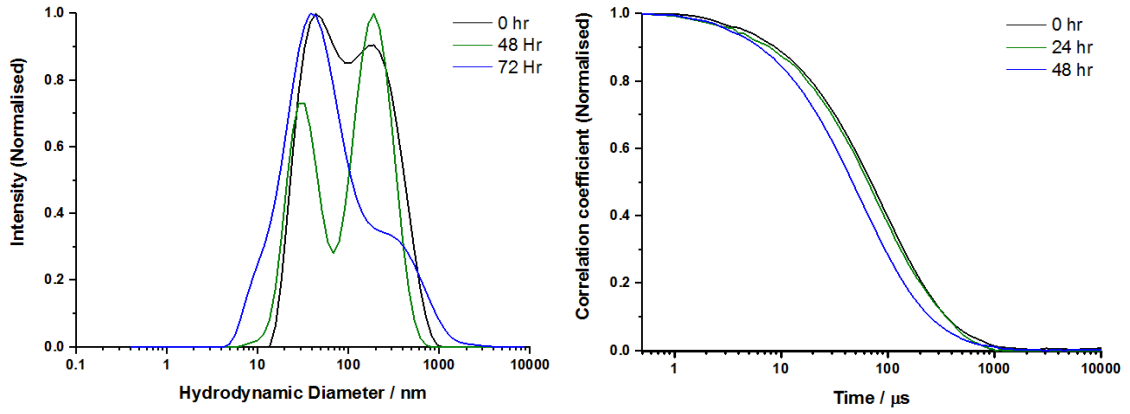

S3.30: DLS Correlation coefficient and intensity distribution for NP_{As-S2} as a function time in aqueous GSH solution (5mM) in Figure 3.30

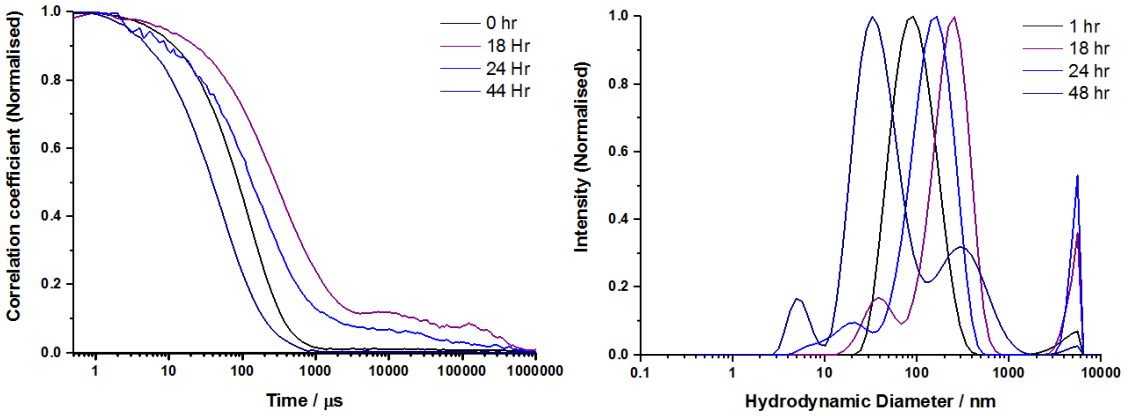

S3.31A: DLS Correlation coefficient and intensity distribution for $NP_{As\text{-}S4}$ as a function time in aqueous hydrogen peroxide solution (5mM) in Figure 3.31

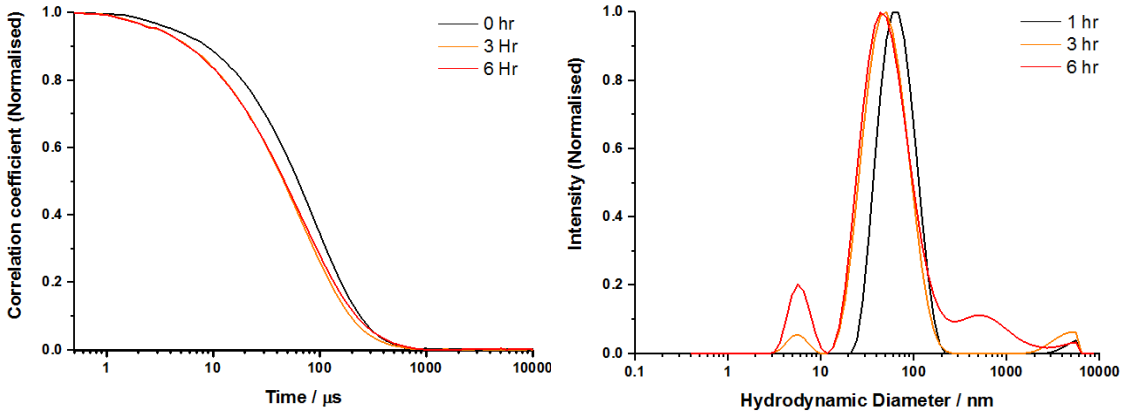

S3.31B: DLS Correlation coefficient and intensity distribution for $NP_{As\text{-}S4/2}$ as a function time in aqueous hydrogen peroxide solution (5mM) in Figure 3.31

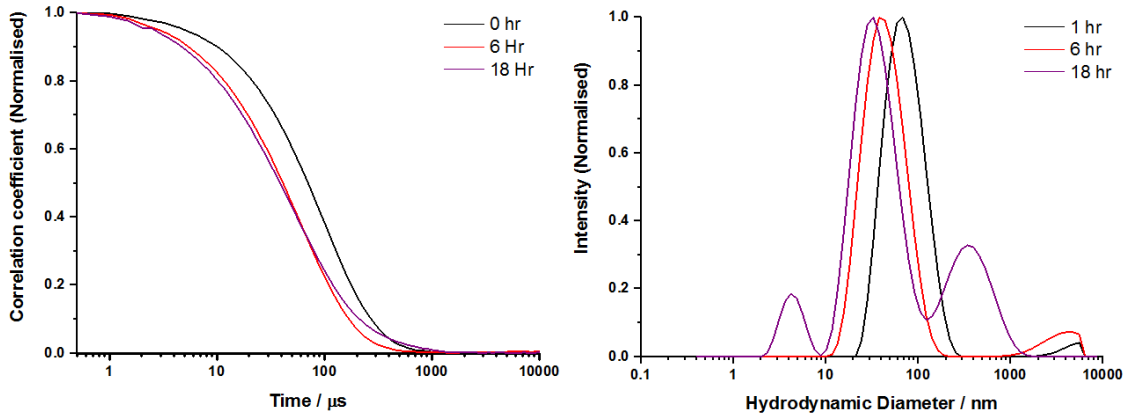

S3.31C: DLS Correlation coefficient and intensity distribution for $NP_{As\text{-}S3}$as a function time in aqueous hydrogen peroxide solution (5mM) in Figure 3.31

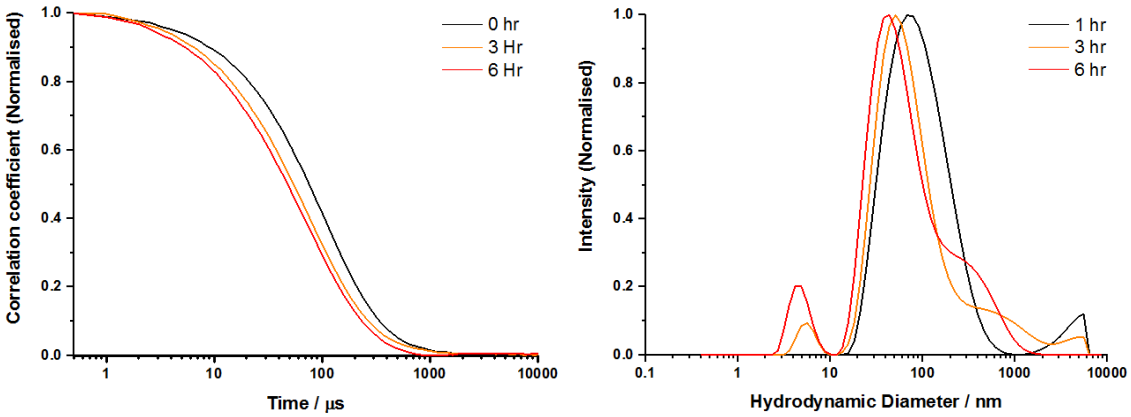

S3.31D: DLS Correlation coefficient and intensity distribution for $NP_{As\text{-}S3/2}$ as a function time in aqueous hydrogen peroxide solution (5mM) in Figure 3.31

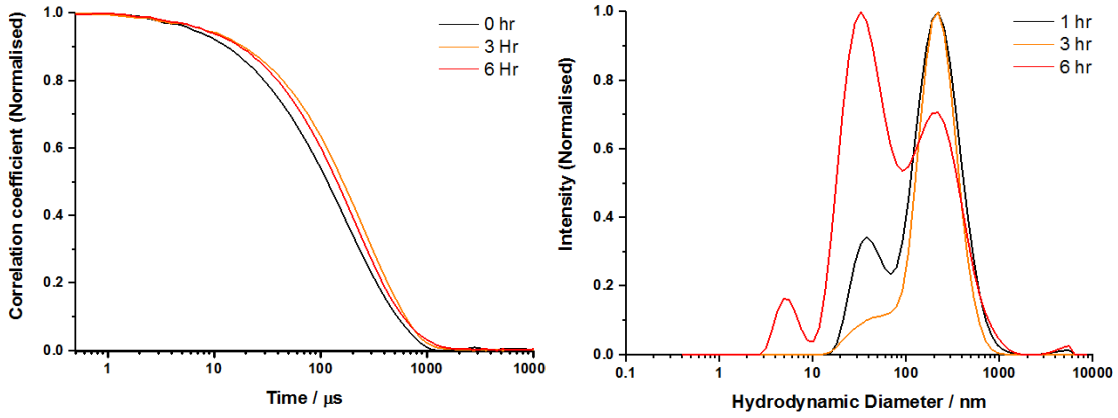

S3.31E: DLS Correlation coefficient and intensity distribution for $NP_{As\text{-}S2}$ as a function time in aqueous hydrogen peroxide solution (5mM) in Figure 3.31

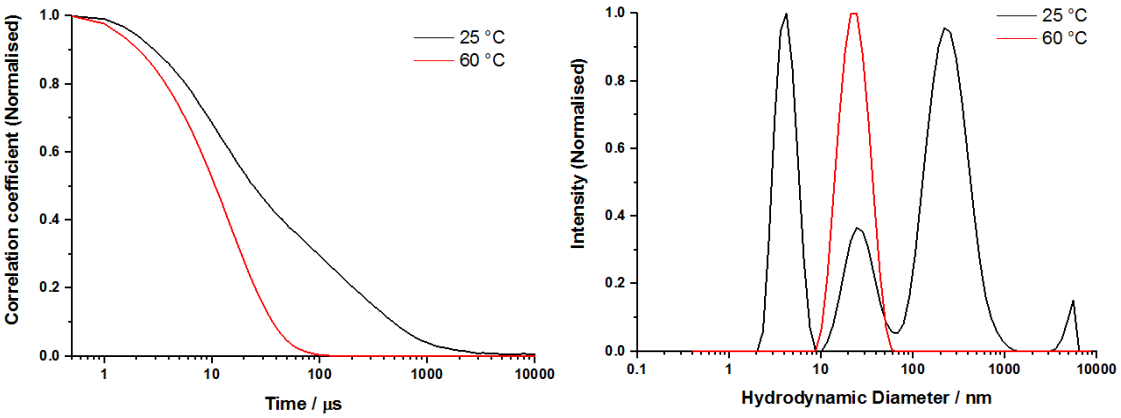

S4.4A: DLS Correlation coefficient and intensity distribution for P4.1 as function of temperature in Figure 4.4

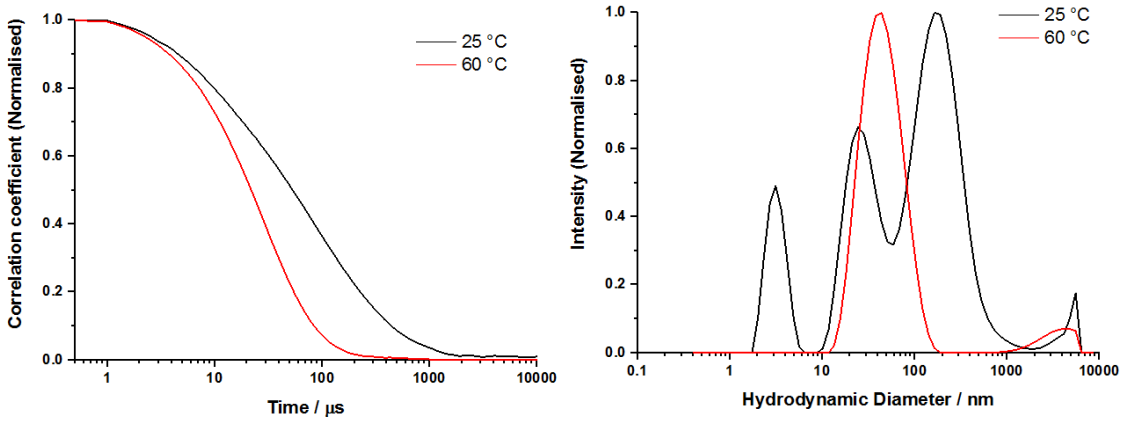

S4.4B: DLS Correlation coefficient and intensity distribution for P4.2 as function of temperature in Figure 4.4

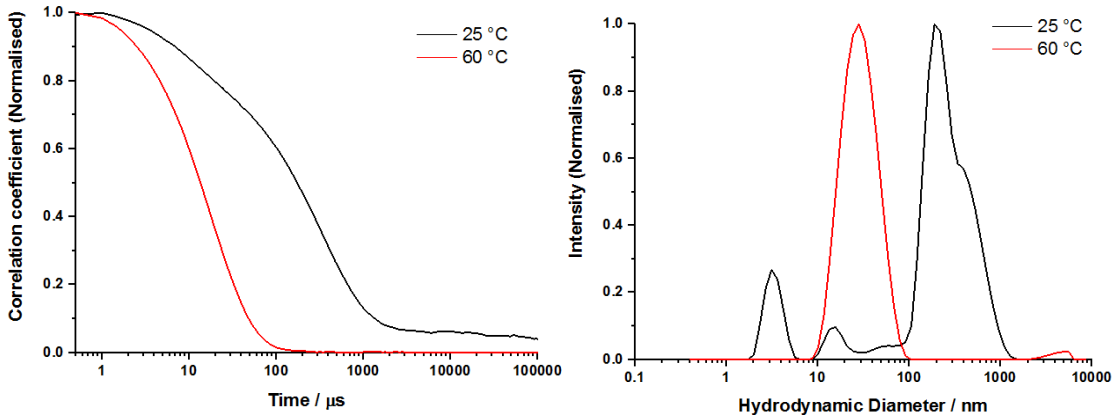

S4.4C: DLS Correlation coefficient and intensity distribution for P4.3 as function of temperature in Figure 4.4

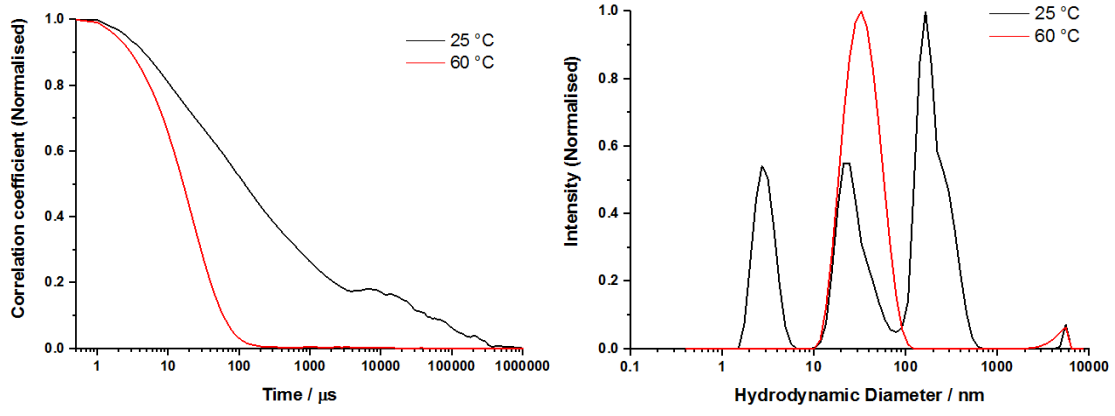

S4.4D: DLS Correlation coefficient and intensity distribution for P4.4 as function of temperature in Figure 4.4

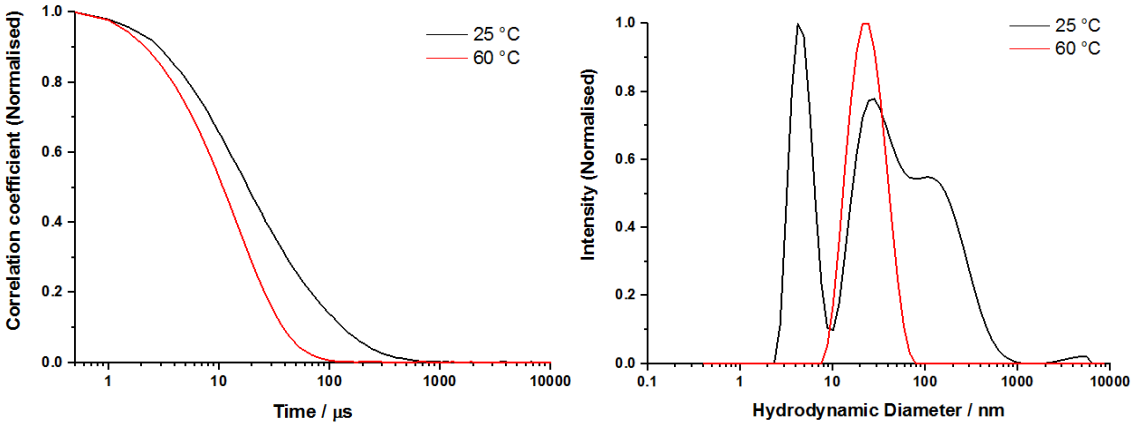

S4.5A: DLS Correlation coefficient and intensity distribution for $NP_{As(I)-4}$ as function of temperature in Figure 4.5

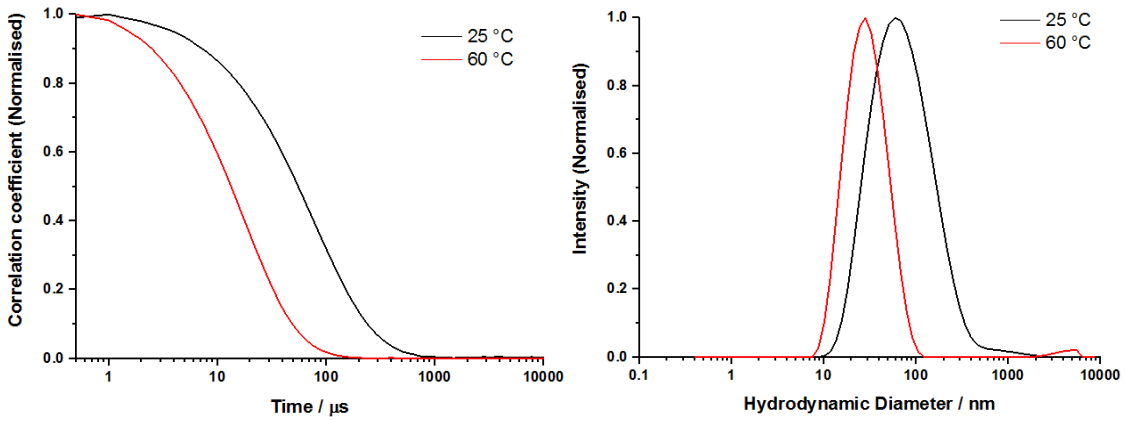

S4.5B: DLS Correlation coefficient and intensity distribution for $NP_{As(I)-11}$ as function of temperature in Figure 4.5

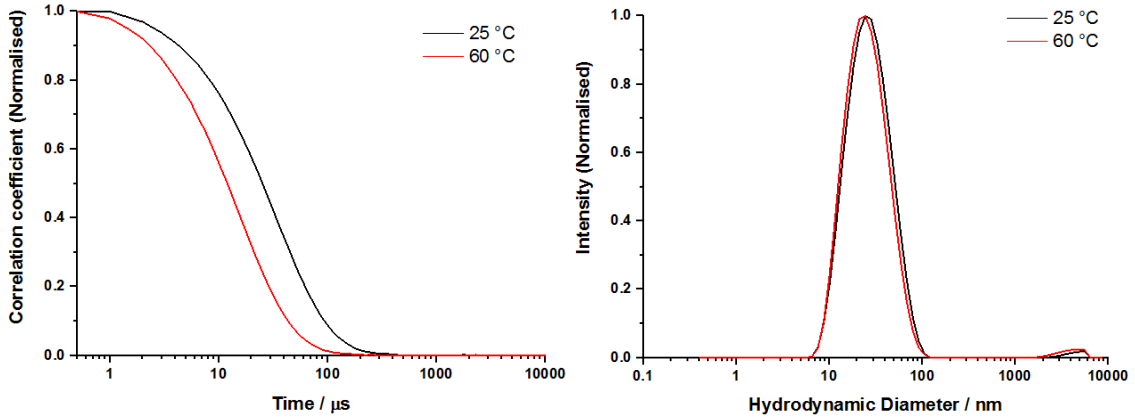

S4.5C: DLS Correlation coefficient and intensity distribution for $NP_{As(I)-15}$ as function of temperature in Figure 4.5

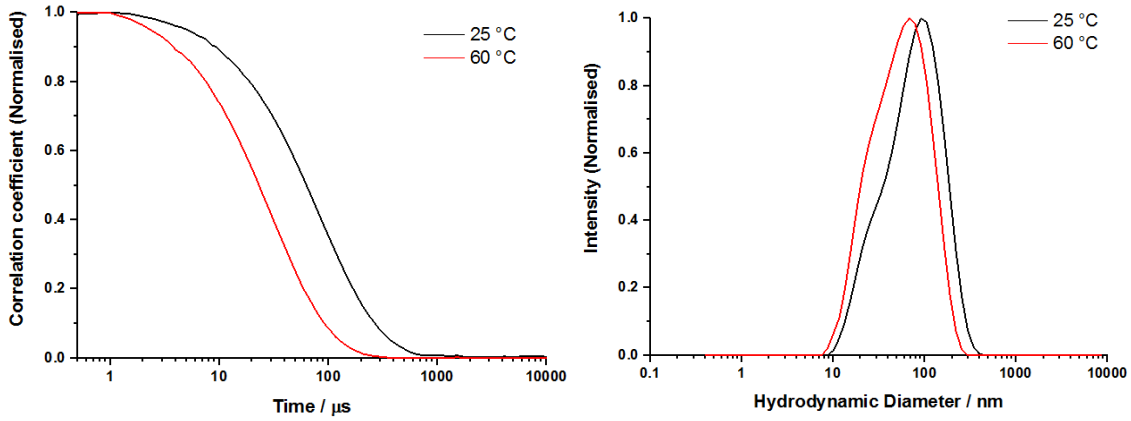

S4.5D: DLS Correlation coefficient and intensity distribution for $NP_{As(I)-18}$ as function of temperature in Figure 4.5

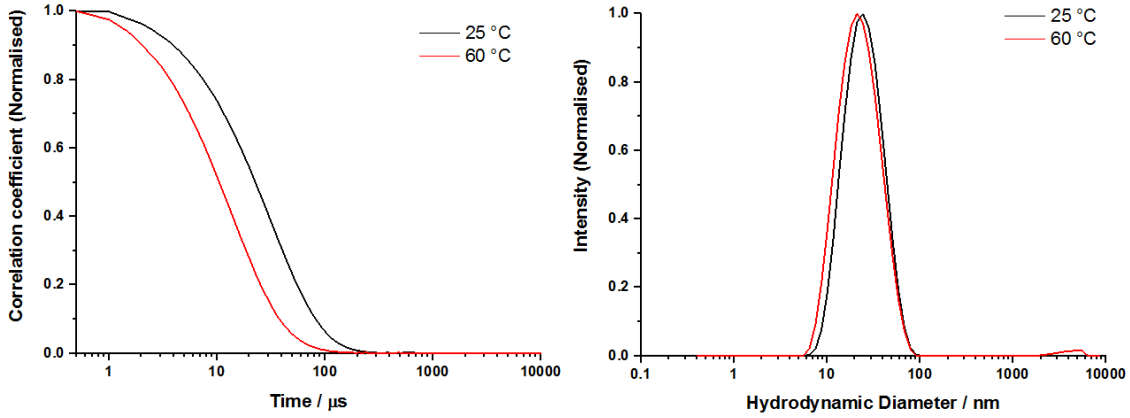

S4.8A: DLS Correlation coefficient and intensity distribution for NP_{PgOH-4} as function of temperature in Figure 4.8

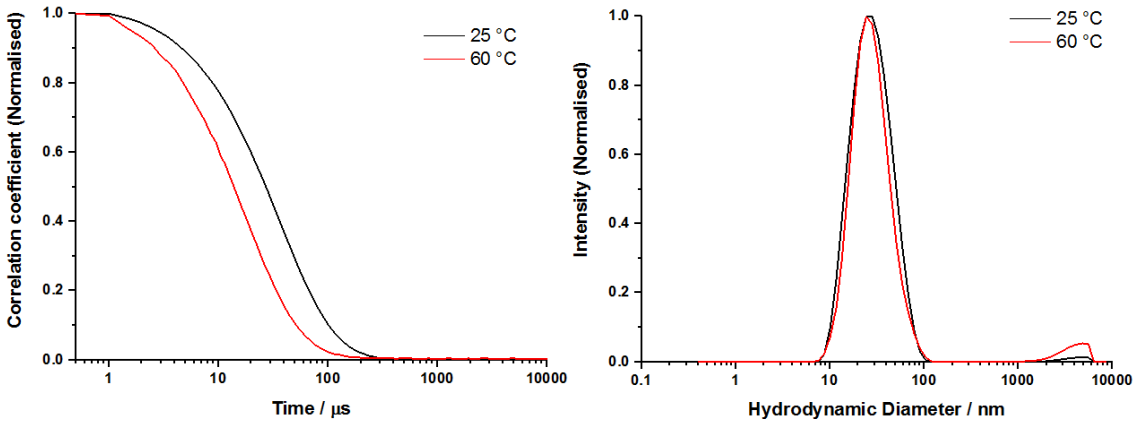

S4.8B: DLS Correlation coefficient and intensity distribution for $NP_{PgOH-11}$ as function of temperature in Figure 4.8

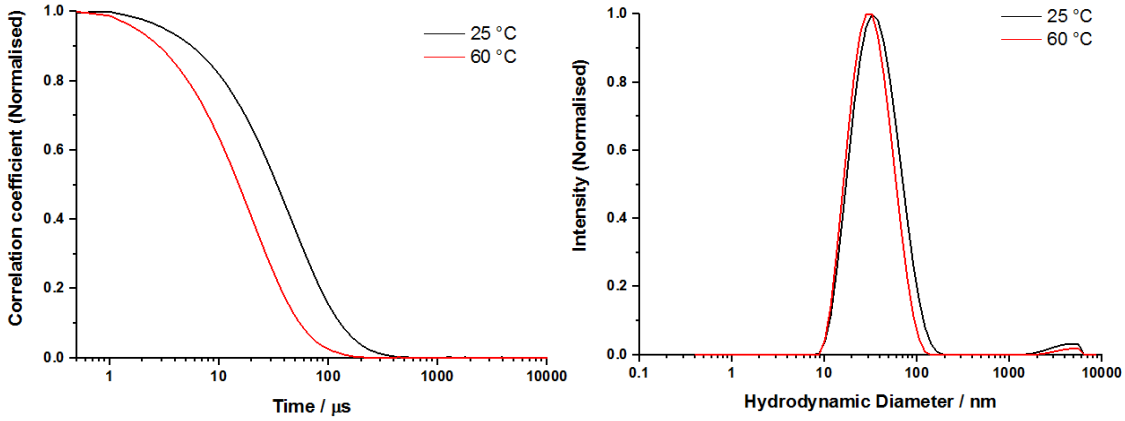

S4.8C: DLS Correlation coefficient and intensity distribution for $NP_{PgOH-15}$ as function of temperature in Figure 4.8

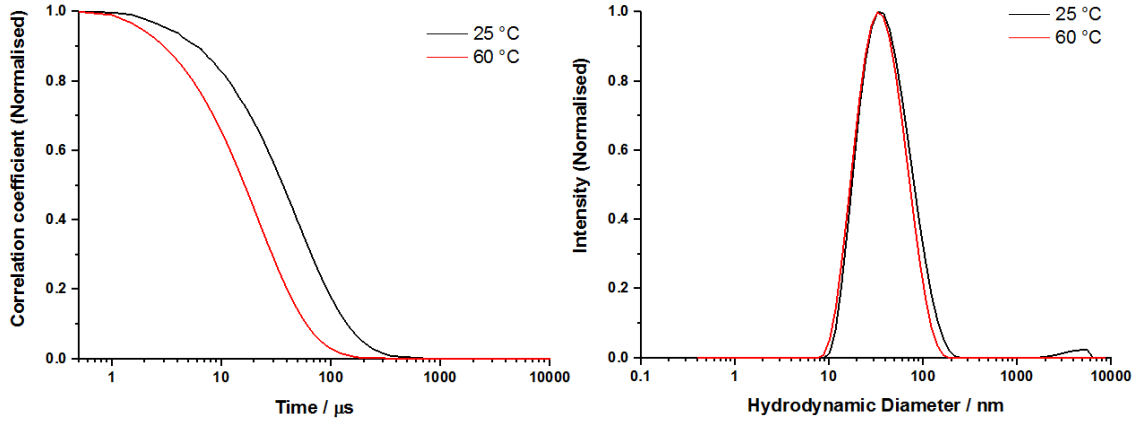

S4.8D: DLS Correlation coefficient and intensity distribution for $NP_{PgOH-18}$ as function of temperature in Figure 4.8

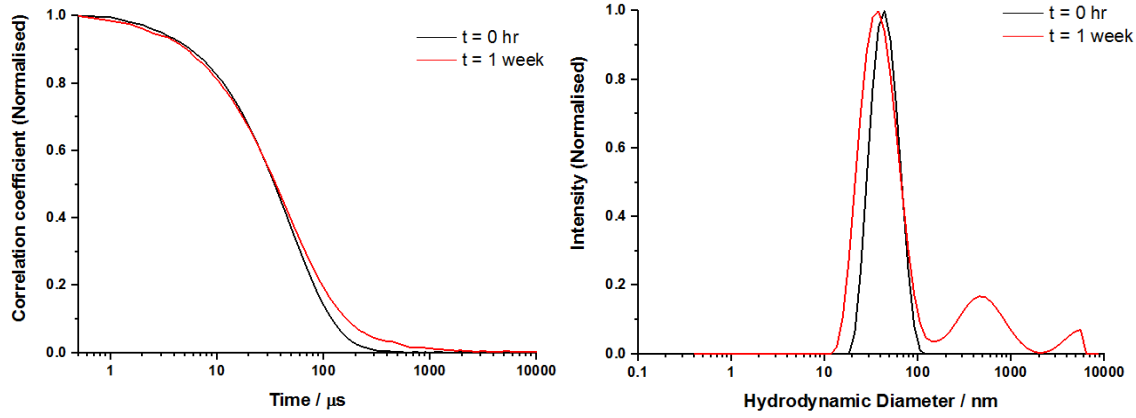

S4.10A: DLS Correlation coefficient and intensity distribution for NP_{PgOH-4} as function of time in aqueous GSH (5 mM) in Figure 4.10

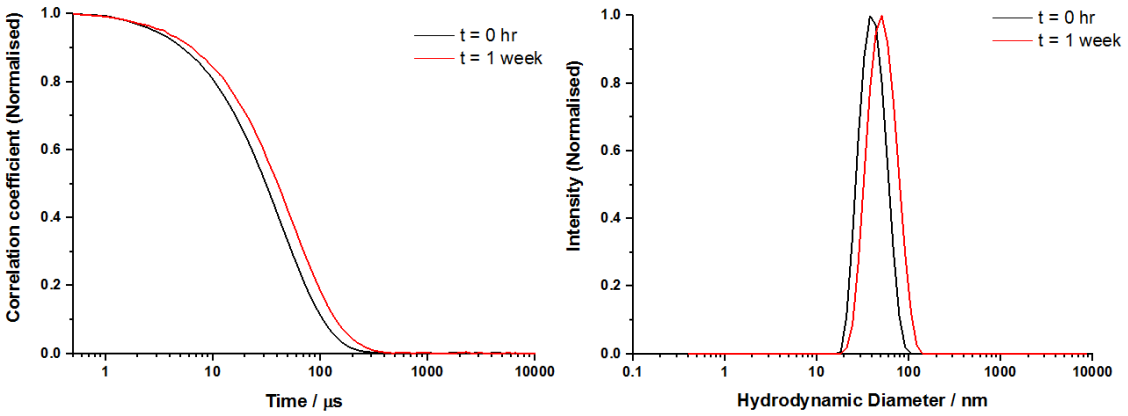

S4.10B: DLS Correlation coefficient and intensity distribution for $NP_{PgOH\text{-}11}$ as function of time in aqueous GSH (5 mM) in Figure 4.10

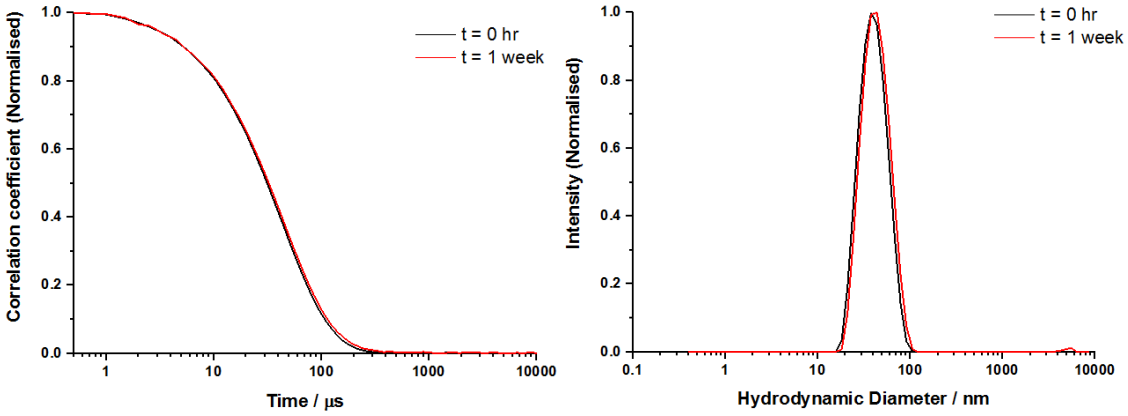

S4.10C: DLS Correlation coefficient and intensity distribution for $NP_{PgOH\text{-}15}$ as function of time in aqueous GSH (5 mM) in Figure 4.10

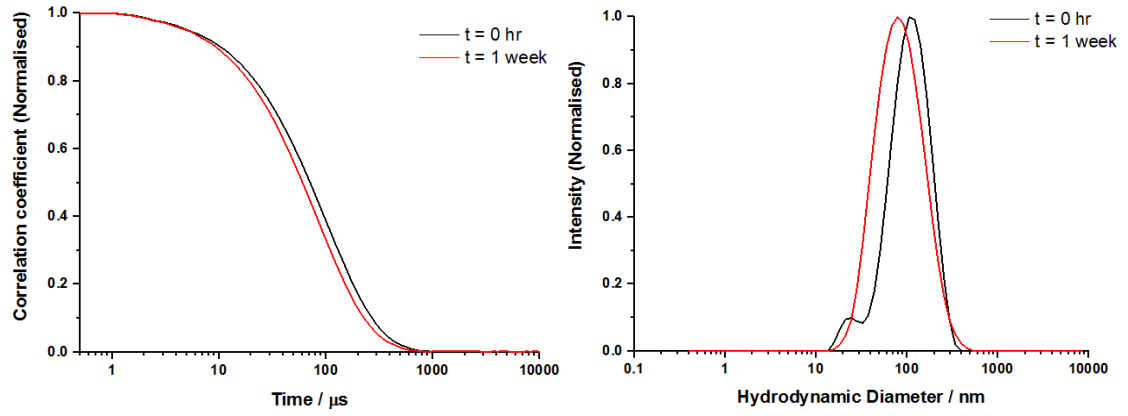

S4.10D: DLS Correlation coefficient and intensity distribution for $NP_{PgOH\text{-}18}$ as function of time in aqueous GSH (5 mM) in Figure 4.10

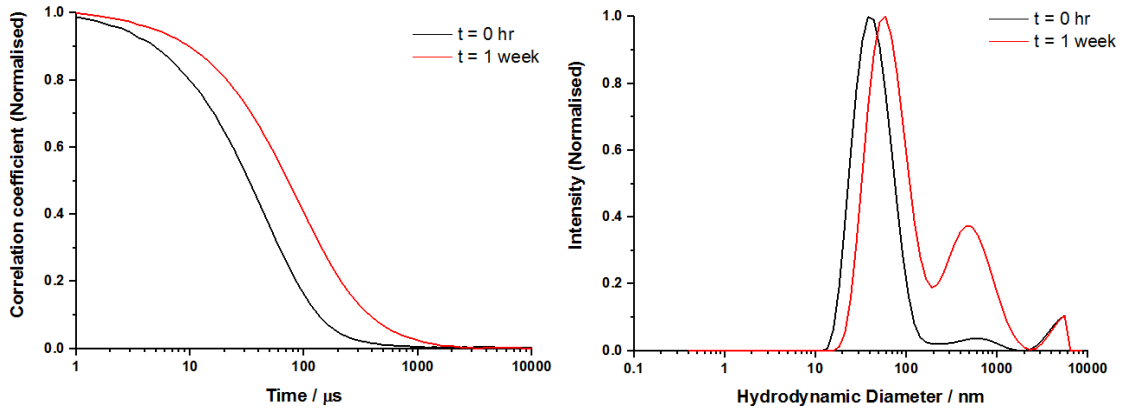

S4.11A: DLS Correlation coefficient and intensity distribution for $NP_{PgOH\text{-}4}$ as function of time in aqueous hydrogen peroxide (5 mM) in Figure 4.11

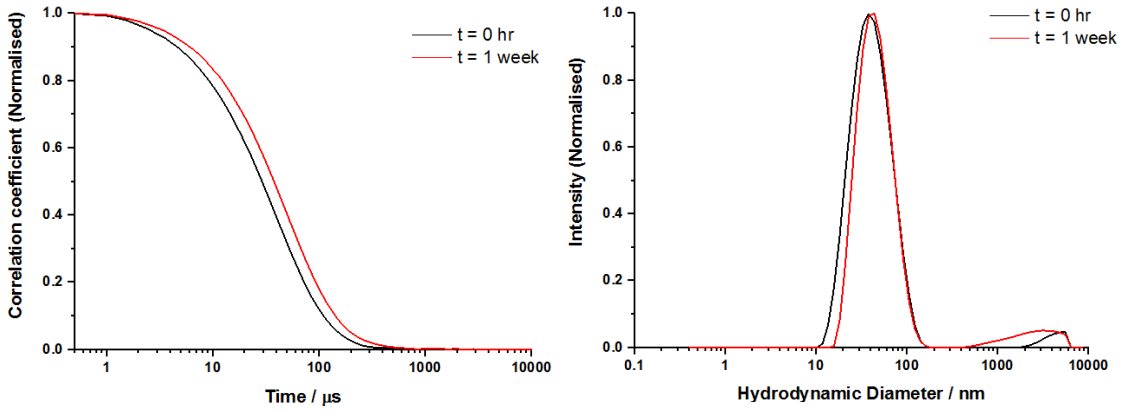

S4.11B: DLS Correlation coefficient and intensity distribution for $NP_{PgOH\text{-}11}$ as function of time in aqueous hydrogen peroxide (5 mM) in Figure 4.11

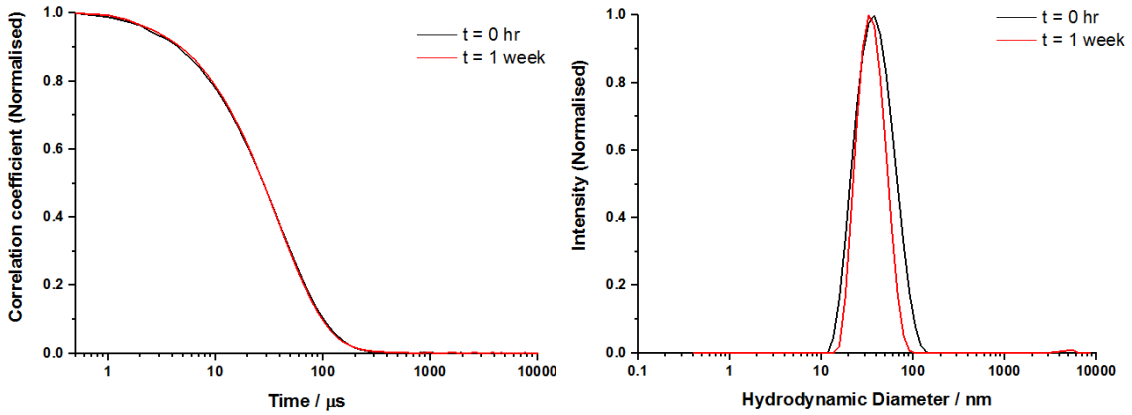

S4.11C: DLS Correlation coefficient and intensity distribution for $NP_{PgOH\text{-}15}$ as function of time in aqueous hydrogen peroxide (5 mM) in Figure 4.11

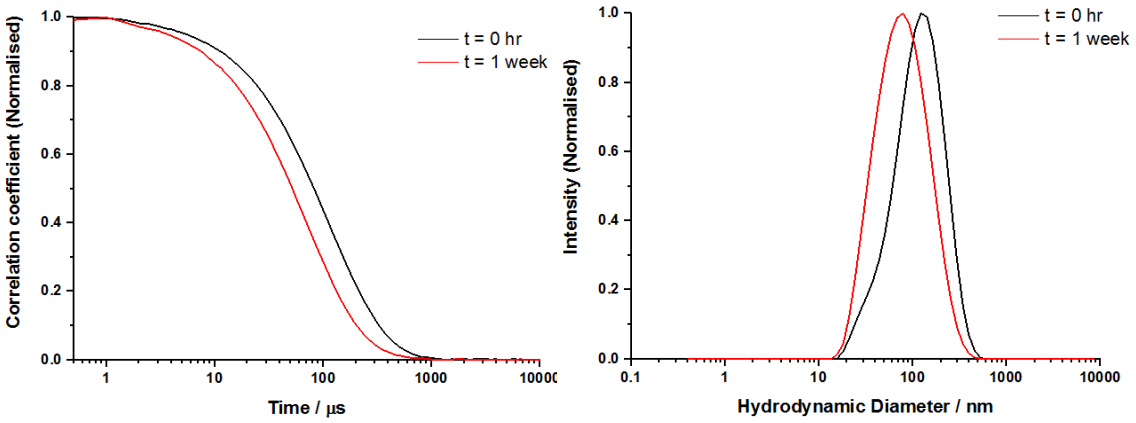

S4.11D: DLS Correlation coefficient and intensity distribution for $NP_{PgOH-18}$ as function of time in aqueous hydrogen peroxide (5 mM) in Figure 4.11

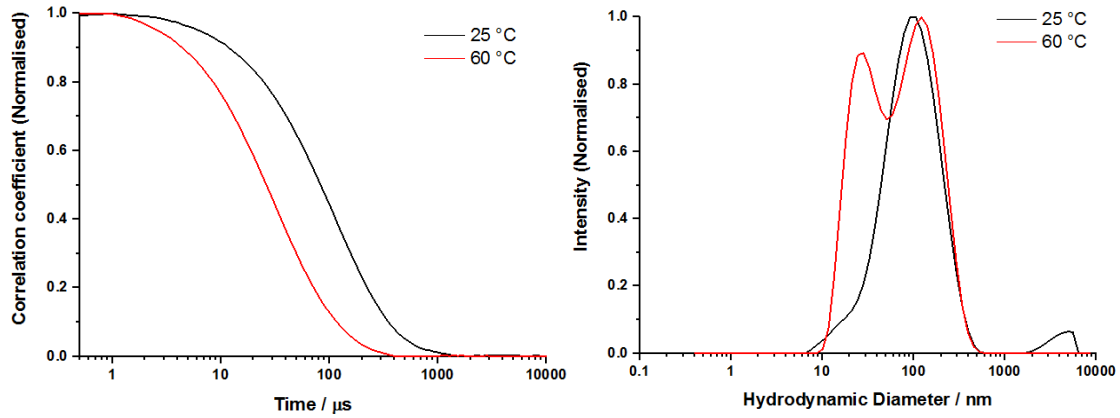

S4.12A: DLS Correlation coefficient and intensity distribution for NP_{PgNH-4} as function of temperature in Figure 4.12

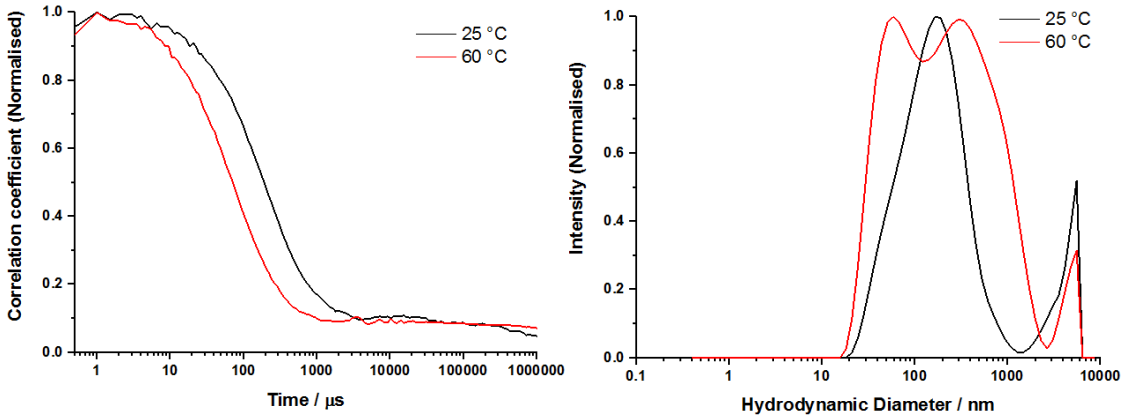

S4.12B: DLS Correlation coefficient and intensity distribution for $NP_{PgNH-11}$ as function of temperature in Figure 4.12

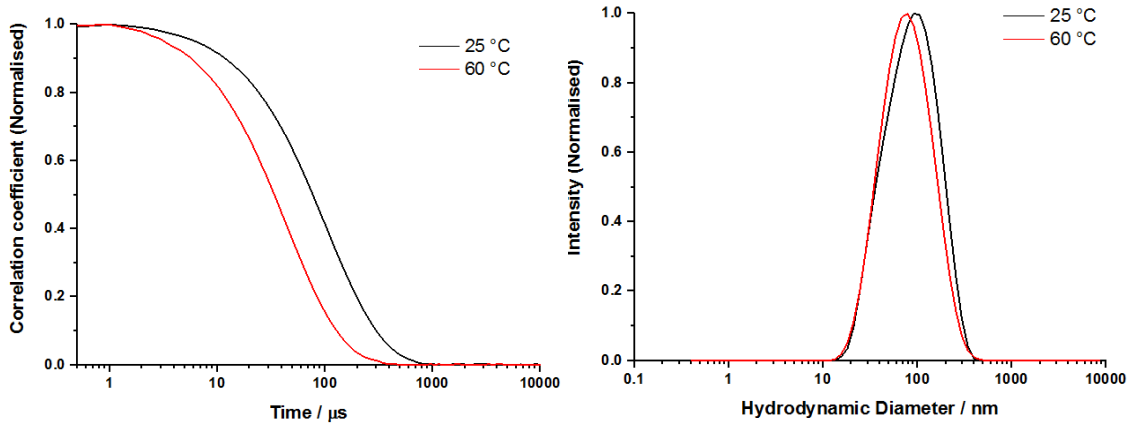

S4.12C: DLS Correlation coefficient and intensity distribution for $NP_{PgNH-15}$ as function of temperature in Figure 4.12

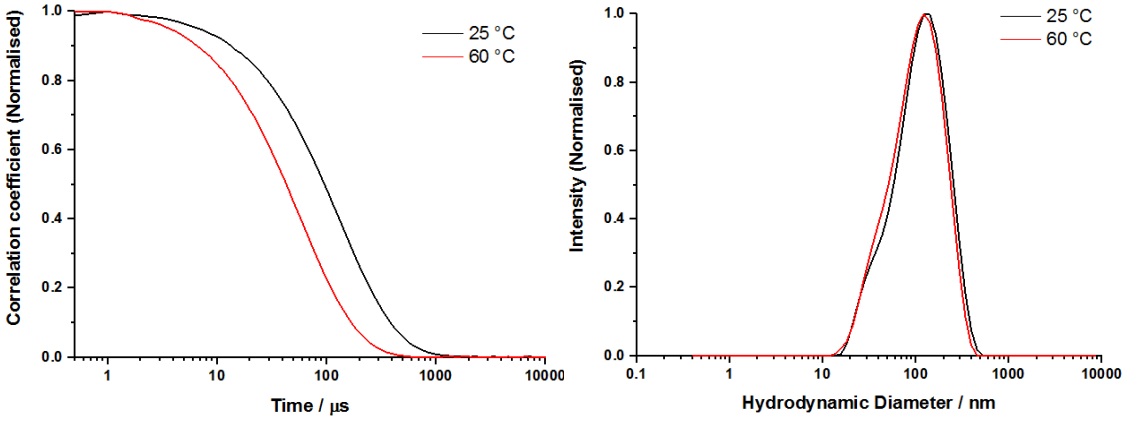

S4.12D: DLS Correlation coefficient and intensity distribution for $NP_{PgNH-18}$ as function of temperature in Figure 4.12

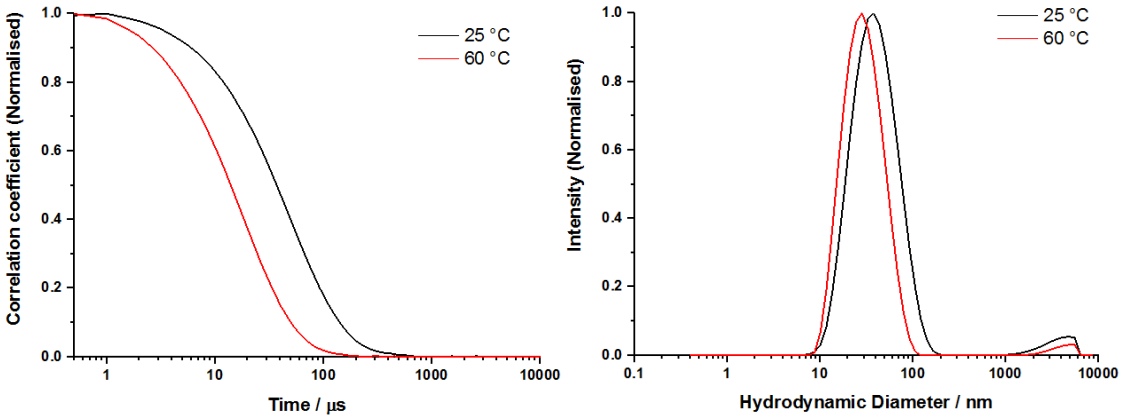

S4.13A: DLS Correlation coefficient and intensity distribution for NP_{PAc-4} as function of temperature in Figure 4.13

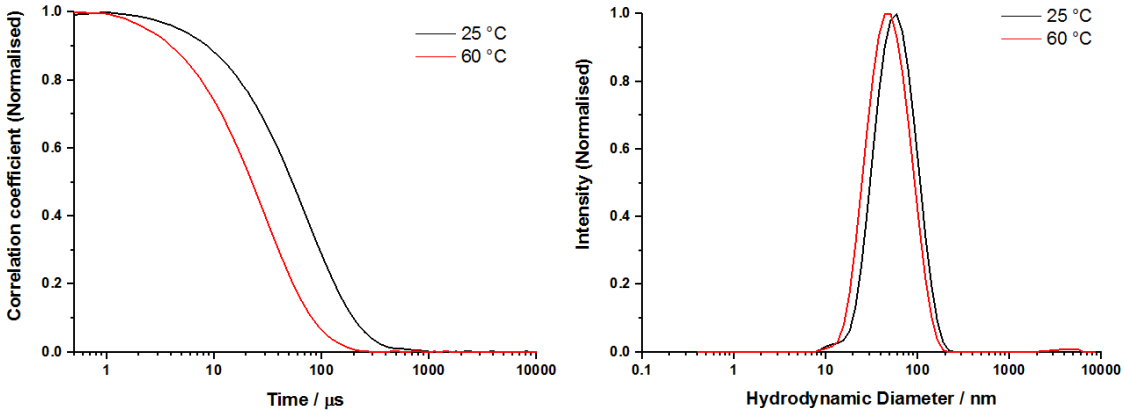

S4.13B: DLS Correlation coefficient and intensity distribution for NP_{PAc-11} as function of temperature in Figure 4.13

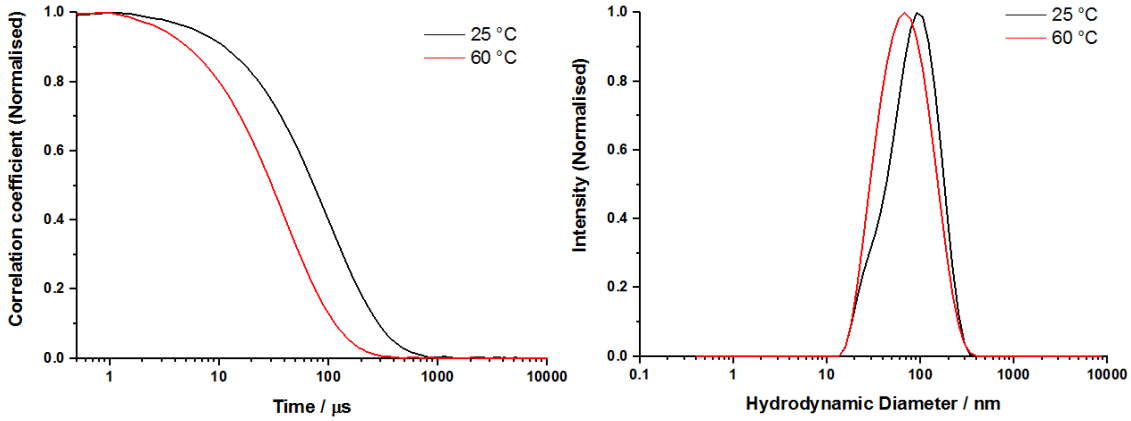

S4.13C: DLS Correlation coefficient and intensity distribution for NP_{PAc-15} as function of temperature in Figure 4.13

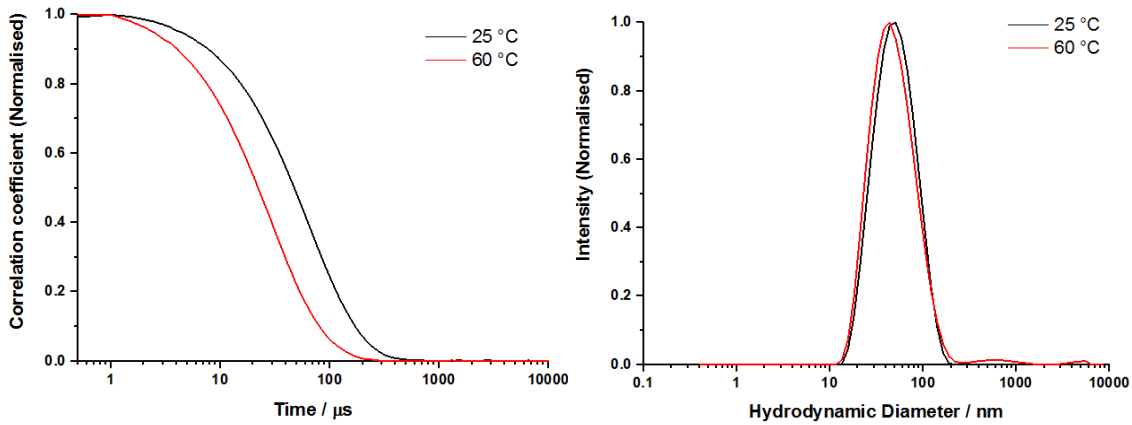

S4.13D: DLS Correlation coefficient and intensity distribution for NP_{PAc-18} as function of temperature in Figure 4.13

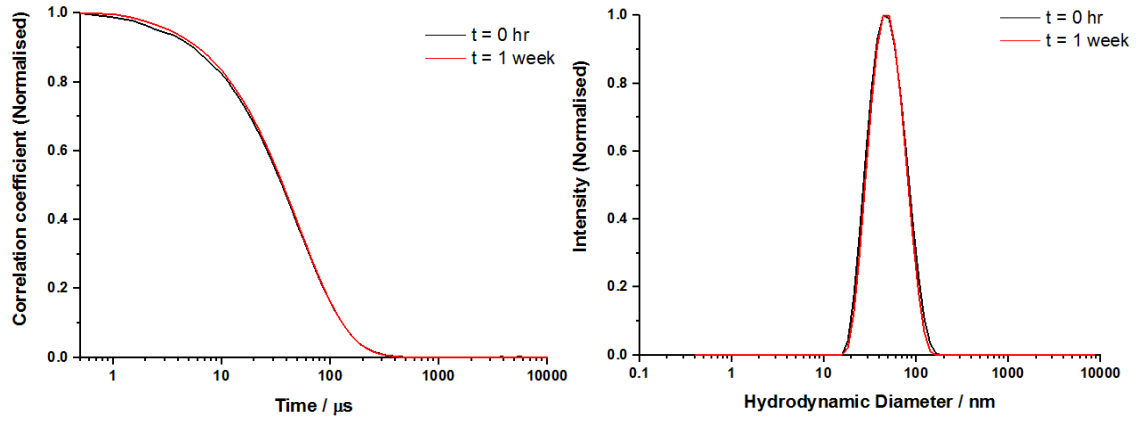

S4.16A: DLS Correlation coefficient and intensity distribution for $NP_{PAc\text{-}18}$ as function of time in hydrogen peroxide solution (5 mM) Figure 4.16

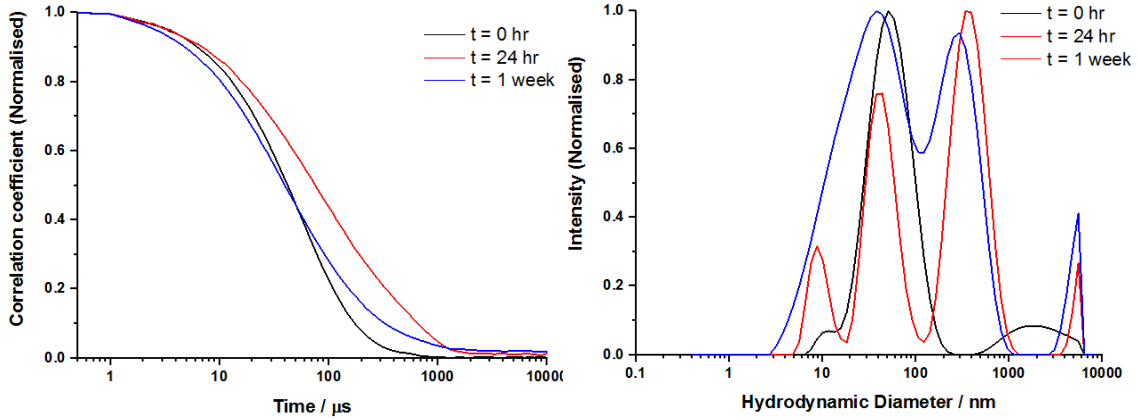

S4.16B: DLS Correlation coefficient and intensity distribution for $NP_{PAc\text{-}4}$ as function of time in hydrogen peroxide solution (5 mM) Figure 4.16

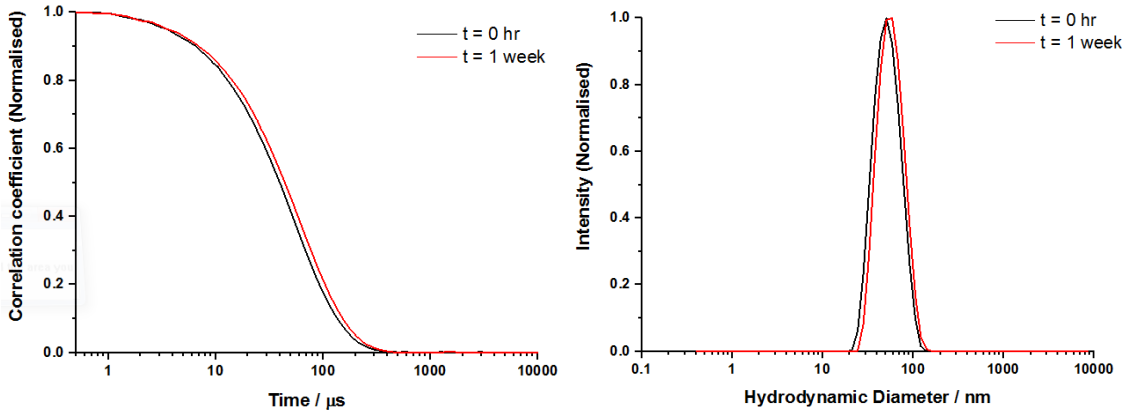

S4.16C: DLS Correlation coefficient and intensity distribution for $NP_{PAc\text{-}18}$ as function of time in GSH solution (5 mM) Figure 4.16

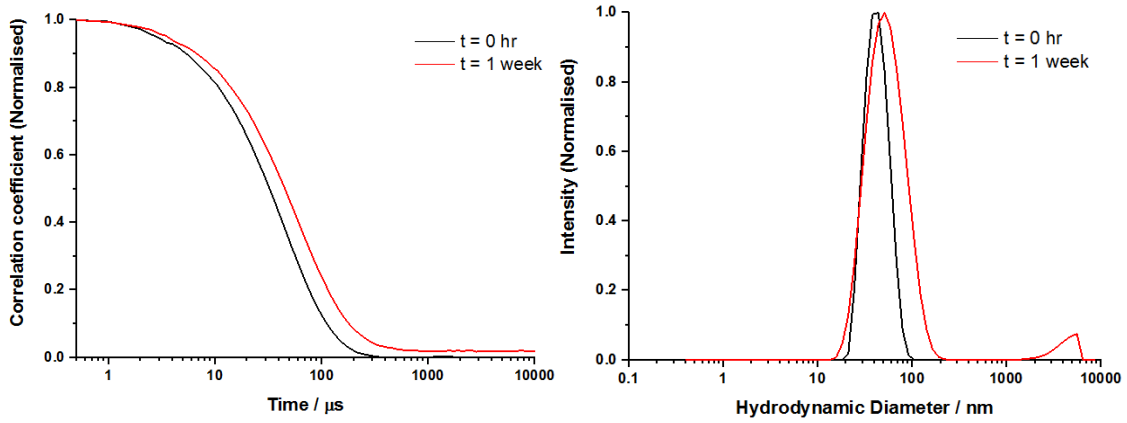

S4.16D: DLS Correlation coefficient and intensity distribution for NP_{PAc-4} as function of time in GSH solution (5 mM) Figure 4.16

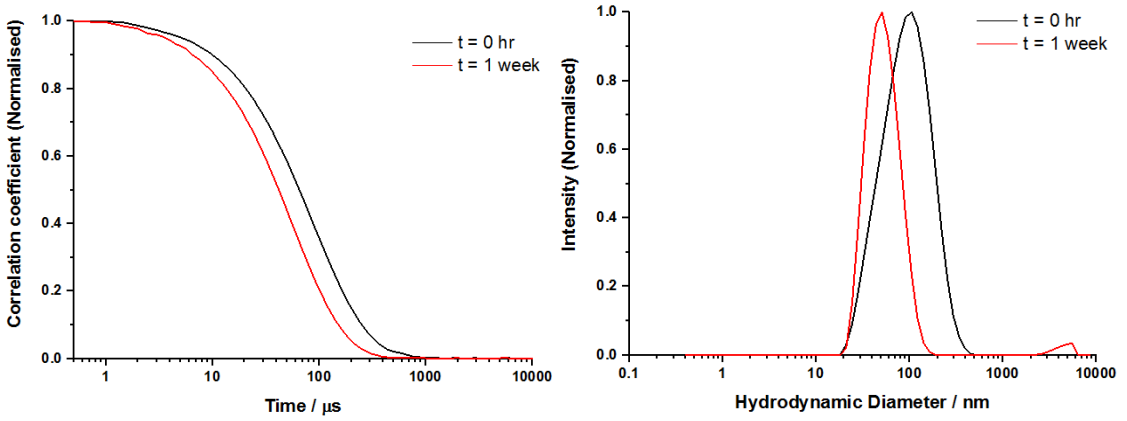

S4.17A: DLS Correlation coefficient and intensity distribution for $NP_{Pg-NH-18}$ as function of time in hydrogen peroxide solution (5 mM) Figure 4.17

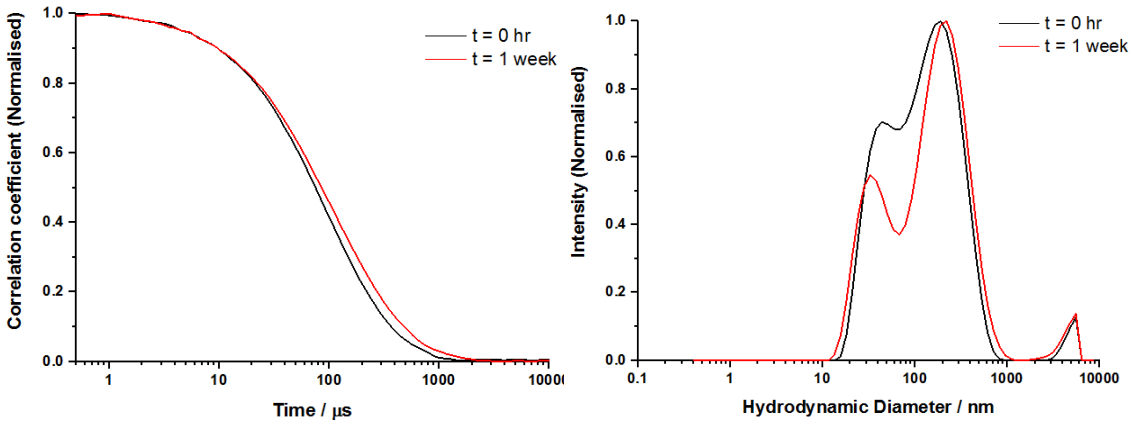

S4.17B: DLS Correlation coefficient and intensity distribution for $NP_{Pg-NH-4}$ as function of time in hydrogen peroxide solution (5 mM) Figure 4.17

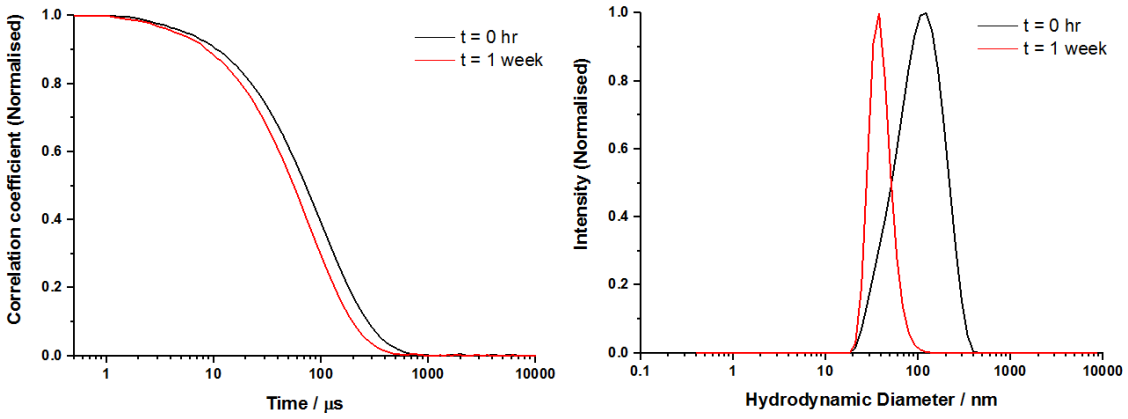

S4.17C: DLS Correlation coefficient and intensity distribution for $NP_{Pg\text{-}NH\text{-}18}$ as function of time in GSH solution (5 mM) Figure 4.17

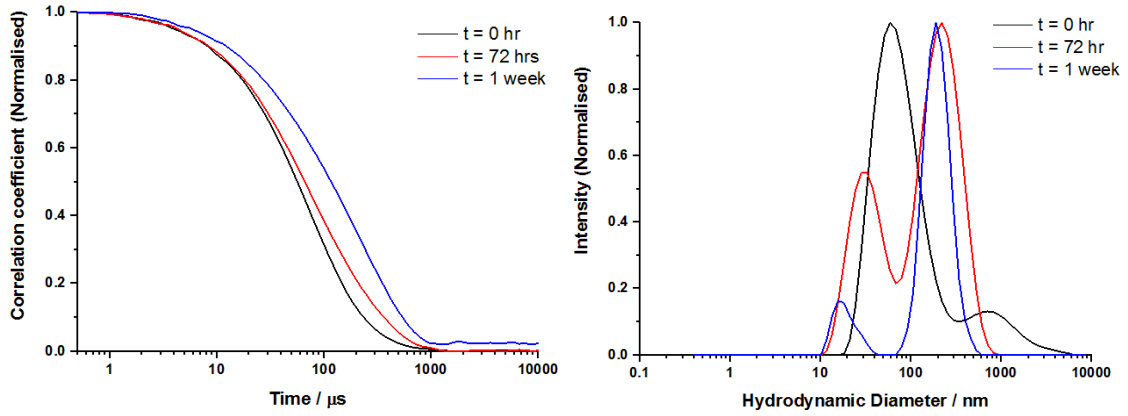

S4.17D: DLS Correlation coefficient and intensity distribution for $NP_{Pg\text{-}NH\text{-}4}$ as function of time in GSH solution (5 mM) Figure 4.17

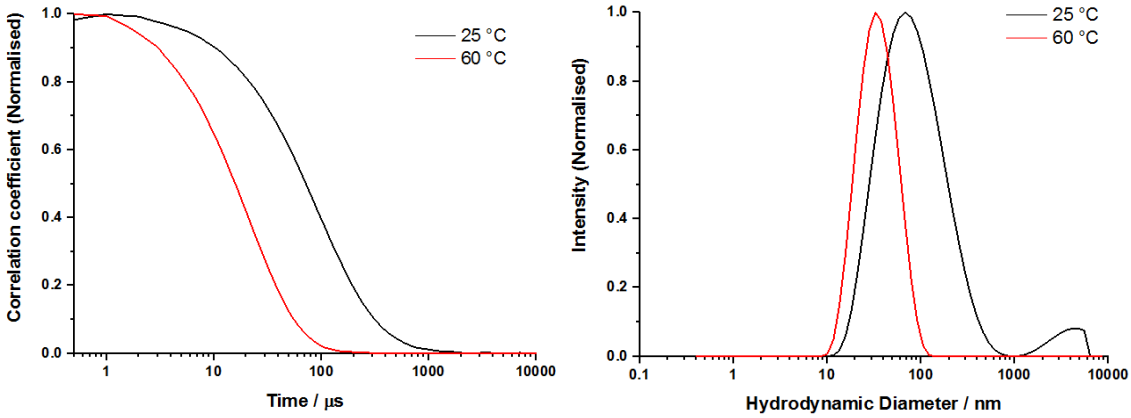

S4.22A: DLS Correlation coefficient and intensity distribution for $NP_{Rh\text{-}4}$ as function of temperature Figure 4.22

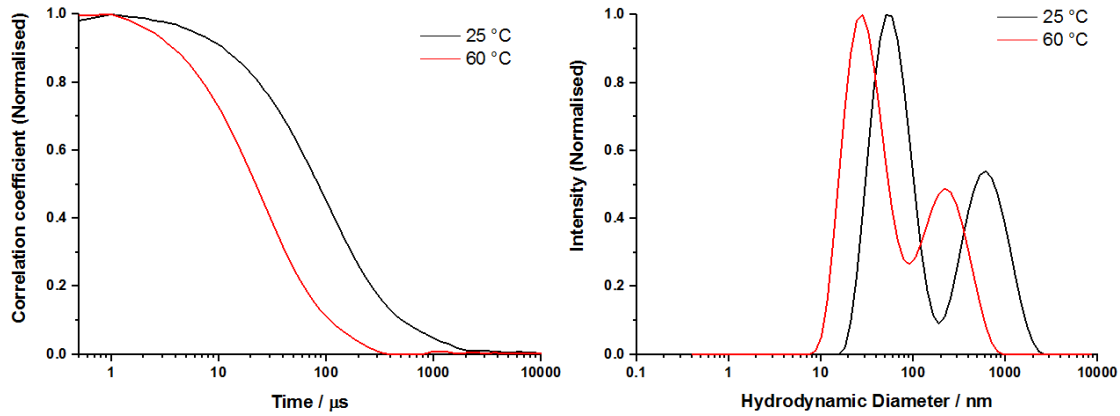

S4.22B: DLS Correlation coefficient and intensity distribution for $NP_{Rh\text{-}11}$ as function of temperature Figure 4.22

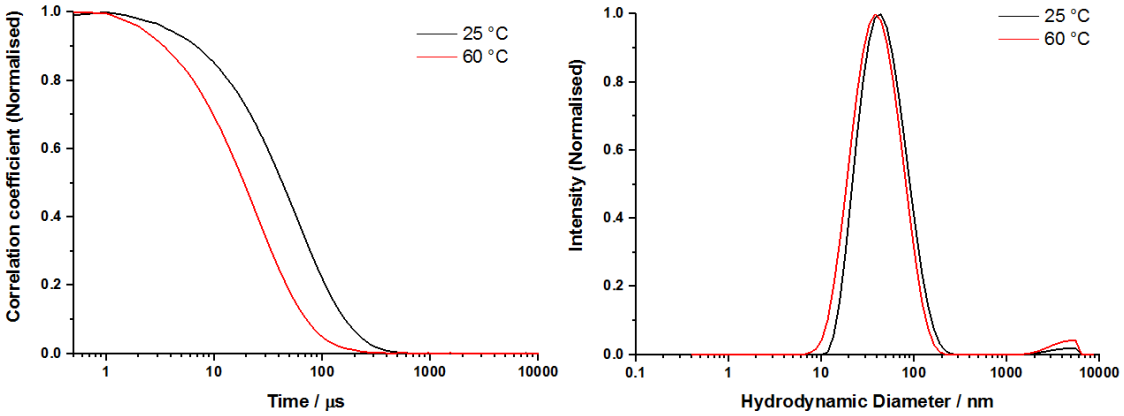

S4.22C: DLS Correlation coefficient and intensity distribution for $NP_{Rh\text{-}15}$ as function of temperature Figure 4.22

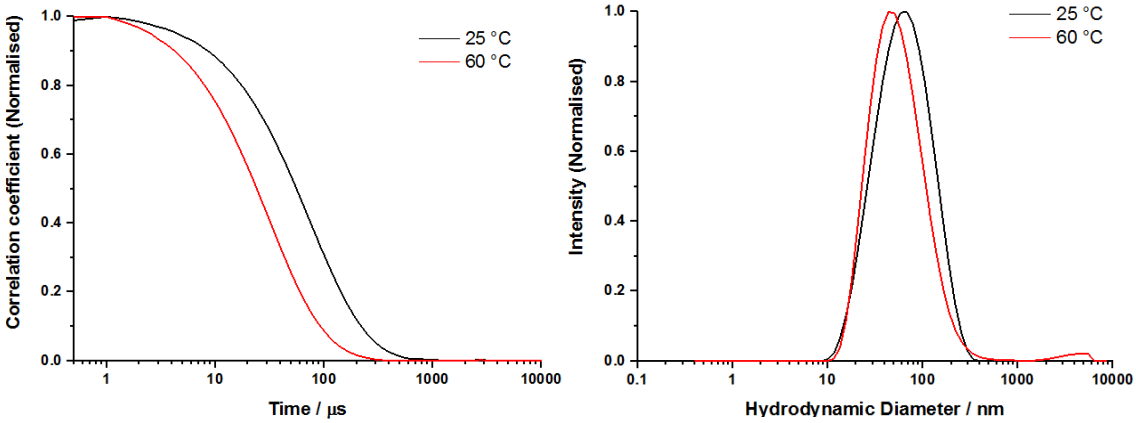

S4.22D: DLS Correlation coefficient and intensity distribution for $NP_{Rh\text{-}18}$ as function of temperature Figure 4.22

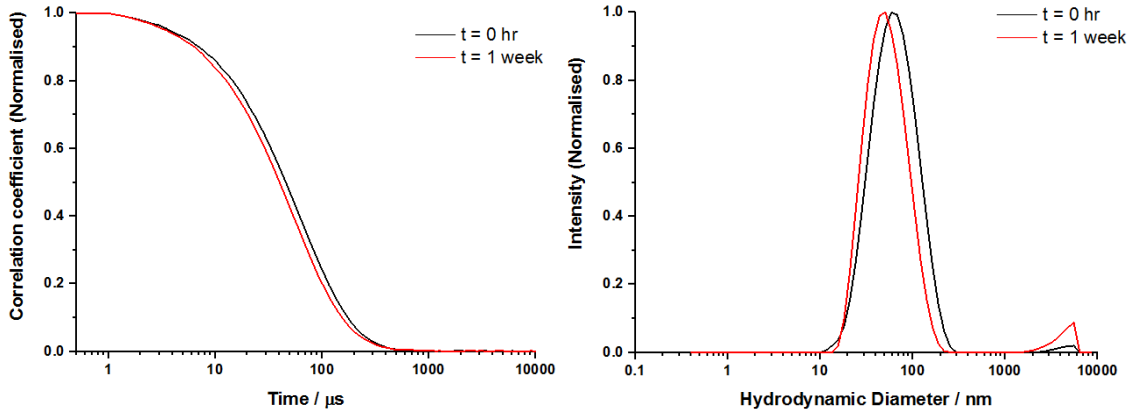

S4.24A: DLS Correlation coefficient and intensity distribution for $NP_{Rh\text{-}18}$ as function of time in aqueous hydrogen peroxide solution (5 mM) Figure 4.24

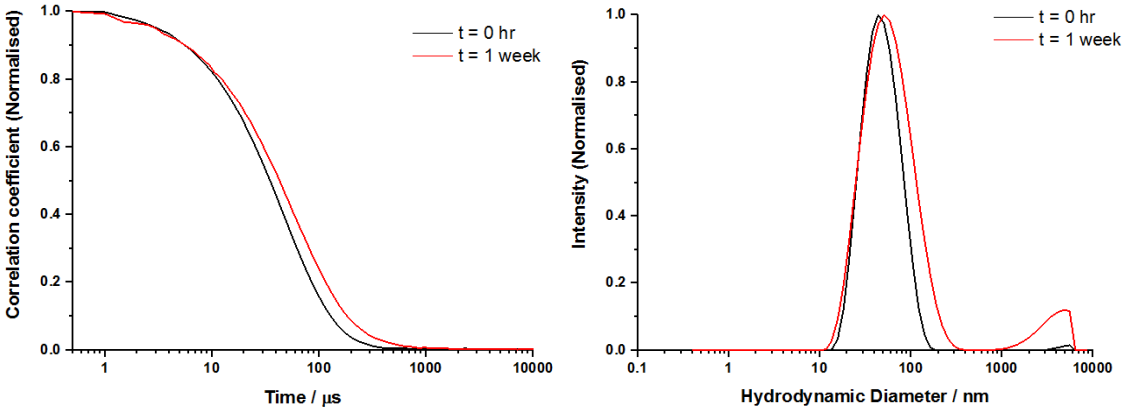

S4.24B: DLS Correlation coefficient and intensity distribution for $NP_{Rh\text{-}4}$ as function of time in aqueous hydrogen peroxide solution (5 mM) Figure 4.24

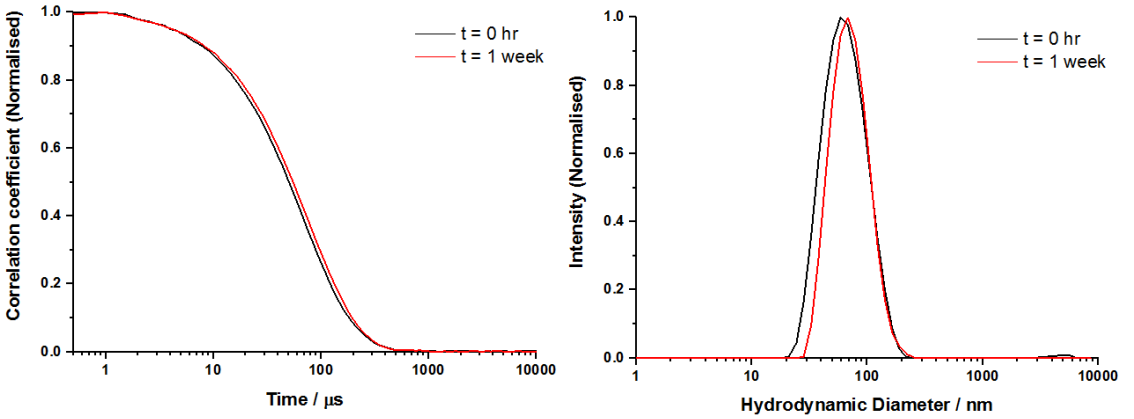

S4.24C: DLS Correlation coefficient and intensity distribution for $NP_{Rh\text{-}18}$ as function of time in aqueous GSH solution (5 mM) Figure 4.24

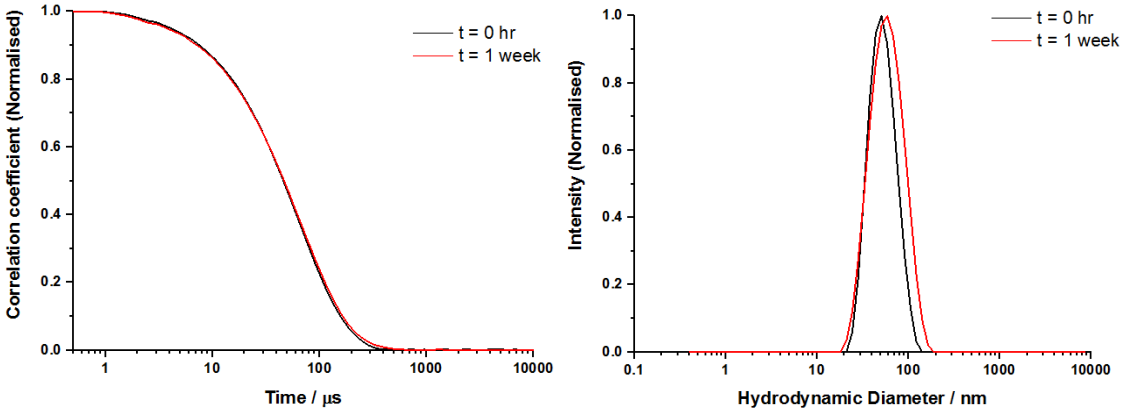

S4.24D: DLS Correlation coefficient and intensity distribution for NP_{Rh-4} as function of time in aqueous GSH solution (5 mM) Figure 4.24

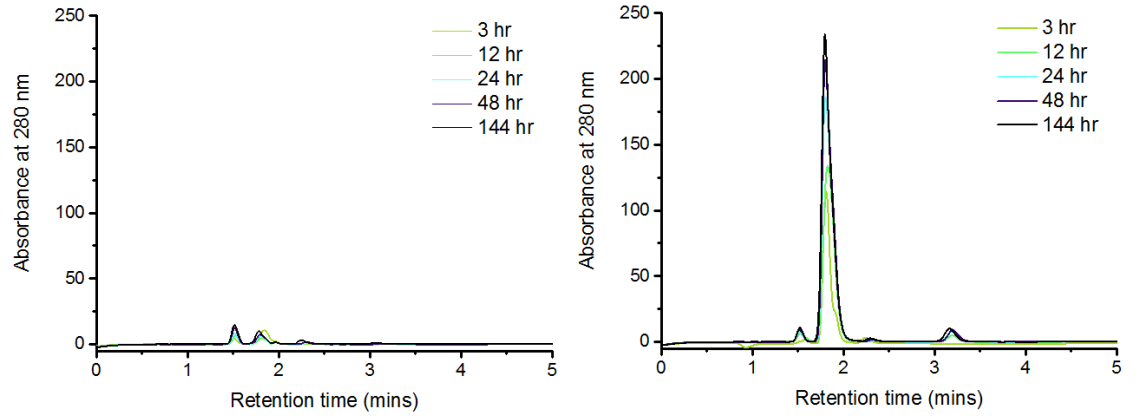

S5.16A: HPLC chromatogram of arsanilic acid released from arsenohydrogels from P5.1 in aqueous solution (left) and under stimulated oxidative stress using stoichiometric H_2O_2 (right)

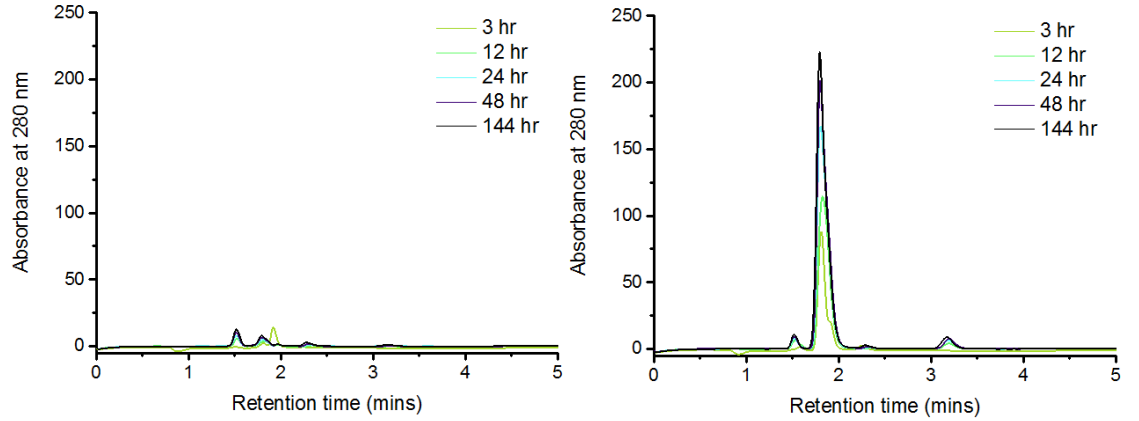

S5.16B: HPLC chromatogram of arsanilic acid released from arsenohydrogels from P5.2 in aqueous solution (left) and under stimulated oxidative stress using stoichiometric H_2O_2 (right)

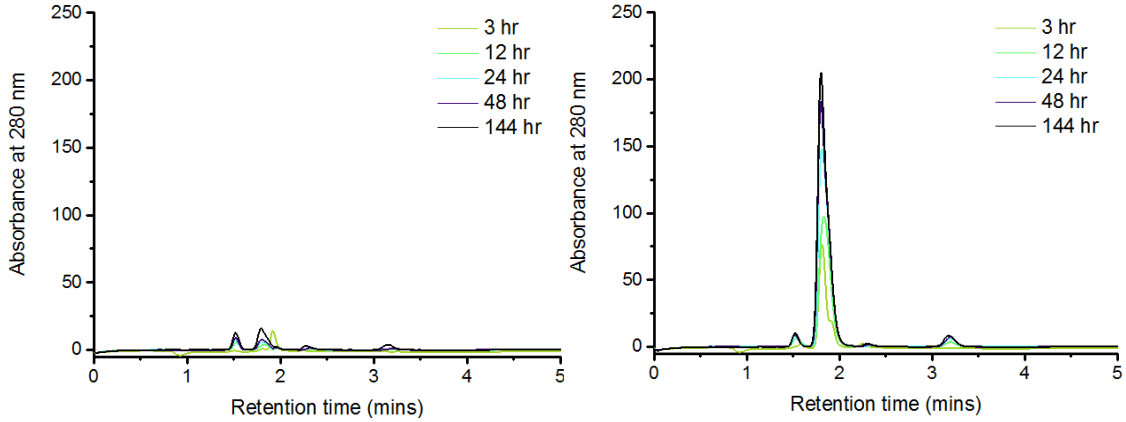

S5.16C: HPLC chromatogram of arsanilic acid released from arsenohydrogels from P5.3 in aqueous solution (left) and under stimulated oxidative stress using stoichiometric H_2O_2 (right)

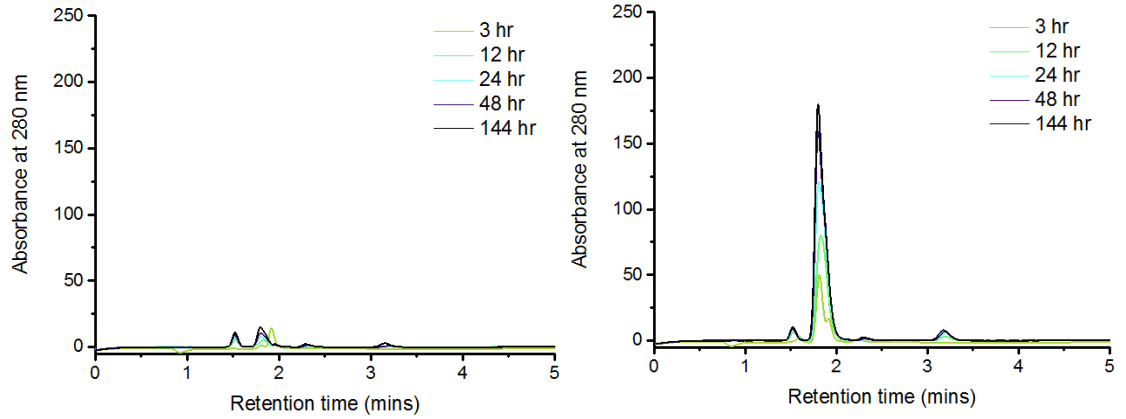

S5.16D: HPLC chromatogram of arsanilic acid released from arsenohydrogels from P5.4 in aqueous solution (left) and under stimulated oxidative stress using stoichiometric H_2O_2 (right)

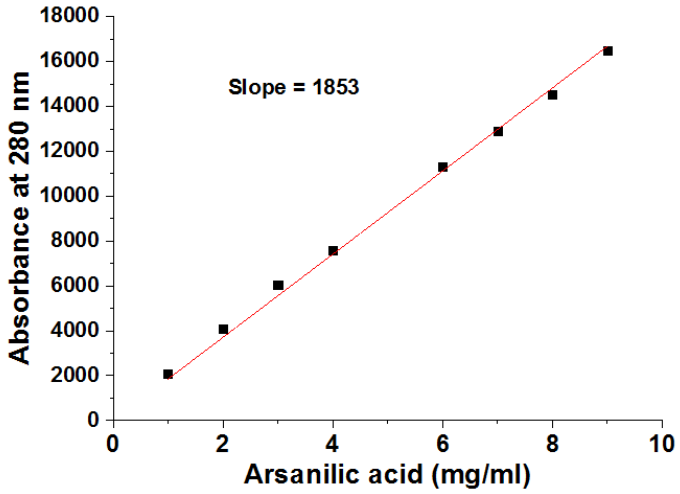

S5.16E: HPLC Calibration curve of arsanilic acid in hypophosphorous acid